OXYGEN IN CATALYSIS

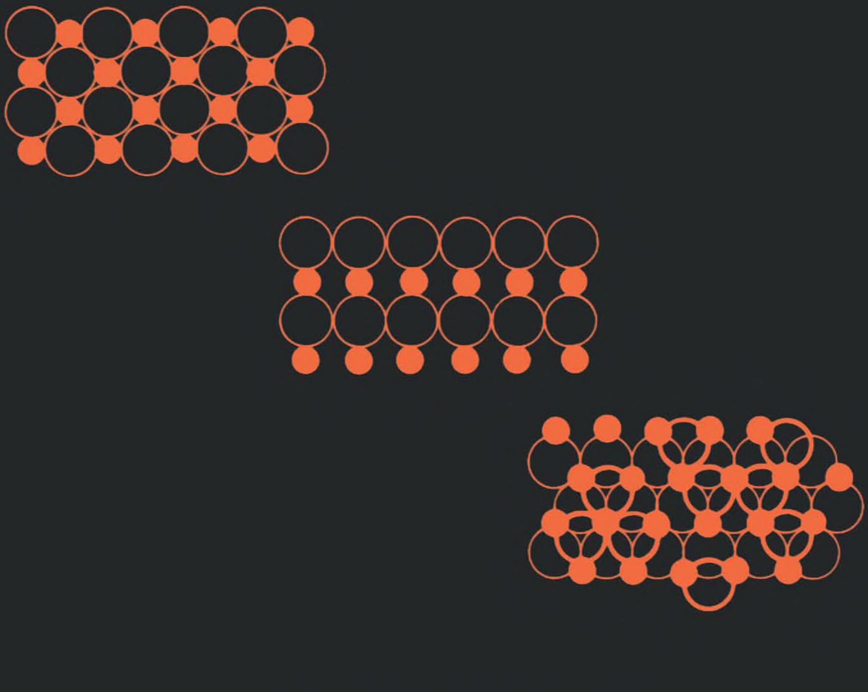

Adam Bielański
Jerzy Haber

OXYGEN IN CATALYSIS

CHEMICAL INDUSTRIES

A Series of Reference Books and Textbooks

Consulting Editor
HEINZ HEINEMANN
Heinz Heinemann, Inc.,
Berkeley, California

Volume 1: Fluid Catalytic Cracking with Zeolite Catalysts, *Paul B. Venuto and E. Thomas Habib, Jr.*

Volume 2: Ethylene: Keystone to the Petrochemical Industry, *Ludwig Kniel, Olaf Winter, and Karl Stork*

Volume 3: The Chemistry and Technology of Petroleum, *James G. Speight*

Volume 4: The Desulfurization of Heavy Oils and Residua, *James G. Speight*

Volume 5: Catalysis of Organic Reactions, *edited by William R. Moser*

Volume 6: Acetylene-Based Chemicals from Coal and Other Natural Resources, *Robert J. Tedeschi*

Volume 7: Chemically Resistant Masonry, *Walter Lee Sheppard, Jr.*

Volume 8: Compressors and Expanders: Selection and Application for the Process Industry, *Heinz P. Bloch, Joseph A. Cameron, Frank M. Danowski, Jr., Ralph James, Jr., Judson S. Swearingen, and Marilyn E. Weightman*

Volume 9: Metering Pumps: Selection and Application, *James P. Poynton*

Volume 10: Hydrocarbons from Methanol, *Clarence D. Chang*

Volume 11: Foam Flotation: Theory and Applications, *Ann N. Clarke and David J. Wilson*

Volume 12: The Chemistry and Technology of Coal, *James G. Speight*

Volume 13: Pneumatic and Hydraulic Conveying of Solids, *O. A. Williams*

Volume 14: Catalyst Manufacture: Laboratory and Commercial Preparations, *Alvin B. Stiles*

Volume 15: Characterization of Heterogeneous Catalysts, *edited by Francis Delannay*

Volume 16: BASIC Programs for Chemical Engineering Design, *James H. Weber*

Volume 17: Catalyst Poisoning, *L. Louis Hegedus and Robert W. McCabe*

Volume 18: Catalysis of Organic Reactions, *edited by John R. Kosak*

Volume 19: Adsorption Technology: A Step-by-Step Approach to Process Evaluation and Application, *edited by Frank L. Slejko*

Volume 20: Deactivation and Poisoning of Catalysts, *edited by Jacques Oudar and Henry Wise*

Volume 21: Catalysis and Surface Science: Developments in Chemicals from Methanol, Hydrotreating of Hydrocarbons, Catalyst Preparation, Monomers and Polymers, Photocatalysis and Photovoltaics, *edited by Heinz Heinemann and Gabor A. Somorjai*

Volume 22: Catalysis of Organic Reactions, *edited by Robert L. Augustine*

Volume 23: Modern Control Techniques for the Processing Industries, *T. H. Tsai, J. W. Lane, and C. S. Lin*

Volume 24: Temperature-Programmed Reduction for Solid Materials Characterization, *Alan Jones and Brian McNicol*

Volume 25: Catalytic Cracking: Catalysts, Chemistry, and Kinetics, *Bohdan W. Wojciechowski and Avelino Corma*

Volume 26: Chemical Reaction and Reactor Engineering, *edited by J. J. Carberry and A. Varma*

Volume 27: Filtration: Principles and Practices, second edition, *edited by Michael J. Matteson and Clyde Orr*

Volume 28: Corrosion Mechanisms, *edited by Florian Mansfeld*

Volume 29: Catalysis and Surface Properties of Liquid Metals and Alloys, *Yoshisada Ogino*

Volume 30: Catalyst Deactivation, *edited by Eugene E. Petersen and Alexis T. Bell*

Volume 31: Hydrogen Effects in Catalysis: Fundamentals and Practical Applications, *edited by Zoltán Paál and P. G. Menon*

Volume 32: Flow Management for Engineers and Scientists, *Nicholas P. Cheremisinoff and Paul N. Cheremisinoff*

Volume 33: Catalysis of Organic Reactions, *edited by Paul N. Rylander, Harold Greenfield, and Robert L. Augustine*

Volume 34: Powder and Bulk Solids Handling Processes: Instrumentation and Control, *Koichi Iinoya, Hiroaki Masuda, and Kinnosuke Watanabe*

Volume 35: Reverse Osmosis Technology: Applications for High-Purity-Water Production, *edited by Bipin S. Parekh*

Volume 36: Shape Selective Catalysis in Industrial Applications, *N. Y. Chen, William E. Garwood, and Frank G. Dwyer*

Volume 37: Alpha Olefins Applications Handbook, *edited by George R. Lappin and Joseph L. Sauer*

Volume 38: Process Modeling and Control in Chemical Industries, *edited by Kaddour Najim*

Volume 39: Clathrate Hydrates of Natural Gases, *E. Dendy Sloan, Jr.*

Volume 40: Catalysis of Organic Reactions, *edited by Dale W. Blackburn*

Volume 41: Fuel Science and Technology Handbook, *edited by James G. Speight*

Volume 42: Octane-Enhancing Zeolitic FCC Catalysts
Julius Scherzer

Volume 43: Oxygen in Catalysis, *Adam Bielański and Jerzy Haber*

Additional Volumes in Preparation

Industrial Drying Equipment: Selection and Application
Kees van't Land

OXYGEN IN CATALYSIS

Adam Bielański
Jagiellonian University
Kraków, Poland

Jerzy Haber
Institute of Catalysis and Surface Chemistry
Polish Academy of Sciences
Kraków, Poland

Marcel Dekker, Inc. New York • Basel • Hong Kong

Library of Congress Cataloging-in-Publication Data

Bielański, Adam
Oxygen in catalysis / Adam Bielański and Jerzy Haber.
p. cm. --(Chemical industries ; 43)
Includes bibliographical references and index.
ISBN 0-8247-8320-4 (acid-free paper)
1. Catalysis. 2. Oxidation. I. Haber, Jerzy. II. Title.
III. Series.
QD505.B54 1991
541.3'93--dc20 90-49153
CIP

Marcel Dekker, Inc.
270 Madison Avenue, New York, New York 10016

Current printing (last digit):
10 9 8 7 6 5 4 3 2 1

PRINTED IN THE UNITED STATES OF AMERICA

Preface

Oxygen plays a fundamental role in catalysis because on the one hand it is a component of the most widely used type of catalysts—oxides—and on the other hand it is the reactant of one of the most important types of catalytic reactions—oxidation. In combination with main group elements, it forms oxides of acidic or basic character which are commonly used as supports for highly dispersed metal catalysts and constitute a vital part of multifunctional catalysts. Finally, oxides are very often used as precursors in the process of preparation of catalytic systems, in which the active phase is metallic or is composed of such metal compounds as sulfides, chlorides, etc. This book is devoted to physical chemistry of oxygen and its compounds in all these aspects.

Oxygen accounts for the greater part of inorganic chemistry, which is concerned with compounds containing oxygen. Simple metallic oxides range from the essentially ionic compounds of the more electropositive elements to the molecular oxides of the nonmetals. Transition metal oxides belong to the compounds of Bertholide class; that is, they show a nonstoichiometry due to the presence of a defect structure in form of point defects or extended defects such as dislocations or shear structures. Understanding of the character of bonding in the solid and of the defect equilibria and their dependence on such parameters as oxygen pressure or the presence of additives enables catalytic properties of these oxides to be predicted and catalysts to be tailored to the requirement of the reaction. In the case of higher valent transition metal oxides anisotropy appears very often, rendering the surface and catalytic properties strongly dependent on the crystal habit of the oxide catalyst. The phenomenon of the structure sensitivity of catalytic reactions on oxides is then observed. Compounds containing two or more elements in addition to oxygen may be grouped into two classes: complex oxides, which may be considered as being composed of close-packed oxygen ions with cations in the octahedral or tetrahedral interstices, and oxysalts containing complex oxy-anions. Physicochemical and catalytic properties of oxides of the first class may be modified by substitution with altervalent cations, whereas interaction of oxides of the second class with surfaces of the appropriate carriers results in the formation of oxide monolayer catalysts. A new field of surface coordination chemistry emerges. The main problems of the physical chemistry of oxides are discussed in more detail in the first three chapters, but the importance of structure–catalytic activity correlations is emphasized and illustrated wherever mechanisms of various reactions are discussed.

Oxygen as reactant of catalytic reactions may enter into these reactions as electrophilic species O_2, O_2^-, and O^-, or as the nucleophilic species O^{2-}. Accordingly, oxidation reactions may be classified as electrophilic or nucleophilic. They constitute the main source of energy exploited by mankind in the form of combustion of fossil fuels, or by living organisms in biological oxidations. Therefore, oxidation of CO and H_2 are extensively discussed in the book as model reactions for combustion. Selective oxidation processes, in which hydrocarbon molecules are oxygenated to form alcohols, aldehydes, or acids, are the basis of the modern petrochemical industry and constitute the largest category of catalytic organic reactions. Practically all monomers used in manufacturing of artificial fibers and plastics are obtained by processes of catalytic oxidation. They may be divided into vapor phase reactions, which are catalyzed by solid oxide catalysts and are carried out as heterogeneous catalytic processes, and liquid phase reactions, which are commonly realized as homogenous catalytic processes. Because of the voluminous literature devoted to these reactions and their importance in both science of catalysis and modern chemical industry, separate chapters have been dedicated to the heterogenous oxidations of aliphatic hydrocarbons and aromatic hydrocarbons. These chapters contain a description of catalytic systems commonly used as model systems in laboratory and as industrial catalysts in large-scale operations, and a discussion of the mechanisms operating in these reactions. Attempts to describe the elementary steps by quantum chemical methods are also shown. In recent years particularly, great efforts have been invested in studying the oxidation of methane, which therefore has been described in more detail in Chapter 9. The last chapter of the book contains the discussion of homogeneous catalytic oxidations.

The essence of catalysis can described briefly as the art of manipulating chemical molecules. A group of atoms, forming the catalyst active site, is made to interact with an organic molecule, resulting in such modification of the molecule's electronic structure and bond distances and angles that its transformation along the desired reaction pathway is favored. The study of this interaction is an interdisciplinary field of research. Contributions from inorganic and organic chemistry, quantum chemistry, solid state, surface science, chemical kinetics, and other branches of science are required to understand the phenomenon of catalysis. The limited size of the book makes necessary the difficult choice of only the most important topics indispensable for the reader to grasp the essence of the mechanisms discussed without having to refer much to other texts. Because the choice of material is arbitrary, the authors hope that not too many interesting problems have been omitted. Thus, the authors will be grateful to all readers who send their comments and criticisms by which subsequent editions may benefit.

The book is intended to be used mainly as a research monograph by a vast community of those working in the field of catalysis. Therefore, ample references to the original literature have been included. However, it may also serve as a supplementary text for postgraduate students studying physical chemistry, industrial chemistry, or chemical technology as well as for university lectures in general chemistry.

Adam Bielański
Jerzy Haber

Contents

1

Molecular Oxygen and Oxygen Compounds

I. MOLECULAR OXYGEN

The usual form in which oxygen is present in the gas phase is dioxygen O_2. Trioxygen O_3 (ozone), thermodynamically unstable under normal conditions, is formed when an electric discharge passes through oxygen gas. It may also be obtained by various forms of irradiation (UV, X- and γ-rays). The formation of small amounts of $(O_2)_2$ in the gas phase occurs only at low temperatures.

Some data concerning the physical properties of O_2 molecules are given in Table 1.1. An orbital diagram of the O_2 molecule is given in Fig. 1.1. Because of the relatively large distance between the energy of electrons in 2s and 2p levels of the O atom (165 eV), no s-p orbital mixing is assumed in the O_2 molecule in contrast to N_2 (2s-2p level separation 12.4 eV) and the σ_g 2p level is situated below that of the π_u 2p orbitals. The electronic configuration of O_2 molecule in its ground state:

$$(\sigma_g 1s)^2(\sigma_u 1s)^2(\sigma_g 2s)^2(\sigma_u 2s)^2(\sigma_g 2p)^2(\pi_u 2p)^4(\pi_g 2p)^2$$

with two unpaired electrons on two π_g2p antibonding orbitals provides the explanation of the observed paramagnetism of oxygen. With 8 electrons on molecular bonding orbitals and 4 on antibonding ones, the bond order in O_2 is 2 [1]. The above sequence of molecular-orbital energy levels was also confirmed by photoelectron spectroscopy.

Several excited states of the O_2 molecule were detected [2]. The ground state with two unpaired electrons, each of them on one

TABLE 1.1 Molecular Properties of O_2

Bond dissociation energy		117.96 kcal mol^{-1} = 493.87 kJ mol^{-1}	(a)
Bond length		0.120741 nm	(a)
Ionization energy		149 kcal mol^{-1} = 623 kJ mol^{-1}	(b)
Electron affinities:			
$O_2 + e^- \longrightarrow O_2^-$		10.15 kcal mol^{-1} = 42.47 kJ mol^{-1}	(c)
$O_2 + 2e^- \longrightarrow O_2^{2-}$		−154.5 kcal mol^{-1} = −646.4 kJ mol^{-1}	(c)
Polarizability	$\alpha_{xx} = \alpha_{yy}$	1.2×10^{-24} cm^3	(d)
	α_{zz}	2.4×10^{-24} cm^3	(d)
	α_0	1.6×10^{-24} cm^3	(d)

(a) R. L. Dekock and H. B. Gray, *Chemical Structure and Bonding*, Benjamin Cummings, Menlo Park, Ca., 1980, p. 229.
(b) D. G. Tuck, *J. Inorg. Nucl. Chem., 26*, 1525 (1964).
(c) M. Che and A. J. Tench, *Adv. Catal., 32*, 1 (1983).
(d) E. A. V. Ebsworth, J. A. Connor, and J. J. Turner, in *Comprehensive Inorganic Chemistry*, Vol. 2 (C. Bailar, H. J. Emeleus, R. Nyholm, and A. F. Trottman-Dickenson, eds.), Pergamon Press, Oxford, 1973, p. 698.

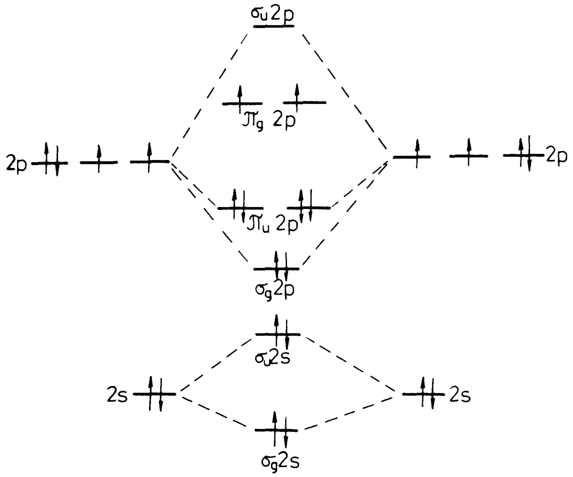

FIGURE 1.1 Molecular-orbital energy diagram for dioxygen molecule.

$\pi_g 2p$ orbital, is a triplet $^3\Sigma_g^-$ state. Both lowest excited states $^1\Delta_g$ and $^1\Sigma_g^+$ (0.98154 and 1.6357037 eV above the ground state, respectively) are singlet ones. Two electrons with antiparallel spins occupy the same $\pi_g 2p$ orbital in the former case and different $\pi_g 2p$ orbitals in the latter case. Singlet oxygen playing an important role in the photochemistry of oxygen may be generated by electrodeless electrical discharge (microwave discharge) in low-pressure oxygen or by the photosensitization method. It is also present in oxygen evolved in a number of chemical reactions, such as hydrogen peroxide reacting with hypochloride [3]. The $^1\Sigma_g^+ \rightarrow {}^1\Delta_g$ transition is symmetry-forbidden and $^1\Delta_g \rightarrow {}^3\Sigma_g^-$ both symmetry- and spin-forbidden. Hence both transitions and especially the latter one are slow and the lifetime of the $^1\Sigma_g^+$ state is 7 sec while that of the $^1\Delta_g$ state is 45 min when extrapolated to zero pressure.

The perturbations from surrounding gases considerably modify and shorten these periods of time. Singlet oxygen when evolved in solutions exhibits characteristic red chemiluminescence, which is mainly due to the double-molecule transition:

$$O_2{}^1\Delta_g + O_2{}^1\Delta_g \rightarrow O_2{}^3\Sigma_g^- + O_2{}^3\Sigma_g^- + h\nu$$

Singlet oxygen is chemically very reactive and in recent years its chemistry developed into a relatively large field of studies comprising such processes as cycloadditions, reactions with alkyl-substituted olefins, reactions of heterocyclic and aromatic systems, and degradation of polymers and dyes. The appearance of chemisorbed singlet oxygen on the surface of some oxides was suggested by several authors [4]. However, there is no direct confirmation of this supposition; also, to date no proof of the participation of singlet oxygen in heterogeneous catalytic reactions has been reported. It is assumed that singlet oxygen molecules may be present in oxygen physically adsorbed. The generation of singlet oxygen in reactions with transition metal ions will be discussed in Chapter 4, Section I.

The molecule of ozone O_3, the allotropic modifcation of oxygen, isoelectronic with NO_2^- ion, has an angular shape and belongs to the C_{2v} symmetry point group. The bond angle 116°45' indicates sp^2 hybridization of the orbitals of the central O atom. The overlap of $2p_x$ orbitals of lateral atoms with hybridized orbitals would give two localized bonds and the overlap of $2p_z$ orbitals of all three atoms directed perpendicularly to the symmetry plane three delocalized π orbitals: bonding, nonbonding, and antibonding ones. More elaborate theoretical treatment leads to a system of delocalized σ and π orbitals and the following ground state configuration of the O_3 molecule [5]:

$$(1a_1)^2(1b_2)^2(2a_1)^2(2b_2)^2(3a_1)^2(1b_1)^2(3b_2)^2(4a_1)^2(1a_2)^2$$

The molecule of ozone is diamagnetic. It exhibits a nonzero dipole moment (Table 1.2), an ionization potential close to that of O_2, and a high positive electron affinity. The additional electron in ozonide ion O_3^- occupies the $2b_2$ level empty in the neutral molecule. The O_3^- ion is one of the chemisorbed oxygen species stable below room temperature.

II. BONDING OF OXYGEN IN ITS COMPOUNDS

A. Introduction

Despite the fact that oxygen seems to be a very familiar element, occurring in most of its compounds in the oxidation state −II, its chemistry is by no means simple and a logical classification of oxygen compounds is not an easy task. In the present chapter we shall discuss only those aspects of oxygen chemistry which are important for understanding catalytic oxidation reactions. To this end it is appropriate to discuss oxygen bonding in the oxides and, rather briefly, oxygen bonding in metal complexes. The fact that the overwhelming majority of oxidation catalysts are oxides justifies inclusion of the paragraphs dealing with the structure of this class of compounds. The structures of superoxides, peroxides, and ozonides will not be discussed here as these substances are thermally unstable and therefore do not play a role in oxidation catalysis.

B. Bonding of Oxygen in Oxides

A synthetic review of oxide chemistry was given by Sanderson [6], on which the following is mainly based, and also by Ebsworth et al. [2].

The oxidation state −II is attributed to oxygen in the oxides. In oxide molecules it can either form two single covalent bonds or one multiple, usually double, bond to the atoms of other elements. In the case of two single covalent bonds the bond angle is somewhere within the limits 100−111°. These are the values mostly deviating from the value 109°28′ corresponding to an equal repulsion of four electron pairs around an O atom core or, alternatively, to the sp^3 hybridization of oxygen orbitals such that in each hybrid orbital there is 25% of s and 75% of p character. The fact that the angle is smaller indicates that the hybrid orbitals involved in both bonds exhibit a smaller participation of s character. In the case of a water molecule with a bond angle equal to 104.52°, the bonding hybrid orbitals exhibit 20% of s character and 80% of p character. Simultaneously, the participation of s orbitals in the nonbonding hybrid orbitals increases to 60% [1].

TABLE 1.2 Properties of O_3 Molecule

Bond length O—O	0.1278(3) nm
Bond angle 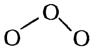	116°45'
Dipole moment	0.58 D = 1.9 × 10^{-30} C m
Ionization potential 1	12.3 ± 0.1 eV
2	12.52 ± 0.05 eV
Electron affinity	44 ± 10 kcal mol^{-1} = 184 ± 42 kJ mol^{-1}
Enthalpy of formation $\Delta H^0{}_f(g)$	34.1 kcal mol^{-1} = 142.7 kJ mol^{-1}

Source: Ref. 2.

There are also known examples of the $\mathrm{O}{<}^{X}_{X}$ angle bond that are appreciably larger than 109°28' as, for example $\mathrm{O}{<}^{P}_{P}$ bond in P_4O_{10} equal to 124° or $\mathrm{O}{<}^{Si}_{Si}$ in SiO_2 (α-quartz) equal to 144° [7]. Such bonds are always shorter than would correspond to a single bond and a certain participation of the "nonshared" electron pairs must be assumed, resulting in an increase of bond order above 1. In the limiting case of P-O-P bonds in ZrP_2O_7, the bond angle reaches as much as 180° [6].

As already stated, oxygen if linked to only one other atom forms a multiple, usually a double, bond. It has been supposed by some authors [8,9] that such doubly bonded oxygen at the surface of transition metal simple or double oxides such as MoO_3, WO_3, or $CaMoO_4$ may play a special role in the selective oxidation of hydrocarbons. This point will be discussed in detail in the next chapter. In some molecules singly coordinated oxygen may exhibit a bond order higher than 2 if two π-bonding orbitals are present. In CO there are three bonding electron pairs $(\sigma^2\pi_1^2\pi_2^2)$ and a bond order equal to 3. In an NO molecule containing one valence electron less and with one of the π orbitals only half-filled $(\sigma^2\pi_1^2\pi_2^1)$, the bond order is $2\frac{1}{2}$.

Oxygen is the most electronegative of all the elements with the exception of fluorine, and hence its bonds to other elements are more or less polar with oxygen acquiring a negative charge. In the limiting case of the oxides of the least electronegative metals, e.g., Cs_2O or Rb_2O, a highly ionic bond forms and the ionic approximation is commonly applied when discussing the properties of metal oxides. However, the ionic approximation in a great many cases is as inadequate as a strictly covalent one. As Sanderson [6] points out, it is very improbable that, say, in CaO an oxide ion which can lose its two extra electrons with a net gain of about 168 kcal mol^{-1} would remain unaffected in a close surrounding of six calcium ions, each of which could acquire two electrons with a net gain of about 415 kcal mol^{-1}. Some overlapping of orbitals and sharing of electrons must evidently occur resulting in the diminishing of the negative charge on the oxygen atom. Based on his own theory of electronegativity, Sanderson [10] calculated the charge on oxygen atoms in some oxides of main group elements and those of some transition metals. Although his data (given in Tables 1.3 and 1.4) can only be taken as a rough approximation, they seem to be useful in comparing the properties of various oxides. Keeping in mind the fact that the electrical charge calculated from the known dipole moment and bond length, where such data are available, are mostly higher than those calculated by Sanderson and the bonds are presumably more polar than is suggested by the data in both tables, we can nevertheless accept the thesis that in real "ionic" oxides the deviation from the ideal ionic bond is quite substantial and that Sanderson's series reflects the real trends in changes of ionicity of the oxygen bonding.

Experimental information concerning the electrical charge on an atom in a compound may be obtained from X-ray photoelectron spectroscopy. Using this method, Nefedov et al. [11] determined the binding energies of oxygen 1s electrons for a number of oxides. In the series of main group oxides—MgO (E_B = 530.2 eV), Al_2O_3 (E_B = 531.8 eV), SiO_2(E_B = 533.1 eV), B_2O_3(E_B = 533.2 eV), and P_2O_5(E_B = 533.8 for terminal and E_B = 532.4 eV for bridging O atoms)—the sequence in which E_B increases and hence the negative charge on oxygen decreases is very similar to the sequence given in Table 3, thus confirming the correctness of the trends indicated by Sanderson's calculations. Unfortunately, the sets of oxides investigated in both papers were partially not overlapping and a more ample comparison of the results is not possible. It should also be observed that the value of E_B = 533.5 eV given by Nefedov for water cannot be included in the above series as presumably it has been obtained not for a solid but for gaseous molecules.

The oxygen atom when combined with other atoms or atom by two single or one double covalent bond still possesses two unshared electron pairs, enabling it to act as an electron pair donor. Usually one unshared electron pair is donated but in some cases, e.g., ice, both nonbonding electron pairs are involved in the formation of hydrogen bonds.

In Sanderson's approach the polarity of bonds and the charge on the oxygen atom play an important role in the interpretation of acid-base properties of the oxides. According to him the principal fundamental characteristic of acidic oxides is a low negative charge

TABLE 1.3 Charge of Oxygen Atom and Coordination Number (CN) in Some Oxides of Main Group Elements According to Sanderson

Charge on O		CN	Acid-base
Cs_2O	−0.96	8	SB
Rb_2O	−0.92	8	SB
K_2O	−0.89	8	SB
Na_2O	−0.81	8	SB
Li_2O	−0.80	8	SB
BaO	−0.67	6	SB
SrO	−0.62	6	SB
CaO	−0.57	6	SB
MgO	−0.42	6	WB
BeO	−0.35	4	AB
Al_2O_3	−0.31	4	AB
H_2O	−0.25	2	AB
B_2O_3	−0.24	2	WA
SiO_2	−0.23	2	WA
P_2O_5	−0.13	2	MA
CO_2	−0.11	1	WA
SO_3	−0.06	1	SA
N_2O_5	−0.05	1 and 2	SA
Cl_2O_7	−0.01	1 and 2	SA

Abbreviations: A, acid; B, base; S, strong; M, medium; W, weak.
Source: Ref. 6.

on the oxygen atom, while that of basic oxides is a high negative charge on the oxygen. Such a correlation, which is supported by the data in Table 1.3, may be explained on the basis of Sanderson's theory of electronegativity. According to this theory, the electronegativities of atoms in a compound are different from the electronegativities of the same atoms when unbonded. Electron density in a compound is distributed in such a way that the electronegativities of all atoms become equal and reach a common value which is the geometric mean of the initial electronegativities of particular atoms.

TABLE 1.4 Charge and Coordination Number (CN) of Oxygen Atoms in Some 18-Shell and Transition Metal Oxides

Approximate charge		CN
Cu_2O	−0.45	4
TiO	−0.37	6
FeO	−0.35	6
CdO	−0.32	6
Ti_2O_3	−0.31	4
ZrO_2	−0.30	4
NbO_2	−0.30	4
ZnO	−0.29	4
Fe_2O_3	−0.25	4
SnO	−0.25	4
PbO	−0.25	4
TiO_2	−0.25	3
VO_2	−0.25	3

Source: Ref. 6.

In the compound the electronegativities of the strongly electronegative atoms therefore decrease and those of weakly electronegative atoms increase. In oxides the electronegativity of oxygen always decreases and the electronegativity of its partner increases, the only exceptions being the oxides of fluorine. The shifts in electron density and hence the changes in electronegativity result in the accumulation of a certain negative charge on oxygen atoms and a positive charge on its partner's atoms.

Now independently of the definition of acid and base we can think of acids as electron attractors and acceptors and of bases as electron donors. Oxygen bonded in an oxide cannot act as electron acceptor because all its valence orbitals are filled. The role of acceptor can only be fulfilled by the other atom and the more it acts as acceptor the higher the electronegativity it reaches in the compound. A small negative charge on oxygen in acidic oxide means that oxygen atoms are bonded with highly electronegative partners which may already be highly electronegative in the unbonded state, e.g., sulfur in SO_3, and/or has been made highly electronegative through electron withdrawal by several competitive, highly electronegative oxygen atoms, e.g., manganese in Mn_2O_7. In both cases the other element by the action of oxygen is rendered more electronegative than it was in the unbonded state and also has orbitals that can become acceptors. The acceptor properties of an orbital are strongly improved by an even slight withdrawal of electrons and the partial positive charge also contributes to the stability of the outer d orbitals. It should be observed here that a high negative charge on oxygen corresponds to a state in which its electronegativity is greatly decreased and the average electronegativity is low. The low electronegativity of the oxygen partner atoms reduces their ability to accept electrons and the oxide becomes much less acidic and more basic.

When considering basic properties of the oxides we must stress the fact that oxygen atoms, when linked with two single covalent bonds or with one double bond, still possess two unshared electron pairs enabling them to act as donors, i.e., to exercise the function of a base. The electron-donating ability of oxygen obviously increases with increasing negative charge, but Sanderson points out that the donating ability of oxygen is stronger when the oxygen atom is attached by single rather than multiple bonds. He believes that this effect is the result of a greater localization of unshared electron pairs in the former case than in the latter. This explanation would be equivalent to the assumption that the localization is greater when unbonding electron pairs occupy sp^3 hybrid orbitals than when they occupy sp^2 hybrids. This explanation seems rather doubtful from the point of view of quantum chemistry as the sp^n hybrids are considered to exhibit higher bonding ability (and hence the higher concentration of electron density) when the participation of s orbitals is higher [12]. As shown by the data in Table 1.3, oxygen atoms in oxides which are known to be very strongly basic, such as the oxides of alkali metals, bear the highest negative partial charge. The amphoteric oxides BeO, Al_2O_3, and H_2O occupy a central position in the series of oxides ordered according to the decreasing negative charge on oxygen. The donating ability of oxygen and the tendency of the other atom to accept an electron pair are comparable in these compounds and, depending on conditions, the compounds may act either as a weak base or a weak acid.

An interesting example of the application of Sanderson's approach to a discussion of physicochemical properties of oxide systems has been given by Mortier [13]. His calculations for various zeolites gave the explanation of the observed fact that the strength of Brönsted acid centers in a given type of zeolite increases with increasing protonation as well as with an increasing SiO_2/Al_2O_3 molar ratio.

Unfortunately, no Sanderson's electronegativities were calculated for most of the transition metals and such calculations usually have to be limited to the main groups of elements.

B. Structural Properties of Oxides

1. Coordination Polyhedra and Close-Packed Ions

The structure of oxide crystals may be discussed from two points of view [7,14-16]. The crystal may be considered to be composed of close-packed rigid spheres of oxygen with cations distributed in the interstices between these spheres, or it may be constructed from coordination polyhedra built of the central metal atom surrounded by oxygen atoms, linked together by corners, edges, or faces into an ordered periodic arrangement in space.

The form of a coordination polyhedron depends on the type of chemical bonds linking the metal atom with the adjacent oxygen atoms. When bonds are covalent the number and position of oxygen ligands are determined by hybridization of the orbitals of the central atom, and when they are ionic, by the ratio of the radii of ions. In crystal these polyhedra are linked together in an ordered mode, whereas in an amorphous substance they exist in a more or less disordered fashion. Thus, crystals are characterized by both short- and long-range order, whereas in amorphous substances only the short-range order is present. It must be emphasized that coordination polyhedra are not equivalent to groups of atoms which could be defined as chemical molecules; they must be considered as arbitrary structural units, which can be chosen in many different ways. The coordination polyhedra acquire a physical sense when the bonds between atoms within the polyhedra are stronger than bonds between them. This is the case when the valence of the central atom is greater than half of the sum of the valences of oxygen ligands. In the limiting case, when the valence of the central atom is equal to the sum of the valences of oxygen ligands, the coordination polyhedron is a chemical molecule. In such case it is obvious that different chemical bonds operate within the coordination polyhedra and between them. Depending on whether the atoms in the crystal are linked together with one type of bond or whether different types of bonds are present in the crystal, we may divide all structures into two groups: homodesmic and heterodesmic. The structure is homodesmic when all the atoms of which it is composed are linked together by the same type of bonds. MgO or ZnS may serve as examples of homodesmic structures with predominantly ionic or predominatly covalent bonds, respectively.

The structure is heterodesmic when its structural elements are linked by at least two different types of bonds. Oxy salts containing complex anions are a typical example. In sulfates, phosphates, and the like, the bonds within the complex anions have a predominantly covalent character, whereas the bonds between these anions and cations are ionic. In this case the representation of the crystal in terms of coordination polyhedra is nearer to physical reality than the model of close-packed rigid spheres. It is also convenient in the discussion of catalytic properties because coordination polyhedra may serve as models of active centers of an oxide catalyst. When they are located at the surface, at least one coordination site is empty and can accommodate the reacting molecule. An intermediate complex is thus formed in which the reacting molecule is one of the ligands of the coordination polyhedron of the oxide lattice.

The approach based on close-packed oxygen spheres essentially comes down to the question of how spheres of equal size can be packed together to fill the space as densely as possible and how the atoms of different metals can be distributed in the interstices appearing between these spheres.

On a plane surface the closest packing is attained when each sphere is in contact with six others. The second identical layer may now be superimposed on the first, so that the spheres in the upper layer are vertically above the centers of the triangles formed by spheres of the lower layer. On superimposing the third layer we have two alternatives: the spheres of this layer may be placed in the centers of triangles formed above the spheres of the first layer or above the interstices in this layer. In the first case a hexagonal close-packed structure is obtained, characterized by the sequence of layers ABABA; in the second case a cubic close-packed structure is obtained with the ABCABC sequence. In both structures each sphere has 12 neighbors.

2. Structures of Simple Metallic Oxides

Crystal structures of some oxides which are of importance in catalysis are summarized in Table 1.5 [7]. The structures are arranged according to type of coordination polyhedra and the mode in which they are linked together. First are the three-dimensional structures of high coordination number, such as ReO_3, rutile, corundum, and sodium chloride; then come those with tetrahedral or lower coordination. Then follow the layer and chain structures. We shall discuss in more detail those most commonly encountered in catalytic studies.

In fluorite the metal cations are surrounded by eight oxide ions located in the apexes of a cube forming the coordination polyhedron. The cubes are linked by common edges (Fig. 1.2), which results in a cation to oxide anion ratio 1:2 as required by the chemical formula MeO_2. This structure may also be regarded as the fcc sublattice of metal ions, in which all tetrahedral interstices are occupied by oxide ions. It can be expected that the fluorite structure will be adopted by compounds for which the ratio of cation to anion radii exceeds 0.732. In fact, oxides of large quadrivalent cations such as Zr, Ce, Th, and V crystallize in this structure.

TABLE 1.5 Crystal Structures of Some Metallic Oxides

Type of structure	Formula type and coordination numbers of M and O		Name of structure	Example
Infinte three-dimensional complexes	MO_3	6:2	ReO_3	WO_3
	MO_2	8:4	Fluorite	ThO_2, CeO_2, HfO_2, NpO_2, PuO_2, AmO_2, PoO_2, CmO_2, PrO_2, UO_2, ZrO_2
		6:3	Rutile	TiO_2, GeO_2, SnO_2, MnO_2, RuO_2, OsO_2, IrO_2, CrO_2, MoO_2, WO_2, TeO_2, ReO_2, PbO_2, VO_2, (NbO_2), TeO_2, TaO_2, PtO_2,
	M_2O_3	6:4	Corundum	α-Al_2O_3,α-Fe_2O_3, Cr_2O_3, Ti_2O_3, V_2O_3, α-Ga_2O_3, Rh_2O_3,
			A'rare earth sesquioxide	La_2O_3, Ce_2O_3, Pr_2O_3, Nd_2O_3
		6:4	C'rare earth sesquioxide	α-Mn_2O_3, Sc_2O_3, Y_2O_3, In_2O_3, Tl_2O_3 Sm_2O_3,and other rare earths oxides M_2O_3
	MO	6:6	Sodium chloride	MgO, CaO, SrO, BaO, CdO, VO, TiO, NbO, FeO, CoO, NiO, MnO
		4:4	Zinc blend wurtzite	BeO ZnO
	MO_2	4:2	Quartz structures	SiO_2, GeO_2
	M_2O	2:4	Cuprite	Cu_2O, Ag_2O
	M_2O	4:8	Antifluorite	Li_2O, Na_2O, K_2O, Rb_2O
Layer structures				MoO_3, As_2O_3, PbO, SnO, Re_2O_7

TABLE 1.5 (Continued)

Type of structure	Formula type and coordination numbers of M and O	Name of structure	Example
Chain structures			Sb_2O_3, CrO_3, SeO_2
Molecular structural units:	polymers		Sb_4O_6, As_4O_6
Molecular structural units:	single molecules		All simple molecular oxides

Source: Ref. 7.

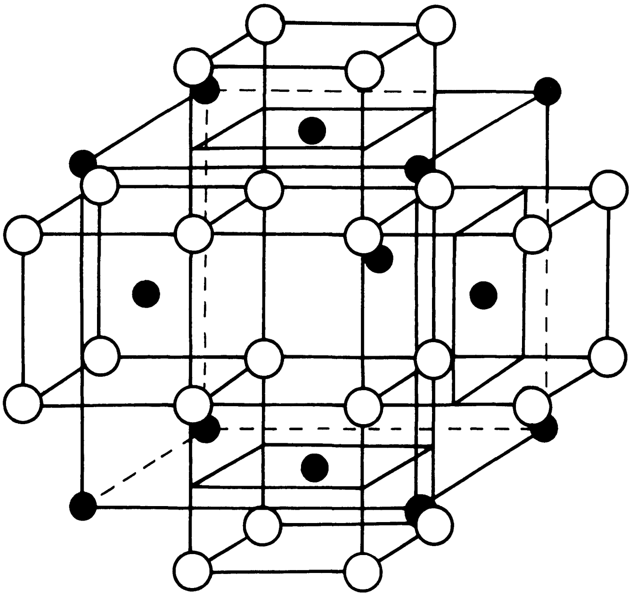

FIGURE 1.2 Fluorite structure. (After [16].)

ReO_3, rutile, corundum, and sodium chloride are built of coordination octahedra linked in different ways. In the ReO_3 structure the octahedra share only vertices as shown in Fig. 1.3. When octahedra share all edges, the sodium chloride structure appears. In the rutile structure (Fig. 1.4) each octahedron shares two opposite edges with the neighboring octahedra. Chains of octahedra are formed which are linked together through the remaining free vertices of the octahedra. Because of the high positive charge on metal ions the repulsive forces between them play an important role and often cause a distortion of the octahedra, resulting in an increase of the intercationic distance. In the rutile lattice the surrounding of the cation has a form of a distorted octahedron, in which two oxygen ions are slightly further than the other four. Some dioxides crystallize with a less symmetric variant of the rutile structure, in which successive pairs of metal atoms in the string of octahedra are alternately closer together and further apart. In some transition metal oxides, such as MoO_3, this distortion is assisted by the formation of π bonds between oxide ions and the metal cations, resulting in a decrease of cation-cation repulsion and in the appearance of a strong tendency to form a layer structure, as in the case of MoO_3 described below [17].

The corundum structure is built of face-sharing pairs of octahedra interlinked through edges to form layers of six-membered rings (Fig. 1.5). The coordination polyhedron of O^{2-} ions around each Al^{3+} ion is essentially regular octahedral and there is no evidence to suggest the existence of metal-metal interactions across the

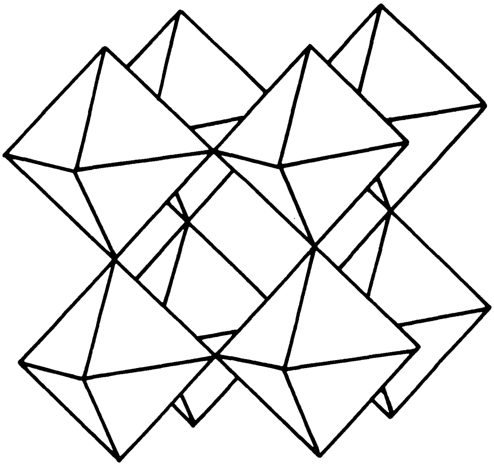

FIGURE 1.3 ReO_3, structure. (After [16].)

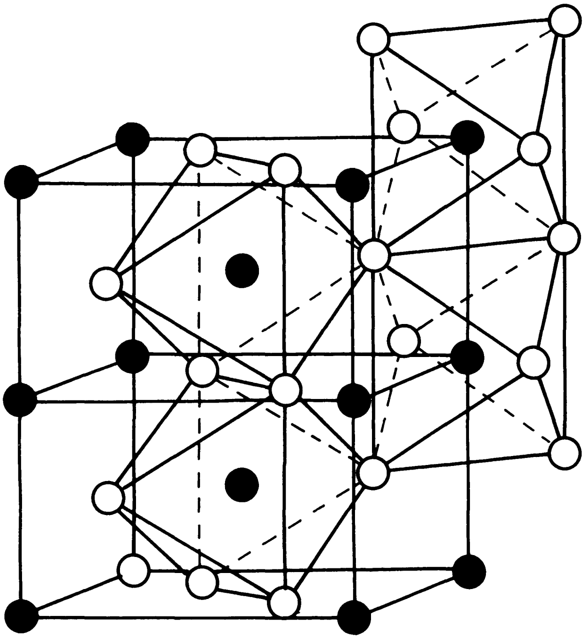

FIGURE 1.4 Rutile structure. (After [16].)

shared face. Thus, it is sometimes more convenient to consider the structure as a hexagonal close-packed array of oxygen ions with metal ions occupying two-thirds of the octahedral holes. Such a structure, represented by the ABAB sequence of close-packed layers, is assumed by α-alumina. There are two other ways of stacking the close-packed layers encountered in aluminas, namely, various sequences of the type ABACAB, ABAC-CABA, etc., represented by χ and κ aluminas, and the cubic close-packed arrangement ABCABC of γ-alumina. In the latter case the aluminum ions occupy tetrahedral and octahedral interstices forming a spinel structure, in which one-third of tetrahedral sites normally occupied remain empty.

Active alumina is not pure Al_2O_3 but contains a certain amount of water in the form of surface hydroxyl groups. Several models of the surface structure of such aluminas were proposed [18,19], the most recent one being that of Knözinger and Ratnasamy [20].

The linking of tetrahedra takes place only through vertices and there are two alternative ways of arranging them to obtain a metal-oxygen atomic ratio of 1:1 as in MeO compounds: a cubic structure of zinc blend and a hexagonal structure of wurtzite. There are, however, many different ways of linking the tetrahedra to satisfy the formula MO_2; thus many different structures are encountered in the case of silica.

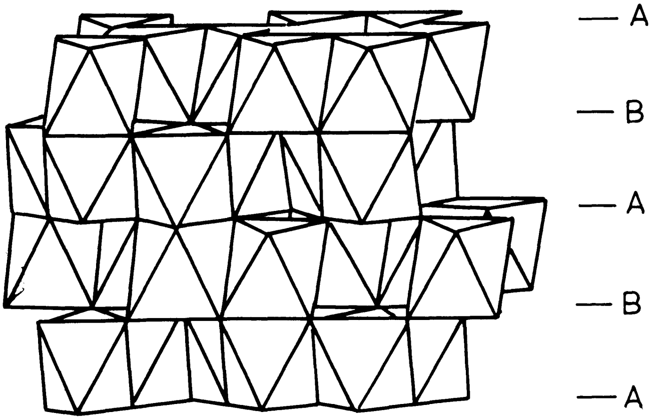

FIGURE 1.5 Packing of AlO_6 octahedra in the corundum structure. (After [16].)

It follows from the Pauling rules [21] that in the structures of silicates each vertex of the SiO_4 tetrahedron is common only for two tetrahedra, and two tetrahedra have only one vertex in common, i.e., they never share edges or faces.

When SiO_4 tetrahedra have no elements in common and are linked only through the polyhedra of other cations, orthosilicates are formed as olivine $(Mg,Fe)_2SiO_4$, granates $(Mg,Fe,Mn,Ca)_3(Cr,Al,Fe)_2(SiO_4)_3$, etc. When each tetrahedron shares only one vertex with another tetrahedron, the silicate is composed of $[Si_2O_7]^{6-}$ as the structural unit. Tetrahedra which share two vertices with other tetrahedra form structures composed either of chain ions ${}^{1}_{\infty}[SiO_3]^{2-}$ (number 1 in the left superscript indicates the one-dimensional chain stretching infinitely as marked by the left subscript ∞ or of cyclic ions $[Si_3O_9]^{6-}$ (three-membered rings) and $[Si_6O_{18}]^{12-}$ (six-membered rings). The Si:O ratio in these compounds amounts to 1.3. A simple silicate chain is shown in Fig. 1.6a; the three- and six-membered rings are illustrated in Fig. 1.6b and c. Simple chain ions may link together through free vertices to form double chains of the composition ${}^{1}_{\infty}[Si_4O_{11}]^{6-}$, in which the Si:O ratio amounts to 1:2.75.

Linkage of a large number of chains through vertices lying in one plane results in the formation of a layer structure, shown in Fig. 1.7a. In this structure each tetrahedron shares three vertices with other tetrahedra, the Si:O ratio thus being 1:2.5. The structure may thus be described as composed of ${}^{2}_{\infty}[Si_2O_5]^{2-}$ units, with the number 2 in the left superscript indicating the bidimensional sheet. Three main classes of layer structures can be distinguished according to the structure of the layer. The first class comprises structures composed of single layers, in which the free vertices of

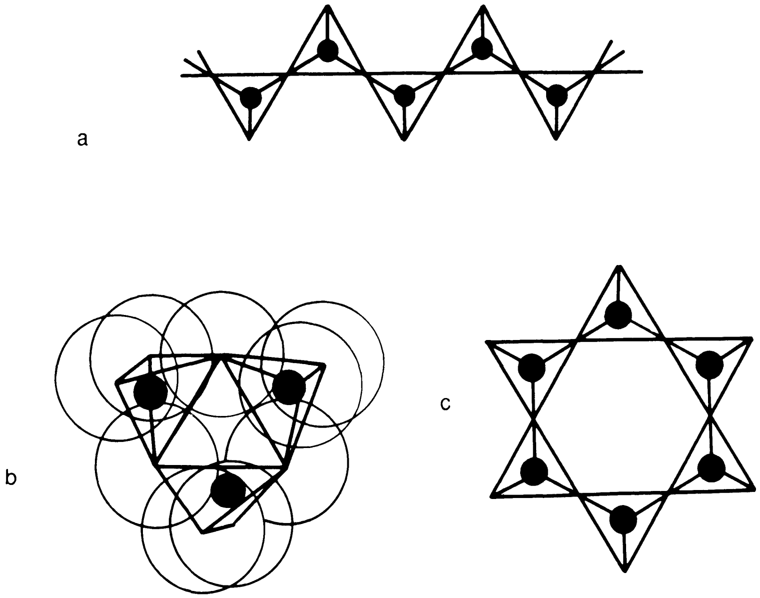

FIGURE 1.6 Arrangement of SiO_4 tetrahedra in the simple chain (a), three-membered ring (b), and six-membered ring (c). (After [16].)

tetrahedra in alternate rings point to opposite sides of the layer, the cations lying between the layers. In the structures of the second class, represented by many aluminosilicates, the layers are built of tetrahedra pointing with free vertices to one side and linked together in pairs to form double layers. If some of the Si^{4+} ions are replaced by Al^{3+} ions, the net negative charge appears on the aluminosilicate layers and is compensated by interlayer cations, which hold together the layers in the crystal (Fig. 1.7b). The third class of structures are composed of sheets of SiO_4 tetrahedra with vertices pointing to one side and linked to sheets of octahedra of such cations as Mg^{+2}, Ca^{+2}, Al^{+3}, etc., coordinated by oxygen ions or hydroxyl groups, to form a composite layer. The octahedral sheet may also be linked on both sides to tetrahedral sheets to form a three-sheet composite layer. Such composite layers are neutral and are held together in the crystal by weak van der Waals forces. This explains the softness of such structures, which are present in, for example, talc. If a certain number of ions, e.g., Al^{3+}, in the octahedral sheet are substituted by divalent ions, the composite layer acquires the charge, which must be compensated by additional cations incorporated between the layers (Fig. 1.7c). In some structures the charged composite layers are interleaved with hydrated ions, as in montmorillonite:

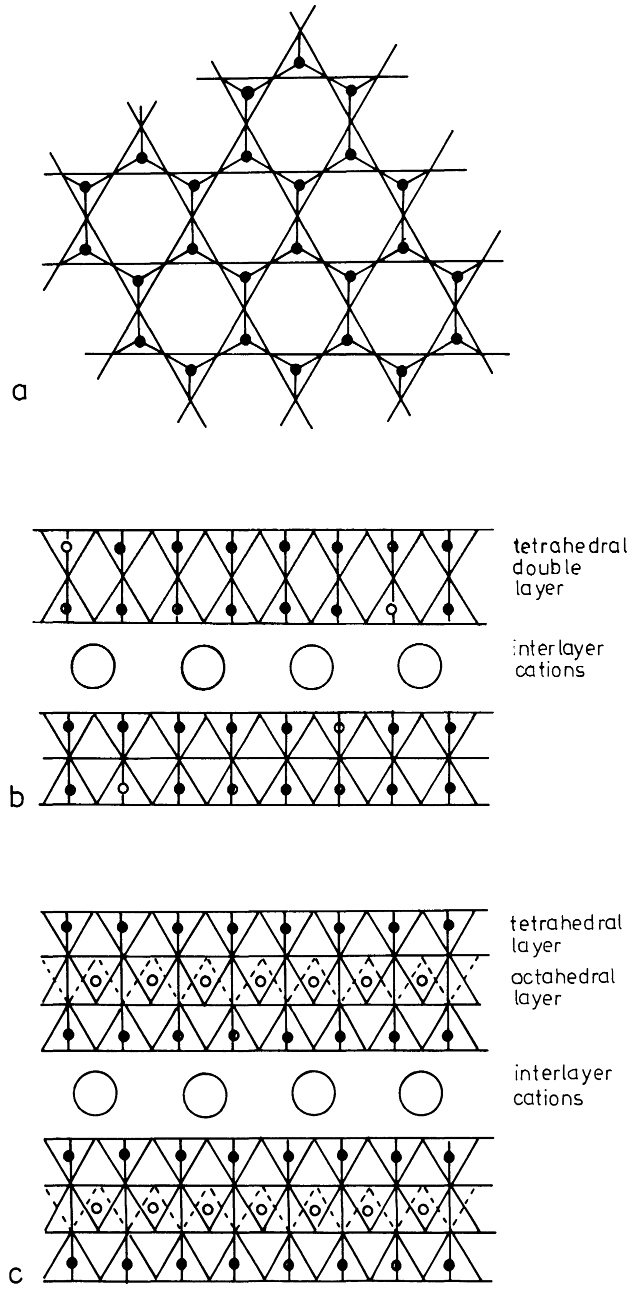

FIGURE 1.7 Structure of layer silicates: (a) single layer, (b) cross-section of the array of double layers, (c) cross-section of array of three-sheet composite layers. (After [16].)

$$Mg_{0.33}Al_{1.67}Si_4O_{10}(OH)_2^{-0.33}Na_{0.33}$$

When all four oxygen atoms of the SiO_4 tetrahedron are shared by two tetrahedra a three-dimensional silicon-oxygen framework is formed, as in all polymorphic modifications of SiO_2 and such minerals as feldspars and zeolites.

Oxides of group IB metals assume a very peculiar structure of cuprite, consisting of two completely interpenetrating and identical frameworks without any cross-connecting bonds.

The stereochemistry of the metal atom in MoO_3 can be best considered as that of a distorted octahedron, although it can be easily deduced from the MoO_3 tetrahedron as a basic unit [22]. Figure 1.8a shows an infinite string of corner-sharing tetrahedra. When such strings are linked together to increase the coordination of molybdenum to 5 (Fig. 1.8b) and other strings are brought from beneath to complete this coordination to 6 (Fig. 1.8c), sheets are formed composed of ribbons of octahedra sharing their two adjacent edges with other octahedra and corners with two adjacent ribbons on both sides (in and out of the plane of Fig. 1.8d). A layer structure of MoO_3 appears in this way.

Closely related to the structure of MoO_3 is that of V_2O_5 [23], which will be discussed in detail in Chapter 8.

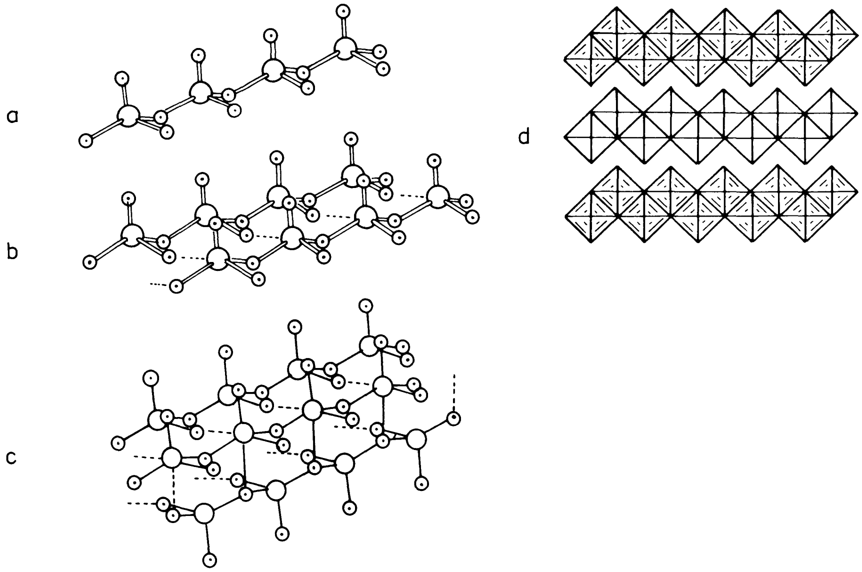

FIGURE 1.8 Elements of MoO_3 structure: (a) string of tetrahedra, (b, c) linking of strings into ribbon and sheet, (d) projection of the structure along the (100) axis.

3. Complex Oxides and Oxy Salts

It is convenient to divide all compounds containing two or more elements in addition to oxygen into two groups according to whether the relation of the oxygen atoms to one kind of atom is different from that to another or no distinction can be made between the bonds of these atoms to oxygen atoms, i.e., whether the structure is heterodesmic or homodesmic. When oxygen atoms in the crystal $A_xY_yO_z$ can be associated with one kind of atoms Y to form oxy ions Y_yO_z, the bonds within these oxy ions having a higher degree of covalency, the structure may be considered as composed of cations A and complex oxy anions Y_yO_z linked by ionic bonds, the oxy anions being either finite or infinite. Such compounds may be called oxy salts. The oxy anions may be composed of two or more kinds of coordination polyhedra containing different central atoms as it is the case in heteropoly oxy salts. When no distinction can be made between the different bonds in the crystal it is convenient to regard the structure as a close-packed array of oxygen ions, with A and Y ions distributed in tetrahedral and octahedral holes. The type of coordination chosen by the given ion depends on its size and ligand field site preference energy. The term complex oxides should be used to describe such phases. If the A ions are approximately the same size as oxygen ions, the structure may be considered to be a close-packed arrangement of O and A ions with Y ions in tetrahedral or octahedral interstices.

The different behavior of atoms in the oxide structure may be related to their electronegativities. When element A is electropositive and element Y electronegative, an oxy salt-type structure will be formed with Y as the central atom of the oxy anion. When both A and Y are electropositive, the structure should be regarded as a complex oxide. Thus, when a diagonal line is drawn across the periodic table from the upper left corner to the lower right one, atoms to the left of this line, which form essentially ionic bonds with oxygen, will appear in crystal structures, which should be considered as complex oxides. The coordination numbers of these ions are determined by their relative sizes. On the other hand, atoms located to the right of this line form oxy anions with a considerable degree of covalency. In the case of transition elements this refers to their ions in the highest oxidation state. Oxides of transition metal ions in lower oxidation states are more ionic.

a. Complex metal oxides: The largest group of complex oxides is the solid solution of one oxide in another, the different ions randomly occupying the cationic sites of a simple oxide structure. Two types of such solid solutions are of particular interest to catalysis: binary complex metal oxides of acid-base properties (e.g., aluminosilicates) and solutions of transition metal ions in diamagnetic matrices (e.g., Cr^{+3} in Al_2O_3, Ni^{+2} in MgO, etc.) used in reactions of the redox type.

Binary oxides with acidic properties: The generation of acidity by substitution of a given ion in the oxide lattice by a different ion may be explained after Tanabe as due to the appearance of a positive or a negative charge at the site of substitution. Tanabe [24] calculates this charge by constructing a hypothetical model structure, in which

The coordination numbers of both atoms in the oxide solid solution remain the same as they were in simple oxides, and

The coordination number of oxygen of the majority component oxide is retained for all oxygens in the solid solution.

As an example, Fig. 1.9a shows the model structure of the TiO_2-SiO_2 system in which TiO_2 is the majority component oxide and Fig. 1.9b that of SiO_2-TiO_2 system, where SiO_2 is the majority oxide. In both cases the coordination numbers of Si and Ti atoms remain 4 and 6, respectively, as in pure SiO_2 and TiO_2, as required by the first assumption, whereas coordination numbers of oxygen are 3 and 2, respectively, according to the second assumption. In the case of the TiO_2-SiO_2 system, in which silicon atoms replace titanium

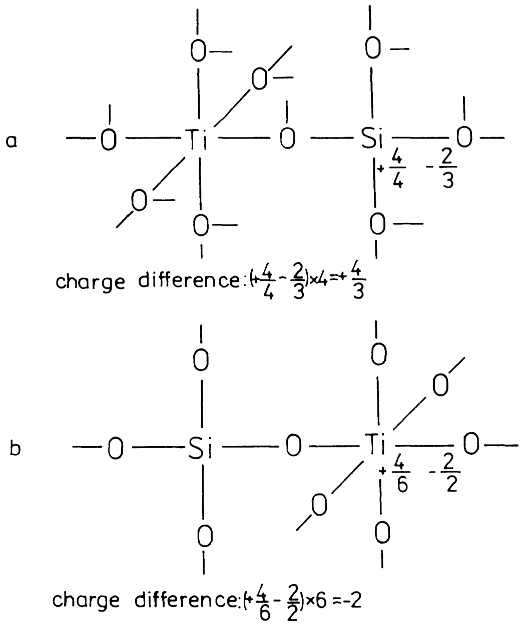

FIGURE 1.9 Model structures of TiO_2-SiO_2: (a) when TiO_2 is major oxide, (b) when SiO_2 is major oxide. (After [24].)

atoms, the four positive charges of the silicon atom are distributed to four bonds, i.e., one valence unit to each bond, while two negative charges of the oxygen atom are distributed to three bonds, i.e., −2/3 of a valence unit for each bond. The charge difference for each bond is 1-2/3 = +1/3; on the Si atom there is thus a charge excess of +1/3 × 4 = + 4/3. This means that a Lewis acid site appeared. In the case of a SiO_2-TiO_2 system with Ti atoms substituting Si atoms, four positive charges of the Ti atom are distributed to six bonds, i.e., +4/6 valence unit to each bond, while two negative charges of the oxygen atom are distributed to two bonds, i.e., one negative charge per bond. The charge difference for each bond is +4/6 − 1 = −1/3; the Ti atom therefore has −2 charges in excess. Tanabe argues that in this case Brönsted acidity appears because two protons must associate with six oxygen atoms to maintain the electric neutrality. Experiments show [25] that the TiO_2-SiO_2 system is indeed characterized by a very high acidity.

The classical representatives of solid acids are aluminosilicates used as catalysts since the 1920s. Using Tanabe's procedure one can calculate that substitution of Al atom for the Si atom in the tetrahedron of the silica structure results in the appearance of one excess negative charge at the Al atom, which must be compensated by adding the proton to one of the oxygen ions (Fig. 1.10a). A center containing a loosely bonded proton is thus formed with properties of a Brönsted acid center. On outgassing at higher temperatures the surface becomes dehydroxylated and the Brönsted acid center is transformed into a Lewis center (Fig. 1.10b). AlO_4 tetrahedra may be substituted into any form of silica, resulting in the formation of amorphous aluminosilicates, those with layer structure like in montmorillonite or a three-dimensional framework as in zeolites.

In zeolites, which are crystalline aluminosilicates built of SiO_4 tetrahedra partially substituted by AlO_4 tetrahedra and linked through all four vertices into a three-dimensional framework, one can distinguish building units such as chains, rings, and regular polyhedra [26], which are the basis of the classification of zeolites. As an example, Fig. 1.11a shows the sodalite unit, which is a cubo-octahedron (truncated octahedron) built of SiO_4 tetrahedra. It can be visualized as obtained by the superposition of an octahedron and a cube, and cutting away all the vertices of the octahedron. When the sodalite units are linked together by the vertices of the tetrahedra, protruding from the hexagonal planes into a three-dimensional array in which every sodalite unit is tetrahedrally surrounded by other sodalite units (diamond-type structure), the structure of the mineral faujasite and its synthetic analogs, zeolites X and Y, is produced (Fig. 1.11b). It can be visualized as composed of cubo-octahedra linked together through hexagonal prisms. This produces

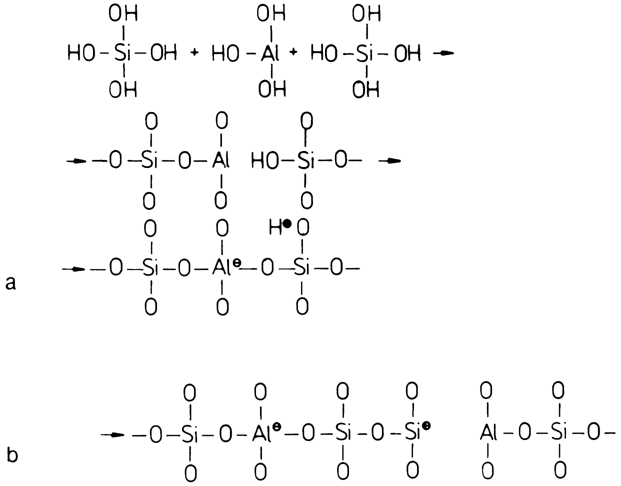

FIGURE 1.10 Generation of Brönsted (a) and Lewis (b) acidity by substitution of aluminum atom into silicate structure.

internal cavities (supercages) of almost spherical shape, with a diameter of 12 Å, interconnected through distorted 12-membered windows of diameter 8–9 Å.

One of the zeolite types used extensively in catalysis is ZSM-5 [27]. It is built of five-membered rings, eight of which form a building unit as shown in Fig. 1.12a. These units are linked through edges to form chains (Fig. 1.12b) connected then through vertices

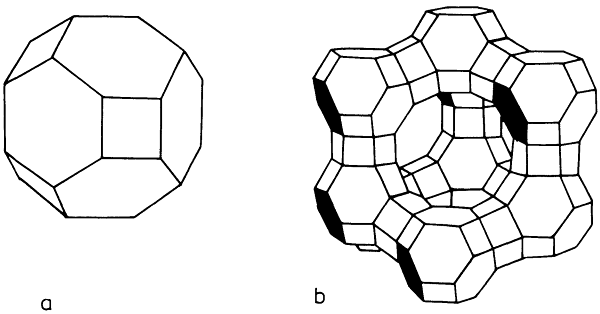

FIGURE 1.11 Structure of faujasite: (a) sodalite unit, (b) linking of sodalite units in tetrahedral arrangement and appearance of supercage. The Si(Al) atoms are situated at the apices of the truncated octahedra.

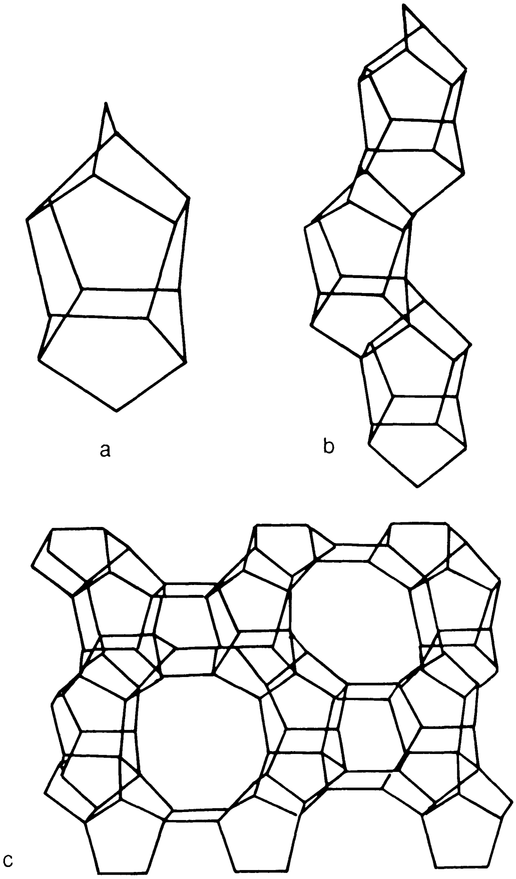

FIGURE 1.12 (a) Building unit, (b) chain, and (c) sheet in ZSM-5 zeolite.

into sheets (Fig. 1.12c), and finally into a three-dimensional framework. Two interconnected channel systems, one sinusoidal and the other straight, are produced, as shown schematically in Fig. 1.13.

The number of AlO_4 tetrahedra which can be incorporated into the silicate framework varies over a wide range, and so does the composition of zeolites, usually expressed in terms of the Si/Al ratio. This ratio is 1 in Linde A or type X zeolites, 3 in type Y zeolites, and assumes values as high as 30 or more in ZSM-type structures. Depending on the Si/Al ratio there are five different environments possible for each SiO_4 tetrahedron. Namely, it can be linked to four other SiO_4 tetrahedra with no adjacent AlO_4 tetrahedron $[Si(OSi)_4]$, or it can have in its surrounding one, two, three, or four AlO_4

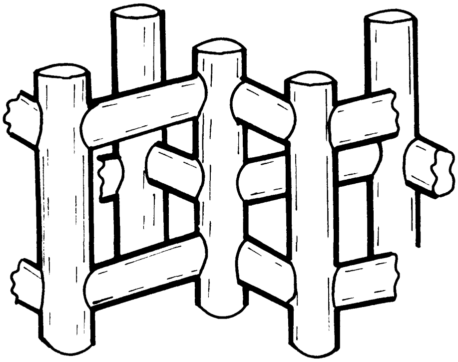

FIGURE 1.13 Channel structure in ZSM-5 zeolite.

tetrahedra and three, two, one, or no SiO_4 tetrahedra, respectively [$Si(OAl)(OSi)_3$, $Si(OAl)_2(OSi)_2$, etc.]. Their concentrations can be determined by using the ^{29}Si magic angle spinning nuclear magnetic resonance (MASNMR) [28]. As an example, Fig. 1.14 shows the ^{29}Si MASNMR spectrum of a synthetic faujasite with an Si/Al ratio of 2.75. It may be seen that four nonequivalent types of SiO_4 tetrahedra are present, the predominant ones being those with one or two adjacent AlO_4 tetrahedra. The negative charge introduced to the framework by each incorporated AlO_4 tetrahedron must be compensated by a cation introduced into the framework. Thus, the number of these cations divided by their valence must equal the number of AlO_4 tetrahedra. The cations are exchangeable; therefore the selection of their type and degree of exchange offers a possibility of wide modifications of adsorptive and catalytic properties

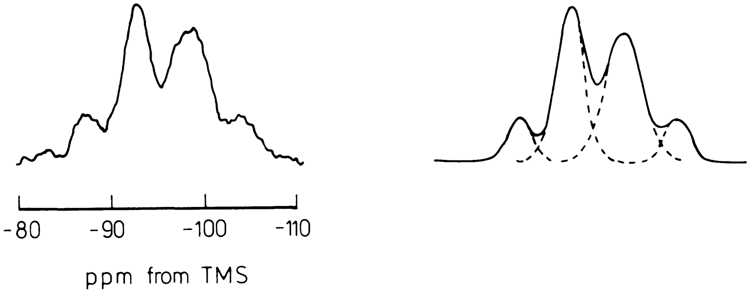

FIGURE 1.14 MASNMR spectrum of faujasite with Si:Al ratio of 2.75. Experimental spectrum (left) and computer simulated spectra (right). The four peaks represent [$Si(OAl)_3(OSi)$], [$Si(OAl)_2(OSi)_2$], [$Si(OAl)(OSi)_3$] and [$Si(OSi)_4$]. (After [28].)

of zeolites. By exchanging them for protons the acidic form of the zeolite may be obtained. Their concentration and acidic properties may be determined by IR spectroscopy. Figure 1.15a illustrates the IR spectrum of the hydrogen form of HZSM-5 zeolite [29]. Two strong bands are visible in the stretching frequency region, at 3620 cm^{-1} and 3740 cm^{-1}, indicating that two types of OH groups are present. Their acidic properties are revealed by the spectra registered after adsorption of a base, e.g., pyridine (Fig. 1.15b). The appearance of a strong band of pyridinium ions at 1552 cm^{-1} and the simultaneous disappearance of the band at 3620 cm^{-1} demonstrates that these hydroxyl groups play the role of strong Brönsted acid centers transforming pyridine into pyridinium ions.

Solid solutions of transition metal ions and diamagnetic matrices: When reacting molecules interact with transition metal ions at the surface of an oxide catalyst, the transfer of electrons takes place between the adsorbed layer and the solid. A fundamental question arises as to what extent the type of bonding between the molecule and the transition metal ion depends on the local properties of this ion, such as the d-electron structure, the character and arrangement of surrounding oxygen ions, etc., and how relevant in this

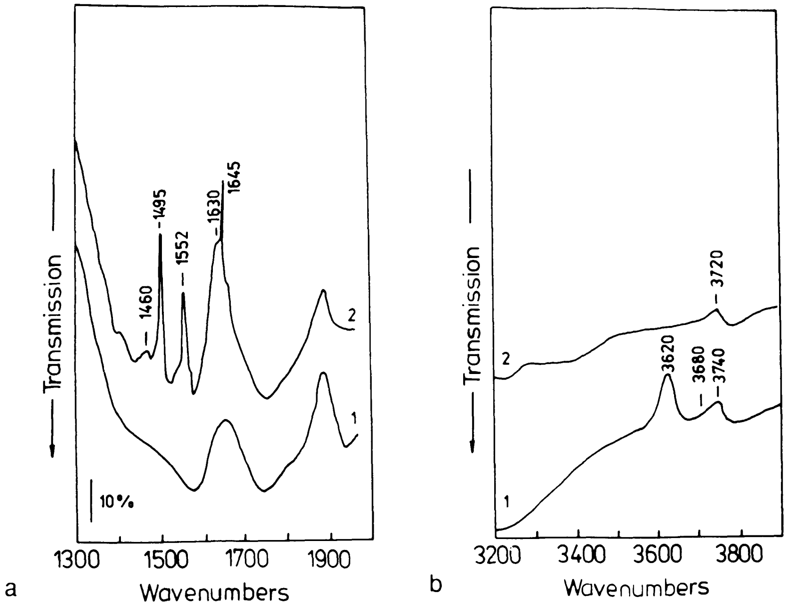

FIGURE 1.15 IR spectrum of type Y zeolite: (a) fresh sample, (b) after adsorption of pyridine. (After [29].)

respect are the collective properties of the solid, in particular the chemical potential of electrons as given by the position of the Fermi level, and the ability of the solid to transport the electrons from one active center at the surface to another expressed by its electric conductivity.

One method of discrimination between the influence of localized and collective properties of the oxide on its behavior in catalytic reactions is the use as model catalysts of the solid solutions of transition metal ions in an insulating, diamagnetic oxide as solvent [30-32]. At very small concentrations it can be assumed that practically no interactions operate between the transition metal ions, and the behavior of isolated ions in adsorption and catalysis can be thus studied. On increasing the concentration one may study the influence of the strength of interaction between the transition metal ions.

MgO as a matrix offering sites with octahedral symmetry and ZnO with tetrahedral symmetry are usually used for such studies. Solid solutions in α-Al_2O_3 with octahedral sites and in $MgAl_2O_4$ with both octahedral and tetrahedral sites have also been investigated.

Spinels and perovskites: Among the complex oxides which can be considered as compounds of the formula $A_xB_yO_z$, two main types can be distinguished: structures with close-packed oxygen ions, and structures in which oxygen and A ions, because of their similar size, are in close-packed arrangement. Representative of the first type, applied widely in catalysis, are spinels; representative of the second type, also of great interest for catalysis, are perovskites.

Spinel structure is assumed by many oxides of the general formula AB_2O_4, which can be divided into groups as follows: (1) $M^{II}M_2{}^{III}O_4$, (2) $M^{IV}M_2{}^{II}O_4$ and (3) $M^{VI}M_2^{I}O_4$. We shall describe the first group in more detail.

The unit cell of the spinel $M^{II}M_2^{III}O_4$ comprises 32 oxygen ions ($8M^{II}M_2^{III}O_4$) in cubic close packing (Fig. 1.16). As follows from simple considerations, the unit cell contains 32 octahedral and 64 tetrahedral holes, in which 8 M^{II} ions and 16 M^{III} ions are arranged. When 8 equivalent tetrahedral holes out of 64 are occupied by M^{II} ions, and 16 octahedral holes out of 32 by M^{III} ions, the spinel is called normal. Other modes of distribution are also encountered. The 8 tetrahedral holes may be occupied by M^{III} ions, the remaining 8 M^{III} ions and all 8 M^{II} ions occupying the 16 octahedral holes. Such spinels which are represented by the formula $M^{III}M^{II}M^{III}O_4$ are called inversed. In some spinels both M^{II} and M^{III} ions are randomly distributed in tetrahedral and octahedral holes. It is convenient to describe different modes of distribution by a parameter η, which gives the fraction of divalent metal ions in octahedral coordination. Thus for the normal spinel $\eta = 0$ and for the inversed one $\eta = 1$. In the case of random distribution $\eta = 0.67$. Values of the

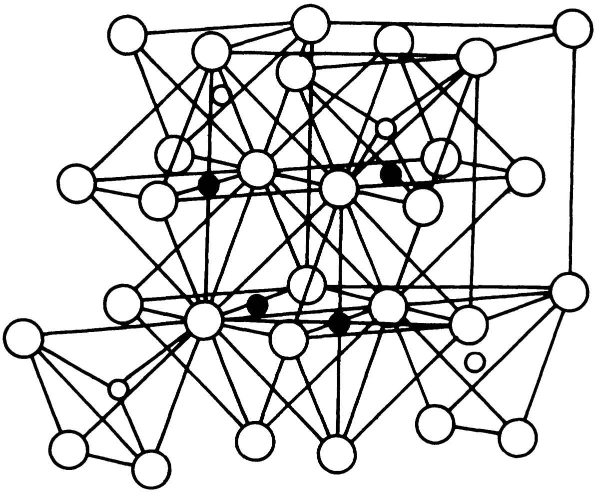

FIGURE 1.16 Spinel structure. (After [16].)

parameter η found experimentally in different spinels are given in Table 1.6 [33].

Calculation of the lattice energy of a spinel formed only by main group metal ions, e.g., $MgAl_2O_4$, indicates that normal distribution of cations is most stable. When, however, the spinel is composed of transition metal cations, the ligand field stabilization energy must be taken into account in the assessment of the stability of different distributions [33]. The greatest tendency to occupy the octahedral position is shown by Cr^{3+} and Mn^{3+} ions. Accordingly, all chromites and manganites except $NiMn_2O_4$ are normal spinels. Conversely, the Fe^{3+} ion is not at all stabilized in the ligand field, similar to the Zn^{2+} ion. Thus, zinc ferrite is a normal spinel because only the lattice energy determines the distribution, whereas ferrites of Cu^{2+}, Ni^{2+}, Co^{2+}, and Fe^{2+} are inversed because the high ligand field stabilization energy of these ions in octahedral coordination is the decisive factor, Fe^{3+} ions being displaced to tetrahedral positions.

There are many ways that defects can form in a spinel structure [34]. The most commonly encountered are vacancies in the cation sublattices, both tetrahedral and octahedral. On the other hand, the spinel structure is fairly empty because only one-eighth of the tetrahedral and one-half of the octahedral sites are occupied. Thus solubility of the component oxides in the spinel phase is observed, resulting in the appearance of excess cations in the interstitial tetrahedral and octahedral sites. The given cations in the spinel structure can be substituted by many other cations. In this

TABLE 1.6 Distribution of Cations in Octahedral Positions in the Spinel Lattice (Values of Parameter η)

Cation	Mg^{2+}	Mn^{2+}	Fe^{2+}	Co^{2+}	Ni^{2+}	Cu^{2+}	Zn^{2+}
Al^{3+}	0	0	0	0	0,76		0
Cr^{3+}	0	0	0	0	0	0,1	0
Fe^{3+}	0,9	0,2	1	1	1	1	0
Mn^{3+}	0	0			1	0	0
Co^{3+}				0			0

Source: Ref. 33.

way multicomponent systems can be obtained, with their properties purposefully regulated by proper selection of the component cations and appropriate adjustment of their composition. This also opens up possibilities for studying various factors influencing the catalytic activity of oxide systems.

The second structure which will be described here is that of perovskite. It is adopted by compounds in which one of the metal ions is of a size similar to that of an oxygen ion. In the case of a binary compound composed of A and O ions with $r_A/r_O \simeq 1$, such a close-packed arrangement of these ions in which the positive ions A are not in contact with each other is possible only at an O/A ratio of at least 3:1, i.e., for compounds of the composition AO_3. The ions may be arranged in two ways, as illustrated in Fig. 1.17 in which single layers of these arrangements are shown. The crystal structures are formed by superimposition of such layers, with ions A having dodecahedral coordination. When metal ions A are mono- or divalent, the excess negative charge must be compensated by a second type of cation, characterized by a small radius and occupying the interstices, in the close-packed structure. Complex oxides, halides, and so forth are formed in this way. By superimposition of layers, as shown in Fig. 1.17, and distribution of cations in octahedral holes, a perovskite structure of the composition ABO_3 is formed (Fig. 1.18). This requires that B be a cation with a preference for octahedral coordination. For stoichiometric ABO_3 compounds there are many combinations of A^{a+} and B^{b+} that satisfy the electroneutrality condition $a + b = 6$, and this structure is adopted by many complex oxides of groups IV, V, and VI transition metal ions with alkali or alkali earth metal cations, e.g., $BaTiO_3$, $KNbO_3$, $PbTiO_3$, $SrZrO_3$, $LaMnO_3$, $LaCrO_3$, $KTaO_3$, $BaHfO_3$, etc. It is interesting to note that the perovskite structure is closely related to that of ReO_3.

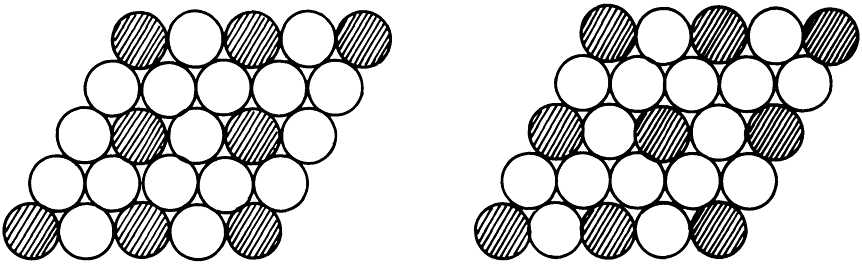

FIGURE 1.17 Close-packed layers of ions A and O with the same radius in the structure of AO_3 compound.

The possible combinations of A and B ions are restricted by geometric and coordination requirements [35].

Both ions A and B can be substituted by other ions to form the full variety of solid solutions. Ordering of the solute ions may also take place, resulting in the formation of definite compounds.

The perovskite phases are usually nonstoichiometric due to the presence of vacancies in the sublattice of cations A as well as vacancies in the oxygen sublattice. This is manifested by the existence of, for example, tungsten bronzes Na_xWO_3 with a very broad range of the variation of x. When the number of A is much smaller than that of B, the A ions may either be distributed randomly in the dodecahedral sites as it is the case in tungsten bronzes, or form an ordered superstructure, as in $La_{2/3}TiO_3$. Nonstoichiometry resulting from the presence of oxygen vacancies also occurs frequently in the perovskite phases [35].

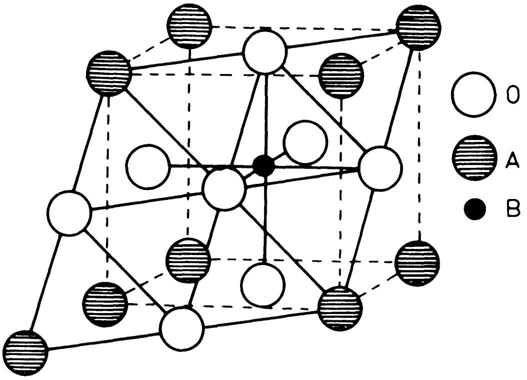

FIGURE 1.18 Perovskite structure. (After [16].)

Of particular importance for the use of perovskites as catalysts is the ability of these structures to stabilize the noble metals. Compounds of Pt, Ir, Is, Re, Rh, and Ra may exist in the perovskite structure, with the noble metal atoms occupying the B sites.

b. Oxy Salts: The stereochemistry of simple oxy ions is shown in Table 1.7. Many of these ions form complex oxy ions by linking through vertices (oxygen atoms), edges, or faces. These complex ions may be symmetric, i.e., every XO_n group may share the same number of O atoms with similar groups, or asymmetric as in $S_3O_{10}^{2-}$ ions, in which the central tetrahedron shares two vertices and the terminal tetrahedra only one. In the case of compounds with octahedral coordination, the XO_6 groups are never linked into complex oxy ions only through vertices or only through edges, but always share vertices and edges. Still more combinations are possible in the case of structures which are composed of two types of oxy ions, e.g., tetrahedral XO_4 and octahedral XO_6 groups, as in the $(Mo_2O_7^{2-})_n$ poly ion.

The usually observed coordination numbers in oxy compounds of some elements are summarized in Table 1.8, in which the dotted line separates the regions of different coordination numbers. The elements in circles—B, Si, Mo, W and Te—are those for which the oxygen coordination number is equal to the number of valency electrons in the atom and which show a very strong tendency to form complex polyions. However, many complex phosphates, vanadates, and chromates are also known.

As an example of the complexity of the oxide chemistry of some elements, we shall discuss the structures of molybdates in more detail. The extensive oxygen chemistry of molybdenum may be partially explained by the fact that molybdenum in oxy compounds readily assumes both tetrahedral and octahedral coordination, which provides an almost infinite number of possible combinations of the spatial arrangement of these coordination polyhedra.

Anhydrous ortho-molybdates contain isolated MoO_4^{2-} tetrahedral ions arranged to form the structure of phenacite (Li_2MoO_4), spinel (Na_2MoO_3), or scheelite ($PbMoO_4$). In appropriate conditions di- and trimolybdates are formed. Dimolybdates contain chain polyion $(Mo_2O_7)_n^{2n-}$, composed of MoO_6 octahedra and MoO_4 tetrahedra linked through vertices. When the condensation of MoO_6 octahedra proceeds further, hepta- and octa-molybdates may be obtained, containing $Mo_7O_{24}^{6-}$ amd $Mo_8O_{26}^{4-}$ ions, built of edge-linked octahedra is shown in Fig. 1.19.

The MoO_6 octahedra may also form a compact grouping around a central atom of some other element. Such compounds are called heteropoly oxy salts. They may be divided into two classes according to whether the central atom is surrounded by four (tetrahedral) or six (octahedral) oxygen atoms. As an example, Fig. 1.20

TABLE 1.7 Shapes of Oxy Ions

Configuration	Anions				
Nonlinear					ClO_2^-
Planar	BO_3^{3-}	CO_3^{2-}	NO_3^-		
Pyramidal				SO_3^{2-}	ClO_3^-
					BrO_3^-
					IO_3^-
Tetrahedral		SiO_4^{4-}	PO_4^{3-}	SO_4^{2-}	ClO_4^-
			AsO_4^{3-}		IO_4^-
			VO_4^{3-}	MoO_4^{2-}	MnO_4^-
Octahedral				TeO_6^{6-}	IO_6^{5-}

shows the structure of the molybdophosphate anion. The central P atom is located at the center of a PO_4 tetrahedron, which shares oxygen atoms with four groups of three edge-sharing MoO_6 octahedra. Such complexes, called Keggin units, are stacked together with the appropriate number of protons (heteropoly oxy acids) or cations (heteropoly oxy salts) into an ionic lattice. Figure 1.21 illustrates the structure of the molybdotellurate anion as a representative of compounds in which the central atom (Te) is octahedrally surrounded by MoO_6 octahedra sharing edges.

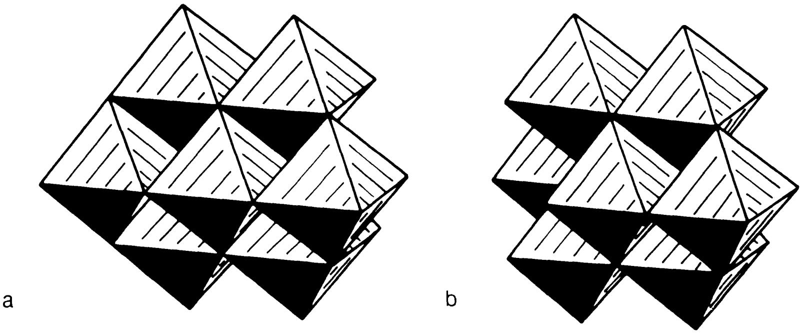

FIGURE 1.19 Structure of (a) heptamolybdate ion $Mo_7O_{24}^{6-}$, and (b) octamolybdate ion $Mo_8O_{26}^{4-}$.

TABLE 1.8 Coordination Numbers in Oxy Compounds

2	3	4	5		6		7		
			A	B	A	B	A	B	
(Be)	B	C	N						RO_3
	Al	Si	P		S		Cl		
		Ge	V	As	Cr	Se	Mn	Br	RO_4
			Nb	Sb	Mo	Te		I	
					W				
									RO_6

Source: Ref. 7.

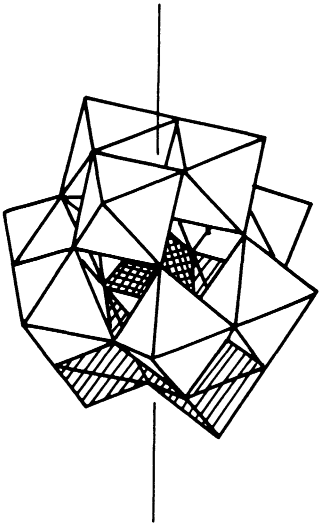

FIGURE 1.20 Keggin unit of molybdophosphates.

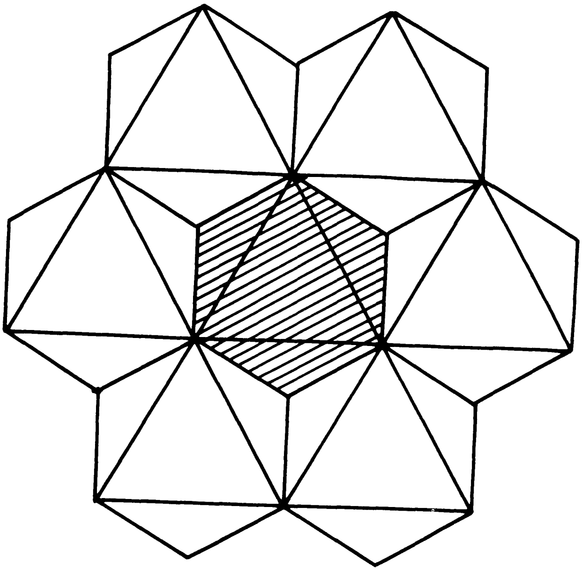

FIGURE 1.21 Structure of $TeMo_6O_{24}^{6-}$ anion.

C. Bonding of Oxygen in Transition Metal Complexes

Molecular oxygen may be activated in different ways. Figure 1.22 shows the potential energy curves of the oxygen molecule in the ground and excited states, with the corresponding equilibrium O-O bond length also given [36]. Thermal excitation of the molecule in its vibrational modes may result in vibronic transition into the first electronically excited state, in which electrons on the antibonding r_g2p orbitals become paired and localized on one of these two orbitals. This is the $^1\Delta_g$ singlet state, which is 22.64 kcal.mol^{-1} above the ground state. Thus, the transition $^3\Sigma_g^- \rightarrow {}^1\Delta_g$ requires a considerable activation energy. However, oxygen may also be activated chemically, by bonding it to an appropriate center which may be the transition metal atom in the coordination complex or at the surface of a solid, e.g., transition metal oxide. Usually the oxygen molecule in the interaction with a metal atom center behaves as an electron acceptor. The character of bonding and hence the properties and reactivity of the oxygen molecule depend on the energy, spacial orientation, and occupancy of the metal d orbitals as well as on the type of surrounding ligands. Complexes with oxygen are formed by compounds of transition metals in lower oxidation states, which have the ability to donate electrons strong enough to effectuate the charge transfer to the oxygen molecule, but not so strong as to cause the rupture of the O—O bond [37,38].

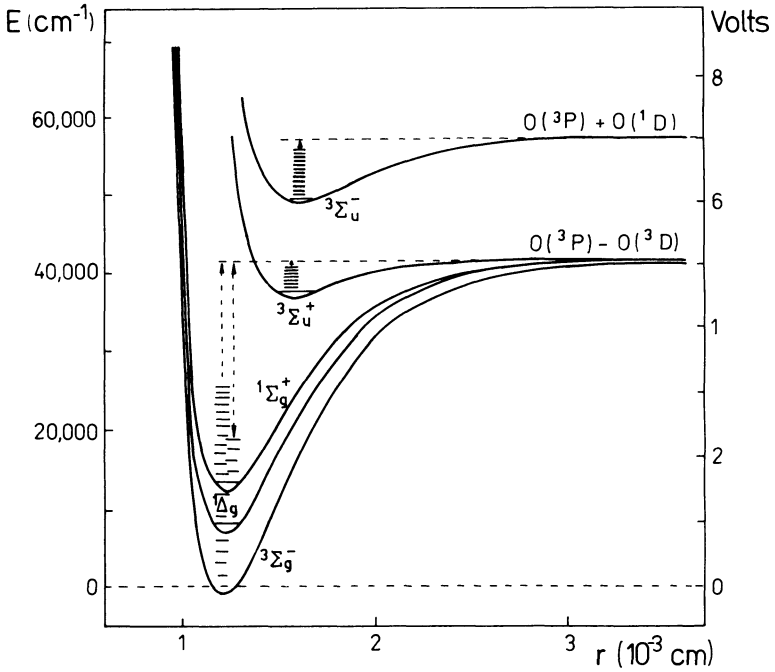

FIGURE 1.22 Potential curves of the observed states of the O_2 molecule. (After [36].)

Metal complexes in low oxidation states can interact with dioxygen in successive steps in which electrons are transferred from the metal to dioxygen forming successively superoxo, μ-peroxo, peroxo, oxo, and μ-oxo complexes [39]. Thus, an important parameter which determines the mode of dioxygen binding is the electron-donating ability of the metal (the energy of the occupied d orbitals). Some transition metal complexes reduce dioxygen reversibly at ambient temperatures. Besides formation of peroxo complexes, dioxygen can also insert into M—H or M—R bonds to form hydroperoxide and alkylperoxo metal complexes, respectively. The latter are intermediates in the oxidation of hydrocarbons catalyzed by metal complexes [40].

There are two ways of bonding the oxygen molecule to the transition metal atom: superoxo (terminal, open) with the C_s symmetry and peroxo (side-on, chelate, closed) with the C_{2v} symmetry, depending on the type of orbitals involved in bonding [41,42].

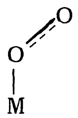

C_s

(Ia)

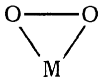

C_{2v}

(IIa)

The O—O bond order in superoxo complexes is 1.5, in peroxo complexes: 1.0. It is noteworthy that the coordinated O_2 molecule shows an almost constant state in either class of compounds as indicated by the very narrow range of frequencies, in which the ν_{O-O} stretching vibrations of different complexes are contained (cf. Table 1.9), and by the remarkable fact that the dioxygen molecule covalently bound in metal complexes resembles either of the two ionic species: superoxide ion O_2^- or peroxide ion O_2^{2-}.

When a second atom becomes linked to the oxygen molecule, dinuclear complexes [μ-superoxo (Ib) or μ-peroxo (IIb)] are formed:

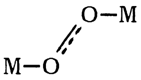

C_1

(Ib$_1$)

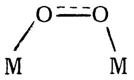

C_{2v}

(Ib$_2$)

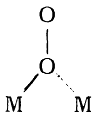

C_s

(Ib$_3$)

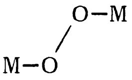

C_1

(IIb$_1$)

The frontier orbitals of the oxygen molecule in the ground state $^3\Sigma_g^-$ are the doubly degenerate, singly occupied, antibonding π_g2p orbitals. Usually such singly occupied orbitals have both electron acceptor and electron donor properties. When a transition metal atom has the appropriate energy and occupancy a peroxo complex is formed by a transfer of the electron from one of the antibonding π_g2p MO of dioxygen onto the empty d-AO of the metal atom, and simultaneous back donation of an electron from the occupied d-AO of the metal onto the singly occupied second π_g2p antibonding MO of dioxygen. This is shown in Fig. 1.23, illustrating orbitals involved in bonding of dioxygen in different types of complexes. The resulting electron configuration of dioxygen is identical to that of the first excited singlet state of the oxygen molecule; formation of the peroxo complex is thus equivalent to the activation of oxygen from the triplet to the singlet state. Such peroxo complexes are diamagnetic and may be represented by the formula M...O_2. On the other hand, when the transition metal atom is in the low oxida-

TABLE 1.9 Dioxygen Vibrational Frequencies in Metal Complexes

									ν_{O_2}, cm^{-1}	
Type				Metal				No	Range	Average
Ia				Fe	Co			9	1103–1195	1134
Ib					Co			5	1075–1122	1110
					Total, superoxo complexes:			14	1075–1195	1125
IIa	Ti	V	Cr		Co	Ni		33	818–932	881
	Zr	Nb	Mo	Ru	Rh	Pd		66	800–929	872
		Ta	W	Os	Ir	Pt	U	75	807–911	850
IIb				Fe	Co			7	790–844	807
					Total, peroxo complexes:			181	790–932	860

Source: Ref. 47.

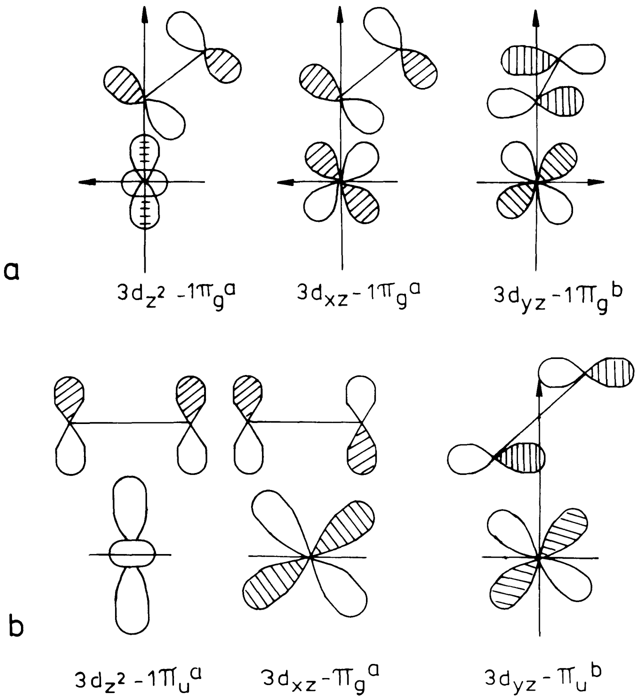

FIGURE 1.23 The main metal 3d-dioxygen interactions: (a) bent structure; (b) side-on structure. (Adapted from [44].)

tion state and has no low-lying empty d-AO, showing a high electron donor potential, only the d → π* transfer of electron takes place, resulting in the formation of the molecular ion O_2^-. By determining the structures of the iridium-oxygen complexes, Ibers [43] discovered that the O—O distance and the tendency to bind oxygen increases as the ancillary ligands become more electron donating. For example, in $Cl\text{-}Ir(CO)L_2O_2$ the O—O distance is 1.30 Å, in the iodide analogue it is 1.51 Å, and in the phosphine chelate $Ir(Ar_2P)_4O_2$ it is 1.66 Å. The valence frequency of the O—O bond is considerably lowered (800–900 cm^{-1}) in comparison with the free molecule (1555 cm^{-1}).

In the superoxo complexes the axis of the oxygen molecule is inclined in respect to the metal-oxygen bond. This angle depends on the type of metal cation and amounts to 126° in the case of Co^{2+}, 120° in Fe^{2+}, and 102.5° in Rh^{1+} complexes, depending on the degree to which different orbitals are involved in the bonding. The scheme of energy levels of the $Co\text{-}O_2$ complexes is shown in Fig. 1.24 [44]. It may be seen that, depending on the value of λ, the

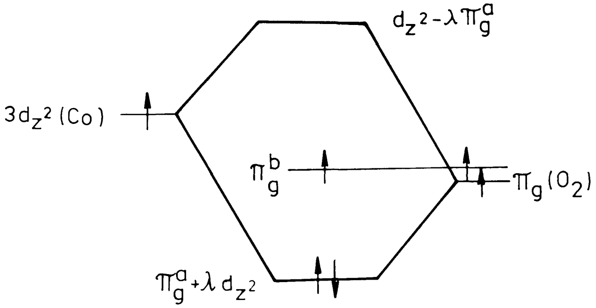

FIGURE 1.24 Simplified interaction diagram and the ground state configuration for the superoxo complex of cobalt. (Adapted from [44].)

electronic structure of the complex becomes $Co^{3+}...O_2^-$ ($\lambda = 0$) Co^{2+},,,O_2 ($\lambda = 1$), or $Co^{+}...O_2^{+}$ ($\lambda = \infty$). The ab initio calculations have shown that the configuration $(\pi_g^*)^2(\pi_g^*)^1$, corresponding to the $Co^{+3}...O_2^-$ case, is more stable than the others, but the difference is small and cannot be taken as an indication of the prevailing structure. However, EPR studies revealed the electron spin density on the coordinated O_2 to be close to 100%, thus confirming that the unpaired electron resides on the dioxygen moiety and the complex is properly represented as $Co^{3+}...O_2^-$ [45].

Theoretically, the third possibility of bonding exists, resulting in the formation of a linear complex. Until now, however, such a configuration was never observed in dioxygen complexes, at variance with the dinitrogen complexes, for which the linear structure is most characteristic. In dioxygen complexes there is only one vacant π-MO (in the singlet state) on which only one electron pair from metal d-AO may be localized, which excludes the possibility of a linear structure. However, the end-on peroxo complex IIb_2 was postulated to explain the results of resonance Raman spectroscopic studies on oxyhemerythrin with ^{18}O-labeled dioxygen which showed that the two oxygen atoms in the bound O_2 molecule have different environments [46].

REFERENCES

1. R. L. DeKock and H. B. Gray, Chemical Structure and Bonding, Benjamin/Cummings, Menlo Park, Vol. 5, 1980, p. 242.
2. E. A. V. Ebsworth, J. A. Connor, and J. J. Turner, in Comprehensive Inorganic Chemistry, Vol. 2 (C. Bailar, H. J. Emeleus, R. Nyhlom, and A. F. Trottman-Dickenson, eds.), Pergamon Press, Oxford, 1973, p. 722.

3. H. H. Wasserman and R. W. Murray, Singlet Oxygen, Academic Press, New York, 1979.
4. M. Che and A. J. Tench, Adv. Catal., 32, 6 (1983).
5. K. Jones, in Comprehensive Inorganic Chemistry, Vol. 2 (C. Bailar, H. J. Emeleus, R. Nyholm, and A. F. Trottman-Dickenson, eds.), Pergamon Press, Oxford, 1973, p. 345.
6. R. T. Sanderson, J. Chem. Ed., 41, 415 (1964).
7. A. F. Wells, Structural Inorganic Chemistry, 4th ed., Clarendon Press, Oxford, 1975.
8. F. Trifiro and I. Pasquon, J. Catal., 10, 86 (1968).
9. L. Ya. Margolis, Okuclenie Uglevodorodov na Geterogennykh katalizatorakh, Khimia, Moscow, 1977, p. 130.
10. R. T. Sanderson, Chemical Periodicity, Reinhold, New York, 1960, Polish translation, WNT, Warszawa, 1965, p. 42.
11. V. I. Nefedov, D. Gati, B. F. Dzhurinskii, N. P. Sergushin, and Ia. V. Salyn, Zhur. Neorg. Khim., 20, 2307 (1975).
12. A. Golebiewski, Chemia kwantowa zwiazköw nieorganicznych-(Quantum Chemistry of Inorganic Compounds), Państwowe Wydawnictwo Naukowe, Warsaw, 1969, p. 352.
13. W. J. Mortier, J. Catal., 55, 138 (1978).
14. G. M. Clark, The Structures of Non-Molecular Solids, Applied Science, London, 1972.
15. I. Naray-Szabo, Inorganic Crystal Chemistry, Academial Kiado, Budapest, 1969.
16. J. Haber, Crystallography of Catalyst Types, in Catalysis: Science and Technology, Vol. 2 (J. R. Anderson and M. Boudart, eds.), Springer-Verlag, Berlin, 1983.
17. C. R. Catlow, in Non-Stoichiometric Oxides (O. T. Sörensen, ed.), Academic Press, New York, 1981.
18. B. C. Lippens and J. J. Steggerda, in Physical and Chemical Aspects of Adsorbents and Catalysis, Academic Press, New York, 1970, p. 171.
19. J. B. Peri, J. Phys. Chem., 69, 211, 220, 231 (1965).
20. H. Knözinger and P. Ratnasamy, Catal. Rev., 17, 31 (1978).
21. L. Pauling, Nature of the Chemical Bond, Cornell Univ. Press, 1960.
22. M. A. Poraj-Koshitz and L. O. Atovmian, Crystalchemistry and Stereochemistry of Coordination Compounds of Molybdenum (in russian), Izd. Nauka, Moscow, 1974.
23. W. Brückner, H. Opperman, W. Reichelt, J. Terukow, F. Tschudnowski, and E. Wolf, Vanadium Oxide, Academie Verlag, Berlin, 1983.
24. K. Tanabe, Solid acid and base catalysts, in Catalysis: Science and Technology, Vol. 2 (J. R. Anderson and M. Boudart, eds.), Springer-Verlag, Berlin, 1983.
25. M. Itoh, H. Hattori, and K. Tanabe, J. Catal., 35, 225 (1974).

26. D. W. Breck, Zeolite Molecular Sieves, John Wiley and Sons, New York, 1974.
27. P. B. Weisz, in New Horizons in Catalysis, Proc., 7th, Int. Congr. Catalysis, Tokyo, 1980 (T. Seiyama and K. Tanabe, eds.), Elsevier, New York, 1981, Vol. 1, p. 3.
28. J. M. Thomas, Proc., 8th Int. Congr. Catalysis, Berlin, 1984, Dechema-Verlag Chemie, Frankfurt, 1984, Vol. 1.
29. S. Dzwigaj, J. Haber, and M. Derewiński, in Zeolites: Synthesis, Structure, Technology and Application (B. Drzaj, S. Hocevar, and S. Pejovnik, eds.), Elsevier, New York, 1985, p. 639.
30. F. S. Stone, J. Solid State Chem., 12, 271 (1975).
31. A. Cimino, Chim. Ind., 56, 27 (1974).
32. K. Dyrek, Bull Acad. Polon. Sci., Ser. Sci. Chim., 21, 675 (1973).
33. J. D. Dunitz and L. E. Orgel, Adv. in Inorg. Chem. Radiochem., 2, 1 (1960).
34. J. D. Trietiakov, Chemistry of Non-stoichiometric Oxides, Izd. MGU, Moscow, 1974.
35. R. J. H. Voorhoeve, in Advanced Materials in Catalysis, Academic Press, New York, 1977, p. 129.
36. G. Herzberg, Atomic Spectra and Atomic Structure, Dover, New York, 1966.
37. R. D. Jones, D. A. Summerville, and F. Basolo, Chem. Rev., 79, 139 (1979).
38. F. Basolo, B. M. Hoffmann, and J. Ibers, Acc. Chem. Res., 8, 384 (1975).
39. R. A. Sheldon and J. K. Kochi, Metal-Catalyzed Oxidations of Organic Compounds, Academic Press, New York, 1981.
40. R. A. Sheldon, in The Chemistry of Functional Groups, Peroxides (S. Patai Woley, ed.), New York, 1983, p. 161.
41. A. V. Savitzkii, V. I. Nieliubin, Usp. Khimii, 44, 214 (1975).
42. J. Lyons, in Fundamental Research in Homogeneous Catalysis (M. Tsutsui and R. Ugo, eds.), Plenum Press, New York, 1977.
43. J. A. McGinnety, R. J. Doeoens, and J. A. Ibers, Science, 155, 709 (1967).
44. A. Dedieu, M. M. Rohmer, and A. Veillard, J. Am. Chem. Soc., 98, 5789 (1976).
45. D. Getz, E. Melemud, B. C. Silver, and Z. Dori, J. Am. Chem. Soc., 97, 3846 (1975).
46. D. M. Kunz Jr., D. F. Shriver, and M. Klotz, J. Am. Chem. Soc., 98, 5033 (1976).
47. L. Vaska, Acc. Chem. Res., 9, 179 (1976).

2

Adsorbed Oxygen Species

I. OXYGEN SPECIES AT THE SURFACE OF OXIDES

A. Introduction

From the point of view of thermodynamics, most of the other elements and a great many chemical compounds including practically all organic substances are not stable with respect to oxygen. However, a small portion of them do react spontaneously at room or even slightly elevated temperatures. The high bond energy in O_2 is one of the reasons that the activation energy of uncatalyzed oxidation reactions is high and at moderate temperatures catalyst must be used. One of the essential functions of the catalyst in oxidation reactions is the activation of oxygen. The way in which oxygen becomes activated is a crucial problem in oxidation catalysis. Generally speaking, oxygen activation is considered to occur by its adsorption and/or incorporation into the oxide crystal lattice, the surface atoms of which may also participate in the catalytic reaction. Therefore the study of the behavior and properties of oxygen adsorbed on the catalyst as well as surface oxygen atoms in oxides is essential for an understanding of the catalytic oxidation processes. In the present chapter these topics are discussed separately for the two main groups of oxidation catalysts: the oxides and the metals.

Oxygen species adsorbed on the surface of oxides and their identification, occurrence, and reactivity were recently reviewed in two comprehensive papers by Che and Tench [1,2]. In this chapter only the main properties of surface oxygen species will be discussed, especially those relevant to catalytic studies. Table 2.1

TABLE 2.1 Oxygen Surface Species

1. Mononuclear surface oxygen species:
    - O^- ion
    - (aggregates of O^- species: dimer, trimer)
    - surface oxygen ion of low coordination O_{LC}^{2-}
    - doubly bonded surface oxygen atom
2. Dioxygen surface species:
    - reversibly bonded O_2 molecules
    - O_2^- ion
    - O_2^{2-}
    - (O_2^{3-} ion)
    - (O_2^+ ion)
3. Oxygen surface species containing more than two nuclei:
    - O_3^- ion
    - (O_4^- ion)

presents the list of various surface oxygen species whose existence was proved or postulated in the literature. It also contains the species discussed in [1] and [2] as well as reversibly bonded molecular oxygen [3]. It is seen that most of the existing oxygen surface species are considered to be negatively charged, although the bond between the formally ionic species and the surface may exhibit a notable amount of covalency.

No thermodynamic data are available concerning the energy of formation of surface oxygen species. Data concerning the formation of mono- and polynuclear species in the gas phase taken from [1] and [2] are given in Table 2.2. It is seen that the only negative oxygen species stable in the gas phase with respect to O_2 is superoxide ion O_2^-, which in fact is a commonly adsorbed oxygen species. In the gas phase the formation of ozonide ion O_3^- from ozone is exoenergetic, which indicates its relative stability in the adsorbed state. All other negative oxygen species are unstable in the gas phase. However, they may be stabilized by the Madelung potential in the bulk of solid oxides or as adsorbed species at their surface. The Madelung potential stabilizes O^{2-} ion in the bulk of oxide crystal lattices and, as it is generally assumed, also in their surface layer despite the fact that it is highly unstable in the gas phase.

TABLE 2.2 Enthalpies of the Formation of Mono- and Dioxygen Species in Gas Phase

Process	ΔH (kJ mol^{-1})
$O_2 \rightarrow 2O$	493.7
$O + e^- \rightarrow O^-$	−441.3
$O^- + e^- \rightarrow O^{2-}$	752.7
$O + 2e^- \rightarrow O^{2-}$	611.3
$O \rightarrow O^+ + e^-$	1273.6
$O^+ \rightarrow O^{2+} + e^-$	3389
$O_2 + e^- \rightarrow O_2^-$	−42.47
$O_2 + e^- \rightarrow O^- + O$	347.4
$O_2 + 2e^- \rightarrow 2O^-$	211.0
$O_2 + 2e^- \rightarrow O_2^{2-}$	646.4
$O_2^- + e^- \rightarrow O_2^{2-}$	688.9
$O_2 \rightarrow O_2^+ + e^-$	1165.0
$O_2^- \rightarrow O + O^-$	394.8
$O_2^- + e^- \rightarrow 2O^-$	253.5
$O_2^{2-} \rightarrow 2O^-$	−435.4
$O_2 + 4e^- \rightarrow 2O^{2-}$	1716[a]
$1\frac{1}{2}O_2 \rightarrow O_3$	142.3[b]
$O_3 + e^- \rightarrow O_3^-$	−189.3
$O^- + O_2 \rightarrow O_3^-$	−144.4

[a] Calculated using the data from note b and Ref. 2.

[b] E. A. V. Ebsworth, J. A. Connor, and J. J. Turner, in Comprehensive Inorganic Chemistry, Vol. 2, (C. Bailar, H. J. Emeleus, R. Nyholm, and A. F. Trottman-Dickenson, eds.), Pergamon Press, Oxford, p. 786.

Source: Data from Ref. 2.

It is considered by many authors [3] that O^{2-} as adsorbed species would also be unstable and the sorption of oxygen resulting in the formation of O^{2-} ions is considered to be equivalent to the incorporation of oxygen into the oxide lattice. The data in Table 2.2 suggest also the possibility of transformation of O^{2-} ions in the surface layer of the oxides into O^- ones as being energetically favorable.

It was suggested that the incorporation of oxygen into the oxide layer may occur stepwise [1,3] according to the following scheme:

$$\begin{tikzcd}
O_{2(g)} \arrow[r] & O^{-}_{2(ads)} \arrow[rr] \arrow[dr] & & O^{-}_{(ads)} \arrow[r] & O^{2-}_{(lattice)} \\
& & O^{2-}_{2(ads)} \arrow[ur] & &
\end{tikzcd}$$

in which a direct transformation of $O^-_{2(ads)}$ into $O^-_{(ads)}$ seems to be more probable than that through the $O^{2-}_{2(ads)}$ intermediate, the formation of which is energetically less favorable.

With the exception of O_2^{2-} and O^{2-}, all other negative oxygen species—mono- as well as polynuclear—are paramagnetic and may be investigated using the EPR method, which in fact has become the most important tool for studying their properties.

Although the compounds containing positively charged dioxygen O_2^+ ions are known, no possibility of formation of such adsorbed species is taken into account because the oxidation of neutral dioxygen occurs only in the presence of the strongest oxidation agents.

B. Mononuclear Surface Oxygen Species

1. O^- Absorbed Species

An O^- anion radical, either on the surface or in the bulk of the oxide crystal lattice, is identified on the basis of its EPR spectra and in particular by the determination of *g* and hyperfine (hf) tensors. The theory of EPR spectra of O^- was given in [4-6] and in a somewhat simplified form in [7]. In orthorhombic symmetry the degeneration of all three 2p orbitals of oxygen is suppressed, as is schematically shown in Fig. 2.1, and according to the latter authors the *g* components of EPR spectrum are given by

$$g_{zz} = g_e \qquad g_{xx} = g_e + \frac{2\lambda}{\Delta E_1} \qquad g_{yy} = g_e + \frac{2\lambda}{\Delta E_2}$$

where $g_e = 2.0023$ is the Lande *g* factor for free electron, λ = the spin-orbit coupling constant, and the meaning of E_1 and E_2 is given by Fig. 2.1.

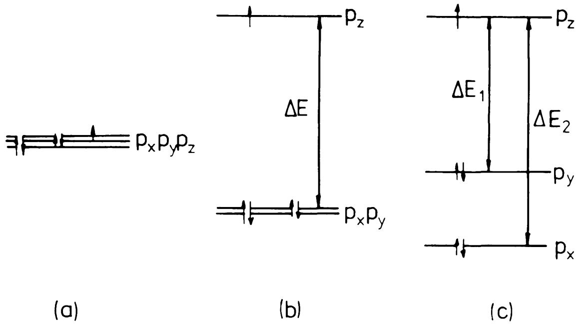

FIGURE 2.1 Energy levels diagram for O^- ion: (a) free ion, (b) in an axial crystal field, and (c) in an orthorhombic crystal field [1].

In the case of axial symmetry only the degeneration of the p_z orbital parallel to the symmetry axis and perpendicular to the surface is abolished while the energy of p_x and p_y orbitals remains the same. The EPR signal in this case is a doublet with

$$g_{11} = g_{zz} \cong g_e \text{ and } g_\perp = g_{xx} = g_{yy} = g_e + \frac{2\lambda}{\Delta E}$$

The signals of adsorbed O^- species most frequently observed correspond to axial symmetry and as such were observed, for example, on prereduced V_2O_5/SiO_2 and MoO_3/SiO_2 catalysts after dissociative adsorption of N_2O [8]. Table 2.3 presents the data concerning g_{11} values of O^- species adsorbed on powders taken from the review by Che and Tench [1]. Important additional information can be obtained from the measurements of EPR signals exhibiting hyperfine structure due to the presence of paramagnetic nuclei either in the adsorbed O^- species itself or in the surface atom on which oxygen is adsorbed. In the former case the adsorbed species is the ^{17}O isotope of oxygen, the nucleus of which exhibits nuclear spin $I = 5/2$ and the signal is composed of six lines (number of lines $(2nI + 1)$ where n is the number of paramagnetic nuclei interacting with unpaired electrons). From the hyperfine tensor spin density on O^- principally may be calculated. However, in the case of O^-/MgO [9] the obtained value depended on the calculation method. When a one-electron wave function was used the values 0.83—0.92 were obtained. The application of a many-electron wave function led to the value of 1.01. When investigating $^{17}O^-$ adsorbed on MoO_3/SiO_2, Ben Taarit and Lunsford [10] showed that 93% of the spin density was localized on the oxygen nucleus of O^- species and they therefore concluded that 7% of spin density is

TABLE 2.3 $g_\perp$ Values of O^- Oxygen Species Adsorbed on Different Oxides and Chlorides

Adsorbate	$g_\perp$ values (axial symmetry)
KCl	2.258
NaCl	2.0806
NaOH + ice	2.070
MgO	2.0385
CaO	2.0697
SrO	2.0705
Al_2O_3	2.033
WO_3/SiO_2	2.026
V_2O_5/SiO_2	2.026
MoO_3/SiO_2	2.019
Al_2O_3/SiO_2	2.012
As_2O_5/SiO_2	2.0055

Source: Data from Ref. 1.

localized on the molybdenum nucleus. The application of ^{17}O to the study of adsorbed oxygen species was amply discussed in [11].

Conclusions concerning the delocalization of electrons from O^- adsorbed species may also be taken from the registration of EPR signals exhibiting hyperfine structure due to the interactions with paramagnetic nuclei of the cations on which O^- species are localized. The EPR splitting in this case is called by Che and Tench [1] superhyperfine splitting. Kolosov et al. [12] investigated the adsorption of oxygen on $^{95}MoO_3$ (95% of ^{95}Mo isotope) and observed an EPR signal of O^- species obtained by the dissociative adsorption of N_2O shown in Fig. 2.2. It is seen that both components $g_\perp$ and $g_\parallel$ were split into six lines corresponding to the nuclear spin of ^{95}Mo equal to 5/2. According to the calculations carried out in this investigation, 1.9% of spin density is localized on molybdenum and 98.1% on O^- species.

Another interesting feature of the EPR signals of adsorbed O^- is the value of the $g_\perp$ tensor. It is seen from Table 2.3 that while the $g_\parallel$ value is contained within very narrow limits, the $g_\perp$ value

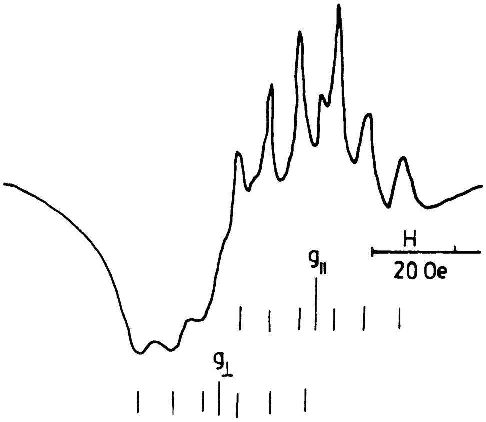

FIGURE 2.2 EPR signal of O^- species in $^{95}MoO_3$ [12].

does distinctly change with the oxidation number of the cation on which the O^- species is adsorbed. It is highest in the case of univalent cations and decreases with increasing cation charge.

Although the EPR is the most important method for detecting and identifying O^- adsorbed species, there exist some cases in which the formation of such species is postulated on the basis of strictly chemical experiments despite the fact that their existence was not confirmed by EPR measurement. Bielański and Najbar [13] proposed a chemical method of the determination of the mean number of elementary electric charges acquired per oxygen atom adsorbed on the surface of such oxides as NiO, CoO, and MnO. It consists of the determination of the volume of oxygen gas adsorbed on a high-surface-area sample of strictly stoichiometric oxide and the subsequent analytical determination (Bunsen-Rupp iodometric method) of the number of metal ions promoted to a higher oxidation state as the result of electron transfer from the adsorbent to the adsorbate. In the course of all experiments the sample is never exposed to air. Using this method it has been shown that, in the case of high-surface-area nickel oxide at room temperature, oxygen is adsorbed predominantly (about 90%) irreversibly. In the irreversible adsorption one electron was transferred per adsorbed O atom, which corresponds to the chemisorption in the form of O^- species or, less probably, from thermodynamic factors in the form of O_2^{2-} ion. At 150°C no reversible adsorption was observed and the number of transferred electrons increased with the time of contact from 1.0 elementary charge per 0 atom after 10 min to 1.52 after 2 hrs which indicated the gradual transformation of O^- into O^{2-} ion, i.e., the incorporation of adsorbed oxygen into the crystal lattice of NiO. It should here be observed that according to our knowledge no detection of EPR signals of O^- on NiO was reported. This may be due either to dipolar interactions between paramagnetic O^- species or—as already said—to the less probable formation of diamagnetic O_2^{2-} ions. Praliaud et al. [14], when applying a similar method consisting of dissolution of the sample in a redox system (Fe^{2+}/Fe^{3+}), showed the presence of oxidizing species in the sample of MgO which had been thermally activated. The results could be due to the presence of O^- species in the bulk or at the surface. It was also supposed [1] that the effect could be due to coordinatively unsaturated O^{2-} ions. This alternative seems to be less acceptable as the O^{2-} species principally does not exhibit oxidizing properties.

The O^- adsorbed species may be obtained at the surface of oxides either by adsorption of oxygen under the proper conditions as already mentioned or by the dissociative chemisorption of N_2O. The O^- species may also be generated by irradiation of oxides and even by their thermal activation. In the course of chemisorption of oxygen, in most cases O^- and O_2^- ions are being formed simultaneously. The results obtained by Shvets and Kazansky [8] can be cited as an example. When adsorbing at −196°C oxygen on prereduced V_2O_5/SiO_2 sample they observed a complex EPR signal with well-resolved superhyperfine structure from ^{51}V nuclei ($\underline{I} = 7/2$), which was identified as the signal of O_2^- species. On heating this sample with adsorbed oxygen to −78°C or higher, the intensity of this signal decreased and a new signal which could be attributed to O^- appeared. When O_2 was adsorbed at temperatures as high as 350°C for 2–3 min the only signal which was registered was that of O^- ion. This experiment shows a high thermal stability of O^- species adsorbed on silica-supported vanadium oxide in which V atoms occupy tetrahedral positions. On the other hand, on prereduced TiO_2/SiO_2 sample the signal of O^- ion could be obtained only at the liquid nitrogen temperature and it vanished by −78°C. Its transformation into O^{2-} and O_2^- was rapid.

The generation of surface O^- ions by dissociative chemisorption of N_2O was applied by many authors:

$$N_2O_{(g)} + e^- \rightarrow O^-_{(ads)} + N_{2(g)}$$

In this way Kolosov et al. [12] produced O^- on prereduced $^{95}MoO_3/SiO_2$ at 100°C. The EPR signals exhibited ultrafine structure due to the magnetic moment of molybdenum 95 nuclei ($\underline{I} = 5/2$). The $\underline{g}$ tensor values were $\underline{g}_\perp = 2.021$ and $\underline{g}_\parallel = 2.006$.

A number of papers also described the formation of O^- ions by γ or UV irradiation of the oxides and especially of MgO. Such methods, although very important for solid state physics, are of lesser interest from the point of view of catalytic research.

High reactivity of the adsorbed O^- species was reported in the literature. It reacted with hydrogen at temperatures as low as 77 K in the case of O^- on previously irradiated MgO. The same reaction was observed on silica-supported Ti, Mo, W, and V oxides and the reactivity followed the pattern V > Mo > W [8]. The latter authors also observed at 77 K the formation of O_3^- ions from O^- species adsorbed on V_2O_5/SiO_2 and O_2 molecules from gas phase. With CO and CO_2 the O^- species gives the CO_2^- and CO_3^- ion radicals [15-17], the plausible intermediates in the catalytic oxidation on transition metal oxides. The reactions of O^- species with hydrocarbons were studied in [15] and [18].

From the above considerations it is clear that the existence of O^- adsorbed species on the oxide surfaces is well established. It is highly reactive even at fairly low temperatures and, despite the fact that in the case of V_2O_5/SiO_2 catalyst it could be detected after heating the sample to 300°C, it is generally not very stable. In an overwhelming majority the conditions under which the properties of O^- were investigated are much different from those typical for the catalytic oxidation processes, i.e., the conditions under which the EPR measurement, because of high temperature and experimental difficulties, cannot be carried out and the identification of transient radicals is very difficult. However, it should be said that the O^- ion is a plausible participant in such catalytic processes and must be taken seriously into account as one of the forms in which oxygen gets activated. The role which O^- species may play in oxidation catalysis was discussed by Kazansky [19], according to whom O^- may participate as an intermediate in the reduction as well as reoxidation of oxide catalyst surface and also may participate directly in reaction with other reagent molecules. In this consideration he refers to the fact that the reduction of V_2O_5 and TiO_2 catalysts is very much faster if the catalyst is illuminated with the light quanta enabling charge transfer from O^{2-} to V^{5+}. The generation of a positive hole on the oxide ion, then, is equivalent to the formation of an O^- ion. The mechanism of such photoreduction of an oxide in the presence of CO can therefore be the sequence of the following two reactions:

$$M^{\underline{n}} + O^{2-} \xrightarrow{h\nu} M^{(\underline{n}-1)} + O^-$$

$$M^{\underline{n}+} + O^- + CO \longrightarrow CO_2 + M^{(\underline{n}-1)} + \square$$

Neither is the formation of CO_2^- anion as an intermediate excluded. A similar scheme with transient O^- species and the formation of a surface anion vacancy may also be proposed for photoreduction with hydrogen:

$$M^{\underline{n}+} + O^{2-} \xrightarrow{h\nu} M^{(\underline{n}-1)} + O^{-}$$

$$O^{-} + H_2 \longrightarrow OH^{-} + H_{ads}$$

$$H_{ads} + O^{2-} + M^{\underline{n}+} \longrightarrow OH^{-} + M^{(\underline{n}-1)}$$

$$2OH^{-} \longrightarrow O^{2-} + H_2O + \square$$

Kazansky argues that the same mechanism can also operate at sufficiently high temperatures without illumination. The charge transfer process is then thermally activated.

The appearance, perhaps momentary, of an O^- intermediate is also very probable in the course of reoxidation of reduced oxide catalyst, which may be represented by the equation:

$$O_2 + 2\square + 4e^{-} \longrightarrow 2O^{2-}$$

There is very little chance for this process to occur in just one stage. As was already stated, more often the O_2^- species usually formed on the prereduced oxides subsequently turns into O^- and this, finally, into O^{2-} ion. The process will be favored by the presence of surface oxygen vacancies:

$$O_2 + e^{-} + \square = O^{-}_{2(\text{surface})}$$

$$O^{-}_{2(\text{surface})} + e^{-} + \square = 2O^{-}_{(\text{surface})}$$

$$2O^{-}_{(\text{surface})} + 2e^{-} = 2O^{2-}_{(\text{surface})}$$

If the reoxidation is fast, the concentration of both O_2^- and O^- species at the surface is low and the oxidation of a reducing gas mixed with oxygen can be effectuated mainly by reducing the catalyst. On the other hand, if reoxidation is slow, the concentration of oxygen radicals is relatively high and the direct reaction between O^- and, say, an organic molecule becomes the main path of the reaction. The problem of both mechanisms of catalytic oxidation will be discussed more fully in Chapter 3.

2. Surface O^{2-} Ions of Low Coordination

Che and Tench in their review [1] emphasize the often neglected role which may be played in catalytic processes by surface oxygen ions O^{2-} exhibiting lower coordination than in the bulk of oxide crystals. Oxide ion O^{2-} is fairly unstable in the gas phase because of its high positive enthalpy of formation amounting to 858 kJ mol^{-1} of O^{2-} ions. The O^{2-} ion in the bulk of oxide lattice is stabilized by the largely coulombic interactions with neighboring ions. It is obvious that the stabilizing Madelung potential is weaker at the surface than in the bulk owing to the decreased coordination number which, for example, in NaCl-type crystal decreases from 6 in the bulk to 5 at (100), 4 at (110), and 3 at (111) crystal face. The sites of diminished coordination exist also at the edges and corners of the crystals and other sites which can be geometrically distinguished, as electron microphotographs show that the surface of a real crystal is never ideally flat but contains imperfections: steps, pits, etc., in which atoms of low coordination may exist. Such a situation is schematically represented in Fig. 2.3, which was taken from the review by Ché and Tench [1]. Following these authors we shall determine the low coordination oxide ions by the symbol O^{2-}_{LC}. In particular cases the coordination number will be substituted for L (O^{2-}_{5C}, an oxide ion in fivefold coordination). The lower the coordination of an surface O^{2-} ion, the lesser is its stability. The decrease of stability with decreasing coordination number will be manifested by (1) the decreasing energy of bonding the O^{2-} surface ion and (2) the increasing tendency to give off an electron and to turn into O^- species or to became the donor of an electron pair in the presence of an electrophilic molecule or ion.

Strong support for such a model is coming from the investigation of heterophase isotopic exchange of oxygen, which will be discussed in Chapter 3. Such investigations show that oxygen in the surface layer of numerous transition metal oxides is heterogeneous with respect to the isotopic exchange, which also indicates the heterogeneity of its bonding.

The electron donor properties of oxides have been the object of increasing interest in recent years. Nitrobenzene (NB) and such related compounds as di- and trinitrobenzene, along with some other substances such as tetracyanoethylene (TCNE), which exhibit high electron affinity when adsorbed on the oxide surface may acquire electrons and convert into negatively charged radicals, the presence of which can be detected by EPR measurement. It is considered that in the case of MgO the role of surface donor centers is mainly played by surface OH^- and O^{2-}_{LC} ions. Ché et al. [20] adsorbed TCNE from benzene solution on MgO activated within the temperature range 150–800°C and, depending on the calcination temperature,

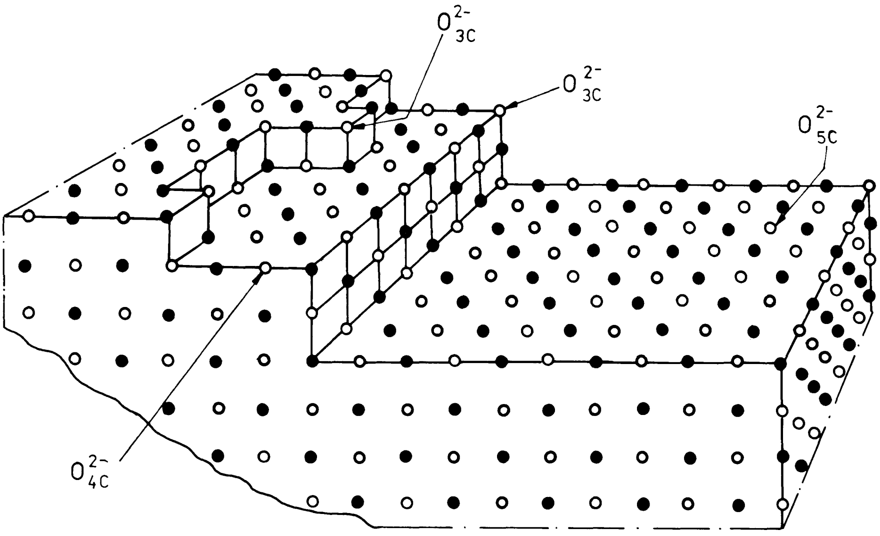

FIGURE 2.3 Representation of a surface (100) plane of MgO showing imperfections which provide sites for ions of low coordination [1].

observed two maxima of TCNE signal intensity—at about 200 and 700°C. Thermogravimetric and IR investigation indicated that the first maximum is connected to the presence of surface OH groups. It decreased parallel to a decrease in OH group concentration. After calcination at about 600°C new donor centers began to operate which, following the earlier suggestion of Tench and Nelson [21], were attributed to the low coordination surface O^{2-} ions. At still higher temperatures sintering of MgO crystallites and a decrease in the amount of O^{2-}_{LC} occurred. Heterogeneity of surface oxygen in MgO was also confirmed in [23].

Very similar results were obtained by Flockhart [22] in the case of adsorption of TCNE on alumina. Maxima of TCNE adsorption appeared in the case of samples calcined at 200 and 800°C, and the interpretation is essentially the same as in the case of MgO.

Kibblewhite and Tench [24] investigated the properties of surface oxygen ions by heating MgO samples with adsorbed halogens at 300°C. Under these conditions chlorine evolved an amount of oxygen corresponding to 20% of surface O^{2-} ions with the parallel formation of an equivalent amount of Cl^- ion. Bromine substituted 10% and iodine only 1% of surface oxygen atoms. These results were compared with the enthalpies of formation of MgO (-143 kcal mol^{-1}) and halides ($MgCl_2$ -153 kcal mol^{-1}, $MgBr_2$ -125 kcal mol^{-1}, and MgI_2 -87 kcal mol^{-1}). The results again indicate the heterogeneity of surface oxygen atoms. The highest is the number of oxygen atoms liberated by chlorine, the strongest electron acceptor, but with decreasing acceptor power the amount of liberated oxygen decreases. A very likely interpretation of these results is that iodine can only react with O^{2-} ions in the lowest coordination, perhaps O^{2-}_{3C}, bromine with O^{2-}_{3C} and O^{2-}_{4C}, and chlorine with a still wider range of oxygen ions.

Surface O^{2-} ions containing oxygen in its lowest oxidation state in contrast to O^- and O_2^- species cannot exhibit oxidizing properties. However, they can play an important role in the mechanism of catalytic oxidation processes because of the fact that they are Lewis and also Brönsted basic sites. Mamoru Ai [25], when discussing the correlation between the acid-base properties of oxide catalysts, shows that both acidic and basic centers may be involved at different stages of the process. Metal atoms in a high state of oxidation, such as Mo(VI) in molybdates of V(V) in V_2O_5 and vanadates, are Lewis acid centers, electron pair acceptors, and can adsorb electrophilic molecules such as olefins. The surface O^{2-} ions may, on the other hand, fulfill two different functions connected with their basic properties, namely, to accept protons splitted by adsorbed hydrocarbon molecules and to act as nucleophilic ligands entering the molecules of the reagent which were turned at the acid sites into nucleophilic intermediates. A detailed model of this kind of process was described by Haber and Grzybowska [26].

3. Doubly Bonded Surface Atoms M=O

As already stated, the largely covalent oxides containing transition metals in their highest oxidation state can contain in their structures O atoms bonded in two different ways. They form either two covalent bonds with two neighboring metal atoms in the chains —M—O—M— or double σ-π bonds with only one metal atom. In the former case each oxygen atom is common for at least two coordination polyhedra MO_n, in the latter they occupy the position of terminal atoms in polyhedra. Such singly coordinated O atoms, when present at the surface, e.g., (010) face in V_2O_5 crystal, differ from the low-coordinated O^{2-}_{LC} oxygen atoms described in the previous section mostly in the sense that the metal-oxygen bond is only weakly polarized. The M=O bond, being stronger than M—O in M—O—M, exhibits stretching vibrations at a higher frequency and is characterized by an IR band between 900 and 1100 cm^{-1}, while the vibrations of M—O—M chains are usually connected with several overlapping bands between 600 and 900 cm^{-1} [27].

Trifiro and Pasquon [28,29], when investigating the catalytic oxidation of CO, ammonia, propene, and methanol, stated that oxide catalysts used by them or investigated by them could be grouped into two classes. Class 1 comprised the oxides: NiO, Co_3O_4, Cu_O, Cr_2O_3, MnO_2, Fe_2O_3, SnO-Sb_2O_3, and $CdMoO_4$, which were active in the oxidation of CO, in homomolecular isotopic oxygen exchange, oxidized methanol and propene to CO_2 and ammonia to N_2O. Class 2 comprised V_2O_5, MoO_3, as well as the molybdates of Fe, Bi, Co, Ni, and Mn, which were not active or only weakly active in the oxidation of carbon monoxide and in homomolecular isotopic oxygen exchange, but selectively oxidized propylene to acroleine and methanol (with the exception of V_2O_5) to CH_2O. Ammonia was oxidized to N_2. Both classes differed also by the fact that class 1 catalysts did not possess a metal-oxygen bond of double-bond character, while all class 2 catalysts exhibited the presence of such a bond, according to IR investigations. Basing on this observation, Trifiro and Pasquon concluded that the metal-oxygen double bond, in the particular case of molybdates a Mo=O bond, plays an essential role in the selective oxidation of hydrocarbons. They suggested that an H atom abstracted from an adsorbed hydrocarbon molecule may add to the metal-oxygen double bond. The opening of the double bond leaves a free valence on the metal which may be used in a bond with the dehydrogenated molecule. In the case of the oxidation of propylene after a possible adsorption as a π-olefin complex this free valence can be used to give an allyl complex.

Analogous results were obtained by Akimoto and Echigoya [30] who investigated the oxidation of butadiene on a series of titania (anatase) catalysts modified by different oxides, and stated that only the catalyst containing as additives the oxides exhibiting doubly bonded oxygen (As_2O_3, Ta_2O_5, P_2O_5, WO_3, and MoO_3) produced certain amounts of maleic anhydride, the catalyst MoO_3-TiO_2 being much more selective than the other. The modification of anatase with the oxides which do not possess doubly bonded oxygen in their structure only converted butadiene to carbon mono- and dioxides. The same authors [31], when investigating oxidation of furan to maleic anhydride on modified molybdena and titania catalysts, concluded that in the former case the active species of oxygen was $Mo^{6+}=0$ and in the latter O_2^- anion radical. They also suggested [32] that the Mo=O bond may behave like radical oxygen, its radical character increasing especially as the result of electron transfer to a nonbonding atomic orbital of Mo^{6+}, and that its reactivity is strongly affected by the electronegativity or acid-base properties of molybdenum ions as modified by the additives with oxides, VA group elements, or alkali metals. The characteristic reactivity of double-bond oxygen participating in allylic oxidations as selective oxidation species is attributed by these authors to the special nature of oxygen in Mo=O.

The importance of the metal-oxygen double bond in selective oxidation was also recognized by Weiss et al. [33], who formulated their argument based on their knowledge of the general rules governing the mechanisms of organic reactions. It may be said that most authors accept the special role of Mo=O in selective oxidation processes on molybdena and molybdates [34]. However, the presence of Mo=O bond in molybdates does not seem to be necessary in all cases. Brazdil and Graselli [35] investigated ammoxidation of propylene to acrylonitrile on $Bi_{2-\underline{x}}Ce_{\underline{x}}(MoO_4)_3$ catalysts and found similar maxima of activity and selectivity occurring in the two single-phase regions, where there is a maximum of solubility of $Ce_2(MoO_4)_3$ in $Bi_2(MoO_4)_3$ phase ($\underline{x} \approx 0.2$) and a maximum of solubility of $Bi_2(MoO_4)_3$ in $Ce_2(MoO_4)_3$ phase ($\underline{x} \approx 1$). However, only in the $Bi_2(MoO_4)_3$ phase was the doubly bonded oxygen Mo=O present.

Also in the case of V_2O_5-based catalysts the role of doubly bonded oxygen in V=O (stretching frequency 1025 cm^{-1}) is not unequivocal. Tarama et al. [36] postulated that the V=O bond strength is a controlling factor for the catalytic activity of V_2O_5 and V_2O_5-MoO_3 catalysts in the reaction of benzene oxidation to maleic anhydride. However, it has been shown that in this case stoichiometric oxides are catalytically nonactive and appreciable reduction (about 100% V^{5+} reduced to V^{4+}) is necessary to make them active and selective [37]. This results in the formation of new phases, V_6O_{13} and V_2O_4 in the case of V_2O_5 catalyst and disappearance of the 1025 cm^{-1} band in their IR spectrum [38]. Full discussion of the present state of the controversy concerning the role of doubly bonded oxygen in vanadia-containing catalysts for benzene oxidation will be given in Chapter 8. Here it should be mentioned that Andersson when investigating 3-picoline ammoxidation [39] on V_2O_5-TiO_2 catalysts suggested that the presence of $V^{4+}=0$ centers favors this reaction.

Generally speaking, the existence of doubly bonded oxygen at the surface of some oxides is well documented by IR investigations [2] and there are suggestions that in particular cases, especially in that of MoO_3 and numerous molybdates, it may play an essential role in selective catalytic oxidation. However, some published results seem ambiguous and there is a distinct lack of theoretical investigation concerning this problem.

C. Dioxygen Adsorbed Species

1. Neutral Adsorbed O_2 Species

At low temperatures oxygen is physisorbed on the surface of solids in the form of neutral triplet molecules. However, this kind of adsorption is not interesting from the point of view of catalytic processes and will not be discussed here. On the other hand, in some cases reversible adsorption of oxygen at around room temperature was observed which does not exhibit properties typical of physisorption. This phenomenon was extensively studied in an O_2-NiO system. It was shown by several authors [40-42] that at room temperature the fast initial adsorption of oxygen on high-surface-area NiO is followed by a slow one, the former being irreversible and accompanied by a distinct increase in the electrical conductivity, and the latter being reversible and not influencing electrical conductivity. It has therefore been concluded that irreversible adsorption is connected with the formation of negatively charged oxygen species which were later shown to be O^- [13] and reversible adsorption is the adsorption of neutral O_2 molecules. Kuchynka and Klier [41], who investigated reversible adsorption within the temperature range −78 to 150°C and called it molecular adsorption, stated that it was a selective process as its extent markedly diminished when oxygen was preadsorbed irreversibly at 100°C. The authors concluded, therefore, that the adsorption forces are not of the type considered in the physical adsorption that is usually little dependent on the character of the adsorbent. This conclusion was supported by the fact that nitrogen was not adsorbed under the same conditions, although the interactions employed in physical adsorption should be the same for both nitrogen and oxygen because of the similar polarizability and dimensions of the two molecules. Considering all these facts Kuchynka and Klier characterized the observed molecular adsorption of oxygen on NiO as a weak chemical interaction of oxygen with Ni^{2+} ions. The heat of molecular oxygen adsorption was estimated by these authors as 7 kcal mol^{-1} in accordance with direct calorimetric measurements [43]. No theoretical interpretation of this kind of oxygen adsorption on NiO has been given. However, it should be observed that Boča [44] in his molecular orbital study of dioxygen ligand in cyanate, chloride, and ammonia complexes of transition metals indicated the possibility of bonding O_2 molecule by the intermediation of its π_g antibonding orbital without acquiring a negative charge.

As already stated, oxygen reversibly adsorbed is the precursor of O^- adsorbed species [13]. This, however, does not exclude the possibility that such transformation is going by the intermediation of O_2^- species which would turn rapidly into O^-.

Adsorption of oxygen in the form desorbable at temperatures below 100°C was observed by TPD method on some other oxides as well (MnO_2 desorption peak at 50°C, Fe_2O_3 55°C, Co_3O_4 30°C, NiO 35°C, Al_2O_3 65°C) [45]. However, no interpretation of such results was given. It can be suggested that we deal here with an analogous phenomenon as in the case of NiO.

2. O_2^- Adsorbed Anion Radical

The data in Table 2.2 show that the O_2^- anion radical is thermodynamically the most stable oxygen-negative species which can exist in the gas phase. In the solid state it is present in superoxides of alkali metals and has been frequently identified as one of the forms in which oxygen may be adsorbed on the surface of oxides and metals. The properties of adsorbed O_2^- species were comprehensively presented and discussed in a review by Ché and Tench [2].

Owing to its paramagnetic properties resulting from the presence of one unpaired electron on an antibonding π_g orbital:

$$(\sigma_g 1s)^2(\sigma_u 1s)^2(\sigma_g 2s)^2(\sigma_u 2s)^2(\sigma_g 2p)^2(\pi_u 2p)^4(\pi_g 2p)^3$$

EPR could be applied as the main method for studying the adsorbed O_2^-. Based on the detailed analysis of its EPR signals and hyperfine and ultrahyperfine structure, a wealth of information concerning the properties of this species could be obtained comprising its identification, concentration, type of bonding, and the nature of adsorption centers. However, the method can be applied only to cases in which O_2^- anion radical is adsorbed on nonparamagnetic surface cations. The interactions between unpaired electrons of O_2^- radicals and the electrons of paramagnetic adsorption centers result in EPR line broadening so intense that the signal cannot be registered.

In most cases of O_2^- formation on the surface of ionic oxides a purely ionic model of adsorption is assumed. Känzig and Cohen [46] derived a set of formulas that based on the crystal field theory gives the relation between the anizotropic values of g tensor, the spin-orbit coupling constant λ, and the values of Δ and $\underline{E}$, the distances between π_g^x and π_g^y, and also the π_g^y and σ_g^z energy levels in adsorbed O_2 molecule as shown in Fig. 2.4. Under the assumption that $\lambda < \Delta << \underline{E}$, which is always the case, the equations take the form:

$$\underline{g_{xx}} = \underline{g_e}$$

$$\underline{g_{yy}} = \underline{g_e} + 2\frac{\lambda}{\underline{E}}$$

$$\underline{g_{zz}} = \underline{g_e} + 2\frac{\lambda}{\Delta}$$

The orientation of $\underline{x}$, $\underline{y}$, and $\underline{z}$ is given in Fig. 2.5 as proposed in [2]: the $\underline{z}$ axis is the axis of the O—O bond in the oxygen molecule. It is assumed that owing to the stronger interaction of the

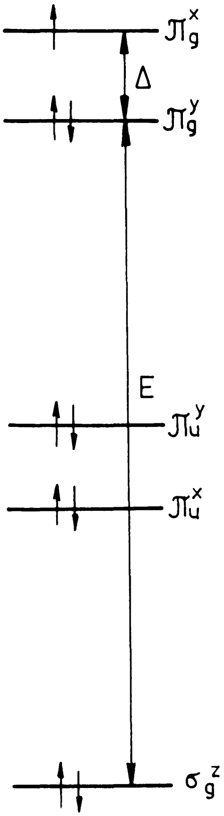

FIGURE 2.4 Energy levels diagram of an O_2^- anion radical in the crystal field acting at the surface of the ionic crystal.

π_g^y orbital with the surface, this orbital has a lower energy and is filled by two electrons while the unpaired electron resides on the π_g^x orbital. Känzing and Cohen's formulas show that the g_{xx} factor is expected to be equal to the value g_e of a free electron (2.0023) and the order of g tensors is $g_{xx} < g_{yy} < g_{zz}$. In fact, the experiment shows that in most cases of O_g^- adsorption on oxides the g_{xx} is contained within the narrow limits 2.001–2.005 and g_{yy} within 2.008–2.010. The greatest variance is exhibited by the value of g_{zz} tensor. This latter value depends—similar to the case of the $g_\perp$ tensor of O^- adsorbed species—on the intensity of crystal field in the vicinity of the adsorbed O_2^- ion and hence on the electrical

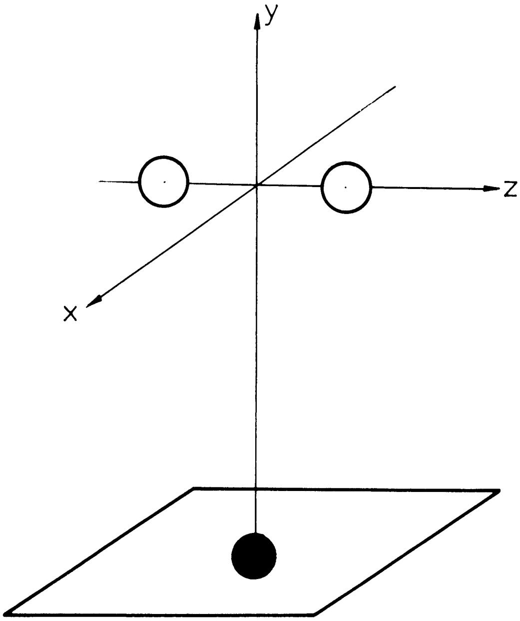

FIGURE 2.5 Orientation of x, y, and z axes with respect to the O_2^- ion and the surface of the crystal [2].

charge of the cation playing the role of adsorption center. This is illustrated in Fig. 2.6 which shows the dependence of the g_{zz} factor on the formal oxidation state of the metal ion [2]. On the basis of the observed values of the g_{zz} tensor conclusions are usually drawn concerning the nature of the adsorption center. For example, in the case of CoO-MgO Dyrek [47] observed the signal with the g_{zz} value 2.025–2.028, which was attributed to O_2^-/Co^{3+} complex, but also the signal with $g_{zz} = 2.070$, which indicated that a certain number of O_2^- radicals were localized on Mg^{2+} ions. However, such a criterion must be applied cautiously because even in the case of adsorption on cations of the same charge the g_{zz} values may differ appreciably. For example, in the series MgO, CaO, and SrO the g_{zz} values were determined at 2.077, 2.093, and 2.102, respectively [48]. When analyzing these results it was concluded that it is the electrostatic field (polarizing power) of the cation expressed by the value q/r (q charge of the cation and r the radius) rather than the absolute value of q which is determining the orbital splitting Δ and hence the value of the g_{zz} tensor.

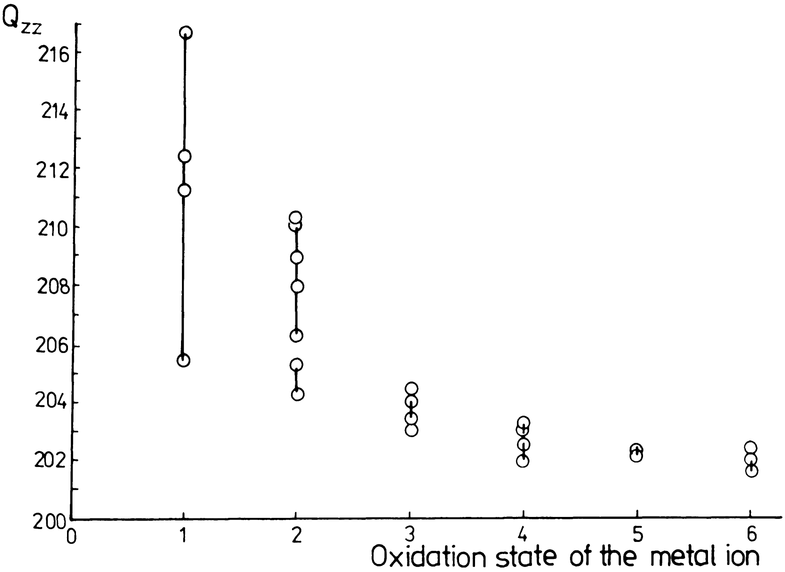

FIGURE 2.6 Variation of $\underline{g}_{zz}$ of the O_2^- adsorbed oxygen species with the oxidation state of the metal ion [2].

The essential feature of the ionic model discussed by Känzig and Cohen [46] is the equivalency of both oxygen atoms in an O_2^- radical oriented parallel to the surface. The equivalency of O atoms can be verified by the investigation of adsorption of isotopically labeled oxygen. As already stated in this chapter, the ^{17}O nuclei exhibit a nonzero nuclear magnetic moment equal to 5/2 and accordingly in the case of equivalent oxygen atoms the adsorption of $^{16}O^{17}O$ molecules should be accompanied by the splitting of each component of EPR signal characterized by a different $\underline{g}$ value into $(2 \times 5/2 + 1) = 6$ lines of hyperfine structure. The adsorption of the $^{17}O^{17}O$ molecule results in the splitting of each component into $(2 \times 2 \times 5/2 + 1) = 11$ lines. The isotopic method which also gives the most unambiguous discrimination between O^- and O_2^- adsorbed species was introduced for the first time by Tench [49] and applied successfully to the investigation of oxygen adsorbed species. The equivalency of O atoms in O_2^- has been confirmed in a number of cases; adsorption of oxygen on MgO]50], CaO [51], SrO [51], and CeO_2/SiO_2 [52] can be mentioned as examples. The hyperfine tensor $\underline{A}$ was also used to calculate the spin densities and values close to unity were obtained in all these cases, confirming the ionic nature of the adsorbed species surface bond.

There are also known examples of adsorbed O_2^- exhibiting nonequivalent oxygen atoms. The EPR spectrum is then more complicated and its analysis is not always straightforward [2]. Often the adsorption of $^{16}O^{17}O$ results in the appearance of two sets of equally spaced lines of hyperfine structure centered around the g_{xx} component. Such effects were observed, for example, by Ben Taarit and Lunsford [53] who studied adsorption of isotopically enriched oxygen on λ-irradiated HY zeolite and silica-supported reduced MoO_3. Both sets in each catalyst exhibited similar intensity, the same thermal stability, and the same behavior when microwave power was being changed. The latter fact indicated that there was only one type of oxygen species present at the surface. If two different species were adsorbed, their behavior could not be identical. In this situation the double signal has to be interpreted as the result of nonequivalency of both oxygen atoms. One oxygen atom is nearer to and the other is farther from the surface. Statistically in half of the O_2^- anions the labeled atom is the inner atom and in half it is the outer one. Different positions of the labeled atom lead to a somewhat different EPR signal of identically bonded species. Similar results were also obtained by Ché et al. [54] for the reduced MoO_3/SiO_2 and MoO_3/Al_2O_3 samples. It was shown in this investigation that inner and outer oxygen atoms have different spin densities and it was suggested that O_2^- is adsorbed at an angle to the surface. The inequivalency of the oxygen atoms is considered to be the result of the covalency of the ion sitting at an angle to an essentially flat surface, or the result of the surface geometry of a particular association of molybdenum and silica. In this latter case an ionic O_2^- could be adsorbed parallel on a ziz-zag surface:

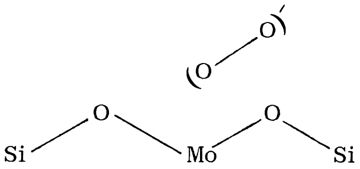

and due to a steric hindrance one oxygen atom would be closer to the adsorption site of Mo^{6+}.

Important information concerning the nature of the bond between adsorbed O_2^- species and the surface of an oxide can also be obtained from the observation of superhyperfine splitting of the EPR signal, i.e., the splitting of the $^{16}O_2^-$ signal resulting from the interactions with the adsorption center containing a cation with a nonzero nuclear moment. In the case of molybdenum oxide catalyst the preparation enriched in ^{95}Mo (I = 5/2) was used. Kazansky et al. [12] studied a $^{95}MoO_3/SiO_2$ system while Ché et al. [55] investigated the same oxide using a wider range of supports (SiO_2, Al_2O_3, and MgO). Adsorption of oxygen on silica-supported $^{95}MoO_3$ resulted in the formation of EPR signals in which each principal value of the g tensor was split into six components, confirming not only adsorption on the Mo^{6+} ion but also delocalization of the unpaired electron onto this ion. It is interesting to observe that in the case of a $^{95}MoO_3/MgO$ system no superhyperfine splitting was observed, proving that Mo atoms were not the adsorption centers. On the contrary, the g_{zz} factor value of 2.070 indicated that oxygen adsorption on Mg^{2+} ions occurred. In the case of $^{95}MoO_3/Al_2O_3$ two different ultrahyperfine EPR signals were registered when adsorption was carried out at 77 and 300 K. Their interpretation was not straightforward because of the fact that ^{27}Al exhibits the same nuclear moment as ^{95}Mo. However, comparison of the splitting parameters a_{xx}, a_{yy}, and a_{zz} with the analogous values obtained for O_2^- adsorbed on γ-irradiated γ-Al_2O_3 made possible the conclusion that at low temperature O_2^- is localized on Mo^{6+} ions. Warming the system to 300 K leads to an increase in the number of O_2^- ions observed due to electron transfer from reduced molybdenum sites to give additional O_2^- adsorbed on Al^{3+} sites on the support.

Another example in which the spin delocalization of O_2^- anion radical onto the adsorption center was observed is given in [56] and [57] describing oxygen adsorption on reduced V_2O_5/SiO_2 samples. In this case tensors g were split into eight components, thus showing that the O_2^- species was adsorbed on V^{5+} ($I = 7/2$).

In cases where oxygen atoms in adsorbed O_2^- species are appreciably unequivalent, the simple ionic model discussed by Känzig and Cohen [46] is no more adequate and must be replaced by a more elaborate model assuming a certain amount of covalency. Tovrog et al. [58] proposed such a model of oxygen bonding in dioxygen-cobalt(II) complexes. He assumed that one of the two orthogonal π_g orbitals of the oxygen molecule containing unpaired electrons overlaps with the d_{z^2} orbital of cobalt(II), also filled with one electron. The second π_g orbital does not participate in the formation of covalent bonds. The electronic configuration of $O_2/Co(II)$ may therefore be represented as $(\Psi_1)^2(\Psi_2)^1(\Psi_3)^0$, where

$$\Psi_1 = \alpha(d_{z^2}) + \beta(\pi_g)$$

$$\Psi_2 = \pi_g$$

$$\Psi_3 = \beta(d_{z^2}) - \alpha(\pi_g)$$

and $\alpha^2 + \beta^2 = 1$. The unpaired electron is residing on π_g orbital of oxygen and the covalency of bonding is due to the occupation of molecular orbital Ψ_1 by a pair of electrons. The interpretation of these results shows that there is wide variation in the amount of electron transfer to O_2 in a series of adducts depending on the ligand field strength around cobalt. With increasing ligand field the energy of d_{z^2} increases with respect to that of the π_g orbital and the complex becomes more ionic. On the other hand, if both energies are nearly equal the bond is covalent and the metal-oxygen bond angle is ~120°. Rough estimates indicate 0.1—0.8 electron transfer as the result of an analysis of the anisotropic cobalt hyperfine coupling for various Co(II) complexes.

Infrared spectroscopy may also supply some information concerning the properties of adsorbed O_2^- anion radical [59]. However, it was used only rarely in this way. Dioxygen in the gas phase as a centrosymmetric molecule is not active in IR. On the other hand, it has been shown that adsorption of oxygen on oxides may be accompanied by the appearance of new IR bands which are attributed to the adsorbed dioxygen species. Evidently in such cases the deformation of the dioxygen molecule occurs rendering it IR-active. Davydov et al. [60] when adsorbing oxygen on anataz samples differently vacuum-reduced at 525°C observed a broad band within the range 700—1000 cm^{-1}, which was interpreted as the consequence of the dissociative adsorption of oxygen. A band at 1630 cm^{-1} was interpreted as the stretching vibration of neutral O_2 molecule polarized by the crystal field at the surface. Its frequency corresponded to that observed for the O_2 molecule in the gas phase in a Raman spectrum. A band at 1180 cm^{-1} was attributed to the vibrations of O_2^- adsorbed species as its frequency was close to that of O_2^- anion in superoxides. In the same spectral region (1160—1180 cm^{-1}) Zecchina et al. [61] observed five overlapping adsorption bands at 77 K after adsorption of oxygen on diluted (5 mol %) CoO-MgO solid solution. They could be slowly desorbed by evacuation at the same temperature at different rates in the order $1088 \simeq 1095 > 1100 > 1124 \simeq 1157$ cm^{-1}. It was therefore concluded that each component band corresponded to a different species. On the basis of isotope substitution and by comparison with homogeneous analogs, it was concluded that O_2 was adsorbed in the superoxide ion O_2^- form.

The results of IR investigation of oxygen adsorption on defected tin dioxide [62] were compared with the results obtained for the same SnO_2 preparation using EPR measurements [63]. The adsorption of oxygen was accompanied by the appearance of two intensive absorption bands at 1190 and 1045 cm^{-1}. The former one disappeared during desorption at temperatures below 200°C while the latter was stable until about 300°C. The study of EPR has shown that two types of O_2^- anion radicals were formed which were stabilized on Sn^{4+} and Sn^{2+}. The radical stabilized on Sn^{4+} was thermally less stable and decomposed below 200°C. It was therefore considered to be identical with oxygen species characterized by an IR band at 1190 cm^{-1}. The O_2^- radical stabilized at Sn^{2+} was stable up to 300°C, which enabled it to be assigned to the vibration frequency of 1045 cm^{-1}.

Generally speaking, IR investigations can supply valuable information concerning the forms of adsorbed oxygen. However, interpretation of data may often be ambiguous.

The formation of O_2^- adsorbed species was observed on more than 30 oxidic system [2] including supported and unsupported main group and transition metal oxides as well as silica and some aluminosilicates, mainly zeolites. Most of these materials, e.g., MoO_3, V_2O_5, TiO_2, Al_2O_3, MgO, ZnO, in the strictly stoichiometric state are nonconducting and contain cations in the highest possible oxidation state. In such a state they do not possess centers capable of donating electrons to the adsorbed O_2 molecules. Such donor centers can be created by various treatments. MoO_3, TiO_2, SnO_2, and ZnO can be activated by vacuum heating or by mild reduction. The oxides which are thermally stable, e.g., Al_2O_3, SiO_2, and MgO, were activated by γ, X, or UV irradiation. On the other hand, transition metal oxides containing cations which can be easily oxidized exhibit a tendency to supply more electrons than are needed for the formation of O_2^- ions and adsorb oxygen as O^- or O^{2-} species [3]. However, the same cations when diluted in a nonconducting diamagnetic matrix become the centers at which oxygen adsorbs as O_2^- radical. This has been observed in the case of diluted solid solutions of CoO in MgO [47,61]. In this system it was possible to correlate the number of isolated Co^{2+} ions in tetrahedral symmetry [65] with the number of O_2^- radicals. The effect of dilution was also observed with MnO-MgO solid solution where, however, the identification of adsorbed oxygen species was less certain because of the overlap of the EPR signal of oxygen and the ultrafine signal of Mn^{2+} [64,66].

The thermal stability of the adsorbed O_2^- species is of great interest from the point of view of the oxidation catalysis. However, there is a distinct lack of systematic studies concerning this problem. Most of the observations of the EPR signals were carried out after adsorption at room temperature or at temperatures as low as 77 K and the authors of the already quoted papers only occasionally give information as to the thermal stability of this species. The range of temperatures at which the EPR signal of adsorbed O_2^- disappeared was wide. The signal obtained with diluted CoO-MgO solid solution and identified as corresponding to O_2^-/Co^{3+} vanished in vacuo at room temperature, but the signal of O_2^-/Mg^{2+} adsorbed on the same sample was stable until 400–500 K [60]. On MoO_3/MgO the localization of O_2^- on Mg^{2+} was observed and the species was stable until 150°C [67]. Also, on MoO_3/Al_2O_3 and Al_2O_3/SiO_2, the

O_2^- disappeared at 150°C [67]. On the reduced SnO_2 the signal of O_2^-/Sn^{4+} vanished at 200°C while that of O_2^-/Sn^{2+} vanished at 300°C [60]. These examples may suggest that the stability of O_2^- adsorbed anion radical decreases with the increasing charge of the stabilizing cation. No information could be found in the literature regarding whether the disappearance of the EPR signal observed in the course of heating was due to the simple desorption or the result of its transformation into other species not visible by EPR, e.g., incorporated into the lattice as O^{2-} ion. The latter possibility is frequently postulated and in fact the O_2^- species is considered as the first intermediate in the formation of other oxygen species more rich in electrons. However, there is a lack of detailed investigations concerning the transformations of adsorbed oxygen species the rate of which may essentially influence the course of catalytic oxidation processes.

There were suggestions in the literature that O_2^{2-} and O_2^{3-} molecular ions can exist as the adsorbed species; however, no convincing proof has been given [2]. It should be observed that the completely filled antibonding $\pi_g 2p$ orbitals renders O_2^{2-} unstable in the gas phase and it can exist in the solid peroxides only because of the stabilizing effect of the crystal field. This effect must be markedly weaker at the surface of oxides. The instability of the hypothetical O_2^{3-} ion with one additional electron on the $\sigma_g 2p$ antibonding orbital would be even more pronounced.

II. OXYGEN SPECIES AT THE SURFACE OF METALS

A. Introduction

Metal catalysts with the exception of platinum and silver are much less important in oxidation catalysis than the oxide catalysts. Platinum is active in the oxidation of H_2, CO, NH_3, and combustion of hydrocarbons, e.g., in the exhaust gases, while silver is used in the catalytic oxidation of methanol to formaldehyde and epoxidation of ethylene. The specific role of these two metals in oxidation catalysis is the reason why in this section our attention will be concentrated on the platinum and silver group metals.

From the experimental point of view the study of oxygen species adsorbed on metal surfaces differs from analogous studies on oxide surfaces by the fact that in this case the EPR measurements, the most powerful tool in the investigation of the oxygen-oxide systems, cannot be applied because of high concentration of delocalized electrons in metals. The only exceptions are systems with highly dispersed metals or evaporated films. The identification of presumed paramagnetic adsorbed oxygen species is therefore less straightforward. On the other hand, the introduction of ultrahigh-vacuum technique and the application of the physical methods of modern "surface science" such as low-energy electron diffraction (LEED), X-ray and ultraviolet spectroscopies (XPS and UPS), Auger electron spectroscopy (AES), electron energy loss spectroscopy (EELS), secondary ion mass spectroscopy (SIMS), and others more recently enabled very rapid progress in the field of chemisorption on metal surfaces. Most of these methods were developed and tested using extremely clean surfaces. The difficulties in obtaining well-defined surfaces of metal oxides, due more than anything to the decomposition of external layers of the solid at conditions of ultrahigh vacuum, very much delayed the application of these methods to the investigation of chemisorption on the oxides.

It is generally agreed [68] that oxygen may be adsorbed on metal surfaces as

1. Weakly adsorbed molecular oxygen
2. Chemisorbed atomic oxygen
3. Oxygen atoms penetrating into the most external layers of metal crystals, thus forming "subsurface" oxygen

The variety of adsorbed oxygen forms and their bond strength at metal surfaces is illustrated by the fact that the adsorption heat of oxygen varies within very wide limits from about 80 kJ mol^{-1} and even less on silver up to about 800 kJ mol^{-1} in the case of tungsten. Adsorption of oxygen on metals occurs in some cases as a practically nonactivated process, but in some other ones activation energy as high as 250—300 kJ mol^{-1} is necessary [69].

B. Oxygen Species on Platinum and Other Platinum Group Metals

The kind of oxygen species, their arrangement at the surface as indicated by LEED, and the kind of metal-oxygen bond depend on the purity of metal surfaces on temperature but also on the crystal face being studied. At the (111) face of platinum molecular adsorption of oxygen is predominant below 120 K [70] and exhibits a desorption peak at 150 K [71] while on the platinum sheet this latter effect was observed at 200 K]72]. The adsorption heat on Pt (111) was estimated on the basis of desorption peak area to be about 37 kJ mol^{-1} [70]. Using EELS the frequency of this species was determined as 870 cm^{-1}. This value is low in comparison with that of the neutral O_2 molecule (1550 cm^{-1}) and in superoxide ion O_2^- (1145 cm^{-1}) corresponds to the vibration frequency of peroxide ion O_2^{2-}, thus indicating a single O—O bond in the adsorbed state. This conclusion is also supported by the observed positive change in the work function of +0.8 eV and the UPS spectra which indicate that the orbitals derived from $\pi_g(2p)$ antibonding orbitals of the O_2 molecule are filled in the adsorbed dioxygen. It should be observed here that, in the case of silica-supported and presumably finely divided platinum, O_2^- species were identified by EPR measurements at room temperature besides which O^- species were also present [73]. No ordered LEED structures were observed after oxygen adsorption at 100 K, indicating that disordered adsorption of dioxygen had occurred [71].

Heating the adsorbed layer on Pt (111) surface to 150–170 K causes some of the adsorbed oxygen to desorb and some to dissociate, which is also signaled by the formation of a (2 × 2) LEED pattern [70]. Molecularly adsorbed oxygen plays the role of precursor of adsorbed atomic oxygen and the process $O_{2(ads)} \rightarrow 2O_{(ads)}$ occurs with an activation energy of about 33 kJ mol^{-1}.

Atomic oxygen at the surface (111) of Pt is the predominant form of adsorbed oxygen within the temperature range 150–500 K [70]. It is characterized by vibrational frequency 490 cm^{-1} appearing parallel to the appearance of (2 × 2) LEED pattern. The surface (111) saturates when one O atom is adsorbed per four Pt atoms [74], which corresponds to the uniform covering of the whole surface by (2 × 2) O-atom arrays. On Pt (100) two surface phases were identified [75]. The average coverage 0.44 ± 0.05 of monolayer gives rise to a (3 × 1) LEED pattern. The second phase is associated with the oxygen-saturated surface (0.63 ± 0.03 monolayer) and is characterized by a very complex LEED pattern.

Heating of platinum in oxygen above 500 K results in the formation of "subsurface" oxide which decomposes at 1250 K [70]. A direct proof of the penetration of oxygen into the near-to-surface layer of the solid was obtained for Pt (111) by ion scattering [68]. In the case of iron, ruthenium, tungsten, and nickel the formation of subsurface oxygen was postulated in order to explain the observed decrease of work function [69]. The subsurface oxygen exhibits reduced reactivity with respect to CO and H_2.

The results of investigations of oxygen adsorption on the other platinum group metals are, generally speaking, analogous to those obtained in the case of platinum. For example, on the iridium (111) surface molecularly adsorbed oxygen stable below 100 K, dissociatively adsorbed oxygen, and the subsurface oxygen forming rapidly above 700 K were observed [76]. The oxide layer saturated at the coverage of 2.4×10^{14} O atoms cm^{-2} and ordered to form a (1× 4) LEED pattern. Different LEED patterns of dissociatively chemisorbed oxygen were observed on clean and oxidized Ir (110). A p(2 × 2) pattern was formed on the clean surface near the coverage of 2.4×10^{14} atoms cm^{-2} whereas a c(2 × 2) pattern appeared on the oxidized surface near 4.8×10^{14} atoms cm^{-2} coverage. Oxygen chemisorption on iridium (110) is not activated since the initial sticking probabilities on the clean and oxidized surfaces are equal to 0.28 and 0.4 irrespective of surface temperature.

C. Oxygen Species on Silver

The practical application of silver as the catalyst for ethylene and alcohol oxidation in the production of ethylene oxide and formaldehyde, respectively, also aroused interest in the investigation of oxygen chemisorption on this metal which had been undertaken in the 1930s [77]. The existing data had been obtained under conditions of oxygen pressures from 10^{-6} to 300 Torr using polycrystalline silver powders, wires, foils, and films [78]. In recent years sophisticated methods of surface physics were applied to the study of oxygen chemisorption on particular faces of Ag monocrystals. These methods resulted in essential progress in our understanding of the behavior of oxygen on the clean surfaces of silver. However, similarly to the case of platinum, the experiments had to be carried out at pressures much lower than 10^{-5} Torr, i.e., under conditions which differ strongly from those of practical catalytic processes. Nevertheless such advanced studies are extremely valuable from the physicochemical point of view and, especially in the case of the Ag (110) face, which was the most frequent object of studies, gave a coherent picture of the behavior of oxygen at the surface of silver. This is why they will be discussed first in this chapter.

At the (110) face of silver all three forms of adsorbed oxygen were identified at appropriate conditions: molecular, atomic, and subsurface oxygen. Molecularly adsorbed oxygen was observed if adsorption was carried out at 150 K and below [79]. Upon heating a desorption peak of this form was registered at 190 K. The amount of this species strongly increased in the measure as the adsorption temperature was lowered. The existence of molecular oxygen under these conditions is well documented. Barteau and Madix [79] carried out a series of isotopic mixing experiments. They introduced $^{16}O_2$ and $^{18}O_2$ on the surface and controlled the isotopic composition of oxygen desorbing at 190 K. In no case could they find the $^{16}O^{18}O$ molecules; hence they concluded that the low-temperature state was solely due to the molecularly adsorbed oxygen. Vibrational spectra of this species were investigated by Sexton and Madix [80] who, using electron energy loss spectroscopy, found vibrational spectra analogous to those observed with the same method in the case of O_2 on Pt (111) [71], mentioned in the preceding section. The difference between the cases consists, however, in the shift of the frequencies observed in the Ag-O_2 system to the lower values. Two bands of O_2 on Ag (110) were observed: 240 cm^{-1} [390 cm^{-1}

on Pt (111)] and 640 cm^{-1} (870 cm^{-1} on Pt]. The former was identified as analogous to the interpretation of data obtained with Pt as a (Ag-O_2) vibration and the latter as a ν(O—O) vibration. However, it should be observed that in the case of Pt (111) the value of the ν(O—O) vibration corresponded well to the frequency of a single O—O bond of dioxygen in [Pt$(PPh_3)_2O_2$] complex in which both π* antibonding orbitals of dioxygen are filled. It is apparent that on Ag (110) the π* orbitals are filled and possibly further donation of electrons into σ* antibonding orbitals occurs.

The exposure of the Ag (110) face to O_2 at 200 K and above resulted in the adsorption of O atoms only [79]. These recombine and desorb at 590 K upon heating of the sample. They are characterized by vibration frequency 490 cm^{-1} as indicated by EELS measurement [80]. This band is attributed to a ν(Ag-O) vibration. The monoatomic form of adsorbed oxygen was also confirmed by isotopic exchange experiments [79].

Dissociative chemisorption of oxygen on the (110) face of silver is accompanied by ordering of the atoms, resulting in a series of LEED patterns of the type ($\underline{n}$ × 1) in which $\underline{n}$ at small exposures assumes the value of 6 and with increasing exposure decreases to 2 [81]. Oxygen is adsorbed on this surface in chains parallel to the [001] direction. The formation of chains implies attractive interactions between oxygen atoms in the [001] direction and repulsion in the [110] direction. A further step in the characterization of the ordered ($\underline{n}$ × 1) structures was done in [82] where, parallel to the LEED examination, low-energy helium ion scattering (IS) was also applied. The observation of strong azimuthal anisotropy of the IS signal led the authors to conclude that oxygen atoms are adsorbed in the bridging position between two Ag atoms of the (110) surface channels, their centers being slightly below the centers of Ag atoms.

The third form of oxygen chemisorbed on Ag (110) and also on Ag (100) and Ag (111) faces was observed in [83], where the samples were exposed to 10^{-3} to 1 Torr of oxygen at temperatures up to 500°C. After oxygen was pumped off and the samples were cooled the surfaces were examined under a condition of ultrahigh vacuum. The samples exposed to oxygen below 300°C exhibited only one desorption peak at about 280°C in good accordance with the observations in [79] corresponding to the dissociatively chemisorbed oxygen. However, if the temperature of exposure was higher than 300°C, another desorption peak appeared at about 500°C, indicating slow oxygen desorption. This form of oxygen was interpreted as subsurface oxygen. According to the authors, this kind of oxygen probably does not cause structural variations of the silver surface but modifies certain electronic properties, which are then reflected in the behavior of the surface. In particular, this kind of oxygen if present in sufficient concentration seems to inhibit the faceting observed on the pure (100) and the dissociative chemisorption. It does not, however, noticeably affect the properties of the (111) face.

As already stated, the conditions at which all the above described investigations with very pure surfaces are carried out are distant from those at which catalytic reactions occur in laboratory and industrial practice, and that is why the earlier studies carried out with more "classical" methods using polycrystalline Ag samples and applying higher pressures, reviewed in [77] and [84], still deserve attention. The results of classical studies differ distinctly in some respects from the results obtained with the application of ultrahigh vacuum and especially purified surfaces. It seems that the most essential difference is the fact that under conditions of ultrahigh vacuum the adsorption of oxygen at room temperature is only dissociative and adsorbed molecular oxygen can be detected exclusively at low temperatures (desorption peak about 190 K), while in the classical studies strong arguments were presented that dioxygen species can exist (besides monoatomic ones) even at temperatures as high as 473 K. The postulated existence of adsorbed dioxygen played an important role in the development of ideas concerning the mechanism of selective oxidation of ethylene [84]. The reasons for the discrepancies between the results of classical and modern studies have not been thoroughly discussed in the literature. However, they seem to be mainly due to the impurities and various defects at the surface of "real" catalysts, but the effect of increased oxygen pressure may also exert an influence.

Here let us mention a few papers in which classical methods gave very convincing evidence that different forms of oxygen adsorbed on polycrystalline samples. Joyner and Roberts [78] adsorbed oxygen at pressures up to 0.5 Torr on a silver foil at 473 K and identified by XPS three oxygen species characterized by oxygen 1s binding energies 528.3, 530.3, and 532.5 eV. The 528.3-eV peak appeared immediately after oxygen admission at a pressure of 5.10^{-3} Torr. After 30 min under the same conditions the intensity of this peak decreased and the 530.3-eV peak appeared, which became dominant after another 10 min. The third least intensive peak was detected after 60 min and rising oxygen pressure to 0.5 Torr. The first peak, corresponding to a transient species, was identified as a surface species and the 530.3-eV peak as corresponding to the subsurface oxygen. Both species were assigned as atomic. The assignment of the remaining peak at 532.5 eV was more tentative, but it was suggested that it was arising from a molecular oxygen species probably present as O_2^- ion. The discrete peak in the UPS spectrum observed at about 9 eV below Fermi level was also evidence in favor of the presence of molecular species being assigned to the orbitals of the O=O bond.

Kilty et al. [85] studied the chemisorption of oxygen on thoroughly reduced silver catalyst supported on α-Al_2O_3. Kinetic investigation clearly indicated that three different types of oxygen adsorption existed. In all cases chemisorption was activated and activation energies were determined as equal to 10, 33, and 60 kJ mol^{-1}. The identification of the adsorbed species was done based on the following two series of experiments: chemisorption of oxygen on the surface poisoned with chlorine and IR studies of the behavior of isotopic mixtures of dioxygen in contact with the catalyst. The poisoning of the surface inhibited the fast initial nonactivated chemisorption of oxygen. It ceased completely when at 373 K the precoverage with chlorine exceeded 3.10^{18} Cl atoms per m^2, which was equal to one Cl atom on flour Ag ones. For higher Cl precoverage each additional Cl atom reduced by two the number of oxygen atoms which could subsequently be adsorbed. These observations can be explained by assuming that the initial fast chemisorption up to the coverage 1.5×10^{18} O_2 molecules per m^2 is dissociative. The fact that this kind of sorption is stopped when one Cl atom is adsorbed for each four Ag atoms suggests that for the dissociation of one O_2 molecule four neighboring Ag atoms are needed:

$$4Ag_{(neighb.)} + O_2 = 4Ag^{+}_{(neighb.)} + 2O^{2-}_{(ads)}$$

This reaction is considered to be only weakly activated ($\underline{E}_a$ = 10 kJ mol^{-1}). However, at temperatures higher than 373 K highly activated chemisorption occurs on the surface saturated according to the above equation. The authors suggest that it is also dissociative and occurs with the participation of four nonneighboring Ag atoms which must migrate in order to form a common ensemble:

$$4Ag_{(nonneighb.)} + O_2 = 4Ag^{+}_{(neighb.)} + 2O^{2-}_{(ads)}$$

This last process presumably needs high activation energy and is identified with the chemisorption occurring with $\underline{E}_a$ = 60 kJ mol^{-1}.

In the IR investigations a band at 848 cm^{-1} was found at 368 K after adsorption of $^{16}O_2$. The supposition that it corresponded to a diatomic species was verified by adsorbing the equilibrated mixture of $^{16}O_2$, $^{16}O^{18}O$, and $^{18}O_2$ (molar ratio 1:2:1). The bands at 870, 855, and 848 cm^{-1} were obtained having the intensivity ratio

1:2:1. Finally and most significantly, a nonequilibrated mixture of $^{16}O_2$ and $^{18}O_2$ (1:1) gave only two bands of equal intensity at 870 and 848 cm^{-1}, thus proving that the two oxygen species involved in the vibration originated from the same oxygen molecule. The introduction of $^{16}O_2$ and $^{18}O_2$ at 433 K resulted in the appearance of all three bands in the IR spectrum, which indicates that under these conditions diatomic species are in equilibrium with dissociated species.

REFERENCES

1. M. Che and A. J. Tench, Adv. Catal., 31, 77 (1982).
2. M. Che and A. J. Tench, Adv. Catal., 32, 1 (1983).
3. A. Bielański and J. Haber, Catal. Revs., 19(1), 1 (1979).
4. J. R. Brailsford and J. R. Morton, J. Chem. Phys., 51, 4794 (1969).
5. S. V. Nistor and G. Stoichescu, Rev. Roum. Phys., 16, 515 (1971).
6. S. V. Nistor and I. Ursu, Rev. Roum. Phys., 16, 495 (1971).
7. R. D. Iyengar, M. Codell, J. S. Karra, and J. Turkevich, J. Am. Chem. Soc., 88, 5055 (1966).
8. V. A. Shvets and V. B. Kazansky, J. Catal., 25, 123 (1972).
9. N. B. Wong and J. H. Lunsford, J. Chem. Phys., 55, 3007 (1971).
10. Y. Ben Taarit and J. H. Lundsford, Chem. Phys. Lett., 19, 348 (1973).
11. M. Che, E. Giamello, and A. Tench, Colloids Surf., 13, 231 (1985).
12. A. K. Kolosov, V. A. Shvets, and V. B. Kazansky, Chem. Phys. Lett., 34, 360 (1975).
13. A. Bielański and M. Najbar, J. Catal., 25, 398 (1972).
14. H. Praliaud, S. Coluccia, A. M. Deane, and A. J. Tench, Chem. Phys. Lett., 66, 44 (1979).
15. C. Naccache and M. Che, Proc. Int. Congr. Catal. 5th, 1972, 2, 1389 (1973).
16. C. Naccache, Chem. Phys. Lett., 11, 323 (1971).
17. A. J. Tench, T. Lawson, and J. F. J. Kibblewhite, J. Chem. Soc. Faraday I, 68, 1169 (1972).
18. K. Aika and J. H. Lunsford, J. Phys. Chem., 81, 1393 (1977).
19. V. B. Kazansky, Kinet. Katal., 14, 95 (1973).
20. M. Che, C. Naccache, and B. Imelik, J. Catal., 24, 328 (1972).
21. A. J. Tench and R. L. Nelson, Trans. Faraday Soc., 63, 2254 (1967).

22. B. D. Flockhart, I. R. Leith, and R. C. Pink, *Trans. Faraday Soc., 65*, 542 (1969).
23. J. Kijeński and S. Malinowski, *Bull. Acad. Polon. Sci., Ser. Sci. Chim., 25*, 329 (1977).
24. J. F. J. Kibblewhite and A. J. Tench, *J. Chem. Soc. Faraday I, 70*, 72 (1974).
25. M. Ai, *Bull. Chem. Soc. Japan, 50*, 2574 (1977).
26. J. Haber and B. Grzybowska, *J. Catal., 28*, 439 (1973).
27. G. G. Barraclough, J. Lewis, and R. S. Nyholm, *J. Chem. Soc.,* 3552 (1959).
28. F. Trifiro, P. Centola, and I. Pasquon, *J. Catal., 10*, 86 (1968).
29. F. Trifiro and I. Pasquon, *J. Catal., 12*, 412 (1968).
30. M. Akimoto and E. Echigoya, *J. Catal., 29*, 19 (1973).
31. M. Akimoto and E. Echigoya, *J. Chem. Soc. Faraday I, 73*, 193 (1977).
32. M. Akimoto and E. Echigoya, *J. Catal., 35*, 278 (1974).
33. F. Weiss, J. Marion, J. Metzgeraud, and J. M. Congnon, *Kinet. Katal., 14*, 45 (1973).
34. L. Ya. Margolis, *Okislenie uglevodorov na geterogennykh katalizatorakh* (Oxidation of Hydrocarbons on Heterogeneous Catalysts), Khimia, Moscow 1977, pp. 129-133.
35. J. Brazdil and R. Graselli, *J. Catal., 79*, 104 (1983).
36. K. Tarama, S. Teranishi, S. Yoshida, and N. Tamura, *Proc. Int. Congr. Catal.,* 3rd, 1964, *1*, 282, 1965.
37. A. Bielański and A. Inglot, *Bull. Acad. Polon. Sci., Ser. Sci. Chim., 22*, 773 (1974).
38. A. Bielański and A. Inglot, *React. Kinet. Catal. Lett., 6*, 83 (1977).
39. A. Anderson, Dissertation, Lund Institute of Technology, Lund, Sweden, 1982.
40. R. P. Marcellini, R. E. Ranc, and S. J. Teichner, *Actes 2^{e} Congr. Int. Catalyse, Paris 1960*, Edition Technip, Paris, 1961, p. 289.
41. K. Kuchynka and K. Klier, *Collection Czech. Chem. Commun., 28*, 148 (1963).
42. H. B. Charman, R. M. Dell, and S. S. Teale, *Trans. Faraday Soc., 59*, 453 (1963).
43. G. El. Shobaky, P. C. Gravelle, and S. J. Teichner, *J. Catal., 14*, 4 (1969).
44. R. Boča, *J. Mol. Catal., 14*, 313 (1982).
45. M. Iwamoto, Y. Yoda, N. Yamazoe, and T. Seiyama, *J. Phys. Chem., 82*, 2564 (1978).
46. W. Känzig and M. H. Cohen, *Phys. Rev. Lett., 3*, 509 (1959).
47. K. Dyrek, *Bull. Acad. Polon. Sci., Ser. Sci., Chim., 21*, 675 (1973).

48. M. Che, S. Coluccia, and A. Zecchina, J. Chem. Soc. Faraday I, 74, 1324 (1978).
49. A. J. Tench and R. L. Nelson, J. Chem. Phys., 44, 1744 (1966).
50. A. J. Tench and P. Holroyd, Chem. Commun., 471 (1968).
51. M. Che, A. J. Tench, S. Coluccia, and A. Zecchina, J. Chem. Soc. Faraday I, 72, 1553 (1976).
52. P. Meriaudeau, C. Naccache, and A. J. Tench, J. Catal., 21, 208 (1971).
53. Y. Ben Taarit and J. H. Lunsford, J. Phys. Chem., 77, 780 (1973).
54. M. Che, A. J. Tench, and C. Naccache, J. Chem. Soc. Faraday I, 70, 263 (1974).
55. M. Che, J. C. McAteer, and A. J. Tench, Chem. Phys. Lett., 31, 145 (1975).
56. V. A. Shvets, V. M. Vorotintsev, and V. B. Kazansky, Kinet. Katal., 10, 356 (1969).
57. V. M. Vorotintsev, V. A. Shvets, and V. B. Kazansky, Kinet. Katal., 12, 1020 (1971).
58. B. S. Tovrog, D. J. Kitke, and R. S. Drago, J. Am. Chem. Soc., 98, 5144 (1976).
59. M. Che, K. Dyrek, M. Kermarec, and A. J. Tench, Rev. Chim. Minérale, 21, 669 (1984).
60. A. A. Davydov and M. Komareva, Seminar on Adsorbed Oxygen in Catalysis, Novosibirsk 1972, preprint 9.
61. A. Zecchina, G. Spoto, and S. Coluccia, J. Mol. Catal., 14, 351 (1982).
62. T. A. Gundrizer and A. A. Davydov, React. Kin. Katal. Lett., 3, 63 (1975).
63. V. E. Anufrienko, N. G. Maksimov, P. V. Schastnev, T. A. Gundritzer, and D. V. Tarasova, Dokl. Akad. Nauk USSR, 209, 372 (1973).
64. K. Dyrek, Bull. Acad. Polon. Sci., Ser. Sci. Chim., 22, 213 (1974).
65. K. Dyrek and Z. Sojka, J. Chem. Soc. Faraday Trans., I, 78, 3177 (1982).
66. K. Dyrek, Bull. Acad. Polon. Sci., Ser. Sci. Chim., 20, 57 (1972).
67. O. V. Krylov, G. B. Pariiskii, and K. N. Spiridonov, J. Catal., 23, 301 (1971).
68. T. Engel and G. Ertl, in Chemical Physicas of Solid Surfaces and Heterogeneous Catalysis, Vol. 4 (D. A. King and D. P. Woodruff, eds.), Elsevier, Amsterdam, 1982, p. 73.
69. O. V. Krylov and V. P. Kiselev, Adsorptsya na Perekhodnykh Metalakh i ikh Okislakh, Khimiya, Moscow, 1981, p. 232.

70. J. L. Gland, B. A. Sexton, and G. B. Fischer, *Surf. Sci., 95*, 587 (1980).
71. J. L. Gland, *Surf. Sci., 93*, 487 (1980).
72. P. R. Norton, *Surf. Sci., 47*, 98 (1975).
73. J. R. Katzer, G. C. Schuit, and J. H. C. Van Hoof, *J. Catal., 59*, 279 (1979).
74. D. R. Monroe and R. P. Merill, *J. Catal., 65*, 46 (1980).
75. K. Griffits, T. E. Jackman, J. A. Davies, and P. R. Norton, *Surf. Sci., 138*, 113 (1984).
76. J. L. Taylor, D. E. Ibbotson, and W. H. Weinberg, *Surf. Sci., 79*, 349 (1979).
77. M. A. Barteau and R. J. Madix, in *Chemical Physics of Solid Surfaces and Heterogeneous Catalysis*, Vol. 4 (D. A. King and D. P. Woodruff, eds.), Elsevier, Amsterdam, 1982, p. 139.
78. R. W. Joyner and M. W. Roberts, *Chem. Phys. Lett., 60*, 459 (1979).
79. M. A. Barteau and R. J. Madix, *Surf. Sci., 97*, 101 (1980).
80. B. A. Sexton and R. J. Madix, *Chem. Phys. Lett., 76,* 294 (1980).
81. H. A. Engelhardt and D. Menzel, *Surf. Sci., 57*, 591 (1976).
82. W. Heiland, F. Iberl, E. Taglaner, and D. Menzel, *Surf. Sci., 53*, 383 (1987).
83. G. Rovida, E. Ferroni, and F. Pratesi, in *Adsorption-Desorption Phenomena* (F. Ricca, ed.), Academic Press, London, 1972, p. 417.
84. W. M. Sachtler, *Catal. Rev., 4*, 27 (1971).
85. P. A. Kilty, N. C. Rol, and W. M. H. Sachtler, *Proc. 5th Int. Congr. Catalysis, Miami Beach 1972* (J. W. Hightower, ed.), North-Holland, Amsterdam, 1973, p. 929.

3

Interactions of Oxygen with the Surfaces of Oxides

I. INTRODUCTION

Each catalytic oxidation process must comprise interactions not only between the catalyst and the oxidizable molecules but interactions between the catalyst and oxygen molecules as well. Various aspects of the interactions between oxide catalysts and oxygen common for many catalytic oxidation processes will be discussed in this chapter. The first topics (Section II) to be tackled are the properties of oxide surface, the geometric arrangement of the atoms, and the chemical composition of the surface layer. Next to be discussed, in Section III, are the chemisorption of oxygen on the oxides and the electronic processes accompanying it. Section IV is devoted to the interactions between oxygen and the bulk of the oxide resulting in the formation or disappearance of a certain number of lattice defects, the presence of which may influence the catalytic properties of the oxides. Section V deals with the isotopic exchange of oxygen on the oxide catalysts. This kind of study supplies us with important information concerning the mobility of oxygen in the bulk of the solid and in the adsorbed layer. Various correlations between the rate and activation energy of isotopic oxygen exchange and the catalytic properties are discussed in Section V, the main subject of which is the studies of oxygen surface bond strength. This latter factor is considered as one of the factors controlling the course of catalytic oxidation reactions. In some special cases, e.g., simple catalytic reactions at the surface of period IV transition metal oxides, surface-oxygen bond strength seems to be the main factor determining the catalytic activity. Because the most important oxidation catalysts are the oxides of transition metals, our attention in this chapter will mainly be focused on this class of substances.

II. SURFACE OF OXIDES

Basic knowledge concerning the geometric structure of the surface of a solid can be obtained from consideration of its crystal structure. Most frequently the models of the surface are obtained by assuming that the crystal has been cleft along a given crystal plane. In the case of an oxide of sodium chloride structure, e.g., magnesium oxide, cleaving along (100) and (110) planes results in the exposition of surfaces containing equal numbers of cations and anions and hence electrically neutral (Fig. 3.1a and b). However, in the case of the (111) plane, which consists alternatively of cationic one anionic layers, the electrical neutrality of both parts of the split crystal is only reached if, for example, the oxide anions from an anionic plane are equally distributed between the surfaces being formed. Such surfaces will contain half of the unoccupied anionic sites (Fig. 3.1c). The ions on the planes created by cleaving the crystal are coordinatively unsaturated. The coordination number of a cation (and also of an anion) in the (100) face of MgO is 5 instead of 6 in the bulk. On the (110) it is reduced to 4 and on (111) to 3, but depending on the distribution of anions in their most external half-filled plane it might also be 4 or 5.

The coordinative unsaturation of surface atoms must be taken into account when considering adsorptive and catalytic properties of the surface. Burwell et al. [1], when discussing the model of the α-Cr_2O_3 surface, indicated that the surface containing anionic vacancies such as those in the (111) face of MgO and also in (001) face of α-Cr_2O_3 may easily chemisorb water molecules forming OH^- ions covering the whole surface:

$$(O_O)_s + (V_O)_s + H_2O_g \rightarrow 2(OH_O)_s \tag{3.1}$$

where $(O_O)_s$ is surface oxygen atom in anionic position, $(V_O)_s$ is surface anionic vacancy, $(OH_O)_s$ is surface hydroxyl group filling anionic vacancy. The dehydroxylation of such a surface results in the exposition of cations and formation of catalytically active centers for various catalytic reactions, e.g., hydrogenation or isomerization of hexene.

Much more complicated are the models of surfaces of the nonionic oxides containing transition metals in high oxidation states. The model of surfaces of MoO_3 recently discussed by Ziólkowski [2] will be taken here as an example. This oxide exhibits a layer structure in which slightly deformed $[MoO_6]$ octahedra are joined in such

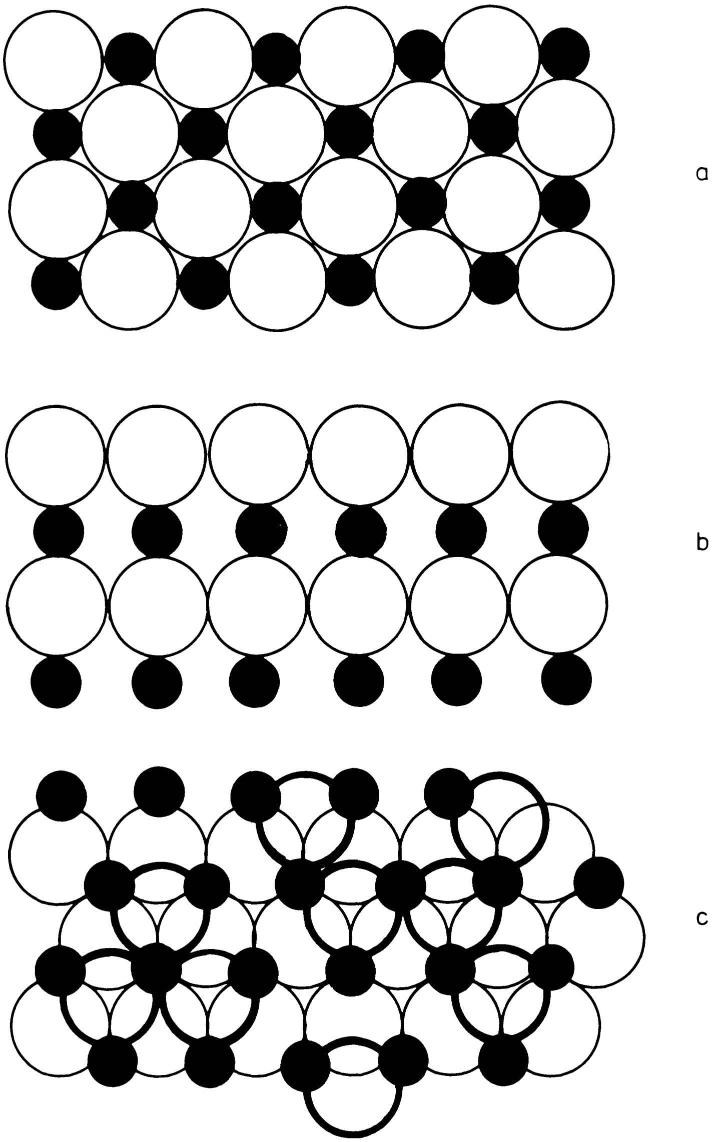

FIGURE 3.1 Geometric arrangement of atoms at different faces of MgO. (a) (100) plane; (b) (110)plane; (c) (111) plane. Large open circles O^{2-}, small shaded circles Mg^{2+}. In (c) large circles traced with a thick line denote O^{2-} anions in the most external plane, only half of which is filled with atoms.

a way that in each octahedron three oxygen atoms are common for three different octahedra as it is seen in the section of the layer along the b plane [3] (Fig. 3.2a). In the direction perpendicular to the sheet of paper (direction of axis a) each octahedron shares two oxygen atoms with two neighboring octahedrons, one before the sheet of paper and another on the other side of the sheet. One oxygen atom is coordinated to only one Mo atom (doubly bonded M=O oxygen atom). The resulting structure contains stoichiometric composite layers with two simple layers of octahedra labeled as m and n in Fig. 3.1a. The neighboring layers parallel to the (010) plane are kept together by weak intermolecular forces and hence it is reasonable to assume that on cleaving the crystal along this plane the layers will separate, exposing their surface as shown in Fig. 3.2b. In this figure the octahedra belonging to the most external sublayer, say sublayer m, are drawn with a thick line and those belonging to sublayer n with a thinner one. On such a surface there are no exposed Mo atoms and three different positions of oxygen atoms are seen. Position 1 is occupied by the most external O atom exhibiting coordination number 1. Somewhat deeper are situated O atoms in positions 2 and 3, the former being common for two octahedra of sublayer m, the latter for two octahedra of sublayer m and one octahedron of sublayer n. Ziółkowski attempted to characterize the oxygen atoms in particular positions by calculating the sum of Pauling's strength of bonds [4] $\Sigma \underline{s}_i$ between a given oxygen atom and the adjacent cations. The values $\Sigma \underline{s}_i = 2.04$, 1.90, and 1.98 were obtained for O_1, O_2, and O_3 oxygen atoms, respectively, suggesting that the most weakly bonded O atom is in position 2 and the most strongly bonded in position 1 (doubly bonded O atom).

Ziółkowski's approach is an attempt not only to give a geometric model of the surface but also to differentiate oxygen atoms at the surface of an oxide and to anticipate their reactivity in the course of catalytic oxidation reactions. However, when considering all such models based on the known crystallographic structure of an oxide, it should be kept in mind that the model concerns an ideal surface and the properties of real surfaces may be very different. First of all, owing to the diminished coordination of surface atoms a reorganization of the surface may occur. The so-called exposed metal atoms must in fact be retracted so as to be optimally coordinated by neighboring oxygen atoms. The surface layer of each crystal is also usually considered to be compressed in some measure owing to the asymmetry of forces at the surface.

The direct verification of surface models deduced by the extrapolation of bulk structure is still difficult. The low-energy electron diffraction (LEED) which has been frequently applied for the study of the surface of metals until the present was seldom used for the study of oxide surfaces. Existing information indicates the

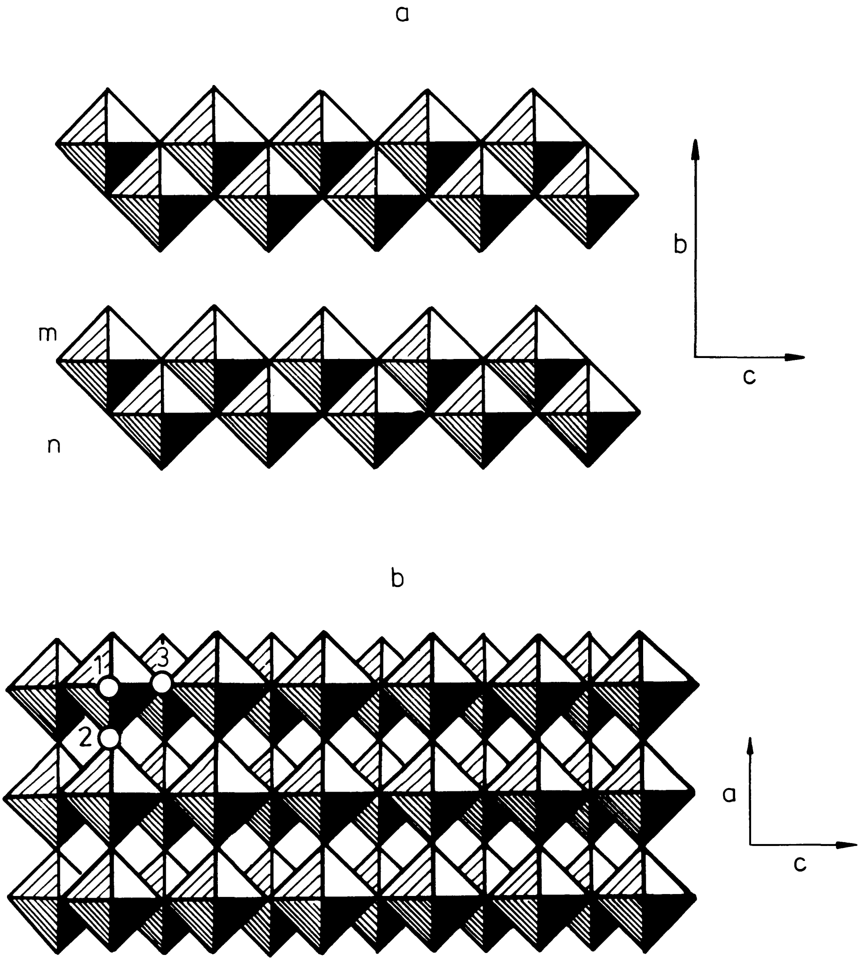

FIGURE 3.2 Structure of MoO_3. (a) Composite layers of [MoO_6] octahedra (section perpendicular to the direction of axis a); (b) (010) plane. The most external octahedra are shown by thick lines (m sublayer), those belonging to the next sublayer (n) by thin lines. 1, Position of an O atom singly coordinated at the surface; 2, doubly coordinated; and 3, triply coordinated.

existence of various possible states but does not allow formulation of a general conclusion. Using this method French and Somorjai [5] showed that the structure of the (0001) face of Al_2O_3 at the surface was distinct from that of the bulk, that the surface layer was oxygen-deficient, and that the aluminum atoms were in a reduced valence state. The composition of the surface layer corresponded to the formula AlO_2 (or AlO). The reconstruction of the (0001) face of ZnO obtained by cleaving a monocrystal was stated after annealing it above 600°C [6]. In particular, a freshly prepared surface has shown a (1 × 1) structure which changed into an overstructure ($\sqrt{3} \times \sqrt{3}/30°$). These experiments show that the reconstruction of the already stabilized surface is possible in some cases. However, surfaces (1010) and (1120) were found to be unreconstructed. The LEED investigations suggested also the presence of regular step arrays on the (0001) cleaved surface appearing after heating at 400°C. They were oriented in three of the six preferential directions and the step height corresponded to two double layers.

The other factors influencing the properties of the real surfaces of oxides are the presence of different lattice defects in the surface layer and its chemical composition, which in many cases may be different from that of the bulk. The most obvious defect is the surface itself with its coordinatively nonsaturated atoms. The presence of the so-called dangling bonds at the surface creates electron energy states, usually named intrinsic states, which are considered to be present even in the case of a pure and strictly stoichiometric surface. On the other hand, the structural defects on the surface or adsorbed impurities create the extrinsic surface states.

The role of intrinsic defects in catalysis has not yet been elucidated. The physics of such defects is still in development. In contrast, the influence of extrinsic defects on chemisorption and catalysis was the object of many investigations.

Crystals with perfect periodical arrangement of all structural elements cannot exist and real crystals show the presence of various imperfections, described as defects of the crystal structure [7]. They are due to the displacement of atoms from the lattice sites, normally occupied by these atoms, into other sites or interstitial positions, the presence of some vacant sites, the displacement of part of the crystal with respect to the other part along a crystal plane, etc. These defects are usually classified according to their dimensions into point defects (vacancies, interstitial or foreign atoms), linear defects (dislocations), flat defects (shear planes and various internal and external grain boundaries), and spatial defects such as pores or foreign inclusions.

From the thermodynamic point of view ideal, crystal can exist only at absolute zero temperature. At every other temperature thermal oscillations of atoms result in the formation of various kinds of point defects because the thermodynamic potential of the defective crystal becomes smaller than that of the ideal one.

The concentration of structural defects in transition metal oxides is dependent on both the pressure of oxygen and temperature. At sufficiently low temperature their creation and vanishing is limited only to the surface layer. At high temperatures the equilibria are established between the defects at the surface, the defects in the bulk, and the gaseous oxygen, which will be discussed in Section IV of this chapter. Here we shall deal only with the effects limited to the surface. In the case of zinc oxide, which can be taken as an example of an n-type semiconducting oxide, slow decomposition localized to the surface layer and resulting in the desorption of oxygen begins in vacuo at 375°C [8]. Zinc atoms, the desorption of which is negligible and diffusion into the bulk very slow, remain in the near-surface layer as interstitial excess atoms forming electron donor centers. The processes can be represented by the following equations expressed with Kröger-Vink symbols:

$$\mathrm{ZnO} \rightleftarrows (\mathrm{Zn_i})_s + \frac{1}{2}\mathrm{O_2} \tag{3.2}$$

Subscript s denotes atoms in the surface layer. The neutral interstitial zinc atoms $(\mathrm{Zn_i})_s$ can supply free electrons e^-, thus increasing the electrical conductivity of the surface layer:

$$(\mathrm{Zn_i})_s \rightleftarrows (\mathrm{Zn_i^{\bullet}})_s + e^- \tag{3.3}$$

In ZnO the formation of defects is enhanced by the treatment of the oxide in vacuo. On the other hand, in the case of p-semiconducting oxides the formation of point defects is favored by increasing oxygen pressure. A typical example is nickel oxide, which when stoichiometric chemisorbs oxygen with the formation of acceptor centers in the form of neutralized cationic vacancies V_{Ni}:

$$\frac{1}{2}\mathrm{O_2} \rightleftarrows (\mathrm{O_O})_s + (V_{\mathrm{Ni}})_s \tag{3.4}$$

$$(V_{\mathrm{Ni}})_2 \rightleftarrows (V'_{\mathrm{Ni}})_s + h^{\bullet} \tag{3.5}$$

The neutral $(V_{\mathrm{Ni}})_s$ center consists of a cationic vacancy which formally bears two negative charges and two $\mathrm{Ni^{3+}}$ ions (positive holes $h^{\bullet}$) localized in the nearest vicinity. The dissociation of $(V_{\mathrm{Ni}})_s$

represented by (3.5) consists of the formation of a free positive hole which is an electric current carrier. The presence of Ni^{3+} ions in the surface layer of NiO preparations was established in the analytical way by Dereń et al. [9], who also stated qualitatively that the black preparation turned to green, the color of stoichiometric NiO, after treatment with hydrochloric acid to remove the nonstoichiometric black external layer of the grains containing an excess of oxygen. Recently, Finster et al. [10], using XPS measurements to investigate NiO samples obtained by the calcination of $Ni(OH)_2$ in air at 220–1000°C, observed a noticeable amount of Ni^{3+} ions in the surface layer the concentration of which increased with the calcination temperature. Simultaneously the concentration of Ni^{3+} in the bulk of NiO crystallites decreased as determined by chemical analysis and the bulk of green samples calcined at 1000°C were stoichiometric. The method applied in this work also enabled the characterization of the state of oxygen atoms in the samples. The O1s line in the XPS spectrum was composed of two components at 529.3 and 531.3 eV. The lower peak was assigned to the lattice oxygen and the higher one to surface or adsorbed species (surface excess oxygen or OH^- groups).

In recent years important information concerning the chemical composition of the surface layer of mixed oxides was gathered mainly due to the photoelectron (XPS and UPS) and Auger electron (AES) spectroscopic investigations. It appears that frequently the surface composition of such oxides is different from that of the bulk. This may be the effect of the tendency of surface energy to reach a minimum, and in such a case enrichment of the surface in one of the components would correspond to an equilibrium state. However, the accumulation of one component at the surface may also be a metastable state reached as a result of some kinetic factors.

Grzybowska et al. [11] using XPS investigated the changes in surface composition of bismuth molybdates Bi_2MoO_6, $Bi_2Mo_2O_9$, and $Bi_2Mo_3O_{12}$ provoked by various treatment of the samples. The ratios of intensities of Bi $4f_{7/2}$ and Mo $3d_{5/2}$ peaks to the intensity of the O1s peak have been taken as the relative measure of the concentration of bismuth and molybdenum in the surface layer. Figure 3.3 shows that the fresh samples outgassed at 120°C exhibited the highest content of bismuth, which decreased linearly with the decreasing bulk content of this element (line IA). The fact that this straight line also includes the point corresponding to pure Bi_2O_3 strongly suggests that in this series of samples surface and bulk compositions are the same. Simultaneously the surface content of molybdenum increased linearly as shown by line IIA on which also lies the point which corresponds to pure MoO_3. Now the prolonged heating of the samples in vacuo at 470°C resulted in a distinct increase of the surface concentration of molybdenum as shown

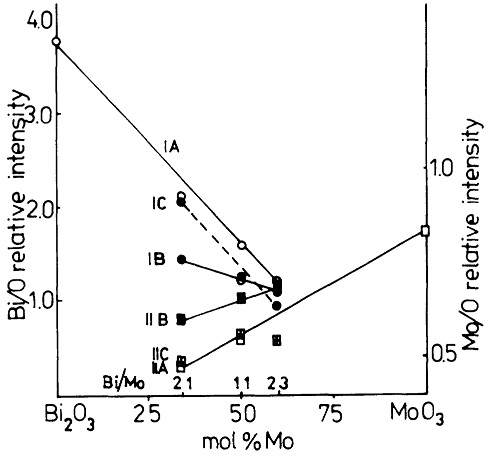

FIGURE 3.3 Relative intensities of XPS peaks Bi 4f 7/2 (I) and Mo $3d_{5/2}$ (II) with respect to the O1s peak in bismuth molybdates [11]. (A) Initial samples outgassed at 120°C, 3 hr, 10^{-8} Torr. (B) After heating the samples in vacuo at 470°C, 10 hr. (C) After treatment of the samples with a mixture of C_3H_6, O_2, and N_2 in molar ratio 23:21:55, 440°C, 5 hr.

by line IIB, the effect being most pronounced in the case of Bi_2MoO_6 sample. The heating of the samples at 440°C in the mixture of propylene, oxygen, and nitrogen resulted in a somewhat different adjustment of the surface composition to the redox potential of the gas phase.

Similar changes in the near-to-surface layer in V_2O_5-MoO_3 solid solutions in the course of the oxidation and reduction of the sample which were observed by Bielański and Najbar [12-14] will be reported in detail in Chapter 8.

Another example of surface enrichment in one component in double oxides was given by Aso et al. [15] who investigated Fe_2O_3-Sb_2O_4 catalysts using XPS. Figure 3.4 shows the ratio of Sb $3d_{3/2}$ and Fe $2p_{5/2}$ peaks as the function of the average composition of the sample. Empty circles indicate the results obtained for mechanical mixtures of Sb_2O_4 and Fe_2O_3, full circles those for the investigated samples obtained by heating for 2 hr of intimate mixtures of $Fe(NO_3)_2$ and Sb_2O_3. It is seen that below Sb/Fe atom ratio 1 the surface compositions of the catalyst samples were practically the same as the bulk compositions. However, at about Sb/Fe = 1 a sudden increase in the concentration of antimony occurred at the surface and increased still further with an increasing total content of Sb. In a later paper Aso et al. [16] studied Fe_2O_3-Sb_2O_4 catalyst

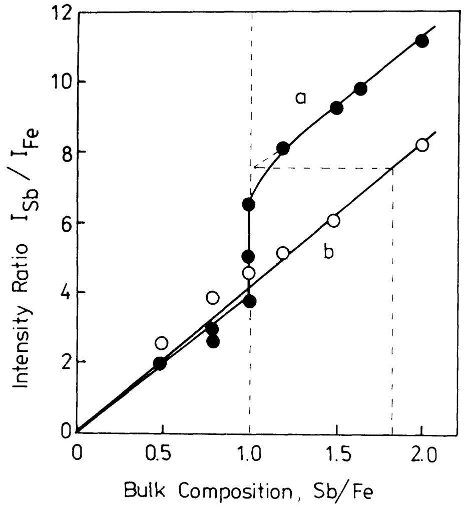

FIGURE 3.4 Correlation between XPS intensity ratio and the bulk composition for (a) catalyst samples and (b) mechanical mixtures of Fe_2O_3 and Sb_2O_4 [15].

with ^{18}O adsorbed using secondary ion mass spectrometry (SIMS). They showed that oxygen is preferentially adsorbed on Sb surface atoms, which is a plausible explanation of the fact that Fe_2O_3-Sb_2O_4 catalysts containing an excess of Sb over $FeSbO_4$ composition exhibit an increased selectivity in the catalytic oxidation of propene to acroleine.

From the catalytic point of view, not only is the geometric structure of the surface of oxide catalyst and its chemical composition important but also the chemical behavior of the coordinatively unsaturated surface atoms, especially those which constitute the catalytically active centers. They are frequently studied by observing the behavior of some adsorbed molecules playing the role of molecular probe [17]. Depending on the kind of probe molecules, acid and basic and also redox centers can be detected at the surface.

Valuable information was obtained, e.g., by IR studies of the adsorption of water molecules on different oxides. H_2O molecules when chemisorbed may either be coordinated to the exposed surface cations $(M_M)_s$, thus forming an adsorption complex H_2O-$(M_M)_s$:

$$H_2O_g + (M_M)_s \rightarrow H_2O\text{-}(M_M)_s \tag{3.6}$$

or, as already mentioned, undergo dissociation at a surface vacancy:

$$(O_O)_s + (V_O)_s + H_2O_g \rightarrow 2(OH_O)_s \tag{3.1}$$

Weak bonding of H_2O molecules by intermediation of the hydrogen bond is less important for catalysis. The properties of surface OH groups on various oxides were discussed frequently in the literature [1,17] as the hydroxylation of oxide surfaces seems to be a rather common effect. The studies of hydroxylated alumina and also of Cr_2O_3, TiO_2, MgO, ZnO, and SiO_2-Al_2O_3 are the most notable examples.

Alumina surfaces of the preparations exposed to water vapor at temperatures above 100°C are covered by hydroxyl groups. If subsequently outgassed at 800°C, five OH stretching bands at 3800, 3780, 3744, 3733, and 3700 cm^{-1} appear in the IR spectrum. Based on this observation, Peri [18] developed a model of the γ-Al_2O_3 surface. He assumed that the (100) plane is exposed predominantly and that there are OH groups in five different positions in the most external layer of the oxide which initially contained only OH groups. According to Peri, after calcination this layer contains OH groups, O^{2-} anions as well as anionic vacancies, the two latters created in the reaction reverse to Eq. (3.1). He postulated that the highest stretching frequency 3800 cm^{-1} corresponded to the situation in which the OH group was situated between four O^{2-} ions; the following frequencies 3780, 3744 and 3733 were attributed to OH groups exhibiting coordination numbers 3, 2, and 1 with respect to O^{2-} ions in the same plane. Such a situation is shown in Fig. 3.5. The lowest frequency 3700 cm^{-1} corresponded in this model to the OH groups having no O^{2-} in the immediate vicinity of the same plane. Peri suggested that the latter OH group was the most acidic and the tetracoordinated (3800 cm^{-1}) OH the least acidic. However, Dunken and Fink [19] when discussing the results of H_2-D_2 isotopic exchange concluded that the highest acidity should be attributed to OH groups tetracoordinated in the surface plane and that the sequence of surface coordination proposed by Peri should be reversed. Thus the assignment of the OH bands is still ambiguous. Knötzinger in his review [17] indicates that the assumption of the (100) face forming predominantly the surface of γ-Al_2O_3 is probably the weakest point in Peri's model and argues that the occurrence of various exposed crystal planes which would offer different local environments for surface OH groups appears likely for polydisperse materials such as the transitional aluminas. He observed also that OH stretching bands very similar to those in γ-Al_2O_3 were also registered in the case of η and δ aluminas. Since

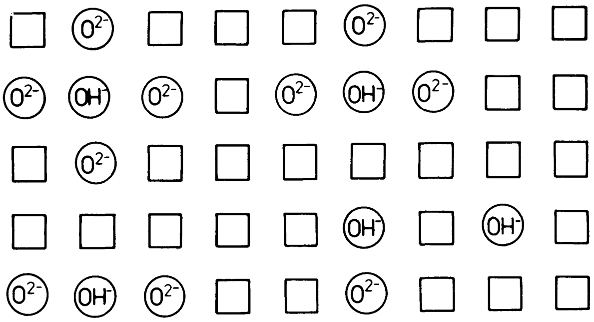

FIGURE 3.5 Different environments of surface OH groups on γ-Al_2O_3 postulated in the model proposed by Peri. Circles represent O^{2-} and OH^- ions in the most external layer of the oxide; squares indicate the positions of O^{2-} ions in the next deeper lattice plane.

equal numbers of OH stretching bands and nicely comparable frequencies were obtained, one may conclude that the respective OH groups reside in comparable local environments on the surface of the three modifications of alumina. The stabilization of comparable surface layers irrespective to the bulk structure may be the reason for this.

As already mentioned, the hydroxylation of the surface of the oxides in the presence of water vapor is a rather common phenomenon. In extreme cases hydroxyl groups may cover the surface forming a complete monolayer. On heating dehydroxylation occurs with the formation of surface anionic vacancies, thus creating the sites which may be preferential for adsorption of other species and among them for the adsorption of oxygen.

It should here be observed that in both reactions (3.6) and (3.1) water molecules are playing a dual role of Lewis base and Brönsted acid. In the former reaction the H_2O molecule is an electron pair donor, behaving as the Lewis base reacting with surface cation functioning as Lewis acid. In reaction (3.1) the water molecule, behaving as a Bröonsted acid, donates a proton to the O^{2-} ion, which is a strong Bröonsted (and also Lewis) base. As was mentioned in Chapter 2, O_s^{2-} often plays an important role as nucleophilic reagent participating in many catalytic oxidation reactions in which oxygen from the lattice of an oxide is inserted into an electrophilic molecule of reagent or an electrophilic reaction intermediate. Surface OH ions, being a weaker base than O^{2-} ions, presumably do not play an important role in oxidation catalysis. On the other hand, OH groups covalently bonded to nonmetal atoms are in many cases strong Brönsted acids catalytically active in numerous acid-base reactions. The surface of an oxide therefore represents an array of acidic and basic centers of the Brönsted as well as the Lewis type. Brönsted acids are formed by covalently bonded OH groups, Brönsted bases by O^{2-} and OH^- ions. Lewis acids by surface cations, and Lewis bases by O^{2-} ions.

From the point of view of oxidation catalysis, of great importance is the presence on the surface of the oxides of redox centers, which may accept or donate odd electrons. This problem was already tackled in Chapter 2, where the possible role of O^{2-} surface ions as one-electron-donor centers was discussed. The same function can also be fulfilled by metal atoms in low oxidation state, e.g., by Co^{2+} ions in CoO or Ni^{2+} in NiO. On the other hand, metal atoms in high valence state, e.g., V^V in V_2O_5, are electron acceptors or, in other words, oxidation centers. Redox centers are frequently connected with the presence of lattice defects in the surface or in the near-to-the-surface layer of the oxides.

III. CHEMISORPTION OF OXYGEN ON TRANSITION METAL OXIDES

Chapter 2 discussed the forms of oxygen chemisorbed on transition metal oxides. In this section the process of adsorption itself and the changes in the most external layers of the solid adsorbent accompanying oxygen chemisorption are discussed.

As previously stated, oxygen is always chemisorbed in the form of species bonded to the surface by a bond exhibiting a high degree of ionicity. This implies the presence in the solid of centers which can supply electrons to the neutral O_2 molecule. Such centers exist in the semiconducting oxides (or the oxides with metallic-type conductivity, which is a much rarer case) and are not present in the oxides which are insulators. The role of donor centers may be played by different lattice defects present in the surface layer and frequently connected with the deviation from the stoichiometry such as the interstitial Zn atoms in ZnO or V^{4+} and V^{3+} in slightly reduced V_2O_5. Such defects appear in n-type semiconducting oxides as the result of even slight reduction. The same effect can be obtained by vacuum treatment of the samples at appropriate temperatures. Oxygen is also chemisorbed on p-type semiconducting oxides containing cations in a low oxidation state which can be easily oxidized by giving off electrons. As examples, the oxides of cobalt and nickel (CoO and NiO) can be mentioned. In all of these cases the transfer of electrons from the solid to the neutral adsorbed oxygen molecule (or atom) forming the surface acceptor level is only possible if the energy of this level $\underline{E}_{\overline{O}}$ is situated on the energy diagram, such as in Fig. 3.6, below the Fermi level of the solid.

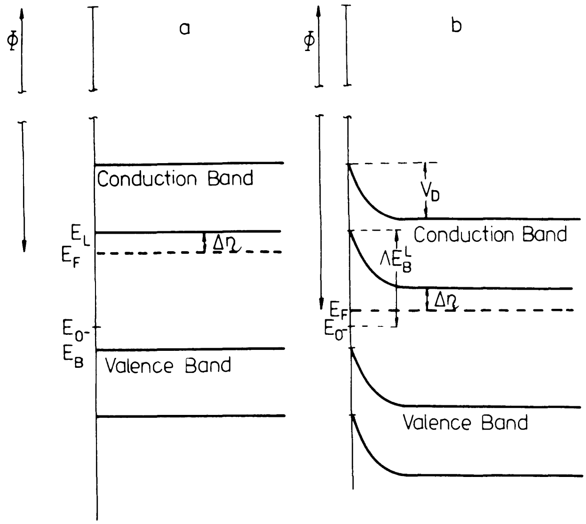

FIGURE 3.6 Energy band scheme of a semiconductor chemisorbing oxygen. (a) Before the transfer of electron, (b) after the transfer of electrons from the solid to the adsorbate. $\underline{E}_F$, Fermi level; $\underline{E}_O$, energy of the surface acceptor level (chemisorbed oxygen molecule or atom); Φ, electrical work function.

Adsorption of oxygen, e.g., as an O_2^- species on an n-type semiconducting oxide, can be represented as

$$O_{2(g)} + e^- \rightarrow O^-_{2(ads)} \tag{3.7}$$

and on a p-type one as

$$O_{2(g)} \rightarrow O^-_{2(ads)} + h^{\bullet} \tag{3.8}$$

where e^- denotes free electron and $h^{\bullet}$ free positive hole in the oxide. Hence supplying of the electrons to the adsorbate by n-type semiconducting oxides is always connected with a decrease of the concentration of free electrons, the predominant current carriers. On the other hand, in the case of p-semiconducting oxides chemisorption of oxygen results in an increase of the concentration of positive holes. The concentration of electrons available for chemisorption of oxygen is much smaller in semiconductors than in metals and hence in the oxides the electrons are given off not only from the surface but also from a layer adjacent to the surface called the Randschicht, the thickness of which is estimated to be 10^{-5} to 10^{-4} cm. In the Randschicht depleted of electrons positive space charge develops, neutralizing the negative charge of chemisorbed oxygen and thus forming an electrical double layer. In the measure as this charge develops an energetic barrier V_D (Fig. 3.6b) is growing which renders the extraction of electrons from the solid increasingly difficult. This results in an increase of the electrical work function Φ. Assuming the energy of an electron in vacuo as equal to zero, one can write according to the band theory of solids:

$$\Phi = -eE_F \tag{3.9}$$

Hence the observed increase of the work function is equivalent to the decrease of Fermi level as shown in Fig. 3.6b. The position of the Fermi level with respect to the conduction and valence bands does determine the concentrations of current carriers: free electrons and holes. These concentrations do not change in the bulk of the semiconductor and the position of the Fermi level with respect to the energy bands there remains unchanged. On the other hand, the decrease of free electron concentration in the Randschicht as well as the increase of free electron holes concentration results at the surface in downwards shifting of Fermi level with respect to the energy bands. Such a situation necessitates a bending of the energy bands in the Randschicht as shown in Fig. 3.6b. It is also seen in this figure that the transfer of electrons to the chemisorbed molecules is accompanied by a decrease of the distance between the Fermi level and the energy level E_O of electrons trapped by adsorbate molecules or atoms. The decreasing value of $(E_F - E_O)$ results in a slowing down of the electron transfer rate.

It is evident that in cases where the E_O level reaches a value equal to E_F, the rate of electron transfer will become zero and chemisorption of oxygen will stop even before all available donor centers in the oxide are ionized. According to Hauffe and Morrison [20], the Langmuir adsorption isotherm must then be modified and should be expressed in the form:

$$\Gamma_B = \Gamma_0 \frac{KP_B\rho}{1 + Kp_B} \tag{3.10}$$

where Γ_B denotes the concentration of adsorbed acceptor molecules B, in our case the surface concentration of adsorbed oxygen species, and $\rho = \exp[-(\Delta\eta + eV_D - \Delta E_B^L)kT]$. K is the adsorption coefficient and the meanings of $\Delta\eta$, V_D, and ΔE_B^L are given in Fig. 3.6.

All the above-mentioned processes are broadly discussed by Wolkenstein [21] and Hauffe [22] in their electronic theory of chemisorption and catalysis on semiconducting catalysts. The most frequently used methods of investigation of such electronic processes accompanying chemisorption of oxygen are measurement of the electrical conductivity of polycrystalline samples and measurement of changes in the electrical work function.

In the case of polycrystalline samples the changes in conductivity are governed by the conductivity of the surface layers. In the case of n-type semiconducting oxides the surface layer is depleted of current carriers—free electrons—and the conductivity decreases. On the other hand, if oxygen is adsorbed on p-type semiconducting oxides, the surface layer becomes enriched in the electron holes, which in this case are the predominant current carriers, and the semiconductivity increases. In both cases of n- and p-type semiconducting oxides chemisorption of oxygen acceptor molecules is accompanied by the increase of electrical work function (Fig. 3.6). It should here be observed that the chemisorption of molecules behaving as electron donors, e.g., hydrogen molecules, is accompanied by effects opposite those of the chemisorption of oxygen or other acceptor molecules. Donor molecules when chemisorbed are positively charged, in the Randschicht a negative space charge develops, energy bands in the Randschicht bend downward, Fermi level shift upward, and electrical work function diminishes.

As was stated, the formation of negatively charged adsorbed oxygen species does result in the formation of an electrical double layer. On the other hand, the incorporation of such species into the oxide lattice results in vanishing of the space charge. In the case of highly dispersed nickel oxide [23] at room temperature, oxygen is adsorbed mainly as the O^- species:

$$\frac{1}{2}O_{2(g)} \rightarrow O^-_{(ads)} + h^{\bullet} \tag{3.11}$$

The positive holes are nickel ions which have lost one electron each, i.e., Ni^{3+} ions. At room temperature slowly, but much faster at temperatures as high as 235°C, O^- ions are turned into O^{2-} incorporated into the external layers of the NiO crystallites.

$$O^-_{ads} = NiO + V^{11}_{Ni} + h^{\bullet} \tag{3.12}$$

It is seen from this equation that the incorporation of one O adsorbed species into the crystal lattice (O^{2-} in an anionic position) is equivalent to the introduction of one negative charge into the Randschicht which results in the vanishing of the positive space charge. Equation (3.12) also shows that in the Randschicht an excess of anions over cations is present. The external layer of crystallites became nonstoichiometric. At high enough temperatures diffusion of vacancies into the bulk takes place and their concentration in the whole crystallite becomes uniform. The incorporation of adsorbed oxygen into the NiO lattice was studied by Dereń and Nowotny [24] and Nowotny [25]. They measured the changes in the value of Φ accompanying the chemisorption of small doses of oxygen (10^{-3} to 10^{-2} of the monolayer coverage) on nickel oxide standardized at 400°C in oxygen and then outgassed for 1 hr at the same temperature (10^{-6} Torr). Chemisorption of oxygen at 400°C was rapid (Fig. 3.7) and, in the case of initials doses, was practically complete after 5—10 min. Rapid chemisorption was accompanied by a rapid increase of the work function Φ, which indicated the formation of a positive space charge in the Randschicht. However, the work function soon reached maximum and then decreased when practically the whole dose of oxygen had been adsorbed. These observed changes in the work function clearly illustrate both chemisorption of oxygen and its incorporation into the lattice. The final value after the first incorporation and the second cycle (10^{-3} and 10^{-2} of the monolayer coverage, respectively) was practically the same as before chemisorption. However, after the third and following cycles it was higher than the initial one. This was the result of an increasing concentration of cationic defects V_{Ni} in the surface layer that formed acceptor levels, lowering, according to the band theory of solids, the position of the Fermi level.

An analogous process accompanying chemisorption of oxygen on n-type semiconducting zinc oxide was observed by Amigues [26], who measured the changes in electrical conductivity. After an initial distinct drop in the conductivity (depletion of electrons from the Randschicht and formation of positive space charge) a minimum was observed followed by an increase in conductivity which was due to the building up of new layers of ZnO lattice. Similar results were also obtained by Fryt [27].

All these processes, including the transformations of adsorbed oxygen species, hampering adsorption by the development of the barrier of electrical potential, and the incorporation of oxygen into the oxide lattice accompanied by the inward or outward diffusion of defects, are rather complicated. Owing to their overlapping, the chemisorption of oxygen on transition metal oxides at the temperatures of catalytic reactions is often nonreversible or only partly reversible, and heating in vacuo to still higher temperatures is frequently necessary to desorb all chemisorbed oxygen. This is the reason why it is rarely possible to observe a true thermodynamic, reversible equilibrium of chemisorbed oxygen with oxygen in the gas phase. Chemisorption equilibrium of oxygen on transition metal

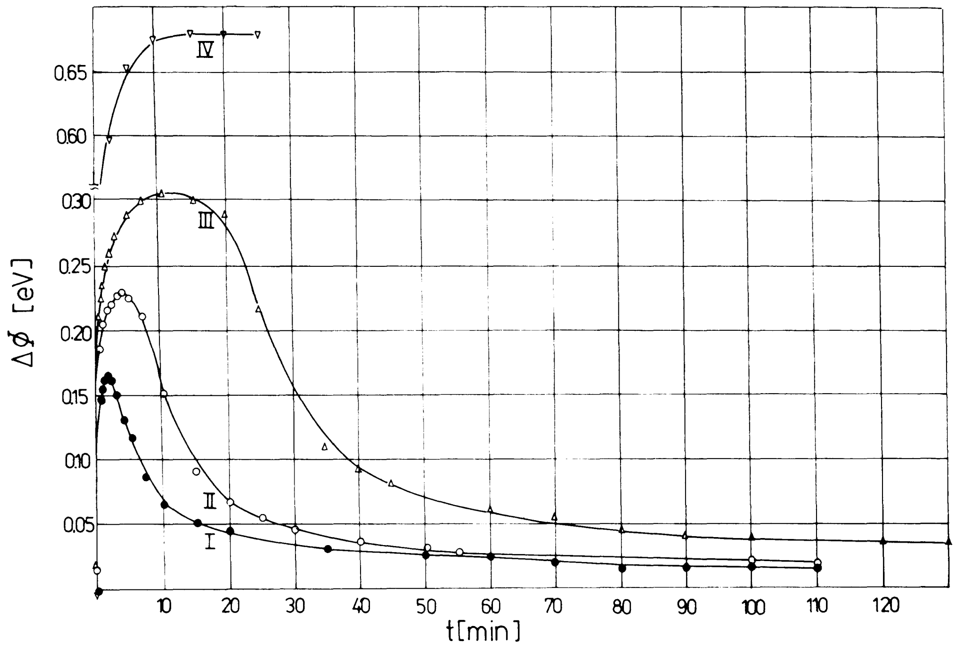

FIGURE 3.7 Changes in work function as a function of time for pure NiO at 400°C. I, first cycle; II, second cycle; III, third cycle; IV, under constant oxygen pressure of 1 mm Hg [25].

oxides is frequently inferred from the shape of the adsorption isobar such as that in Fig. 3.8 [28]. The descending portion of the curve above 300°C is reversible and corresponds to the adsorption equilibrium states while the low-temperature ascending branch is irreversible and corresponds to the nonequilibrium metastable states. Thermodynamic equilibria between oxygen in the gas phase, chemisorbed oxygen, and the bulk of the oxide were studied by many authors at much higher temperatures, e.g., in polycrystalline NiO at 800–1200°C [29]. However, although the reversibility condition is fulfilled, the experimental discrimination between oxygen adsorbed and that incorporated into the lattice is not possible.

The lack of experimental data to enable the calculation of free enthalpy changes ($\Delta \underline{G}_a$) accompanying chemisorption of oxygen under conditions of catalytic reaction is the reason why in practice only the adsorption heat is taken as a measure of the tendency to get chemisorbed at the surface of transition metal oxides. This is also justified by the fact that in the equation $\Delta \underline{G}_a = \Delta \underline{H}_a - T \Delta \underline{S}_a$ the absolute value of the entropy term in adsorption processes is usually much smaller than that of the enthalpy term.

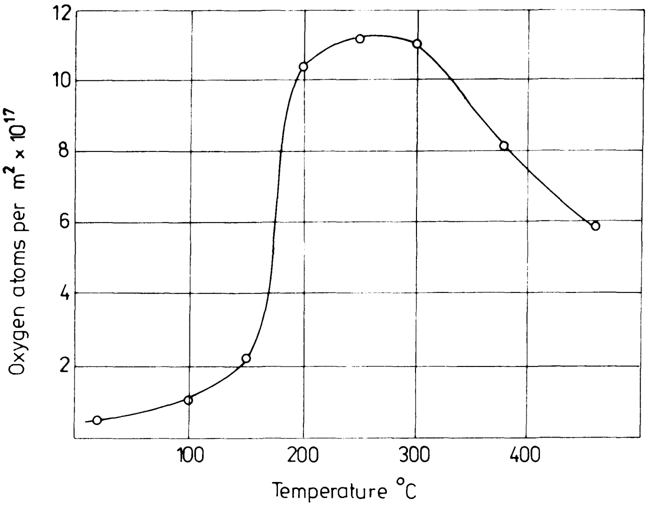

FIGURE 3.8 Isobar of oxygen adsorption on nickel oxide; $p = 6.10^{-2}$ Torr [28].

Several factors determine the value of chemisorption heat ΔH_a of oxygen adsorbed on transition metal oxides. When oxygen is adsorbed as an O_2^- species, ΔH_a can be calculated as the sum of enthalpies of the following sequence of elementary steps:

$$\text{Solid} \rightarrow \text{solid}^+ + e^-$$

$$O_{2(g)} + e^- \rightarrow O^-_{2(g)}$$

$$O^-_{2(g)} + \text{solid}^+ \rightarrow [O_2^- - \text{solid}^+]$$

The enthalpy of the first process is equal to the work function of the solid, that of the second process equal to the negative value of electron affinity E_{O_2} of the O_2 molecule. The enthalpy of the last process is that of the bond between O_2^- species and the surface atom or atoms constituting the adsorption center ΔH_B:

$$\Delta H_a = \Phi - E_{O_2} + \Delta H_B \qquad (3.13)$$

If oxygen is adsorbed dissociatively in the form of O^- species, an elementary step corresponding to the dissociation of the O_2 molecule must be included:

$$\text{Solid} \rightarrow \text{solid}^+ + e^-$$

$$\frac{1}{2}O_{2(g)} \rightarrow O_{(g)}$$

$$O_{(g)} + e^- \rightarrow O^-_{(g)}$$

$$O^-_{(g)} + \text{solid}_+ \rightarrow [O^- - \text{solid}^+]$$

Denoting the dissociation energy of O_2 as $\underline{D}_{O_2}$ we can write:

$$\underline{H}_{ads} = \Phi + \frac{1}{2}\underline{D}_{O_2} - \underline{E}_O + \Delta\underline{H}_B \tag{3.14}$$

In both Eqs. (3.13) and (3.14) the terms characterizing the properties of the oxygen molecule and atom ($\underline{E}_{O_2}$, $\underline{E}_O$, and $\underline{D}_{O_2}$) are constant. The value of $\Delta\underline{H}_B$ is largely determined by the nature of the atom or atoms constituting the adsorption center and depends mainly on local interactions. On the other hand, the value of Φ characterizes collective electronic properties of the solid and there is no direct correlation between both factors $\Delta\underline{H}_B$ and Φ. The effect of the electronic factor in chemisorption (and catalysis) can best be studied using a series of samples of an oxide doped with different amounts of the dopant changing the position of the Fermi level—examples of such studies will be presented in Chapter 5—or studying the kinetics of chemisorption. In all these cases the nature of the bond in the adsorption complex does not change and in Eqs. (3.13) and (3.14) the changes in Φ determine the changes in $\Delta\underline{H}_{ads}$.

When comparing different oxides one should principally take into account changes in both Φ and $\Delta\underline{H}_B$. However, this is not an easy task. The data concerning the electrical work function of particular transition metal oxides, both simple and mixed, and much more frequently used as catalysts, are not complete and, owing to the dependence of the measurements on experimental conditions and the state and nature of reference electrodes, the correlations based on the existing values do not seem to be very trustworthy. Also $\Delta\underline{H}_B$ is not liable for the direct determination. In this situation many attempts were undertaken to characterize and compare the behavior of different oxides by determining in some experimental way the enthalpy of oxygen chemisorption $\Delta\underline{H}_{ads}$, also called oxygen bonding strength. These investigations will be described in detail in Section VI of this chapter.

Since the early 1960s there has been an increasing tendency to represent in the literature chemisorption on transition metal oxides, and in particular chemisorption of oxygen, as an essentially local phenomenon, i.e., the result of interactions between the ad-molecule and the adsorption center with the exclusion of the participation of delocalized free current carriers, electrons, and holes, as postulated by the electronic theory of chemisorption on semiconductors. In such a model electrons are supplied to the adsorbed molecules not from the energy bands but from the cations constituting adsorption centers, and their ionization energy is used as a value characterizing local properties instead of as an electrical work function characterizing collective properties of the solid. This approach was originated by Dowden and Wells [30], who suggested that chemisorption on surface cations in transition metal oxides can be interpreted in terms of coordination chemistry, in particular in terms of crystal field theory assuming that adsorption is equivalent to the addition of a new ligand to a coordinatively unsaturated surface atom. As stated in Section II, the coordination of a surface cation on the (100) face of a crystal exhibiting an NaCl (e.g., NiO) structure is 5, on the (110) face is 4, and on the (111) face is 3. These situations are presented once more in Fig. 3.9 [28], where the middle column represents the (100), (110), and (111) surfaces as they appear at the instant of cleavage. The relaxation of such surfaces results in the small shifts of Ni^{2+} ions tending to occupy positions in which they are uniformly surrounded by the oxygen ions. In the case of the (100) face Ni^{2+} enters a square pyramid depicted in the left column; in the case of the (110) and (111) face it enters a tetrahedron and a triangle, respectively. In the (100) face one additional atom can be coordinated to the surface cation, thus increasing the coordination number to 6; in (110) one or two atoms, increasing the cation coordination number to 5 or 6, respectively; and in the (111) face, one, two or three atoms increasing the coordination number to 4, 5, or 6, respectively. The situation after completing the coordination number to 6 is depicted in the right column in Fig. 3.9. In each case the change in coordination number is accompanied by the change in the crystal field stabilization energy (CFSE) as is shown in Table 3.1. The values of CFSE are expressed in Dq units and correspond to the weak field of the ligands, which is the case in transition metal oxides. Taking into account the values of 10 Dq determined for particular oxides of transition metals, Dowden and Wells calculated the absolute values of the changes in CFSE, which are given in Table 3.2. Negative values of $\Delta \underline{E}_c$ correspond to the increasing stability. It is seen that the contribution of the changes in CFSE to the chemisorption heat in particular cases are as high as about 40 kcal mol^{-1} but they are zero for d^0, d^5, and d^{10} cations.

Chemisorption of oxygen restoring, say, coordination number 6 on the surface of crystals exhibiting NaCl structure results in different changes of CFSE on different faces. In the case of CoO the

TABLE 3.1 Crystal Field Stabilization Energies E_c of Various Configurations of d-Electron Cations Expressed in D_q Units (Weak Field Approximation)

Number of d electrons	Examples	Coordination			
		Trigonal	Tetrahedral	Square-pyramidal	Octahedral
0	Ca^{2+}, Sc^{3+}	0	0	0	0
1	Ti^{3+}	− 3.86	−2.67	− 4.57	− 4.0
2	Ti^{2+}, V^{3+}	− 7.72	−5.34	− 9.14	− 8.9
3	V^{2+}, Cr^{3+}	−10.92	−3.58	−10.0	−12.0
4	Mn^{3+}	− 5.46	−1.78	− 9.14	− 6.0
5	Mn^{2+}, Fe^{3+}	0	0	0	0
6	Fe^{2+}, Co^{3+}	− 3.86	−2.67	− 4.57	− 4.0
7	Co^{2+}, Ni^{3+}	− 7.72	−5.34	− 9.14	− 8.0
8	Ni^{2+}	−10.92	−3.56	−10.0	−12.0
9	Cu^{2+}	− 5.46	−1.78	− 9.14	− 6.0
10	Cu^{+}, Zn^{2+}	0	0	0	0

Source: Data from Ref. 30.

2 Changes in Crystal Field Stabilization Energy ΔE_c Corresponding to Changes of Coordi
tion Metal Cations in Oxides (Weak Field, kcal mol^{-1})

f ns	Ion (2)	Trigonal→ tetahedral (3)	Tetraedral→ square-pyramidal (4)	Square-pyramidal→ octahedral (5)	Tetraedral→ octahedral (6)	Trig octah (7
	Ca^{2+}	0	0	0	0	0
	Ti^{3+}	+ 6	− 9.5	+ 2.9	− 6.7	− 0.
	V^{2+}	+11	−18	+ 5.5	−13	− 1.
	Cr^{3+}	+34	−30	− 9.2	−39	− 2.
	Mn^{3+}	+20	−39	+17	−22	− 2.
	Mn^{2+}, Fe^{3+}	0	0	0	0	0
	Fe^{2+}	+ 3.6	− 5.7	+ 1.7	− 4	− 0.
	Co^{2+}	+ 6.7	−11	+ 3.2	− 7.4	− 0.
	Ni^{2+}	+17	−15	− 4.6	−19	− 2.
	Cu^{2+}	+14	−27	+12	−16	− 2
	Zn^{2+}	0	0	0	0	0

Data from Ref. 30.

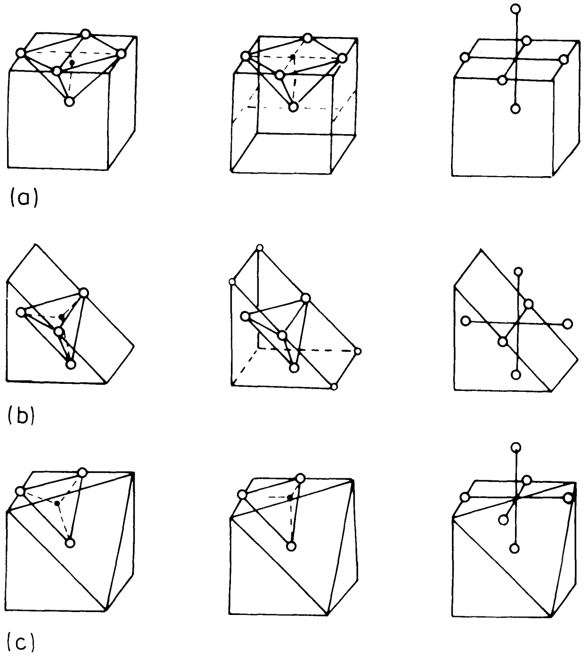

FIGURE 3.9 Changes in nickel ion coordination during the chemisorption of oxygen on nickel oxide. a, (100) plane; b, (110) plane; c, (111) plane. Diagrams in the middle column refer to a bare surface at the instant of cleavage. Left column, bare surface, relaxed position; right column, after adsorption of oxygen. •, nickel ion, o, lattice oxygen ions, or, adsorbed oxygen ions [28].

greatest gain in the stabilization energy has been calculated for the (110) face (column 6 in Table 3.2) and it diminished successively for (100) and (111) faces (column 5 and 7, respectively). Haber and Stone [28] pointed out that in the same order should decrease the coverage with adsorbed oxygen and the heat of adsorption. These conclusions have not been yet checked by direct experiment. However, they are in good accordance with the results obtained by Volpe and Reddy [31], who investigated the catalytic decomposition of N_2O on monocrystalline plates of CoO. The rate-determining step of this reaction is desorption of oxygen. Its energy of activation must therefore be large if oxygen is strongly held at the surface and decrease if the bonding becomes weaker. In fact, Volpe and Reddy found the highest activation energy on the (110) face, i.e., at the face at which the contribution of CFSE to the chemisorption heat of oxygen is largest.

The model of chemisorption based on crystal field theory is fairly simplified and it can be expected that the best results will be obtained when comparing the behavior of oxides with the same crystallographic structure and similar physical properties. Here only two further applications of this approach to the interpretation of chemisorption of oxygen on transition metal oxides will be mentioned. One of them concerns photodesorption of oxygen from nickel oxide and the other one chemisorption of oxygen on some oxy salts.

Photodesorption of oxygen from nickel oxide was investigated by Haber and Stone [28] who stated that the photoactivity is almost entirely confined to wavelengths of 650 and 900 nm comprising the $^3A_{2g} \rightarrow {}^1E_g$ and $^3A_{2g} \rightarrow {}^3T_g$ transitions (Fig. 3.10), and was not active in oxygen desorption. The authors assumed that desorption occurs mainly from the (110) face, which is supposed, as already mentioned, to be the most densely covered with chemisorbed oxygen owing to the highest crystal field stabilization effect. It was also postulated that two oxygen atoms are desorbed simultaneously from one adsorption center, thus changing the coordination from octahedral to tetrahedral. In such a model the photoactivation of the nickel ion to the ^1E_g or $^3T_{1g}$ state renders the octahedral adsorption complex unstable with respect to the tetrahedral one, as is shown in the Orgel diagram in Fig. 3.10. As a consequence the simultaneous desorption of two oxygen atoms should occur.

The study of chemisorption of oxygen on oxy salts of transition metals was undertaken in order to check the effect of the ionization potential of cations [32] and the effect of the crystal field on the chemisorption of oxygen [33]. In the former case chemisorption of oxygen was studied on a series of Fe, Ni, Co, Mn, and Bi molybdates. The highest coverage exhibited manganese and cobalt molybdates, the lowest one iron molybdate. Bismuth molybdate virtually did not adsorb oxygen. It should now be remembered that the investigated molybdates are heterodesmic compounds in which oxygen atoms are linked to molybdenum by the essentially covalent bond while the transition metal cations form predominantly ionic bonds with oxygen atoms. The cations are coordinated by the oxygen atoms (of MoO_4^{2-} anions) bearing in all cases practically the same negative charge, and hence the crystal field acting on the cations can be taken as identical in all the molybdates. The authors argue that in this situation the coverage with chemisorbed oxygen must depend on the ease with which transition metal ions forming adsorption centers can supply electrons, i.e., on their ionization potentials. In fact, the following data indicate that the correlation between coverage and ionization potential $\underline{B}$ really exists.

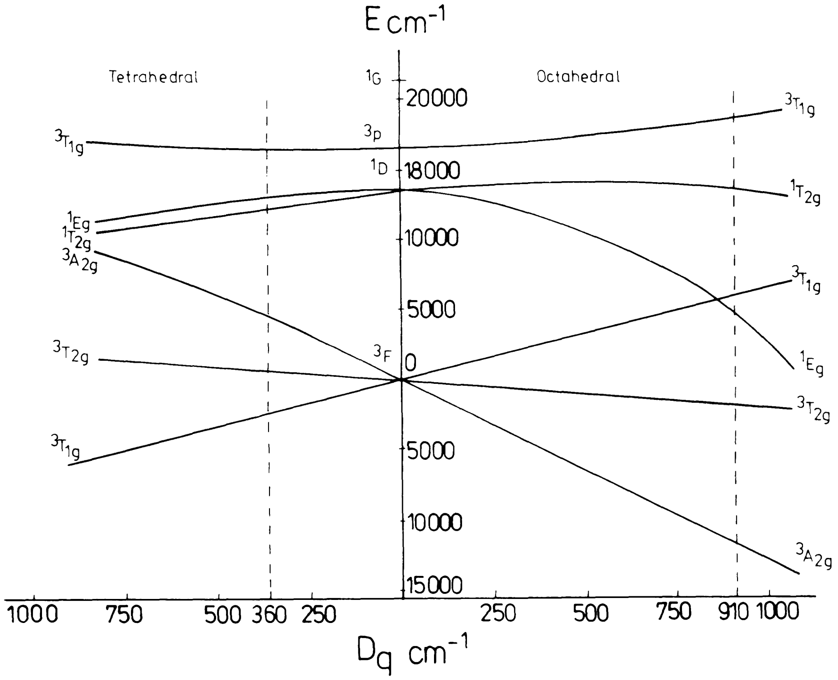

FIGURE 3.10 Orgel diagram for the Ni^{2+} ion in tetrahedral and octahedral fields. Dashed lines indicate the D_q(tetra) and D_q(octa) values as determined for Ni^{2+} ion coordinated tetrahedrally and octahedrally, respectively, by oxygen atoms [28].

Cation	Co^{2+}	Mn^{2+}	Ni^{2+}	Bi^{3+}	Fe^{3+}
B (eV)	33.5	33.7	36.2	45	56
(% of monolayer)	1.26	1.28	0.36	0.05	0.04

The coverage was measured at 635 K and 0.15 Torr.

In the above experiments all samples contained the same oxy anion but the cations were changing, which enabled the investigators to follow the effect of cation ionization energy. On the other hand, Dziewiecki et al. [33] synthesized a series of oxy salts in which oxy anions were changing but the cation Co^{2+} was always the same, aiming to study the effect of crystal field strength on the cation. It has been shown that the smallest amount of oxygen was adsorbed on cobalt phosphate and it increased in the following sequence:

$$Co_3(PO_4)_2 < CoMoO_4 < CoTiO_3 < CoFe_2O_4 < Co_3O_4$$

Co_3O_4 adsorbed unusually large amounts of oxygen in comparison with the analogous compound $CoFe_2O_4$. This was explained by the fact that Co_3O_4 dissolves large quantities of oxygen, forming a nonstoichiometric β phase.

In all investigated cobalt oxy salts Co^{2+} ions are adsorption centers but their properties as shown by the experimental results are modified by the nature of oxy anions present. Qualitatively it can be inferred that the negative charge on oxygen atoms belonging to oxy anions $XO_{\overline{m}}^{n-}$ but simultaneously coordinated to Co^{2+} depend on the ionicity of the X–O. This should be smallest in the case of predominantly covalent bond in PO_4^{3-} and the largest in $Fe_2O_4^{2-}$ or $Co_2O_4^{2-}$, where the X–O bond is predominantly ionic. A large negative charge on oxygen atoms does increase the action of the crystal field on Co^{2+} ion, thus diminishing its ionization energy. Dziewiecki et al. [33] took a further step and estimated quantitatively the ionicity of the X—O bond based on the concept of relative electronegativity A developed by Goerlich [34]. The results of calculations given in Table 3.3 show clearly that the changes in ionicity are appreciable and that a distinct correlation exists between ionicity and the amount of chemisorbed oxygen, thus confirming the above qualitative discussion.

IV. OXYGEN-OXIDE EQUILIBRIA AND THE DEFECT STATE OF TRANSITION METAL OXIDES

In the preceding section the formation and vanishing of lattice defects at the surface and in the near-to-surface layer of transition metal oxides was discussed as the result of interactions of the oxide surface with oxygen in the gas phase. At temperatures that are low with respect to the melting temperature of a given oxide diffusion of defects into the bulk is slow and the changes in the concentration of defects are limited to the surface layer only. At high temperatures the defects are mobile and the equilibrium between the bulk of the oxide and gaseous oxygen may be reached.

In the state of equilibrium the concentration of defects depends on the partial oxygen pressure. As shown by Eqs. (3.2) and (3.4), the interactions with gas phase result in the formation of interstitial atoms or vacancies which are so-called point defects. If the concentration of point defects is low, they do not interact and the crystal can be considered as an ideal solution of defects in the crystal lattice [35]. Under these conditions the equilibria of defects can be easily described by the methods of statistical thermodynamics. However, at higher concentrations of defects their mutual in-

TABLE 3.3 Bond Ionicities in Anionic Groups and the Adsorption of Oxygen

Ion X	Relative electronegativity of X A	Ionicity of X—O bond I (%)	Oxygen coverage at 0.05 Torr, 583 K (%)
P^{5+}	67.9	27.5	0.45
Mo^{6+}	66.6	28.9	0.76
Ti^{4+}	52.1	44.3	1.64
Fe^{3+}	45.7	51.2	5.99
Co^{3+}	46.8	50.1	Absorption

Source: Ref. 33.

teractions cannot be neglected. As a consequence of the interaction of complexes, clusters or superstructures of defects are often formed which are called extended defects.

The presence of defects strongly influences the electrical, optical, adsorptive, and catalytic properties of the oxides. It also controls transport phenomena in solids. Here we shall discuss only the most important features of the defect state in the oxides and simple oxygen-oxide equilibria which determine the deviations from stoichiometry. However, it should be noticed that point defects can also be present in stoichiometric oxides. In a stoichiometric oxide MO two kinds of such defects are of special interest: the Schottky and the Frenkel defects. Schottky defects can be described as the result of migration of a cation-anion pair to the surface, leaving behind in the bulk a pair of cation and anion vacancies V_M'' and $V_O^{\bullet\bullet}$

$$MO \rightleftarrows V_M'' + V_O^{\bullet\bullet} \tag{3.15}$$

Both vacancies bear formal charges: the cationic one 2— and the anionic one 2+.

Applying mass action law, we can write:

$$\underline{K}_{\underline{s}} = [V_M''][V_O^{\bullet\bullet}] \tag{3.16}$$

The Frenkel defect in ionic crystal is the result of migration of a cation into an interstitial position ($M_i^{\bullet\bullet}$) leaving behind a cationic vacancy. The anti-Frenkel defect, comprising an anion in the interstitial position and an anionic vacancy, appears only exceptionally in the oxides (e.g., UO_2) owing to the relatively large size of the oxygen anion. The formation of a Frenkel defect is represented by the equation:

$$M_M \rightleftarrows M_i^{\bullet\bullet} + V_M'' \tag{3.17}$$

where the M_M cation is in cationic position. Also in this case, mass action law can be applied to the equilibrium of defects:

$$\underline{K_F} = [M_i^{\bullet\bullet}][V_M''] \tag{3.18}$$

The formation of both kinds of defects is an endoenergetic process and hence equilibrium constants $\underline{K_S}$ and $\underline{K_F}$, as well as the total concentrations of Schottky and Frenkel defects, increase with increasing temperature. It should here be observed that by appropriate cooling the equilibrated samples one can easily "freeze" the defect state corresponding to a high temperature.

As already stated, the deviations from stoichiometry in the oxides are the effect of incorporation of oxygen into the lattice, resulting in the deficiency of the metallic component, or the giving off of oxygen from the lattice, resulting in the appearance of excess metal. The equilibrium of defects in nonstoichiometric NiO can be represented by an equation analogous to Eq. (3.4) which, however, was limited to the surface layer only:

$$\frac{1}{2}\,O_2 \rightleftarrows V_{Ni} + O_O \tag{3.19}$$

Here the symbols V_{Ni} and O_O—electrically neutral nickel ion vacancy and oxide ion on the anionic site—refer to the bulk of the crystal. According to the Kröger-Vink notation system, the symbol V_{Ni} corresponds to the cationic vacancy the formal negative charge of which (2−) is neutralized by two Ni^{3+} ions in the nearest neighborhood. From the point of view of the band theory of solids, Ni^{3+} ions represent positive holes $h^{\bullet}$ localized at the cationic vacancy. Electrically neutral cationic vacancy is an acceptor center, i.e., can accept one or two electrons from adjacent Ni^{2+} ions, thus forming a free positive hole $h^{\bullet}$:

$$V_{Ni} \rightleftarrows V_{Ni}' + h^{\bullet} \tag{3.20}$$

$$V_{Ni}' \rightleftarrows V_{Ni}'' + h^{\bullet} \tag{3.21}$$

Assuming that the concentration of defects is low enough for the laws of ideal solutions to still be valid, we write:

$$k_1 = \frac{[V_{Ni}]}{p_{O_2}^{1/2}} \tag{3.22}$$

$$k_2 = \frac{[V'_{Ni}][h^{\bullet}]}{[V_{Ni}]} \tag{3.23}$$

$$k_3 = \frac{[V''_{Ni}][h^{\bullet}]}{[V'_{Ni}]} \tag{3.24}$$

Because the NiO crystal is electrically neutral, its electroneutrality condition is

$$[V'_{Ni}] + 2[V''_{Ni}] = [h^{\bullet}] + 2[V_O^{\bullet\bullet}] \tag{3.25}$$

However, the concentration of V''_O (due to the presence of Schottky defects) is always low in comparison with that of $h^{\bullet}$ and one can write:

$$[V'_{Ni}] + 2[V''_{Ni}] = [h^{\bullet}] \tag{3.26}$$

From Eqs. (3.22)–(3.24) and (3.26), one obtains:

$$k_1 k_2 p_{O_2}^{1/2} \{[h^{\bullet}] + 2k_3\} = [h^{\bullet}]^3 \tag{3.27}$$

The latter equation enables us to calculate the concentration of positive holes in two limiting cases, i.e., when $2k_3 \ll [h^{\bullet}]$ and when $2k_3 \gg [h^{\bullet}]$. The first case corresponds to the situation in which the single ionization of cationic vacancies predominates and the double one can be neglected. Then:

$$[h^{\bullet}] = \sqrt{k_1 k_2}\; p_{O_2}^{1/4} \tag{3.28}$$

In the second limiting case it is the double ionization of cationic vacancies which predominates and:

$$[h^{\bullet}] = \sqrt[3]{2k_1 k_2 k_3}\; p_{O_2}^{1/6} \tag{3.29}$$

In the intermediate cases the exponent at the partial pressure of oxygen assumes the values between 1/4 and 1/6. Both Eqs. (3.28) and (3.29) can be verified by the measurement of electrical conductivity σ which is proportional to the concentration of free positive holes and hence $\sigma = \beta p_{O_2}^{1/4}$ (β = proportionality constant). In fact, the measurements of conductivity carried out by various authors at temperatures above 900°C within the pressure range 10^{-3} to 1 atm the values of the exponent equal 1/4 to 1/6 were obtained.

In a similar way, the formation of defects in ZnO can be discussed. However, here the formation of defects is favored by the low pressure of oxygen:

$$ZnO \rightleftarrows Zn_i + \frac{1}{2}O_2 \tag{3.30}$$

Here Zn_i denotes the interstitial electrically neutral atom of zinc. This can easily give off one or, less easily, two electrons and hence is an electron donor center:

$$Zn_i \rightleftarrows Zn_i^{\bullet} + e^- \tag{3.31}$$

$$Zn_i^{\bullet} \rightleftarrows Zn_i^{\bullet\bullet} + e^- \tag{3.32}$$

The electroneutrality condition of the lattice is expressed here as

$$[e^-] = [Zn_i^{\bullet}] + 2[Zn_i^{\bullet\bullet}] \tag{3.33}$$

Applying mass action law in an analogous way to the previous case of NiO, one arrives in the limiting case of single ionization of donors to the quation in the form:

$$[e^-] = \sqrt{k_4k_5}\ P_{O_2}^{-1/4} \tag{3.34}$$

and in the case of double ionization:

$$[e^-] = \sqrt[3]{k_4k_5k_6}\ P_{O_2}^{-1/6} \tag{3.35}$$

k_4, k_5 and k_6 are equilibrium constants of reactions (3.30), (3.31) and (3.32) respectively. Equations (3.34) and (3.35) indicate that in the equilibrated system the concentration of free electrons $[e^-]$ does increase in the measure as oxygen pressure decreases. Parallel the concentration of interstitial zinc atoms and the deviations from stoichiometry are growing. Similarly as in the case of NiO, in ZnO the applicability of Eqs. (3.34) and (3.35) can also be checked by the measurements of changes in electrical conductivity at different oxygen pressures.

The changes in the electrical conductivity of nonstoichiometric transition metal oxides are the effect of the formation of acceptor or donor centers in the crystal lattice. Another effect is the change in the work function which increases with the formation of acceptor centers and decreases with that of donor centers. All these phenomena may also be described as being due to changes in the position of the Fermi level which is shifted downward by the increasing concentration of acceptor centers and upward by that of donor centers. However, the deviations from stoichiometry are usually small and the shift in the position of the Fermi level in this case is not significant. Greater changes of Fermi level, more important from a catalytic point of view, can be achieved by doping semiconducting oxides with other altervalent oxides according to the controlled valency principle of de Boer and Verwey [36].

Similarly as in the case of inducing nonstoichiometry, doping involves also the participation of oxygen from the gas phase. For example, doping of NiO with Li_2O usually occurs according to the equation:

$$Li_2O + \frac{1}{2}O_2 \rightleftarrows 2Li_{Ni} + 2O_O \qquad (3.36)$$

The acceptor center Li_{Ni} consists of a lithium cation in the cationic position (Li_{Ni}), the formal charge of which (−1) is neutralized by an Ni^{3+} ion in its immediate vicinity, i.e., by a positive hole localized at this foreign atom. The neutral acceptor center Li_{Ni} becomes ionized according to

$$Li_{Ni} \rightleftarrows Li'_{Ni} + h^{\bullet} \qquad (3.37)$$

If the ionization is complete, instead of the two last equations one can write:

$$Li_2O + \frac{1}{2}O_2 \rightleftarrows 2Li'_{Ni} + 2O_O + 2h^{\bullet} \qquad (3.38)$$

On the other hand, doping nickel oxide with Fe_2O_3 is accompanied by the giving off of elemental oxygen and the formation of donor centers Fe_{Ni}:

$$Fe_2O_3 \rightleftarrows 2Fe_{Ni} + 2O_O + \frac{1}{2}O_2 \qquad (3.39)$$

These ionize with the formation of free electrons e^-:

$$Fe_{Ni} \rightleftarrows Fe^{\bullet}_{Ni} + e^- \tag{3.40}$$

Owing to the recombination of the excess free electrons with positive holes which are predominant current carriers in NiO, this last process can also be represented as

$$Fe_{Ni} + h^{\bullet} \rightleftarrows Fe^{\bullet}_{Ni} \tag{3.41}$$

If ionization of donor centers is complete, instead of Eqs. (3.39) and (3.41) one can write:

$$Fe_2O_3 + 2h^{\bullet} \rightleftarrows 2Fe^{\bullet}_{Ni} + 2O_O + \frac{1}{2}O_2 \tag{3.42}$$

In zinc oxide doping with Li_2O results in diminishing of the concentration of free electrons the predominant electrical current carriers and doping with tervalent oxide to its increase. The equations analogous to equations (3.38) and (3.42) are in this case [37]

$$Li_2O + \frac{1}{2}O_2 + 2e^- \rightleftarrows 2Li'_{Zn} + 2O_0 \tag{3.43}$$

and

$$Ga_2O_3 \rightleftarrows 2Ga^{\bullet}_{Zn} + 2O_0 + 2e^- + \frac{1}{2}O_2 \tag{3.44}$$

The results of work function measurements on a series of Li_2O-doped nickel oxide will be presented in Chapter 6 in connection with catalytic oxidation of CO on such samples.

It should be stressed that the simple interpretation of defect equilibria in oxides given above concerns only the oxides in which the concentration of defects is low enough and the laws of ideal solutions are still valid. In nickel oxide, for example, the concentration of defects even at temperatures as high as 1300°C does not exceed the limit of 0.1 mol %. However, there is a large group of oxides containing much higher numbers of defects. Wüstite FeO belongs to the most notable examples of such behavior. This phase is thermodynamically stable only above 570°C and can exist as a nonstoichiometric compound within wide limits of concentration. In the range 800—1200°C the composition of ferrous oxide was found to vary between $FeO_{0.947}$ and $FeO_{0.906}$ indicating a deficit of iron between 5.3 and 9.4 mol % [38]. In oxides with large deviations from stoichiometry the interactions between the point defects result in the formation of various complexes and clusters of defects which exhibit short- or long-range order [35]. The superstructures of defects may appear in some oxides and often in such cases homologous series of intermediate phases exist. Some examples of extended defects will be mentioned here. However, there is no need here for systematic presentation.

From the point of view of oxidation catalysis, of particular importance are crystallographic shear defects which appear in the groups IV—VII transition metal oxides containing these metals in high oxidation states. The presence of such defects is considered to be connected to a high mobility of lattice oxygen and to be one of the essential factors controlling catalytic properties of these oxides. Formally the formation of a shear defect can be represented as the result of specific ordering of anionic defects which are subsequently eliminated by a local reconstruction of the lattice. This is shown schematically in Fig. 3.11 representing a cross-section of ReO_3 structure in which $[ReO_6]$ octahedra are linked by the intermediation of O^{2-} ions in such a way that each of them is common for two neighboring octahedra. On the left side of Fig. 3.15 the supposed positions of ordered anionic vacancies are shown by empty circles. The shift in the direction of the arrow of one of the two parts of the lattice separated by the rows of vacancies would result in the formation of a defect zone, an extended defect, called the crystallographic shear plane as shown on the right side of Fig. 3.11. In this zone the coordination number 6 of cations remains unchanged. The change is suffered only by the coordination of anions. It can easily be seen in Fig. 3.11 that in the defect zone oxygen atoms are present which belong to three neighboring octahedra. In the shear plane the cation-anion number ratio therefore increases and in order to preserve locally electroneutrality condition cations of lower valency must occupy octahedra with tricoordinated oxygen atoms. Reduction of appropriate number of cations to a lower oxidation state must have occurred at the moment when the lattice lost some oxygen atoms (formation of oxygen vacancies). Now these reduced atoms are ordered in the shear plane.

At a sufficiently high concentration of crystallographic shear planes, called also Wadsley defects, the planes interact among themselves and get ordered at equal distances, forming a homologous series of the oxides (Magneli phases). In the case of molybdenum oxides the composition of the members of the series is given by the formula $Mo_{\underline{n}}O_{3\underline{n}-1}$ ($\underline{n}$ = 4, 5, 8, 9, 17, 18) [39]. A series of vanadium oxides of the composition $V_{\underline{n}}O_{2\underline{n}-1}$ with $\underline{n}$ = 2—8 was described [40,41].

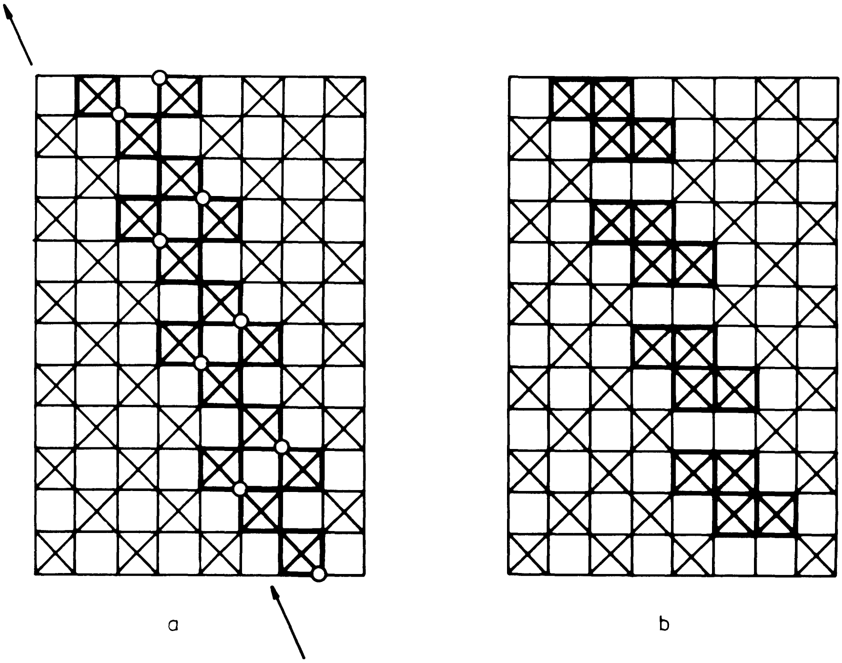

FIGURE 3.11 Scheme of crystallographic shear defects formation: (a) hypothetical ordering of anionic vacancies before defect formation, (b) defect resulting from the shift in the direction of the arrow.

The real mechanism of the formation of crystallographic shear defects is not fully understood. Wadsley and Anderson [42,35] assumed that it is due to the ordering of anionic vacancies. Bonnet and Ouillon [43] suggested recently that in the case of nonstoichiometric WO_3 the initial point defects—interstitial metal atoms and anionic vacancies—tend to aggregate in the form of W_4O_{11} clusters. The grouping of these clusters would lead to the formation of shear planes. Independently of the detailed mechanism the formation of Magneli phases must be connected with the release of oxygen either by the evacuation at elevated temperatures or under the influence of reducing gases. At the conditions of many catalytic oxidation reactions the inward diffusion of vacancies from the surface into the bulk of crystallites equivalent to the outward diffusion of oxygen is considered to be quite rapid and the surface reduced by the reagents can be regenerated to some extent, even without the presence of gaseous oxygen. This can be illustrated by the results of butene oxidative dehydrogenation to butadiene on Bi_2MoO_6

catalyst obtained by Haber and Grzybowska [44]. At first pulses of the mixture of hydrocarbon with oxygen were injected into a flow microreactor and conversion determined as the function of the number of pulses (Fig. 3.12A). After eight such pulses a series of pulses containing only pure butene was injected. The yield of butadiene remained unchanged (Fig. 3.12E); however, as the gas contained no oxygen, the lattice oxygen of the molybdate must have been used for the reaction. The yield of butadiene remained unchanged even after extracting from the lattice an amount of oxygen corresponding to 7% reduction of the solid. Hence it can be concluded that the lattice of bismuth molybdate can readily supply oxygen for the reaction with hydrocarbon at a rate much higher than that of the surface reaction itself.

V. ISOTOPIC EXCHANGE OF OXYGEN ON SOLID CATALYSTS

The isotopic exchange of oxygen:

$$^{18}O_2 + ^{16}O_2 \rightleftarrows 2\,^{16}O^{18}O \qquad (3.45)$$

belongs to the simplest reactions involving molecular oxygen. It occurs in the gas phase as a homogeneous reaction at high temperatures only because of a considerable and necessary weakening of the O—O bond. However, in the presence of solid catalysts it can be observed within the temperature range 200—400°C, at which many catalytic heterogeneous reactions occur. In some cases catalytic isotopic oxygen exchange could be observed at room temperature and even at the temperature of liquid nitrogen.

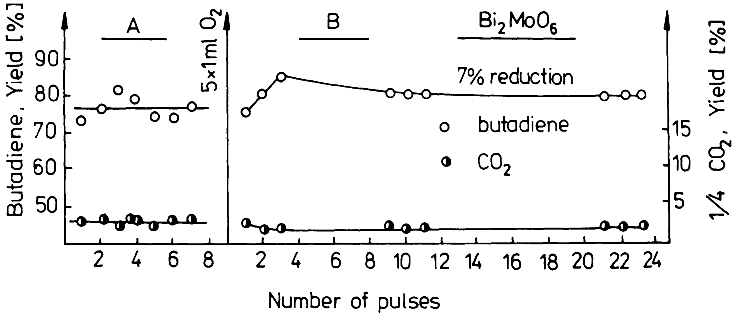

FIGURE 3.12 Activity of Bi_2MoO_6 in the oxidation of butene in the presence of gaseous oxygen (A) and in its absence (B).

Studies of catalytic oxygen exchange contributed greatly to the elucidation of the interactions between molecular oxygen and the catalyst surface. They enabled characterization of the mobility of oxygen atoms at the oxide surface and frequently that of lattice oxygen atoms as well. In a number of cases they also supply valuable information concerning some simple reactions occurring with the participation of molecular oxygen. The main contributions to the knowledge of catalytic exchange of oxygen on the surface of oxides were given by Winter [45], Boreskov [46], and by the Czech group of Jiru, Novakova, and Klier [47]. Much less attention has been given to the isotopic exchange of oxygen on metal catalysts, evidently due to the fact that metals are used only rarely as oxidation catalysts.

Isotopic exchange of oxygen on the oxide catalysts occurs either with or without the participation of the oxide's oxygen. In the former case we deal with hetero- and in the latter with homomolecular exchange. The heteromolecular exchange may occur in such a way that one oxygen molecule from the gas phase does exchange only one oxygen atom with the surface of the catalyst:

$$^{18}O_2 + {}^{16}O_s \rightleftarrows {}^{18}O^{16}O + {}^{18}O_s \tag{3.46}$$

or in such a way that the oxygen molecule from the gas phase exchanges both its atoms with the surface:

$$^{18}O_2 + 2\,{}^{16}O_s \rightleftarrows 2\,{}^{18}O_2 + {}^{16}O_2 \tag{3.47}$$

Subscript s denotes here a surface atom (or vacancy) of the solid. On the other hand, no lattice oxygen atoms appear in the equation representing homomolecular exchange:

$$^{18}O_2 + {}^{16}O_2 \rightleftarrows 2\,{}^{18}O^{16}O \tag{3.48}$$

The possible mechanism of such processes was discussed by Winter [48] who assumed that reaction (3.46) occurs in one stage only by the interaction of an O_2 molecule with an oxygen surface atom. The transition complex in such a case would be composed of at least three atoms:

$$^{18}O_2 + {}^{16}O_s \rightleftarrows ({}^{18}O^{18}O^{16}O)_s \rightleftarrows {}^{16}O^{18}O + {}^{18}O_s + {}^{18}O_s \tag{3.49}$$

For simplicity's sake no possible electrical charges of adsorbed oxygen are given in this equation. The same process can also occur in several stages including the dissociation of the O_2 molecule on the surface of the oxide:

$$^{18}O_2 \rightleftarrows 2\,^{18}O_{ads} \tag{3.50a}$$

$$^{18}O_{ads} + {}^{16}O_s \rightleftarrows {}^{16}O^{18}O + (V_O)_s \tag{3.50b}$$

$$^{18}O_{ads} + (V_O)_s \rightleftarrows {}^{18}O_s \tag{3.50c}$$

or by the adsorption of $^{18}O_2$ on a surface anionic vacancy $(V_O)_S$:

$$^{18}O_2 + (V_O)_s = {}^{18}O_s + {}^{18}O_{(ads)} \tag{3.51a}$$

The adsorbed $^{18}O_{ads}$ atom would react with a surface $^{16}O_s$ atom, thus regenerating surface vacancy in the same way as in (3.64b):

$$^{18}O_{ads} + {}^{16}O_s = {}^{16}O^{18}O + (V_O)_s \tag{3.51b}$$

As was shown by Boreskov [46], the three mechanisms (3.49), (3.50), and (3.51) cannot be discriminated by the kinetic measurements. However, it should be observed that, in the case of a slightly reduced V_2O_5/SiO_2 catalyst, Kazansky et al. [49] showed using EPR measurement that a negatively charged O_3^- complex is the intermediate species for homomolecular isotopic exchange of oxygen occurring between −140 and 20°C.

Heteromolecular exchange with the participation of two oxide oxygen atoms for one exchanged O_2 molecule from the gas phase may occur in one stage through the formation of a transition complex composed of four atoms:

$$^{18}O_2 + 2\,^{16}O_s \rightleftarrows ({}^{18}O^{18}O^{16}O^{16}O)_s \rightleftarrows {}^{16}O_2 + 2\,^{18}O_s \tag{3.52}$$

or by the incorporation of an oxygen molecule at the site of two neighboring surface oxygen vacancies and the simultaneous desorption of O_2 molecule from another site at the surface:

$$^{18}O_2 + (V_OV_O)_s \rightleftarrows 2\,^{18}O_s \tag{3.53a}$$

$$^{18}O_s + {}^{16}O_s \rightleftarrows {}^{16}O_2 + (V_OV_O)_s \tag{3.53b}$$

where $(V_OV_O)_s$ denotes a pair of neighboring surface anionic vacancies.

Homomolecular oxygen exchange can be observed only on the condition of no isotopic equilibrium in the gas phase. Its mechanism may comprise formation of an active complex composed of four oxygen atoms from the gas phase. One can also conceive a process in which dissociative adsorption of oxygen molecules takes place and subsequently molecular oxygen is again produced from adsorbed O atoms:

$$^{18}O_2 = 2\,^{18}O_{ads} \tag{3.54a}$$

$$^{16}O_2 = 2\,^{16}O_{ads} \tag{3.54b}$$

$$2(^{18}O_{ads} + {}^{16}O_{ads}) = 2\,^{16}O^{18}O \tag{3.54c}$$

The latter mechanism can play a noticeable role only if the rate of heteromolecular exchange is significantly lower than that of homomolecular exchange.

Statistical considerations show that the isotopic exchange of oxygen should obey first-order law with respect to the mole fraction of a given isotopic species independently of exchange mechanism [50]. In accordance with this the results of measurements of the catalytic homomolecular exchange can be expressed by the equation:

$$\underline{K} = \frac{1}{\underline{t}} \ln (1 - \underline{F}) \tag{3.55}$$

where $\underline{F} = \underline{C}_o - \underline{C}_t/\underline{C}_o - C_\infty$ and $\underline{C}_o$, $\underline{C}_t$, and $\underline{C}_\infty$ represent the initial concentration of ^{18}O (at %) in the gas phase, the concentration after time $\underline{t}$, and the concentration at the isotopic equilibrium state, respectively. If the exchange was not limited to the gas phase but occurred also with the participation of surface or lattice oxygen of the catalyst instead of Eq. (3.55), the following equation was used by Jiru and Novakova [51]:

$$\underline{R} = -\frac{\underline{n}_s \ln(1 - \underline{F})}{\underline{S}(1 + \lambda)\underline{t}} \tag{3.56}$$

in which $\underline{S}$ is the surface area of the oxide, $\lambda = \underline{n}_s/\underline{n}_g$, $\underline{n}_s$ is the number of exchangeable oxygen atoms in the solid (surface and bulk), and $\underline{n}_g$ is the number of oxygen atoms in the gas phase.

The overall rate constant $\underline{R}$, often referred to as the rate of exchange, depends both on the total pressure of oxygen $\underline{p}_{O_2}$ and on the temperature

$$\underline{R} = A\underline{p}_{O_2}^{\underline{m}}\left(\exp - \frac{\underline{E}_{\underline{a}}}{RT}\right) \qquad (3.57)$$

Using this equation the reaction order $\underline{m}$ with respect to oxygen and the apparent activation energy $\underline{E}_{\underline{a}}$ can be calculated from the experimental data.

The discrimination between the rate constant of homomolecular oxygen exchange $\underline{R}_0$ and the rate constants of heteromolecular exchange occurring with the participation of one oxide oxygen atom $\underline{R}_1$, or with the participation of two oxide oxygen atoms $\underline{R}_2$, can be done on the basis of detailed kinetic considerations. This has been done by Klier et al. [52] and by Boreskov [46]. Although the two approaches are not quite the same, algebraic results may readily be shown to be identical [48].

The results of the investigations of isotopic oxygen exchange at the surface of oxide catalysts show that the rate and the mechanism of this process largely depend on the pretreatment of the catalyst surface. The results obtained for the samples previously heated in vacuo, the surface of which are partially reduced and contain different defects, can be satisfactorily reproducible only on the condition that a given experimental procedure be strictly reproduced in each run. Oxygen isotopic exchange is in this case much faster than in the case of samples which were equilibrated with oxygen before experiments. Such equilibration is usually carried out by heating the sample in the atmosphere of oxygen of natural isotopic composition at a pressure and temperature corresponding to those which are subsequently applied in the catalytic exchange experiment. Reproducibility of the results so obtained is quite satisfactory, e.g., results obtained by Winter [45] and Boreskov [46] for MgO, NiO, ZnO, CuO, Cr_2O_3, Fe_2O_3, and TiO_2 do not exhibit any striking discrepancies in the values of the apparent activation energy. On the other hand, the data published by Winter [53] and Minachev [54] concerning isotopic oxygen exchange on rare-earth sesquioxides show significant discrepancies which were attributed to different ways of synthetizing the samples. The samples prepared by Winter by the decomposition of oxalates were heated before experiments for 16 hr at 900°C in air while those obtained by Minachev were prepared from nitrates via hydroxides heated for 6 hr at 600°C and outgassed for 6 hr at 500°C.

The most extensive compilation of results obtained by different authors is given in [47]. A selection of the data collected in this paper is given in Table 3.4, containing the following information: temperature range in which the experiments were carried out, activation energy $\underline{E}_{\underline{a}}$, and reaction order $\underline{m}$ with respect to oxygen pressure, the latter both calculated from Eq. (3.57). Column 4 gives the number of layers in which the exchange took place in the oxide. Column 5 informs about the type of exchange $\underline{R}_0$, $\underline{R}_1$, or $\underline{R}_2$ provided that the authors themselves mentioned it. As the data in Table 3.4 show, depending on the nature of the oxide only a fraction of surface oxygen takes part or the oxygen atoms from only several subsurface layers. From this point of view quite peculiar behavior is exhibited by V_2O_5, MoO_3, and WO_3 in which practically all the lattice oxygen can participate in the isotopic exchange [55]. The notable mobility of oxygen proven by these experiments is a plausible explanation of the fact that all three oxides easily undergo reduction accompanied by the formation of crystallographic shear defects and, in consequence, the formation of lower oxides of the Magneli series (as V_nO_{2n+1} or Mo_nO_{3n-1}). The common feature of these oxides in the pure state or in the form of mixed oxides is their remarkable catalytic properties in the selective oxidation of hydrocarbons.

TABLE 3.4 Oxygen Isotopic Exchange on Oxide Catalysts

Oxide (1)	Reaction temp. °C (2)	Energy of activation kJ·mol^{-1} (3)	$\underline{n}$ number of oxygen layers in solid in which exchange takes place (4)	Mechanism (5)
CuO	230–330[a]	92	2.5–3	R_2
	300			$6R_0 = 7R_1 = R_2$
	275–350	109	0–0.8	
AgO	90–130	142		$10R_1 < R_2$
MgO	370–450[a]	159	0.8–3	R_1
	350–440[f]	159	1.4–2.4	$(R_0)R_1$
	400–500	168		
ZnO	350–410[a]	151	1.5–3	R_1
	360–420[f]	168	1–3	$(R_0)R_1$
	425–475	166,2		
CdO	250–350	84	2–2.5	R_1
La_2O_3	350–450[f]	96	7–10	$(R_0)R_1$
	220–300[a]	46	0.8–2.5	

TABLE 3.4 (Continued)

Oxide (1)	Reaction temp. °C (2)	Energy of activation kJ·mol^{-1} (3)	n number of oxygen layers in solid in which exchange takes place (4)	Mechanism (5)
Al_2O_3	α500–600[a]	188	2–3	R_1
	γ480–580	163	2–3	R_1
	γ400–500	134		
In_2O_3	550–650[a]	239	6–9	$R_1 > 10R_2$
TiO_2	500–580[a]	147	2–4	R_1
(rutile)	630–730	134	6–9	R_1
ZrO_2	550–650[f]	63	2–3	R_1
	350–450[a]	126	1	R_1
V_2O_5	480–540	84	all	R_1
	520–600	335	all	R_2
	400–550	188	all	
	450–550	193	all	
Cr_2O_3	270–370[a]	142	1–1.5	$R_1(R_2)$
	270–400[f]	134	1–2	$R_1 > 6R_2$
MoO_3	600–660	117	all	R_1
	630–690	251	all	R_2
	630–750	172	all	
	650		all	$R_0 = R_1 = R_2$
WO_3	700–750	63	all	R_1
	720–790	209	all	R_2
	700–800	214	all	
α-Fe_2O_3	290–400	80	2–4	$R = R_1 = 4R_2$
	260–340[a]	113	1.5–2	$R_1 = 2R_2$
NiO	330–400[a]	188	1–2	$R_1 = 4R_2$
	200–370[f]	147	0–1,5	R_1
Pd	200–350	126		
Pt	200–250	69.0		
	20–427	151		

[a] Sample heated in oxygen prior to the exchange reaction.
[f] Sample heated in vacuum prior to the exchange reaction.
Source: Ref. 47.

The rate of heteromolecular oxygen exchange in the equilibrated samples of such oxides as Co_3O_4, NiO, CuO, and MnO_2 rapidly decreases with the exchange degree. The changes are distinct even within the monolayer thus indicating nonuniformity of surface oxygen atoms relative to the isotopic exchange with the gas phase. On the other hand, Fe_2O_3, Cr_2O_3, ZnO, and V_2O_5 exhibited appreciable uniformity of surface oxygen [56].

Various correlations between the rate of isotopic oxygen exchange on equilibrated oxides or activation energy of this process E_a and different physicochemical parameters were proposed. In the case of a series of equilibrated oxides of transition metals belonging to the fourth group of the periodic system, Boreskov [46] stated a correlation between the enthalpy of the formation of oxide calculated per mole of oxygen and the activation energy of oxygen exchange. In the same series of oxides parallel changes of E_a and the activity of a number of catalytic oxidation reactions was also stated [57]. These observations, which will be described in more detail in the next section, led Boreskov to the conclusion that there exists a link between the mechanism of heteromolecular isotopic exchange and that of the investigated catalytic oxidation reactions. At first one could suppose that in all cases there is the same rate-limiting step, e.g., chemisorption of oxygen. However, distinct differences in activation energies render such an assumption inplausible. Facing this fact, Boreskov arrived at the conclusion that although the rate-limiting steps are different, the formation of active complex must in each case involve breaking the bond between oxygen atoms participating in the given reaction and the surface of the catalyst. The energy of the oxygen-catalyst bond, "oxygen bonding strength," must therefore, according to Boreskov's theorem, be one, but not the sole, factor determining the activation energy. If the same reaction is studied on different oxides, the other factors are approximately constant and the observed changes in the catalytic activity are mainly due to the oxygen bonding strength. This rule also comprises isotopic oxygen exchange and hence the exchange activity of an oxide is considered by Boreskov to be a value characterizing oxygen-surface bond strength.

VI. OXYGEN-SURFACE BOND STRENGTH

The problem of catalytically active oxygen on the surface of oxide catalysts was tackled in the previous sections mainly from the perspective of different forms of oxygen available at the surface. However, it should be observed that the practical discrimination between oxygen species participating in a catalytic reaction is by no means a simple task and can be solved only with rather elaborate experimental methods. In addition, the studies on adsorbed oxygen species are most frequently carried out at conditions rather distant from the usual conditions of catalytic reactions. These difficulties can in some measure be overcome by the study of the energetics of oxygen bonding at the surface. This approach brought success in the interpretation of the catalytic properties of the oxides of group IV transition metal oxides. These oxides exhibit in a number of catalytic oxidation reactions a characteristic, almost universal reactivity pattern with three maxima at the Co, Cu, and Mn oxides [58]:

$$\mathrm{Ti} < \mathrm{V} < \mathrm{Cr} < \mathrm{Mn} > \mathrm{Fe} < \mathrm{Co} > \mathrm{Ni} < \mathrm{Cu} > \mathrm{Zn}$$

As the example, specific activities of these oxides in the catalytic oxidations of hydrogen and carbon monoxides as well as in oxygen isotopic exchange are shown in Fig. 3.13. The data were taken from [46,59,60]. Similar activity patterns were obtained for the total oxidation of CH_3OH, C_3H_6, C_6H_6 [61], NH_3 [62], $C_6H_5{\cdot}CH_3$ [63], etc. The fact that the same activity pattern is observed for the catalytic oxidation of different oxidizable substances led to the conclusion that this pattern reflects in some way the reactivity of oxygen at the surface of metal oxides, frequently also described as the "mobility" of surface oxygen [58].

The postulated role of this value becomes clear if we consider the general scheme of heterogeneous catalytic oxidation [58]:

$$A_{(g)} + \text{K-ox} \rightarrow AO_{ads} + \text{K-red} \tag{3.58a}$$

$$AO_{ads} \rightarrow AO_{g} \tag{3.58b}$$

$$\text{K-red} + \frac{1}{2} O_{2g} \rightarrow \text{K-ox} \tag{3.58c}$$

where K-ox and K-red represent oxidized and reduced states of the catalyst and A and AO substrate and the product of the catalytic reaction, respectively. The first step in this scheme is the reaction of substrate with chemisorbed or lattice oxygen, the second one is the desorption of the product from the surface, and the third is the reoxidation of the catalyst with oxygen from the gas phase. At low temperatures (approximately −80 to 100°C for the oxides) adsorption and desorption processes are slow and in fact determine the overall rate of oxidation. If CO is oxidized at room temperature on MnO, CoO, and NiO, the most difficult step is desorption of CO_2, while on some preparations of MnO_2 the rate-determining

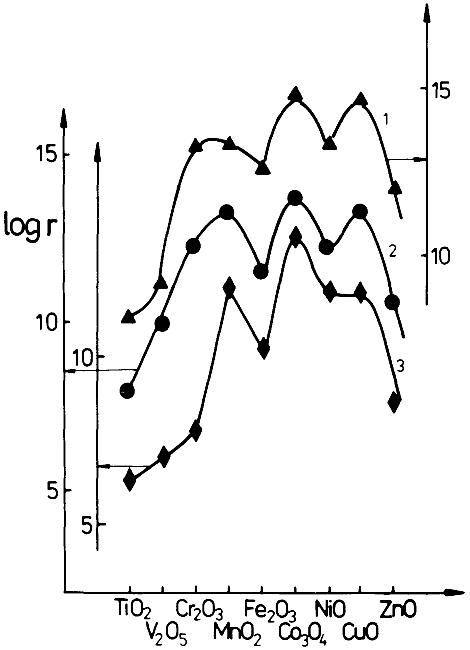

FIGURE 3.13 Specific activities r (molecules cm^{-2} sec^{-1}) of the oxides of group IV transition metals. 1, Catalytic oxidation of carbon monoxide at 227°C, p_{CO} = 2 Torr, p_{O_2} = 1 Torr [59]. 2, Catalytic oxidation of hydrogen at 300°C, p_{H_2} = 11.8 Torr, p_{O_2} = 750 Torr [60]. 3, Isotopic exchange of oxygen at 300°C, p_{O_2} = 40 Torr [46].

step is chemisorption of oxygen on the reduced surface of the oxide [64]. On the other hand, at temperatures above 150—200°C adsorption and desorption processes are definitely faster and stage (3.58a) becomes the rate-determining step. Now the formation of active complex must involve the breaking of the oxygen-surface bond, as was already mentioned in the preceding section, and hence the activation energy must depend on the oxygen bonding strength. If we assume that in all oxidation reactions exhibiting the same activity pattern (high-temperature region, excess of oxygen (in gas phase) step (3.58a) is the rate-limiting step, the similarity of activity patterns will be understood and explained by different oxygen bonding strengths at different oxide surfaces.

In order to verify this hypothesis it is necessary to determine oxygen bonding strength and to compare it with catalytic activities.

This has been attempted in various ways which were recently reviewed by Golodets [60]. The most direct method consists of calorimetric measurements of the heat of adsorption q_s of oxygen on the oxide surface. However, the value of q_s strongly depends on both the coverage and the pretreatment of the oxide. Sazonov and colleagues [65] determined chemisorption heat of oxygen on the oxides of period IV transition metals as a function of the amount of oxygen removed from the surface. In these experiments the stoichiometric surface of the oxide was at first treated with a small amount of CO and then thoroughly evacuated. From the amount of desorbed CO_2 the degree of surface deoxygenation was calculated and expressed as θ, the percentage of oxygen monolayer removed. In most of the investigated oxides (Co_3O_4, V_2O_5, NiO, CuO, MnO_2) q_s increased with the deoxygenation of the surface. It remained practically constant in the case of Fe_2O_3 and in that of ZnO exhibited a small increase after about 0.25% of monolayer of oxygen was removed and then remained constant. It could be shown [60] on the example of nickel oxide that q_s values obtained at 327°C for the surfaces of a given θ were also dependent on the time which elapsed between prereduction and chemisorption. With the prolongation of this time the q_s value decreased. This was interpreted as the result of partial regeneration of the surface due to the diffusion of oxygen from the deeper layers of the crystallites. This effect was stronger with increasing deoxygenation but vanished for θ approaching 0. The values of q_s obtained for $\theta = 0$ reproduced well and could be taken as the measure of oxygen bond strength.

In Boreskov's laboratory studies were also undertaken in which the bonding energy of oxygen was estimated on the basis of measurements of oxygen equilibrium pressure over the oxides within an appropriate range of temperature. The measurement were carried out in a bivariant region where the elimination of oxygen still did not involve the generation of a new phase. The experiments in this area suffer some complications the most important of which is connected with the impossibility of fixing up the initial state of oxides with a certain stoichiometric composition. The treatment aiming at the elimination of impurities usually results in a significant change in the concentration of oxygen in the surface layer of oxide. However, when the proper standarization of samples was applied (vacuum treatment for 4 hr at 500°C and then keeping in oxygen at the same temperature (for 1 hr at $p_{O_2} = 10$ Torr), the reproducible results were obtained and the values corresponding to stoichiometric surface calculated from the Clapeyron-Clausius equation were in good accordance with the calorimetric values determined when $\theta = 0$. The data taken from [66] are given by the lower curve in Fig. 3.14.

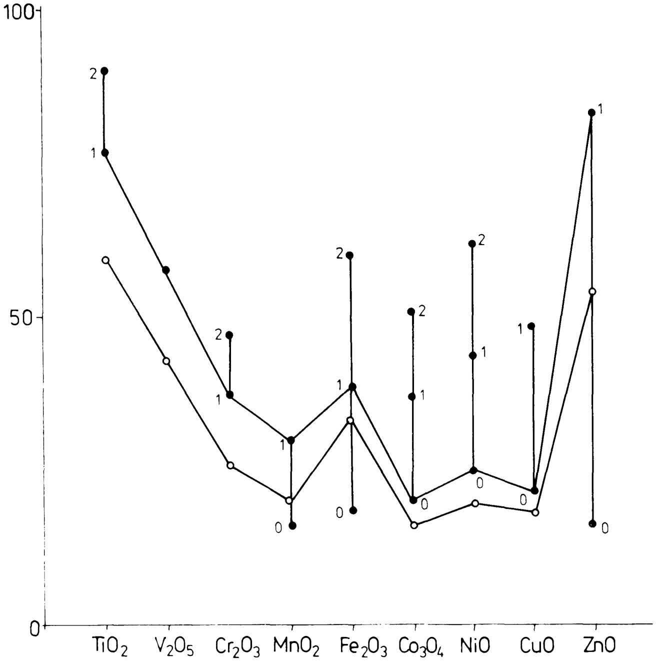

FIGURE 3.14 Activation energies $\underline{E}_d$ of oxygen desorption as determined by Halpern and Germain and oxygen bonding strength $\underline{E}$ as determined by Boreskov and colleagues by the measurement of oxygen equilibrium pressure [67].

Boreskov's results correlate well with the results of "flash" thermodesorption obtained by Germain et al. [67,68]. In this case the samples were standardized by heating them in vacuo (500—700°C) and then in oxygen. After cooling and evacuating the sample was heated rapidly (in the course of 20—40 sec) to 800—900°C by using a strong beam of light. The evolution of oxygen was followed mass spectrometrically. Depending on the nature of the oxide, one to three desorption peaks were registered and labeled as 0, 1 and 3. An example of a desorption spectrum is shown in Fig. 3.15. The pressure of several peaks indicated heterogeneity of labile oxygen. This method was therefore more sensitive than the method consisting of measurement of oxygen equilibrium pressure. With temperatures of the peaks and the heating rate known, the activation energies of oxygen desorption $\underline{E}_d$ for particular oxides could be calculated. The results are given in Fig. 3.14. The line joining the points corresponding to the activation energy of peak 1 for the oxides of Ti, V, Cr, Mn, Fe, and Zn and the points corresponding

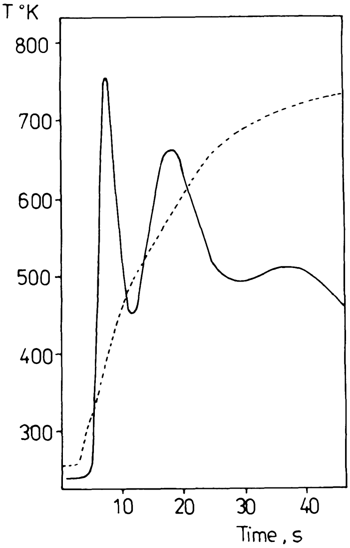

FIGURE 3.15 Flash desorption spectrum of oxygen from Co_3O_4. Full line, mass spectrometer current; dashed line, heating curve [67].

to peak O for the oxides of Co, Ni, and Cu is parallel to the line showing Boreskov's q_s values (lower curve in Fig. 3.14) [66]. It can therefore be concluded that the first species detected by Boreskov's method are oxygen in state 1 for the former group of oxides and oxygen in state 0 for the latter one. The parallelism between q_s and E_d values indicates that in this case the Polanyi-Evans correlation between the heat of reaction and its activation energy can be applied. This correlation obtained for homogeneous reactions was applied to heterogeneous catalytic reactions for the first time by Temkin and Balandin [69]:

$$E_d = a \pm dq_s \tag{3.59}$$

The plus corresponds to the situation in which oxygen-surface bond is broken in the course of formation of the active complex and the minus to that when the oxygen-surface bond is formed. The values a = 3.61 kcal mol^{-1} and b = 1.32 were obtained in [67].

To the methods used for the characterization of oxygen bonding strength also belongs isotopic exchange of oxygen, described in detail in the preceding section. As was stated, only the results obtained for heteromolecular exchange on the samples which were previously equilibrated with oxygen can be taken for the characterization of oxygen bond strength. Owing to the fact that in some cases surface oxygen is not uniform and its activity does change with the exchange degree, the best reproducibility is obtained when only the initial rate of exchange is taken into account [66]. The correlation between the activation energy of isotopic oxygen exchange and the oxygen bonding strength determined at standard conditions is experimentally confirmed. The parallelism between the specific activities of oxygen exchange and catalytic oxidation of CO and H_2 is shown in Fig. 3.13. When comparing both correlations it can be inferred that the catalytic activity increases with decreasing oxygen-surface bond strength, which makes easier the formation of active complex occurring with the breaking of this bond. Another example of such a correlation was reported in [66] where the specific activities of a series of Mn, Ca, Ni, Zn, Co, Mg, and Cu cobaltites (spinels) in the catalytic oxidation of H_2 and CH_4 as well as in oxygen exchange were investigated.

However, it should be stressed that the correlations obtained in the case of simple nonselective oxidation catalytic reactions occurring on the oxides of period IV transition metals do not possess a general character, nor are they observed in the same form with the oxides of periods V and VI transition metals or mixed oxides containing Mo, W, Sn, Sb, V, etc., frequently used in the selective oxidation of hydrocarbons. Gelbstein et al. [70] confirmed Boreskov's correlations in the case of nonselective oxidation of olefins on the oxides of period IV transition metals but stated that it is not valid in the case of MoO_3, Sb_2O_5, Bi_2O_3, and V_2O_5. All these oxides exhibit high oxygen bonding strength (activation energies of oxygen isotopic exchange between 35 and 75 kcal mol^{-1}) and low activity in the complete oxidation of olefins independent of oxygen bond strength. The most probable cause of low catalytic activity of these oxides in reactions of complete oxidation lies in the high-energy of surface-oxygen bond. At the same time typical of these oxides is high selectivity of catalytic action with respect to olefin oxidation reactions.

The situation is much more complicated in selective oxidation than in complete oxidation. The oxygen bonding energy should be weak enough to enable the formation of the product of partial oxidation but at the same time strong enough to render its further oxidation possibly difficult. Sachtler [71] indicated that such a situation can be expected if the surface oxygen bonding strength does strongly increase with the deoxidation of the surface expressed as its reduction degree $\underline{x}$. In the stationary state of the catalytic reaction the optimal oxygen bonding strength can be established. The high value of $\underline{dq_s}/\underline{dx}$ should, according to Sachtler's hypothesis, indicate high selectivity. In fact, when comparing the behavior of MnO_2 nonselective in the oxidation of benzaldehyde with that of V_2O_5 fairly selective and highly selective V_2O_5-SnO_2 (selectivities 0, 70—80, and 90—100%, respectively), he found that the enthalpy gradient increased in the sequence 8, 80, 200.

It is clear that in the selective oxidation the energy of oxygen bonding to the surface must not necessarily be the only factor controlling the kinetics and selectivity of the reaction. In selective oxidation of hydrocarbons dissociative adsorption of a substrate molecule, i.e., hydrogen splitting off in a C—H bond and formation of a species subsequently reacting with surface oxygen, is another step which may control the overall catalytic process [71].

REFERENCES

1. R. L. Burwell Jr., G. L. Haller, K. C. Taylor, and J. F. Reed, Adv. Catal., 20, 7 (1969).
2. J. Ziółkowski, J. Catal., 80, 263 (1983).
3. L. Kihlborg, Arkiv Kemi, 21, 357 (1963).
4. L. Pauling, The Nature of Chemical Bond, Cornell University Press, Ithaca, 1945, p. 384.
5. T. M. French and G. A. Somorjai, J. Phys. Chem., 74, 2489 (1970).
6. D. Hofmnn, Current Topics in Material Science, Vol. 7 (E. Kaldis, ed.) North Holland, Amsterdam, 1981, p. 305.
7. F. A. Kröger, Chemistry of Imperfect Crystals, North Holland, Amsterdam, 1964.
8. M. Grade, Current Topics in Materials Science, Vol. 7 (E. Kaldis, ed.), North Holland, Amsterdam, 1981, p. 339.
9. J. Dereń, J. Haber, and J. Sloczynski, Bull. Pol. Ac. Chem., 9, 245 (1961).
10. J. Finster, P. Lorenz, F. Fievet, and M. Figlarz, Proc. 9th Symposium on the Reactivity of Solids, 1980, Vol. 1, Elsevier, New York, 1981, p. 391.
11. B. Grzybowska, J. Haber, W. Marczewski, and L. Ungier, J. Catal., 42, 327 (1976).
12. A. Bielański and M. Najbar, J. Catal., 57, 326 (1979).
13. M. Najbar and S. Niziol, J. Solid State Chem., 26, 3 (1978).
14. M. Najbar and E. Bielańska, Proc. 9th Int. Symposium on the Reactivity of Solids, Vol. 2 (K. Dyrek, J. Haber, and J. Nowotny, eds.), Elsevier, 1982, p. 657.
15. I. Aso, T. Amamoto, N. Yamazoe, and T. Seiyama, Chem. Lett., 365 (1980).
16. I. Aso, T. Amamoto, N. Yamazoe, and T. Seiyama, Chem. Lett., 1435 (1980).
17. K. Knötzinger, Adv. Catal., 25, 184 (1976).
18. J. B. Peri, J. Phys. Chem., 69, 220 (1965).

19. H. Dunken and P. Fink, Z. Chem., 6, 194 (1966).
20. K. Hauffe and S. Roy Morrison, Adsorption, Walter de Gruyter, 1974.
21. Th. Wolkenstein, Physico-chimie de la surface des semiconducteurs, Mir, Moscow, 1977.
22. K. Hauffe, Angew. Chem., 67, 189 (1955).
23. A. Bielański and M. Najbar, J. Catal., 25, 398 (1972).
24. J. Dereń and J. Nowotny, Oxid. Metals, 1, 73 (1969).
25. J. Nowotny, Bull. Pol. Acad. Chem., 10, 743 (1973).
26. P. Amigues, Thesis, Lyon, 1964.
27. E. Fryt, Thesis, Cracow, 1967.
28. J. Haber and F. S. Stone, Trans. Faraday Soc., 59, 192 (1963).
29. Z. M. Jarzebski, Semiconducting Oxides, Pergamon Press, New York, 1973.
30. D. A. Dowden and D. Wells, Actes du deuxième congrés sur la catalyse, Vol. 2, Technip, Paris, 1960, p. 1499.
31. M. L. Volpe and J. F. Reddy, J. Catal., 7, 76 (1967).
32. J. Haber and E. Mielczarska, Zhurn. Phys. Khim, 53, 2909 (1979).
33. Z. Dziewiecki, J. Haber, and E. Mielczarska, React. Kinet. Catal. Lett., 3, 55 (1975).
34. E. Goerlich, Papers of the Commission of Technical Sciences, Polish Academy of Sciences, Ceramics, 4, Cracow, 1965.
35. S. Mrowec, Defects and Diffusion in Solids, Elsevier, New York, 1980.
36. J. H. de Boer and E. J. Verwey, Proc. Phys. Soc., 49, 59 (1937).
37. P. Roussel and S. J. Teichner, Catal. Rev., 6, 133 (1972).
38. A. K. Cheetham, B. E. F. Fender, and R. I. Taylor, J. Phys. Solid State Phys., 4, 2160 (1971).
39. A. F. Wells, Structural Inorganic Chemistry, 4th ed., Clarendon Press, Oxford, 1975, p. 474.
40. H. Horiuchi, N. Morimoto, and Tokonami, J. Solid State Chem., 17, 407 (1976).
41. H. Horiuchi, M. Tokonami, and N. Morimoto, Mater. Res. Bull., 6, 833 (1971).
42. A. D. Wadsley and J. S. Anderson, Nature, 211, 58 (1966).
43. J. P. Bonnet and M. Onillon, Solid State Ionics, 12, 337 (1984).
44. J. Haber and B. Grzybowska, Tagungsberichte der III Int. Katalyse Konferenz, Vol. 2, Bad Reinhardsbrunn, DDR, 1984, p. 224.
45. E. R. S. Winter, Adv. Catal., 10, 196 (1958).
46. K. G. Boreskov, Adv. Catal., 15, 285 (1964).
47. J. Novakova, Catal. Rev., 4, 77 (1971).

48. E. R. S. Winter, *J. Chem. Soc., A*, 2889 (1968).
49. V. V. Nikisha, B. N. Shelimov, V. A. Shvets, A. P. Griva, and V. B. Kazansky, *J. Catal., 28*, 230 (1973).
50. A. Ozaki, *Isotopic Studies of Heterogeneous Catalysis*, Kodansha and Academic Press, 1977.
51. P. Jiru and J. Novakova, *Coll. Czech. Chem. Commun., 28*, 1 (1963).
52. K. Klier, J. Novakova, and P. Jiru, *J. Catal., 2*, 479 (1963).
53. E. R. S. Winter, *J. Chem. Soc., A*, 1832 (1969).
54. Kh. M. Minachev and G. V. Antoshin, *Dokl. Akad. Nauk USSR, 161*, (1), 122 (1965).
55. J. Novakova and P. Jiru, *Coll. Czech. Chem. Commun., 29*, 1114 (1964).
56. G. K. Boreskov and V. V. Pokrovsky, *Kinet. Katal., 2*, 657 (1961).
57. G. K. Boreskov, *Problemy kinetiki i kataliza, 9*, 49 (1966).
58. J. E. Germain, *Intra-Science Chem. Rep., 6*, 101 (1972).
59. G. K. Boreskov and B. I. Marsheva, *Dokl. Akad. Nauk USSR, 213*, 112 (1973).
60. G. I. Golodets, *Geterogenno-kataliticheskie reaktsii s uchastiem molekularnogo kisloroda*, Naukova Dumka, Kiev, 1977.
61. G. K. Boreskov, *Kinet. Katal., 14*, 7 (1973).
62. N. Giordano, E. Cavaterra, and D. Zema, *Chim. Ind. (Milan), 45*, 15 (1963).
63. J. E. Germain and R. Laugier, *Bull. Soc. Chim. F.,* 541 (1972).
64. K. Klier, *J. Catal., 8*, 14 (1968).
65. V. A. Sazonov, V. V. Popovskii, and K. G. Boreskov, *Kinet. Katal., 9*, 307, 313 (1968).
66. G. K. Boreskov, V. V. Popovskii, and V. A. Sazonov, *Proc. 4th Int. Congress on Catalysis*, Moscow, 1968, Akademiai Kiado, Budapest, 1971, p. 439.
67. B. Halpern and J. E. Germain, *J. Catal., 37*, 44 (1975).
68. L. Gonzales-Cruz, J. P. Jolly, and J. E. Germain, *J. Chim. Phys., 75*, 324 (1978).
69. A. A. Balandin, *Adv. Catal., 19* (1969).
70. A. I. Gelbstein, S. S. Stroeve, Yu. M. Bakshi, and Yu. A. Mischenko, *Proc. 4th Int. Congr. on Catalysis,* Moscow, 1968, Akademiai Kiado, Budapest, 1971, p. 297.
71. W. M. H. Sachtler, G. J. Dorgelo, and R. J. Voorhoeve, *Proc. 4th Int. Congr. on Catalysis*, Moscow, 1968, Akademiai Kiado, Budapest, 1971, p. 454.

4

Mechanism of the Catalytic Oxidation:
General Considerations

I. GENERATION OF REACTIVE SPECIES

Molecular oxygen contains in its ground state two unpaired electrons, which are localized on the degenerate antibonding $\pi_g 2p$ orbitals; the ground state is thus a triplet $^3\Sigma^-_g$ (see Section I of Chapter 1). Because of the rule of spin conservation, reactions between this triplet oxygen and organic molecules which are in the singlet state experience high activation energies. This symmetry barrier may be overcome either by activating oxygen to the singlet state or by activating the organic molecule to make it susceptible to the reaction with molecular or atomic ions in the doublet or singlet state. Of particular importance is the nucleophilic attack by the oxide ion O^{2-}.

Crystallites of transition metal oxides may exhibit two types of crystal faces [1]:

Those whereby all constituent atoms are chemically fully saturated but have either exposed transition metal cations with empty d orbitals, which may play the role of LUMO of the oxide; or free electron pairs of the oxide ions, which may act as the oxide HOMO.

Those which are composed of coordinatively unsaturated cations and anions, whereby excess charges are accumulated generating considerable variations of the potential along the surface.

The first type may be considered as hydrophobic. Exposed transition metal ions with empty d_{xz} and d_{yz} orbitals, which are LUMOs, may play the role of electron acceptor sites. Oxygen ions bridging the M-O_x polyhedra have free electron pairs at HOMOs, which may act as electron donors [2]. When a hydrocarbon molecule approaches such a surface, the C—H bonds may react with the empty d orbitals of the transition metal ions, the protons being shifted to the bridging oxide ions and the alkyl radicals attached to the transition metal ions. Hydrocarbon molecules thus become activated and rendered prone to the nucleophilic attack of other bridging oxide ions.

Different interactions prevail at crystal planes of the second type, which may be considered as hydrophilic [3,4]. These planes show a strong tendency to dissociatively adsorb water. The OH groups generated as the result of hydroxylation may show more or less acidic character and interact with the hydrocarbons to form carbonium ions. On heating at higher temperatures dehydration of the surface takes place, leaving coordinatively unsaturated cations and anions, on which considerable excess charge is accumulated. Such sites may induce a heterolytic bond scission in the adsorbed reactant molecules. Simultaneously the reducing atmosphere of the hydrocarbon reaction medium usually causes some reduction of the catalyst surface so that lower valent metal cations are generated. Such ions may function as sites activating oxygen molecules to their electrophilic active forms.

The type of product formed as the result of an electrophilic attack of oxygen on the hydrocarbon molecule depends on the structure of the oxygen adsorption complex. That is, quantum chemical calculations of, for example, the reactions of oxygen with benzene and toluene revealed [5,6] that the type of product formed depends on the direction of approach and mutual orientation of the reacting molecules and on the mode of oxygen activation. An oxygen molecule may be bound to the surface of an oxide in many different forms, derived from the metal-dioxygen complexes described in Chapter 1. On the basis of ESR studies, different forms of oxygen molecules adsorbed at the surface of the CoO-MgO solid solution (Fig. 4.1) could be distinguished [7]: species linked to the surface Co^{3+} cations side-on and end-on, forming different angles to the surface, from a vertical orientation to a horizontal one. It is noteworthy that at the steps and kinks a two-site adsorption may take place. Also surface OH groups may interact with adsorbed oxygen molecules.

II. ELECTROPHILIC AND NUCLEOPHILIC OXIDATION

As discussed in Chapter 2, dioxygen adsorbed at oxide surfaces is present mainly in form of superoxide ions. The existence of peroxide ions has not been proved directly; however, it cannot be excluded a priori. At higher temperatures both adsorbed superoxide

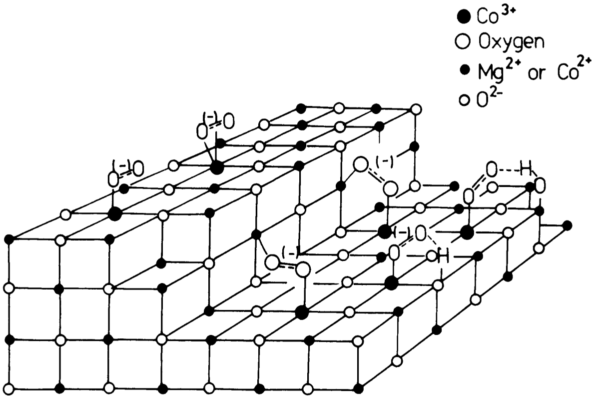

FIGURE 4.1 Different adsorption complexes of dioxygen at the surface of CoO-MgO solid solution. (Adapted from [7].)

and peroxide dioxygen species are unstable and presumably decompose with the formation of the ion radical species O^-. All three activated oxygen forms—the neutral singlet O_2 and the ionic O_2^- and O^- species—are strongly electrophilic reactants which attack the organic molecule in the region of its highest electron density, i.e., the π bonds. At variance with their behavior in the liquid phase, the peroxy and epoxy complexes formed as the result of an electrophilic attack of O_2^- or O^- species on the π bonds of hydrocarbon molecule at the surface of an oxide are intermediates which lead to the degradation of the carbon skeleton under heterogeneous catalytic reaction conditions. In the case of, say, oxidation of olefins, saturated aldehydes are formed in the first stage (upper left of Fig. 4.2). These are usually much more reactive than unsaturated aldehydes or anhydrides and at higher temperatures undergo a rapid total oxidation.

The presence of O_2^- or O^- species at the surface of an oxide may be detected by different techniques (see Chapter 2). One of the methods which permits the quantitative determination of the number of electrons transferred between the solid and the adsorbed layer is the measurement of the changes of work function in the course of adsorption. Thus, when changes of work function due to exposure to oxygen are followed upon temperature variation and the amount of oxygen adsorbed is simultaneously measured, the number of electrons localized per oxygen atom adsorbed may be determined and hence the type of oxygen species residing at the surface may be found. Results of such experiments [8] carried out with different oxides are summarized in Table 4.1 and compared with the catalytic properties of these oxides. They indicate that whenever electro-

TABLE 4.1 Oxygen Species at Surfaces of Various Oxides

Catalyst	Temperature range (K)	Oxygen species	Catalytic behavior
Co_3O_4	293–423	O_2^-	Total oxidation
	573–673	O^-	Total oxidation
V_2O_5 and V_2O_5-TiO_2	293–393	O_2^-	Total oxidation
	533–653	O^-	
	653	O^{2-}	Selective oxidation of aromatics
$Bi_2Mo_3O_{12}$	538–673	O^{2-}	Selective oxidation of olefins

Source: Ref. 8.

philic oxygen species O_2^- or O^- is present at the surface, total oxidation is observed in the course of the catalytic oxidation of hydrocarbons.

The second route of heterogeneous oxidation is the reaction with lattice oxide ion O^{2-}. At variance with all other oxygen species, these ions have no oxidizing properties but as already mentioned in Chapter 2, are nucleophilic reactants which can be inserted into the activated hydrocarbon molecule by a nucleophilic addition, resulting in the formation of an oxygenated product. This reaction path starts with the activation of organic molecules, which thus become prone to undergo an attack by nucleophiles, and consists of a series of consecutive steps of hydrogen abstraction and nucleophilic oxygen addition, with each of these steps requiring different active centers to be present at the catalyst surface. It is the cations of the catalyst which act as oxidizing agents in some of the consecutive steps of the reaction sequence, forming the activated hydrocarbon species. In subsequent steps these undergo a nucleophilic attack by lattice oxygen ions and the oxygenated product is desorbed, leaving oxygen vacancies at the surface of the catalyst. Such vacancies are then filled with oxygen from the gas phase, simultaneously reoxidizing the reduced cations. It should be noted that incorporation of oxygen from the gas phase into the oxide surface does not necessarily take place at the same site from which surface oxygen is inserted into the hydrocarbon molecule and is transported through the lattice. This mechanism may be represented by the cycles represented in Fig. 4.3.

In the case of complex hydrocarbon molecules, the nucleophilic addition of oxygen may take place at different sites of the molecule. Specifically, it will take place at that site which is made most electropositive by appropriate bonding of the molecule at the active center

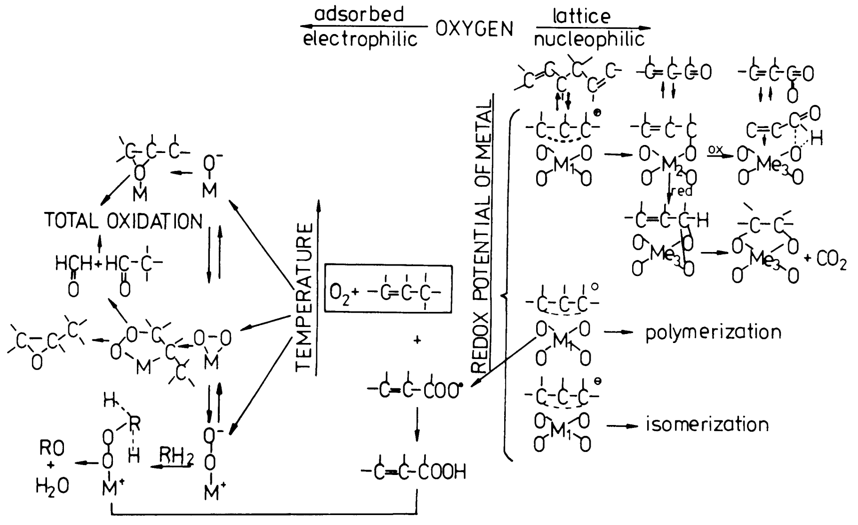

Activation of oxygen to electrophilic forms O_2^-, O_2^{2-}, O^-

Activation of hydrocarbon and insertion of nucleophilic oxygen O^{2-}

FIGURE 4.2 Mechanism of the catalytic oxidation of hydrocarbons.

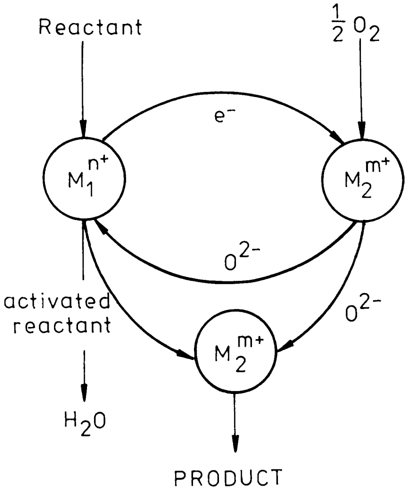

FIGURE 4.3 Oxidation-reduction cycles in selective catalytic oxidation.

of the catalyst. As an example, Fig. 4.4 shows schematically the different pathways of the oxidation of butene-1. The butene-1 molecule activated to a methylallyl species can react in three directions: it can lose the second hydrogen atom and form butadiene, or undergo a nucleophilic attack by the oxide ion, either on the carbon-1 atom to form crotonaldehyde, or on the carbon-2 atom resulting in the formation of methyl vinyl ketone.

When adsorption of the hydrocarbon molecule results in the formation of a radical, interaction between adsorbed molecules is favored and dimerization or polymerization occurs; when the adsorbed species are negatively charged, isomerization may be favored (cf. Fig. 4.2).

Reactions of catalytic oxidation may thus be divided into two categories [9]: (1) electrophilic oxidation, proceeding through the activation of oxygen, and (2) nucleophilic oxidation, in which activation of the hydrocarbon molecule is the first step, followed by consecutive steps of nucleophilic oxygen insertion and hydrogen abstraction. They may be conveniently systematized [10] according to the number of elementary structural transformations introduced into the reacting molecule (Table 4.2). The mildest electrophilic oxidation is the addition of oxygen to the double bond resulting in the formation of epoxides, or the oxy hydration of the double bond to form respective saturated ketones (e.g., propene → acetone). A more pronounced structural change is the fission of the double C—C bond, saturated aldehydes being formed from olefins ($CH_3—CH=CH_2 \longrightarrow CH_3—CHO + CH_2O$), or the fission of the aromatic

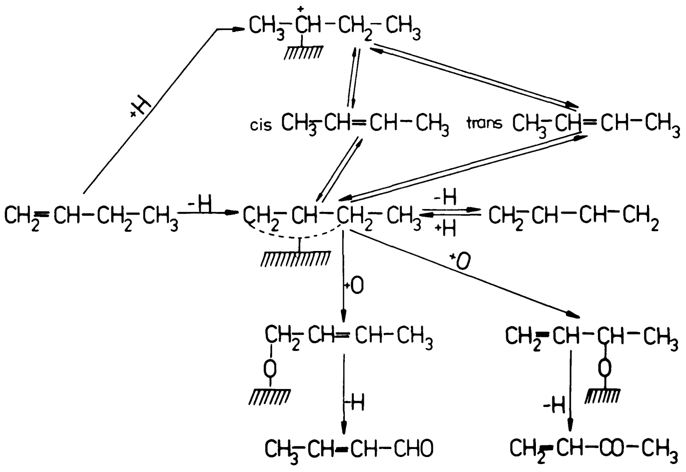

FIGURE 4.4 Scheme of reactions of butene-1.

TABLE 4.2 Heterogeneous Oxidation of Hydrocarbons

Electrophilic oxidation reaction type	Catalyst	Nucleophilic oxidation reaction type	Catalyst
1. With double bond fission		1. Without introduction of the heteroatom	
1.1. oxidation of olefins to oxides	Ag_2O	1.1. oxidative dehydrogenation to alkanes and alkenes to dienes	Bi_2O_3-MoO_3-P_2O_5
1.2. oxy hydration of olefins to saturated ketones	SnO_2/MoO_3	1.2. oxidative dehydrodimerization and dehydrocyclization of alkenes	MoO_3-Al_2O_3
2. With C—C bond fission			
2.1. oxidation of olefins to saturated aldehydes	V_2O_5	2. With introduction of heteroatom	
2.2. oxidation of aromatics to anhydrides and acids with ring rupture	V_2O_5/MoO_3	2.1. with introduction of heteratom into hydrocarbon chain	
		2.1.1. introduction of oxygen	
3. Total oxidation to CO_2 and H_2O	Co_3O_4 $CuCo_2O_4$ $CuCr_2O_4$	a) oxidation of olefins to unsaturated aldehydes and ketones	Bi_2O_3-MoO_3
		b) oxidation of alkyl aromatics to aldehydes	Bi_2O_3-MoO_3
		2.1.2. introduction of nitrogen	
		a) ammoxidation of olefins to nitriles	UO_3-Sb_2O_4
		2.2. introduction of heteroatom into acyl group	
		a) oxidation of aldehydes to acids	NiO-MoO_3
		b) oxidation of alkyl aromatics to anhydrides	V_2O_5-MoO_3

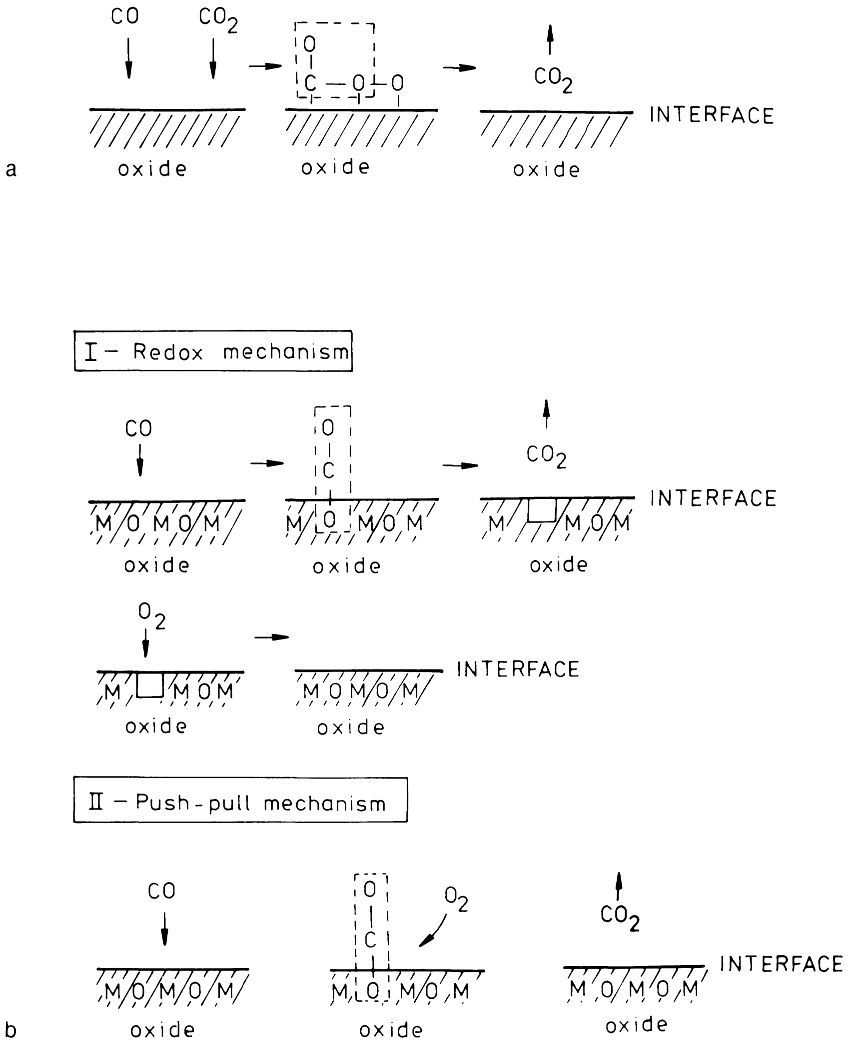

FIGURE 4.5 Extrafacial (a) and interfacial (b) reactions.

ring resulting in the appearance of anhydrides. The final stage is total oxidation to $CO_2 + H_2O$. Along the nucleophilic route the first, smallest structural change is the abstraction of hydrogen in the process of oxidative dehydrogenation of alkanes and alkanes to dienes, or the dehydrodimerization and dehydrocyclization. Deeper structural changes are involved in reactions in which a heteroatom is introduced into the hydrocarbon molecule by a nucleophilic addition. This may be oxygen, sulfur, nitrogen, etc. Introduction of the first, e.g., oxygen, results in the formation of aldehydes; the introduction of the second one in the formation of acids or anhydrides. In all these processes the carbon skeleton remains unchanged.

As shown earlier, it is the oxygen species O_2, O_2^-, and O^- generated on adsorption at the surface of an oxide catalyst which are responsible for electrophilic oxidation; both reactants of this reaction are located at the gas phase side of the gas-solid interface. Such catalytic reactions are called extrafacial, or reactions without transfer (WT) (Fig. 4.5a). On the other hand, the nucleophilic oxidation is a reaction between the adsorbed reactant and the oxide ion of the catalyst lattice, which is transferred across the gas-solid interface. Therefore this type of catalytic reaction is called interfacial (Fig. 4.5b, I and II).

Two kinds of interfacial reactions may be distinguished. One kind is reactions which are considered to proceed in two steps: (1) reaction between the reactant and the oxide to give oxygenated products and partially reduced catalyst, and (2) reoxidation of the reduced catalyst with gaseous oxygen to restore the catalyst to its initial state. Because in this kind of reaction the reduction part and oxidation part are considered to be separate steps, it is called the redox mechanism. A mechanism of this type was postulated by Mars and van Krevelen [11] to explain the kinetics of the oxidation of aromatics on V_2O_5 catalysts; therefore it is also known as the Mars-van Krevelen mechanism.

To the second kind of interfacial reactions belong those in which both reduction and oxidation steps are performed in one transformation. They are thus called concerted or push-pull reactions. An example would be the oxidation of CO on ZnO catalyst [12]. It was shown that tearing away of the surface oxide ions of the catalyst by the desorbing product and the reoxidation of the reduced catalyst proceed simultaneously on the same site in a concerted operation, as illustrated in Fig. 4.5b, II.

III. ROLE OF OXYGEN BOND ENERGY AT CATALYST SURFACE

Let us consider in general terms a reaction of the oxidation of a reactant RH_2 by gas phase oxygen on an oxide catalyst, given by the equation:

$$RH_2 + O_2 \longrightarrow RO + H_2O \qquad \Delta \underline{G}^{\theta} \qquad (4.1)$$

It was stated in Chapter 3 that any catalytic oxidation process occurring at the surface of an oxide can be represented by a scheme comprising the reaction between the oxidizable reactant and the active oxygen of the surface, resulting in the formation of an oxidized product desorbing from the surface and the reaction, in which the reduced surface of the catalyst becomes reoxidized by gas phase oxygen (redox mechanism). In the case of a hydrogen-containing reactant RH_2, e.g., a hydrocarbon, the two stages may be represented by following:

(a) Reaction of the reactant with oxygen bound at the surface of the catalyst KO:

$$RH_2 + 2KO \longrightarrow RO + H_2O + 2K \qquad \Delta \underline{G}_{\underline{a}}^{\theta} \qquad (4.1a)$$

(b) Replenishment of the catalyst surface with gas phase oxygen to restore the catalyst to its initial state:

$$K + \frac{1}{2}O_2 \longrightarrow KO \qquad \Delta \underline{G}_{\underline{b}}^{\theta} \qquad (4.1b)$$

The rate of the overall reaction (4.1) attains the highest value when rate constants of both stages (a) and (b) are equal:

$$\underline{k}_{\underline{a}} = \underline{k}_{\underline{b}} \qquad (4.2)$$

Taking into account the Brönsted-Polanyi equation,

$$\underline{k} = \underline{gK}^{\alpha} \qquad (4.3)$$

and assuming that the constants $\underline{g}$ and α in Eq. (4.3) do not differ much for the two steps of the reaction, we find that catalytic oxidation has the highest rate when equilibrium constants $\underline{K}_{\underline{a}}$ and $\underline{K}_{\underline{b}}$ are equal:

$$\underline{K}_{\underline{a}} = \underline{K}_{\underline{b}} \qquad (4.4)$$

Using the equation correlating the equilibrium constant with the change of the Gibbs free energy of the reaction:

$$\Delta G^{\theta} = -RT \ln K$$

we obtain

$$(\Delta G_a^{\theta})_{opt} = (\Delta G_b^{\theta})_{opt}$$

the subscript opt indicating that it is the condition for the optimal reaction rate. As, however, for reaction (4.1),

$$\Delta G^{\theta} = \Delta G_a^{\theta} + \Delta G_b^{\theta} \tag{4.5}$$

we finally arrive at the conclusion that

$$(\Delta G_b^{\theta})_{opt} = \frac{\Delta G^{\theta}}{2} \tag{4.6}$$

from which it follows that

$$(Q_b)_{opt} \approx \frac{Q}{2} + \delta \tag{4.7}$$

where Q's are heats of the respective reactions, and

$$\delta = T\left(\frac{\Delta S}{2} - \Delta S_a\right) \tag{4.8}$$

For many catalytic reactions the values of δ are small and the condition for the optimal catalyst may be expressed in a simple form:

$$(Q_b)_{opt} \approx \frac{Q}{2} \tag{4.9}$$

Equation (4.9) indicates that for a reaction (4.1) proceeding in two separate steps (4.1a) and (4.1b), when $Q_a < Q_b$, it is the interaction of the reactant with oxygen at the surface of the catalyst which is rate determining, the replenishment of the surface with oxygen being very rapid. On increasing the heat of interaction Q_a of the reactant with surface oxygen from a small value this step is accelerated and so is the overall reaction (4.1) until Q_a becomes equal to Q_b. From this moment step b begins to be rate-determining and on further increasing Q_a the overall rate now decreases because of the decreasing heat Q_b of the replenishment of catalyst surface with oxygen. A volcano-shaped curve is thus obtained, which is the manifestation of a very general relationship, constituting the basis of many theoretical considerations.

It should be emphasized at this point that Eqs. (4.1a) and (4.1b) are of general validity and describe both nucleophilic and electrophilic oxidations depending on the meaning attached to the symbols KO and K. When KO and K represent the oxidized and reduced state of the catalyst, respectively, the symbol O in KO being the lattice O^{2-} ion located at the surface of the catalyst, Eqs. (4.1a) and (4.1b) describe the redox mechanism. In this case $\Delta \underline{G}_a^\theta$ represents the Gibbs free energy of the reaction between the reactant RH_2 and the metal oxide used as catalyst, and $\Delta \underline{G}_b^\theta$ is the Gibbs free energy of the reoxidation of the oxide reduced in step (a). Depending on the defect structure of the oxide $\Delta \underline{G}_b^\theta$ may have different meaning. Namely, when the catalyst is a transition metal oxide which can accommodate a relatively high concentration of defects, generated on its reduction, $\Delta \underline{G}_b^\theta$ is simply the Gibbs free energy related to the defect equilibria. If, however, the transition metal forms several oxide phases in which it assumes different oxidation states, these phases having narrow homogeneity composition ranges, $\Delta \underline{G}_b^\theta$ may be approximated by the Gibbs free energy of the oxidation of a lower valent oxide into a higher valent one.

When the symbol O in KO of Eqs. (4.1a) and (4.1b) is assumed to represent oxygen adsorbed at the surface of the catalyst K, step (a) is then equivalent to the oxidation of reactant RH_2 by the adsorbed oxygen, and step (b) readsorption of oxygen at the surface of the catalyst K. Under such an assumption the set of Eqs. (4.1) describes the electrophilic oxidation, $\Delta \underline{G}_a^\theta$ being the Gibbs free energy of the reaction between reactant RH_2 and oxygen adsorbed at the surface of the catalyst, and $\Delta \underline{G}_b^\theta$ the Gibbs free energy of oxygen adsorption.

In the last 20 years many attempts have been undertaken to prove the validity of this approach. In studies of the catalytic activity–heat of adsorption correlation different parameters were taken as the measure of the heats of adsorption, the experimental values being accessible only for a very limited number of oxides. Most often the discussions were based on the observation that a linear dependence exists between the heat of adsorption of oxygen and the heat of formation of the respective oxide (Fig. 4.6); the latter value may thus be used instead of the heat of adsorption in seeking a correlation with catalytic activity. As an example, Fig. 4.7 shows the dependence of the rate of total oxidation of propene on the heat of formation of the higher valent oxide from a lower one, found by Roiter and Golodetz [13]. It may be seen that a volcano-shaped curve was indeed obtained, the position of maximum corresponding to half of the heat of burning propene, recalculated per oxygen atom.

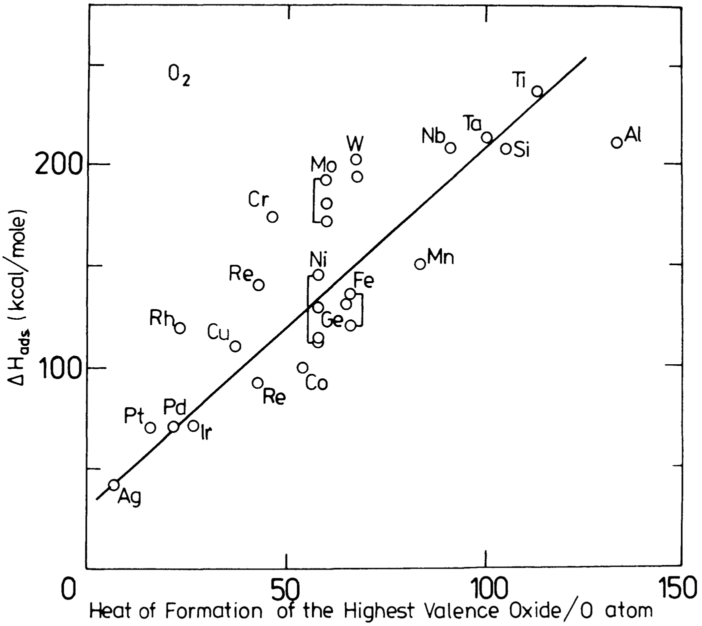

FIGURE 4.6 Heat of adsorption of oxygen as function of the heat of formation of oxides. (After [47].)

Different approach was used by Boreskov and his school [14]. It is based on the assumption that on heating an oxide, only the surface at first becomes equilibrated with the gas phase, the equilibrium with the bulk being established only at higher temperatures:

$$O_2 \text{ (gas)} \rightleftarrows O_2 \text{ (ads)} \rightleftarrows 2O \text{ (ads)} \rightleftarrows O^{2-} \text{ (lattice)}$$

low temperatures high temperatures

Thus, as already described in Chapter 3, by measuring the temperature dependence of oxygen pressure over different oxides in the appropriate temperature range the heat of adsorption could be calculated from the Clapeyron equation and correlated with the catalytic activity in various oxidation reactions. Figure 4.8 summarizes the results of the studies, in which heat of adsorption of oxygen on oxides of metals of the first transition period was correlated with the activation energy of the total oxidation of hydrogen (curve I) and methane (curve II) as well as activation energy of the homomolecular isotopic exchange of oxygen (curve III). Similar correlations were also obtained in the case of total oxidation of many other

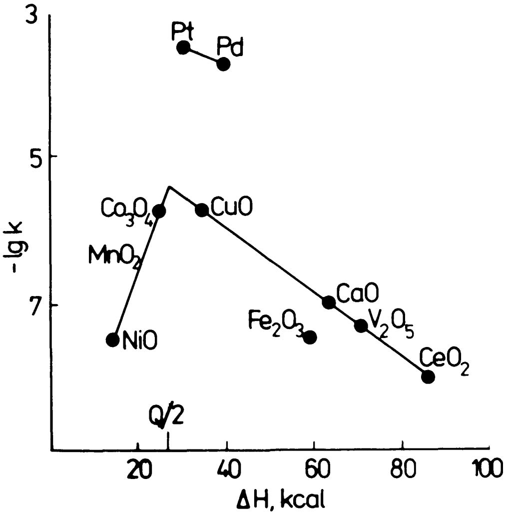

FIGURE 4.7 Logarithm of the rate constant of total oxidation of propene as a function of the heat of formation of the higher valent oxide from the lower valent one. (After [13].)

reactants such as acetylene, ethylene, benzene, cyclopropene, etc. These examples demonstrate clearly that a correlation indeed exists between the rate of total oxidation of different molecules and the heat of oxygen adsorption or such parameters as the heat of formation of an oxide, which are related to the former.

On the other hand, Germain and Laugier [15] measured the rate of selective oxidation of toluene to benzaldehyde using as catalysts a large number of different transition metal oxides, but obtained no correlation with the heat of formation of these oxides (Fig. 4.9). When the series of oxides of Cu, Co, Mn, Fe, Cr, V, U, Ti, Th, and Ta is chosen, the rate of toluene oxidation decreases with the increasing heat of the formation of the oxide, but when oxides of Bi, Mo, W, Sn, Zn, V, Cr, U are selected, an opposite relation is obtained. On analyzing the data represented in Fig. 4.9 it may be also noticed that oxides, characterized by similar values of the heat of formation, show catalytic activity in toluene oxidation, differing by many orders of magnitude. This may be easily understood, because in the case of selective oxidation of hydrocarbons it is the rate of adsorption of hydrocarbon molecules which is rate determining, and this rate depends not on the energy of bonding of oxygen but on such parameters as the nature and electronic structure of active centers responsible for the activation of reactant molecules.

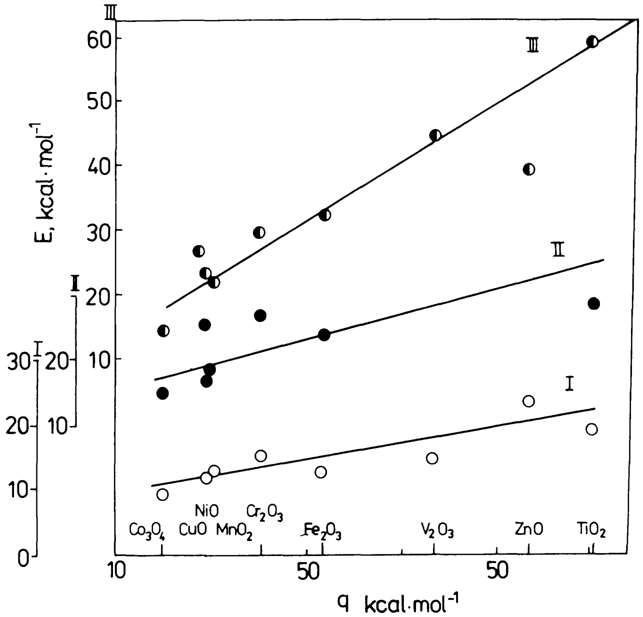

FIGURE 4.8 Activation energy of the total oxidation of hydrogen (curve I), methane (curve II), and homomolecular isotopic oxygen exchange (curve III) as function of the heat of adsorption of oxygen at the surface of transition metal oxides. (After [14].)

IV. KINETICS OF GAS PHASE CATALYTIC OXIDATION

It has been pointed out that both electrophilic oxidation, in which adsorbed oxygen species take part, and nucleophilic oxidation with the participation of lattice oxide ions, proceeding by a redox mechanism, may be described within the same kinetic formalism based on elementary steps of the oxidation of reactant to form water and the oxygenated product, and of replenishment of oxygen at the catalyst surface from the gas phase as given by Eqs. (4.1a) and (4.1b). If both steps are assumed to be first order with respect to the reactant and oxygen, respectively, the rate expressions for the individual steps can be written as

$$r_a = k_a C_R \theta \qquad (4.10a)$$

$$r_b = k_b P_{O_2} (1 - \theta) \qquad (4.10b)$$

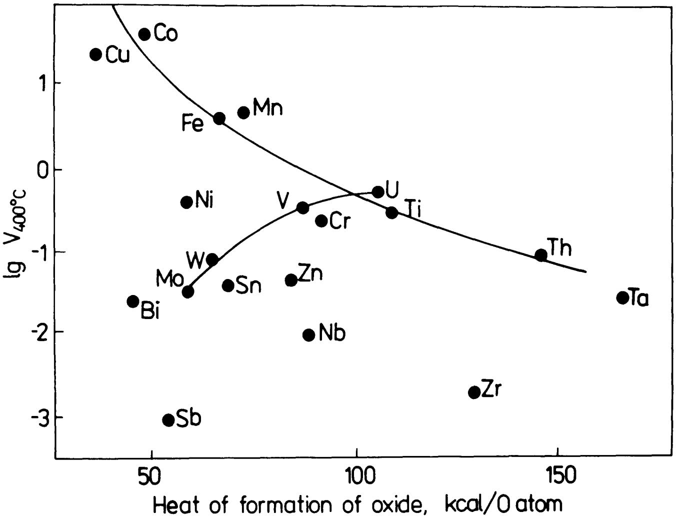

FIGURE 4.9 Rate $\underline{V}$ (mmol m^{-2} hr^{-1}) of the oxidation of toluene at 400°C as function of the heat of formation $\underline{Q}_f$ of oxides, recalculated in kcal per oxygen atom. (After [15].)

where θ is the fraction of oxygen sites at the surface of the catalyst available for oxidation of the reactant, i.e., fraction of sites, where active oxygen species reside, and $\underline{C}_R$ is the concentration of the reactant. In the steady state,

$$\underline{r}_b = \underline{n}\underline{r}_a \tag{4.11}$$

where $\underline{n}$ is the number of oxygen molecules used per mole of reactant oxidized.

Equations (4.10a), (4.10b), and (4.11) yield the fraction of active sites available for the reaction:

$$\theta = \frac{\underline{k}_b\underline{P}_{O_2}}{\underline{k}_b\underline{P}_{O_2} + \underline{n}\underline{k}_a\underline{C}_R} \tag{4.12}$$

and hence the overall rate of the oxidation of a reactant to a single product is given by

$$r = r_a = \frac{k_b k_a C_R P_{O_2}}{k_b P_{O_2} + n k_a C_R} \tag{4.13}$$

This approach can be extended to a more complex reaction network involving parallel and consecutive reaction steps. Three limiting cases may be distinguished as shown in Fig. 4.10:

(I) From the given substrates the same intermediate complex is always formed, but depending on the catalyst different products are formed.

(II) Depending on the catalyst different intermediate complexes are formed, which then transform into different products.

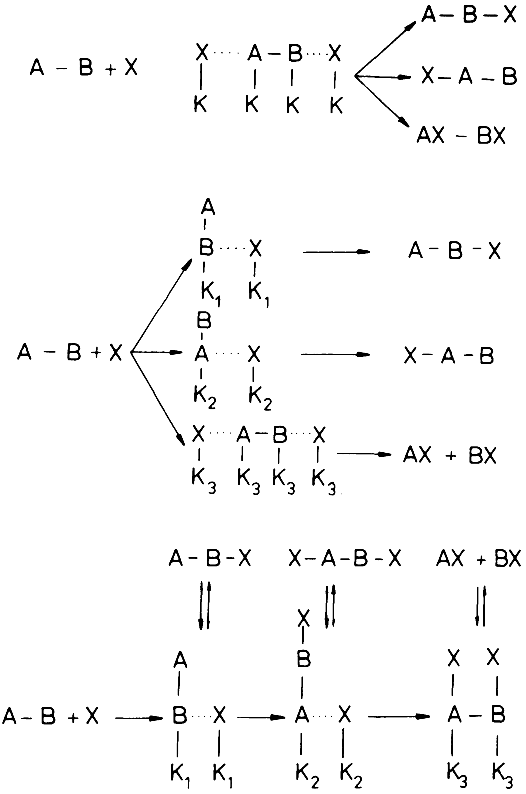

FIGURE 4.10 Role of intermediate complex in determining the selectivity of catalytic reaction.

(III) In a series of consecutive steps several intermediate complexes are formed, which either decompose to give one of the products or transform consecutively into the next one in the series.

Let us take as an example the oxidation of propene. Ample experimental evidence indicates that the conversion selectivity data can be described by the reaction sequence which is the combination of cases II and III of Fig. 4.10:

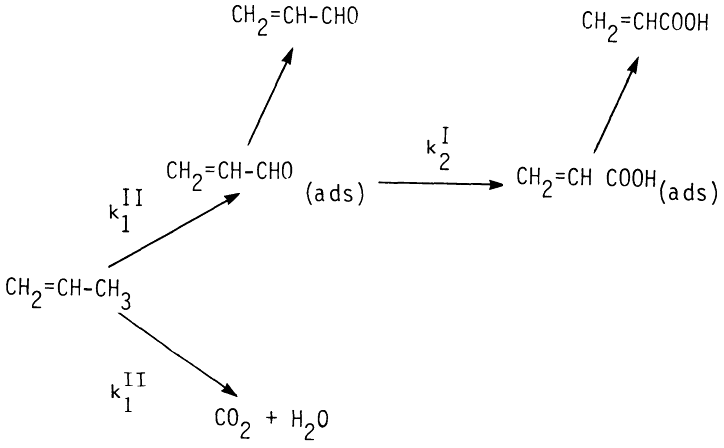

On Bi_2O_3—MoO_3 catalysts the reaction pathway II is negligible and the pathway I ends at the formation of acrolein. The rate constant k_1^I is simultaneously much smaller than the rate constant of catalyst reoxidation k_b. In terms of redox sequence given by Eqs. (4.1a) and (4.1b) it is step (4.1a) which is rate determining. Thus the overall rate of propene oxidation given by Eq. (4.13) reduces to a simple equation:

$$r = k_1^I [C_3H_6]^{1.0} [P_{O_2}]^0 \qquad (4.14)$$

Conversely, in the case of Cu_2O catalysts the interaction of propene with oxygen of the catalyst (step 4.1a) is rapid in comparison with step (4.1b) and the rate equation assumes the form:

$$\underline{r} = \frac{\underline{k}_1^I[C_3H_6]^0[\underline{P}_{O_2}]^{1.0}}{1 + \underline{b}[C_3H_4O]} \qquad (4.15)$$

In this case the reaction is hindered by the adsorption of products.

V. THE REDOX MECHANISM

As shown in Section II of this chapter, all reactions of catalytic oxidation can be categorized as electrophilic or nucleophilic ones. It is the nucleophilic addition of oxide ions O^{2-} which results in the formation of oxygenated product molecules without destruction of the carbon skeleton in reactions which are called selective oxidation. They include such important industrial processes as oxidation of olefins to oxygenated allylic compounds (e.g., oxidation of propene to acrolein or acrylic acid, or oxidation of butene to maleic anhydride) and oxidation of functional groups in aromatic molecules (e.g., oxidation of toluene to benzaldehyde). However, thermodynamic data concerning the formation of different oxygen species, discussed in Chapter 2, indicate that formation of an oxide ion O^{2-} requires the expenditure of very large amount of energy, this ion being stabilized only by the Madelung potential of the crystal lattice. It may thus be concluded that it is the lattice oxide ions, located at the surface of the oxide, which must be involved in nucleophilic oxidation.

The experimental evidence of this mechanism comes mainly from two types of experiments: comparison of the catalytic activity of the oxide catalyst in the oxidation of a given reactant in the presence and in the absence of gas phase oxygen, and determination of the distribution of isotopic oxygen in the products of the oxidation of a given reactant in the presence of labeled gas phase oxygen or oxide catalyst.

Figure 3.12 in Chapter 3 illustrates the reactivity of lattice oxygen of a Bi_2MoO_6 catalyst in the reactions with butene [16]. As was said, the experiments were carried out in the following way: at first, pulses of the mixture of butene-1 with oxygen were injected into the flow microreactor containing the molybdate catalyst, and the conversion to different products was determined as a function of the number of pulses. Oxidative dehydrogenation took place yielding about 80% butadiene (section A). After eight such pulses a series of pulses was injected containing pure butene (section B). The yield of butadiene remained pratically unchanged. However, as the gas now contained no oxygen, the lattice oxygen of the molybdate must have been used for the reaction. The yield of butadiene remained unchanged even after extracting from the lattice the amount of oxygen corresponding to a 7% reduction of the solid. Thus, it may be concluded that the lattice of the molybdate can readily supply oxygen for the reaction with the hydrocarbon at a rate much higher than that of the surface reaction itself.

It should be remembered that even in the absence of oxygen in the gas phase electrophilic oxygen species may appear at the surface as intermediates in the transfer of oxygen from the lattice into the gas phase in the process of dissociation of the solid, or in the course if its reduction, by, for example, a hydrocarbon molecule (Fig. 4.11). Thus, not only the gas phase but also the lattice of the oxide may serve as the source of electrophilic oxygen. Indeed, total oxidation of hydrocarbons is often observed on contacting them with transition metal oxides even in the absence of oxygen in the gas phase, decreasing the expected high selectivity of reactions of selective oxidation.

Boreskov et al. [17,18], for the simple reaction of the oxidation of hydrogen, measured parallely the rate of the catalytic reaction at the surface of a number of simple transition metal oxides (Fe_2O_3, Co_3O_4, MnO_2, ZnO, Cr_2O_3, NiO and CuO), the rate of reduction of these oxides with hydrogen, and the rate of their reoxidation in oxygen as function of the fraction of the oxygen surface layer removed. The cross-points of the reduction and oxidation curves correspond to the steady-state conditions prevailing at the surface of the oxide during the catalytic oxidation of hydrogen. As shown in Chapter 5, the values of the rate at these points agree very well with the rates of catalytic reaction measured directly. Similarly, very good agreement was obtained in the case of the oxidation of carbon monoxide, which led the authors to conclude that it is the oxide ions which are responsible for the oxidation of H_2 and CO, with a redox mechanism operating in both cases. On the other hand, in the case of oxidation of CO on TiO_2 the rate of catalytic reaction

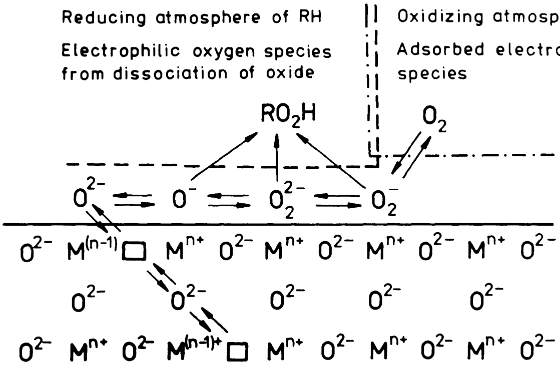

FIGURE 4.11 Formation of electrophilic oxygen at the oxide surface.

is one order of magnitude higher than the rate of reduction or the rate of reoxidation, corresponding to the steady state. Similarly, on V_2O_5 the rate of catalytic oxidation of hydrogen was found to be five times higher than the steady-state rates of reduction or oxidation.

At this point it should be noted that in the case of simple molecules such as H_2 or CO the distinction between electrophilic and nucleophilic oxidation loses its meaning because both reactions result in the formation of the same—the only possible—product. However, from the point of view of the source of oxygen used for the oxidation, i.e., for analysis of the parameters determining the activity of the catalyst, it is informative to differentiate between extrafacial and interfacial reactions. Indeed, Boreskov et al. [17] found that in the case of V_2O_5 catalysts the rate of CO oxidation is at temperatures below 450°C almost one order of magnitude higher than the steady-state rates of reduction and reoxidation. On raising the temperature the rate of catalytic reaction decreases and by 590°C becomes equal to the rates of reduction and oxidation. This result clearly indicates that at lower temperatures catalytic oxidation proceeds mainly through the extrafacial pathway. When the temperature rises, surface coverage with oxygen decreases and so does the extrafacial reaction, whereas lattice oxygen ions become more and more mobile and the interfacial mechanism takes over as the main reaction pathway. In the case of the oxidation of hydrocarbons this switch from electrophilic to nucleophilic surface oxygen species entails a dramatic change in the selectivity of reaction. As an example, the oxidation of o-xylene to phthalic anhydride on V_2O_5 catalysts may be quoted. When a mixture of o-xylene and oxygen is passed over V_2O_5 catalyst at temperatures below 350°C, only total oxidation is observed because of the predominance of electrophilic oxygen species at the catalyst surface. At about 370°C the complete change of selectivity occurs, phthalic anhydride becoming the major product above this temperature. In these conditions the reaction proceeds by the nucleophilic, redox mechanism.

The second way of determining the contribution of lattice oxide ions to the reaction of oxidation at an oxide catalyst consists of carrying out the reaction in gas phase oxygen enriched in ^{18}O isotope. As an example, Fig. 4.12 shows the results obtained by Keulks et al. [20] in a classical experiment in which propene was oxidized over $Bi_2O_3-MoO_3$ catalyst in oxygen containing $^{18}O_2$. Acrolein appearing in the first moment of the reaction contained only ^{16}O isotope, indicating that exclusively the oxygen from the lattice of the catalyst participated in its formation. In the course of the reaction the ^{18}O content of acrolein builds up because the catalyst lattice contains more and more of this isotope which was incorporated in the process of catalyst reoxidation. From the dependence of the ^{18}O distribution in the products on time of the reaction the number of the layers of

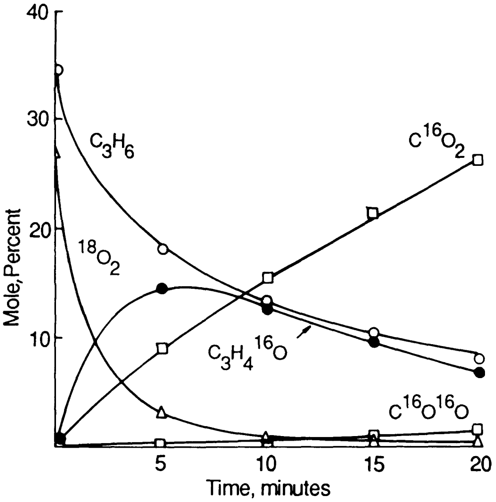

FIGURE 4.12 Distribution of ^{18}O in the products of the oxidation of propene in gas phase $^{18}O_2$ as function of reaction time. (After [20].)

oxide ions of the catalyst crystal lattice involved in this process may be calculated. In the case of the $Bi_2(MoO_4)_3$-based multicomponent catalyst, the mobility of oxide ions in the lattice is so high that ^{18}O ions incorporated into the lattice during reoxidation become uniformly distributed in the whole lattice before they have the chance to be extracted from the lattice due to insertion into the reactant molecule in the reduction step. Table 4.3 summarized the results obtained by Moro-oka et al. [21] for a number of different mixed oxide catalysts. It may be seen that in all MoO_3-based catalysts the mobility of oxide ions is high and many layers of the lattice are involved in the redox mechanism of the oxidation of propene, whereas in the Sb_2O_4-based catalysts only the uppermost surface layers participate in the exchange of oxygen.

Further information on the role of electrophilic and nucleophilic oxygen species in oxidation reactions yields the comparison of the rate of homomolecular isotopic oxygen exchange with rates of catalytic oxidation (see Chapter 3, Section V). Homomolecular isotopic exchange requires the activation of oxygen molecules at the surface of the catalyst; its rate may be thus taken as the measure of the ability of the catalyst surface to generate electrophilic oxygen species. In Fig. 4.13 the selectivity of ammoxidation of propene to acrylonitrile (curve I) ad CO_2 (curve II) on $Fe_2O_3-Sb_2O_5$ catalysts as determined by Boreskov et al. [22] is compared with the activity of these catalysts in isotopic oxygen exchange as measured by Muzykantov et al. [23]. We may see that selective in partial oxidation are those catalysts which are not active in isotopic oxygen exchange, whereas the appearance of higher activity in the exchange is accompanied by the increase in total oxidation [24]. This observation is substantiated by the results given in Table 4.4 which summarized the selected data on the activity in isotopic oxygen exchange of four double oxide systems known to be selective in partial oxidation as well as their components, some of which are very active in total oxidation. It may be seen that very selective Bi–Mo catalysts show no activity in oxygen exchange, i.e., no adsorbed oxygen species

TABLE 4.3 Number of Lattice Oxide Ion Layers Involved in Oxidation of Propylene to Acrolein [21]

Catalyst	Temp (°C)	Number of oxide ion layer involved	Other catalysts[a]
Fe_2O_3-Sb_2O_4			
Fe/Sb = 1:4	450	6–7	M—Sb—O (M/Sb = 1:4) M = Ni, Co, Mn, Zn
1:2	450	5	
	350	3	
1:1	450	4	
4:1	350	0–2	
Sb_2O_4-MoO_3 (1:1)	450	20–40[b]	
$CoTeMoO_6$	450	55–75[b]	$MnTeMoO_6$ TeO_2-MoO_3 (1:1)
$Bi_2(MoO_4)_3$	430	75[c]	
Bi_2MoO_6	430	286[c]	
Cu_2O/Celite	260	0–1	
$Co_{17/18}Bi_{1/18}MoO_{4+\underline{x}}$	450	Whole $Bi_2(MoO_4)_3$ phase	M—Bi—Mo—O M = Co, Mn, Mg, Ni
$Pb_{11/12}Bi_{1/12}MoO_{4+\underline{x}}$	450	Whole oxide	M—Bi—Mo—O M = Pb, Ba, Sr

[a] Other catalysts which gave similar results in the ^{18}O experiment.
[b] Values obtained by rough approximation.
[c] Values taken from the data by Keulks et al. [20].

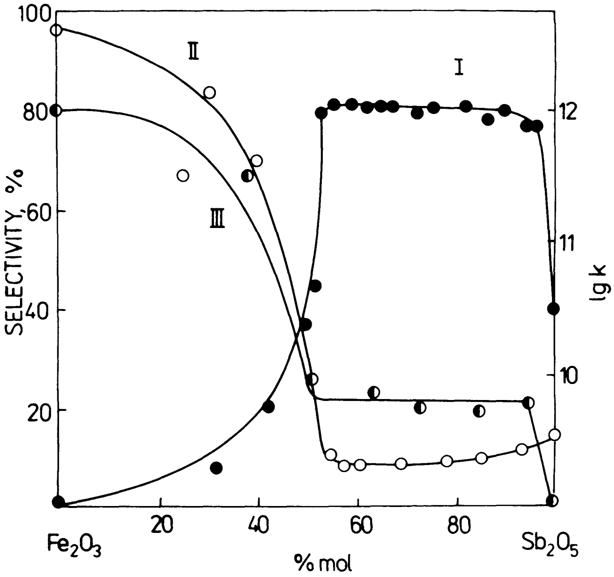

FIGURE 4.13 Selectivity of the ammoxidation of propylene to acrylonitrile (curve I) and CO_2 (curve II) at 425°C as a function of the composition of Fe_2O_3–Sb_2O_5 catalysts. (After [22].) Curve III shows the rate of homomolecular oxygen isotopic exchange on these catalysts. (After [23].)

TABLE 4.4 Activity of Oxides in Oxygen Isotopic Exchange

Catalyst	T (°C)	Rate (g $O_2/m^2\cdot h$)
MoO_3	580–601	9×10^{-4}
Bi/Mo = 2:1	250–500	No exchange
Bi/Mo = 1:1	474–500	No exchange
Co/Mo = 1:1.7	599–634	1.8×10^{-4}
Co/Mo = 2:1	401–462	2.9×10^{-2}
Co_3O_4	125–250	12.7
Fe/Mo = 1:1.7	511–551	7×10^{-3}
Fe/Mo = 1:1	508–552	1×10^{-3}
Fe_2O_3	350–450	4×10^{-1}
Fe/Sb = 1:2	530–598	1×10^{-5}
Fe/Sb = 1:1	548	1.7×10^{-7}
Sb_2O_5	538–600	1.7×10^{-6}

are present at their surface. Indeed, direct adsorption measurements indicate that no chemisorption of oxygen takes place at the surface of these catalysts [25]. Similarly, a selective Co—Mo catalyst of composition 1:1.7 shows a very slow exchange, the much less selective Co—Mo = 2:1 catalyst shows a higher rate of exchange, and on Co_3O_4, which is a good catalyst for total oxidation, the rate of exchange has the value three orders of magnitude higher. The same is true for Fe—Mo and Fe—Sb systems. These results confirm the conclusion that in the conditions of the heterogeneous catalytic oxidation of such hydrocarbons as olefins the electrophilic oxygen attack results in the formation of total oxidation products.

VI. DEPENDENCE OF SELECTIVITY ON REACTION PARAMETERS

It seems appropriate at this point to draw attention to the fact that technologically most valuable chemicals obtained by oxidation are hydrocarbons containing different functional groups such as —CHO, —COOH, 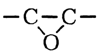 $-\underset{\diagdown O \diagup}{C-C}-$, —CN, and so forth. They are intermediates on the way to total oxidation to the thermodynamically stable products CO_2 and H_2O. Therefore the selectivity of their formation strongly depends on the conditions of the reaction. All oxidation processes are strongly exothermic and the temperature of the catalyst bed usually rises downstream of the inlet until high conversion into products has been attained, when the reaction slows down and so does the heat evolution, the temperature now decreasing on approach to the outlet. A characteristic temperature profile with a well-pronounced maximum is obtained, the region of high temperature being known as the hot spot (Fig. 4.14).

If the temperature in the hot spot rises above a certain critical value, the total oxidation may start. Because of the high exothermicity of this reaction, rapid heat evolution occurs and combustion takes place. However, total combustion in the presence of a selective catalyst becomes rapid only at high temperatures; a more or less wide temperature range exists, which corresponds to maximum rates of partial oxidation relative to total oxidation (Fig. 4.15a). If the removal of heat from the reactor is efficient enough to keep the temperature within this range, the stationary performance is maintained. If not, the temperature rises suddenly and the reaction "runs away."

As discussed above, electrophilic oxygen responsible for the total oxidation may be generated at the surface of an oxide either as the result of its dissociation at high temperature or in the course of the adsorption of oxygen at lower temperatures. If in the case of a given oxide electrophilic oxygen is generated by both mechanisms,

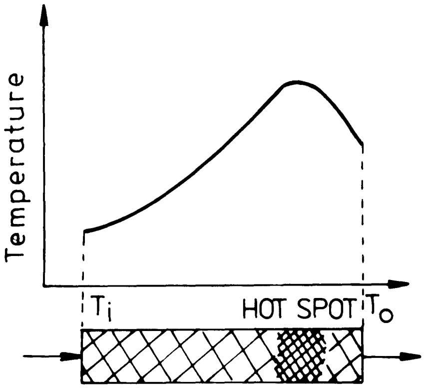

FIGURE 4.14 Axial temperature profile in a fixed-bed oxidation reactor.

the temperature range wherein selective oxidation takes place is surrounded on both sides by temperature ranges in which total oxidation occurs (Fig. 4.15b). On raising the temperature total oxidation is at first observed, then switching on of selective oxidation occurs, but if the temperature is raised too high, or removal of heat is not efficient enough, or the catalyst is characterized only by a narrow temperature range corresponding to selective oxidation, then the reaction may run away.

The preceding discussion clearly shows that selectivity of an oxidation reaction not only depends on the properties of the catalyst but is also strongly influenced by the conditions under which the reaction is carried out: temperature, contact time, diffusional parameters, efficiency of heat transport, flow rate, etc. As an illustration, Fig. 4.16 shows the results of experiments [26] in which oxidation of propene was carried out over a series of catalysts composed of Bi_2O_3—MoO_3—P_2O_5 supported on samples of alumina, which previously were annealed at different temperatures and therefore were characterized by different surface areas. It may be seen that on increasing the surface area of the catalyst the selectivity of the oxidation to acrolein strongly decreases and that of the total oxidation to CO_2 rapidly increases.

There exists also a possibility of secondary homogeneous reactions of the products of partial oxidation or reactions initiated by these products. Pure hydrocarbons may not undergo reactions, so that the latter may not be detectable in blank experiments. The importance of these reactions for the selectivity of the catalyst oxidation was demonstrated in an elegant experiment carried out by Germain and Cathala [53]. The principle of this experiment and its results are summarized in Fig. 4.17. A gas mixture or propene, ammonia, and air was passed under the exact same conditions through a reactor filled in different ways by the same amounts of a bismuth molybdate catalyst and SiO_2 support. In a blank run through an empty reactor not a trace of reaction was observed. When the catalyst was placed near the outlet so that the products formed as the result of the catalytic oxidation at the surface of the catalyst were leaving the reactor immediately after the reaction, the selectivity to acrylonitrile was 74%. When, however, the catalyst was placed near the inlet to the reactor the observed selectivity dropped to only 60%, the yield of acrylonitrile being practically the

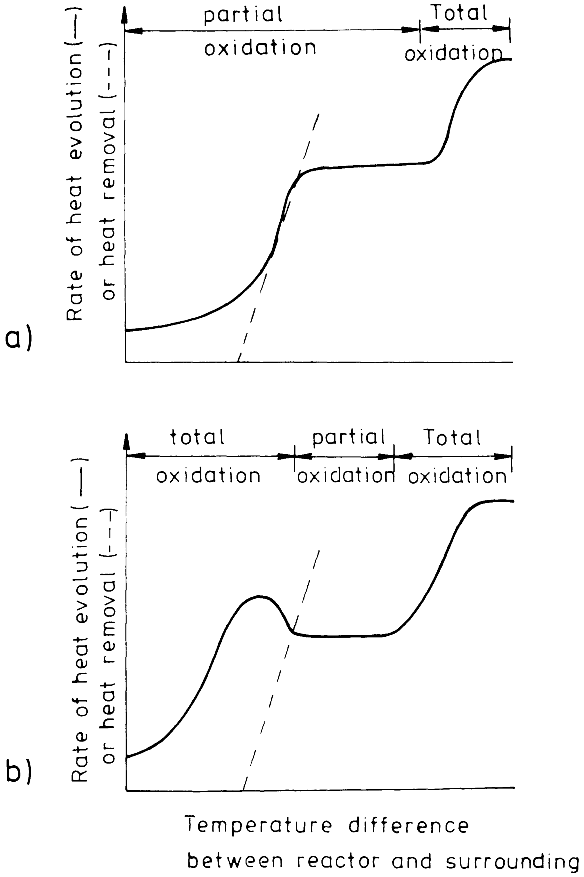

FIGURE 4.15 Energy balance in an oxidation reactor.

same but the total conversion having increased because of the increased yield of CO and CO_2. It can be concluded that the conversion of propene to acrolein at the catalyst surface remained the same, but an additional amount of propene reacted in the empty volume of the reactor behind the catalyst bed. However, the blank experiment showed that pure propene does not undergo any reaction in the empty reactor. Apparently, the homogeneous chain reaction of propene must have been initiated by the presence of products of catalytic oxidation. Indeed studies of homogeneous oxidation of hydrocarbons showed that aldehydes act as very efficient indicators of radical chain reactions of olefins. After filling the empty volume of the reactor with SiO_2, the homogeneous chain reaction was strongly hindered and conversion dropped back to the value observed in run 2. When the catalyst was mixed with the support and the mixture used to fill the reactor, conversion strongly decreased because now the conditions of the heat removal were improved and a more uniform temperature profile was achieved,

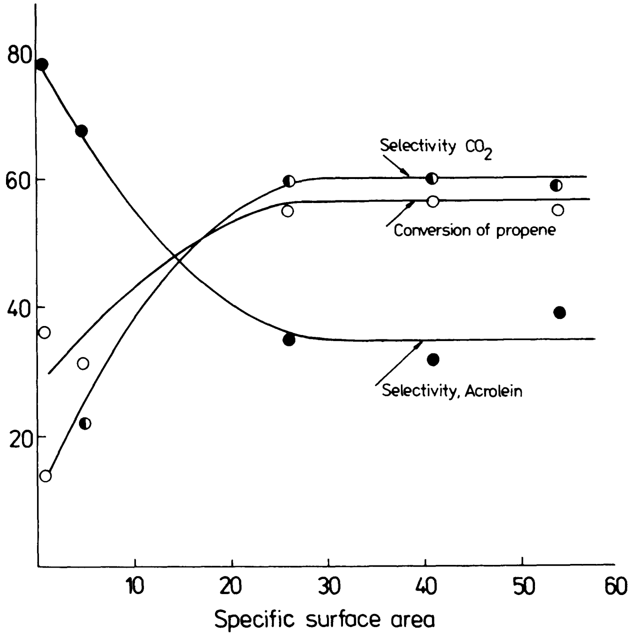

FIGURE 4.16 Oxidation of propene to acrolein on Bi_2O_3–MoO_3–P_2O_5 catalyst supported on Al_2O_3 of different surface areas. (After [26].)

Ammoxidation of propene

1g $Bi_2O_3 \cdot 2MoO_3$ + 14g SiO_2

C_3H_6 : NH_3 : Air = 1 : 1,5 : 10

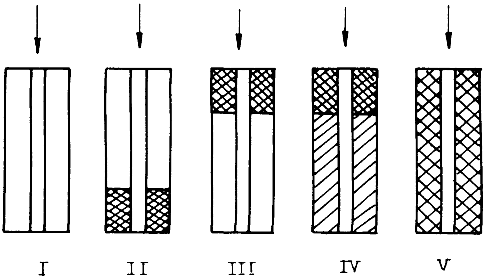

Conversion of propene	I	II	III	IV	V
total	–	44.1	52,5	46.5	21.0
to acrylonitrile	–	32,9	32,9	32,6	15,1
to acetonitrile	–	3,0	2,3	1,6	1.6
to $CO + CO_2$	–	2.6	7.0	1.9	1.6
to ethylene	–	1,2	3.0	1,0	1.0
to acetaldehyd	–	-	3,5	-	2.0
to acrolein	–	1.8	1,7	1.5	1,8

FIGURE 4.17 Dependence of the product composition of the ammoxidation of propene on the mode of filling the reactor with 1 g of catalyst (K) and 14 g of support (S). Reaction temperature 460°C; flow rate of gas: 7.5 liters/hr. I, empty reactor; II, (K + S) in the lower part of the reactor; III, (K + S) in the upper part of the reactor; IV, (K + S) in the upper part of the reactor with the remaining volume of the reactor filled with additional amount of the support: V, this additional amount of the support mixed with (K + S) and the reactor filled uniformly. (After [53].)

which prevented the increase of temperature of the catalyst bed due to the evolution of the reaction heat.

VII. ROLE OF ACID-BASE PROPERTIES

Many reactants participating in the reactions of catalytic oxidation are characterized by pronounced acidic or basic properties and therefore may interact with acid-base centers present at the surface of an oxide catalyst. This may affect the process of oxidation in two ways: (1) As the result of an acid-base reaction between the reactant and the catalyst; an active species may be generated which then more easily undergoes the redox process, the acid-base reaction being one of the elementary steps of the oxidation. (2) Due to acid-base interaction with the catalyst strong chemisorption of reactants may take place, and their residence time at the catalyst surface may be changed, the conditions of their interaction with oxygen are thus strongly modified.

Let us discuss some examples of these two effects. In the process of the oxidation of olefins the first step is the activation of the olefin molecule, consisting of the abstraction of the α-hydrogen. This activation may proceed as either a homolytic or a heterolytic bond rupture. Although the homolytic rupture of the C—H bond in a homogeneous reaction is energetically more favorable than the heterolytic one, the latter may be rendered much easier by interaction with the surface of an oxide exhibiting acid-base properties. In the presence of lattice oxide ions of basic character the first step of the oxidation of, say, propene could be envisaged as

$$CH_2{=}CH{-}CH_3 + O^{2-}\ (s) \longrightarrow [\overline{CH_2{-}CH{-}CH_2}]^- + OH^-\ (s)$$

which may be considered as an acid-base reaction of proton transfer. The adsorbed allyl anion before further reaction must now undergo an electron transfer to the metal cation of the catalyst lattice, rendering the allyl species positive:

$$[\overline{CH_2{-}CH{-}CH_2}]^- + 2M^{+\underline{n}} \longrightarrow [\overline{CH_2{-}CH{-}CH_2}]^+ + 2M^{+(\underline{n}-1)}$$

This is a redox step. It is obvious that the two stages may proceed as one concerted reaction of mixed acid-base redox character.

The second step in the selective oxidation consists of the nucleophilic addition of the lattice oxygen ion to the allyl species:

$$[\overline{CH_2{-}CH{-}CH_2}]^+ + O^{2-}\ (s) \longrightarrow CH_2{=}CH{-}CH_2 - O^-\ (s)$$

In terms of the Guttmann definition it is an acid-base process with O^{2-} transfer. Decomposition of the surface complex with desorption of acrolein may also be considered to proceed in two stages, of which one is of acid-base character:

$$CH_2{=}CH{-}CH_2{-}O^-\ (s) + O^{2-}\ (s) \longrightarrow CH_2{=}CH{-}CH{-}O^{2-} + OH^-\ (s)$$

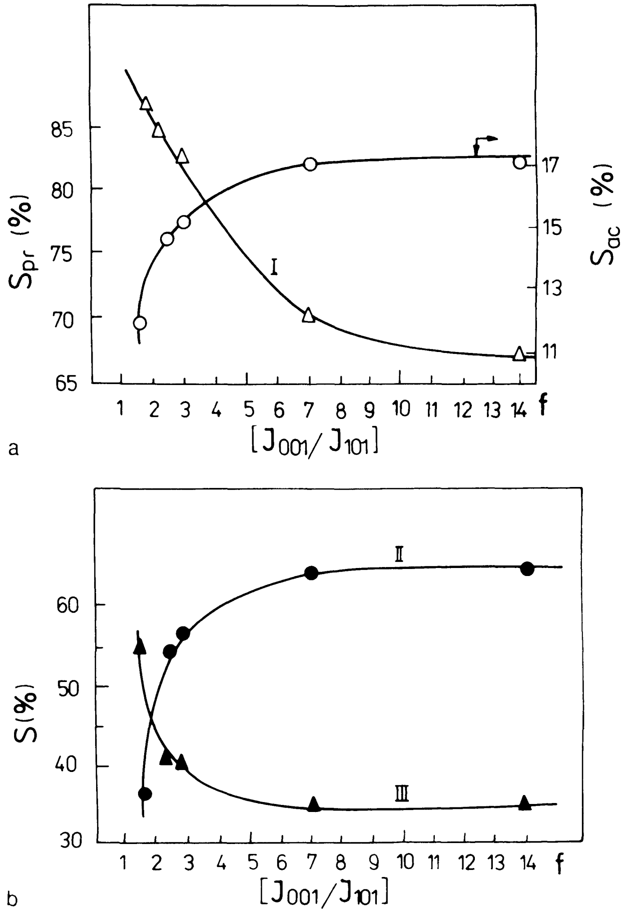

FIGURE 4.18 Correlation between surface acidity and selectivity in the oxidation of o-xylene on V_2O_5 catalyst. (a) curve I, selectivity of isopropanol decomposition to propene; (b) curve II, selectivity of the oxidation of o-xylene to total combustion; curve III, to phthalic anhydride; as function of the morphological factor f. (Adapted from [29].)

and the second of redox character:

$$CH_2{=}CH{-}CH{-}O^{2-}\ (s) + 2M^{+\underline{n}} \longrightarrow CH_2{=}CH{-}CHO + 2M^{+(\underline{n}-1)}$$

Oxidation of an olefin molecule into aldehyde may be thus considered as proceeding through a series of consecutive steps, of which some are acid-base reactions and others redox reactions. A correlation may thus be expected between catalytic activity and acidity under the condition that catalytic systems are compared which are characterized by similar redox properties. The role of acid-base properties of oxide catalysts in the oxidation of different reactants has been extensively studied and discussed by Ai [27,28].

The influence of acid-base properties on catalytic oxidation through modification of the adsorption of the reactant is encountered particularly often in the case of oxidation of aromatic hydrocarbons, which are characterized by considerable basicity and interact with Lewis acid centers at the surface of the catalyst. This is illustrated in Fig. 4.18 in which the selectivity in oxidation of o-xylene to phthalic anhydride is compared with the acidity for a series of V_2O_5 catalysts of different crystal habit, described by the morphological factor f. The acidity was determined by measuring the conversion

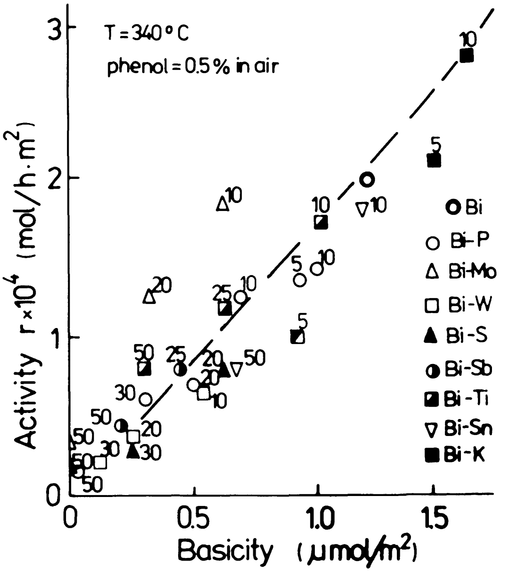

FIGURE 4.19 Activity in the total oxidation of toluene as function of the basicity of catalysts. (After [28].)

of isopropanol to propene, considered to proceed only on acid centers [29]. It may be seen that acidity is deleterious for the selective oxidation of o-xylene because interaction of aromatic electrons with acid centers results in prolongation of the residence time of o-xylene molecules at the surface, which increases the probability of an electrophilic attack of adsorbed oxygen and combustion of the molecules. An opposite correlation is obtained in the case of the total oxidation of phenol (Fig. 4.19), which shows acidic properties and whose combustion is therefore accelerated on increasing the basicity of the surface [27].

VIII. INFLUENCE OF SURFACE GEOMETRY

The importance of the geometric structure of the surface to its catalytic behavior has been discussed since the beginning of catalysis studies. The simplest case of the influence of the lattice parameter on the activation energy of the reaction may be demonstrated by an example of dissociative chemisorption of a reactant A on the catalyst B (e.g., oxygen on platinum):

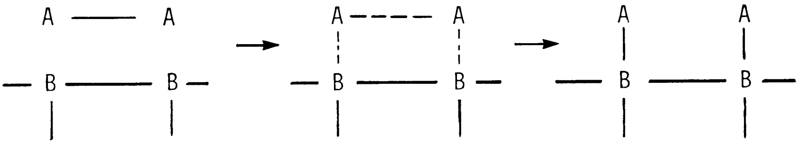

It can easily be shown that at a certain distance B—B a minimum of the activation energy of this process appears, namely, at small distances the repulsion between the adsorbed species A makes the adsorption process difficult, whereas at long distance the two adsorption centers cannot simultaneously exert their influence on the molecule and the A—A bond must become completely split before dissociative adsorption takes place.

The requirement that geometry of the arrangement of atoms forming the active center at the surface of the catalyst should match the geometry of atoms in the reacting molecule for the catalyst to be active in transformation of this molecule was introduced by Balandin [30] as the basis of his theory of multiplets. Let us discuss as an example the transformation of alcohols which can proceed along two different paths: dehydrogenation to give aldehydes or ketones, and dehydration resulting in the formation of olefins. According to Balandin, both reactions require that appropriate doublet active centers be present at the catalyst surface to weaken the two bonds in the reacting molecule (white dots) and other doublet active centers to facilitate the formation of the two new bonds (black dots):

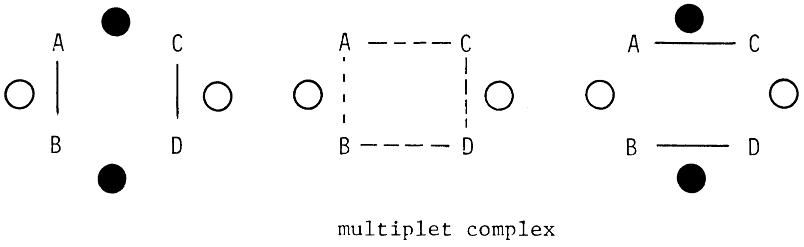

However, in the case of dehydrogenation the alcohol molecule must be linked to the catalyst surface in the form of the multiplet complex shown in Fig. 4.20a, whereas for dehydration to occur the multiplet complex must assume the form shown in Fig. 4.20b. Comparison of the interatomic distances in the reacting molecule corresponding to these two multiplet complexes leads to the conclusion that when appropriate active centers exist at the catalyst surface, smaller distances between atoms in these center should favor dehydrogenation, whereas longer distances should favor dehydration. Indeed, on studying [31] the reactions of <u>n</u>-butanol on MgO as catalyst it has been found that the selectivity to dehydrogenation as compared to dehydration decreases when the lattice parameter of MgO increases (Fig. 4.21). In the 1960s Schuit et al. [32] and then Matsura [33] drew attention to the implications of the arrangement of ions at different crystal faces of bismuth molybdate for their catalytic activity in the oxidation of butene. Recently, the influence of the geometric

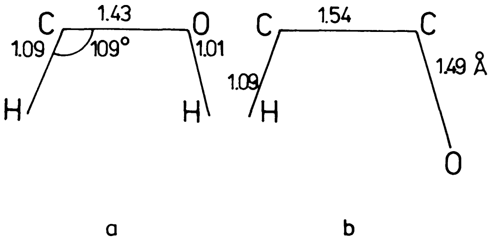

FIGURE 4.20 Multiplet complexes formed in the course of dehydrogenation (a) and dehydration (b). The respective interatomic distances in an alcohol molecule are given by the bonds.

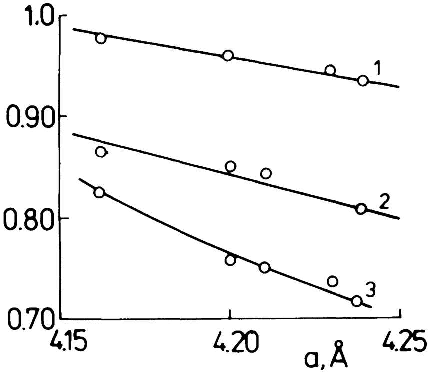

FIGURE 4.21 Selectivity coefficient (ratio of the percentage of dehydrogenation to the sum of the percentages of dehydrogenation and dehydration) of n-butanol as a function of the lattice parameter a of magnesium oxide used as catalyst. 1, 400°C; 2, 440°C; 3, 460°C.

arrangement of ions at different crystal planes of several oxide catalysts on the reactivity of adsorbed reactants of a number of catalytic reactions was discussed by Ziółkowski [34] on the basis of the bond strength—bond length model.

In the last 10 years a number of observations have been accumulated indicating that the habit of oxide crystallites may have a pronounced influence on the selectivity of oxidation reactions. Many studies were devoted to the elucidation of the behavior of different crystal faces of MoO_3. Tatibouet and Germain [35] measured the catalytic activity of crystallites of orthorhombic MoO_3 of different habit in the vapor phase reaction of methanol-oxygen mixtures. Two reaction paths are possible: dehydrogenation to formaldehyde and its acetal, or dehydration to dimethyl ether:

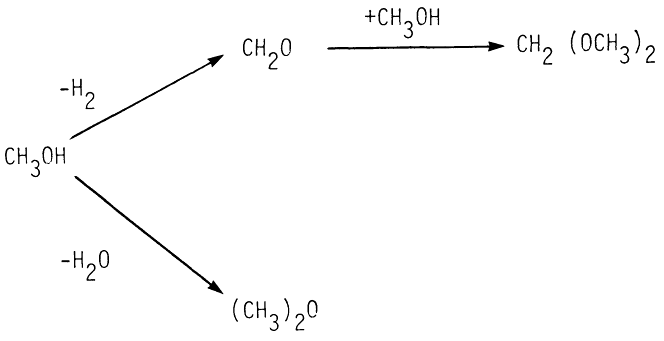

By comparing the selectivities observed, when crystallites of different shape were used, with the percentage of the exposed MoO_3 faces the authors came to the conclusion that (010) faces (cleavage or basal plane of MoO_3 (cf. Fig. 0.00)) carry active centers for dehydrogenation while (100) faces also contain Lewis acid centers responsible for dehydration. Thus, different crystal faces show distinct catalytic specificity in the oxidation of methanol. However, comprehensive investigations of the reactions of methanol over monocrystals of MoO_3 carried out by Sleight et al. [36] demonstrated that it is the dissociative chemisorption of methanol leading to the formation of surface alkoxy groups which is a necessary first step in the oxidation sequence. This chemisorption takes place at Lewis acid sites which are located on the side faces of MoO_3 crystal. Upon heating chemisorbed methoxy groups are transformed nearly quantitatively into formaldehyde and desorbed. There is a concurrent loss of oxygen from the catalyst. A typical desorption spectrum is shown in Fig. 4.22. The conclusion that the basal (010) crystal face of MoO_3 is inactive in this reaction has been confirmed by direct evidence obtained with ultraviolet photoelectron spectroscopy.

Considerable attention was also devoted to the selectivity of different crystal faces of MoO_3 in the oxidation of propene and butene. Volta et al. [37], using oriented graphite supported MoO_3 catalysts, reported differences in activity and selectivity for crystal-

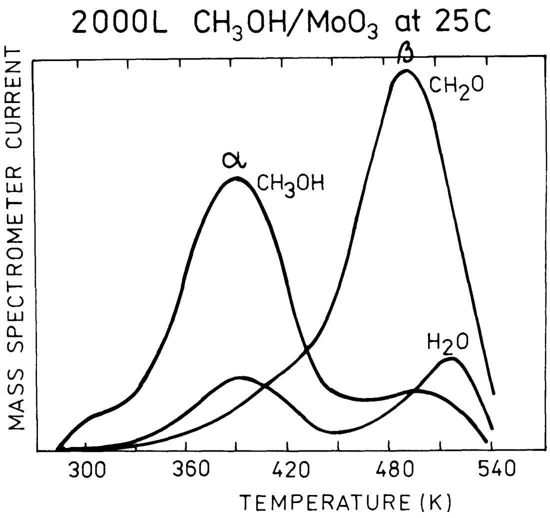

FIGURE 4.22 Results of the TPD-MS experiment carried out after exposure of a MoO_3 crystal to 2000 liters of methanol at 25°C. (After [36].)

lites with various faces exposed and concluded that it is the (100) face which is mainly responsible for the selective oxidation of propene to acrolein and isobutene to methacrolein. This face also showed considerable activity in the total oxidation of isobutene, whereas propene was oxidized to CO_2 only at the (010) face. Haber et al. [38] compared the behavior of propene and allyl compounds over MoO_3 crystallites of different habit, which permitted separation of the two elementary steps of the selective oxidation: activation of the propene molecule and insertion of oxygen. A linear dependence of the yield of acrolein from allyl compounds on the surface area of the (010) face was observed (Fig. 4.23). This indicates that insertion of oxygen takes place at the (010) face, whereas it is the dissociative chemisorption of propene resulting in its activation which

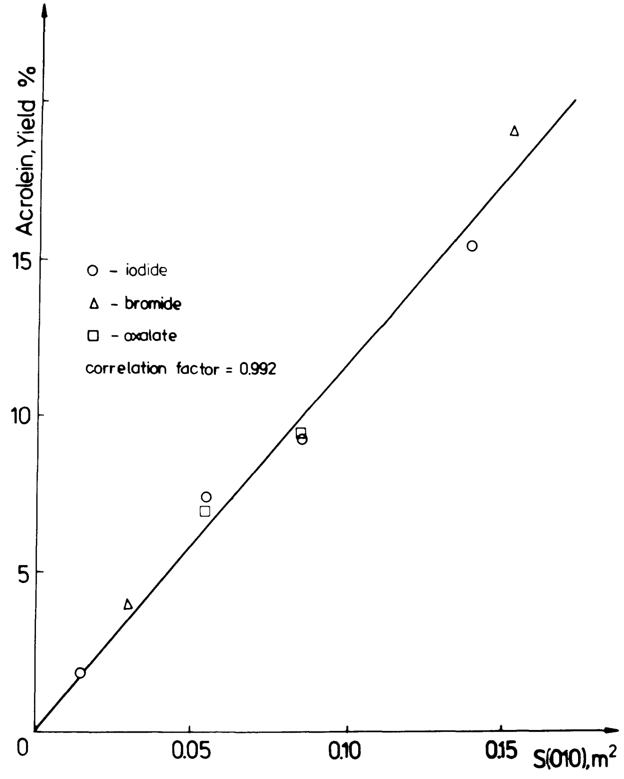

FIGURE 4.23 The yield of acrolein in the oxidation of propene on MoO_3 crystallites of different habits as a function of the area of the (010) crystal face exposed. (After [38].)

takes place at the side face (100), which may explain the observation of Volta et al., who studied only the overall reaction.

A pronounced influence of geometry on the pathway of the catalytic reaction is visible in the case of the oxidation of o-xylene on V_2O_5 studied by Gasior and Machej [39]. Figure 4.24 shows the selectivity for phthalic anhydride and the selectivity for products of total oxidation as a function of the textural factor of V_2O_5 crystallites, which is expressed as the ratio of intensities of (001) to (110) reflections. Comparison with the arrangement of VO_6 octahedra on these crystal faces shown in Fig. 8.13 indicates that high selectivity for phthalic anhydride is observed in the case of samples composed of crystallites exposing mainly the (001) faces with the V=O groups sticking out of the surface. However, when the crystallites expose

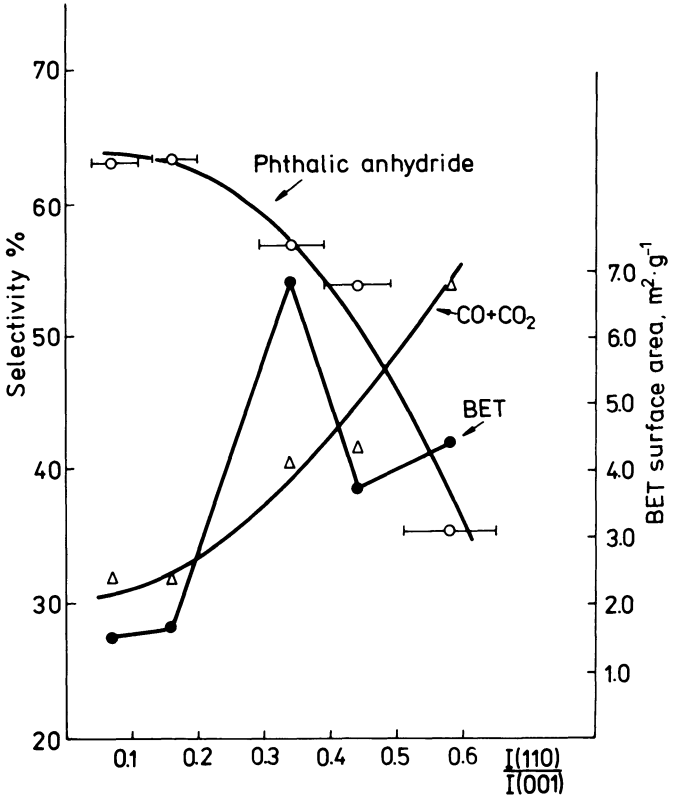

FIGURE 4.24 Selectivities in oxidation of o-xylene on V_2O_5 as a function of the textural factor. (After [39].)

mainly the (110) faces, at which the shear planes may be nucleated and whole perpendicular layers of oxygen may be extracted, total oxidation becomes the predominant reaction pathway. A general conclusion may thus be formulated that in compounds of those transition elements, in which the phenomenon of the displacement stabilization results in the strong anisotropy of properties, differences in surface and catalytic properties of different crystal faces may be encountered.

IX. DYNAMICS OF THE CATALYST SURFACE

The last decade has equipped surface chemistry with a variety of new techniques which supply detailed information on both atomic and electronic structures of solid surfaces and their interactions with adsorbed species. Results accumulated in this field in recent years show that the reactants of the catalytic reaction are in dynamic interaction with the solid catalyst and the continuous exchange of matter and energy between the reactants and the catalyst may result in many phenomena, such as the shift of defect equilibria both at the surface and in the bulk of the solid, ordering of defects at the surface and surface reconstruction, formation of new bidimensional phases at the catalyst surface, etc., all of them having a profound influence on the catalytic properties. They may be due either to the shift of chemical equilibria or to the kinetic effects. Specifically, in the case of oxide catalysts the system may respond to the change in composition of the reacting catalytic mixture in three different ways:

The defect equilibria at the surface of the oxide or in the whole bulk may be shifted and the change of the concentration of the given type of defects involved in the catalytic transformation may cause a change of catalytic properties. Usually a gradual shift of selectivity with the changing composition of the gas phase is then observed.

When concentration of defects at the surface of the oxide surpasses a certain critical value, ordering of defects or formation of new bidimensional surface phases may occur, often resulting in a dramatic change of catalytic properties. It should be borne in mind that due to the contribution from the surface free energy the phase transformation may take place at the surface at thermodynamic parameters values differing considerably from those corresponding to bulk phase transformations. Thus, new bidimensional surface phases may appear under conditions in which bulk phases could never be formed.

In the case of redox mechanism operating in the catalytic reaction, the ratio of rates of the catalyst reduction and its reoxidation may be different for various oxide phases. A hysteresis of the dependence of catalytic properties on the composition of the gas phase may appear, catalytic activity and selectivity being strongly influenced by the pretreatment of the catalyst. In such a case a highly active and selective catalyst may be obtained by appropriate activation, whereas the same system subjected to other activation procedures may turn out to be completely inactive.

The change of catalyst composition under the influence of changing partial pressures of the reactants was observed many years ago in the case of the oxidation of SO_2 on V_2O_5 catalyst by Weychert [40], who tried to correlate the activity of the catalyst with its chemical composition. Such an effect was clearly demonstrated by Bielański and Inglot [41] in the reaction of the oxidation of benzene to maleic anhydride on V_2O_5–MoO_3 catalyst. The increase of the ratio of benzene to oxygen in the gas phase is followed by an appropriate rise of the degree of reduction of the catalyst, expressed in terms of the concentration of V^{4+} ions which in turn results in the increase of selectivity of the reaction to maleic anhydride (Fig. 4.25). Catalytic activity of a Fe_2O_3–Sb_2O_4 catalyst in the oxidative dehydrogenation of butene as a function of the degree of surface reduction resulting from the change of the gas phase composition as found by Boreskov et al. [42] is shown in Fig. 4.26. An increase in the content of butene is followed by more and more considerable surface reduction, resulting in a proportional increase of the rate of the catalytic reaction.

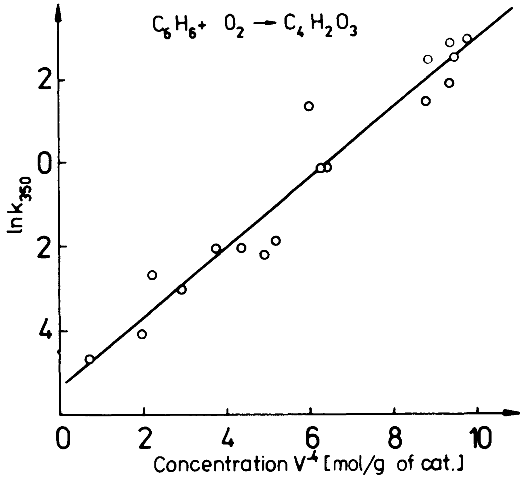

FIGURE 4.25 Selectivity of V_2O_5–MoO_3 catalysts in the oxidation of benzene as function of the concentration of V^{4+} ions. (After [41].)

The above examples illustrate the influence of the change of gas phase composition when the oxide catalyst is a nonstoichiometric compound with a wide homogeneity range which can respond to this change by the shift of defect equilibria. Different phenomena take place when the homogeneity range is narrow and a change of stoichiometry can only be accommodated by formation of a new phase. As an example, Fig. 4.27 shows the results of an experiment in which a mixture of propene and oxygen of the composition 1:1 was at first pulsed over the $Cu^{I}_{2}Mo_{3}^{VI}O_{10}$ catalyst. Total oxidation was only observed with the conversion of about 25% [43]. Then pulses of oxygen started to be introduced between the pulses of the reacting mixture. This resulted in the dramatic shift of the reaction pathway to selective oxidation, with acrolein appearing in the products with selectivity which after a certain number of pulses attained a constant high value. When pulses of oxygen were stopped, selectivity to acrolein rapidly dropped back to the very low level. Such cycles could have been repeated many times. Parallel to catalytic experiments the changes in surface composition were followed

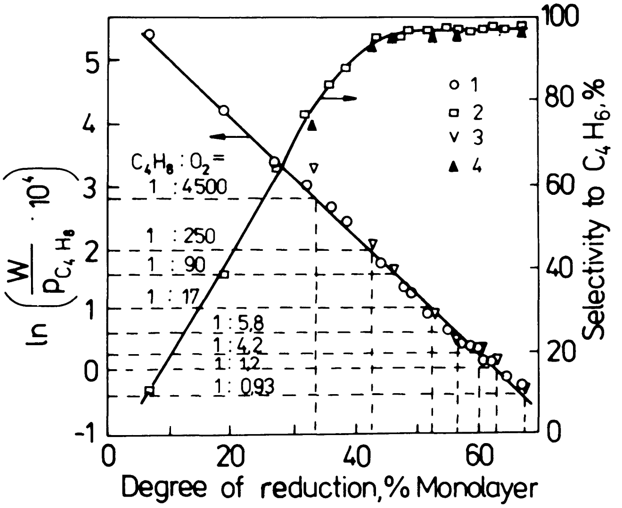

FIGURE 4.26 Changes of the activity of a Fe_2O_3–Sb_2O_5 catalyst in the dehydrogenation of butene and its selectivity to butadiene with the change of the degree of reduction of the catalyst surface, due to the change of the composition of the reacting mixture. 1, activity and 2, selectivity, observed on reduction of the oxidized catalyst with the C_4H_8 + He mixture; 3, activity and 4, selectivity observed under steady-state conditions. (After [42].)

by photoelectron spectroscopy. The presence of a single peak at the binding energy of 932 eV in the spectrum of the initial sample (curve I in Fig. 4.28) indicates that only Cu^+ ions in the environment of the $Cu_2Mo_3O_{10}$ lattice are present at the surface. After the additional oxygen pulses, i.e., in the state when high selectivity to acrolein is attained, the photoelectron spectrum (curve II in Fig. 4.28) indicates the presence of Cu^{2+} ions in the coordination similar to that in $CuMoO_4$. Comparison of spectra 3 and 4, registered after subsequent reducing and oxidizing cycles, indicates that the reconstruction is reversible. It may thus be concluded that the drastic change of selectivity is related to the surface transformation consisting of the appearance of surface clusters of $CuMoO_4$, responsible for the insertion of oxygen and formation of acrolein. Simultaneously, the adsorption of oxygen and its activation to eletrophilic species, leading to total oxidation, is depressed. A general conclusion was formulated by Haber [44] that the catalyst surface is in dynamic interaction with the gas phase. Depending on the properties of the

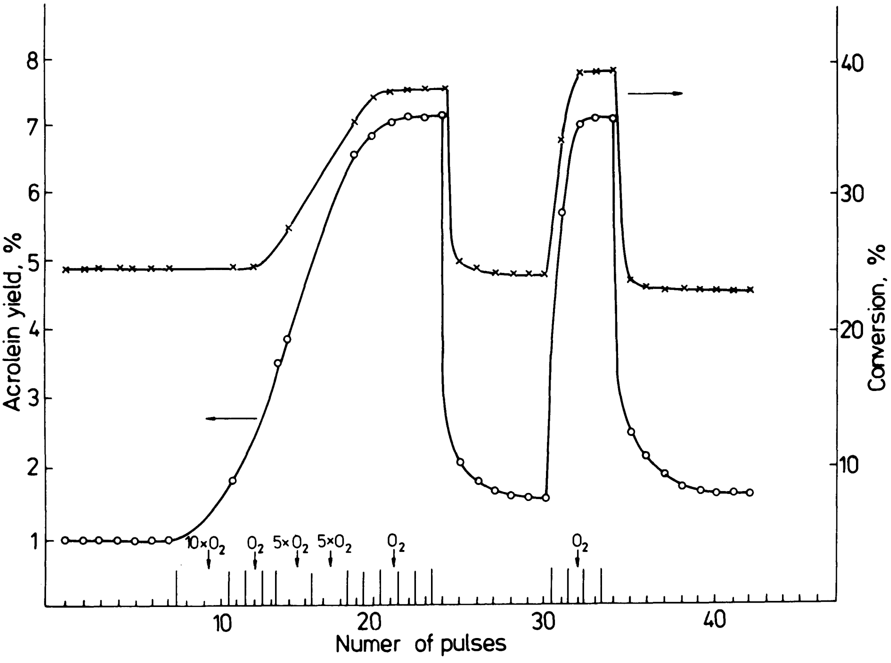

FIGURE 4.27 Conversion and selectivity to acrolein in the oxidation of propene over $Cu_2Mo_3O_{10}$ catalysts as a function of the number of $C_3H_6 + O_2$ and O_2 pulses at 350°C. (After [43].)

reacting mixture, different surface phases may be formed at the surface of the catalyst, directing the reaction along different reaction pathways. When the steady-state conditions of the reaction are changed, the structure and composition of the catalyst surface may also change, modifying the activity and selectivity of the catalyst itself. This means that in the equation describing the rate of the catalytic reaction:

$$r = kf(\theta_i) \tag{4.16}$$

it is not only the concentration term $f(\theta_i)$ which depends on the pressures of the reactants, but also the rate constant k:

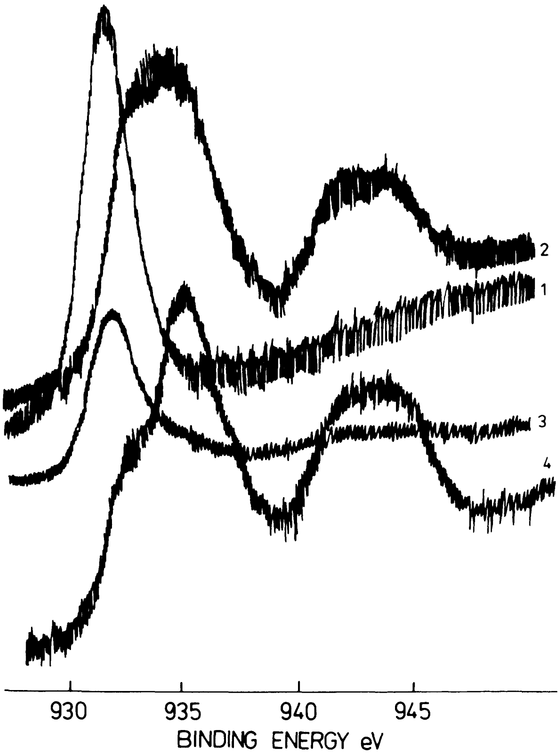

FIGURE 4.28 Photoelectron spectra of Cu (2p) electrons from $Cu_2Mo_3O_{10}$ catalysts: 1, initial sample; 2, after exposing to O_2 pulses; 3, after outgassing at 350°C; 4, after reoxidation.

$$k = k(T, p_i)$$

These conclusions open new possibilities of carrying the catalytic reactions under conditions in which the catalyst shows high selectivity to the given product, although the state of its surface, responsible for this selectivity, may be unstable and its maintenance may require periodic changes of the composition of the gas phase.

Kinetic analysis of a system built of a transition metal oxide interacting with the gas phase composed of oxygen and a reactant with reducing properties was given by Wagner [45] some time ago, but was recently verified experimentally by Rieckert et al. [46]. Let us consider an oxidation reaction proceeding by a redox mechanism. Wagner assumed that rates of the elementary steps—reduction of the oxide by the reactant and its reoxidation by oxygen—are functions of the oxygen thermodynamic potential a_{Ox} in the solid, being defined as p_{O_2} at equilibrium between gaseous oxygen and the nonstoichiometric solid under consideration. Thus, in the presence of a gas phase reactant with reducing properties such as hydrogen, CO, or hydrocarbons, $(a_{OX})_s < p_{O_2}$. The rates of the two elementary steps are then given by equations:

$$R(g) + 2O_O \longrightarrow RO_2(g) + 2V_O \qquad r_- = r_-(P_R, a_{OX}, T) \qquad (4.17)$$

$$O_2(g) + 2V_O \longrightarrow 2O_O \qquad r_+ = r_+(P_{O_2}, a_{OX}, T) \qquad (4.18)$$

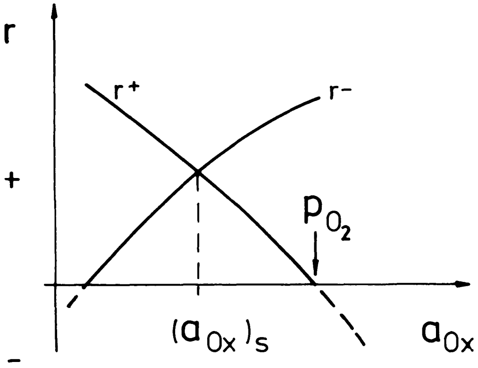

FIGURE 4.29 Rates of oxygen uptake (r_+) and removal (r_-) at a solid surface as a function of oxygen potential a_{OX} in the solid (schematic), for constant composition (p_{O_2}, p_R) of the gas phase. (After [46].)

The oxygen potential $(\underline{a}_{OX})_S$ at the steady-state results from the condition $\underline{r}_+ = \underline{r}_-$, as illustrated in Fig. 4.29, and is determined by the kinetics. Different solid phases will show different parameters of Eqs. (4.17) and (4.18), and the value of $(\underline{a}_{OX})_S$ at a given non-equilibrium composition of the gas phase will depend on the phase composition of the solid. If $(\underline{a}_{OX})_S$ is plotted as function of $\underline{P}_{O_2}$, all other partial pressures being constant, one line will be obtained for each solid phase. For two phases α and β two possibilities exist for the relative location of these lines as illustrated schematically in Fig. 4.30, where $\underline{a}^*$ represents the value of $(\underline{a}_{OX})_S$ corresponding to the coexistence of the two phases α and β. In the situation

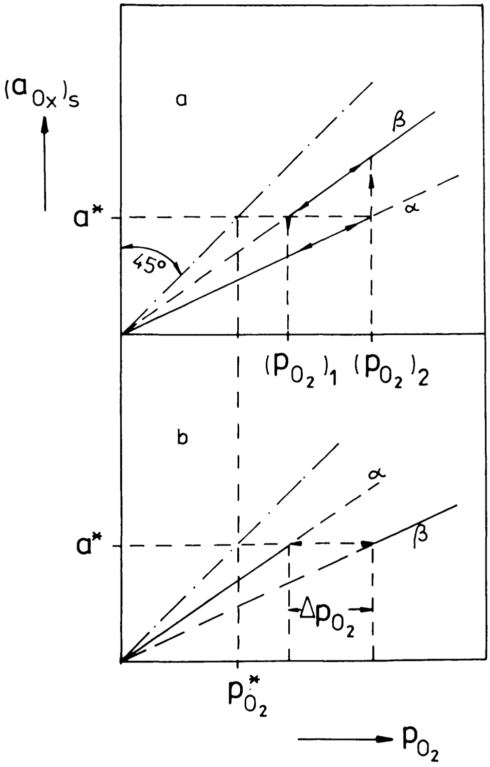

FIGURE 4.30 $(\underline{a}_{OX})_S$ at steady state in two solid phases α and β as a function of $\underline{P}_{O_2}$, at constant $\underline{T}$ and constant partial pressures of other components in the gas phase. Phase α is stable at $(\underline{a}_{OX})_S < \underline{a}^*$, phase β is stable at $(\underline{a}_{OX})_S > \underline{a}^*$. The two solid phases α and β and $O_2(g)$ coexist in an equilibrium system at $\underline{P}_{O_2} = \underline{a}^*$. (After [46].)

shown in Fig. 4.30a, phase α will be oxidized to β only when $\underline{P}_{O_2} > (\underline{P}_{O_2})_2$, whereas phase β will be reduced to phase α only when $\underline{P}_{O_2} < (\underline{P}_{O_2})_1$. A hysteresis of the phase composition versus oxygen pressure cycle is to be expected when oxygen pressure will be changed in this range. Let us suppose that we are increasing oxygen pressure from the value $(\underline{P}_{O_2})_1$ over the system composed of phase α. When it reaches the value of $(\underline{P}_{O_2})_2$, oxidation to phase β takes place. However, when the pressure is lowered, phase β will exist until the pressure drops below the value of $(\underline{P}_{O_2})_1$, when reduction of β to α will occur. Thus, in the pressure range $(\underline{P}_{O_2})_2-(\underline{P}_{O_2})_1$ either phase α or phase β will exist depending on whether we approach this pressure range from the side of lower or higher pressures, respectively. The state of the system depends on its pretreatment. In the case represented by Fig. 4.30b, the two phases α and β will coexist in the pressure range $\Delta\underline{P}_{O_2}$ and the phase composition of the system will be independent of its history. The experimental results obtained by Rieckert et al. [46] on studying the oxidation of propene to acrolein over copper oxide catalyst are shown in Fig. 4.31, in which the ratio $\underline{K}$ of selectivities to acrolein and carbon oxides is plotted as a function of the variation of oxygen partial pressure, the arrows indicating the direction of this variation. When $\underline{P}_{O_2}$ is decreased from point e, in which the catalyst is composed of CuO, mainly total oxidation takes place and the value of $\underline{K}$

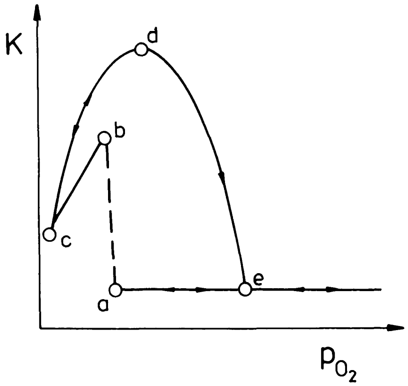

FIGURE 4.31 The ratio $\underline{K}$ of the rate of partial oxidation of propene to acrolein to the rate of oxidation of propene to carbon oxides, as a function of the changes of oxygen pressure $\underline{P}_{O_2}$. The arrows indicate the direction of the change of $\underline{P}_{O_2}$. (After [46].)

is low. When point a is reached, suddenly the selectivity to acrolein increases considerably. Chemical analysis showed that CuO was reduced to Cu_2O. This phase exists on further decrease of oxygen pressure and its subsequent increase to point d, well above the pressure corresponding to point a, selectivity to acrolein being now at maximum. Only on raising further the oxygen pressure does oxidation of Cu_2O to CuO start and does selectivity to acrolein drop until the system attains the initial state at e. Such cycles could then be repeated. The results show that the steady state of a solid catalyst can be indeterminate, the latter showing a distinct memory of its history.

X. THE CONCEPT OF REMOTE CONTROL

Ample experimental evidence was accumulated in recent years which indicates that when mechanical mixtures of two different oxides are used as catalysts in selective oxidation, a strong synergistic effect appears and the catalytic activity, but particularly the selectivity of such mixtures are much higher than those expected from the simple addition of the properties of separate oxides [49,50]. Such cooperation between oxides was observed when mixtures of MoO_3 and Sb_2O_4, SnO_2 and Sb_2O_4, MoO_3 and $BiPO_4$, $Fe_2(MoO_4)_3$ and Sb_2O_4 were used as catalysts in oxidation of isobutene to methacrolein. However, detailed structural investigation with such techniques as XRD, AEM, CTEM, SEM, ESR, Mössbauer spectroscopy and XPS did not reveal any interaction between the oxides in the mixture, nor could any migration be detected of one oxide over the surface of the other oxide.

To explain the observed phenomenon of the influence of the presence of one solid oxide on the catalytic properties of another solid oxide, Delmon and his school [51] advanced a hypothesis that such influence is exerted by means of the spillover of oxygen. In the case of the mechanical mixture of $SnO_2-Sb_2O_4$ it is SnO_2 which is responsible for the catalytic activity in oxidation of hydrocarbons. As the oxidation reactions are proceeding by the redox mechanism (cf. Section V) and surface lattice oxygen atoms become inserted into hydrocarbon molecules, a steady-state of the reduction of SnO_2 surface is established, the rate of overall process being determined by the rate of the supply of oxygen to the surface of SnO_2, which controls its degree of reduction. The supply of oxygen is enhanced by the presence of Sb_2O_4, at the surface of which oxygen molecules from the gas phase are easily dissociated and oxygen atoms then migrate through spill-over effect to the surface of SnO_2, maintaining its degree of reduction at the level corresponding to the highest concentration of active sites, i.e., highest rate of reaction (Fig. 4.32). In this way, Sb_2O_4 exerts a remote control on the catalytic

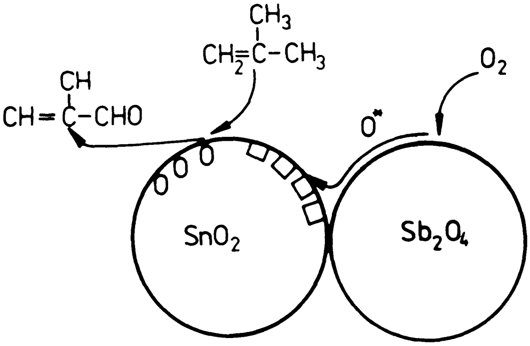

FIGURE 4.32 Remote control of catalytic properties of SnO_2 by spillover of oxygen from Sb_2O_4, which reoxidizes surface oxygen vacancies of SnO_2 generated in the course of the oxidation of isobutene.

properties of SnO_2. Thus, the synergy of catalytic properties observed in the mixtures of oxide phases may be due to cooperation between a compound playing the role of an oxygen donor and a compound which is an oxygen acceptor. Results of the experiments with Sb_2O_4 enriched in ^{18}O are consistent with the hypothesis that remote control may indeed be performed through the oxygen spillover mechanism [52].

REFERENCES

1. J. Haber, in Structure and Reactivity of Surfaces (C. Morterra, A. Zecchina, and G. Costa, eds.), Elsevier, 1989.
2. J. Haber and E. Serwicka, React. Kinet. Catal. Lett., 35, 369 (1987).
3. G. A. Parks, Chem. Rev., 65, 177 (1965).
4. J. P. Bonnelle, Pure Appl. Chem., 50, 1211 (1978).
5. M. Witko, E. Broclawik, and J. Haber, J. Mol. Catal., 35, 179 (1986).
6. M. Witko, E. Broclawik, and J. Haber, J. Mol. Catal., 45, 183 (1988).
7. E. Giamello, Z. Sojka, M. Che, and A. Zacchina, J. Phys. Chem., 90, 6084 (1986).
8. J. M. Libre, Y. Parbaux, B. Grzybowska, P. Conflant, and J. P. Bonnelle, Appl. Catal., 6, 315 (1983).
9. J. Haber, Proc. 8th Int. Congr. Catalysis, Vol. 1, Plenary Lectures, West Berlin, 1984, DEHEMA, Frankfurt Main, 1984, p. 85.
10. J. Haber, in Solid State Chemistry in Catalysis (R. K. Greaselli

and J. F. Brazdil, eds.), ACS symposia Series No. 279, Washington, D.C., 1985, p. 3.

11. P. Mars and D. W. van Krevelan, Chem. Eng. Sci., 3, 41 (1954).
12. W. D. Sokolovkij, G. K. Boreskov, A. A. Davydov, T. A. Gundrizer, W. F. Anufrienko, E. G. Izmailov, A. A. Bundieva, and N. G. Maksimov, Dokl. An SSSr, 216, 599 (1974).
13. V. A. Roiter and G. I. Golodetz, Proc. 4th Int. Congr. Catalysis, Moscow, 1968.
14. G. K. Boreskov, V. V. Popovskij, and V. A. Sazonov, Proc. 4th Int. Congr. Catalysis, Moscow, 1968.
15. J. E. Germain and R. Laugier, Bull. Soc. Chim. France, 541 (1972).
16. B. Grzybowska and J. Haber, Tagungsberichte III Int. Katalysekonferenz der DDR, Vol. 2, Bad Reinhardsbrunn, 1974, p. 244.
17. G. K. Boreskov, Kinet. Kataliz, 14, 7 (1973).
18. E. A. Mamedov, W. W. Popovskij, and G. K. Boreskov, Kinet. Katal., 10, 852 (1969); 11, 969 (1970); 11, 979 (1970).
19. G. K. Boreskov, Kinet. Kataliz., 8, 1020 (1967).
20. G. N. Keulks, J. Catal., 19, 232 (1970).
21. Y. Morooka, W. Ueda, S. Tanaka, and T. Ikawa, in New Horizons in Catalysis, Proc. 7th Int. Congr. Catalysis, Tokyo, 1980, (T. Seiyama and K. Tanabe, eds.), Elsevier-Kodansha, 1981, p. 1086.
22. G. K. Boreskov, S. A. Vanjaminov, V. A. Dzisko, D. V. Tarasova, V. M. Dindoin, N. N. Sazonova, I. P. Olenkova, and L. M. Keteli, Kinet. Kataliz, 10, 1350 (1969).
23. V. S. Muzykantov, G. I. Panov, and G. K. Boreskov, Kinet. Kataliz, 10, 1270 (1969).
24. J. Haber, Z. Chem., 13, 241 (1973).
25. R. D. Wragg, P. G. Ashmore, and J. A. Hockey, J. Catal., 22, 49 (1971).
26. J. Bereś and J. Haber, unpublished results.
27. A. Ai and S. Suzuki, Bull. Japan Petroleum Inst., 16, 118 (1974).
28. M. Ai, in New Horizons in Catalysis, Proc. 7th Int. Congr. Catalysis, Tokyo, 1980, (T. Seiyama and K. Tanabe, eds.), Elsevier-Kodansha, 1981, p. 1060.
29. M. Gasior and B. Grzybowska-Świerkosz, React. Kinet. Catal. Lett., 32, 281 (1986).
30. A. A. Balandin, Multipletnaia Tieoria Kataliza, Izd. Moskovskovo Universiteta, Moscow, 1963.
31. A. M. Rubinstein and N. A. Pribytkowa, Izv. AN SSSR, Otd. Khim. Nauk, 509 (1945).
32. G. C. A. Schuit, Chimica Ind. Milano, 51, 1307 (1969); Proc. 1st Int. Conf. Chemistry and Uses of Molybdenum, Reading, 1973, (P. C. H. Mitchell, ed.), Climax, 1974.

33. I. Matsuura, *J. Catal.*, 35, 452 (1974); *Proc. 6th Int. Congr. Catalysis*, Vol. 2, London, 1976, (G. C. Bond, P. B. Wells, and F. C. Tompkins, eds.), The Chemical Society, London, 1977, p. 819.
34. J. Ziólkowski, *J. Catal.*, 80, 263 (1983).
35. J. M. Tatibouet and J. E. Germain, 72, 375 (1981).
36. W. E. Farneth, F. Ohuchi, R. H. Staley, U. Chowdhry, and A. W. Sleight, *Proc. 5th Int. Conf. Chemistry and Uses of Molybdenum*, Newcastle-upon-Tyne, 1985.
37. J. C. Volta, W. Desquesnes, B. Moraweck, and J. M. Tatibouet, *New Horizons in Catalysis*, Proc. 7th Int. Congr. Catalysis, Tokyo, 1980, (T. Seiyama and K. Tanabe, eds.), Elsevier, Amsterdam, 1981, p. 1398.
38. K. Brückman, R. Grabowski, J. Haber, A. Mazurkiewicz, J. Sloczyński, and T. Wiltowski, *J. Catal.*, 104, 71 (1987).
39. M. Gasior and T. Machej, *J. Catal.*, 83, 472 (1983).
40. S. Weychert, *Roczniki Chemii*, 30, 291 (1956).
41. A. Bielański and A. Inglot, *Bull. Acad. Polon. Sci., Ser. Sci. Chim.*, 22, 773 (1974).
42. G. K. Boreskov, *Kinet. Kataliz*, 21, 5 (1980).
43. J. Haber and T. Wiltowski, *Bull. Acad. Polon. Sci., Ser. Sci. Chim.*, 27, 785 (1979); *New Horizons in Catalysis*, Proc. 7th Int. Congr. Catalysis, Tokyo, 1980, (T. Seiyama, K. Tanabe, eds.), Elsevier, Amsterdam, 1981, p. 1402.
44. J. Haber, in *Surface Properties and Catalysis by Non-metals* (J. P. Bonnelle, B. Delmon, and E. Derouane, eds.), Reidel, Dordrecht, 1983.
45. C. Wagner, *Ber. Bunsenges. Phys. Chem.*, 74, 401 (1970).
46. M. Greger, B. Ihme, M. Kotter, and L. Rieckert, *Ber. Bunsenges. Phys. Chem.*, 88, 427 (1984).
47. G. C. Bond, *Heterogeneous Catalysis: Principles and Application*, Clavendon Press, Oxford, 1974.
48. W. D. Sokolovskij, in *Mechanism and Kinetics of Catalytic Processes* (in Russian), Akademia Nauk SSSR, Sibirskoie Otdielenie, Institut Kataliza, Novosibirsk, 1977, p. 41.
49. B. Delmon and P. Ruiz, *Catal. Today*, 1, 1 (1987).
50. L. T. Weng, B. Zhou, B. Yasse, B. Doumain, P. Ruiz, and B. Delmon, *Proc. 9th Int. Congr. Catalysis*, Vol. 4, Calgary, 1988, (M. J. Philips and M. Ternan, eds.), Chemical Institute of Canada, Ottawa, 1988, p. 1609.
51. L. T. Weng, S. Y. Ma, P. Ruiz, and B. Delmon, *J. Mol. Catal.* (in press).
52. L. T. Weng, P. Ruiz, B. Delmon, and D. Duprez, *J. Mol. Catal.*, 52, 349 (1989).
53. M. Cathala and J. E. Germain, *Bull. Soc. Chim. France*, 2174 (1971).

5

Catalytic Oxidation of Hydrogen

I. INTRODUCTION

The catalytic oxidations of small inorganic molecules such as H_2 and CO occurring without formation of any side products are considered to belong to the simplest catalytic reactions and were applied by numerous authors as the catalytic test reactions carried out in order to characterize various catalysts, metallic as well as the nonmetallic. However, the simplicity of such reactions is only apparent and establishing of their unambiguous reaction paths encountered frequently serious difficulties.

The catalytic oxidation of hydrogen was discovered by Döbereiner in 1822 who showed that at ambient temperatures platinum sponge can induce spontaneous combustion of hydrogen in oxygen. This observation was followed by the discovery of Dulong and Thénard that some other metals—gold, silver, and even glass—exhibited similar behavior if temperature was sufficiently raised [1]. These processes were among the examples on which Berzelius formulated his ideas of catalysis in 1835–1836.

Studies of catalytic oxidation of hydrogen carried out with contemporary methods of surface science have contributed appreciably in the present time to the general understanding of the mechanism of catalytic reactions, especially those which occur on the surface of platinum group metals. Besides purely scientific reasons, the interest in the catalytic burning of hydrogen is nowadays stimulated by the prospect of its future application in hydrogen-based energetics including the development of hydrogen fuel cells [2]. Another reason for practical interest in this reaction is the application of hydrogen as the fuel for rocket propulsion.

The equilibrium constant of the highly exothermic (ΔH°_{298} = −241.83 kJ mol^{-1}) reaction:

$$H_{2(g)} + \frac{1}{2}O_{2(g)} = H_2O_{(g)} \tag{5.1}$$

assumes the value 1.175 × 10^7 at 1300 K [3], which indicates that below this temperature practically no dissociation of water vapor into the elements has to be taken into account. The homogeneous reaction at room temperature does not take place because of the strong chemical bonds in O_2 and H_2 which must be broken. It runs with an observable rate at 450 K in stoichiometric mixture of gases through a chain mechanism. Above 770 K branching of the reaction chains greatly accelerates the reaction and an explosion occurs. The catalytic investigations of H_2 oxidation are hence limited to temperatures below 770 K. It has been studied mainly on transition metals, from which platinum and platinum metals are most active, and on transition metal oxides. The other types of catalysts, such as metal carbides, sulfides, and zeolites containing transition metal cations are less important and will not be discussed here.

II. OXIDATION OF HYDROGEN ON METAL CATALYSTS

The catalytic activity in hydrogen oxidation resulting in the formation of water as the only product is exhibited by transition metals. The fact that they are also the catalysts of H_2–D_2 isotopic exchange indicates their ability to chemisorb hydrogen dissociatively. The sequence of specific activities at 180°C determined at a high excess of hydrogen was given in [4]:

$$\mathrm{Pt} > \mathrm{Pd} > \mathrm{Ni} > \mathrm{Rh} > \mathrm{Co} > \mathrm{Fe} > \mathrm{Au} > \mathrm{Ag} > \mathrm{Cu} >$$
$$\mathrm{Mn} > \mathrm{V} > \mathrm{Cr} > \mathrm{Ti} > \mathrm{Zn}$$

On the other hand, the main group metals are poor catalysts for both hydrogen oxidation and hydrogen-deuterium isotopic exchange.

The most important and best-studied catalyst for the oxidation of hydrogen is platinum as well as other platinum group metals and that is why the present section will deal mainly with catalysis on these metals. Considerable progress in the understanding of the behavior of such catalysts was obtained in recent years by the study of definite crystal faces (on monocrystals) and the application of modern UHV techniques such as XPS, UPS, LEED, EELS, etc.

A number of investigations partially based on classical methods have also been carried out on polycrystalline samples: wires and sheets as well as on supported Pt catalysts.

A. Adsorption of Substrates and Products of Hydrogen Oxidation on Platinum Metals

The elucidation of the mechanism of catalytic hydrogen oxidation also requires separate studies on the adsorption of reactants and products: oxygen, hydrogen, and water vapor. Chemisorption of oxygen on platinum metals was discussed in Section 2.II.B. Here it should only be remembered that at the lowest temperature oxygen is adsorbed on platinum in a molecular form which below 200 K either desorbs or dissociates. Atomic oxygen is the predominant form within the temperature range 150–500 K and heating of platinum at temperatures higher than 500 K results in the incorporation of oxygen atoms into the most external layers of Pt crystallites as the so-called subsurface oxygen.

As already stated, the chemisorption of hydrogen on platinum was investigated in recent years using definite crystal faces and paralleled by the LEED determinations of the surface structure. It should here be observed that the stable surface of a metal is not necessarily identical to the corresponding crystal plane in the bulk. Owing to coordination asymmetry the surface atoms are frequently reorganized thus reaching lower surface energy [5]. Lyon and Somorjai [6] studied the structure of (111), and (110) crystal faces of platinum over a wide range of temperature, from 300 up to 1769°C (mp). The (111) and (100) substrates were stable at all temperatures. However, the (110) plane exhibited faceting above 600°C. Several surface structures were found to exist on the stable Pt substrates, which can be divided into two types: ordered and disordered. The ordered structures appear during the annealing of the crystal after ion bombardment. They exhibit long-range order and their thermal stabilities overlap on a given substrate. They are believed to be ordered arrays of vacancies in the substrate plane. The ordered structures thus obtained on Pt (100) were (5 × 1) and (2 × 1) observed within the temperature range 350–500°C and 300–500°C, respectively. On Pt (111) the structures (2 × 2) and (3 × 3) were observed after annealing at 800–1000°C.

The disordered surface structures appear at high temperatures above the stability range of most of the ordered structures. They are characterized by a ringlike LEED pattern which develops gradually as a function of increased heating time or temperature. These structures exhibit surprisingly high stability and can only be removed by ion bombardment.

Thermal desorption spectroscopy enabled the discrimination of at least three different states of hydrogen adsorbed on platinum.

Nieuwenhus [7] stated in field emission microscope studies the existence of a β state of hydrogen desorbing above 300 K, an α state desorbing around 230 K, and a very weakly bound γ state with maximum adsorption heat of 6 kcal mol^{-1} desorbing at still lower temperatures. This, is in accordance with the results of Sephans et al. [8] who observed desorption peaks of hydrogen at 120, ~200, and 330 K. In the (111) region of Pt tip in the field emission microscope the dominating hydrogen state was α and only small amount of β was present. On the other hand, on (100) and (210) regions all three states could be detected. The results of [7] and [8] cannot be unequivocally correlated with those obtained by Lu and Rye [9], who investigated chemisorption of hydrogen on various faces of Pt monocrystal. After adsorption at 190 K they observed a single desorption peak at 330 K from the Pt (111) face but five peaks on Pt (100) which were grouped around 250 and 430 K. Two poorly resolved peaks were observed on Pt (211) and Pt (110), at ~300 and ~430, and at ~260 K and ~350 K, respectively. The important result is that in all cases the desorption kinetics were proportional to $(1 - \theta)^2$, which proves that hydrogen desorbing above 200 K is adsorbed dissociatively. Evidently this can also be referred to the states α and β described in [7] and [8] while the low-temperature γ state, considering its low adsorption heat and low desorption temperature, must be assumed to be molecular adsorption.

Further information concerning the nature of chemisorbed hydrogen atoms was presented by Sayers [10], who studied hydrogen chemisorbed on Pt (111) surface using electron energy loss spectroscopy, which indicated three vibrations at 550, 860, and 1230 cm^{-1}. The peaks at 550 and 1230 cm^{-1} were assigned to vibrations of hydrogen adsorbed on a two-coordinated site, the former being associated with vibration parallel and the latter to vibration perpendicular to the surface. The nearest neighbor distance in this site was $\underline{R}_{H\ Pt}$ = 1.93 Å. These observations are in good accordance with the results of elastic neutron scattering: peaks at 500 and 1296 cm^{-1}. The weak EELS feature at 860 cm^{-1} and neutron-scattering peaks at 856 and 936 cm^{-1} were assigned to the hydrogen motion perpendicular and parallel to the surface at a three-coordinated site with bond length $\underline{R}_{H\ Pt}$ = 1.905 Å. Such sites were also assumed in [11].

The adsorption of water on clean Pt (111) [12-13] and Pt (100) [14] surfaces was investigated at temperatures below 200 K using high-resolution electron loss spectroscopy (HREELS) and in both cases the main vibrations characteristic of molecular water were registered corresponding to the H—O—H scissor vibrations at 1630 cm^{-1} and to the OH stretching vibrations. Only one vibration at 3420 cm^{-1} in the latter region was observed on Pt (111) surface but three vibrations on Pt (100). Two of them at 2750 and 3380 cm^{-1} (the strongest one) were assigned to the OH stretching vibrations in H_2O molecules bonded to Pt or to O atoms, respectively. The third vibration at 3670 cm^{-1} was attributed to the free OH group. The vibrations below 1000 cm^{-1} were in the case of Pt (111) assigned to the Pt—O stretching (550 cm^{-1}) and vibration (~700 cm^{-1}). In the studies of the Pt (100) face a somewhat different interpretation was given to the vibrations observed in the same spectral region (frequency 460 cm^{-1} is the vibration of the Pt—O bond in which oxygen is coordinated by its lone electron pair to the metal atom and the frequencies 560 and 920 cm^{-1} are described by the authors as H_2O "rotations"). The frequencies of the vibrations do not change with the coverage in the low-coverage region; however, their shifts observed at higher coverages indicate the formation of ice.

The heat of adsorption of water on the Pt (111) surface was estimated based on the results of thermal desorption spectroscopy [12]. Water adsorbed at 100 K desorbs with approximately zero-order kinetics and a monolayer has a maximum desorption rate at 180 K. Heavier coverages exhibit additional desorption from multilayer water (ice), which peaks at about 165 K. Since the adsorption of water on platinum is a nonactivated process, the activation energy of 180 K peak desorption (65 kJ mol^{-1}) can be equated to the adsorption heat. The fact that this value is higher than the sublimation heat of ice indicates that we are dealing here with weak chemisorption rather than with simple physisorption.

Very much similar were the results of investigation of water desorption from the Ru (111) face where two states desorbing at ~230 and 200 K were registered [15].

The rapid desorption of water from the surface of platinum group metals observed at about 200 K indicates that above this temperature desorption of water cannot be expected to be the rate-limiting step in the catalytic oxidation of hydrogen.

The formation of surface OH groups as the intermediate species in the oxidation of hydrogen on Pt was postulated by some authors [13,16,17].

B. Reactivity of Oxygen and Hydrogen Chemisorbed on Platinum Metals

Very illuminating results were obtained by the study of the catalytic H_2—O_2 reaction under conditions whereby one of the reactants was chemisorbed and the other was present in the gas phase. The application of modern surface techniques permitted the obtaining of very strict and unambiguous results. Much of this work was done with oxygen chemisorbed and hydrogen in the gas phase at temperatures above 200 K where the absorption of water is very fast.

The common feature of the results obtained by all of the above authors was that the rate of chemisorbed oxygen consumption increased at first (an induction period was observed by some of the authors), passed over a maximum, and subsequently decreased. The appearance of such a maximum indicates that adsorption of both components is necessary, suggesting a Langmuir-Hinshelwood mechanism. Norton [17,18] proposed the following kinetic equation:

$$\frac{d\theta_0}{dt} = \frac{k_1 k_2 [H_{2(g)}]\theta_0(1 - \theta_0)}{k_{-1} + k_2\theta_0} \tag{5.2}$$

based on the assumption that the reaction comprises two steps, a rapid establishing of hydrogen adsorption equilibrium:

$$H_{2(g)} + [Pt]_{site} \underset{k_{-1}}{\overset{k_1}{\rightleftarrows}} 2H_a \tag{5.3}$$

and the slow reaction between adsorbed species supplying rapidly desorbing water molecules:

$$2H_a + O_a \xrightarrow{k_2} H_2O_{(g)} \tag{5.4}$$

It has been also assumed that in the steady state $\theta_H \ll \theta_O$. Further assumption that $k_{-1} \gg k_2\theta_O$, i.e., that the adsorbed hydrogen is much more quickly removed from the surface by desorption than by chemical reaction led the author to the equation:

$$\frac{d\theta_0}{dt} = K[H_{2(g)}]\theta_0(1 - \theta_0) \tag{5.5}$$

where $K = \dfrac{k_1 k_2}{k_{-1}}$

It should be noted that in order to obtain a good fit of experimental results to the first-order kinetics with respect to chemisorbed oxygen, Norton assumed that a single site on the surface was required for dissociative chemisorption of hydrogen. This assumption seems to be rather artificial in view of the results of Sayers [10] who postulated on the basis of his EELS investigations two- and three-coordinated positions of hydrogen atoms chemisorbed on the Pt (111) face. An alternative interpretation of the first-order kinetics with respect to hydrogen was given by Yates et al. [19], who carried out an analogous study of O_a–$H_{2(g)}$ reaction on the Rh (111) face. They found that oxygen was adsorbing, at first producing a mixture of ordered and disordered domains. Extensive ordering occurred only in the very last stages of monolayer formation. The reaction of the ordered O layer with hydrogen from the gas phase took place rapidly above 275 K in the range of 10^{-8} to 10^{-6} Torr and exhibited kinetics which were first order in H_2 pressure similarly to that observed by Norton on Pt. However, in the interpretation of their results they suggest that there exists an efficient trapping mechanism for hydrogen adsorbed on the ordered O-layer. The desorption of dissociatively bonded hydrogen would be very slow. The mechanism of O_a-H_2 reaction proposed by Yates comprises the subsequent formation of OH species as the intermediates in the formation of water molecules:

$$H_{2(g)} + 2[Rh]_{site} \longrightarrow 2H_a \tag{5.6}$$

$$H_a + O_a \rightleftharpoons OH_a + [Rh]_{site} \tag{5.7}$$

$$OH_a + H_a \longrightarrow H_2O_g + 2[Rh]_{site} \tag{5.8}$$

The rate of the reaction would be determined by step (5.8). Norton when discussing this latter scheme [18] indicated that although the idea of surface traps may adequately explain first-order reaction with respect to hydrogen, it does not explain the dependence of the reaction rate on the $\theta_O(1 - \theta_O)$ value and in conclusion states that his own mechanism appear to be the simplest one capable of rationalizing all the observations even though it contains the assumptions that are difficult to explain.

Norton studied also the behavior of oxygen on Pt (100) surface at temperature below 200 K, i.e., at the conditions at which no desorption of water occurs [18]. The surface precovered with about 0.5 monolayer of oxygen exhibited 01s peak in the XPS spectrum at 530.1 ± 0.2 eV characteristic of atomic oxygen. At 77 K the sample was contacted with hydrogen ($\sim 3.10^{-5}$ Pa) and slowly warmed. The first changes in the XPS spectrum were registered above 130 K. The temperature was maintained for sometime at 135 K, then hydrogen pumped out and the XPS spectrum again registered. A new peak at 532.4 ± 0.2 eV appeared corresponding to the adsorbed water molecules besides which a shoulder was present at 530.1 eV indicating that some adsorbed oxygen atoms were still present. However, there was no peak observed at 531 eV, characteristic of adsorbed OH groups. The presence of adsorbed H_2O and O species was confirmed by the parallel UPS measurements, which, on the other hand, similarly as XPS measurements, gave no indication of the presence of adsorbed OH groups. It can therefore be concluded that at temperatures below 170 K there is no evidence of the OH groups as reaction intermediates.

Ogle and White [20] investigated at 120—153 K the reaction of hydrogen from gas phase (10^{-9} to 10^{-6} Torr) with oxygen preadsorbed on the Pt (111) surface and forming a p (2 × 2) overstructure. The temperature range applied by them was well below 180 K about which water desorbs from platinum. The fact that water molecules remained at the surface made it possible to apply H_3O^+ SIMS intensity for the determination of the concentration of reaction products. One of the main results of this investigation was the statement that at temperatures below 153 K only a fraction of adsorbed oxygen is available for the reaction during H_2 exposure.

The studies of the reaction of chemisorbed hydrogen with oxygen from the gas phase are much less complete than the studies of the behavior of chemisorbed oxygen. This can partially be due to the fact that owing to the lower adsorption heat the coverage of platinum metals with chemisorbed hydrogen at comparable conditions is lower than that with oxygen. In addition, the presence of hydrogen cannot be monitored, e.g., by XPS or UPS, as it is in the case of chemisorption of oxygen and also no LEED patterns of chemisorbed hydrogen can be obtained. Norton [17] described a few experiments in which the surface of platinum saturated with hydrogen (273 K, 10^{-6} Torr, and evacuation) has been contacted with gaseous oxygen (10^{-2} Torr). The XPS spectrum indicated the presence of chemisorbed oxygen atoms. In an analogous experiment carried out at 200 K, an "induction period" was observed during which chemisorbed hydrogen was oxidized after which peak 530.2 eV of adsorbed O atoms appeared. With increasing temperature this peak decreased and a peak around 533 eV appeared which was attributed to the reaction product H_2O or OH.

The studies of the interaction of coadsorbed hydrogen and oxygen represent a further step in deciphering the mechanism of the catalytic reaction of both elements. In this case hydrogen and oxygen were adsorbed in a definite sequence at temperatures as low as to eliminate the immediate reaction between them. After pumping off thermal desorption experiments were carried out [18]. In one experiment Pt (111) surface exposed to 2.7×10^{-4} Pa sec of O_2 at 100 K and hence covered with molecular oxygen was exposed at the same temperature to 1.3×10^{-4} Pa sec of H_2. A desorption peak at about 150 K appeared on heating the sample, indicating departure of O_2 molecules, and a broader one beginning about 170 K and reaching its maximum around 200 K, which is typical of water desorption. On the other hand, if oxygen was preadsorbed dissociatively (saturation of the surface with oxygen at 100 K, heating to 300 K, and again cooling to 100 K) and exposed to hydrogen (4×10^{-4} Pa sec) besides the peak of desorbing water above 170 K also a peak with maximum about 215 K was observed. Its position was the same as that of the peak which was obtained after reaction of dissociatively preadsorbed oxygen with water vapor which resulted in the formation of surface OH species desorbing at the temperature of this peak. This strongly suggests that some water molecules forming about 170 K were reacting with excess oxygen adsorbed atoms. However, such an interpretation was questioned by Norton [18] on the basis of the already-mentioned fact that the XPS (and also the work function measurements) did not confirm the presence of OH species on the oxygen-precovered Pt surface when exposed to hydrogen under the same conditions. He was rather inclined to interpret the peak around 215 K as indicating the presence of nonequilibrium water.

C. Catalytic Reaction of H_2 and O_2 on Platinum Metal Catalysts with Both Reactants in the Gas Phase

Before presenting the results of mostly earlier "classical" investigations of catalytic hydrogen oxidation carried out at and above room temperature under conditions whereby no ultrahigh-vacuum cleaned surface could be used, we shall present more recent investigations in which molecular beam technique was applied. In particular this technique has been used by Pacia and Dumesic [21], who studied hydrogen oxidation in an apparatus in which a supersonic molecular beam of hydrogen was directed on the surface of platinum ribbon situated in a chamber in which a low isotropic pressure of oxygen (10^{-9} to 10^{-6} Torr) was dynamically kept. Oxygen was introduced by a leak valve and constantly pumped out. The concentration of oxygen and hydrogen either isotropic or reflected from the ribbon was controlled with a mass spectrometer. A system of metallic interrupters permitted the interception of the incident or reflected molecular beam. When using them in an appropriate way the authors could determine the reactive sticking probability β_{H_2}. The product $g_{H_2}\beta_{H_2}$ where g_{H_2} is collision density (proportional to the hydrogen pressure) gives the rate of hydrogen consumption, i.e., the difference between the rates of H_2 adsorption and desorption at the given moment. At the stationary state hydrogen is consumed by its reaction with oxygen or by atomization (desorption of free H atoms). The latter process is predominant only at temperatures above 1350 K and at lower ones can be neglected. Hence in this latter region β_{H_2} is at the stationary state proportional to the reaction rate. An analogous value β_{O_2} can also be introduced. At the stationary state $\beta_{O_2} = 1/2\beta_{H_2}$. At constant pressures of hydrogen and oxygen in the reaction chamber the β_{H_2} value plotted as the function of temperature exhibits a maximum around 1000 K, then decreases, and above 1350 K again increases owing to the strongly increasing atomization process of hydrogen. As Fig. 5.1 shows at constant β_{H_2} the position of the β_{H_2}—$\underline{T}$ curve depends on the isotropic oxygen pressure. In order to visualize this better, the values of β_{H_2}, corresponding to the temperature 750 K taken from Fig. 5.1, are plotted in Fig. 5.2 as the function of oxygen pressure. A distinct maximum is seen on this curve indicating that below 1350 K there exists an optimal $\underline{p}_{H_2}/\underline{p}_{O_2}$ ratio at which the reaction rate reaches a highest value. Pacia and Dumesic when discussing the shape of this curve indicate that it is incompatible with the kinetic equation $\underline{r}_{ER1} = \underline{k}\underline{p}_{H_2}\theta_O$, which would be obtained in the case of Eley-Rideal mechanism assuming the reaction between chemisorbed oxygen and hydrogen from the gas phase. The rate expressions $\underline{r}_{ER2} = \underline{k}\underline{p}_{O_2}\theta_H$ (ER mechanism describable as the reaction between chemisorbed hydrogen and oxygen from the gas phase) or $\underline{r}_{LH} = \underline{k}\theta_O\theta_H$ (Langmuir-Hinshelwood mechanism: reaction between chemisorbed oxygen and chemisorbed hydrogen) are thus needed to explain the maxima in β_{H_2} with oxygen pressure. The discrimination between both latter cases was possible owing to the measurement of transient value of β_{H_2}, i.e., the measurement of β_{H_2} as the function of time which

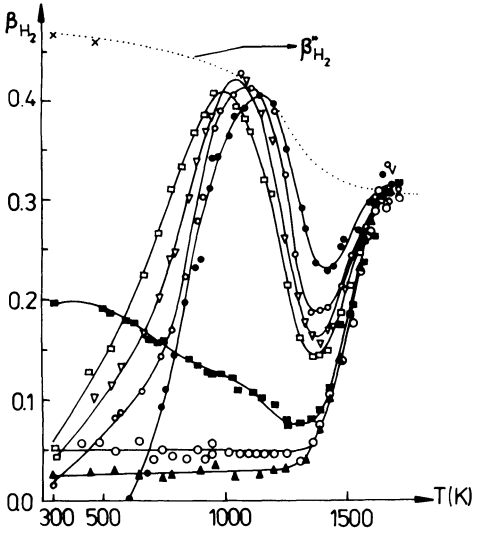

FIGURE 5.1 Variation of β_{H_2} with $\underline{T}$ for a constant H_2 beam intensity and at different values of oxygen pressure. $\beta^*_{H_2}$ is identical to the zero coverage sticking probability. $\underline{p}_{H_2}$ (Torr) = 8 × 10^{-8}; $\underline{p}_{O_2}$ (Torr): •, 2.9 × 10^{-6}; ✖, 1.3 × 10^{-6}; ∇, 6.7 × 10^{-7}; x, 4.5 × 10^{-7}; ■, 9.5 × 10^{-8}; o, 1.9 × 10^{-8}; ▲, 5.7 × 10^{-9} [21].

elapsed since the moment of introduction of the H_2 molecular beam on the Pt sheet. As Fig. 5.3 shows, the initial value of β_{H_2} ($\underline{t}$ = 0) was zero and then before reaching the stationary value it passed over a maximum. The initial rate of reaction equal to zero is not compatible with the $\underline{r}_{ER1}$ or the $\underline{r}_{ER2}$. In the former case the initial rate cannot be zero, in the latter the only time-dependent term is θ_H, which would unrealistically be required to pass through a maximum in time to explain the data. On the other hand, the transient behavior of β_{H_2} corresponds perfectly to the LH mechanism in which θ_O and θ_H, respectively, decrease and increase smoothly with time while their product passes over a maximum value. Such a mechanism correlates well with the mechanism proposed by Norton [17] for the reaction of chemisorbed oxygen and gaseous hydrogen described in the preceding section. The main differences between Pacia and Dumesic's and Norton's papers consist of the fact that the former considered strongly bonded oxygen as active in the catalytic reaction

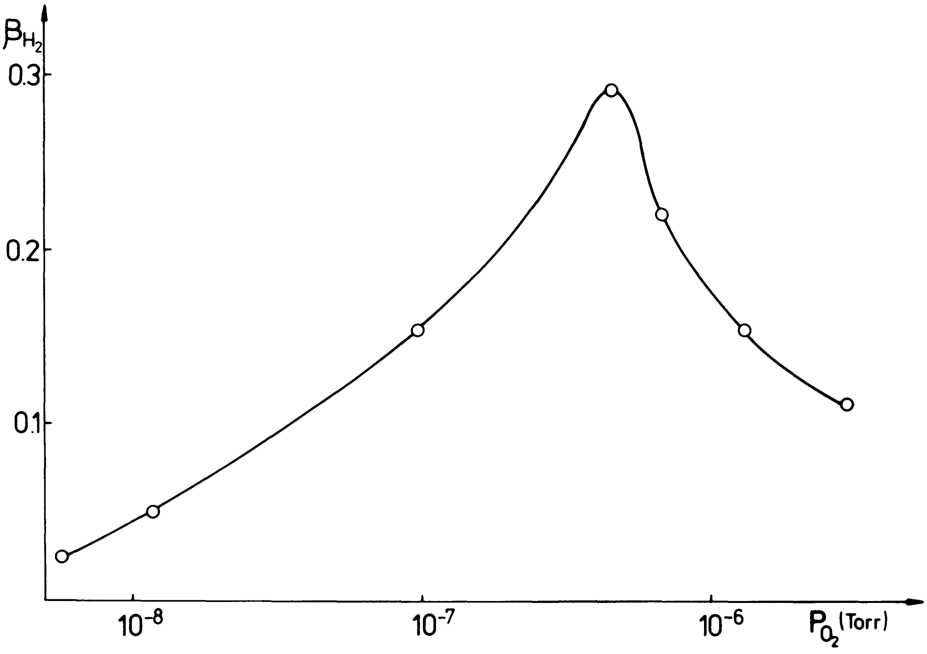

FIGURE 5.2 Variation of β_{H_2} with the oxygen pressure $\underline{p}_{O_2}$ (Torr) at a constant H_2 beam intensity and constant temperature 750 K. (Data taken from Fig. 6 in [21].)

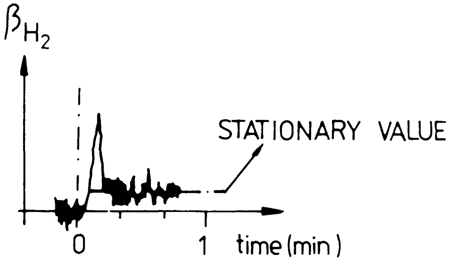

FIGURE 5.3 Transient behavior of β_{H_2} at 300 K [21].

while the latter postulated the participation of "weakly" chemisorbed oxygen.

The LH mechanism can also be used for qualitative interpretation of the β_{H_2}–$\underline{T}$ curve. The maximal possible value of β_{H_2} is $\beta^*_{H_2}$. The sticking coefficient (in other words, the rate of reaction) is limited by the number of H_2 molecules sticking to the surface. The value of $\beta^*_{H_2}$ is given in Fig. 5.1 by a dotted line and it is seen that at the maximum of the β_{H_2}–$\underline{T}$ curve $\beta_{H_2} = \beta^*_{H_2}$; the reactants are then optimally coadsorbed. Below and above the temperature of maximum the ratio of θ_H and θ_O, both changing with temperature in a rather complicated way, assume less favorable values.

The molecular beam technique was also applied to the study of hydrogen oxidation by Engel and Kuipers [22], who investigated this reaction on the Pd (111) surface. Palladium catalyst is of particular interest because of the high solubility of hydrogen in this metal. The rapid transport between the surface and the bulk provides a reservoir of atomic hydrogen for surface reactions which can be available to the surface within 10^{-3} sec.

The formation of H_2O in a mixed H_2–O_2 beam proceeded differently under the conditions of excess oxygen and excess hydrogen. In the excess of hydrogen the kinetics are dominated by the transport of atomic hydrogen between the bulk and the surface. In an excess of oxygen, diffusion of hydrogen into the bulk is blocked by adsorbed oxygen and the hydrogen reservoir available for reaction at the surface is decreased by several orders of magnitude. This results in a drastic reduction of the reaction rate which, on the other hand, can be reversed by increasing the partial pressure of hydrogen.

Engel and Kuipers assumed the following scheme for hydrogen oxidation on palladium:

$$H_{2(g)} \rightleftarrows 2H_a \qquad (5.9)$$

$$O_{2(g)} \longrightarrow 2O_a \quad (5.10)$$

$$H_a \rightleftarrows H_{bulk} \quad (5.11)$$

$$H_a + O_a \rightleftarrows OH_a \quad (5.12)$$

$$OH_a + H_a \longrightarrow H_2O_{(g)} \quad (5.13)$$

In the experiments with the excess of oxygen the authors found the first order of reaction with respect to hydrogen pressure and arrived at the conclusion that the rate-limiting step was reaction (5.12) followed by a fast step (5.13).

Kuchaev and Temkin [23—25] obtained further interesting results concerning the mechanism of the H_2—O_2 catalytic reaction by studying isotopic exchange of oxygen and hydrogen simultaneously with this reaction. The conditions applied by them—polycrystalline Pt foil, temperature range 300—600°C, low dynamic pressure of reaction components 10^{-6} to 10^{-5} Torr—were similar to the conditions of Pacia and Dumesic's investigations. In addition, the concentration of reactants was measured mass spectrometrically.

Kuchaev and Temkin carried out a series of experiments in which at constant oxygen feed rate (and also constant pumping rate) the pressure of hydrogen was changed. Curve 1 in Fig. 5.4, showing the rate of H_2—O_2 catalytic reaction at 560°C as the function of hydrogen pressure (expressed as the pressure of deuterium in the constant H/D ratio), is typical for the results of the authors. There are two distinct portions of the curve. At deuteruim pressures below ~6 × 10^{-6} Torr (pressure range I) the reaction rate $\underline{r}$ increases with hydrogen pressure. In this range $\underline{r}$ is increasing with hydrogen and at lowest deuteruim pressures the reaction order with respect to $\underline{p}_{H_2}$ is 1. At deuteruim pressures higher than about 6 × 10^{-6} Torr (pressure range II) reaction rate is hydrogen pressure-independent and assumes a constant value. Curve 3 in Fig. 5.4 indicates that the pressure of oxygen despite its constant supply does decrease within $\underline{p}_{D_2}$ range I and becomes constant in the range II. When changing the supply of oxygen in a series of experiments it has been shown that the rate $\underline{r}$ in pressure range II was changing proportionally to the steady-state oxygen pressure, i.e., that in this range the H_2—O_2 reaction is of the first order with respect to oxygen.

The rate of isotopic exchange of oxygen in the course of a catalytic reaction is shown by curve 2. It is seen that the exchange is fast at lowest hydrogen pressures and decreases to zero in the intermediate area between ranges I and II. The coverage of platinum

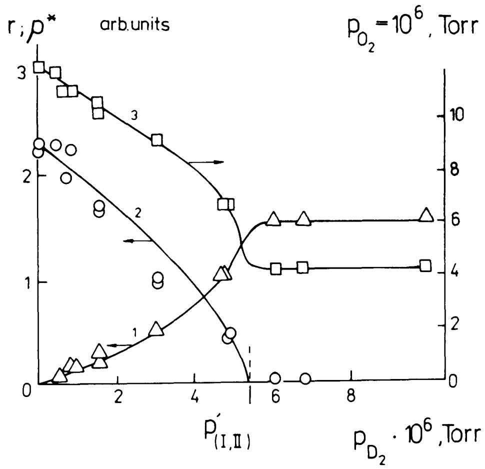

FIGURE 5.4 Dependence of catalytic hydrogen oxidation rate (1), homomolecular oxygen isotopic exchange (2), and oxygen dynamic pressure (3) on deuterium presure at constant oxygen feed rate. Temperature = 560°C [25].

with oxygen in the absence of hydrogen was estimated by the authors on the basis of their measurements to be very close to unity. At a high coverage with oxygen and a low rate of H_2—O_2 reaction only a small fraction of dissociatively chemisorbed oxygen participates in the chemical reaction and the rest can participate in isotopic exchange. The drop of the exchange rate to zero indicates that in the hydrogen pressure range II the coverage with oxygen is close to zero and the rate of water formation is governed by the rate of chemisorption of oxygen. On the other hand, at lowest hydrogen pressure and the surface nearly saturated with oxygen, the reaction rate is determined by the rate with which hydrogen from gas phase reacts with chemisorbed oxygen. The authors conclude that under these conditions the Eley-Rideal mechanism is operating. The arguments in favor of such a mechanism are also supplied from experiments with H_2—D_2 isotopic exchange under catalytic reaction conditions. The rate of this exchange is highest in the hydrogen pressure range II and reaches zero in the pressure range I, indicating very low coverage with dissociatively chemisorbed oxygen.

Kuchaev and Temkin carried out a detailed analysis of their kinetic results and showed that at least three different reaction schemes can be reconciled with the observed kinetics. However, independently of the assumed mechanism kinetic data analysis indicates that a drop of oxygen coverage occurs from $\theta_O = 1$ at $p_{H_2} = 0$

to $\theta_O = 0$ at p_{H_2}, corresponding to the transition from range I to range II. This conclusion found interesting support in the secondary ion mass spectrometric (SIMS) investigations carried out by the same authors in parallel to the kinetic studies. At the transition from kinetic pressure range I to range II a distinct drop was observed in the intensity of all peaks corresponding to oxygen-containing ions, PtO_2^- and also CaO^+ and $CaPtO^+$, thus confirming a strong decrease in oxygen coverage. According to the authors, the intensity of peaks of Ca-containing ions, despite the fact that this metal is present only in traces, is due to the very high sensitivity of SIMS for such ions connected with the low ionization energy of Ca.

Platinum catalysts used for various practical purposes are usually supported catalysts. The problem of the properties and particle size of such dispersed platinum was investigated by many authors. Boreskov [26] when studying the oxidation of hydrogen over a series of unsupported and supported Pt catalysts found that their specific activity determined at the stationary state was almost independent of their total surface area. It changed by a factor less than 3 while the specific surface area varied by four orders of magnitude (Table 5.1).

The effect of platinum dispersion was thoroughly investigated by Hanson and Boudart [27] who studied the samples with still higher dispersion of the metal than Boreskov. The specific activities in H_2 oxidation were practically independent of dispersion D (the ratio of the number of surface metal atoms to the total number of metal atoms) of platinum in the catalysts if the reacting mixture contained an excess of oxygen. On the other hand, no such effect was observed when the experiments were carried out with an excess of hydrogen. An increase of specific activity with increasing dispersion occurred in this case. The authors suggest that in the case of

TABLE 5.1 Catalytic Activity of Platinum Catalysts of Various Dispersion Degrees in the Oxidation of Hydrogen as Calculated per cm^2.

		Pt wire 0.1 mm	Pt foil	$Pt\text{-}SiO_2$
Surface area of platinum ($cm^2\ g^{-1}$)		1.53×10^3	6.7×10^2	7.8×10^7
Specific activity ($cm^3\ H_2\ sec^{-1}\ cm^2$)	100°C	535	900	1400
	50°C	74	97	260

Source: Data from Ref. 26.

samples working under conditions of an excess of oxygen the surface becomes covered by a monolayer of platinum oxide (corrosive chemisorption), which eliminates any crystal plane specificity for hydrogen oxidation.

On the other hand, Marshneva et al. [28] in a more recent study could not confirm the existence of surface structure sensitivity of catalytic activity determined at the excess of hydrogen. They used supported Pt catalysts with crystalline size determined by several available methods (electron microscopy, small angle diffraction of X rays, and chemisorption) and found it to vary from 11—14 Å to 1730 Å. In both oxygen-rich (O_2/H_2 = 7:1) and oxygen-deficient (O_2/H_2 = 1:3) reacting gas mixtures, specific activities were dispersion-independent and equal to the specific activity of massive platinum. The reasons for the discrepancies in the latter results of Boreskov's group and those of Hanson and Boudart are not clear and further investigation is needed.

The independence of specific activity in H_2 oxidation on dispersion is not limited to the platinum catalysts. It has also been observed in the case of Pd and Rh supported catalysts [29].

The fact that at an excess of oxygen the specific rate of hydrogen oxidation is structure insensitive suggests that it is also the case with chemisorption of oxygen on the platinum surface. This enabled application of the reaction between chemisorbed oxygen and gas phase hydrogen for the determination of surface area of dispersed platinum as proposed by Benson and Boudart [30] and reviewed by Prasad et al. [31].

III. CATALYTIC OXIDATION OF HYDROGEN ON METAL OXIDES

Catalytic oxidation of hydrogen on metal oxides, mainly on transition metal oxides, is a process more complicated than oxidation on noble metal catalysts. Oxygen in this case is present not only in elemental form in the gas phase but also as a component of the catalyst itself and in this form can also participate in the catalytic reaction. In the extreme case hydrogen can be oxidized even without the presence of oxygen in gas phase by reducing the catalyst to a lower oxide or metal. Also, at the presence of both reagents H_2 and O_2 in the gas phase, depending on their molar ratio, various defects can be introduced into or removed from the solid thus changing its catalytic properties. Another factor influencing the catalyst's properties is the presence of surface OH groups, which frequently form upon contact of the surface with water vapor.

The fact that the surface transition metal oxides can more or less easily give off oxygen when heated in vacuum renders inapplicable the methods of obtaining a clean surface used in the study of metal catalysts in which ultrahigh-vacuum conditions are applied. Also the application of some of the UHV methods of modern surface science, such as low-energy electron diffraction or Auger electron spectrometry, becomes more complicated because of the building of electrical charge on the oxide surfaces exposed to electron beams. In these circumstances recent progress in the investigation of catalytic H_2 oxidation on transition metal oxides was less spectacular than in the case of metal catalysts.

A. Chemisorption of Hydrogen on Transition Metal Oxides

The existing data indicate that at least three forms of hydrogen adsorbed on transition metal oxides exist, one of which is molecular physisorption observed at low temperatures. In the other two cases we deal with chemisorption which is either fast and exhibiting only low activation energy or slow and activated [32].

Chemisorption of hydrogen was studied most extensively in the case of zinc oxide. Kokes et al. [33] observed at room temperature fast chemisorption of hydrogen, which has been called chemisorption I. Such rapidly sorbed hydrogen can be removed by evacuation at the same temperature. Chemisorption I is independent of simultaneous slow chemisorption II, which is observed after the fast sorption has ceased. Chemisorption II cannot be removed by evacuation at room temperature even after several hours.

Chemisorption I is accompanied by the appearance of two bands in the IR spectrum of zinc oxide, at 3484 and 1709 cm^{-1}. These bands were observed for the first time by Eischens et al. [34] and are assigned to OH and ZnH species, respectively. Accordingly, the course of chemisorption I can be formulated as the heterolytic fission of the H_2 molecule:

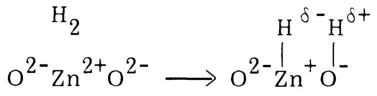

$$\overset{H_2}{O^{2-}Zn^{2+}O^{2-}} \longrightarrow O^{2-}\overset{\overset{H^{\delta-}}{|}}{Zn^{+}}\overset{\overset{H^{\delta+}}{|}}{O^{-}} \qquad (5.14)$$

It is assumed that the hydrogen atom bonded to oxygen has a protonic character and the hydrogen atom bonded to zinc has a hydridic character. The presumed largely ionic character of both bonds is consistent with relatively high intensity of the corresponding IR bands. More recently, Boccuzzi et al. [35] observed in the lower wavenumber region the bands at 817 and 850—845 cm^{-1} of reversibly adsorbed hydrogen and deuterium associated with bending modes of Zn—H and Zn—D bonds, respectively. According to Eq. (5.14), chemisorption of type I does not involve the participation of free electrons of the solid. Gerasimova et al. [41] confirmed that no changes in the electrical conductivity of ZnO occur during chemisorption of hydrogen at room temperature.

Type II chemisorption occurs rapidly initially, but slowly in later stages and continues at an observable rate for several days. No IR bands attributable to type II hydrogen were observed in the earlier investigations [33,34]. However, recently Boccuzzi et al. [35] were able to identify the bands around 3400 and 1475 cm^{-1} as arising from type II irreversibly adsorbed hydrogen. They arrived at the conslusion that hydrogen atoms in this state are bonded in bridged structures between two Zn or O atoms (Zn—H—Zn or OH...O) in the subsurface cavities.

The third form of hydrogen adsorbed on zinc oxide described by Kokes [36,37], hydrogen type III, is observed at -78°C and below. Infrared bands were registered at 4017, 3507, and 2887 cm^{-1} corresponding to the molecularly adsorbed H_2, HD, and O_2. The observed frequencies are shifted into lower values in comparison with the frequencies in the gas phase. For example, the shift in the case of D_2 adsorbed molecule is nearly 100 cm^{-1} (frequency in free D_2 molecule 2990 cm^{-1}). This value is larger than could be expected for pure physisorption and that is why the authors interpret the IR bands as being due to a weak molecular chemisorption. They believe that this type of chemisorption may be common for certain dehydrated oxides.

In later investigations it was shown by thermal desorption experiments that adsorption of hydrogen on zinc oxide is giving rise to more than three adsorption states as could be inferred from Kokes' experiments. Narvaez and Taylor [38] found four different desorption peaks at 60, 150, 250, and 400°C, and Barański and Galuszka [39] in their study discovered seven peaks between -68°C and 400°C (peak O_A, 68°C; O_B, -16°C; I_A, 9°C; I_B, 36°C; II, 100°C; III, 225°C; and IV, 400°C). Watanabe [40], investigating low-temperature desorption of hydrogen, confirmed the presence of Barański's O and I peaks but also observed two peaks designed as L_a and L_B at temperatures -134 and -95°C, respectively.

Chemisorption of hydrogen on zinc oxide at higher than room temperature (25—300°C) was investigated by Gerasimova et al. [41], who parallel to the adsorption measurements carried out under analogous conditions also measured changes in electrical conductivity accompanying hydrogen adsorption. As already mentioned, at room temperature, i.e., under the conditions in which Kokes' adsorption type I occurs, no changes in electrical conductivity were observed. At temperatures above room temperature Gerasimova et al. observed three kinds of hydrogen chemisorption on ZnO:

1. Within a temperature range below 100°C chemisorption occurred as a practically nonactivated process (activation energy 3 kcal mol^{-1}) with a simultaneous decrease in electrical conductivity.

Therefore it was connected with the formation of acceptor species. The authors argue that the centers in the solid which are donating electrons to an adsorbed hydrogen species are donor centers the presence of which is manifested by an EPR signal at $\underline{g}$ = 1.957 ($\Delta\underline{G}$ = 9 Gs). This signal is considered in the literature as being due either to anionic vacancies at which unpaired electrons are localized $V_{\dot{0}}$ (F centers) or to interstitial zinc atoms singly ionized (Zn_i) [42].

2. Within the temperature range about 100 to 200—250°C chemisorption dominated accompanied by an increase in the electrical conductivity of ZnO and a simultaneous appreciable change in the activation energy of conductivity. Gerasimova et al. suggest that here a donor-type adsorption reaction occurs in which $V_{\dot{0}}$ centers (F centers) are playing the role of electron acceptors.
3. At temperatures above 200°C donor-type chemisorption of hydrogen was observed different from chemisorption as described in item 2, but without a significant change in the activation energy of electrical conductivity. This was considered to be the first step in the reduction of the oxide

$$O^{2-} + \frac{1}{2}H_2 \longrightarrow OH^- + e^- \qquad (5.15)$$

Further investigation is necessary in order to find whether the discrimination between states 2 and 3 is real and to confirm the proposed mechanisms.

The number of papers dealing with adsorption of hydrogen on transition metal oxides other than zinc oxide is surprisingly small. However, it can be assumed that the basic information gathered in the case of ZnO has a general meaning. Without doubt it is the case with low-temperature adsorption of H_2 on oxides. It has been investigated by Maslov et al. [43], who observed one IR adsorption band on Ga_2O_3, Sc_2O_3, ZrO_2, and SiO_2 and two to four bands on ZnO, Al_2O_3, TiO_2, and SiO_2–Al_2O_3 appearing after adsorption of hydrogen at 60–77 K and corresponding to the stretching vibration of the H_2 molecule. It should be remembered here that a centrosymmetric H_2 molecule when free in the gas phase is IR nonactive. Adsorption considered to occur on metal cations playing the role of Lewis acid centers evidently results in such deformation of H_2 molecules that their symmetry is changed and the space distribution of electron density is no more centrosymmetric.

The reversible molecular adsorption of hydrogen on Co_3O_4 at liquid air temperature was also observed by Shigehara and Ozaki [44]. The coverage with molecular hydrogen decreased on heating to -75°C but the sorption of hydrogen increased again at room temperature thus indicating activated chemisorption. The same authors [45] determined chromatographically the hydrogen adsorption isobar on prereduced Cr_2O_3. Also in this case activated chemisorption with maximum coverage at about room temperature was observed. Supposedly this kind of chemisorption corresponds to the Kokes' chemisorption type I of hydrogen on ZnO which was suggested by Burwell [46,47].

At high enough temperatures reductive adsorption of hydrogen on oxides takes place in which OH groups form as an electron is simultaneously given to the lattice as shown by Eq. (5.15), which may be used for the reduction of a cation to a lower oxidation degree. The range of temperature in which such a process becomes significant depends on the nature of the oxide. As already stated, at different ZnO preparations it was observed above 200°C [41] but in the case of Sc_2O_3 the formation of OH groups was observed at 400—500°C [48]. The molecular adsorption of H_2 on this oxide was observed between -78 and 200°C.

Andreev et al. [32,49] carried out a series of quantum chemical calculations of the interactions of the hydrogen molecules with the surface of transition metal oxides. The geometry of surface complexes taken for the calculations is schematically given in Table 5.2. Two orientations of the H_2 molecule with respect to the surface—normal and parallel—were taken into account. As the results obtained for nickel oxide show, owing to the better overlap of 3d orbitals of cation with 1s orbitals of H atoms, adsorption heat is always greater in the case of parallel orientation, thus indicating that this type of molecular adsorption should be expected. Simul-

TABLE 5.2 Adsorption Heat and Bond Order in H_2 in Different Surface Complexes on NiO.

	I	II	III	IV	V
Surface complex	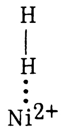	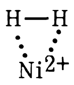	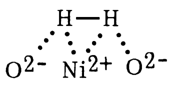	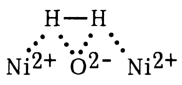	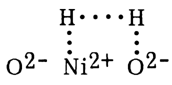
Adsorption heat, eV	5.51	6.03	10.12	7.81	10.62
H—H bond order	0.847	0.792	0.821	0.912	-0.058

Source: Data from Ref. 32.

taneous weakening of the H—H bond is manifested by diminished bond order. This is connected with increasing occupancy of σ^* antibonding orbitals of H_2 molecules, thus indicating a certain negative charge on H_2 adsorbed molecule. The data in Table 5.2 show that among the four possible parallel positions the most stable is that in surface complex V. In this case the adsorption heat is largest and a very low bond order calculated for the H_2 molecule indicates it dissociation. This situation corresponds to the formation of M—H and OH surface species which, as already mentioned, were experimentally detected in ZnO.

B. Catalytic Oxidation of Hydrogen on Transition Metal Oxides

An extensive investigation of catalytic oxidation of hydrogen on transition metal oxides was undertaken by Boreskov and his collaborators [50,51], who used a stationary-circulating type of apparatus that allowed study of the catalytic activity in a well-determined stationary state. In order to compare the behavior of different oxides, the activities measured at a high excess of oxygen within different temperature ranges (depending on the activity of particular oxides) were extrapolated to 300°C and the following series of specific activities was obtained: $Co_3O_4 > CuO > MnO_2 > NiO > Cr_2O_3 > CdO > SnO_2 > Fe_2O_3 > PbO > ZnO > WO_3 > V_2O_5, MoO_3 > TiO_2$. Specific activity changed in this series by as much as six orders of magnitude from 5.50×10^{13} O_2 molecules$\cdot$cm^{-2} sec^{-1} for Co_3O_4 to 8.6×10^7 O_2 molecules$\cdot$cm^{-2} sec^{-1} for TiO_2. Very low activity was observed in the case of the dielectric oxides MgO and Al_2O_3.

The kinetic equation which has been shown to have the widest applicability was given by Golodets [4], based on a reaction scheme comprising the following steps:

$$\begin{aligned}
&(1)\quad O_{2(g)} + (\quad) \xrightarrow{k_1} (O_2) \xrightarrow[\text{fast}]{(\ )} 2(O)\\
&(2)\quad H_{2(g)} + (O) \xrightarrow{k_2} (H_2O)\\
&(3)\quad (H_2O) \xrightarrow{k_3} H_2O_{(g)}
\end{aligned}\tag{5.16}$$

in which symbol ( ) denotes surface adsorption site and (O_2), (O), and (H_2O) adsorbed O_2, O, and H_2O species, respectively. Not specified here were the chemisorbed oxygen species. The scheme therefore comprises the situation in which ( ) is a surface anionic vacancy and (O) a surface oxygen atom of low coordination O_{LC}. The kinetic equation given in [4]:

$$r = \frac{k_1 k_2 p_{O_2} p_{H_2}}{k_1 p_{O_2} + \frac{k_1 k_2}{k_3} p_{O_2} p_{H_2} + 1/2 k_2 p_{H_2}} \tag{5.17}$$

where r = reaction rate, can be linearized by plotting $1/r$ against $1/p_{H_2}$:

$$\frac{1}{r} = \frac{1}{2k_1 p_{O_2}} + \frac{1}{k_3} + \frac{1}{k_2 p_{H_2}}$$

If a high excess of oxygen is present, $k_1 p_{O_2} >> [(k_2 k_2/k_3) p_{O_2} p_{H_2}] + 1/k_2 p_{H_2}$ and Eq. (5.17) is reduced to

$$r = k_2 p_{H_2} \tag{5.18}$$

indicating that at these conditions a zero-order reaction with respect to oxygen and a first-order reaction with respect to hydrogen should be expected. In fact, in Boreskov's experiments with a high excess of oxygen an order of 1 or close to 1 with respect to hydrogen was observed.

In reaction scheme (5.16) and Eq. (5.17) it was assumed that the rate constant of water desorption k_3 is comparable to rate constants k_1 and k_2, i.e., desorption of water can become the rate-limiting step. Under these conditions:

$$\frac{k_1 k_2}{k_3} p_{O_2} p_{H_2} >> k_1 p_{O_2} + \frac{1}{2} k_2 p_{H_2}$$

and

$$r = k_3 \tag{5.19}$$

The reaction becomes zero order with respect to both oxygen and hydrogen. Such a situation was observed in [52] where the oxidation of hydrogen on NiO films was investigated at 0—137°C.

On the other hand, if desorption of water is very fast and $k_3 >> k_1$ and $k_3 >> k_2$, the term $[(k_1 k_2/k_3) p_{O_2} p_{H_2}$ in Eq. (5.17) can be omitted and

$$r = \frac{k_1 k_2 p_{O_2} p_{H_2}}{k_1 p_{O_2} + 1/2 k_2 p_{H_2}} \qquad (5.20)$$

The reaction can now be considered as being composed of two steps only:

$$\begin{aligned} &(\ell) \quad O_{2(g)} + (\ \ ) \longrightarrow (O_2) \xrightarrow{\text{fast}} 2(O) \\ &(o) \quad H_{2(g)} + (O) \longrightarrow H_2O_{(g)} + (\ \ ) \end{aligned} \qquad (5.21)$$

Reaction (o) represents here a reduction step in which some surface oxygen species are reduced, while reaction (ℓ) represents the reoxidation of the catalysts. In their extensive studies, Boreskov and his collaborators [51] showed that at the stationary state the rate of catalytic oxidation of hydrogen on group IV transition metal oxides is equal to the rate of catalyst reduction and simultaneously to the rate of catalyst reoxidation. This can be understood if the dependence of both latter rates on the amount of oxygen removed from the surface is taken into account. It was already mentioned in Section VI of Chapter 3 that oxygen-surface bond strength is also influenced by oxygen deficiency of the surface. Figure 5.5 shows that with an increasing amount of oxygen removed from the surface θ_O (expressed as the percentage of monolayer), the rate of reduction at a given pressure of hydrogen p_{H_2} does decrease and the rate of catalyst reoxidation H_2 at a constant pressure of oxygen p_{O_2} does increase. At the point of intersection of curves $r_{red} = f((p_{H_2})$ and $r_{ox} = f(p_{O_2})$ both rates are equal and are also equal to the overall catalytic oxidation rate at the stationary state. This stationary state evidently must be reached under the conditions at which the pressures p_{H_2} and p_{O_2} in the reacting mixture are the same as those applied when the separate rates of catalyst reduction and reoxidation were determined. The data collected in Table 5.3 show that at the stationary surface composition of Fe_2O_3, Cr_2O_3, and CuO, the rate of catalytic oxidation of hydrogen was really close to the rates of reduction and reoxidation. Similar results were obtained by Boreskov and his collaborators for Co_3O_4, MnO_2, and ZnO, thus confirming their proposed mechanism of catalytic oxidation (the deviations from this rule exhibited by V_2O_5 will be discussed later).

As already stated, reaction path (5.21) does not imply any determined form of oxygen which participates in the sequence of reduction-oxidation steps. Principally this may be any form of oxygen present at the surface, i.e., negatively charged adsorbed oxygen

TABLE 5.3 Reaction Rates of Catalytic Oxidation of Hydrogen r, and Rates of Catalyst Reduction r_{red} and Catalyst Reoxidation r_{ox} at the Stationary State of the Surface Characterized by Amount of Oxygen Removed from Surface θ_0[a]

Oxide	$r_{red} = r_{ox}$ (10^{-3} cm^3 O_2/m^2 min)	r (10^{-3} cm^3 O_2/m^2 min)	Temp. (°C)	Oxygen removed from the surface (% of monolayer)
Fe_2O_3	1.50	1.36		0.6
Cr_2O_3	1.70	1.44	201	1.3
CuO	2.40	2.50	102	0.4
V_2O_5	0.70	1.24	440	1.3

[a] Experiments carried out at $p_{O_2} = p_{H_2} = 80$ Torr.

Source: Data from Ref. 51.

species as well as lattice oxygen from the most external surface layer. However, it should be observed that under the conditions at which Boreskov's experiments were carried out, i.e., at temperatures mostly above 150—200°C, one can expect only a very small concentration of adsorbed species O_2^- or O^-. It was stated in Chapter 2 that such species have a tendency to accept additional electrons and transform into O^{2-} ions incorporated into the oxide crystal lattice according to the sequence:

$$O_{2(\underline{g})} \longrightarrow O^-_{2(\underline{a})} \longrightarrow O^-_{(\underline{a})} \longrightarrow O^{2-}_{lattice}$$

This transformation is enhanced by increased temperature and by prereduction of the surface which creates new centers supplying electrons. It can therefore be concluded that the most probable

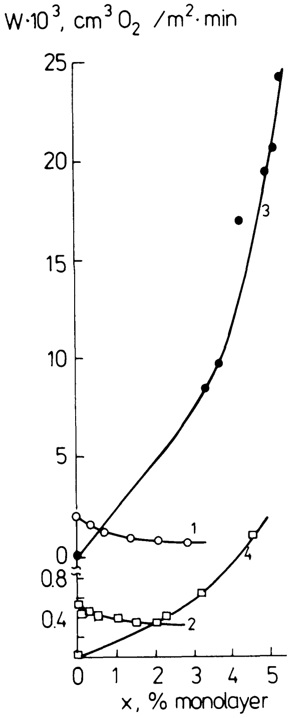

FIGURE 5.5 Dependence of the rate of reduction (1, 2) and the rate of reoxidation (3,4) on the amount of oxygen removed from surface θ_0 for Co_3O_4 (1, 3 at 63°) and MnO_2 (2, 4 at 101°C) [51].

form of oxygen participating in the catalytic oxidation of hydrogen on the oxides of group IV transition metals is lattice oxygen.

Of special interest are the data shown in Table 5.3 concerning the result obtained for V_2O_5 catalyst. In this case the rate of catalytic oxidation of hydrogen was nearly twice as high as the velocities of catalyst reduction and reoxidation in the stationary state. A similar result was also obtained for TiO_2 where the rate of catalytic reaction was six times as high as the rates of reduction and reoxidation. The simplest explanation of such an effect would be to assume that it is due to the presence on the surface of such species as O_2^- or O^-. It can be supposed that they are much more reactive than the surface O^{2-} ions and even at low stationary concentration, virtually not changing the oxidation state of the surface, the reaction path including these species effectively increases the total reaction rate. This explanation seems to be plausible in the case of TiO_2 as well as in the case of one strictly stoichiometric preparation of NiO studied by Boreskov. However, in the case of V_2O_5 Ilchenko et al. [53] suggested a different interpretation. It has been shown that on this catalyst the rate of catalytic reaction exceeds the rates of catalyst reduction and reoxidation if the $\underline{p}_{O_2}/\underline{p}_{H_2}$ ratio is contained within the limits 0.1 and 30, at still higher excess of oxygen and at a high excess of hydrogen when $\underline{p}_{O_2}/\underline{p}_{H_2} < 0.1$ or $\underline{p}_{O_2}/\underline{p}_{H_2} > 30$ all three rates are equal. For the intermediate values of this ratio Ilchenko et al. suggested a different interpretation according to which the observed effect is due to the presence of an additional reaction path in which a chain in the gas phase is being originated at the surface of the solid, e.g., by the desorption of OH or H species. This hypothesis was supported by the experiment in which the empty space in the reactor was filled with catalytically inert ground quartz glass, thus reducing the volume at which the presumed homogeneous chain reaction can develop. Simultaneously, the probability of chain breaking in the gas phase was strongly increased. In fact, under these conditions the rate of catalytic hydrogen oxidation was appreciably reduced.

In Section VI of Chapter 3 it was mentioned that a parallelism exists between oxygen bonding strength $\underline{q}_s$ and the rate of catalytic hydrogen oxidation. This was illustrated by Fig. 3.13 in which parallelism of the reaction rate of hydrogen oxidation $\underline{r}$ is shown to change for different oxides parallel to the rate of isotopic oxygen exchange which was proved to be directly correlated with $\underline{q}_s$. The direct dependence of log $\underline{r}$ on $\underline{q}_s$ is shown in Fig. 5.6; Boreskov's data from [54] and [4] were taken for constructing the graph, indicating distinct correlation between both values. With decreasing oxygen-catalyst bond strength catalytic activity does increase. This correlation can be understood on the basis of

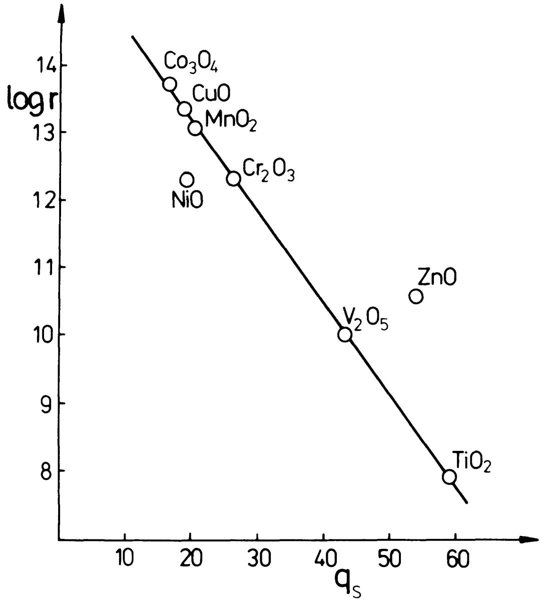

FIGURE 5.6 Dependence of the rate of hydrogen oxidation $\underline{r}$ on the oxygen-surface bonding strength $\underline{q}_s$ in different oxides. Temperature of the catalytic reaction = 300°C, $\underline{p}_{O_2}$ = 750 Torr, $\underline{p}_{H_2}$ = 11.8 Torr. (Data from 54,4].)

Boreskov's reaction scheme. Let us consider the curves representing the rates of catalyst reduction and catalyst reoxidation as the function of the amount of oxygen removed from the surface such as those already shown in Fig. 5.5. Figure 5.7 schematically shows the situation existing in the case of two different oxides (oxide 1 and 2) which at $\theta_O = 0$ exhibit different oxygen bonding strengths. It is reasonable to assume that the rate of reduction of oxide 2 characterized by a lower $\underline{q}_s$ value at $\theta = 0$ will be higher than that of oxide 1. On the other hand, the rate of reoxidation of oxide 2 extrapolated to $\theta_O = 0$ will be lower than that of oxide 1. This implies the shift of both curves, $\underline{r}_{red} - \underline{f}(\theta_O)$ and $\underline{r}_{ox} = \underline{f}(\theta_O)$, as shown in Fig. 5.7. It is seen that the intersection point of both curves at which $\underline{r}_{red} = \underline{r}_{ox} = \underline{r}$ corresponds in the case of oxide 2 to higher catalytic reaction rate $\underline{r}_2 > \underline{r}_1$.

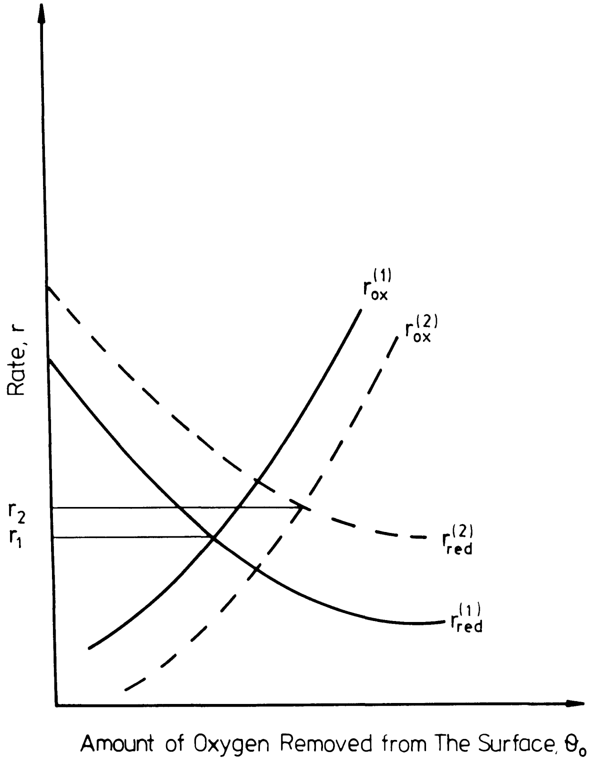

FIGURE 5.7 Schematic diagram showing the dependence of catalyst reduction rate $\underline{r}_{red}$ and catalyst reoxidation $\underline{r}_{ox}$ on the amount of oxygen removed from the surface θ_O for a catalyst 1 showing higher $\underline{q}_s$ value at $\theta_O = 0$ and catalyst 2 showing lower $\underline{q}_s$ value at $\theta_O = 0$.

REFERENCES

1. E. K. Rideal and H. S. Taylor, Catalysis in Theory and Praxis, Macmillan, London, 1926.
2. J. O'M. Bockris, Pure and Appl. Chem., 47, 25 (1976).
3. Gmelins Handbuch der anorganischen Chemie, 8 Aufl., Sauerstoff, Lieferung 5, System-Nummer3, Verlag Chemie, 1963, p. 1209.
4. G. I. Golodets, Geterogenno-katalititcheskye reaktsii s utchastiem molekularnogo kisloroda (Heterogeneous Catalytic Reactions with the Participation of Molecular Oxygen), Naukova Dumka, Kiev, 1977, p. 238.
5. T. N. Rhodin and G. Brodén, Surf. Sci., 60, 446 (1976).

6. H. B. Lyon and G. A. Somorjai, J. Chem. Phys., 46, 2539 (1967).
7. B. E. Nieuwenhus, Surf. Sci., 59, 430 (1976).
8. J. J. Sephans, V. Ponec, and W. M. H. Sachtler, J. Catal., 37, 81 (1975).
9. K. E. Lu and R. R. Rye, Surf. Sci., 45, 677 (1974).
10. C. M. Sayers, Surf. Sci., 143, 411 (1984).
11. J. Lee, J. P. Covin, and L. Wharton, Surf. Sci., 130, 1 (1983).
12. G. B. Fisher and J. L. Gland, Surf. Sci., 94, 446 (1980).
13. G. B. Fisher and B. A. Sexton, Phys. Rev. Lett., 44, 683 (1980).
14. H. Ibach and S. Lehwald, Surf. Sci., 91, 187 (1980).
15. T. E. Madey and J. T. Yates, Jr., Chem. Phys. Lett., 51, 77 (1977).
16. B. A. Morrow and P. Ramamurthy, J. Phys. Chem., 77, 3052 (1973).
17. P. R. Norton, J. Catal., 36, 211 (1975).
18. P. R. Norton, in The Chemical Physics of Solid Surfaces and Heterogeneous Catalysis, Vol. 4 (D. A. King and D. P. Woodruff, eds.), Elsevier, Amsterdam, 1982, p. 27.
19. J. T. Yates, Jr., P. A. Thiel, and W. H. Weinberg, Surf. Sci., 82, 45 (1979).
20. K. M. Ogle and J. M. White, Surf. Sci., 139, 43 (1984).
21. N. Pacia and J. A. Dumesic, J. Catal., 41, 155 (1976).
22. T. Engel and H. Kuipers, Surf. Sci., 90, 181 (1979).
23. V. L. Kuchaev and M. I. Temkin, Kinet. Katal., 13, 719 (1972).
24. V. L. Kuchaev and M. I. Temkin, Kinet. Katal., 13, 1024 (1972).
25. V. L. Kuchaev, L. M. Nikitushina, and M. I. Temkin, Kinet. Katal., 15, 963 (1974).
26. G. K. Boreskov, J. Chim. Phys., 51, 759 (1954).
27. F. V. Hanson and M. Boudart, J. Catal., 53, 56 (1978).
28. V. I. Marshneva, G. K. Boreskov, and A. A. Pankratova, Kinet. Katal., 23, 1349 (1982).
29. M. Ladacki, T. J. Houser, and R. W. Roberts, J. Catal., 4, 239 (1965).
30. E. Benson and M. Boudart, J. Catal., 6, 704 (1965).
31. J. Prasad, K. R. Murthy, and P. G. Menon, J. Catal., 52, 512 (1978).
32. A. Andreev and D. Shopov, Khimicheskaya sviaz pri Adsorptsii ii Katalize, II Okisly (Chemical Bond and Upon Adsorption and Catalysis, II Oxides), in Russian, Bulgarian Academy of Sciences, Sofia, 1979, p. 119.
33. R. J. Kokes and A. L. Dent, Adv. Catal., 22, 1 (1972).
34. R. P. Eischens, W. A. Pliskin, and M. J. Low, J. Catal., 1, 180 (1962).

35. F. Boccuzzi, E. Borello, A. Zecchina, A. Bossi, and M. Camia, J. Catal., 51, 150 (1978).
36. C. C. Chang and R. J. Kokes, J. Am. Chem. Soc., 93, 7107 (1971).
37. C. C. Chang, L. T. Dixon, and R. J. Kokes, J. Phys. Chem., 77, 2634 (1973).
38. R. Narvaez and H. A. Taylor, J. Phys. Chem., 69, 2500 (1965).
39. A. Barański and J. Galuszka, J. Catal., 39, 259 (1960).
40. M. Watanabe, J. Res. Inst. Catalysis, Hokkaido Univ., 26, 63 (1976).
41. G. F. Gerasimova, N. P. Keier, and L. I. Isaenko, Kinet. Katal., 14, 1239 (1973).
42. G. Neuman, in Current Topics in Materials Science, Vol. 7, Zinc Oxide (E. Caldis, ed.), North Holland, Amsterdam, 1981, p. 270.
43. S. Y. Maslov, L. A. Demisienko, A. A. Tsyganenko, and V. N. Filimonov, React. Kinet. Catal. Lett., 20, 273 (1982).
44. Y. Shigehara and A. Ozaki, J. Catal., 21, 78 (1971).
45. Y. Shigehara and A. Ozaki, Bull. Soc. Chem. Japan, 45, 634 (1972).
46. R. L. Burwell, Jr., A. B. Littlewood, M. Cardew, G. Pass, and C. T. H. Stoddart, J. Am. Chem. Soc., 82, 6272 (1960).
47. R. L. Burwell, G. L. Haller, K. C. Taylor, and J. F. Read, Adv. Catal., 20, 1 (1969).
48. L. Gonzales Tejuca, C. Jandula Cordoba, and J. L. Garcia Fierro, Z. Phys. Chem. (Wiesbaden), 118, 99 (1979).
49. A. A. Andreev, N. M. Neshev, L. T. Prakhov, and D. M. Shopov, Kinet. Katal., 13, 1005 (1972).
50. V. V. Popovskii and G. K. Boreskov, Problemy Kinetki i Kataliza, Publishing House of the Academy of Sciences USSR, 10, 67 (1960).
51. E. A. Mamedov, V. V. Popovskii, and G. K. Boreskov, Kinet. Katal., 10, 852 (1969); 11, 969 (1970); 11, 979 (1970).
52. T. Gray and P. W. Darby, J. Phys. Chem., 60, 209 (1956).
53. N. I. Ilchenko, G. I. Golodets, and Yu. I. Pyatnitskii, Kinet. Katal., 13, 1444 (1972).
54. G. K. Boreskov, V. V. Popovskii, and V. A. Sazonov, Proc. Fourth Int. Congr. on Catalysis, Moscow, 1968, Akademiai Kiado, 1971, p. 439.

6

Catalytic Oxidation of Carbon Monoxide

I. INTRODUCTION

The catalytic oxidation of carbon monoxide is one of the most comprehensively studied and best understood catalytic reactions. Owing to the fact that, with rare exception, chemisorption of CO is nondissociative under the conditions of catalytic oxidation, this latter reaction is a relatively simple process that has been frequently applied as a catalytic test reaction. It served as the basis for studies of fundamental problems of catalysis, e.g., verification of the electronic theory of chemisorption and catalysis on semiconductors or the reduction-oxidation mechanism of catalytic oxidation.

The revival of interest in this process in recent years was due, on the one hand, to the introduction of new methods of surface science which supplied a wealth of entirely new information in the case of metal catalysts concerning the behavior of chemisorbed reaction partners and the molecular mechanism of CO oxidation. On the other hand, the problem of pollution of air by exhaust gases in which CO is usually the most toxic component needs the synthesis of effective and durable catalysts enabling rapid oxidation of CO to CO_2 under technical conditions.

There are two groups of catalysts usually applied for CO oxidation: platinum group metals and simple or mixed transition metal oxides. In both cases the nature of the carbon monoxide-catalyst bond is considered to be essentially the same as in metal carbonyls. Hence, it seems appropriate to precede the chapters on chemisorption of CO on metals by a short summary of the present state of knowledge concerning the bonding of CO in carbonyls.

II. CARBON MONOXIDE BONDING IN METAL CARBONYLS

A schematic diagram of molecular orbitals in the carbon monoxide molecule is given in Fig. 6.1, and the spatial representation of orbitals in Fig. 6.2. The orbital most strongly contributing to the formation of the bond is orbital 1σ, which in order to make Fig. 6.2 more clear has been symbolized by a line. The highest electron density corresponding to this orbital is localized between both nuclei C and O. The two other σ orbitals, 2σ and 3σ, are directed along the C—O axis outside the molecule and accommodate lone pairs of electrons. The overlap of p_y and p_x orbitals of both atoms results in the formation $1\pi_y$ and $1\pi_x$ doubly degenerated bonding orbitals as

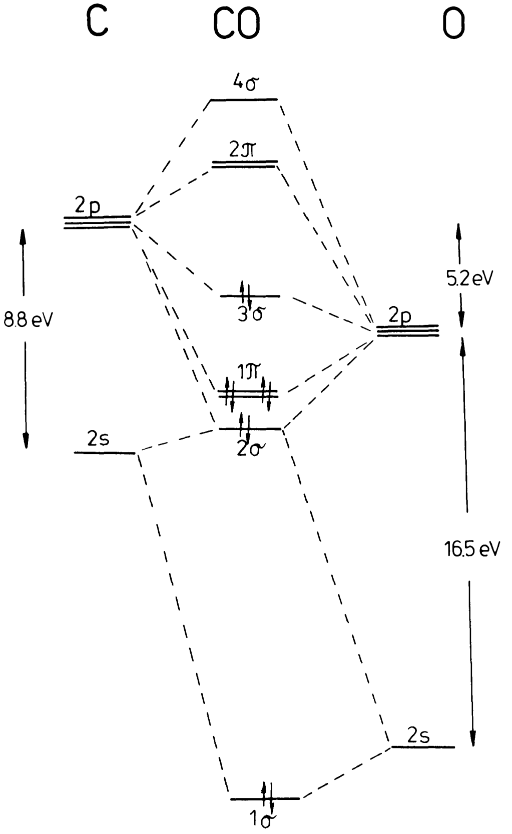

FIGURE 6.1 Schematic diagram of molecular orbitals in CO molecule.

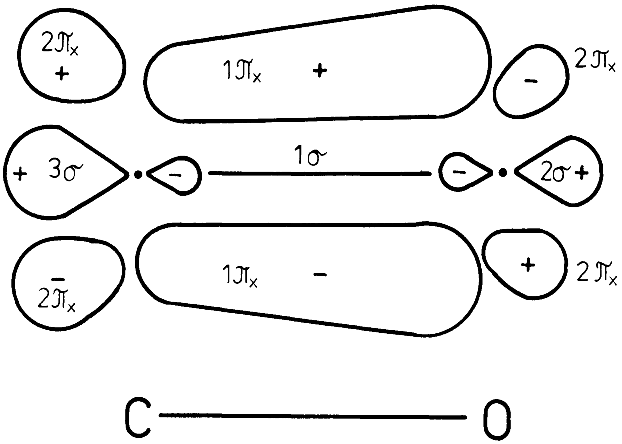

FIGURE 6.2 Shape of orbitals in CO molecule.

well as $2\pi_y$ and $2\pi_x$ antibonding ones. Only one from each pair of π orbitals ($1\pi_x$ and $2\pi_x$) is shown schematically in Fig. 6.2, with the sheet of paper being its symmetry plane. The symmetry plane of the other pair of π orbitals is perpendicular to the sheet of paper. The electron density corresponding to 1π bonding orbitals is asymmetrically distributed with respect to both atomic nuclei, and it is estimated that the probability of finding a 1π electron near the oxygen nucleus is about four times greater than the probability of finding one around the carbon nucleus. The dipole moment of these bonds, however, is compensated by the dipole moment of opposite direction, due to the fact that the lobe of the 3σ orbital protrudes much more outside the molecule than does the lobe of the 2σ orbital with another lone pair of electrons. The resulting dipole moment of the CO molecule is 0.12 D [1,2].

The scheme in Fig. 6.1 indicates that the electronic configuration of the carbon monoxide molecule is $(1\sigma)^2(2\sigma)^2(1\pi)^4(3\sigma)^2$. There are four bonding electron pairs and one antibonding, and hence the bond order is three.

A CO molecule is bonded in carbonyls either linearly with one transition metal atom or forming a bridge between two or, less frequently, between three metal atoms as shown by the following scheme:

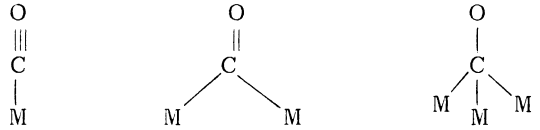

In all three cases it is the carbon atom which is immediately linked to the metal atom or atoms. The linear bonding is realized owing to the overlap of filled 3σ orbital of CO molecule with the empty σ orbital of the metal atom, e.g., $d_{z}2$ orbital with the simultaneous back-donation of electrons from the filled $d\pi$ orbitals (e.g., d_{xz} and d_{yz}) to the overlapping empty $2\pi_y$ and $2\pi_x$ antibonding orbitals. This back donation contributes to the strengthening of M—C bond by the compensation of the polarization of σ bond. The shift of electron density to the 2π antibonding orbitals weakens the C—O bond in carbon monoxide molecule thus decreasing its stretching frequency from 2143 cm^{-1} in free CO molecule to 2100–2000 cm^{-1} for neutral, unsubstituted linearly bonded one [3].

In the case of CO molecule forming a bridge between two metal atoms a sp^2 hybridization of carbon atom must be assumed. Two of the hybridized orbitals are forming bonds with two metal atoms while the third one is used for the formation of the σ bond in CO molecule. There is only one p orbital, e.g., p_z orbital, which can be used for the formation of a π bond. Consequently carbon–oxygen bond order decreases to 2. Still further decrease of the bond order occurs if CO molecule is coordinated to three metal atoms. In this case sp^3 hybridization is assumed. Three of the hybridized orbitals are forming bonds with metal atoms and one a σ bond in CO molecule. Here there are no disponible p orbitals for the formation of a π bond in CO molecule and oxygen–carbon bond order is 1. The decrease in bond order and bond strength also results in the decreased stretching frequency of the CO molecule, which is contained within the range 1750–1850 cm^{-1} for doubly coordinated CO molecules.

As was already stated, carbon monoxide when chemisorbed on transition metals and transition metal oxides forms a similar bond to the surface atoms as metal carbonyls. The most frequent form is the linearly bonded carbonyl group (terminal CO) but the formation of bridged forms was also confirmed by LEED measurement on platinum metals. However, it should be observed that at the surface the situation is much more complicated than in the case of metal carbonyls in which only one or two transition metal atoms are taken into account. Here the frequency criterion is partially valuable; it means that from the observed IR frequency between about 2000 and 2100 cm^{-1} one can conclude that CO is linearly bonded. However, the lower frequencies may correspond to the bridged as well as linearly bonded molecules. This was discussed by Blyholder [4], who calculated Hückel molecular orbitals for the metal–carbon–oxygen linear bond. The π delocalized orbitals ψ_1, ψ_2, and ψ_3 were calculated as a linear combination of a metal d orbital ($\underline{X}_1$), carbon 2p orbital ($\underline{X}_2$), and oxygen 2p orbital ($\underline{X}_3$). The energy sequence corresponding to these orbitals is:

$$\underline{E}_1 < \underline{E}_2 < \underline{E}_3$$

The form of the lowest orbital ψ_1 indicates that the corresponding electron density is localized mainly on the oxygen and carbon atoms and this adds to the bond strength for both C—O and M—C bonds. However, the second orbital, whose energy indicates that it is lower energy than a metal d orbital, is bonding for the M—C bond but antibonding for the C—O bond, since the wave function has a node between C and O atoms. There are two sets of ψ_1, ψ_2, and ψ_3 orbitals for each linearly bonded CO molecule—one for the set of p_y and one for the set of p_x orbitals of C and O atoms. Now when counting electrons, e.g., in the $Cr(CO)_6$ molecule, we may assume that the electrons forming the lone pair at the carbon atom in CO are filling the σ molecular orbital while the electrons from π_y and π_x orbitals of CO are filling two ψ_1 orbitals. To fill the ψ_2 orbitals the electrons from the outer shell of the Cr atom must be used. However, for 12 ψ_2 orbitals only six such electrons are available and there is competition among the ligands for electrons to be put in these orbitals. The occupancy of ψ_2 orbitals is consequently small and the antibonding effect of the ψ_2 occupied orbital not appreciable. On the other hand, although the ψ_1 orbitals are bonding ones, the strength of the C—O π bond is lower than in free CO molecule and the observed frequency ν_{CO} is lower than in free molecule and is equal to 2000 cm^{-1}.

Blyholder applies the same simple theory to the chemisorption of CO on metals and regards a metal atom on the surface as a central atom in a complex with the surrounding metal atoms and the chemisorbed molecule as ligand. However, here the high symmetry of metal carbonyls is no longer preserved. For the transition metals, the metal ligand atoms partially surrounding a particular surface metal atom will have available partially filled d orbitals with appropriate symmetry to form π bonds with the chosen surface atom and thereby compete with the adsorbed carbon monoxide for electrons from the adsorbant atom. Now the frequency of the stretching vibration in the CO ligand will be determined by the extent of this competition for electrons and the resulting occupancy of ψ_2 orbitals. This can be largely influenced by the position and hence by the coordination of the surface atom bonding CO molecule.

Blyholder gives as the example the (111) and (100) faces of nickel at which a given surface atom has nine or eight surrounding atoms. The number of ligands competing for d electrons of the central atom is therefore high, rendering the occupancy of ψ_2 orbitals rather small, and the stretching frequency ν_{CO} is still above 2000 cm^{-1}. On the other hand, if chemisorption occurs on the atoms situated on the crystal edges or corners, the number of metal atoms surrounding the adsorption center strongly decreases and the occupancy of the ψ_2 orbital does increase, thus lowering ν_{CO} frequency below 2000 cm^{-1}. This is Blyholder's interpretation of the fact that on nickel besides the band or bands of chemisorbed

CO around 2060 cm^{-1} a broad band around 1940 cm^{-1} is usually observed. The bands around 1900 cm^{-1} are especially intense in the case of evaporated Ni samples in which the proportion of corner and edge atoms is increased owing to the small size of crystallites.

Blyholder's theory has also been used to explain the fact that with increasing coverage of metal surface with CO, high- and low-frequency bands are shifted to higher values. This is considered to be due to the increased competition for the electrons of the surface atoms and the diminished number of electrons available for filling ψ_2 orbitals. Similarly interpreted was the effect of coadsorbed gases. The chemisorption of strongly electronegative oxygen does decrease the number of available electrons and, as was observed for CO chemisorbed on Fe and Cu, shifts the CO stretching frequency to lower values [5]. On the other hand, if H_2 is added to CO chemisorbed on Pt forming electron donor centers, the CO band is shifted to lower frequencies.

III. OXIDATION OF CARBON MONOXIDE ON THE PLATINUM GROUP METALS

A. Chemisorption of Reactants on Platinum Group Metals

Chemisorption of oxygen on platinum group metals was treated in Section 2.II.B. Here only the overlayer structures of chemisorbed oxygen are listed in Table 6.1.

No adsorption of carbon dioxide on platinum metals was observed. Hence the present section deals only with chemisorption of carbon monoxide and the interactions of all three reactants—oxygen, carbon monoxide, and carbon dioxide—at the surface of platinum metals.

1. Nature of CO Surface Bond and the Overstructures of Adsorbed CO Molecules

Carbon monoxide if chemisorbed on clean platinum metal surfaces forms bonds with the surface atoms which are the same kind as the bonds in transition metal carbonyls. Important information concerning the nature of this bond has been obtained by electron energy loss spectrometry (EELS) and high-resolution electron energy loss spectrometry (HREELS). Using this latter method, Bare et al. [6] registered the frequencies 2105 and 475 cm^{-1} of CO chemisorbed on Pt (110) surface and forming a (2 × 1) overstructure. The former band corresponded to C—O stretching vibrations and its frequency is of the same order as the frequency of CO molecules linearly bonded in carbonyls. The latter band has been attributed to the Pt—CO stretching vibration. At high coverages the (1 × 1) and (2 × 1) surface phases were formed and the new frequency 420 cm^{-1}

was registered, which has been attributed to the frustrated rotation of tilted, linearly bonded CO molecules. On the Pd (111) surface a C—O stretching frequency of 1823 cm^{-1} was observed at low coverages [7], indicating a strong diminution of the bond order. Considering the fact that the $(\sqrt{3} \times \sqrt{3})$ R 30° CO overstructure is forming simultaneously [8], the location of CO molecules in threefold coordinated sites can be assumed. With increasing coverage the C—O stretching frequency is in most cases shifted to higher values as was observed in the case of Pd (111) and Pd (100) [7] as well as Pt (111) [9] planes. This effect is due to the dipole-dipole coupling interaction between the adsorbate molecules in the overlayer. That is why the frequency-based conclusions concerning the properties of the bond between CO molecules should be limited to situations in which the coverage is low and the interactions between adsorbed molecules are not important.

The net transfer of electronic charge accompanying the formation of the σ bond with π back donation results in an increase of the work function, indicating that the electron density is shifted from the metal to the adsorbed CO molecules. The calculated dipole moment of CO molecules adsorbed on different planes of Pd crystals ranges from 0.29 to 0.35 D [10] and hence it is about three times larger than the dipole moment of the free CO molecule.

The LEED investigations of CO overstructures exhibit a distinct parallelism between the behavior of analogous planes of different platinum group metals, as is shown in Table 6.1 containing the data collected in [11] supplemented by more recent results. Included in the table is information concerning oxygen overstructure which will be used in further discussion. In most cases several different overstructures can be formed by a given adsorbate depending on the coverage. Most of the clean platinum metal surfaces exhibit the same arrangement of atoms that is expected from the undistorted termination of the bulk [12]. Such structures are labeled (1 × 1) in the LEED investigations. Only in the (100) and (110) planes of Pt and Ir are such structures unstable and they reconstruct when reaching the equilibrium state. In Table 6.1 chemisorption of CO on unstable and stable Ir (100) and Pt (100) surfaces was taken into account.

As a typical example we shall discuss the formation of carbon monoxide overstructures on Pd (111) and Pd (100) faces. Conrad et al. [8] when adsorbing CO on Pd (111) at 200 K observed the formation of a $(\sqrt{3} \times \sqrt{3})$ R 30° overstructure around the coverage $\theta = 1/3$ with the molecules presumably located in threefold coordinated sites (Fig. 6.3a). Increasing exposure to CO resulted in the splitting of LEED pattern spots and the development of c (4 × 2) structure (Fig. 6.3b) to which the coverage $\theta = 0.5$ corresponds. In this case bridge positions of the CO molecule between two Pd atoms are assumed as most probable. A strong decrease of adsorp-

TABLE 6.1 Surface Structures of Chemisorbed Carbon Monoxide and Oxygen on the (111) and (100) Surfaces Rh, Pd, Ir, and Pt and the (001) Surface of Ru.*

Gas	Rh (111)[a]	Pd (111)[b,c]	Ir (111)[a,e,f]	Pt (111)[g,h]	Ru (001)[i]
CO	$(\sqrt{3} \times \sqrt{3})$ R 30° split (2×2) (2×2)	$(\sqrt{3} \times \sqrt{3})$ R 30° c (4×2) compression hexagonal hexagonal	$(\sqrt{3} \times \sqrt{3})$ R 30° $(2\sqrt{3} \times 2\sqrt{3})$R 30° split $(2\sqrt{3} \times 2\sqrt{3})$ R 30°	$(\sqrt{3} \times \sqrt{3})$ R 30° c (4×2) hexagonal	$(\sqrt{3} \times \sqrt{3})$ R 30° (2×2) disorder
O_2	(2×2)	(2×2) $(\sqrt{3} \times \sqrt{3})$ R 30°	(2×2)	(2×2)	(2×2)
	Rh (100)[a]	Pd (100)[j,k]	Ir (100)(1×1)[k]	Pt (100)(1×1)[h]	
CO	c (2×2) split (2×1)	c (4×2) R 45° compressed c (4×2) R 45°	c (2×2)	c (2×2)	
O_2	(2×2) c (2×2)	p (2×2) c (2×2)	(2×1)	(1×1)	
			Ir (100)(5×1)[k,l,m]	Pt (100)(5×20)[h,n]	

CO	(2 × 2)	(1 × 1)
	(1 × 1)	c (4 × 2)
		(2 × 2)
O_2	(2 × 1)	

---

*The different overstructures on a given crystal surface are listed in the order of increasing coverage.

[a] D. G. Castner, R. A. Sexton, and G. A. Somorjai, Surf. Sci., 71, 519 (1978); [b] H. Conrad, G. Ertl, and J. Küppers, Surf. Sci., 76, 323 (1978); [c] H. Conrad, G. Ertl, J. Küppers, and E. E. Latta, Surf. Sci., 65, 245 (1977); [d] D. I. Hagen, B. E. Nieuwenhuys, G. Rovida, and G. A. Somorjai, Surf. Sci., 57, 632 (1976); [e] J. Küppers and A. Plagge, J. Vacuum Sci. Technol., 13, 259 (1976); [f] C. M. Comrie and W. H. Weinberg, J. Chem. Phys., 64, 250 (1976); [g] G. Ertl, M. Neuman, and K. M. Streit, Surf. Sci., 64, 393 (1977); [h] C. R. Helms, H. P. Bonsel, and S. Kelemen, J. Chem. Phys., 65, 1773 (1976); [i] H. P. Bonzel and G. Pirug, Surf. Sci., 62, 45 (1977); [j] J. C. Tracy and P. W. Palmberg, J. Chem. Phys., 51, 4852 (1969); [k] J. T. Grant, Surf. Sci., 18, 228 (1969); [l] T. N. Rhodin and G. Broden, Surf. Sci., 60, 466 (1976); [m] G. Broden and T. N. Rhodin, Solid State Commun., 18, 105 (1976); [n] G. Kneringer and F. P. Netzer, Surf. Sci., 49, 125 (1975).

Source: Data from Ref. 11.

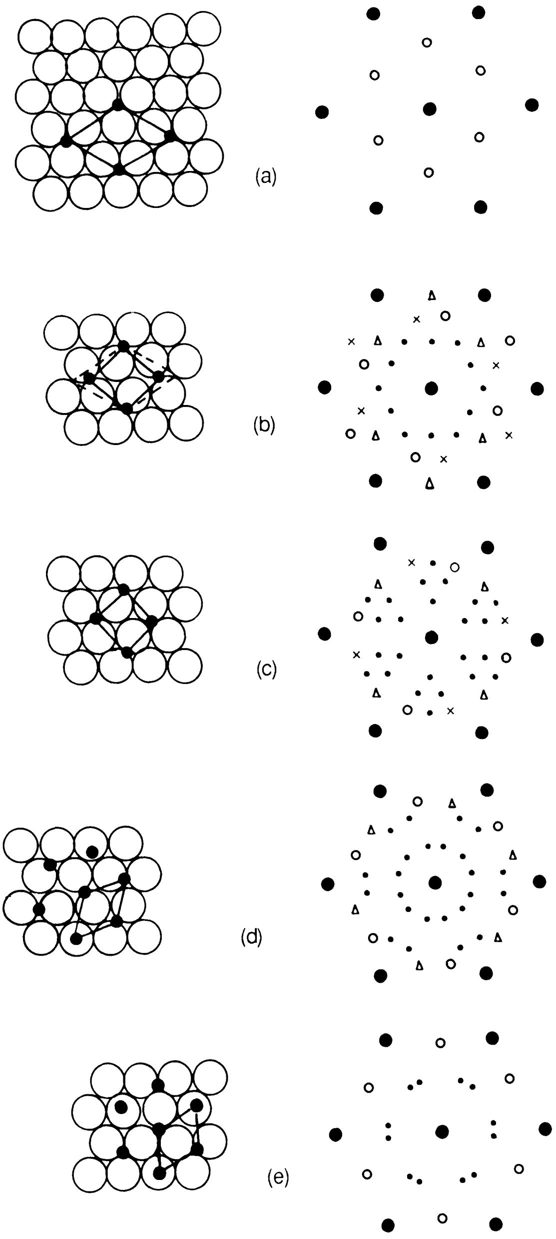

FIGURE 6.3 Overlayer unit cells and proposed structure models for CO molecules adsorbed on a Pd (111) surface at various coverages. Dark circles denote the proposed positions of the CO molecules. (a) $\theta = 0.33$ ($\sqrt{3} \times \sqrt{3}$) R 30° structure; (b) $\theta = 0.5$ (c 4×2 structure); (c) $\theta = 0.6$; (d) $\theta = 0.63$; (e) $\theta = 0.66$ [8].

tion energy in this coverage range prevents further adsorption at room temperature. However, at 200 K such adsorption can occur along with the compression of overlayers, which is reached by the formation of more densely populated islands rather than by continuous transformation. Figure 6.3c shows the overlayer structure reached at the coverage $\theta = 0.6$. Additional uptake of CO at 200 K causes the formation of two further CO overstructures with hexagonal arrangements of adsorbed molecules which are represented in Fig. 6.3d and e. The axis of the surface unit cell of the first of them, corresponding to the coverage $\theta = 0.63$, is rotated by $18.4 \pm 0.5^\circ$ with respect to that of the substrate lattice. The other one, reached at the coverage $\theta = 0.66$, is the most densely packed overstructure of CO molecules chemisorbed on Pd (111) (1.01×10^{15} molecules CO per cm^2). Table 6.1 shows that the $(\sqrt{3} \times \sqrt{3})$ R 30° overstructure is the structure forming at lower coverages also on the (111) face of Rh, Pd, Ir, and Pt as well as on the (001) face of Ru.

In the case of the (100) face of Pd, Rh, Ir, and Pt, the variety of overstructures is less than in the case of the (111) face. The most common and mostly the only overstructure appearing at the (100) face is c(2 × 2) (Fig. 6.4). Pd (100) is an exception; a c (4 × 2) R 45° overlayer of CO molecules forms on it (Fig. 6.5) [13]. The axis of the unit cell is rotated in this case by 45° with respect to that of the substrate. The only possible arrangement of the adsorbate molecules in this pattern is to locate them in equivalent positions in bridge sites [12]. In fact, only one frequency ($\nu_{CO} = 1859\ cm^{-1}$) has been detected in the IR spectra at low coverage which continuously increased to $1949\ cm^{-1}$ at $\theta = 0.5$ owing to the dipole-dipole interaction. The appearance of a single band in the IR spectrum is an additional argument indicating the presence of only one CO species at the surface.

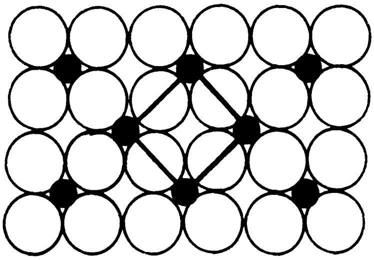

FIGURE 6.4 c (2 × 2) surface structure of CO molecules adsorbed on Rh (100) surface.

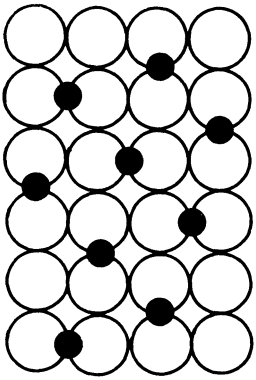

FIGURE 6.5 c (4 × 2) R 45° surface structure of CO molecules adsorbed on Pd (100) surface.

The adsorption energies of carbon monoxide on platinum group metals as measured at low coverages are contained within the relatively narrow limits of 26 and 40 kcal mol^{-1} in analogy to the CO bonding energy in metal carbonyls [12]. Also there is not any correlation between the initial adsorption energy and the structure of low-index planes (111), (110), and (100) on which chemisorption energy was studied. With increasing coverage the adsorption energy of CO does decrease. This can be due both to the changes in the overlayer structure and to the increasing repulsion of chemisorbed dipole molecules. The effect of the former factor can be illustrated by the results of Ertl and Koch [14], who determined the isosteric adsorption heat of CO on the Pd (111) face and observed a constant value of 34 kcal mol^{-1} up to the coverage 0.3. In this case, as already said, the ($\sqrt{3} \times \sqrt{3}$) R 30° overlayer is completed in which threefold coordinated CO molecules participate. After completion of this overlayer a drop of about 2 kcal mol^{-1} was observed and subsequently adsorption heat changed rather slowly up to the completion of the c (4 × 2) overstructure (CO molecules twofold coordinated, when it rapidly dropped to about 23 kcal mol^{-1}.

3. Kinetics of Carbon Monoxide Adsorption and Desorption

The kinetics of CO chemisorption on metals can best be characterized by the sticking coefficient, which is defined as the fraction of molecules impinging the surface which remain chemisorbed. The values of the initial sticking coefficients s(0) of CO on a bare surface are rather high in the case of platinum group metals. They were determined as 0.96 for Pd (111) [15] and 0.84 for Pt (111) [16]. According to the classical model of Langmuir, the sticking coefficient should depend on the coverage because it is assumed that no adsorption occurs on a surface already covered with adsorbed molecules. At the given coverage θ, the sticking coefficient $\underline{s}(\theta)$ should be equal to $\underline{s}(0)(1 - \theta)$ in the case when only one adsorption site is needed for one molecule of adsorbate or to $\underline{s}(0)(1 - \theta)^2$ if two adjacent sites are needed for one adsorbed molecule. However, the measurements show that for platinum group metals, with few exceptions, the $\underline{s}(\theta)$ value at low coverages does decrease much more slowly with θ than could be expected from Langmuir's model or even remains constant as happens in the case of the Pt (111) face [17], where it is constant up to the coverage $\theta = 0.15$. This indicates that at these conditions the CO molecules are being adsorbed not only on the bare surface but on the existing layer of adsorbate as well. Such a case was discussed by Kisluk [18], who proposed a model of chemisorption occurring with the formation of a precursor state in which a molecule striking the already covered portion of the surface is at first weakly adsorbed, presumably physisorbed, and in this state remains long enough to migrate in this second layer until it encounters a vacant site for chemisorption.

The formation of short-living adsorbed molecules on the Pt (111) face around room temperature and at temperatures up to 1000 K was confirmed by measurement of the angle distribution of the CO molecular beam scattered from the surface [16]. In the ideal case of strictly elastical reflection of molecules impinging on the surface the molecular beam would be reflected in the specular direction without any appreciable broadening. The so reflected particles essentially retain the initial gas temperature, i.e., are not accommodated at the surface [19]. On the other hand, if collision of a molecule with the surface is connected with a weak adsorption, the molecules are accommodated to the temperature of the substrate and are desorbed in different directions, which statistically results in cosine distribution. In the case of a clean Pt (111) surface, the angular distribution of reflected beam is predominantly specular, and the collisions are mainly elastic. However, with increasing coverage the angular distribution becomes more and more cosine-like, indicating a weak bonding of molecules in the second layer. From this state they can either be released back into the gas phase or diffuse to a vacant chemisorption site.

Desorption of carbon monoxide from platinum group metals occurs above 100°C. Thermal desorption spectra obtained for Pd (100) contained only one peak at 242°C for the coverages between 0.01 and 0.22 [20]. At $\theta = 0.53$ a second peak appeared at 105°C. Most probably the appearance of this new peak was due to the formation of islands of a new compressed overstructure besides the c (4×2) R 45° initial one. At still higher coverage a third peak was present in the TDS spectrum at −15°C, presumably corresponding to physisorbed carbon monoxide. On Pd ribbon two peaks were detected at 212 and 112°C corresponding to peaks observed in the case of Pd (100) [21]. On the Ru (111) face at low coverages a peak at 275°C was registered which was shifted to 225°C with increasing coverage [11]. A similar set of TDS was obtained for the Ru (100) surface, the only difference being that the peak maxima occurred at temperatures about 20°C lower.

No chemisorption of carbon dioxide on platinum group metals was observed [19] and hence it must be assumed that CO_2 moleclues forming in the catalytic oxidation of CO are immediately desorbed.

B. Coadsorption and Interaction of Oxygen and Carbon Monoxide on the Surface of Platinum Group Metals

The key to the understanding of the microscopic mechanism of CO oxidation on platinum group metals is the study of the interactions of the coadsorbed reactants. A thorough investigation of the behavior of coadsorbed oxygen and carbon monoxide on the Pd (111) surface was carried out by Conrad et al. [8]. It is interesting to observe that their results were different depending on the sequence of adsorption of both reactants carried out at 200 K. If the surface concentrations of O_{ads} and CO_{ads} were small and did not exceed 10% of the saturation coverage, no ordered overlayer structures were observed and adsorbed molecules were statistically distributed over the surface at relatively large distances from each other, as is schematically shown in Fig. 6.6a. On heating CO_2 was forming and the heating curves exhibited a shape similar to that shown in Fig. 6.7. The activation energy calculated on the basis of such curves is 25 kcal mol^{-1} in good accordance with the value 24 kcal mol^{-1} in the molecular beam experiments carried out under similar conditions [22].

Figure 6.6b shows schematically the situation reached by preadsorption of CO forming an incomplete $(\sqrt{3} \times \sqrt{3})$ R 30° overlayer ($\theta_{CO} < 1/3$) and subsequent chemisorption of oxygen. The latter forms islands of (2×2) structure with local coverage, $\theta_O = 0.25$. On heating, similar to the previous case, CO_2 is produced and immediately desorbed as is shown by the curves in Fig. 6.7 corresponding to the different initial coverages of CO and subsequent exposure to oxygen. The schematic sketch in Fig. 6.6b shows that the reaction can only occur along the boundaries of CO_{ads} and O_{ads} islands, the mean diameter of which has been estimated as not lower than 100 Å. The area under desorption curves in Fig. 6.7 is proportional to the total amount of CO_2 produced. This amount will be maximal when equal numbers of O and CO species are present at the

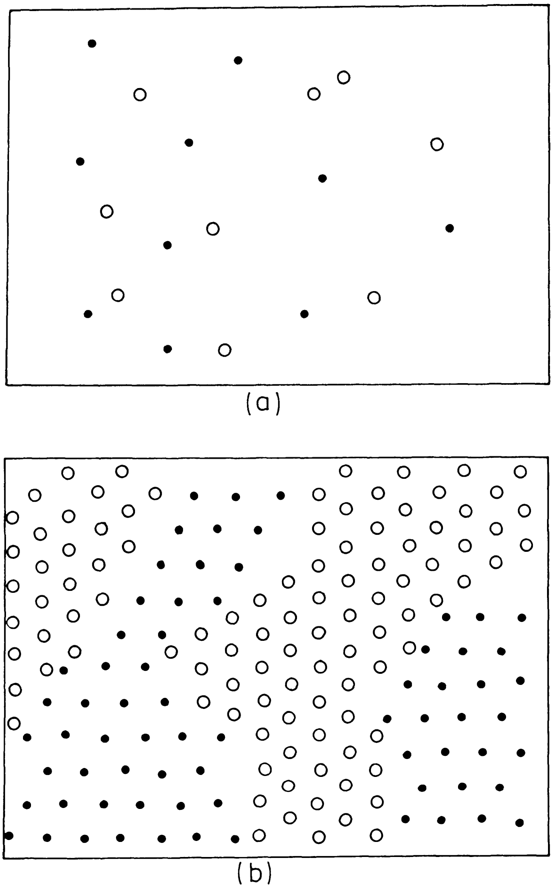

FIGURE 6.6 Schematic sketches of the surface configuration of oxygen (dark circles) and carbon monoxide (open circles) adsorbed on Pd (111) surface. (a) Very low concentrations of O_{ads} and CO_{ads}; (b) formation of islands of the O (2 × 2) and CO ($\sqrt{3} \times \sqrt{3}$) R 30° structures [8].

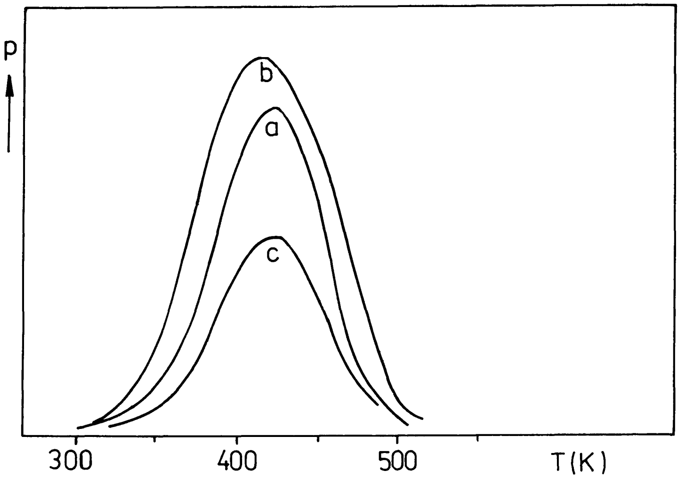

FIGURE 6.7 Thermal desorption spectra from Pd (111) surface for CO_2 after successive exposures to CO and O_2: (a) 0.2 L CO + 5 L O_2; (b) 0.5 L CO + 2 L O_2; (c) 1 L CO + 2 L O_2 [8].

surface. This will be reached when the ratio of areas of $(\sqrt{3} \times \sqrt{3})$ R 30° CO and (2 × 2) O overlayers will be 3/7:4/7. Additional experiments have shown that this is reached after exposing the surface first to 0.7 L CO and then saturating with oxygen. Accordingly, curve b in Fig. 6.7, obtained after exposing the surface to 0.5 L CO, exhibits a larger area than that corresponding to curve a (0.2 L CO) and c (1 L CO). If the surface was saturated with CO, forming a complete overlayer of $(\sqrt{3} \times \sqrt{3})$ R 30° structure, no adsorption of oxygen took place at 200 K and no oxidation of CO occurred.

A different picture was obtained when CO was contacted with a Pd (111) surface covered with preadsorbed oxygen. At an oxygen coverage of about 0.15, the formation of (2 × 2) LEED pattern was observed with rather diffuse diffraction spots. However, they became sharper after admission of small portions of CO, which indicated that O_{ads} islands grew because they were squeezed by chemisorbed CO molecules ordering into islands of $(\sqrt{3} \times \sqrt{3})$ R 30° overstructure. As illustrated by Fig. 6.8b), carbon monoxide can also be adsorbed on the surface completely saturated with preadsorbed oxygen in contrast to the behavior of the surface saturated with CO on which no chemisorption of oxygen occurs. Chemisorption of CO on such an oxygen-saturated surface is possible due to the squeezing of the (2 × 2) O structure into a $(\sqrt{3} \times \sqrt{3})$ R 30° one. This indicates that at this stage there is a repulsive interaction between both chemisorbed species, resulting in the formation of separate islands but still inhibiting the formation of the mixed structure. It is interesting that on the partial removal of CO_{ads} and O_{ads} by the formation of rapidly desorbing CO_2, the less densely packed (2 × 2) structure of oxygen islands is restored. This indicates that between O_{ads} species repulsive interactions also exist.

Figure 6.8c illustrates the situation which is reached if at 200 K CO exposure of an oxygen-saturated surface is continued. LEED investigations exhibit, in this case, the formation of a new (2 × 1) overstructure which never was observed after chemisorption of oxygen or CO alone, and hence must be assumed to be a mixed overstructure containing both species O_{ads} and CO_{ads} in the unit cell. This conclusion is also supported by the XPS measurements exhibiting a shift in the CO-derived valence levels which was not observed when separate islands of O_{ads} and CO_{ads} were present. The observed lowering of the ionization energy of the CO 2σ level was explained in terms of partial electron transfer from CO to the neighboring atoms [23]. The local coverages within the domains of this mixed-surface phase are $\theta_O = \theta_{CO} = 0.5$. This means that the adsorbed O atoms are further compressed. As the consequence nearly half of the surface becomes accessible for additional chemisorption of CO and in fact the appearance of a (2 × 1) structure was always accompanied by the simultaneous appearance of a $(\sqrt{3} \times \sqrt{3})$ R 30° structure of CO_{ads}.

Thermal desorption curves obtained after successive exposure of the Pd (111) surface to oxygen and subsequently to carbon monoxide are shown in Fig. 6.9. It is seen that with the surface covered with preadsorbed oxygen after a short exposure to CO the maximum rate of CO_2 formation was observed at about 480 K but is continuously shifted to lower temperatures with increasing exposure to CO. The simplest explanation of this effect is to assume that squeezing of the initial (2 × 2) overstructure of oxygen by increasing amounts of chemisorbed CO into the $(\sqrt{3} \times \sqrt{3})$ R 30° structure is accompanied by a decrease of oxygen bonding energy which also results in the lowering of activation energy of CO_2 formation. At higher exposures, e.g., 1 L of oxygen and more than 2 L of CO, a new peak at about 290 K is the result of formation of mixed-surface phase in which both O_{ads} and CO_{ads} species are in intimate contact. In such a situation the activation energy of the reaction between both adsorbed species must be appreciably lower and the temperature of the new TDS peak must also be lower.

An analogous study of the coadsorption of oxygen and carbon monoxide was recently undertaken on the Pd (100) face by Stuve and Madix [20], who found many similarities but not the identical behavior of the Pd (111) face reported by Conrad et al. [8]. As is seen from Table 6.1, oxygen chemisorbed at the Pd (100) face forms p (2 × 2) and c (2 × 2) structures, the coverages of θ_O =

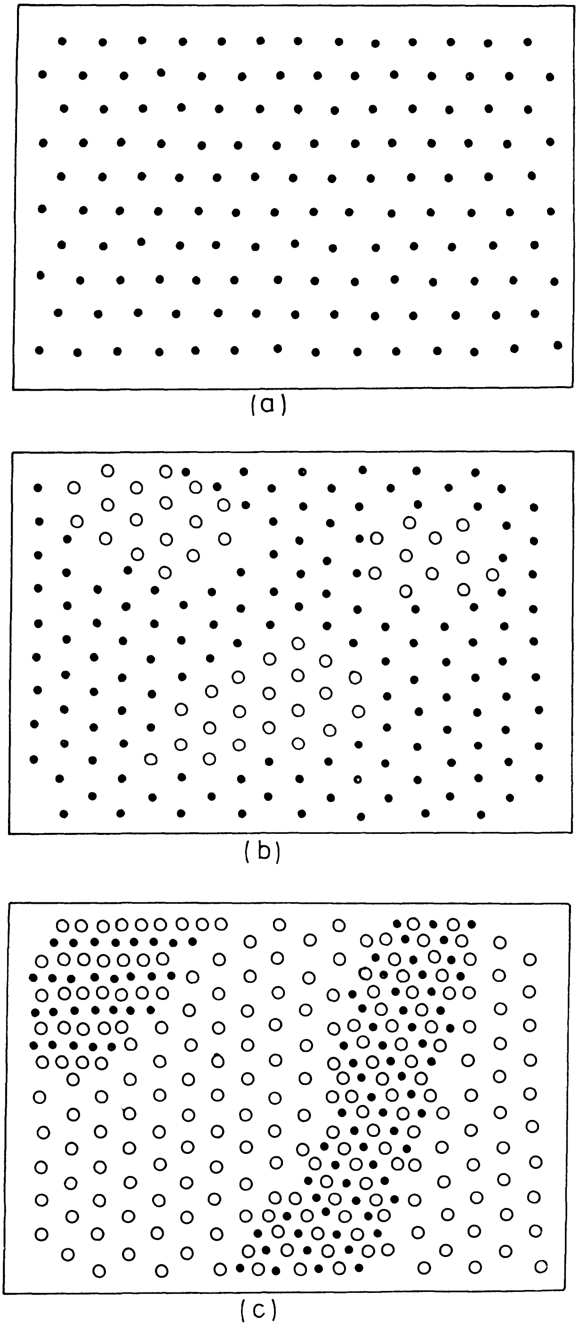

FIGURE 6.8 Schematic sketches of the structural transformations which may take place if an oxygen-saturated Pd (111) surface.

0.25 and 0.5, respectively. The transformation from p (2 × 2) to c (2 × 2) structure does not change the frequency of the Pd—O bond which, according to EELS measurements, is equal in both cases to 390 cm^{-1} thus indicating the same type of adsorption sites in both structures. It is assumed by the authors to be a fourfold coordination position. As was stated by Stuve and Madix, the p (2 × 2) structure completely covering Pd (100) surface gets disordered by the additional chemisorption of CO and its LEED pattern vanishes completely at $\theta_{CO} = 0.1$. This CO-induced disordering was interpreted by the authors as the redistribution of O atoms into small p (2 × 2) and c (2 × 2) patches that have no long-range order.

The thermal CO_2 desorption curves of the same kind as those in Figs. 6.7 and 6.9 exhibited the existence of three different reaction states on the surface precovered with oxygen on which, in addition, different amounts of CO were adsorbed at 80 K:

1. Desorption peak at 420 K was observed for $\theta_O < 0.05$ and $\theta_{CO} < 0.4$ when no LEED detectable phase of CO_{ads} or O_{ads} was present and CO could react with isolated O_{ads} atoms or small clusters of O atoms in next-nearest-neighbor positions. At higher oxygen coverages, but always below $\theta_O = 0.25$, this peak appeared also in the situation when both p (2 × 2) islands of oxygen and ($\sqrt{3} \times \sqrt{3}$) R 30° islands of carbon monoxide were present ($\theta_O \approx \theta_{CO} \approx 0.15$) and the reaction could occur at the perimeter of oxygen islands.
2. Disordering of p (2 × 2) O phase was accompanied by a second peak, at 360 K, in the thermal desorption spectrum. In this case carbon monoxide also reacted with oxygen atoms which presumably are contained in the small patches of p (2 × 2) and c (2 × 2) structures not detectable by LEED. The authors concluded that such a disordered oxygen phase is more reactive because of the energetic reasons.
3. Exposure of the p (2 × 2) O overlayer to 1 L of CO ($\theta_{CO} > 0.25$) produced adsorbed oxygen and carbon monoxide in an intimate contact. The authors assume that in this case CO is adsorbed in the interior of oxygen islands thus forming a structure which they labeled a CO—Pd—O complex. Under these conditions chemisorbed CO exhibits a C—O stretching frequency (EELS) of 2125 cm^{-1}, which suggests a linear bonding of the

---

((2 × 2) O structure, $\theta_O = 0.25$) is exposed to CO: (a) (2 × 2) O structure, $\theta_{CO} = 0$, $\theta_{O,loc} = 0.25$; (b) domains from the ($\sqrt{3} \times \sqrt{3}$) R 30° O structure ($\theta_{O,loc} = 0.33$) and from the ($\sqrt{3} \times \sqrt{3}$) R 30° CO structure ($\theta_{CO,loc} = 0.33$); (c) domains from the "mixed" (2 × 1) O—CO structure ($\theta_{O,loc}$, $\theta_{CO,loc} = 0.5$) and from CO domains ($\theta_{CO,loc} > 0.33$) [8].

CO molecule. CO chemisorbed in CO—Pd—O complex within the temperature range 100–300 K was observed on the samples containing this CO species.

Another metal on the surface of which coadsorption of oxygen and carbon monoxide was studied was platinum. Behm et al. [24] followed the changes of LEED patterns when Pt (100) surface covered with preadsorbed CO or O was exposed to the pressures of O_2 or CO of 10^{-5} to 10^{-8} Torr. The temperature of the experiments (355 K) was low enough to prevent the reconstruction of the surface and to keep O_{ads} immobile while the surface diffusion of CO was rapid. Under these conditions the separate islands of O_{ads} and CO_{ads} species can coexist and react with the rate, enabling continuous registration of the intensity of diffraction spots with a fast video system. The only surface phase of CO which appears on (100) face is c (2 × 2). The changes of its coverage were characterized by the intensity of (1/2, 1/2) diffraction spot. Oxygen was forming a (3 × 1) structure monitored by the (0, 1/3) beam. Figure 6.10 shows the behavior of the surface saturated with preadsorbed carbon monoxide after exposure to oxygen for different periods of time. At saturation the CO_{ads} coverage was about 0.65, exceeding the value 0.5 corresponding to the c (2 × 2) structure. It is seen

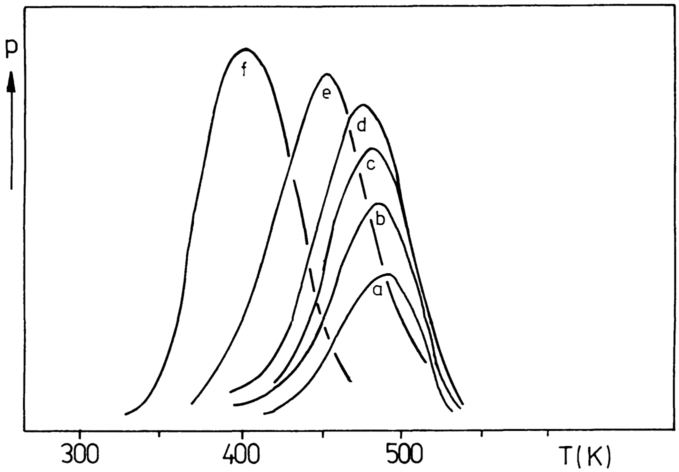

FIGURE 6.9 Thermal desorption spectra of CO_2 from the Pd (111) surface after successive exposures to O_2 and CO: (a) 0.4 L O_2 + 0.05 L CO; (b) 0.1 L O_2 + 0.1 L CO; (c) 0.1 L O_2 + 0.15 L CO; (d) 0.1 L O_2 + 0.2 L CO; (e) 0.1 L O_2 + 0.5 L CO; (f) 0.1 L O_2 + 1 L CO [8].

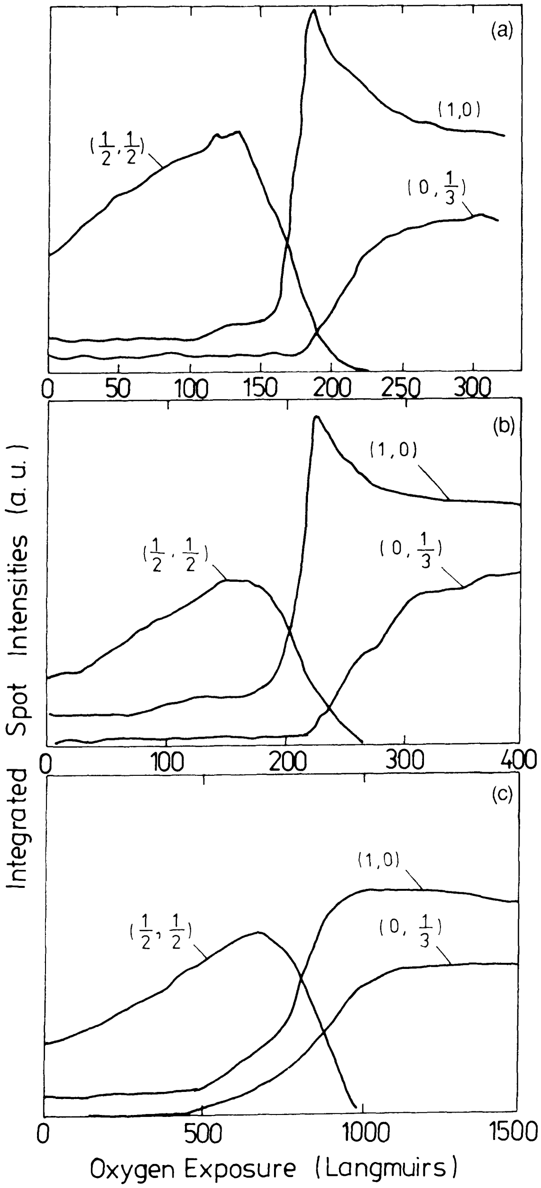

FIGURE 6.10 LED spot intensities during O_2 exposure of a CO-saturated Pt (100) surface at 355 K. (1/2, 1/2) spot = c (2 × 2) phase of CO; (0, 1/3) spot = (3 × 1) phase of oxygen. (a) $\underline{p}_{CO}$ = 5 × 10^{-7} Torr; (b) $\underline{p}_{O_2}$ = 1 × 10^{-6} Torr; (c) $\underline{p}_{O_2}$ = 1 × 10^{-5} Torr [24].

that on exposure to oxygen the intensity of the (1/2, 1/2) beam increased, showing that at these conditions the CO adlayer was not stable with respect to oxygen. The area of the c (2 × 2) layer reached a maximum and subsequently decreased exposing the Pt (100) surface (considered by the authors as the surface of Pt covered with a certain, definitely small number of disordered O_{ads} atoms), characterized by a (1.0) beam. On continuing the exposure to oxygen the latter beam intensity reached a steep maximum immediately after which the formation of oxygen (3 × 1) islands began, the area of which increased up to a certain saturation. Before the c (2 × 2) CO structure vanished completely, both structures c (2 × 2) CO and (3 × 1) O could coexist at low coverages.

Figure 6.11 shows the intensities of LEED diffraction spots observed when the sample saturated with oxygen was exposed to carbon monoxide. It is seen that the (3 × 1) pattern of oxygen began immediately to fade and the (1.0) beam simultaneously increased in intensity. Under these experimental conditions no c (2 × 2) CO overstructure existed simultaneously with a (3 × 1) O structure. The latter one vanished before the (1.0) beam reached its maximal intensity and further appeared only when the (1.0) beam was weak. The surface passed, therefore, through the stage in which only the LEED pattern of the Pt (100) surface was detectable. However, as was already stated, there are indications that the maximum in the (1.0) beam intensity is not related to the clean (1 × 1) surface of metal but to the (1 × 1) surface with low oxygen coverage. The authors considered that the concentration of such disordered O_{ads} atoms decreases with prolonging exposure to carbon monoxide owing to the reaction with CO. The latter then begins to accumulate on an almost clean surface of platinum.

The depleting of O_{ads} from the surface of polycrystalline Pt foil after exposure to CO at 300–800 K was observed by Matsushima et al. [25], who applied Auger electron spectroscopy to determine oxygen coverage. At temperatures above 800 K a new species of oxygen also appeared that was characterized by an Auger signal shift of about 6 eV and by low reactivity toward carbon monoxide. This unreactive oxygen is apparently identical with "subsurface oxygen" described in Chapter 2.

C. Mechanism of Carbon Monoxide Oxidation on Platinum Metal Surfaces

1. General Remarks

The general scheme of carbon monoxide oxidation on the surface of platinum group metals may possibly involve the following steps [12]:

$$O_2 \xrightarrow{k_1} 2O_{ads} \qquad (6.1)$$

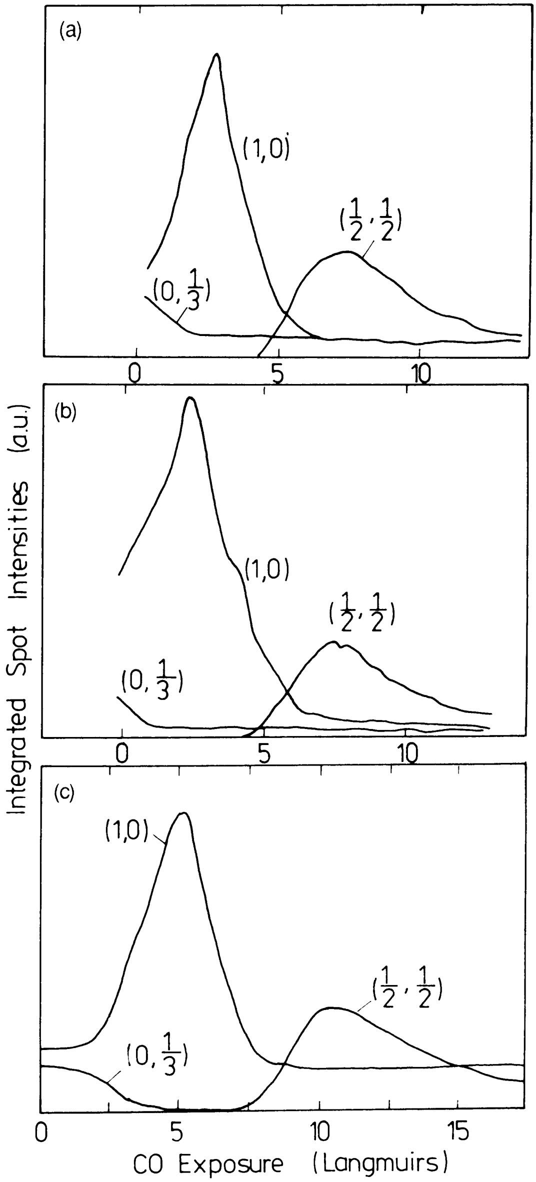

FIGURE 6.11 LEED spot intensities during CO exposure of an oxygen-saturated Pt (100) surface at 355 K. (1/2, 1/2) spot = c (2 × 2) phase of CO; (0, 1/3) spot = (3 × 1) phase of oxygen. (a) $\underline{p}_{CO} = 5 \times 10^{-8}$ Torr; (b) $\underline{p}_{CO} = 1 \times 10^{-7}$ Torr; (c) $\underline{p}_{CO} = 1 \times 10^{-6}$ Torr [24].

$$CO \underset{}{\overset{k_2}{\rightleftarrows}} CO_{ads} \qquad (6.2)$$

$$CO_{ads} + O_{ads} \xrightarrow{k_4} CO_2 \qquad (6.3)$$

$$O_{ads} + CO \xrightarrow{k_5} CO_2 \qquad (6.4)$$

$$2CO_{ads} + O_2 \xrightarrow{k_6} 2CO_2 \qquad (6.5)$$

The dissociative chemisorption of oxygen was described in Chapter 2 and in the preceding section in this chapter. No reverse reaction of oxygen desorption needs to be taken into account when discussing the mechanism of CO oxidation, which is studied at temperatures not exceeding 600 K because vacuum desorption of O_{ads} from platinum group metals occurs above 700 K. On the other hand, chemisorption of CO is reversible at temperatures at which most of the catalytic experiments were carried out. As was already stated, no detectable adsorption of CO_2 on platinum group metals was reported and hence in the reaction scheme the immediate desorption of CO_2 after its formation is assumed. The reaction path comprising steps (6.1), (6.2), and (6.3) as the rate-limiting step corresponds to the Langmuir-Hinshelwood (LH) mechanism. Reaction path with (6.4) or (6.5) as the rate-limiting step corresponds to the Eley-Rideal (ER) mechanism. However, the latter possibility, i.e., the reaction of oxygen molecule with two chemisorbed CO molecules, has to be ruled out as it has frequently been observed that no oxidation occurs if the surface is precovered with a saturated overlayer of CO.

Different ultrahigh-vacuum (UHV) methods were applied for the study of CO catalytic oxidation on platinum metals: those applying steady-state conditions as well as those applying nonsteady, transient conditions. The former enables above all the study of the formal kinetics comprising the determination of overall kinetic equation, reaction order with respect to the particular reagents, etc. However, the latter render available much deeper insight into the molecular reaction mechanism. This will be illustrated in the next section by example of the palladium catalysts.

2. Carbon Monoxide Oxidation on Palladium Catalysts

Figure 6.12 shows the rate of steady-state formation of CO_2 at the Pd (111) surface as a function of temperature, as was given by Engel and Ertl [22]. The measurements were carried out at three

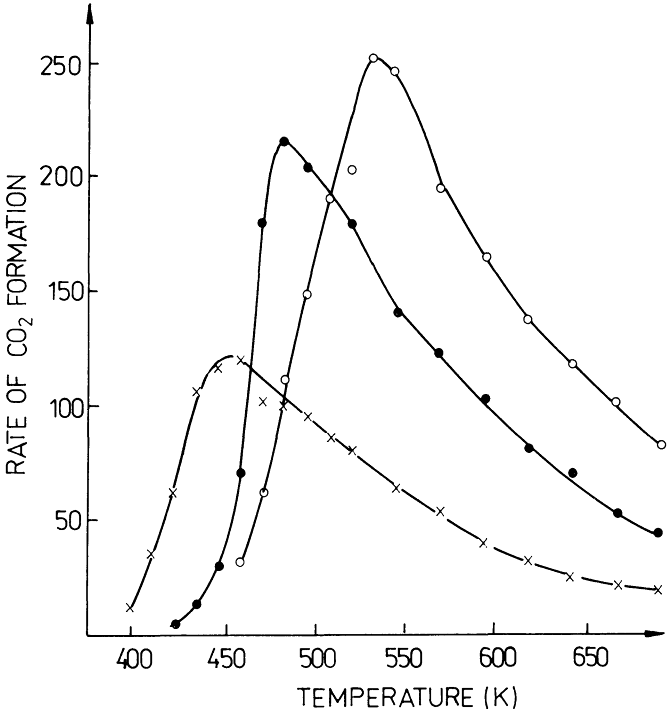

FIGURE 6.12 Steady-state of CO_2 production on Pd (111) surface as the function of substrate temperature for an O_2 beam (equivalent pressure 4×10^{-7} Torr) and CO pressures: 1×10^{-7} (x), 3×10^{-7} (•), and 1×10^{-6} (o) Torr [22].

different CO dynamic pressures (1×10^{-7}, 3×10^{-7}, and 1×10^{-6} Torr). Oxygen was introduced as a molecular beam the intensity of which corresponds to a pressure of 4×10^{-7} Torr. The production of CO_2 was controlled with a quadrupole mass spectrometer. The shape of the $r = f(T)$ curve with a maximum at T_{max}, the position of which depended on p_{CO}, is typical for all other platinum group metals. In some cases the maximum was so flat that within certain limits of temperature the maximum rate could be assumed to be constant as it was in the case of Golchet and White's [26] studies of CO oxidation on polycrystalline platinum. The effect of the change of oxygen pressure at constant p_{CO} in the case of the Pd (111) surface is shown in Fig. 6.13 [22]. Curves a, taken at $p_{CO} = 10^{-7}$ Torr, correspond to the situation in which the maximum on the corresponding curves in Fig. 6.12 was situated below the temperatures 485 and 522 K at which the experiments were carried out. It is seen that within the region of low p_{O_2} reaction is first order with respect to oxygen but above a certain p_{O_2} (~2 × 10^{-7} Torr) it is practically zero order. On the other hand, curves c with p_{CO} = 1 × 10^{-6} Torr correspond to the curve in Fig. 6.12, the maximum of which is above 522 K. Here the order of reaction with respect to oxygen is low at lowest oxygen pressures but it gradually increases with increasing p_{O_2}. Hence in both cases different kinetic laws are valid. Similar experiments were carried out by Engel and Ertl [22] in which the rate of CO_2 production was investigated at constant T and p_{O_2} and variable p_{CO}. It has been shown that if T_{max} from the corresponding curve in Fig. 6.12 was below the working temperature, the reaction rate increased linearly with increasing p_{CO} to a saturation value above which no changes in $r = f(P_{CO})$ were observed. For high CO beam intensities oxygen coverage is depleted by the reaction, which results in an apparent decrease of reaction order in CO from 1 to 0 with increasing beam intensity. On the other hand, if T_{max} in Fig. 6.12 is higher than the working tem-

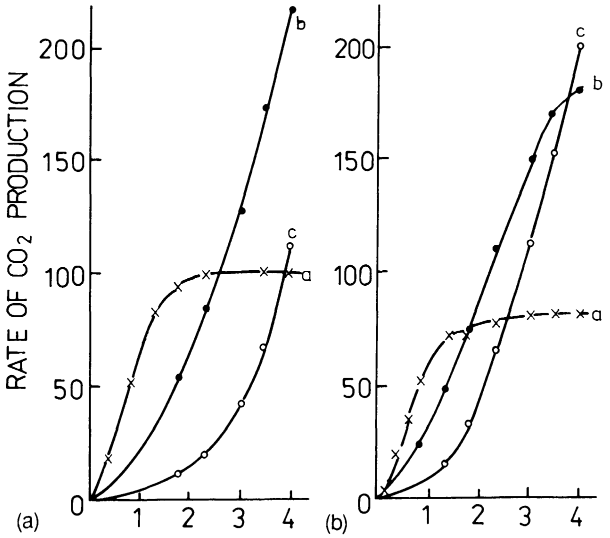

FIGURE 6.13 Steady-state rate of CO_2 production on Pd (111) surface as the function of O_2 beam intensity (equivalent pressures) for various CO pressures. CO pressures: 1 × 10^{-7} (x), 3 × 10^{-7} (•), and 1 × 10^{-6} (o) Torr [22]. (a) 485 K; (b) 522 K.

perature, then carbon monoxide acts as an inhibitor and the rate becomes approximately proportional to $1/p_{CO}$.

Before further discussing the curves in Fig. 6.12, some results concerning the nonsteady-state measurements should be presented. More recent investigations of this kind did not confirm the ER mechanism of CO oxidation on Pd, which formerly was frequently assumed in the literature, and indicated that it is LH mechanism which is operating. This latter mechanism seems also be be predominant in the case of other platinum group metals. Figure 6.14 shows the results of an experiment carried out by Engel and Ertl [22] in which the Pd (111) surface was at first precovered with O_{ad} to $\theta_O = 0.25$, then the O_2 atmosphere pumped off and the CO beam with an effective pressure $p_{CO} = 6 \times 10^{-8}$ Torr switched on. The rate of CO_2 formation, $d[CO_2]/dt$, was under these conditions directly proportional to the recorded CO pressure. It is seen that the CO_2 formation rate was initially zero and has begun to increase after a short induction period. It reached maximum when the

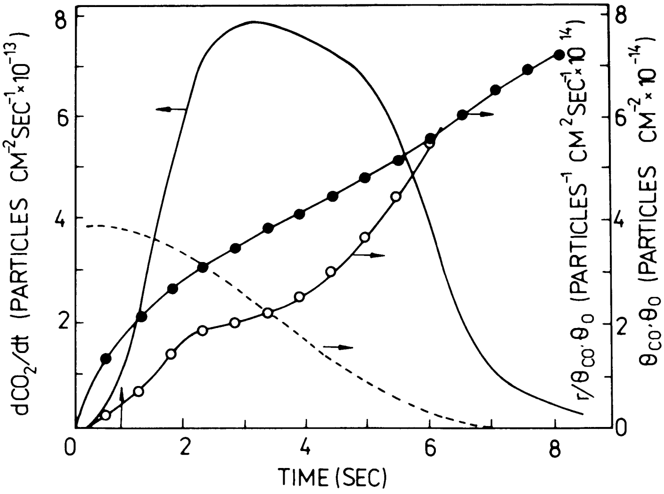

FIGURE 6.14 Rate of CO_2 production on Pd (111) surface, r (——), θ_O (----), and θ_{CO} (○) as the function of time for T = 374 K. The curve (•) shows $r/\theta_O\theta_{CO}$ as a function of time [22].

coverages θ_O and θ_{CO} were approximately equal and decreased with a further increase of θ_{CO}. All of these facts can only be reconciled by the LH mechanism. In the case of the ER mechanism the initial rate obviously should be maximal and monotonically decrease with decreasing oxygen coverage. Another confirmation of the LH mechanism was obtained by the same authors in the modulated beam experiments. These were carried out at $T > 500$ K when the stationary coverage with CO is small and the reaction rate changes linearly with p_{CO}. The effective pressure of CO beam changed as $p_{CO} = p^o_{CO} + \alpha e^{i\breve{\omega}t}$ where $\breve{\omega} = 779\ sec^{-1}$ is the frequency. The isotropic oxygen pressure was chosen in such a way that θ_O was high enough to suffer only minor changes during the fluctuations of CO pressure and, therefore, the reaction rate was independent of p_{O_2}. The mathematical analysis of the process occurring under such conditions indicated that in the case of the ER mechanism no time lag would exist in the fluctuations of CO_2 signal in comparison with CO beam fluctuations, while such a lag would appear in the case of the LH mechanism, as in fact it was observed. Also predictions concerning the effect of temperature in the case of the LH mechanism were confirmed by the experiment.

When summarizing their work on Pd (111), Engel and Ertl discussed the problem of obtaining a kinetic equation in the usual form $r = d[CO_2]/dt = f(T, p_{CO}, p_{O_2}, p_{CO_2})$ describing the overall kinetics of the reaction $2CO + O_2 = 2CO_2$. Considering the fact that the ER mechanism can be excluded and only the three elementary steps (6.1), (6.2), and (6.3) should be taken into account, the formulation of such an equation should be quite easy. This is, however, by no means the case since the rate constants k_1–k_4 depend not only on temperature but, in a rather complicated way, also on the concentrations and mutual configurations of both reacting species which were described in the preceding section. In fact, the behavior of the surface species ordering into various LEED patterns differs very much from the ideal behavior of noninteracting chemisorbed molecules randomly distributed at the surface assumed in the Langmuir adsorption theory.

Engel and Ertl concluded that, owing to all these circumstances, no analytical expression for the rate law of the overall reactions can be proposed, but rather several approximations for limiting cases can be presented. Hence they discuss the following situations:

1. Low surface concentration of CO_{ads} and O_{ads}. Chemisorption of both components CO and O_2 is a nonactivated and hence fast process, and $O_{ads} + CO_{ads} \longrightarrow CO_2$ is the rate-limiting step. At very low concentrations of O_{ads} and CO_{ads}, far below the saturation, the adsorbed molecules can be assumed to be randomly distributed and the interactions between them to be neglected. At these conditions the rate equation:

$$\underline{r} = \underline{k}_4 \theta_O \theta_{CO} \tag{6.6}$$

is expected.

This equation can be fulfilled only if the temperature is high enough and CO pressure low enough to shift appreciably the equilibrium $CO_g \rightleftarrows CO_{ads}$ to the left-hand side. This is reached when the reaction temperature is higher than the temperature of maximum $\underline{T}_{max}$ on the curves in Fig. 6.12, i.e., generally above 500 K and $\underline{p}_{CO} \leq 10^{-6}$ Torr. With increasing temperature the coverage with CO does decrease and this is the reason why the rate of catalytic CO oxidation decreases with increasing temperature.

It should now be observed that initial sticking coefficients of CO and O_2 are $\underline{S}_{CO} = 1$ and $\underline{S}_{O_2} = 0.4$. This indicates that at equal pressures of both reactants roughly equal probabilities exist for the simultaneous formation of one CO_{ads} and one O_{ads}. If $\underline{p}_{O_2} < \underline{p}_{CO}$, each oxygen atom is immediately consumed after being chemisorbed and oxygen chemisorption becomes the rate limiting step. Hence

$$\underline{r} = 2\underline{k}_1 \underline{p}_{O_2} \tag{6.7}$$

as is shown by the initial portions of the curves a in Fig. 6.13.

2. Low CO coverages, $\theta_O \geq 0.08$. If at low CO pressure and $\underline{T} > 500$ K oxygen pressure is higher than that of carbon monoxide, accumulation of oxygen must occur at the surface and θ_O continuously increases. Under steady-state conditions catalytic reaction occurs on the surface, the appreciable fraction of which is covered with oxygen. The rate may now become independent of oxygen pressure as is seen on portions of curves a in Fig. 6.13 corresponding to $\underline{p}_{O_2} > \underline{p}_{CO}$. Under such conditions oxygen is forming the islands of (2 × 2) structure with local coverage 0.25. Oxygen exhibiting chemisorption heat roughly twice as high as carbon monoxide is at the temperature of experiments immobile, but CO_{ads} can easily diffuse and it can be concluded that reaction between CO_{ads} and O_{ads} occurs at the boundaries of oxygen islands. As long as the mean free path for CO_{ads} diffusion is larger than the average distance of oxygen islands, the rate is independent of the total oxygen coverage. However, as the temperature is augmented the average diffusion path of CO_{ads} decreases and a trend of the reaction order with respect to oxygen appears to increase from 0 to 1. The reaction order with respect to CO is 1 and hence within the region of temperature in which the rate is independent of $\underline{p}_{O_2}$ the rate equation is

$$\underline{r} = \underline{k}_4 \theta_O \theta_{CO} = \underline{k}'\underline{p}_{CO} \qquad (6.8)$$

3. Moderate and high CO coverages. The moderate and high CO surface concentrations can be reached at temperatures below 500 K and appropriate CO pressures. Under these conditions an oxygen-saturated adlayer is compressed into domains of $(\sqrt{3} \times \sqrt{3})$ R 30° structure with local coverage 0.33. The increased repulsion of O_{ads} species causes a decrease of the activation energy from the value 25 kcal mol^{-1} in case (2) to 14 kcal mol^{-1}. As was already stated, adsorbed CO inhibits the chemisorption of oxygen, thus slowing down the catalytic reaction, and its rate may be expressed as

$$\underline{r} = \underline{k}''\underline{p}_{O_2}/\underline{p}_{CO} \qquad (6.9)$$

where the apparent activation energy is roughly equal to the adsorption energy of CO under the respective conditions of coverage. With increasing temperature θ_{CO} does decrease, enabling the faster chemisorption of oxygen and an increase in the reaction rate. At temperatures of maximum rate the coverage with CO becomes small.

3. Carbon Monoxide Oxidation on Platinum Metals Other than Palladium

Catalytic CO oxidation was also studied on the other platinum group metals including Pt as well as less intensively investigated Ir, Ru, and Rh. Stationary and nonstationary experiments were applied and the general features of the catalytic reaction were very much similar to those of the Pd catalytic reaction [12]. In steady-state investigations on Pt [26—28], Ir [29], and Ru [30], temperature dependence of reaction rate was observed similar to that shown in Fig. 6.13. Generally the ascending portion of the curve ($\underline{T} < \underline{T}_{max}$) corresponds to the situation when the $CO_g \rightleftarrows CO_{ads}$ equilibrium is shifted to the right-hand side, the coverage with CO is high, and hence the sticking coefficient of oxygen is low. With increasing temperature θ_{CO} diminishes and parallel to it $\underline{S}_{O_2}$ and $\underline{r}$ increase. At $\underline{T}_{max}$ the surface contains a small concentration of CO_{ads} and, as was shown by Pacia et al. [28], the reactive sticking coefficient β_{O_2} of oxygen (the fraction of O_2 molecules impinging on the surface and entering into the reaction) on polycrystalline Pt is equal to the sticking coefficient $\underline{S}_{O_2}$ determined for the clean metal surface. The temperature $\underline{T}_m$ is shifted to the higher values of $\underline{p}_{CO}$ obviously because of the shift of $CO_g \rightleftarrows CO_{ads}$ equilibrium to the right-hand side. At temperatures above $\underline{T}_{max}$ the rate of reaction is determined by θ_{CO}, which decreases with increasing temperature, and the negative apparent activation energy is observed.

At constant temperature the rate of CO catalytic oxidation and the reaction order changes with the p_{CO}/p_{O_2} ratio. Similar to that observed on Pd catalysts, in the case of Pt in the low-pressure, steady-state oxidation, the rate order with respect to CO also changes sharply from first order to zero or even negative order as the CO pressure approaches that of O_2 from below. Matsushima et al. [25] showed that this is accompanied by a drastic change in oxygen coverage. Figure 6.15 shows the results of their measurements in which the changes in θ_O were followed by steady-state Auger signal of oxygen at 483 K. During these experiments p_{O_2} was kept constant and p_{CO} was variable. It is seen from Fig. 6.15 that at lowest p_{CO} (below 0.1 p_{O_2}) oxygen coverage was reaching

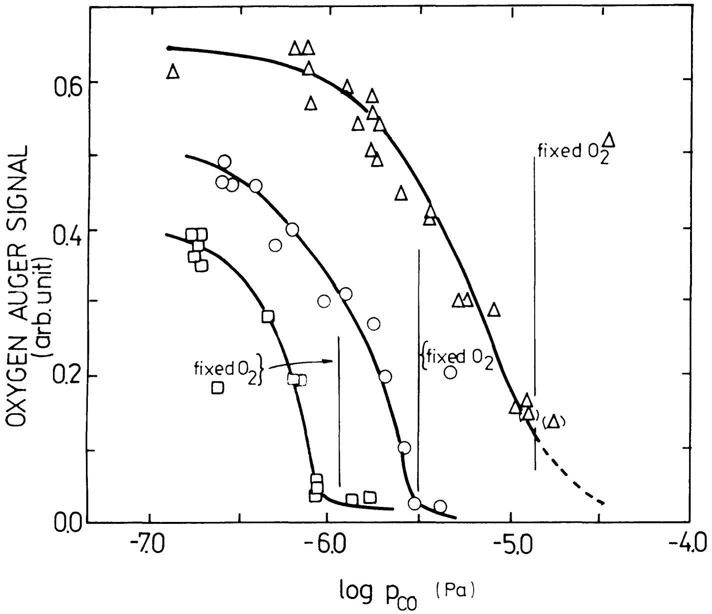

FIGURE 6.15 Steady-state oxygen Auger signal at polycrystalline platinum at 483 K as a function of carbon monoxide pressure for several fixed oxygen pressures. Triangles enclosed in brackets indicate the presence of detectable concentration of adsorbed carbon monoxide. The fixed oxygen pressures were 1.3 × 10^{-6} Pa (□); 3.2 × 10^{-6} Pa (○), and 1.4 × 10^{-5} Pa (△) [25].

the highest and almost constant value; at higher $\underline{p}_{CO}$ it sharply decreased; and at about $\underline{p}_{CO}/\underline{p}_{O_2} = 1$ it became very small. At $\underline{p}_{CO}$ lower than 10^{-5} Pa no presence of CO_{ads} (no Auger signal of carbon) was registered in the region of $\underline{p}_{CO}$ somewhat higher than $\underline{p}_{O_2}$. However, above $\underline{p}_{CO} \approx 10^{-5}$ Pa chemisorption of CO was detected, and the experimental points enclosed in brackets in Fig. 6.15 indicate the presence of a detectable concentration of CO_{ads} species. Qualitatively similar results were obtained by Golchet and White [26], who determined the coverage by O_{ad} and CO_{ad} on polycrystalline Pt by flash desorption.

As was already stated, the transient state experiments gave evidence of the Langmuir-Hinshelwood mechanism in the case of Pd catalyst. This suggests that this is also the case with other platinum group metals. In their review paper, Engel and Ertl [12] state that this mechanism can surely be assumed for Pt catalysts when $\underline{p}_{CO} \approx \underline{p}_{O_2}$, $\underline{T} < \underline{T}_{max}$, and for total pressures not exceeding 10^{-4} Torr. The most convincing argument is the retarding effect of CO chemisorption on the reaction rate at high θ_{CO}. However, as was already stated, for $\underline{T} > \underline{T}_{max}$, this effect is no longer observed. The reaction rate falls off slowly with increasing temperature, whereas θ_{CO} decreases by several orders of magnitude in the same temperature range. This fact was the reason why most authors in the past proposed the Eley-Rideal mechanism. It has also been argued that the ER mechanism can easily explain the fact that the rate of CO_2 formation on the surface of Pt precovered with oxygen is almost independent of temperature. However, Engel and Ertl argue that the simple ER mechanism cannot be accepted in this latter case since at $\underline{T} > \underline{T}_{max}$ the reaction rate is not of the first order with respect to θ_O [25]. Also the nonstationary experiments of Bonzel [31,32] and Pacia [28], in which no measurable induction period was observed for CO impinging on an oxygen-precovered Pt surface, cannot be taken as conclusive. Engel and Ertl point out that in the case of Pd (111) similar behavior was observed and has been shown to be consistent with the LH mechanism when smallest detectable relaxation time is not limited to several seconds by the experiment equipment [22].

4. Structure Insensitivity of Platinum Metal Catalysts in the Oxidation of Carbon Monoxide

In Section II.C of Chapter 5 the problem of the effect of surface structure in platinum group metal catalysts on their activity in hydrogen oxidation was discussed and it has been shown that this catalytic system is "structure-insensitive" [33]. This means that the turnover rate, the reaction rate calculated per surface stom, is independent of the surface structure and hence also on the catalyst dispersion as the participation of particular crystal faces in the total surface area may vary strongly with the particle size. The same problem pertaining to carbon monoxide oxidation on platinum group metals was tackled for the first time by Ertl and Koch [34], who studied the clean Pd (111), (100), and (110) single-crystal planes as well as a polycrystalline Pd wire. In all cases the temperature dependence of CO_2 production in the steady-state experiments carried out at a total pressure of the order of 10^{-7} Torr was the same. The curves $\underline{r} = \underline{f}(\underline{T})$ exhibited maxima at $\underline{T}_{max}$ equal to about 500 K. As the absolute values of surface areas of the catalysts were not known, the curves obtained for different catalysts were normalized to their respective maximum. This resulted in a shift of all experimental points to the positions close to a common line of the same shape as the lines shown in Fig. 6.12. The fact that different crystal planes as well as a polycrystalline sample gave practically the same result has been an important indication that this catalytic system is also structure-insensitive.

More exact and strictly quantitative study on alumina-supported palladium catalyst was undertaken by Ladas et al. [35]. They investigated the catalysts containing Pd particles of average diameter 1.5–8 nm obtained by the evaporation of palladium on α-Al_2O_3 single-crystal support under the conditions of UHV. The number of surface metal atoms was determined by combining transmission electron microscopy with temperature-programmed desorption. This enabled calculation of the turnover rate and demonstration that at 445 K, i.e., below $\underline{T}_{max}$, the turnover rate is independent of the particle size in supported Pd catalysts. It is interesting to observe that the same turnover rate value was obtained by Engel [36] for the Pd (111) face. Under these conditions catalytic CO oxidation on palladium appears to be totally structure-insensitive, thus confirming the earlier results of Ertl and Koch.

When the reaction was carried out at 518 K, i.e., at temperature near $\underline{T}_{max}$, the agreement of the data for the particles larger than 4 nm and the Pd (111) face was again excellent. However, below a particle size of 4 nm a distinct increase of turnover rate was observed. The reasons for such behavior are not very clear. The authors suggested the possibility that in the case of the smallest particles in which the proportion of Pd atoms on crystal edges and corners are necessarilly high the accessibility of surface atoms to the molecules impinging from the gas phase should be higher than that of the atoms on a flat surface.

Ladas et al. [35] also compared their own results obtained at low pressure (10^{-5} to 10^{-4} Torr) with those obtained by Cant et al. [37] for the steady-state oxidation of CO over Pd–SiO_2 near atmospheric pressure and below 450 K. It has been shown that despite the fact that the increase of pressure was about seven orders of magnitude, the turnover rate increased only from 0.012 sec^{-1} for low-pressure experiments to 0.035 sec^{-1} for high-pressure. This remarkable invariance of the turnover rate over a large range of pressure must be related to the fact that at 450 K the rate depends only on the p_{CO}/p_{O_2} ratio and not on the total pressure. It also suggests that the same mechanism is applicable in both cases. The authors conclude, therefore, that the oxidation of CO on Pd below 450 K is structure-insensitive at high pressures as well.

IV. OXIDATION OF CARBON MONOXIDE ON METAL OXIDE CATALYSTS

A. Chemisorption of Carbon Monoxide and Carbon Dioxide on Metal Oxide Catalysts as Investigated by IR Spectroscopy

1. General Remarks

Chemisorption of carbon monoxide and carbon dioxide on metal oxides and especially on transition metal oxides, which are important catalysts for CO oxidation, is much more complicated than in the case of metal catalysts due to the fact that, besides carbonyl-like species, carbonate- and carboxylate-type species may also be present at the surface. In addition, application of the modern UHV methods is limited as most of the transition metal oxides when exposed to high vacuum and temperature give off some amounts of oxygen, thus changing the chemical composition of the surface. This renders it difficult or even impossible to attain a stoichiometric clean surface. Another difficulty which may be met in applying such methods as AES or LEED, in which cathode rays are directed toward the surface, is the acquiring of a static electrical charge by samples which do not exhibit high enough electrical conductivity. The method which is supplying the most valuable information concerning the nature of chemisorption of CO and CO_2 on the metal oxides is infrared spectroscopy, with which we shall deal in the present section. Another method which has been used with success is calorimetry. Its application will be discussed in the following Section IV.B.

It is convenient to discuss separately the IR bands of chemisorbed CO and CO_2 and their assignment in the following three spectral ranges [38]:

1. 2140–2200 cm^{-1} where the bands appear at frequencies higher than the stretching frequency of a free CO molecule
2. 1800–2140 cm^{-1} where the frequencies typical for metal carbonyls are registered
3. 1200–1800 cm^{-1} region comprising the frequencies characteristic of carbonate and carboxylate species

2. IR Bands of Adsorbed CO Within the Region 2140–2200 cm^{-1}

Infrared bands of adsorbed CO exhibiting higher frequency than the stretching frequency 2143 cm^{-1} of free CO molecule were observed on different oxides. Some examples are listed in Table 6.2. The adsorbed species corresponding to the bands within this spectral region are weakly adsorbed and in most cases can be desorbed at least partially in vacuum at room temperature. However, some authors observed an increase of the coverage with increasing temperature [3,38], which indicated that chemisorption, although fast at room temperature, is a slightly activated process.

Different interpretations of the CO bands of frequency above 2143 cm^{-1} were proposed in the literature. They were reviewed in [3] and [39]. Unfortunately, none of them is generally accepted. Eischens and Pliskin's [5] suggestion that the 2200 cm^{-1} species on NiO corresponds to the $\text{Ni}{-}{-}{-}\overline{\text{O}{-}\text{C}{-}\text{O}}$ complex seems to be incompatible with the fact that in desorbate only CO molecules are detected and no CO_2 is present. The dipole interactions [40] as the explanation for this band are questioned by Little [3] who argued that in this case a shift of the frequency of free CO molecule to the opposite direction should be expected. More convincing seems to be the suggestion of Gardner and Petrucci [42] according to which the species responsible for the high-frequency bands are partially or completely ionized. The former possibility is much more probable as the complete ionization of CO molecule needs rather high energy (1350 kJ mol^{-1}). The idea of partial localization of positive charge on the adsorbed CO species was strongly supported by quantum chemical calculations carried out by Politzer and Kasten [41] for the system composed of CO molecules and nickel atoms in different oxidation states (Ni^0, Ni^+, Ni^{2+}, and Ni^{3+}) and also to some extent by the calculations carried out by Colburn and Mackrodt [43] in which chemisorption of CO on the (001) surface of MgO was studied.

3. IR Bands of Adsorbed CO Within the Region 1800–2140 cm^{-1}

The adsorbed CO molecules exhibiting IR bands within this spectral region are the molecules bonded to the surface cations essentially in the same way as the CO ligands in metal carbonyls as described in Section II. The frequencies above 2000 cm^{-1} are assigned to the CO molecules bonded linearly. The bridged CO species are characterized by frequencies below 2000 cm^{-1}. However, linearly bonded species may also exhibit frequencies below 2000 cm^{-1} as it was shown in Blyholder's paper [4] discussed in Section II. In the case of metals the discrimination between bridged and linear molecules can frequently be done on the basis of LEED investigations. Unfortunately, this method is rarely applied for the studies of adsorption on oxide surfaces. In addition, the observation of frequencies corresponding to

TABLE 6.2 IR Bands of Carbon Monoxide Adsorbed on Different Metal Oxides Registered within Spectral Range 2140–2200 cm^{-1}

Adsorbent	Ir band (cm^{-1})	Assignment proposed by the author	Ref.
Ni/NiO	2200	Ni—O—C—O species	a
NiO	2175–2190	CO weakly adsorbed on surface O atom	b
NiY zeolite	2212	CO adsorbed on O atom bridging between two Ni atoms	c
Cr_2O_3/Al_2O_3	2200	CO adsorbed on Cr^{3+}	
	2230	CO adsorbed on Al^{3+}	
	2180	CO adsorbed on C^{2+}	d
Cr_2O_3/Al_2O_3	2200	CO^+	e
ZnO	2188	P and Q bands of physically adsorbed CO	
	2120		f
ZnO	2174	CO adsorbed by dipole interaction	g
	2198		g
V_2O_5/SiO_2			
Mildly reduced	2192, 2205	CO complex on V^{4+}	
Strongly reduced	2178, 2185	CO complex on V^{3+}	h
Al_2O_3	2200	CO adsorbed by dipole interaction	i
Al_2O_3	2200	CO^+	e
MgO	2200	CO weakly adsorbed on cationic site	j

[a] R. P. Eischens and W. A. Pliskin, Adv. Catal., 9, 662 (1957); [b] C. E. O'Neil and D. J. Yates, Spectrochim. Acta, 17, 953 (1965); [c] N. N. Bobrow, A. A. Daydow, and K. G. Ione, Kinet. Katal., 16, 1272 (1975); [d] J. B. Peri, J. Phys. Chem., 78, 588 (1974); [e] L. H. Little and C. H. Amberg, Can. J. Chem., 40, 1997 (1962); [f] G. Kortüm and H. Knehr, Z. Physik. Chem.N. F., 89, 194 (1974); [g] J. H. Taylor and C. N. Amberg, Can. J. Chem., 39, 535 (1961); [h] A. A. Davydow, A. A. Budnewa, and N. G. Maksimow, React. Kinet. Catal. Lett., 20, 93 (1982); [i] N. D. Parkyns, J. Chem. Soc. (A), 1910 (1967); [j] E. Guglielminotti, S. Coluccia, E. Garrone, L. Cerruti, and A. Zecchina, J. Chem. Soc. Faraday I, 75, 96 (1979).

the metal-carbon stretching vibrations was not applied in the case of transition metal oxides in which generally no spectral region below 1000 cm^{-1} is studied.

When two bands appear in the 1800–2140 cm^{-1} region the higher one is usually ascribed to the linearly bonded carbonyl species and the lower one to bridged species. Chemisorption of CO on nickel oxide is an example. Courtois and Teichner [44] observed a band at 2060 cm^{-1} which was assigned to a linearly bonded carbonyl group and a band at 1965 cm^{-1} assigned to a bridged CO molecule. Both species, observed also by Roginskii et al. [45], differed by their reversibility. The former could be desorbed in vacuum at room temperature; the latter could not. Conclusions concerning the form of carbonyl species could also be formulated based on the results of the measurements carried out with a series of solid solutions containing transition metal cations dispersed in a diamagnetic matrix. Matushak et al. [46] on a CoO–MgO solid solution observed several IR bands between 1800 and 2000 cm^{-1} which could be grouped into two sets. The intensities of the bands belonging to one of the sets (1875 and 1930 cm^{-1}) decreased with increasing concentration of cobalt while the intensities of the bands belonging to the second set (1805, 1845, and 1965 cm^{-1}) increased. The authors assigned the bands of the first group to the CO molecules chemisorbed on isolated Co ions and those of the second group to CO molecules chemisorbed on interacting Co ions. It would be logical to assume as a consequence that the first group species is adsorbed linearly and the second one is a bridged species.

4. IR Bands of Adsorbed CO and CO_2 Within the Region 1200–1800 cm^{-1}

IR bands within this spectral region can be obtained by adsorption of CO and CO_2 on the oxides and it happens that the same species are produced by chemisorption of each substance on the same adsorbent as was observed for examples by Goodsel [47] who identified the same bidentate carbonate complex after adsorption of either CO or CO_2 on Co_3O_4. Absorption bands within this region can be grouped into sets comprising two or three bands which suffer all the changes simultaneously and hence must be ascribed to the same adsorbed species. The species exhibiting in this spectral region two or more bands must be composed of more than two atoms. The comparison of such spectra of chemisorbed CO and CO_2 with the IR spectra of different carbonates, bicarbonates, mono- and bidentate carbonato complexes, organic carbonates, etc. enabled the interpretation of the numerous results of IR studies of chemisorption of carbon oxides [39]. The properties of the particular carbonate and carboxylic species were summarized by Krylov and Kiselev [39] and are given in Table 6.3. Generally the carbonate surface complexes are thermally stable and decompose only at high temperatures. Lesser stability is exhibited by carboxylate and bicarbonate anions. The latter decomposes somewhat above room temperature.

Recently, the existence of several polymeric CO surface species was described. Guglielminotti et al. [48] when studying chemisorption of CO on well outgassed MgO samples observed among the others a set of four IR bands (1480, 1275, 1197, and 1066 cm^{-1}) growing slowly upon adsorption and very sensitive to oxygen. Upon all treatments the intensities of these bands changed parallel to each other and hence had to be assigned to the same species. The relatively high number of IR bands indicated polyatomic species and the formation of polymeric complex $(CO)_n^{x-}$ with $2 < n \le 4$ and $x = 2$ or 4 has been suggested in analogy to the cyclic carbanions such as

TABLE 6.3 Carbonate and Carboxylic Surface Species Detected on the Transition Metal Oxides

Surface species	Formula	Characteristic IR bands (cm^{-1})
Simple carbonate ion	CO_3^{2-}	ν_{as} = 1415–1470
Monodentate carbonate	$M{-}O{-}CO_2^{2-}$	ν_{as} = 1420–1540 ν_{sym} = 1330–1390 ν = 980–1050
Bidentate carbonate	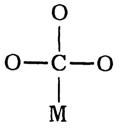 $O{-}\overset{\overset{O}{\mid}}{\underset{\underset{M}{\mid}}{C}}{-}O$	ν_{C-O} = 1600–1670 ν_{as} = 1280–1310 ν_{sym} = 980–1050
Bridged carbonate	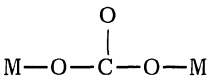 $M{-}O{-}\overset{\overset{O}{\mid}}{C}{-}O{-}M$	ν_{C-O} = 1780–1840 ν_{as} = 1250–1280 ν_{sym} = 1000
Carboxylate ion	COO^-	ν_{as} = 570–1630 ν_{sym} = 1350–1390
Bicarbonate ion	CO_3H^-	ν_{as} = 1615–1650 ν_{sym} = 1400–1500 ν_{OH} = 3600 δ_{OH} = 1225
Formate ion	$HCOO^-$	ν_{as} = 1580–1620 ν_{sym} = 1340–1390

Source: Data from Ref. 39.

$(CO)_p^{2-}$ known in inorganic chemistry. Upon depletion such species transform into the forms exhibiting only two IR modes which presumably are dimeric structures as:

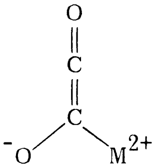

The dimeric forms transform depending on the conditions into stable carbonate-like species, or disproportionate with the formation of C and O_{CUS} (CUS - coordinatively unsaturated) atoms which results in the observed darkening of the sample. The existence of dimeric form was confirmed by later studies with CoO—MgO and NiO—MgO solid solutions. Cordischi et al. [49] studied adsorption of CO on the diluted CoO—MgO solid solutions of high surface area using EPR measurements and observed at 298 K a signal with the $g_{xx} = 2.0021$, $g_{yy} = 2.0050$ and $g_{zz} = 2.0060$ values which was weak on MgO pure but much stronger on the CoO solid solution. The use of ^{13}CO + ^{12}CO mixtures enabled to prove that the paramagnetic species contained two equivalent carbon atoms. The species was tentatively identified as $C_2O_2^-$.

Cordischi et al. [49] in their EPR study could also identify a radical containing four nonequivalent carbon nuclei. The species containing four CO molecules were also observed in the IR studies on CoO—MgO [50—52] and NiO—MgO by Zecchina et al. [53]. In the former case the formation of $Co(CO)_4^-$ species and carbonate-like groups was assumed to be formed on clustered Co^{2+} ions:

$$10CO + 3O^{2-} + 2Co^{2+} \longrightarrow Co(CO)_4^- + 2CO_3^{2-}$$

The vibrational assignment of the $Co(CO)_4^-$ species has been made on the basis of a complete set of isotopic substitution experiments. Another species containing three carbon nuclei $[(CO_2)_2Co(CO)]^{2-}$ was assumed to be formed on the $O^{2-}Co^{2+}O^{2-}$ triplets situated on the edges of the crystallites. On NiO—MgO a similar surface complex $[(CO)_3Ni(CO_2)]^{2-}$ Mg^{2+} was assumed which can be interpreted as $Ni(CO)_4$ adsorbed on $Mg^{2+}O^{2-}$ pairs.

B. Catalytic Oxidation of CO on the Surface of Oxides at and about Room Temperature

From the practical point of view, catalytic oxidation of carbon monoxide at and about room temperature is of special interest. Nevertheless toward the end of World War I Lamb et al. discovered a highly active four-component oxide catalyst (MnO_2, CuO, Co_2O_3, Ag_2O) called hopcalite [54]. In later years this catalyst type, which was used, for example, for filling gas mask canisters, was further developed, and some other new industrial catalysts were introduced, the most prominent examples being promoted argentic oxide or activated silver permanganate [55]. The hopcalite-type catalysts are characterized by low activation energy, mostly in the limits 5–7 kcal mol^{-1}. All these catalysts represent fairly complicated physicochemical systems and the modern study of the low-temperature mechanism of carbon monoxide oxidation had to be carried out on simpler catalysts containing only one oxide component. The present section deals with the interactions of carbon monoxides and oxygen on such systems, mainly on high surface area Cu_2O and NiO. The study of these catalysts supplied us with important information concerning the CO oxidation at and about room temperature.

The comprehensive studies of Cu_2O were undertaken by Garner et al. [56–58]. The main tools of their research were the calorimetric and electrical conductivity measurements. They used the high surface area samples obtained by the partial oxidation of very fine copper grains. The oxide film was about 100 Å thick and the presence of underlying metal enabled the oxide surface to be cleaned more readily after exposure to oxygen. The remaining oxygen which is difficult to desorb can be, under such conditions, very easily incorporated into the film on the expense of metal without the danger of formation of the film of higher oxide.

In their now classical experiments Garner et al. proved that no CO_2 is produced if CO is contacted with the fresh surface of Cu_2O at room temperature and its adsorption is reversible. On the other hand, if CO is adsorbed on oxygen precovered surface the slow distillation of CO_2 into the liquid air trap occurs. Adsorption of CO in this latter case created new adsorption sites for oxygen corresponding to 50 mol % of adsorbed CO. This observation led to the conclusion that a CO_3 complex has been forming at the oxygenated surface according to the scheme:

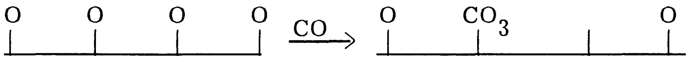

The same was observed on nickel [59] and cobalt [60] oxides.

Such a complex was decomposing at room temperature with the formation of CO_2

$$CO_{3/ads/} \longrightarrow CO_{2/g/} + O_{/ads/}$$

It can also react with an excess of CO in accordance with the reaction:

$$CO_{3/ads/} + CO_{/g/} \longrightarrow 2CO_{2/g/}$$

It should be observed that the CO_3 complex exhibiting the same properties can also be formed in the reaction of CO_2 with chemisorbed oxygen [57].

$$CO_{2/g/} + O_{/ads/} \longrightarrow CO_{3/ads/}$$

A strong support for the proposed schemes was obtained from the calorimetric measurements. This could be done by comparing the heat of chemisorption of oxygen on carbon monoxide precovered surface as determined in a direct experiment with the heat of the same process calculated from thermochemical cycles in which the composition of surface complex was assumed to correspond to CO_2 or CO_3 [56]. In the case of high surface area NiO the two following thermochemical cycles were taken into account:

Cycle I

$$2CO_{(g)} + O_{2(g)} = 2CO_{2(g)} + 2 \times 67 \text{ kcal mol}^{-1} \quad (6.10)$$

$$2CO_{(ads)} = 2CO_{(g)} - 2 \times 26 \text{ kcal mol}^{-1} \quad (6.11)$$

$$2CO_{2(g)} = 2CO_{2(ads)} + 2 \times 28 \text{ kcal mol}^{-1} \quad (6.12)$$

$$2CO_{(ads)} + O_{2(g)} = 2CO_{2(ads)} + 138 \text{ kcal mol}^{-1} \quad (6.13)$$

Cycle II

$$CO_{(g)} + \frac{1}{2} O_{2(g)} = CO_{2(g)} + 67 \text{ kcal mol}^{-1} \quad (6.14)$$

$$CO_{(ads)} = CO_{(g)} - 26 \text{ kcal mol}^{-1} \quad (6.15)$$

$$\frac{1}{2} O_{2(g)} = O_{(ads)} + 22.5 \text{ kcal mol}^{-1} \quad (6.16)$$

$$CO_{2(g)} + O_{(ads)} = CO_{3(ads)} + 37 \text{ kcal mol}^{-1} \quad (6.17)$$

$$CO_{(ads)} + O_{2(g)} = CO_{3(ads)} + 100.5 \text{ kcal mol}^{-1} \quad (6.18)$$

The directly determined heat of chemisorption of 1 mol of oxygen on CO precovered surface of NiO was 100 kcal mol^{-1} in good accordance with cycle II in which the formation of CO_3 surface complex was assumed. Similar results were also obtained with CoO and Cu_2O.

Garner et al. [58], when discussing the mechanism of room temperature oxidation on Cu_2O, remarked that this process being not inhibited by the product CO_2 is inconsistent with simple Langmuir-Hinshelwood mechanism. Taking into account all arguments concerning the existence of CO_3 complex under these conditions, they assumed that it is the reaction intermediate and proposed the following scheme:

$$CO_{(g)} \longrightarrow CO_{(ads)} \tag{6.19}$$

$$O_{2(g)} \longrightarrow 2O_{(ads)} \tag{6.20}$$

$$CO_{(ads)} + 2O_{(ads)} \longrightarrow CO_{3(ads)} \tag{6.21}$$

$$CO_{3(ads)} + CO_{(ads)} \longrightarrow 2CO_{2(g)} \tag{6.22}$$

The investigations initiated in Garner's laboratory were widely developed by Teichner, Gravelle, and their collaborators in later years. The work of this group reviewed in [61] was concerned with two preparations of high-surface-area (~ 150 m^2 g^{-1}) nickel oxide obtained by vacuum decomposition of nickel hydroxide at 200 (NiO_{200}) and 250°C (NiO_{250}) on which very extensive calorimetric measurements were carried out. They were also supplemented by the measurements of electrical conductivity and IR spectra of chemisorbed CO and CO_2. The essential progress in these investigations was achieved by taking for thermochemical calculations the data of chemisorption heat determined at the known coverages of the surface with particular reagents. The results obtained by Gravelle and Teichner present a very thoroughly documented example of the work showing that even small differences in the preparation mode of the sample may result in distinct differences in adsorptive and catalytic properties and also that the mechanism of a catalytic reaction may change with changing coverage. The authors confirmed the formation of CO_3 surface species as the product of the interaction of oxygen and carbon oxide at the surface of finely divided NiO and proved that it is negatively charged, presumably bearing one negative charge CO_3^-.

When summarizing the whole of their results, Gravelle and Teichner [61] arrive at the conclusion that on their NiO preparations two mechanisms of room temperature CO oxidation are operating, Mechanism II represents a single reaction path on NiO_{200}:

$$2CO_{(g)} \longrightarrow 2CO_{(ads)} \qquad \text{fast} \qquad (6.23)$$

$$CO_{(ads)} + O_{2(g)} + Ni^{2+} \longrightarrow CO^{-}_{3(ads)} + Ni^{3+} \qquad \text{fast} \qquad (6.24)$$

$$CO^{-}_{3(ads)} + CO_{(ads)} + Ni^{3+} \longrightarrow 2CO_{2(g)} + Ni^{2+} \qquad \text{slow} \qquad (6.25)$$

On the surface of NiO_{250}, in addition to mechanism II mechanism I is also operating and in fact the latter is faster. Hence:

$$\frac{1}{2}\, O_2 + Ni^{2+} \longrightarrow O^{-}_{(ads)} + Ni^{3+} \qquad \text{fast} \qquad (6.26)$$

$$CO_{(g)} \longrightarrow CO_{(ads)} \qquad \text{fast} \qquad (6.27)$$

$$O^{-}_{(ads)} + CO_{(ads)} + Ni^{3+} \longrightarrow CO_{2(g)} + Ni^{2+} \qquad \text{slow} \qquad (6.28)$$

A somewhat different mechanism has been suggested in the case of room temperature oxidation of CO on Li_2O-doped high-surface-area nickel oxide:

$$O_{2(g)} + 2Ni^{2+} \longrightarrow 2O^{-}_{(ads)} + 2Ni^{3+} \qquad (6.29)$$

$$2O^{-}_{(ads)} + CO_{(g)} + 2Ni^{3+} \longrightarrow CO^{-}_{3(ads)} + Ni^{2+} + Ni^{3+} \qquad (6.30)$$

$$CO^{-}_{3(ads)} + CO_{(g)} + Ni^{3+} \longrightarrow 2CO_{2(g)} + Ni^{2+} \qquad (6.31)$$

Two further mechanisms proposed by Gravelle and Teichner concern the behavior of high-surface-area NiO catalyst at 200°C. In the case of oxygen-rich gas mixtures, mechanism IV, including the formation of carbonate intermediate, is probable:

$$O_{2(g)} + 2Ni^{2+} \longrightarrow 2O^{-}_{(ads)} + 2Ni^{3+} \qquad (6.32)$$

$$2O^{-}_{(ads)} + CO_{(g)} + 2Ni^{3+} \longrightarrow CO^{2-}_{3(ads)} + 2Ni^{3+} \qquad (6.33)$$

$$CO^{2-}_{3(ads)} + 2Ni^{3+} \longrightarrow CO_{2(g)} + O^{2-}_{(ads)} + 2Ni^{2+} \qquad (6.34)$$

On the other hand, in the case of carbon monoxide-rich gas mixtures mechanism V is highly probable at 200°C:

$$CO_{(g)} + NiO \longrightarrow Ni + CO_{2(g)} \tag{6.35}$$

$$Ni + \frac{1}{2} O_{2(g)} \longrightarrow NiO \tag{6.36}$$

Besides cuprous and nickel oxides, important studies on the catalytic carbon monoxide oxidation at and near room temperature were also undertaken in the case of manganese dioxide, which is of special interest from a practical point of view as the main component of hopcalite-type catalysts. Roginsky and Zeldovich in their early paper [62] arrived at the conclusion that this reaction proceeds by the interaction between chemisorbed carbon monoxide and oxygen from gas phase. Brooks [63], when comparing the "heterogeneous" oxidation of CO on MnO_2 with "depletive" oxidation (oxidation of CO by the reduction of the oxide), found a first-order reaction and similar activation energies in both cases and interpreted the observed facts in favor of the Eley-Rideal mechanism in a similar way as was proposed in [62]. Klier and Kuchynka [64] showed that oxidation of carbon monoxide by the lattice oxygen of MnO_2 is a rapid process producing gaseous and, to some extent, adsorbed carbon dioxide, the subsequent reoxidation being a very difficult reaction step. This behavior is markedly different from that of NiO and MnO.

In more recent years a thorough study of catalytic CO oxidation on MnO_2 was carried out by Kobayashi and Kobayashi [65—67] who successfully applied the transient response method in their investigations. The essential feature of this method using a constant-flow catalytic reactor consists of the sudden change of gas composition introduced into the catalyst and observing the changes in concentration at the reactor outlet.

Parallel to the studies based on the transient response method, Kobayashi and Kobayashi determined the distribution of the oxidation power of surface oxygen species using the iodometric method described in an earlier paper [68]. It consists of the analytical determination of iodine produced in KI solutions of different pH values in contact with the surface of the oxide covered with adsorbed oxygen. If the oxidation power is high, iodine is evolved in solutions of high pH value. Using this method it was shown [65] that there were two kinds of oxygen species on the oxygenated surface of MnO_2: the O_s^h species of higher oxidation power constituting only a small fraction of adsorbed oxygen and O_s^l species of lower oxidation power which are the predominant oxygen surface species. The O_s^h species are negatively charged and are considered to be either O_2^- or O^- ions. However, it should be observed that the detailed analysis of kinetic data suggested that the former species is the predominant one.

The Kobayashi and Kobayashi experiments show that gaseous CO reacts directly with the oxygen species at the surface, thus forming a certain intermediate which successively decomposes to form gaseous CO_2. Carbon dioxide formed in the course of surface reaction is being reversibly adsorbed on sites different from those where the intermediate is formed. Reversibly adsorbed CO_2 is electrically neutral, which has been verified by measurements of the electrical conductivity of the catalyst.

From the analysis of their kinetic data the authors also concluded that the rate-determining step in the room temperature oxidation of CO on MnO_2 is the reaction between surface O_2^- ions and CO from the gas phase. This result is in accordance with IR investigations carried out by Davydov et al. [69], who showed that the reaction between chemisorbed oxygen and carbon monoxide from the gas phase results in the formation of carbonate-type intermediates. They could also discriminate between more and less strongly bonded oxygen surface species. Surface carbonates formed by the less strongly bonded oxygen are not stable and decompose with the formation of CO_2 at room temperature. On the other hand, the carbonate species formed with the participation of more strongly bonded oxygen are stable at room temperature and decompose only at and above 150°C.

It should be observed here that room temperature oxidation of CO on MnO, similar to the case of its oxidation on finely divided NiO and Cu_2O around room temperature, is characterized by low apparent activation energy. For example, in [70] it was determined as equal to 2.7 kcal mol^{-1}.

C. Catalytic Oxidation of Carbon Monoxide on Transition Metal Oxides at High Temperatures

In the preceding section the catalytic carbon monoxide oxidation on high-surface-area metal oxides occurring at and near room temperature was discussed. As was already stated, such processes are characterized by the low values of the apparent activation energy, which is usually of the order 2–4 kcal mol^{-1}. The most probable intermediate, at least in a number of cases, is the CO_3^- ion, the existence of which was documented by calorimetric measurements. However, no catalytic oxidation of CO is observed at room temperature if the metal oxides exhibiting small specific surface area (of a few m^2 per g) are used as catalysts. This may be due not only to the diminished surface area but to the fact that such preparations are obtained by the calcination of appropriate substrates at high temperatures (600–1000°C in most cases) and they contain much smaller concentrations of lattice defects than finely divided preparations which are usually obtained at temperatures not higher than 200—250°C and frequently calcined in vacuum. On the other hand, low-surface-area transition metal oxides are quite good catalysts of carbon monoxide oxidation at temperatures of the order 200—400°C. The fact that the apparent activation energies at these conditions are much higher than in the vicinity of room temperature (10—25 kcal mol^{-1}) indicates that the mechanism of high-temperature oxidation is different from that at low temperatures. This is why the problem of high-temperature oxidation of CO is discussed in a separate section.

As will be shown later on some chosen examples, also in this case the kinetics and activation energy of CO oxidation on a given transition metal oxide may change depending on the experimental conditions and the way in which catalyst was obtained, thus indicating that different CO oxidation mechanisms can operate. They may include either the interactions between chemisorbed molecules (e.g., Langmuir-Hinshelwood mechanism) or the sequence of the independent catalyst's surface reduction and reoxidation steps (Mars-Van Crevelen mechanism), similar to that observed in the case of hydrogen oxidation on transition metal oxides. Boreskov in his numerous papers showed that in the series of IV period transition metal oxides above a certain characteristic temperature range the latter mechanism is operating. As was stated in Section III.B of Chapter 5, in order to discriminate between both principal mechanisms, the rate of catalytic oxidation at the stationary state is compared with the rates of reduction and reoxidation of the surface. The latter measurements must be carried out at the surface, the oxidation state of which corresponds to that reached in the course of the catalytic reaction. Boreskov and Marshneva [71,72] carried out a series of measurements in which at first the catalytic activity of oxide catalysts was determined in a constant-volume apparatus with circulation of gases (CO, O_2, and He as the carrier gas) and removal of CO_2 in a liquid air trap. After reaching the stationary state the reacting gas mixture was changed in such a way that helium gas was mixed with only one of both reagents, CO or O_2, at the same partial pressure applied during the catalytic test. The rates of catalyst surface reduction and reoxidation were measured in this way. In most cases (Co_3O_4, Mn_2O_3, NiO, Cr_2O_3, Fe_2O_3, ZnO) the dependence of stationary reaction rate W on temperature expressed in $\log - \frac{1}{T}$ coordinates represented a plot comprising two linear sections. The apparent activation energy calculated for the lower temperature sections was 9—10 kcal mol^{-1}; that corresponding to the high-temperature region was contained within the limits 24—30 kcal mol^{-1}. The more or less sharp temperature at which the inversion of activation energy occurred depended on the nature of the oxide and ranged from about

245°C for Fe_2O_3 to 410—510°C for Mn_2O_3. The important result was that above this temperature the points representing the rate of the catalytic reaction fell on the same line as the points representing the rates of reduction and reoxidation (equal at the stationary state of catalytic reaction) of the catalyst surface. Hence at these conditions the rates of catalytic reaction and surface reduction-oxidation processes are the same, thus giving proof of the Mars-Van Crevelen consecutive mechanism. Boreskov's data clearly indicate that this mechanism corresponds to the highest regions of temperature and is characterized by high activation energies.

Principally the participation of the oxide oxygen in the catalytic oxidation of CO can be confirmed or rejected by the investigations with isotopically labeled oxygen. However, as was observed by Boreskov [73], numerous complications do not always permit formulation of clear-cut conclusions and this means that allowance should be made in each case for the direct isotopic exchange of all reactants: O_2, CO, and CO_2. In fact, the results obtained by different authors who undertook such measurements on transition metal oxides were frequently contradictory. The early investigators [74,75] arrived at the conclusion that oxide oxygen does participate in the catalytic reaction. On the other hand, no noticeable changes in the isotopic compositions of manganese peroxide and copper oxide (both enriched in ^{18}O) were detected by Vainstain and Turovski [76,77]. Nor did Roiter [78] detect $C^{18}O^{16}O$ molecules during the oxidation of CO on ^{18}O-enriched MnO_2 at 178°C and CuO at 300°C. However, it should be observed that both temperatures are apparently below the range at which Boreskov proved the reduction-oxidation mechanism to be valid. Winter [79], who contributed very extensive and highly competent studies of oxygen isotopic exchange, showed that in the case of CO catalytic oxidation on $Cu_2\,^{18}O$ oxide oxygen does participate in the reaction at temperatures as low as 15 and 38°C. The proportion of surface O atoms participating in this process was estimated to be about 10 and 15%, respectively. The sites reacting with CO were subsequently regenerated with oxygen of normal isotopic composition from the gas phase and accordingly the content of ^{18}O in the reaction product exhibited a tendency to decrease. Similar results were also obtained by Winter for NiO and Cr_2O_3. The fraction of surface O atoms participating in the catalytic reaction, however, was low. In the former case it amounted to 0.34% at 49°C and increased to 2.28% at 211°C. In the latter case it was 2.05% at 44°C and the same value was obtained at 155°C.

Very convincing proof of the participation of the lattice oxygen in the oxidation of carbon monoxide was recently given by Takasu et al., who studied the behavior of Pr_6O_{11} [80,81] and $Tb_{11}O_{20}$ [82] catalysts. They showed that if the oxide of natural isotope composition was exposed to a mixture of $^{18}O_2$ and CO, most of the carbon dioxide formed was composed of $C^{16}O_2$ molecules with only a little of $C^{16}O^{18}O$, indicating that the lattice oxygen atoms in both oxides play an important role in the catalytic oxidation.

When summarizing all the above results it can be stated that in the temperature region above 250–300°C the catalytic oxidation of CO usually occurs on the oxide catalysts according to the Mars-Van Crevelen mechanism, comprising consecutive steps of catalyst reduction and reoxidation characterized by the apparent activation energy above 20 kcal mol^{-1}. There are many indications that these processes occur with the participation of lattice oxygen forming the surface of the solid. Presumably not all such oxide oxygen atoms participate in the reaction but only those whose bonding energy is lowest.

D. Catalytic Oxidation of Carbon Monoxide on Oxide Catalysts Within the Intermediate Temperature Region 150–300°C

As was already stated in the case of group 4 transition metal oxides, the redox mechanism of carbon monoxide oxidation operates at temperatures above 250–300°C for which apparent activation energies above 20 kcal mol^{-1} are characteristic. On the other hand, the same reaction can proceed with quite appreciable rates at and about room temperature if highly dispersed oxides Cu_2O, NiO, or MnO_2 are used as catalysts. The mechanism of such low-temperature oxidation most probably includes the formation of CO_3^- ion as an intermediate which subsequently reacts with the CO molecule, producing two molecules of carbon dioxide. The apparent activation energy of such a process is only a few kcal mol^{-1}. None of these two low- and high-temperature mechanisms can be accepted for the intermediate temperature region roughly contained between 150 and 300°C. Here CO oxidation can be observed on many oxides the specific surface area of which is small (of the order of a few m^2 g^{-1}) and the activation energies are usually between 10 and 20 kcal mol^{-1}. No generally valid mechanism can be proposed in this case. This can be illustrated by a diversity of kinetic equations which were found to fit the experimental results, an example of which will be given. The reaction mechanism changes depending not only on the kind of oxide but also on its defect state, pretreatment, additives, as well as the conditions of the catalytic experiments. This is the reason why the results obtained on oxide catalysts within this range of temperature will be presented here based on the examples nickel oxide and chromium sesquioxide, on which perhaps the most interesting results were obtained.

1. Nickel Oxide Undoped Catalyst

Nickel oxide was the most frequently studied catalyst with which carbon monoxide oxidation was investigated in order to verify the electronic theory of chemisorption and catalysis. The diversity of kinetic equations which, depending on the conditions, can be obtained may be illustrated by the results published by Parravano [83]. In this case a constant-volume reactor with the circulation of gases was used in which CO_2 was removed on a column filled with ascarite. The NiO catalyst obtained by the calcination of nickel nitrate in air had a specific surface area of 2.2 $m^2\ g^{-1}$. The catalyst was initially undergoing irreversible changes during the course of a few initial runs and in this period the rate of CO oxidation could be expressed by a Roginskii-Zeldovich (called also Elovich) equation (160—212°C):

$$\frac{d\underline{q}}{dt} = \underline{a}\ e^{-\alpha \underline{q}} \tag{6.37}$$

where $\underline{q}$ is the amount of conversion and $\underline{a}$ and α are constants. However, after being used for a sufficient time, the activity of the catalyst reched a minimum value, which could be considered constant for all practical purpose. The initial rate of the reaction equal to $\underline{a}$ was found to increase with increasing temperature according to Arrhenius law and the apparent activation energy, equal to 9.7 kcal mol^{-1}, was calculated for the experiments in which a stoichiometric $CO-O_2$ gas mixture was used.

The form of empirical kinetic equation obtained for the samples which reached the constant activity depended on temperature. Within the temperature range 106—174°C reaction rate could be well represented by the formula:

$$-\frac{d\underline{p}}{dt} = \underline{k}\underline{p}_{O_2}^{0.5}\,\underline{p}_{CO}^{0.5} \tag{6.38}$$

but at 205—222°C

$$-\frac{d\underline{p}}{dt} = \underline{k}\underline{p}_{O_2}^{0.2}\,\underline{p}_{CO} \tag{6.39}$$

was valid.

The Roginskii-Zeldovich equation can be deduced from different assumptions. Kinetics of this kind may be due to the fact that the surface of an adsorbent or catalyst is heterogeneous and in the course of reaction most active centers get successively poisoned. The remaining less active ones need higher activation energy the linear change of which with time results in an equation of the form

(6.37). Hauffe [84] showed that the same kinetics can result from the formation of space charge in the Randschicht when electron exchange occurs between adsorbate and adsorbent (see Section III in Chapter 5). Parravano in his paper [83] assumed that Roginskii-Zeldovich kinetics were the result of the gradual removing of a large excess of surface oxygen. However, it should be observed that Herzog and Schlosser [85] proved that the NiO surface is poisoned by the reaction product carbon dioxide. This effect can be essentially reduced if CO_2 formed is removed from the reactor by freezing it out in a liquid nitrogen trap.

The activation energy found by Parravano in the 160–174°C temperature region for the samples which reached a constant activity was 2.2 kcal mol^{-1}, which suggests that in this case the already described low-temperature reaction mechanism was still operating. Parravano's Eq. (6.39) seems to be a transition to the equation of the form:

$$-\frac{dp}{dt} = kp_{O_2}^{0}p_{CO} \qquad (6.40)$$

which was given by several authors investigation CO catalytic oxidation on nickel oxide [86–89]. It corresponds, for example, to situations in which the surface is saturated with chemisorbed oxygen which reacts either with gaseous (Eley-Rideal mechanism) or chemisorbed (Langmuir-Hinshelwood mechanism) carbon monoxide.

Some interesting information concerning the coverage of nickel oxide with reagent molecules in the course of catalytic CO oxidation could be obtained from measurements of electrical conductivity. The conductivity of NiO, which is a p-type semiconductor, does increase when oxygen, an electron acceptor, is chemisorbed producing electron holes $h^{\bullet}$ in the Randschicht as described in Section III of Chapter 3.

The effect of carbon monoxide chemisorption on the electroconductivity of NiO depends on temperature. According to Gravelle and Teichner [61], adsorption of CO on high-surface-area nickel oxide at room temperature is not accompanied by any change in the electrical conductivity of the solid. This is easy to understand since at these conditions CO appears at the surface mainly as the carbonyl species bonded by acceptor-donor bonds not involving any localization or delocalization of electrons at the adsorption sites. However, at temperatures as high as 200–300°C a distinct decrease in the electrical conductivity of NiO is observed [85,90,91] in the course of chemisorption of CO. All of the above authors assume in this temperature region the donor-type chemisorption of CO:

$$CO_{(g)} + h^{\bullet} \text{ —— } CO^{+}_{(ads)} \qquad (6.41)$$

Unfortunately, no IR data were published concerning the spectra of CO adsorbed on nickel oxide at high temperature. It should here be observed that irreversible donor-type chemisorption of carbon oxide must not necessarily result in the formation of CO^+ species. The carbonate-like complexes, for example, are also conceivable as:

$$CO_{(g)} + 2O^{2-} + 2h^{\bullet} \longrightarrow CO^{2-}_{3(ads)} \qquad (6.42)$$

No changes in the NiO electrical conductivity of NiO accompany adsorption of CO_2 [91].

Changes in the electrical conductivity of nickel oxide, obtained by the calcination of nickel basic carbonate in air at 600°C, were studied by Bielański et al. [91]. Figure 6.16 shows the results obtained at 300°C with the samples which were at first standardized in oxygen at the experimental temperature until the conductivity reached a constant level and then the portions of CO were introduced permitting the CO/O_2 molar ratios indicated in the figure. The progress of the catalytic reaction was followed parallel to the measurements of electrical conductivity. It is seen that in the case of experiments in which an excess of oxygen was present the introduction of CO resulted in only minor changes in conductivity, indicating that the catalytic reaction proceeded on the surface practically saturated with oxygen. On the other hand, if the reacting mixture of gases was either stoichiometric or contained an excess of CO, the conductivity decreased by three orders of magnitude. This indicated that acceptor-type processes occurred at the surface. Besides the donor-type chemisorption of CO, this could also be the vanishing of some negatively charged reaction intermediates such as carbonate, O^-, or O^{2-} species. The deepest and most constant conductivity level in such cases was obtained after the reaction ceased completely because of oxygen exhaustion. In the case of the 3:1 $CO-O_2$ mixture, after the reaction was over the system was pumped off and then a rapid increase in conductivity was observed showing that an appreciable fraction of chemisorbed species, most probably $CO^+_{(ads)}$, was desorbed with the simultaneous transfer of electrons from the solid.

The kinetics of CO oxidation in [91] followed the Roginskii–Zeldovich law. The values of the initial reaction rate were dependent on the gas phase composition and at 225°C and higher temperatures reached a maximum at CO/O_2 molar ratio equal to 3:1. The apparent activation energy calculated from the initial reaction rates, on the other hand, changed monotonically with gas composition and, as Fig. 6.17 shows, increased from the value 6.4 kcal mol^{-1} for 1:2 $CO-O_2$ mixtures to 22.5 kcal mol^{-1} for the 4:1 mixture richest in CO. This result, obtained with the catalysts from the same batch, clearly

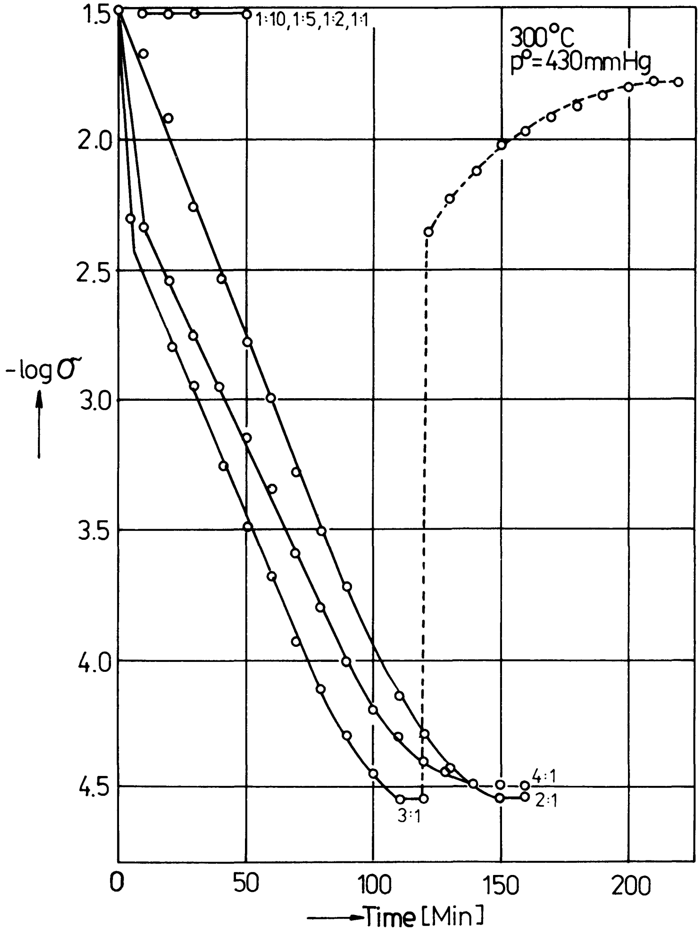

FIGURE 6.16 Changes in the electrical conductivity of NiO catalyst in the course of carbon monoxide oxidation in CO/O_2 mixtures of different compositions at 300°C with constant volume reactor and circulating gas. Catalyst standardized in oxygen. Broken line shows behavior of the catlyst in the course of desorption [91].

indicates how strongly the kinetic parameters and hence also the mechanism of catalytic CO oxidation on transition metal oxides may depend on the experimental conditions.

2. Nickel Oxide Catalyst Doped with Altervalent Oxide Additives

Catalytic experiments with transition metal oxides doped with altervalent metal oxide additives played an important role in the verification of the electronic theory of chemisorption and catalysis on semiconductors. As was mentioned in Secion IV of Chapter 3, doping changes the position of the Fermi level and hence the work function of the solid. According to the electronic theory [92—94], the increase in work function should enhance the catalytic reactions in which the rate-determining step is a donor-type reaction (reaction supplying electrons to the solid from the chemisorbed molecules) and the decrease in work function should enhance the catalytic reactions in which the rate-determining step is an acceptor process. Hence it was hoped that by carrying out the oxidation of carbon monoxide

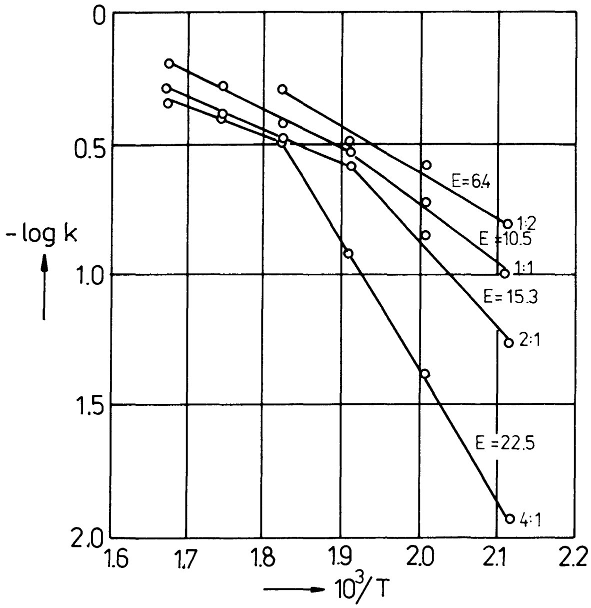

FIGURE 6.17 Changes in the apparent activation energy of CO oxidation in NiO catalysts as a function of reacting gas mixture composition [91].

on the doped samples and observing the changes in activation energy, one will be able to obtain valuable information concerning the mechanism of this reaction.

Much of this type of investigation was carried out with nickel oxide doped with the oxides of mono- (Li_2O) and tervalent (Fe_2O_3, Ga_2O_3, Cr_2O_3) oxides. According to the controlled valency principle of de Boer and Verwey (Section IV of Chapter 3), the incorporation of Li_2O into the NiO lattice occurs according to the reaction:

$$Li_2O + \frac{1}{2} O_2 \longrightarrow 2Li^{1}_{Ni} + 2O_0 + 2h^{\bullet} \qquad (6.43)$$

Increasing the concentration of positive holes $h^{\bullet}$ (and hence decreasing the concentration of free electrons e^-) is equivalent to shifting the Fermi level to the lower values and increasing the work function of the solid. The effect of Fe_2O_3 dopant is opposite. The incorporation of Fe_2O_3 into the NiO crystal lattice occurs with the consumption of positive holes, shifts the Fermi level to the higher values, and decreases the work function:

$$Fe_2O_3 + 2h^{\bullet} \longrightarrow 2Fe^{\bullet}_{Ni} + 2O_0 + \frac{1}{2} O_2 \qquad (6.44)$$

The experiments with doped nickel oxide catalysts and CO oxidation as the catalytic test reaction were carried out by several authors. However, the results obtained by them were not congruent. Parravano [94] and Keier et al. [95] observed that doping NiO with monovalent cations increased the apparent activation energy of catalytic CO oxidation while Cr_2O_3 and CeO_2 decreased. On the other hand, Schwab and Block [96] and Dry and Stone [86] found just the opposite. In addition, Herzog and Schlosser [85] did not observe any influence of doping NiO with Li_2O on the activation energy of CO oxidation.

Considering all these discrepancies, Bielański and Dereń undertook a more complete series of investigations, reviewed in [97], in which besides the catalytic experiments other physicochemical properties were also extensively studied. The NiO samples were obtained by the calcination of basic nickel carbonate impregnated with Li_2CO_3. Their homogeneity was checked by fractional dissolution in hydrochloric acid. The Li/Ni ratio was determined in the so obtained solutions.

It is seen in Fig. 6.18 that the specific surface area, lattice parameter, and magnetic susceptibility exhibit relatively sharp maxima corresponding to the concentration of lithium of about 0.1 at.% [98,99]. It has also been shown that the incorporation of small amounts of lithium up to 0.1 at.% occurs without simultaneous incorporation of the amount of excess oxygen corresponding to the stoichio-

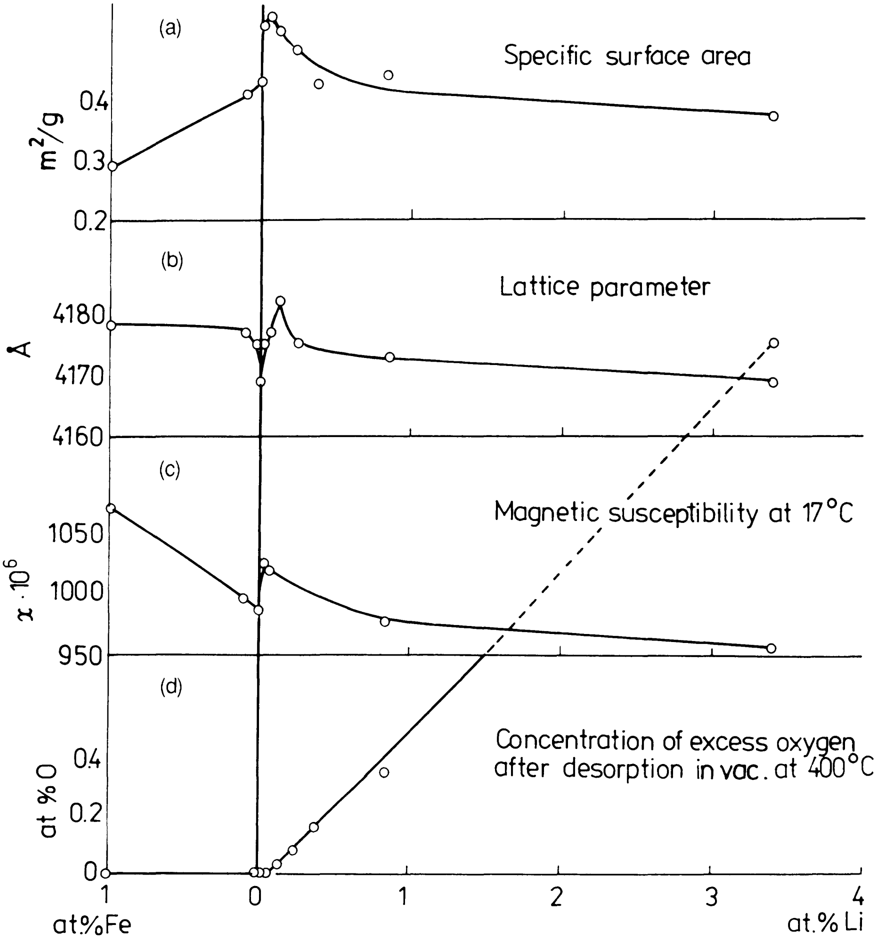

FIGURE 6.18 (a) Specific surface area; (b) lattice parameter; (c) magnetic susceptibility; and (d) concentration of excess oxygen of lithium-doped NiO catalysts. All values as the function of lithium concentration in the sample [98].

metry of reaction (6.43). The fact that in these samples the lattice parameter does increase with respect to the undoped NiO suggests that Li atoms are partially introduced into the interstitial positions. Such incorporation has been suggested to occur according to the equation [99]:

$$Li_2O \longrightarrow Li'_{Ni} + Li_i^{\bullet} + O_0 \qquad (6.45)$$

This kind of lithium incorporation is predominant at and below 0.1 at. % Li but at higher concentrations lithium was introduced with simultaneous incorporation of an appropriate amount of oxygen from the gas phase as indicated by Eq. (6.43).

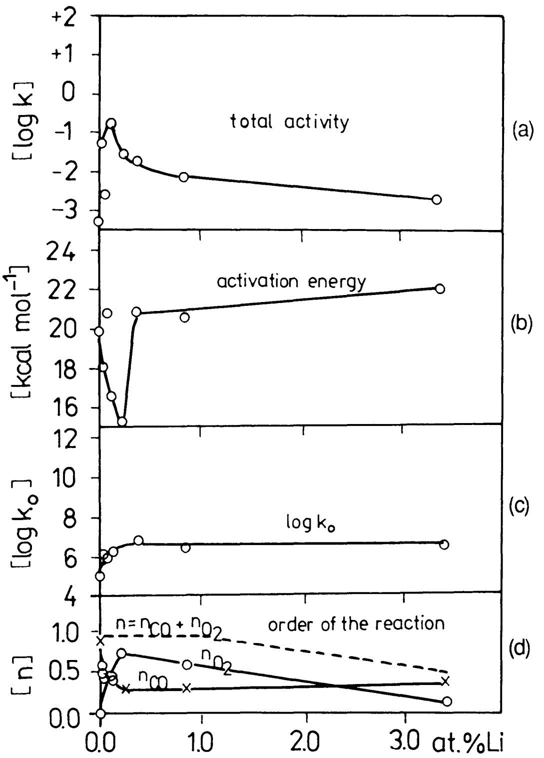

FIGURE 6.19 Catalytic oxidation of carbon monoxide on nickel oxide catalysts containing various additions of lithium oxide: (a) logarithm of the rate constant k corresponding to a temperature of 247°C; (b) apparent energy of activation; (c) logarithm of the preexponential factor k_0 [97].

Figure 6.19 shows that in analogy to the above described non-monotonous changes of lattice parameter, specific surface area, and magnetic susceptibility, the apparent activation energy and the catalytic activity also exhibit extrema at low lithium concentrations [97]. Analogous extrema in the catalytic properties were also observed on Li-doped monocrystal obtained by the Verneuil method [100]. Such behavior was rather unexpected and would be difficult to interpret on the basis of the electronic theory of chemisorption and catalysis if it would be assumed, as was done by earlier authors, that the position of the Fermi level in nickel oxide does change monotonously with the incorporation of lithium. However, the measurements of work function carried out by Dereń et al. [101,102] on the same series of samples proved that the real $Li_2O-NiO-O_2$ system is much more complicated than that. Figure 6.20 shows the dependence of work function on lithium concentration. Curve a corresponds to the measurements carried out in vacuum, curve b to those carried out in oxygen of 1 Torr. All the values are given with respect to the value for pure NiO measured in vacuum which has been assumed conventionally as equal to zero. It is seen that the shape of both curves is the same. The shift of curve b with respect to curve a shows that chemisorption of oxygen increased the work function. However, it did not change the dependence on the lithium concentration. In both cases small amounts of lithium increase work function, those greater than 0.1 at. % decreased it. The possible reasons for such behavior are discussed in [100]. The correlation between the changes in work function $\Delta\Phi$ and the changes of activation energy (with respect to the undoped sample) of the catalytic carbon monoxide ΔE_a postulated by the electronic theory of chemisorption and catalysis is therefore obvious. It can be better visualized by plotting $\Delta \underline{E_a}$ values as the function of $\Delta\Phi$. Quite a

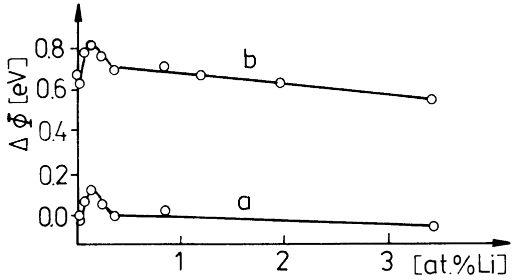

FIGURE 6.20 Changes in $\Delta\Phi$ value of lithium-doped NiO catalysts as the function of lithium concentration [97]: (a) in vacuo; (b) in oxygen (1 Torr).

good linear relation is then obtained (Fig. 6.21). It follows that the apparent activation energy does decrease with increasing work function and decreasing Fermi energy E_F since $\Delta\Phi = -\Delta E_F$. A reaction which is facilitated by a low-value Fermi level and hence a high concentration of positive holes $h^\bullet$ is a donor or p-type reaction according to the classification proposed by Wolkenstein [92]. In this case the rate-determining step must be accompanied by the consumption of positive holes $h^\bullet$. For example, it might be the following reaction:

$$CO_{(ads)} + O^-_{(ads)} + h^\bullet \longrightarrow CO_{2(g)} \qquad (6.46)$$

It should be observed here that the parallelism between the changes in activation energy was confirmed in the cases in which the reacting gas mixtures were either stoichiometric or contained an excess of oxygen. In such cases the dependence of E_a on lithium content exhibited a similar shape characterized by a minimum at about 0.1 at. % Li as is shown in Fig. 6.22. On the other hand, if the reacting gas mixture contained an excess of carbon monoxide, the apparent activation energy decreased monotonously with lithium concentration. Unfortunately, no work function data carried out at such conditions are available. The data shown in Fig. 6.21 clearly indicate that the effect of doping NiO with Li_2O on the catalytic

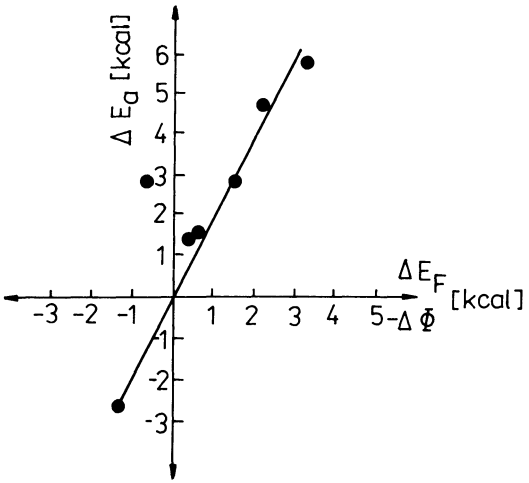

FIGURE 6.21 Apparent activation energy of carbon monoxide oxidation as the function of $\Delta\Phi$ value of lithium-doped NiO catalysts [97].

behavior may be different depending on the conditions of the catalytic experiments. This seems to be the source of already mentioned discrepancies in the results of different authors.

It should here be observed that very similar curves representing the dependence of the activity, the activation energy of CO oxidation, and the position of the Fermi level were also obtained for a series of lithium-doped cobaltous oxide [103,104]. Also in this case a linear dependence of $\Delta \underline{E}_a$ and $\Delta\Phi$ was obtained, indicating that the rate-determining step was a donor-type reaction.

C. Chromium Sequioxide

An extensive study of the oxidation of carbon monoxide oxidation over chromium sesquioxide catalyst was published by Kobayashi and Kobayashi [105–107]. These authors used the method of transient flow response already described in Section IV.B, much as they did in their investigation of MnO_2 catalyst. The chromium sesquioxide

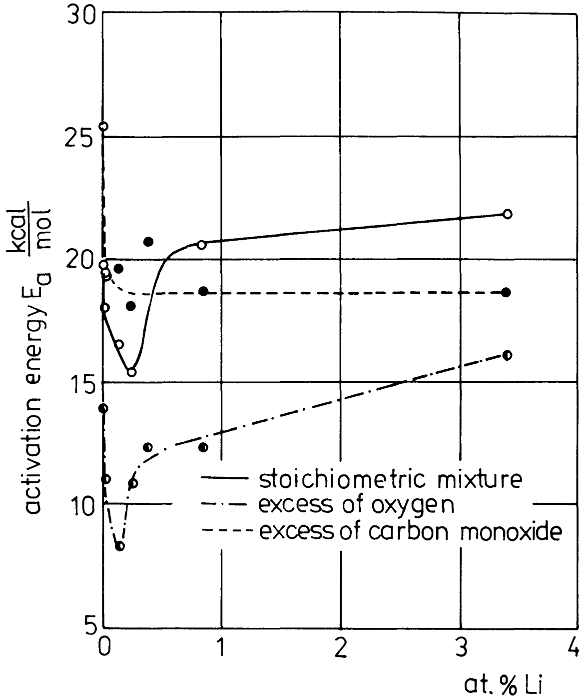

FIGURE 6.22 Apparent energy of activation of carbon monoxide oxidation in mixtures of various compositions.

used by them was α-Cr_2O_3 with a specific surface area of 21 $m^2\ g^{-1}$. The experiments were carried out with the oxidized (24 hr in a stream of air at 131°C) as well as with reduced (the treatment with 6% CO in nitrogen stream at 131°C until no CO_2 in the effluent was detected) catalyst samples. Two kinds of active oxygen were detected by iodometric method [108] on the oxygenated samples. Active oxygen atoms designated as O_s^h present in oxygen-saturated samples in the concentration of 3.3×10^{-5} mol g^{-1} exhibited a higher oxidation power and reacted faster with carbon monoxide, producing irreversibly bonded carbon dioxide. However, the latter could be displaced by oxygen from the gas phase. The second kind of active oxygen, the O_s^l species, was present in much higher concentration which in the oxygen-saturated samples reached the value of 1.17×10^{-4} mol g^{-1}. They reacted much more slowly with carbon monoxide and produced rapidly desorbing CO_2.

Based on information gained by the transient response method, Kobayashi and Kobayashi proposed a model of CO catalytic oxidation [107] in which the following assumptions were made:

1. There are two kinds of centers on which oxygen is chemisorbed on Cr_2O_3: S_I and S_{II}. Less numerous O^-S_I species exhibit higher oxidative power and S_I sites are always saturated with oxygen at the steady state of the catalytic reaction. Simultaneously O^-S_{II} species have lower oxidation power and are slowly regenerated. The concentration of O^-S_{II} species does decrease with the increasing pressure of CO.
2. Under steady reaction conditions both kinds of oxygen species react with CO at different rates.
3. CO_2 produced by the interaction of O^-S_{II} with CO is irreversibly adsorbed on S_I when oxygen is not present in the gas phase. On the other hand, in the presence of oxygen such CO_2 adsorbed molecules are quickly removed from the surface due to the competetive adsorption of oxygen on S_I. The desorption of CO_2 produced from O^-S_{II} is rapid and is not affected by the presence of oxygen in the gas phase. Under the steady state conditions of the reaction the amount of adsorbed CO_2 on S_{II} is negligible.

These assumptions led the authors to the formulation of two reaction paths:

Reaction path I:

$$CO_{(g)} + O^-S_I \xrightarrow{k_1} CO_2\cdot S_I + e^- \tag{6.47}$$

$$O_{2(g)} + 2CO_2\cdot S_I \xrightarrow{k_2} 2CO_{2(g)} + 2O^-S_I \tag{6.48}$$

Reaction path II:

$$CO_{(g)} + O^-\cdot S_{II} \xrightarrow{k_3} CO_2\cdot S_{II} + e^- \qquad (6.49)$$

$$CO_2\cdot S_{II} \xrightarrow{k_4} CO_{2(g)} + S_{II} \qquad (6.50)$$

$$O_{2(g)} + 2S_{II} + 2e^- \xrightarrow{k_5} 2O^-S_{II} \qquad (6.51)$$

A system of differential equations representing the rates of all these steps was proposed by the authors and then numerically solved with the help of a computer using the experimental data obtained from the transient response measurements. Such a procedure enabled the calculation of values of the rate constants of the particular steps in the above reaction scheme:

$k_1 = 4.15 \times 10^{-6}$ mol/g min atm

$k_2 = 1.75 \times 10^{-4}$ mol/g min atm

$k_3 = 1.2 \times 10^{-5}$ mol/g min atm

$k_4 = 3.21 \times 10^{-5}$ mol/g min

$k_5 = 4.8 \times 10^{-6}$ mol/g min atm

It is seen that k_2 is much larger than k_1 in accordance with the previous conclusion reached experimentally that the regeneration of $O^-\cdot S_I$ is rapid and $O^-\cdot S_I$ always contributes to the reaction. The slow regeneration of $O^-\cdot S_{II}$ during the steady state is also confirmed by the fact that k_5 is much smaller than k_3 and k_4.

Knowing the concentration of $O^-\cdot S_I$ and $O^-\cdot S_{II}$ at the steady state of reaction, the turnover numbers k' and k'' of both types of sites can be calculated:

$k_1 = 1.26 \times 10^{-1}$ min^{-1} atm^{-1}

$k_2 = 1.17 \times 10^{-1}$ min^{-1} atm^{-1}

thus showing the higher activity of S_I centers.

Knowing k_i values it was possible to numerically simulate the response data. The simulated curves agreed with the experimental points.

REFERENCES

1. R. L. Dekock and H. B. Gray, Chemical Structure and Bonding, Benjamin Cummings, Menlo Park, California, 1980, p. 256.
2. A. K. Holliday, G. Hughes, and S. M. Walker, in Comprehensive Inorganic Chemistry, Vol. 1 (J. C. Bailar, H. J. Emeleus, R. Nyholm, and A. F. Trottman-Dickenson, eds.), Pergamon Press, Oxford, 1973, p. 1225.
3. L. H. Little, Infrared Spectra of Adsorbed Species, Academic Press, New York, 1966, pp. 47–89.
4. G. Blyholder, J. Phys. Chem., 68, 2773 (1964).
5. R. P. Eischens and W. A. Pliskin, Adv. Catal., 10, 1 (1958).
6. S. R. Bare, P. Hofmann, and D. A. King, Surf. Sci., 144, 347 (1984).
7. A. M. Bradshaw and F. M. Hoffman, Surf. Sci., 72, 513 (1978).
8. H. Conrad, G. Ertl, and J. Küppers, Surf. Sci., 76, 323 (1978).
9. A. Crossley and D. A. King, Surf. Sci., 68, 528 (1977).
10. H. Conrad, G. Ertl, J. Koch, and E. E. Latta, Surf. Sci., 43, 462 (1974).
11. D. G. Castner, B. A. Sexton, and G. A. Somorjai, Surf. Sci., 71, 519 (1978).
12. T. Engel and G. Ertl, Adv. Catal., 28, 1 (1979).
13. J. C. Tracy and P. W. Palmber, J. Chem. Phys., 51, 4852 (1969).
14. G. Ertl and J. Koch, Z. Naturforsch., A25, 1906 (1970).
15. T. Engel, J. Chem. Phys., 69, 373 (1978).
16. C. T. Campbel, G. Ertl, H. Kuipers, and J. Segner, Surf. Sci., 107, 207 (1981).
17. G. Ertl, M. Neumann, and K. M. Streit, Surf. Sci., 64, 393 (1977).
18. P. J. Kisliuk, J. Phys. Chem. Solids, 3, 95 (1957); 5, 78 (1958).
19. T. Engel and G. Ertl, in The Chemical Physics of Solid Surfaces and Heterogeneous Catalysis, Vol. 4 (D. A. King and D. P. Woodruff, eds.), Elsevier, New York, 1982, p. 73.
20. E. M. Stuve and R. J. Madix, Surf. Sci., 146, 155 (1984).

21. N. Van Hieu and J. H. Craig, Jr., Surf. Sci., 145, L493 (1984).
22. T. Engel and G. Ertl, J. Chem. Phys., 69, 1267 (1978).
23. H. Conrad, G. Ertl, J. Küppers, and E. E. Latta, Surf. Sci., 57, 475 (1976).
24. R. J. Behm, P. A. Thiel, P. R. Norton, and P. E. Bindner, Surf. Sci., 147, 143 (1984).
25. T. Matsushima, D. B. Almy, and J. M. White, Surf. Sci., 67, 89 (1977).
26. A. Golchet and J. M. White, J. Catal., 53, 266 (1978).
27. H. P. Bonzel and R. Ku, J. Vac. Sci. Technol., 9, 663 (1972).
28. N. Pacia, A. Cassuto, A. Pentenero, and B. Weber, J. Catal., 41, 455 (1976).
29. J. L. Taylor, D. E. Ibbotson, and W. H. Weinberg, J. Catal., 62, 1 (1980).
30. T. E. Madey, H. A. Engelhardt, and D. Menzel, Surf. Sci., 48, 304 (1978).
31. H. P. Bonzel and R. Ku, Surf. Sci., 40, 85 (1973); 33, 91 (1972).
32. H. P. Bonzel and J. J. Burton, Surf. Sci., 52, 223 (1975).
33. M. Boudart and G. Djega-Mariadassou, Kinetics of Heterogeneous Catalytic Reactions, Princeton University Press, 1984, p. 155.
34. G. Ertl and J. Koch, Proc. 5th Int. Congress of Catalysis, Miami Beach, 1972, J. E. Hightower (ed.), Elsevier, New York, 1973, pp. 67–96.
35. S. Ladas, H. Poppa, and M. Boudart, Surf. Sci., 102, 151 (1981).
36. T. Engel, J. Chem. Phys., 69, 373 (1978).
37. N. W. Cant, P. C. Hicks, and B. S. Lennon, J. Catal., 54, 372 (1978).
38. L. H. Little and C. H. Amberg, Can. J. Chem., 40, 1997 (1962).
39. O. V. Krylov and V. P. Kiselev, Adsorptsya i kataliz na perekhodnykh metallakh i ikh oksidakh (Adsorption and Catalysis on Transition Metals and their Oxides), Khimia, Moscow, 1981.
40. J. H. Taylor and C. H. Amberg, Can. J. Chem., 39, 535 (1961).
41. P. Politzer and S. Kasten, Surf. Sci., 36, 186 (1973).
42. R. A. Gardner and R. H. Petrucci, J. Phys. Chem., 1376 (1963).
43. E. A. Colburn and W. C. Mackrodt, Surf. Sci., 143, 391 (1984).
44. M. Courtois and S. J. Teichner, J. Chim. Phys., 272 (1962).
45. S. Z. Rogniskii, V. A. Seleznev, and A. A. Kadushin, Zh. Fiz. Khim. (USSR), 43, 1075 (1969).
46. V. A. Matushak, A. A. Kadushin, and O. V. Krylov, Izv. Akad. Nauk USSR, Ser. Khim., 2677 (1977).
47. J. A. Goodsel, J. Catal., 30, 175 (1975).

48. E. Guglielminotti, S. Coluccia, S. Garrone, I. Cerutti, and A. Zecchina, J. Chem. Soc. Faraday I, 75, 96 (1979).
49. D. Cordischi, V. Indovina, and M. Occhiuzzi, J. Chem. Soc. Faraday I, 76, 1147 (1980).
50. A. Zecchina, G. Spoto, S. Coluccia, and E. Guglielminotti, J. Phys. Chem., 88, 2575 (1984).
51. A. Zecchina, G. Spoto, S. Coluccia, and E. Guglielminotti, J. Phys. Chem., 88, 1582 (1984).
52. A. Zecchina, G. Spoto, S. Coluccia, and E. Guglielminotti, J. Phys. Chem., 88, 2587 (1984).
53. A. Zecchina, G. Spoto, S. Coluccia, and E. Guglielminotti, J. Chem. Soc. Faraday I, 80, 1975 (1984).
54. A. B. Lamb, W. C. Frazer, and J. C. Frazer, Ind. Eng. Chem., 12, 213 (1920).
55. M. Katz, Adv. Catal., 5, 177 (1953).
56. F. S. Stone, Adv. Catal., 13, 1 (1962).
57. W. E. Garner, T. J. Gray, and F. S. Stone, Disc. Faraday Soc., 8, 246 (1950).
58. W. E. Garner, T. J. Gray, and F. S. Stone, Proc. Royal Soc. (London), A211, 472 (1952).
59. R. M. Dell and F. S. Stone, Trans. Faraday Soc., 50, 50 (1954).
60. R. Rudham and F. S. Stone, in Chemisorption, Proc. Chem. Soc. Symposium, 1956 (E. W. Garner, ed.), Academic Press, New York, 1957, p. 205.
61. P. C. Gravelle and S. J. Teichner, Adv. Catal., 20, 167 (1969).
62. S. Z. Roginsky and Y. Zeldovich, Acta Physicochem. USSR, 1, 554, 545 (1934).
63. C. S. Brooks, J. Catal., 8, 272 (1967).
64. K. Klier and K. Kuchynka, J. Catal., 6, 62 (1966).
65. M. Kobayashi and H. Kobayashi, J. Catal., 27, 100 (1972).
66. M. Kobayashi and H. Kobayashi, J. Catal., 27, 108 (1972).
67. M. Kobayashi and H. Kobayashi, J. Catal., 27, 114 (1972).
68. M. Kobayashi, H. Matsumoto, and H. Kobayashi, J. Catal., 21, 48 (1971).
69. A. A. Davydov, Y. M. Shchekochikhin, and N. P. Keier, Kinet. Katal., 11, 1230 (1970).
70. G. Rienacker and E. Scheve, Z. Anorg. Allg. Chem., 330, 18 (1964).
71. G. K. Boreskov and V. I. Marshneva, Doklady Akad. Nauk USSR, 213, 112 (1973).
72. G. K. Boreskov and V. I. Marshneva, Doklady Akad. Nauk USSR, 199, 1091 (1971).
73. G. K. Boreskov, Adv. Catal., 15, 285 (1964).

74. T. Chitani, S. Nakata, and A. Kanome, *Bull. Chem. Soc. Jpn.*, *17*, 288 (1942); Chem. Abstr. *2974*, 4366 (1947).
75. C. M. Karpacheva and A. M. Rozen, *Doklady Akad. Nauk USSR*, *68*, 1057 (1949).
76. F. M. Vainstein and G. J. Turovskii, *Doklady Akad. Nauk USSR*, *72*, 297 (1950).
77. G. J. Turovskii and F. M. Vainstein, *Doklady Akad. Nauk USSR*, *79*, 1173 (1951).
78. W. A. Roiter, *Actes du deuxieme Congr. Int. de Catalyse, Paris 1960*, Vol. 1, Technip, Paris, 1961, p. 759.
79. E. R. S. Winter, *Adv. Catal.*, *10*, 196 (1958).
80. Y. Takasu, M. Matsui, H. Tamura, S. Kawamura, Y. Matsuda, and I. Togoshima, *J. Catal.*, *69*, 5 (1981).
81. Y. Takasu, M. Matsui, and Y. Matsuda, *J. Catal.*, *76*, 6 (1982).
82. Y. Takasu, T. Yoko-o, M. Matsui, Y. Matsuda, and I. Togoshima, *J. Catal.*, *77*, 485 (1982).
83. G. Parravano, *J. Am. Chem. Soc.*, *75*, 1348 (1953).
84. K. Hauffe, *Adv. Catal.*, *7*, 232 (1955).
85. W. Herzog and E. G. Schlosser, *Ber. Bunsenges Physik. Chem.*, *71*, 344 (1967).
86. M. E. Dry and F. S. Stone, *Disc. Faraday Soc.*, *28*, 192 (1959).
87. A. Bielański and R. Dziembaj, *Bull. Pol. Ac. Chem.*, *16*, 269 (1968).
88. G. M. Schwab and J. Block, *Z. Physik. Chem. N. F.*, *1*, 42 (1954).
89. E. G. Schlosser, *Ber. Bunsenges Physik. Chem.*, *71*, 352 (1967).
90. T. J. Gray and P. W. Darby, *J. Phys. Chem.*, *60*, 209 (1956).
91. A. Bielański, J. Dereń, J. Haber, and J. Sloczyński, *Z. Physik. Chem. N. F.*, *24*, 345 (1960).
92. Th. Wolkenstein, *Physico-chimie de la Surface des Semiconducteurs*, Editions Mir, Moscow, 1977, p. 171.
93. Th. Wolkenstein, *Adv. Catal.*, *12*, 189 (1960).
94. G. Parravano, *J. Am. Chem. Soc.*, *75*, 1452 (1953).
95. N. P. Keier, S. Z. Roginskii, and I. S. Sazonova, *Doklady Akad. Nauk USSR*, *106*, 859 (1956).
96. G. M. Schwab and J. Block, *J. Chim. Phys.*, *51*, 664 (1954).
97. A. Bielański and J. Dereń, *Symposium on Electronic Phenomena in Chemisorption and Catalysis on Semiconductors* (K. Hauffe and Th. Wolkenstein, eds.), Walter de Gruyter, 1969, p. 149.
98. A. Bielański, K. Dyrek, and Z. Kluz, *Bull. Pol. Ac. Chem.*, *13*, 285 (1965).
99. A. Bielański, K. Dyrek, Z. Kluz, J. Sloczyński, and T. Tobiasz, *Bull. Pol. Ac. Chem.*, *12*, 657 (1964).

100. J. Dereń, Z. Guzik, and J. Sloczyński, Bull. Pol. Ac. Chem., 20, 361 (1972).
101. J. Dereń, J. Nowotny, and J. Ziólkowski, Bull. Pol. Ac. Chem., 16, 45 (1968).
102. J. Dereń and J. Nowotny, Bull. Pol. Ac. Chem., 15, 115 (1967).
103. A. Bielański and Z. Kluz, Bull. Pol. Ac. Chem., 20, 597 (1972).
104. A. Bielański, J. Dereń, R. Dziembaj, Z. Kluz, and J. Nowotny, Bull. Pol. Ac. Chem., 20, 587 (1972).
105. M. Kobayashi and H. Kobayashi, Bull. Chem. Soc. Jpn., 49, 3009 (1976).
106. M. Kobayashi, T. Date, and H. Kobayashi, Bull. Chem. Soc. Jpn., 49, 3014 (1976).
107. M. Kobayashi and H. Kobayashi, Bull. Chem. Soc. Jpn., 49, 3018 (1976).
108. M. Kobayashi and H. Kobayashi, J. Catal., 27, 100 (1972).
109. A. Zecchina, S. Coluccia, E. Guglielminotti, and G. Chiotti, J. Phys. Chem., 75, 2774, 2790 (1971).

7

Oxidation of Aliphatic Hydrocarbons

I. INTRODUCTION

Reactions of the catalytic oxidation of hydrocarbons have been extensively studied [1—8] because of their great importance for the development of the chemical industry. The introduction of bismuth molybdate as catalyst for the selective oxidation of propene to acrolein by Veatch and Callahan and the development of the synthesis of acrylonitrile by ammoxidation of propene on this catalyst may be considered milestones in the history of modern petrochemistry. However, some older catalytic processes, such as production of phthalic anhydride, have also been intensively studied because, although they have been operated in industry for almost 70 years, their mechanism is not yet fully understood and considerable improvement in their catalytic performance may still be expected. Selective oxidation of particular functional groups in complex organic molecules opens new perspectives on the cheaper and wasteless production of many important chemicals. Today catalytic oxidation is the basis of the production of almost all monomers used in the manufacturing of synthetic fibers, plastics, and many other products (Table 7.1). With the increasing cost of energy and the shrinking supply of cheap hydrocarbons, much effort is now being expended on the development of new oxidation processes of higher selectivity and lower energy consumption. Substitution of dehydrogenation by oxidative processes as in the production of styrene from ethylbenzene and selective oxidation of paraffins can be quoted as an example.

TABLE 7.1 Important Industrial Oxidation Processes

Product	Reaction	Catalyst	Company
Maleic anhydride	$C_6H_6 + O_2$	$V_2O_5-MoO_3/Al_2O_3$	Halcon
Terephthalic acid	p-Xylene + O_2	$CoBr_2$	Halcon/Amoco
Acetaldehyde	$C_2H_4 + O_2$	$PdCl_2/C$	Wacker/Hoechst
Acrylonitrile	$C_3H_6 + O_2$	$Bi_2O_3-MoO_3-P_2O_5/Al_2O_3$	SOHIO
Vinylacetate	$C_2H_4 + CH_3COOH + O_2$	$PdCl_2/C$	Bayer, Celanese
Phthalic anhydride	o-Xylene + O_2	V_2O_5/TiO_2	BASF
Ethylene oxide	$C_2H_4 + O_2$	Ag	UCC, Shell, Halcon
Maleic anhydride	$C_4H_8 + O_2$	$V_2O_5-P_2O_5$	Amoco, Monsanto, Halcon
Aerolein	$C_3H_6 + O_2$	$Bi_2(MoO_4)_3/Al_2O_3$	SOHIO
Acrylonitrile	$C_3H_6 + NH_3 + O_2$	Oxides of Ni, Co, Fe, Bi, Mo, K, Mn, Si	SOHIO
Hydrogen cyanide	$CH_4 + NH_3 + O_2$	Pt, Rh	Degussa
Ethylene glycol	$C_2H_4 + O_2 + CH_3COOH$	TeO_2	Halcon
Formaldehyde	$CH_3OH + O_2$	$Fe_2(MoO_4)_3$	ICI

Source: Adapted from Ref. 9.

II. OXIDATION OF ETHYLENE

A. Introduction

Selective oxidation of ethylene to ethylene oxide in the gas phase is one of the major petrochemical processes because of the importance of ethylene oxide as the most versatile chemical intermediate. It is converted by thermal hydration into a mixture of glycols used in the manufacturing of artificial fibers and plastics and as freezing point depressants in cooling systems of motor cars. Polyglycols found many applications in cosmetic and pharmaceutical industries, the printing industry, and the textile industry as spinning lubricants and antifoam agents. Ethylene oxide readily reacts with ammonia to produce ethanolamines, used in fabrication of cosmetics. Reactions of ethylene oxide with alcohols produce glycol ethers, which are widely applied as high boiling solvents in processes of coating as well as components in hydraulic and brake fluids. Another important application of ethylene oxide is its use as an ethoxylation agent of long chain alcohols and alkylphenols to obtain surface active compounds for the detergent industry. The distribution of ethylene oxide utilization in EC countries and its world production is shown in Table 7.2 [10].

Oxidation of ethylene with gas phase oxygen may proceed along three different pathways:

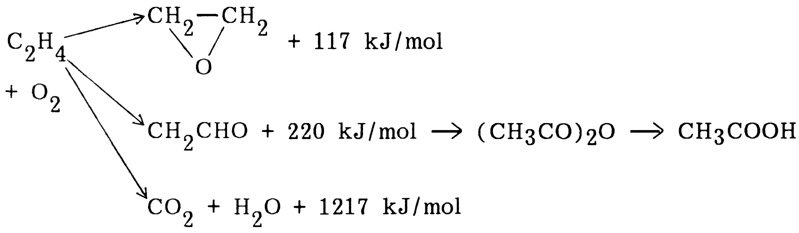

(7.1)

(7.2)

(7.3)

Reactions along these pathways are accelerated by different metals [11]. The most important metals for the selective oxidation by route 2 are Pd and Ir. The selectivity for products along this route decreases with increasing temperature, decreasing oxygen pressure, and can be modified by alloying Pd. As an example, Fig. 7.1 shows the dependence of selectivity to acetaldehyde as a function of the composition of the Pd-Au alloy [12]. It can be seen that a sharp maximum appears at a concentration of about 20% of Pd in Au. It has been suggested that total oxidation starts with a deep dehydrogenation of ethylene. Such dissociative adsorption of ethylene is inhibited by alloying Pd with Au, the latter interacting with hydrogen only very weakly.

TABLE 7.2 Distribution of Ethylene Oxide Utilization (%) in EEC Countries

	1960	1970	1980
Ethylene glycols	46.5	52	55
Polyglycols	6	4	4
Ethanolamines	12.5	8.5	7
Glycol ethers	15.3	13.5	12
Surface active agents	14.5	13	12
Polyols	—	3	4
Others	7	6	6
Worldwide ethylene oxide production in millions tons/year	1.4	4.0	5.8

Source: Ref. 10.

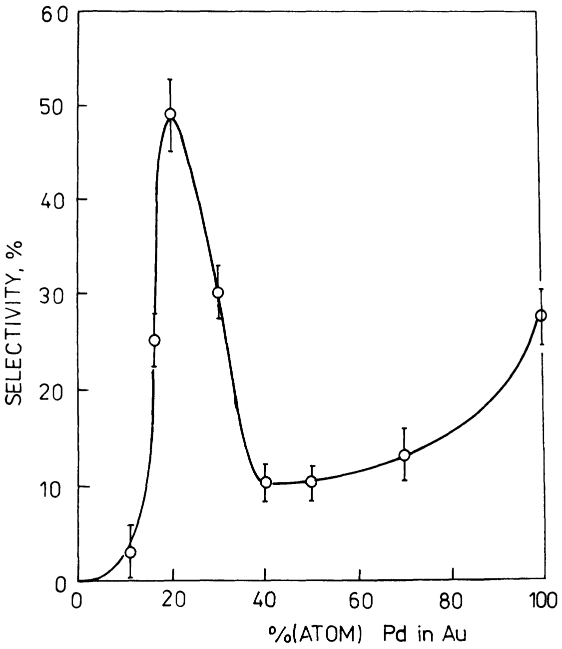

FIGURE 7.1 Selectivity of the oxidation of ethylene to acetaldehyde as a function of the composition of the Pd–Au catalyst [12].

The only metal which has been found to effectively catalyze the reaction along pathway 1 is Ag. The question of why silver is so unique remains one of the most puzzling questions of catalysis by metals, although many attempts have been undertaken to answer it [13]. One of the explanations may lie in the very peculiar behavior of silver in its interaction with oxygen.

B. Adsorption of Oxygen on Silver

The adsorption of oxygen on silver has received by far the most extensive treatment in the literature [14]. Numerous experimental methods and techniques of surface science have been employed in these studies, which have been carried out with silver monocrystals, films, powder, and clusters supported on different carriers.

Many experimental data indicate that three types of oxygen sorbed at the surface of silver may be distinguished. As an example, Fig. 7.2 shows the calorimetrically determined heat of adsorption of oxygen on silver as a function of oxygen coverage [15]. The curve reveals two breaks thereby suggesting three adsorbed oxygen species. The existence of three kinetically distinguishable oxygen adsorption processes with activation energies of < 10, 33, and 60 kJ/mol, respectively, was confirmed by Kilty et al. [16]. Chlorine may be used to selectively poison the different centers of oxygen adsorption, as illustrated in Fig. 7.3. At the temperature of the

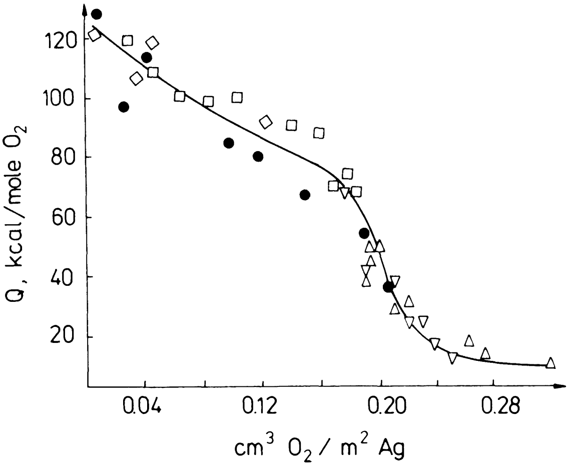

FIGURE 7.2 Heat of adsorption of oxygen on silver as a function of the coverage [15].

experiment (373 K), adsorption of 3×10^{18} atoms of chlorine per m^2 on the surface of silver containing 1.2×10^{19} Ag atoms/m^2 completely stopped the fast oxygen adsorption of low activation energy, each Cl atom blocking adsorption of one oxygen atom. The authors thus concluded that the fast adsorption characterized by a low activation energy of less than 10 kJ/mol is dissociative and requires adsorption sites consisting of four silver surface atoms. At the same time a second oxygen adsorption process proceeds practically unaffected. Only when more than 3×10^{18} chlorine atoms/m^2 have been adsorbed at the surface of silver does this second process (activation energy = 33 kJ mol^{-1}) become inhibited, with each Cl atom blocking adsorption of two oxygen atoms. Apparently, in this case O_2 molecules are adsorbed nondissociatively. Positive evidence of molecular oxygen adsorption was provided by Clarkson and Cirillo [17] who detected the EPR signal of O_2^- species after adsorption of oxygen on silver, and by Tanaka and Yamashima [18] who observed the signal of superoxide ion on silver oxide. Such a signal was also registered by Shimizu et al. [19] after adsorption of oxygen on silica-supported silver, but the signal was absent upon adsorbing N_2O instead of O_2. Three peaks appeared in the photoelectron spectra after adsorption

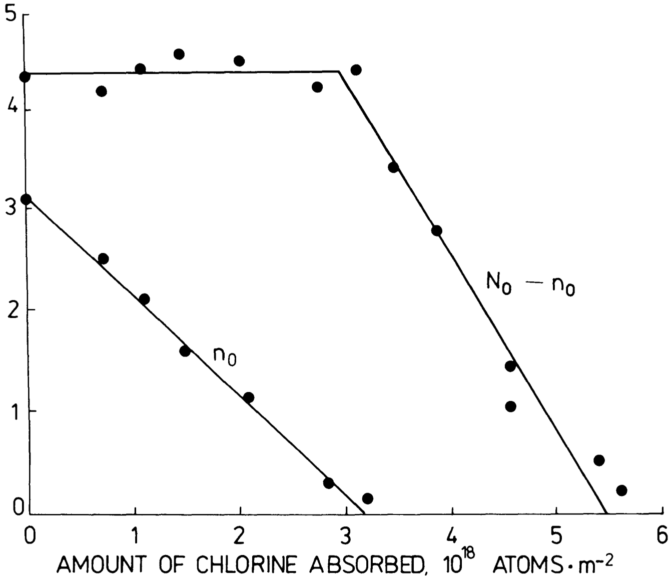

FIGURE 7.3 Correlation between the amount of chlorine preadsorbed and the amounts of oxygen subsequently adsorbed at 373 K by fast process ($\underline{n}_0$) and by an activated process ($\underline{N}_0 - \underline{n}_0$) [16].

of oxygen on silver foils [20], two of which were due to atomic oxygen while the third could be assigned to a molecular species, its intensity increasing in the presence of chlorine.

More information on the nature of the adsorbed oxygen species was quite recently obtained by Backx et al. [21] from studies with EELS. Figure 7.4 shows the electron energy loss spectra of the (110) plane of silver after adsorption of oxygen. At −160°C two peaks appear: at 30 meV (242 cm^{-1}) and 78 meV (629 cm^{-1}), which

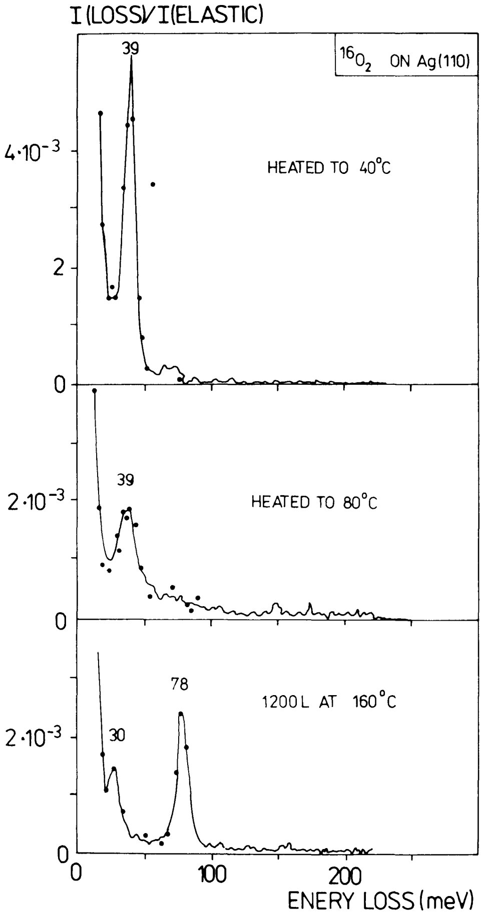

FIGURE 7.4 EELS spectra of the (110) plane of silver exposed to 1200 L $^{16}O_2$ at −160°C and after subsequent heating to −80 and 40°C. Electron beam energy 2.4 eV [21].

can be assigned to the O_2—Ag and O—O vibrations, respectively. When a mixture of $^{16}O_2$ and $^{18}O_2$ is adsorbed the desorbate does not contain the $^{16}O^{18}O$ molecules. After heating to −80°C the diatomic oxygen dissociates. However, as oxygen after dissociation into atoms requires more sites for adsorption than in its molecular form, partial desorption of dioxygen take place. The peaks of molecular oxygen disappear and a peak at 39 meV (314 cm^{-1}) appears instead assigned to a vibration normal to the surface of an oxygen atom linked to four silver atoms. Upon further heating, a desorption peak is observed at 583 K, from which the activation energy of 150 kJ mol^{-1} can be estimated. LEED studies reveal that this oxygen forms ordered superstructures. When all oxygen detectable by LEED and HREELS has been removed from the surface and the sample exposed to another isotope of oxygen (e.g., $^{18}O_2$ when the first adsorption was carried out with $^{16}O_2$), the subsequent desorbate contained significant quantities of $^{16}O^{18}O$ which indicates that part of the oxygen from the first experiment remained in the sample, albeit not at the surface. It has been identified as oxygen dissolved in the subsurface region, the existence of this region playing an important role in catalytic behavior of silver.

C. Ethylene-Oxygen Interaction at the Surface of Silver

It is generally accepted that ethylene is not adsorbed on reduced metallic silver [22,23], but its adsorption was observed after preadsorption of oxygen [24] or chlorine [25]. Force and Bell [26] demonstrated by infrared spectroscopy that on oxygenated silver surface ethylene adsorbs as π-complex, without the C=C bond rupture, and assumed that Ag^+ ions are the adsorption sites:

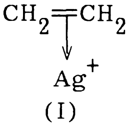

$CH_2{=}CH_2 \rightarrow Ag^+$

(I)

The related coordination of ethylene with Ag^+ ions was reported earlier [27]. Later the interaction of C_2H_4 with Ag (110) face precovered with adsorbed oxygen has been studied [28]. Adsorption of C_2H_4 was found to be promoted by the presence of monoatomic oxygen. No significant shift of the C—H stretch or bending vibrations was observed, indicating that no significant rehybridization has taken place. Thus, it was concluded that the molecule is adsorbed with the molecular plane parallel to the surface. The vibration of the oxygen atoms is not influenced which confirms the conclusion that ethylene is adsorbed on silver atoms carrying a positive charge induced by adsorbed oxygen atoms. This ethylene complex is desorbed at 170 K without reaction, which becomes observed after heating the oxygen-covered surface in ethylene to 320 K. Atomic oxygen EELS peak disappears while a carbonate-like surface complex is formed. This is consistent with the observation that ethylene is adsorbed on the oxygenated surface in part reversibly and in part irreversibly [22]. The amount of reversibly adsorbed ethylene decreases with increasing temperature, whereas the amount of irreversibly adsorbed ethylene increased with temperature.

Infrared studies of the interaction of oxygen and ethylene with Ag—SiO_2 showed that on exposing the catalyst first to O_2 and then to ethylene at 363 K, an adsorption band appeared at 870 cm^{-1}, interpreted as the O—O vibration in the organic peroxide species $CH_2—CH_2—O—OAg$ [29]. Heating the sample to 383 K resulted in a new IR spectrum identical to that obtained when ethylene oxide was adsorbed on a reduced silver surface. When using an equilibrated mixture of $^{16}O_2 + {}^{16}O^{18}O + {}^{18}O_2$, three bands were observed at 870, 859, and 848 cm^{-1} confirming that the 870 cm^{-1} band is due to an O—O vibration [16]. A nonequilibrated gaseous mixture of $^{16}O_2 + {}^{18}O_2$ gave rise to only two bands at 870 and 848 cm^{-1}, which proved that the two oxygen atoms in adsorbed peroxide species originate from the same gaseous O_2 molecule. However, when oxygen was adsorbed above 433 K, subsequent admission of ethylene at lower temperatures generated three bands, indicating that above 433 K dissociation of molecular oxygen took place at the surface, resulting in equilibration of the $^{18}O_2 + {}^{16}O_2$ mixture.

Interpretation of IR spectra led to proposals [26] of the following structures for adsorbed ethylene oxide:

In the absence of oxygen

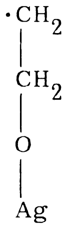

(II)

and

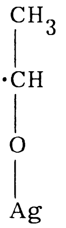

(III)

Coadsorbed with oxygen

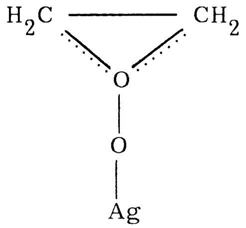

(IV)

Ethylene oxide is adsorbed more strongly than ethylene, the activation of the latter being thus inhibited.

IR spectra indicate also that CO_2 adsorbs in the form of three species, one with the molecule parallel to the surface attached to a silver atom and two others of the carbonate type:

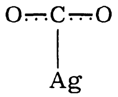

(V)

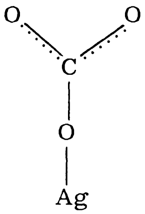

(VI)

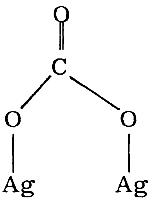

(VII)

D. Kinetics of Ethylene Oxidation

In the oxidation of ethylene on silver the only by-products besides ethylene oxide are carbon dioxide and water. They are formed in three stoichiometric reactions:

$$C_2H_4 + 1/2\ O_2 \longrightarrow C_2H_4O \qquad \Delta H^o = -117\ \text{kJ/mol},\ \ \Delta G^o = -50.6\ \text{kJ/mol} \tag{7.1}$$

$$C_2H_4 + 3O_2 \longrightarrow 2CO_2 + 2H_2O \qquad \Delta H^o = -1217\ \text{kJ/mol},\ \ \Delta G^o = -1249\ \text{kJ/mol} \tag{7.2}$$

$$C_2H_4O + 2\ 1/2O_2 \longrightarrow 2CO_2 + 2H_2O \qquad \Delta H^o = -1334\ \text{kJ/mol},\ \ \Delta G^o = -1294\ \text{kJ/mol} \tag{7.3}$$

The chemical equilibrium strongly favors the formation of total oxidation products. Therefore, the reason that ethylene oxide is not further oxidized is purely kinetic.

It is now generally accepted [30] that the kinetics of ethylene oxidation on silver can be described by a triangular scheme:

$$\begin{tikzcd}
C_2H_4 \arrow[rr, "+\ 1/2\ O_2", "r_1"'] \arrow[dr, "+\ 3O_2"', "r_2"] & & C_2H_4O \arrow[dl, "r_3"', "+\ 2\ 1/2\ O_2"] \\
& 2(CO_2 + H_2O) &
\end{tikzcd}$$

On a good industrial catalyst the ratio of the rates can be $r_1/r_2 \sim 6$ and $r_2/r_3 \sim 2.5$. They strongly depend on the catalyst and reaction conditions.

The rates of the two parallel reactions of ethylene may be expressed by the following equations:

$$r_1 = k_1 P_{C_2H_4}^{m_1} P_{O_2}^{n_1}$$

$$r_2 = k_2 P_{C_2H_4}^{m_2} P_{O_2}^{n_2}$$

The published values of parameters m and n of these equations are scattered in the very wide range between 0 and 1. Figure 7.5 shows the initial rate r_1 of ethylene oxide formation as a function of oxygen partial pressure [31]. It may be seen that $n_1 = 1$ at low oxygen pressure but becomes 0 at higher pressures. Also the dependence of the rate r_1 on ethylene pressure is not linear, deviating at higher pressures. Similar changes of the reaction order were observed for the rate of total oxidation r_2.

Many authors [26,32,33] found that the activation energies of the two reaction pathways r_1 and r_2 are equal. This may indicate that the two reactions have the same rate-determining step. Oxidation of ethylene is inhibited by the adsorption of ethylene oxide as the reaction product, but there are conflicting results as to the effect of adding ethylene oxide to the reaction mixture on the selectivity of the reaction. The rate equations accounting for the effects of temperature and partial pressures of the reactants, products, inhibitors, and paraffin hydrocarbons used in the design of reactors are proprietary information of the companies and are not published.

At this point interesting experiments should be mentioned [34] in which ethylene was oxidized with N_2O on silver as catalyst. No ethylene oxide was formed, whereas after replacing N_2O with O_2 high selectivity to epoxidation was observed. At higher temperatures, where the decomposition of N_2O into O_2 and N_2 becomes important, small amounts of ethylene oxide were formed. These observations confirm the conclusions drawn from spectroscopic studies that dioxygen molecules are responsible for epoxidation of ethylene on silver. This conclusion was corroborated [35] by the results of the oxidation of ethylene in the absence of gaseous O_2, using silver oxides Ag_2O and Ag_2O_2 as oxidants. When Ag_2O_2 was used, considerable amounts of ethylene oxide appeared in the initial oxidation products, whereas with Ag_2O initially no ethylene oxide was formed. Results of pulse experiments [36] with $Ag/\alpha\text{-}Al_2O_3$ were also reported, in which high amounts of ethylene oxide were observed on injecting pulses of ethylene after pulses of oxygen, but no ethylene oxide was formed on reversing the sequence of pulses. When deuterated ethylene is used [37] in the oxidation reaction, the pathway to epoxidation is enhanced in comparison with that of C_2H_4, whereas the pathway to the total oxidation product is hindered, resulting in a considerable increase of the selectivity to ethylene oxide. This would be consistent with the hypothesis that diatomic oxygen leads to ethylene oxide and monoatomic oxygen to $CO_2 + H_2O$ if reaction of dioxygen were faster with C_2D_4 than with C_2H_4. Unfortunately, the observed isotope effect is large, whereas no carbon-hydrogen bonds are broken in epoxidation, which makes the interpretation unconvincing.

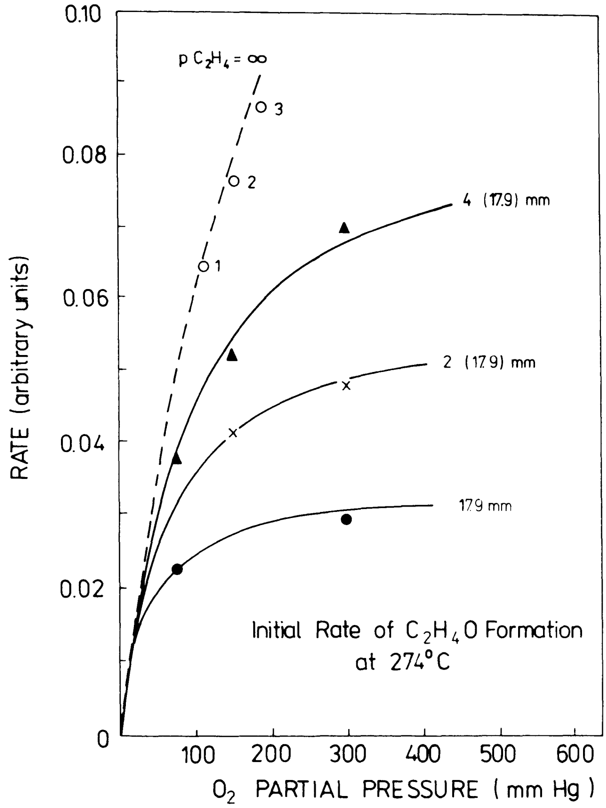

FIGURE 7.5 Initial rate of ethylene oxide formation as a function of oxygen partial pressure at different ethylene partial pressures [31].

The complex and extensive experimental data on ethylene oxidation on silver were recently summarized [38] in a reaction network shown in Fig. 7.6. Reaction (a) represents the formation of an oxygen-deficient, subsurface oxide film, which seems to be an essential element of the silver catalyst surface. The concentration of defects in this layer may be modified by incorporation of chloride ions on exposure of the silver catalyst to chlorine (b) or chlorinated hydrocarbons. Oxygen is then adsorbed on silver atoms forming the outermost surface layer over the subsurface oxide layer (c). The existence of the latter as well as the presence of surface and subsurface chloride ions will inhibit the dissociative adsorption.

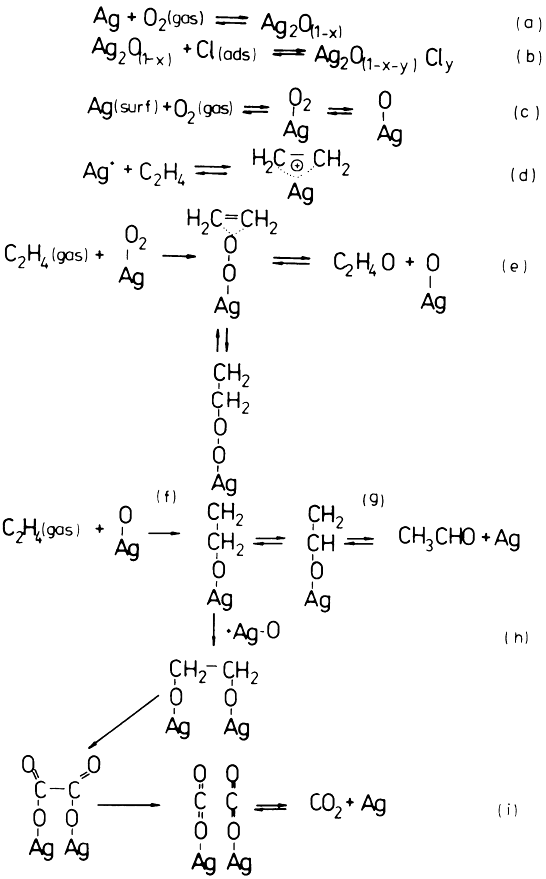

FIGURE 7.6 Mechanism of the interaction of silver surface with oxygen and ethylene [38].

Ethylene is reversibly adsorbed on Ag^+ (d) ions or irreversibly adsorbed on the two types of adsorbed oxygen species: molecular and atomic (reactions e and f). Reaction e leads to the formation of peroxo intermediate which then decomposes giving off ethylene oxide and leaving the surface covered with adsorbed atomic oxygen species. These react with gaseous ethylene (reaction f) to form adsorbed alcoxy radicals, which either isomerize and desorb as acetaldehyde (reaction g) or interact with another adsorbed oxygen atom to form glycoxide intermediate (reaction h), which further oxidizes to the products of total combustion (reaction i).

E. Manufacturing Processes

The large-scale operation of the oxidation of ethylene over a silver catalyst requires a very strict control of reaction conditions so that while maintaining an adequate production rate the formation of wasteful CO_2 and H_2O becomes as limited as possible. A compromise must be found between several contradictory requirements. The flammable limit of ethylene in air is about 3%. Above that concentration oxygen must be limited to a relatively low concentration, depending on pressure, temperature, and gas composition. On the other hand, the higher the oxygen partial pressure the better is the probability of ethylene oxide formation, so that considerations of how close one should approach the dangerous flammable limit involve balancing safety with the benefits in productivity.

As ethylene oxide is the intermediate compound in the series of consecutive steps in the oxidation of ethylene to carbon dioxide and water, the selectivity of its formation decreases as conversion of ethylene is increased by raising temperature or contact time. Thus a low conversion per pass of ethylene is required to attain high enough selectivities. However, the relatively high cost of ethylene dictates the need for its overall conversion greater than 85–90%, which may be attained by recycling a large fraction of the reactor effluent after scrubbing to remove ethylene oxide. Nitrogen accumulates in the recycle gas and must be purged, but the purge gas still contains a significant quantity of unconverted ethylene. A reasonable compromise may be attained by introducing a second purge reactor system, operating at lower ethylene concentration and higher conversion per pass. In order to avoid construction of a purge reactor different in size from a primary reactor, the purge gas from 5–10 primary reactors running in parallel is used to feed one purge reactor.

Many of these difficulties can be avoided by using oxygen instead of air. This offers major advantages in terms of reaction kinetics and eliminates the large nitrogen stream entering the system with oxygen, reducing the amount of purge gas to such an extent that the use of a purge reactor is no longer necessary. A single-stage reactor system can thus be operated at a high ethylene concentration and a low conversion rate per pass, with inherent selectivity and productivity advantages over a two-stage air-based process, compensating the cost of oxygen production.

The most important factor in the design of ethylene oxidation reactors is the efficient and economic removal of reaction heat while maintaining high productivity and good selectivity. It should be borne in mind that the heat evolved in the total oxidation of both ethylene and ethylene oxide [Eqs. (7.2) and (7.3)] is one order of magnitude greater than the heat of the formation of ethylene oxide [Eq. (7.1)]; therefore, even small changes of selectivity may cause the reactor to run away if the removal of heat is not controlled efficiently enough. Therefore all commercial processes operate with a multitude of packed-bed reactors. Cooling is accomplished either by circulating heat transfer fluids or by boiling organic fluids. The use of newer, more active catalysts operating at lower temperatures permits the direct cooling with water boiling in the reactor shell; the generated high-pressure steam is applied for further use. The first commercial production based on an air oxidation process was started at Union Carbide in 1937, followed by Halcon/Scientific Design in 1940. Oxygen-based direct oxidation was put into operation by Shell in 1958 [10,30,39].

III. OXIDATION OF PROPENE TO ACROLEIN

A. General Properties

The heterogeneous catalytic oxidation of olefins to aldehydes started with the discovery of the oxidation of propene to acrolein over cuprous oxide by Hearne and Adams [40]. This process was later commercialized by the Shell Chemical Company. Detailed studies of the kinetics and mechanism of the oxidation on copper oxides followed [41—43], much attention having been paid to the redox behavior of copper oxides in the course of the catalytic reaction. However, the modern era of the now worldwide application of catalytic oxidation of olefins to produce aldehydes began with the introduction of bismuth phosphomolybdate catalyst for the oxidation of propene to acrolein by Veatch and coworkers [44,45], and in the presence of ammonia, to acrylonitrile by Idol [46], both processes having been carried to commercial operation by SOHIO. It was also shown by Hearne and Furman [47] that diolefins could be made from C_4 and higher olefins by oxidative dehydrogenation over bismuth molybdate catalyst. Since then the number of studies on olefin oxidation has increased very rapidly and many different catalytic systems have been developed and introduced into industrial use. Tables 7.3 and 7.4 summarize some of the patented catalysts for the oxidation of

3 Active Phase in Multicomponent Metal Oxide Catalysts for the Oxidation of Propene
n

n,	Temp. of reaction (°C)	Composition of the feed, % (vol)			Conversion (%)	Select. to acrolein (%)	Yield of acrolein (%)	R
		C_3H_6	Air	H_2O				
a, Mn, , Co, Te	300	5.4	64.6	30	84	74	63	
i, W, Si	250–450	4–7	51	40–45	96	90–93	88	
o, Fe, K	330–350	6	56	38	94	81	76	
e, Ni, Mg	350	4	50	46	98	95	85	
o, Fe, K	300	6	48	46	87	97	89	

ent 1920247 (1970); ^{2}U.S. Patent 3,825,600 (1974); ^{3}FRG Patent 2020791 (1970); ^{4}Belgian
974); ^{5}Japan Patent 48-16450 (1973).

4 Active Phase in Catalysts for Ammoxidation of Propene to Acrylonitrile

n,	Temp. of reaction (°C)	Composition of the feed, % (vol)			Conversion (%)	Select. to acrylonitrile (%)	Yield of acrylonitrile (%)
		C_3H_6	NH_3	Air			
	500	7.4	8.5	66.4 He 17.7 O_2	26.9	75.3	20.3
, Co, Fe	450	3.5	4.5	92.0	92.2	73.0	68.2
	450	8.0	9.3	82.7	91.5	77.0	70.8
o, P	450–490	8.5	81.5	10.0	96.0	74.0	
Io	440				84.0		65.0
	500	7.0	8.5	84.5	55.9		62.3
, Te	480	5.0	5.0	90.0	93.0	82.0	77.0
e, Co,	480	3.5	4.5	92.0	97.0	78.0	76.0

fen. 2,013,915 (1970); 2-Jap. Pat. 45-35287 (1970); 3-Jap. Pat. 71,03,438 (1971); 4-Ger. (1972); 5-Franch Pat. 1,538,997 (1968); 6-Ger. Offen. 2,163,319 (1972); 7-Jap. Pat. 47- -Ger. Offen. 2,104,016 (1971).

propene to acrolein and ammoxidation of propene to acrylonitrile, respectively. It is noteworthy that all of these catalyst formulations contain at least two metal oxides, one of them being usually molybdenum or tungsten oxide.

B. Mechanism of the Activation of Propylene Molecules

It is now well established [3,8] that the first step of the allylic oxidation of propene to acrolein consists of the abstraction of α-hydrogen and formation of a symmetric allylic species, which uses its π orbitals to form a σ bond with the metal cation at the oxide surface. McCain et al. [48] showed that in the oxidation of 1-^{13}C-prop-1-ene, both ends of the molecule could be converted to the carbonyl group of acrolein with equal probability. Isomerization of labeled propene before the addition of oxygen was shown to be negligible, so it was concluded that the first step of the oxidation must involve the reaction:

$$\mathrm{CH_2{=}CH{-}CH_3 \xrightarrow{-H} CH_2 \underline{\overline{-CH-}} CH_2}$$

This conclusion was confirmed by Sachtler and de Boer [49] who used 1-^{14}C-prop-1-ene, 2-^{14}C-prop-1-ene, and 1-^{14}C-prop-2-ene molecules. Acrolein formed as the result of propene oxidation was decomposed photochemically:

$$\mathrm{H_2C{=}CH{-}CHO \xrightarrow{h\nu} H_2C{=}CH_2 + CO}$$

and the radioactivity of the products was determined. In the case of $^{14}CH_2{=}CH{-}CH_3$ and $CH_2{=}CH{-}^{14}CH_3$ molecules the radioactivity was evenly distributed between $CH_2{=}CH_2$ and CO, whereas after oxidation of $CH_2{=}^{14}CH{-}CH_3$ the activity as found only in the unreacted propene molecules and in $CH_2{=}CH_2$. This clearly indicates that dissociative chemisorption takes place in the first step, resulting in the formation of symmetric allyl species, with both terminal carbon atoms having an equal chance of forming a C=O bond. Confirmation of this mechanism was obtained by Adams and Jennings [50] using propene labeled with deuterium in various positions.

Adams [54] examined the behavior of a large number of $C_3{-}C_8$ olefins of various structures. The initial products were mainly conjugated dienes and unsaturated aldehydes formed with high selectivity. He found that monounsaturated aldehydes were formed only in the case of olefins of the structure:

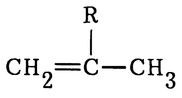

$$\mathrm{CH_2{=}\overset{\overset{\displaystyle R}{|}}{C}{-}CH_3}$$

Where allowed, conjugated dienes were formed at a much faster rate than the conjugated unsaturated aldehydes from the same molecule. As discussed above, the initial step involves hydrogen abstraction from the methyl group adjacent to a double bond (α position) to form a symmetric allyl intermediate. A study of the kinetic isotope effect in the oxidation of propene has shown that this is the slow step. The probability of initial removal of allylic hydrogen is determined in part by the relative strength of this bond.

Skeletal isomerization normally does not occur under the conditions of catalytic oxidation, so that the rates and selectivities depend on the structure of the olefin, i.e., the position of the double bond and the nature of the substituent. Tertiary α-hydrogens are more reactive than secondary, which in turn are more reactive than primary hydrogens (Table 7.5). The effects of olefin structure on reactivity in oxidation are very similar to those reported for hydrogen abstraction by free radicals [56].

As in the majority of partial oxidation reactions, the first step consisting of activation of the hydrocarbon molecule is the rate-determining one and studies of the kinetics of these reactions cannot yield any information on the next stages of the reaction. One of the ways by which further steps of the oxidation reactions could be studied in more detail is to bypass the first step by generating the allyl radicals in situ in the catalytic reactor by some other route. This was effected by using allyl halides and allyl oxalate [51,52] or

TABLE 7.5 Bond Dissociation Energies of Olefins

Bond	$\underline{D}$ (kcal mol^{-1})
$H—H$	103
$CH_3—H$	102
$\underline{n}$-$C_3H_7—H$	99
$\underline{i}$-$C_3H_7—H$	94
$\underline{i}$-$C_4H_9—H$	90
$CH_2{=}CH—H$	105
$C_6H_5—H$	103
$CH_2{=}CH—CH_2—H$	77
$C_6H_5—CH_2—H$	77

azopropene [53], which readily decompose into allyl radicals. A new facile route of the production of allyl radicals is thus provided making possible the examination of the conditions, which are necessary for the insertion of oxygen in the next step of the reaction. Comparison of the behavior of propene and allyl compounds thus enables the identification of surface sites responsible for the activation of hydrocarbon molecules and those which are involved in the insertion of oxygen in the second step of the reaction. The way of reasoning will be illustrated by studies of the reactions of propene and allyl iodide on Bi_2O_3, MoO_3, and Bi_2MoO_6 [51], their results being summarized in Table 7.6. When allyl iodide is passed over MoO_3, at 310°C practically total conversion is observed with 98% selectivity to acrolein. Under the same conditions MoO_3 is completely inactive with regard to propene. On contacting allyl iodide with Bi_2O_3 total conversion at 310°C was also observed; however, in this case 70% of the product formed was 1,5-hexadiene, with practically no acrolein being detected. Comparison with the results for homogeneous reaction indicates that hexadiene was formed mainly as the result of heterogeneous reaction at the surface of Bi_2O_3 because at 310°C only about 20% conversion is observed in homogeneous reactions. 1,5-Hexadiene as the principal product was also obtained in the reaction of propene on Bi_2O_3. These results led to the conclusion that in the case of Bi_2O_3—MoO_3 oxidation catalysts the role of Bi centers consist of the generation of allyl species. When no other centers are present at the surface, these species recombine to give hexadiene irrespective of whether they are formed from propene at Bi centers at the surface of the catalyst or generated in situ in the reactor as the result of the decomposition of allyl iodide. The situation is different in the case of MoO_3. Its surface contains active centers which are able to perform the insertion of oxygen into the organic molecule, but no centers are available for the efficient generation of allyl species. MoO_3 is thus inactive in propene oxidation. However, when such species are formed by some other route, their total conversion to acrolein at the MoO_3 surface takes place.

An efficient catalyst for the oxidation of propene to acrolein is characterized by two functions: activation of propene by formation and bonding of allylic species, and insertion of oxygen into these species. In complex oxide catalysts these functions are played by different lattice constituents, as Bi—O and Mo—O polyhedra. The overall reaction network consists of a series of consecutive and parallel steps:

TABLE 7.6 Interaction of Propene and Allyl with Molybdates

	Propylene				Allyl iodide				
		Yield (%)				Yield (%)[a]			
Catalyst	Temp. (°C)	Hexadiene	Benzene	Acrolein	Temp (°C)	Propene	Hexadiene	Benzene	Acrolein
Bi_2O_3	480	8.6	—	—	310	— (2.0)	70.0 (8.0)	— (—)	5.0 (—)
MoO_3	480	—	—	—	310	—	—	—	98.0 (—)
Bi_2MoO_6	460	—	—	13.0	310	—	12.0	1.0	15.0
$Mg_2Mo_3O_{11}$	480	—	—	1.0	370	15.0 (25.0)	10.0 (25.0)	— (2.0)	25.0 (0)
$MgMoO_4$	480	—	—	—	400	61.0 (62.0)	0.7 (7.0)	1.3 (7.0)	— (0)

[a] Numbers in parentheses are for the homogeneous reaction.

Source: Ref. 51.

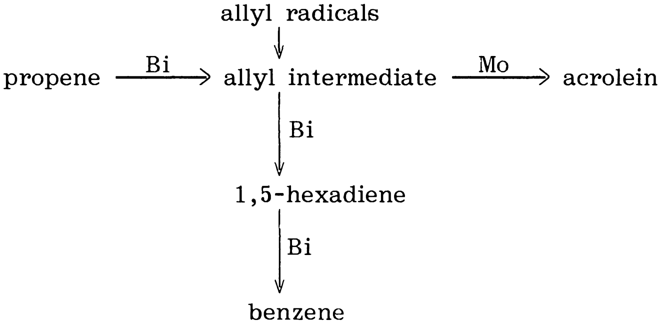

The acrolein/diene ratio depends on the ratio of the rate constants. In the case of the oxidation of propene, its adsorption (which is equivalent to its activation to allylic intermediate) is rate determining [54]. In such conditions the surface of the catalyst is sparsely populated with allylic intermediates, which immediately react to acrolein, the selectivity to this product being thus very high. However, when the surface is contacted with allyl radicals generated in the gas phase by decomposition of allyl iodide, the coverage of the surface with adsorbed allylic intermediate may attain much higher values and the probability increases that two such species will be adsorbed at adjacent centers and recombine to form 1,5-hexadiene. In fact Table 7.6 shows that the reaction of allyl iodide at the surface of Bi_2MoO_6 results in the formation of certain amount of 1,5-hexadiene and benzene, and consequently much lower selectivity to acrolein than that observed in the oxidation of propene. When active centers for oxygen insertion are removed by replacing molybdate anions with, say, phosphate, the reaction path to acrolein is eliminated and a high conversion to benzene is observed [55].

Direct evidence of the formation of allylic species and their role as intermediates in the mild oxidation of propene to acrolein was provided by the studies of IR spectra of propene adsorbed on catalysts for partial and total oxidation [57—59]. It was found that on Cu_2O, CuO, and CuO—MgO solid solution [58] propene is adsorbed reversibly giving an IR band at 1440 cm^{-1} assigned to ν_{AS} $\underline{C-C-C}$ in the π-allyl species and irreversibly in the form of the π complex, responsible for the appearance of $\nu_{C=C}$ at 1510 cm^{-1}. The intensities of the absorption band characteristic of the π-allylic surface complexes $\underline{C-C-C}$ increase with rising concentration of copper. Also increased was the amount of acrolein formed from propene. This is shown in Fig. 7.7 in which the rate of the oxidation of propene to acrolein, the amount of reversibly adsorbed propene, and the intensity of the band at 1440 cm^{-1} assigned to π-allylic species are plotted as the function of the CuO content in CuO—MgO catalysts.

Thus it may be concluded that complexes of the allylic type which are weakly adsorbed at the surface are indeed the intermediates in the formation of products of partial oxidation.

Important evidence substantiating the assumption that a polyhedron composed of a cation coordinated by oxide ions, located at the surface of a metal oxide, may indeed be considered as an active site for activation of the hydrocarbon molecule was quite recently obtained by using model catalysts prepared by supporting isolated Bi^{3+} ions at the surface of MoO_3 crystallites [60]. Analysis by XPS confirmed that these ions are indeed located in the surface layer. Catalytic activity of a series of such catalysts containing different amounts of supported Bi^{3+} ions was then determined in the oxidation of propene and allyl iodide by using the pulse technique. The only products obtained from the propene plus oxygen mixture were acrolein and products of total combustion, whereas only acrolein was obtained when allyl iodide was introduced. Figure 7.8 shows the

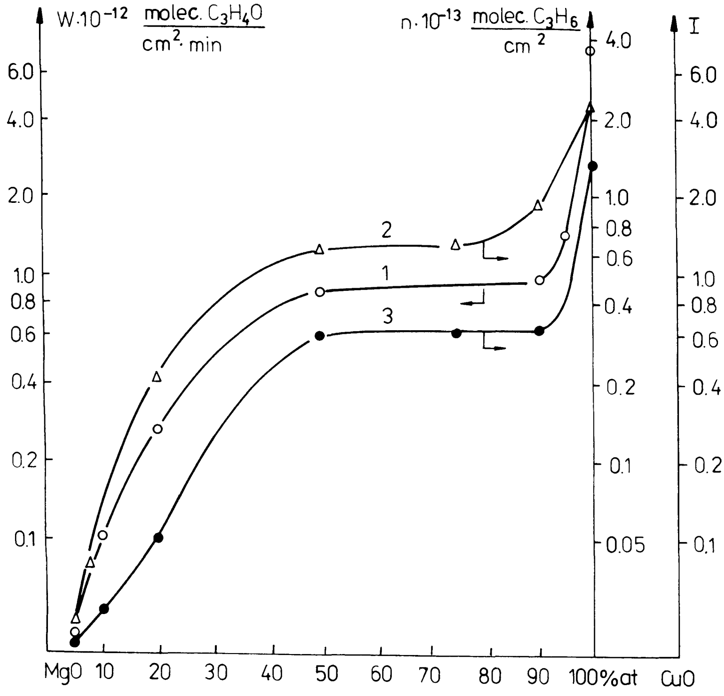

FIGURE 7.7 Rate with respect to acrolein (1), the adsorption value of propene in the reversible form (2), band intensity of a π-allylic complex (3) versus catalyst composition [58].

yields of acrolein and CO_2 as the function of the concentration of Bi^{3+} ions at the surface of MoO_3 crystallites, expressed in terms of surface coverage. The yield of acrolein observed when allyl iodide was introduced was constant and independent of the number of bismuth ions and was identical to the value observed for the pure MoO_3. This is in agreement with the above-mentioned conclusion that the lattice of MoO_3 is very efficient in adding oxygen to allyl species once they have been generated, e.g., by decomposition of allyl iodide in situ in the catalytic reactor. The yield of acrolein from propene increases at first proportionally to the number of these ions. This indicates that isolated Bi^{3+} ions serve as active centers which convert propene into allylic species. At higher surface coverages the yield of acrolein levels off, attaining a constant value independent of further increase of the amount of supported bismuth. This is due to the formation of a thicker and thicker layer of bismuth molybdate phase at increasingly higher Bi^{3+} loadings.

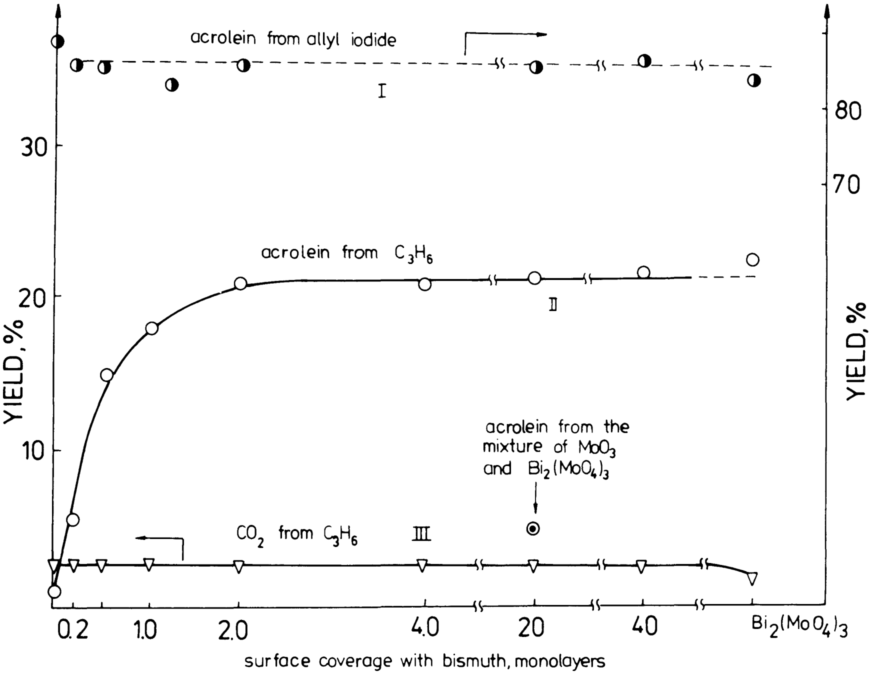

FIGURE 7.8 Yield of acrolein and CO_2 in oxidation of propene and allyl iodide as function of coverage of the MoO_3 surface with bismuth ions [60].

It should also be noted that the amount of CO_2 formed in the course of the reaction remains constant for all catalysts independent of the amount of supported Bi^{3+} ions. This clearly indicates that complete oxidation of propene takes place at active centers different from those responsible for the activation of propene in the first step of its selective oxidation to acrolein and does not result from the consecutive oxidation of acrolein but is formed in a parallel reaction. The rate of CO_2 formation is not limited by the activation of hydrocarbon in agreement with the classification of total combustion as an electrophilic oxidation (see Chapter 4).

An important question should be raised at this point as to whether the Bi ions in the model catalysts uniformly cover the whole surface of the support crystallites or are deposited only on certain planes. In answer to this question an experiment was carried out [60] in which large, plate-like crystallites of MoO_3 were suspended in the solution of $Bi(NO_3)_3$ at a concentration sufficient to form a multilayer deposit of Bi^{3+} ions, and then annealed in the same condition in which the model catalysts were obtained. Micorgraphs of two parts of a platelet are shown in Fig. 7.9. It may be seen that the basal (010) crystal plane of MoO_3 remained practically unchanged, whereas at the side on the (100) and (001) planes a new phase is clearly visible. STEM and EDAX as well as X-ray diffraction analyses revealed that this phase represents the α phase of bismuth molybdate $Bi_2(MoO_4)_3$ with the scheelite structure. At those locations on the (010) plane, where steps and kinks were present, Bi ions were deposited on the (100) and (001) fragments exposed at these steps. A conclusion may thus be formulated that on impregnation no adsorption takes place on the basal (010) crystal plane, whereas bismuth ions are adsorbed selectively only on the crystal faces perpendicular to the basal faces, e.g., on (100) or (001). As this phenomenon of crystallographically specific deposition is of more general significance for the preparation and behavior of oxide catalysts, it will be examined in more detail later.

C. Quantum Chemical Description of the Activation

Several attempts have been undertaken in recent years to use quantum chemical methods to obtain more information as to which properties are required for the active centers of oxide catalysts to abstract the hydrogen atom from the olefin molecule and generate the allylic species. Haber et al. [61,62] carried out the SINDO quantum chemical calculations of the interaction of propene with the surface of the oxide catalyst. A complex consisting of cobalt or magnesium ion surrounded by five oxygen atoms and the propene molecule as the sixth ligand in octahedral coordination has been used as a model of the active center at the catalyst surface. Curve I in Fig. 7.10 shows

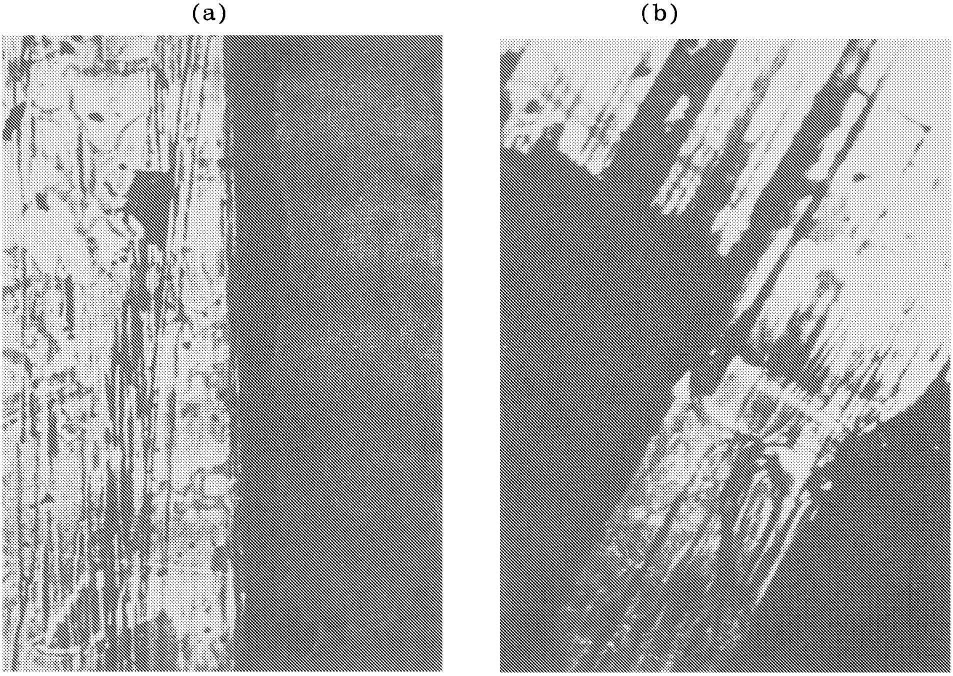

FIGURE 7.9 Micrographs of the MoO_3 platelet after impregnation with Bi^{3+} ions and annealing. (010) plane with: (a) (100) edge, magnification 200x, and (b) (100) and (001) edges, magnification 130x [60].

the total energy as a function of the distance of propene molecule from the plane of cobalt complex. A minimum, appearing at the distance of 1.95 Å, corresponds to the formation of a stable intermediate surface complex. The dotted line represents the change of total energy of the system when not the whole propene molecule but only the allylic species is being removed from the surface, one hydrogen atom remaining at the surface attached to an oxygen atom. Apparently, this process is energetically much more favorable than removal of propene.

Curves II and III represent the diatomic contributions $\underline{E}_{AB}$ of the C—H and O—H bonds, respectively, to the total energy plotted as a function of the distance of the propene molecule from the plane of cobalt complex. It may be seen that on approach of the propene molecule to the complex, the C—H bond is being continuously destabilized, whereas the strength of the O—H bond increases reaching a maximum value at the distance of about 2.1 Å. When the allyl

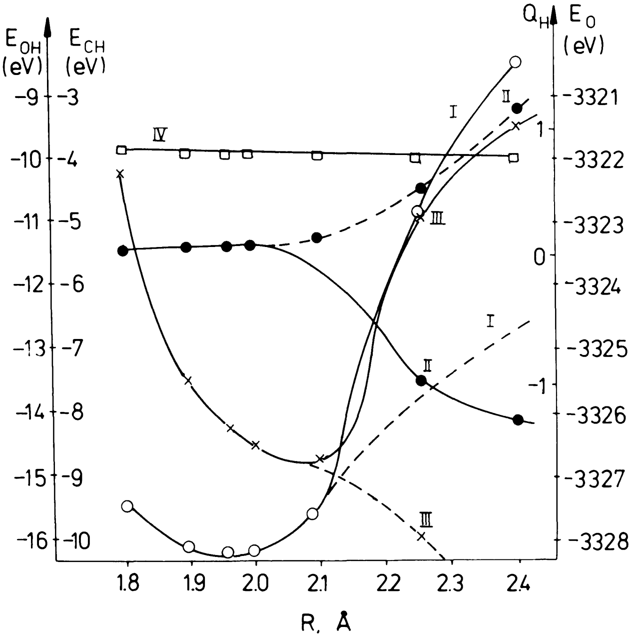

FIGURE 7.10 Total energy (curve I) and diatomic energy contributions of C–H (curve II) and O–H (curve III) interactions as well as charge on hydrogen atom (curve IV) as a function of the distance of the propylene molecule from the plane of the cobalt complex. Dotted curves refer to allyl species [61].

species is now removed from the surface, the O—H bond is further strengthened (dotted part of curve III), its energy attaining −17.2 eV, which agrees very well with the value of −18.8 eV obtained for the O—H bond in $(H_3O)^+$. These results clearly indicate that on contacting propene with the surface of cobalt oxide, its reactive chemisorption takes place, in which the C—H bond becomes cleaved and an intermediate adsorption complex of the allyl type is being formed. It is noteworthy that in the course of the approach of the propene molecule to and the removal of the allyl radical from the surface, the charge on the moving hydrogen atom remains practically constant and amounts to about +0.7 (curve IV in Fig. 7.10). This indicates that the movement of hydrogen along the reaction path may be visualized as composed for two operations—transfer of a proton from the olefin molecule to a surface oxide ion:

$$CH_2{=}CH{-}CH_2{-}H + O^{2-}(s) \longrightarrow [CH_2{=}CH{=}CH_2]^- + OH^-$$

which may be considered as an acid-base reaction, and the electron transfer from adsorbed allyl to the metal cation of the catalyst lattice to render the allyl species positive and susceptible to the nucleophilic attack of oxygen:

$$[CH_2{=}CH{=}CH_2]^- + 2M^{\underline{n}+} \longrightarrow [CH_2{-}CH{-}CH_2]^+ + 2M^{+(\underline{n}-1)}$$

which is a redox process.

A different approach was adopted by Anderson et al. [63], who based their discussion on the results of the ASEO-UO calculations of the energy band structures of $Bi_2Mo_3O_{22}{}^{20-}$ cluster taken as a model of α-bismuth molybdate surface, and $Bi_4Mo_2O_{28}{}^{32-}$ cluster representing the fragment of the layered γ-Bi_2MoO_6 structure. It was assumed that it is a coordinatively unsaturated Mo^{VI} site where the reaction starts by adsorption of propene and the bonding interactions between different propene orbitals and orbitals of Mo^{VI}, O^{2-}, and Bi^{III} of the clusters in consecutive steps of the transformation of propene to acrolein were discussed. Figure 7.11 shows the model of propene adsorption on a $Bi_2Mo_3O_{20}{}^{12-}$ cluster representing the α-bismuth molybdate surface, and Fig. 7.12 the respective bonding interactions between the adsorbed propene molecule and a surface Mo^{VI} cation. The bonding is predominantly π-donation from the π-bonding orbital of propene to the empty d_z2 orbital of molybdenum. There is no significant Mo 4d backbonding into the propene antibonding π* orbital because the d band is empty. If the adsorbed propene molecule is now rotated until the out-of-plane methyl C—H bond is directed toward an oxygen anion coordinated to bismuth, this bond becomes activated by forming a three-center CH—O σ-donation bond. This leads to the transformation into π-coordinated allyl and the OH^- group.

D. Nucleophilic Addition of Oxygen

Nucleophilic addition of oxygen to an activated olefin molecule resulting in the formation of aldehyde or acid may be performed by many different oxides, provided that centers exist at the oxide surface which are able to activate the hydrocarbon molecule. However, there is a fundamental difference in the catalytic behavior of oxides and oxy salts of group V, VI, and VII transition metal oxides, as compared to other transition metal oxides and their oxy salts of main group elements [64]. As an illustration Fig. 7.13 shows the catalytic properties of nickel phosphate and nickel molybdate in the oxidation of propene as a function of the reaction temperature [65]. In the case of such compounds as NiO or $Ni_3(PO_4)_2$ high selectivity to acrolein is observed only at low temperature, when the overall activity is low. On rising temperature, selectivity to acrolein drops

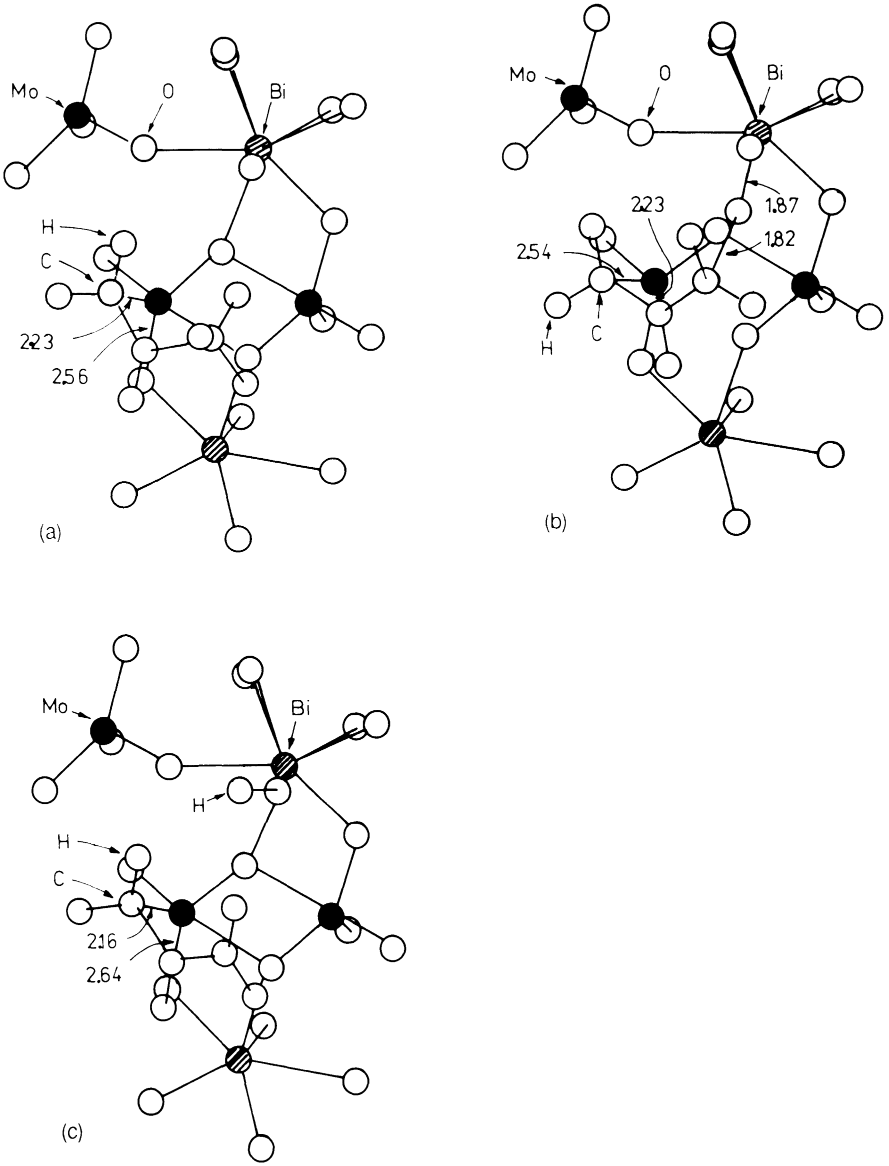

FIGURE 7.11 Reaction of propene on a cluster model of an α-bismuth molybdate surface: (a) adsorption, (b) transition state, (c) allyl and OH [63].

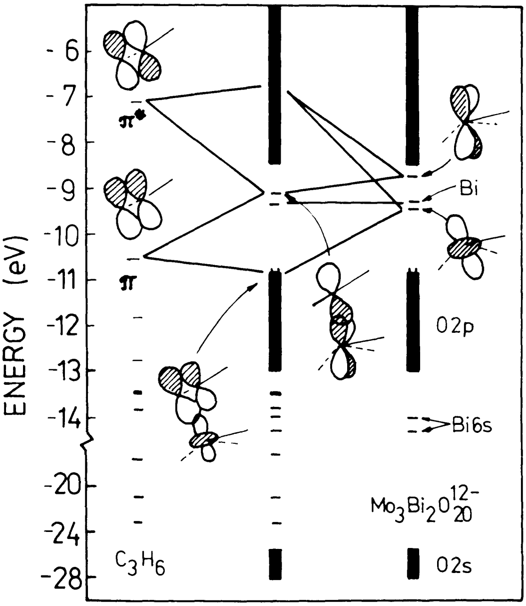

FIGURE 7.12 Bonding interactions between adsorbed propene and a surface Mo^{VI} cation [63].

rapidly and CO_2 appears in increasing quantity. It may be concluded that at higher and higher temperatures the dissociation pressure of the oxide increases, oxygen adsorption equilibria shift toward the formation of electrophilic oxygen species, and total oxidation becomes the predominant process.

An entirely different picture is obtained in the case of nickel molybdate. At lower temperatures the main products are acrolein and acetaldehyde. However, when the temperature is raised, the amount of acetaldehyde decreases and the amount of acrolein increases, appearing with higher and higher selectivity so that at about 500°C acrolein becomes practically the only product. As shown in Section III.B of this chapter, active and selective oxidation catalysts must perform two functions: activate propene and insert nucleophilic oxygen into the activated species, this latter function being very efficiently performed by group V, VI, and VII transition metal oxides and the corresponding anionic sublattices in their oxysalts. A question may be raised as to which properties of these oxides are responsible for the very high activity and selectivity involved in the insertion of oxygen. The chemistry of such elements as vanadium or molybdenum is dominated by the consequences of the considerable extension of their d orbitals and positions of the d-electron redox potentials relative to the anion valence band edge [66]. In the octahedral coordination of oxide ions, in which d^2sp^3 hybridized orbitals are used by the metal to form σ bonds, the remaining $\underline{d}_{xy}$, $\underline{d}_{yz}$, and $\underline{d}_{xz}$ orbitals extend far enough to considerably overlap with the π-p orbitals of oxygen. As the result π bonds with oxygen atoms are formed and the cation becomes displaced from the center of the octahedron toward terminal oxygen atoms. The softness of the metal-oxygen potential is the cause of large cation displacement polarizabilities, which give rise to the high relaxation energy. As a result it becomes energetically more favorable for such an oxide to change on reduction the stoichiometry by the change of the mode of linkage between the coordination polyhedra instead of generating the point defects, the usual mechanism responsible for the nonstoichiometry of transition metal oxides. Namely, removal of

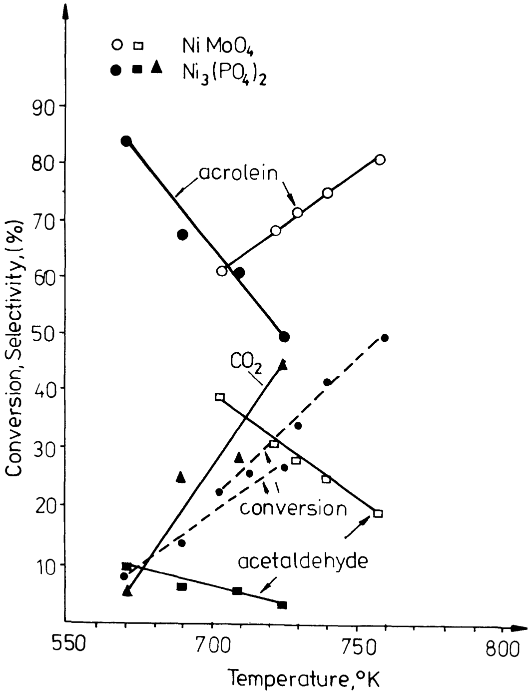

FIGURE 7.13 Selectivity of the oxidation of propene to acrolein, acetaldehyde, and CO_2 on $NiMoO_4$ and $Ni_3(PO_4)_2$ as a function of temperature.

oxygen ions from the lattice group V, VI, and VII transition metal oxides results in the formation of ordered arrays of oxygen vacancies, followed by a very facile rearrangement of the layers of initially corner-linked metal oxygen octahedra into an arrangement of edge-linked octahedra, resulting in the formation of a shear plane. The mechanism of such crystallographic shearing is illustrated in Fig. 7.14, this phenomenon being responsible for the characteristic chemical properties of this group of oxides [67]. It may be expected that on raising the temperature the rearrangement of the corner-linked metal-oxygen polyhedra into an edge-linked array proceeds more and more readily, in particular at the surface of the oxide, providing a facile and efficient route for the addition of a nucleophilic lattice oxygen into the hydrocarbon molecule [64] without the generation of point defects which could be involved in the formation of electrophilic oxygen species and create a pathway for a stray reaction of total combustion. The mechanism of such nucleophilic insertion of oxygen is shown in Fig. 7.15. Results of experiments with different tungsten oxides [68] as well as quantum chemical

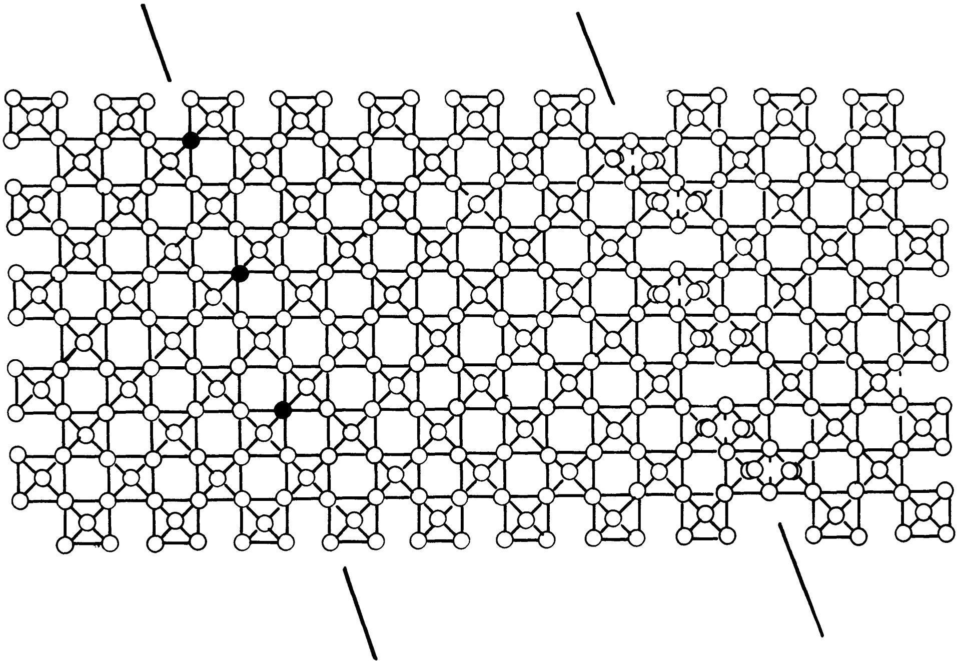

FIGURE 7.14 Formation of a crystallographic shear plane.

calculations [42,43] supplied strong evidence for the conclusion that the ability of group V, VI, and VII transition metal oxides to form different types of bonding between the coordination polyhedra indeed plays an important role in determining the mode of their operation in nucleophilic addition of oxygen into activated organic molecules.

The most widely used partial oxidation catalysts are based on MoO_3 and its compounds. MoO_3 has a layer structure, in which MoO_3 octahedra are linked together by edges to form a double zigzag chain; the chains are linked through corners into infinite sheets [69]. Each octahedron has one unshared corner, the free corners in one layer pointing down between those of neighboring layers. The idealized structure may be considered as fcc oxygen packing with Mo in one-third of the octahedral interstices. The left side of Fig. 7.16 shows (010), (100), and (001) projections of the arrangement of octahedra, and the right side of Fig. 7.16 illustrates the idealized arrangement of molybdenum and oxygen atoms on the appropriate crystal planes. On the (010) plane all molybdenum and oxygen atoms are coordinatively saturated and therefore this plane, in the absence of defects, is inert in chemisorption processes. A clean (100) plane contains coordinately unsaturated Mo^{6+} ions with one bridging O^{2-} ion missing from their coordination sphere thus acquiring the formal uncompensated charge +1. This plane also contains unsaturated bridging O^{2-} ions with one Mo^{6+} missing and a formal uncompensated charge of 1—. A compensation of local charge difference is achieved by dissociative chemisorption of water with proton going to oxygen and a hydroxyl group being attached to the Mo^{6+} ion; this reduces the formal charge to zero. Analogous considerations show that the charges M^{6+} and O^{2-} ions exposed on the (001) plane would be +2/3 and −2/3, respectively; hydroxylation reduces these charges

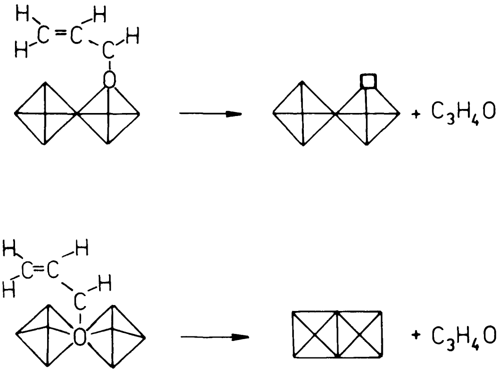

FIGURE 7.15 Mechanism of the nucleophilic addition of oxygen to activated hydrocarbon molecule [64].

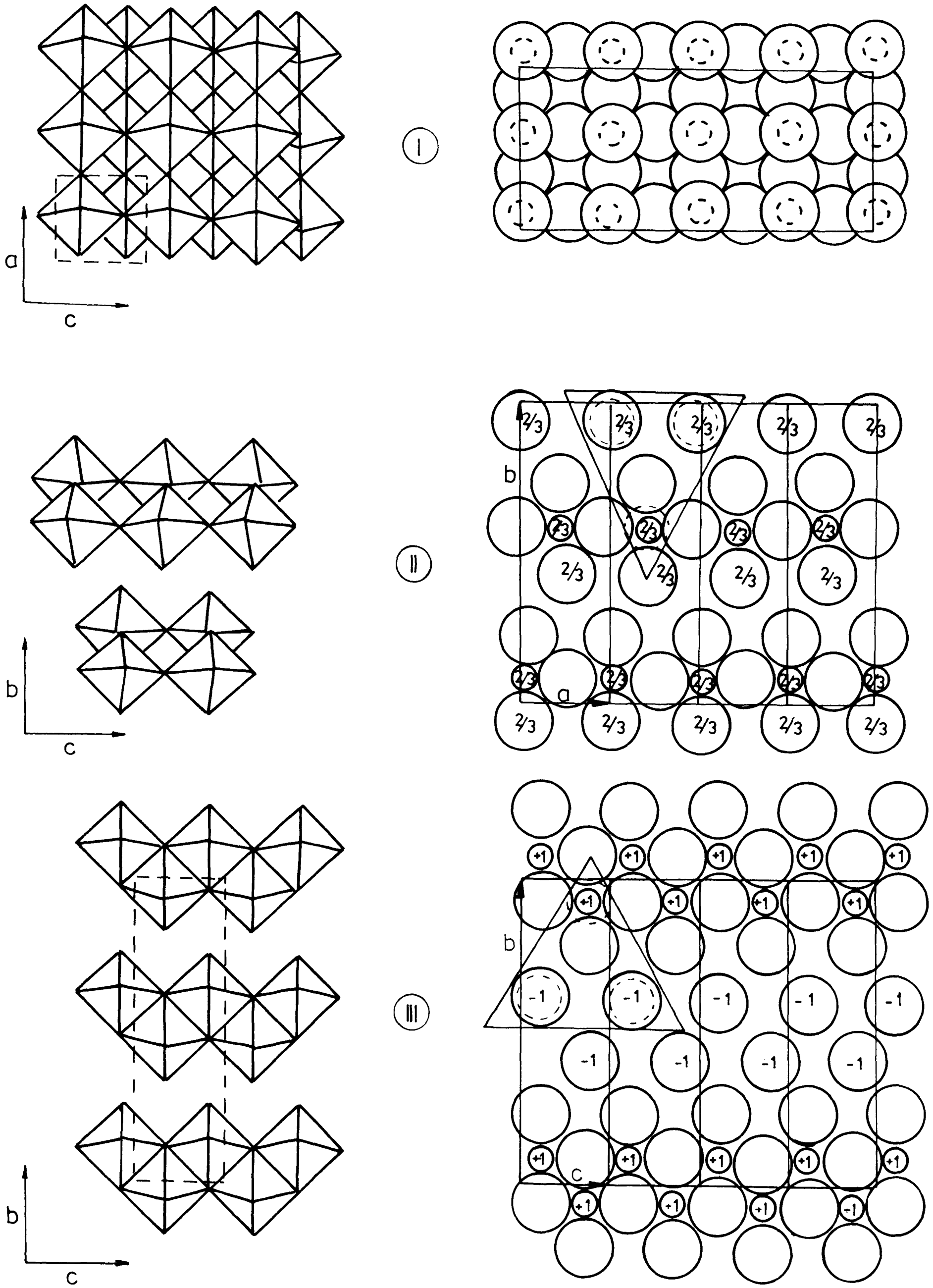

FIGURE 7.16 Idealized structure of the (010), (001), and (100) crystal planes in MoO_3 [60].

to −1/3 and +1/3. It may thus be concluded that in acid-base interaction only (100) and (001) planes of MoO_3 will take part. Indeed, studies of the transformations of methanol on MoO_3 monocrystals revealed that acid-base type reaction takes place on the (100), (001) and (110) planes, as described in Section VIII of Chapter 4. This also explains why in the course of preparation of the model catalysts containing Bi^{3+} ions supported on MoO_3, which were described in Section III.B, the Bi^{3+} ions were deposited only on the (100) and (001) planes, where they could react with the acidic hydroxyl groups and replace protons. The dehydroxylation of these planes on heating leaves the Mo^{6+} ions coordinatively unsaturated, acting as electron traps liable to interact with oxygen molecules generating active electrophilic forms. This may provide a route for electrophilic oxidation to saturated aldehydes and finally to total oxidation.

An entirely different situation exists on the (010) crystal plane. As mentioned before, in the strong $\sigma\pi$ bond of terminal $Mo{=}O_t$ on the (010) plane there is sufficient transfer of electron density onto the metal orbitals to render the terminal oxygen O_t only weakly basic. Conversely, the exposed bridging oxygens are more basic and their lone pairs are capable of performing a nucleophilic attack on an organic molecule. These electron pairs form the HOMO at the surface of MoO_3. Its LUMO is the Mo 4d [71], but this orbital is relatively inaccessible to the reactants of the catalytic reaction because it is screened by the close-packed surface oxygen atoms. The HOMO and LUMO of allyl species are illustrated in Fig. 7.17. The HOMO in the allyl cation is the bonding three-nuclear π orbital, the LUMO consists of the nonbonding π orbital. The reaction between allyl species and MoO_3 to form a chemisorbed species is governed by HOMO-LUMO interactions, of which there are two possibilities: (1) an electrophilic attack by the catalyst Mo 4d empty orbital on the allyl radical and (2) a nucleophilic attack by the surface bridging oxygen lone pair orbitals on the empty π orbital of allyl. In view of the inaccessibility of the Mo 4d orbitals and the more pronounced electron acceptor properties of the allyl cation or allyl radical, pathway 2 seems to be more probable, all conditions of the swift reaction being fulfilled.

Indeed, by comparison of the behavior of propene and allyl compounds over MoO_3 crystallites of different habit [72], it was possible to separate the two elementary steps of the selective oxidation: activation of propene molecules to form the allyl species and nucleophilic addition of oxygen. The yield of acrolein from allyl compounds was found to be a linear function of the surface area of (010) crystal planes (Fig. 7.18), indicating that it is at this plane where the addition of oxygen takes place.

Strong evidence hinting at the role of bridging oxygens was obtained from the ESR spectra of MoO_3 in the course of its interaction with different atmospheres [73]. As an example, Fig. 7.19a shows the ESR spectra of MoO_3 after outgassing at the temperature of 430°C for 5 min (curve A) and 35 min (curve B). Analysis of the values of the g tensor reveals the appearance of two different Mo^{5+} centers: type A, formed at the early stage of the reduction and characterized by rhombically distorted square-pyramidal surrounding of axial symmetry along the $\sigma\pi$ double-bonded oxygen, and type B, of distorted octahedral symmetry and appearing in strongly reduced samples. Comparison of these results with the situation at the surface of MoO_3 crystallites (Fig. 7.19b) leads to the conclusion that the only surface oxygen ion which can be removed leaving reduced molybdenum cation in square-pyramidal surrounding with double-bonded oxygen in the

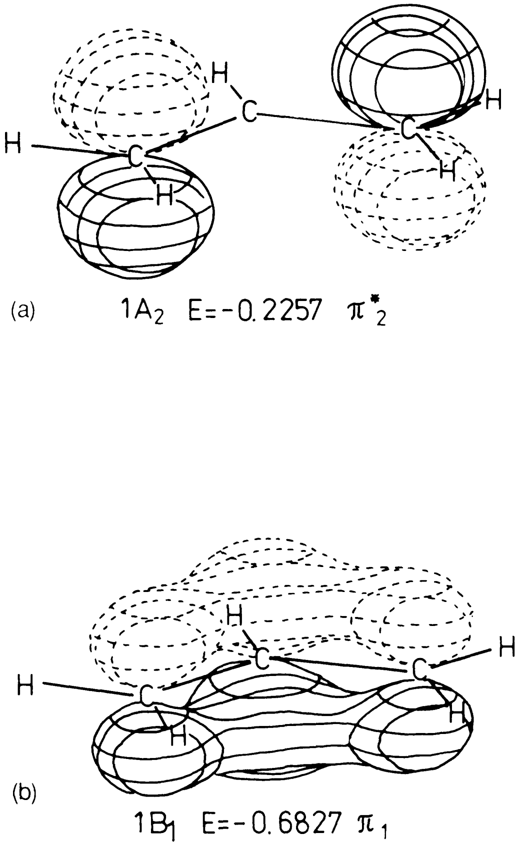

FIGURE 7.17 The (a) LUMO and (b) HOMO of allyl species [136].

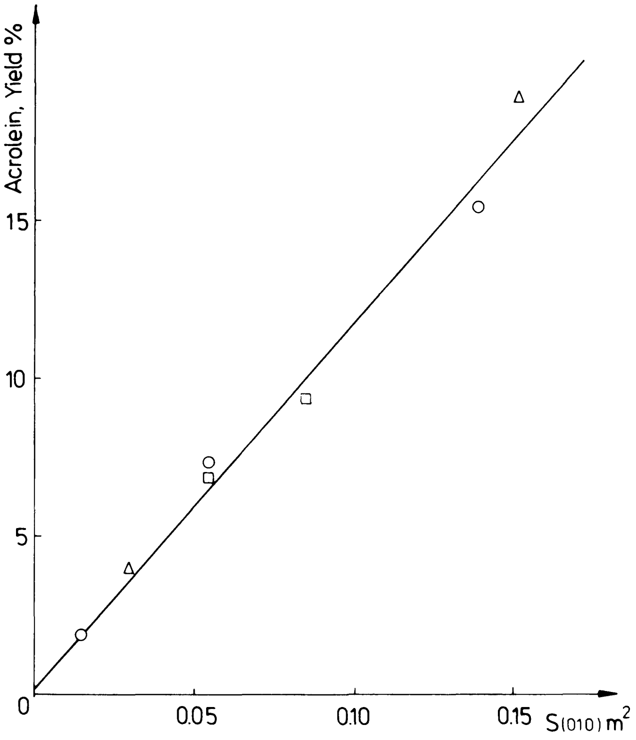

FIGURE 7.18 Yield of acrolein obtained on interaction of allyl compounds with MoO_3 as function of the surface area of the (010) crystal face [72]. o-iodide, Δ-bromide, □-oxalate. Correlation factor = 0.992.

opposite apex is the surface oxygen bridging two adjacent octahedra in the double string of edge-linked Mo—O octahedra. When concentration of vacancies increases, crystallographic shear takes place and Mo^{5+} cations assume octahedral coordination along the shear planes. These results are consistent with the assumption that the side crystal planes which contain the acid-base sites are responsible for activation of propene, whereas nucleophilic addition of oxygen takes place on the basal (010) face. A general conclusion emerges that different steps of the multistep catalytic reaction may proceed at active centers located on different crystal planes, the intermediate species being transported along the surface. As the result a pronounced structure sensitivity of reactions on oxide catalysts may appear.

A question may be raised as to what extent the idealized structure of the surfaces of MoO_3 crystallites represent the real structure of MoO_3 samples used in catalytic research. A detailed study of MoO_3 single crystals with many sophisticated physical techniques such as LEED, XPS, UPS, and EELS revealed [73] that the basic (010) crystal plane of the oxidized sample is indeed stoichiometric and shows the same periodicity as that of the bulk. Heating MoO_3 in vacuum to 600 K reduces the surface region, the O/Mo atomic ratio decreasing to 2.85. On sputtering the MoO_3 lattice disorders, oxygen is lost and the final product is MoO_2, as determined by XPS and electron diffraction. Annealing above 770 K causes the reappearance of the LEED pattern of the (010) plane of MoO_3, and the valence band structure becomes indistinguishable from that of stoichiometric MoO_3. As the only source of oxygen to replenish the surface is the bulk of the sample, so oxygen diffusion must be rapid. Recently it was claimed that very thin steps on the (010) plane of MoO_3 platelets may be visible by the electron microdiffraction technique [70].

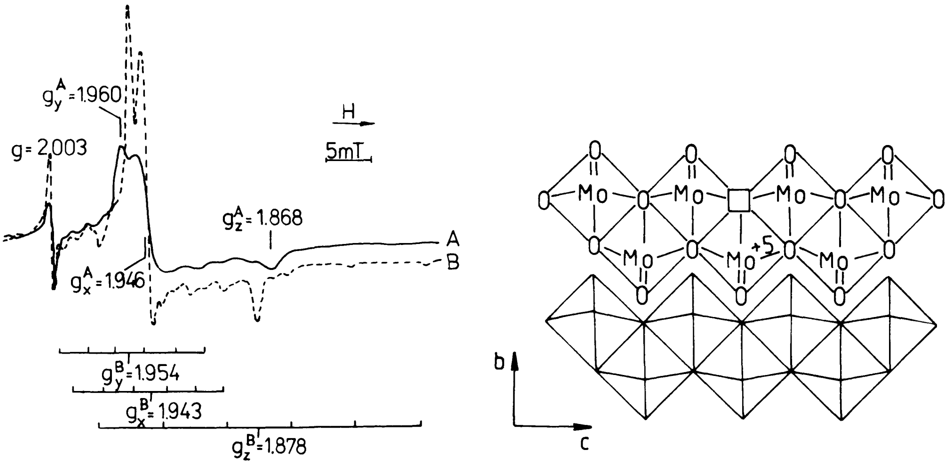

(a) (b)

FIGURE 7.19 (a) ESR spectra of MoO_3 after outgassing at 430°C for 5 min (curve A) and 35 min (curve B); (b) Section of MoO_3 lattice [8].

E. Formation of Acrolein

Nucleophilic addition of oxygen to the allylic species results in the first step in the formation of a σ-bond between the allyl initially π-bonded to the metal cation and the lattice oxygen, situated at the surface of the catalyst. This adsorbed complex must now get rid of one hydrogen atom linked to the carbon atom of the C—O group, before it can be desorbed in the form of acrolein. In earlier studies [50] it has been postulated that the second abstraction of hydrogen precedes the addition of oxygen so that the latter step is directly followed by desorption of acrolein and formation of an oxygen vacancy at the catalyst surface. These two possible routes may be described by the following scheme:

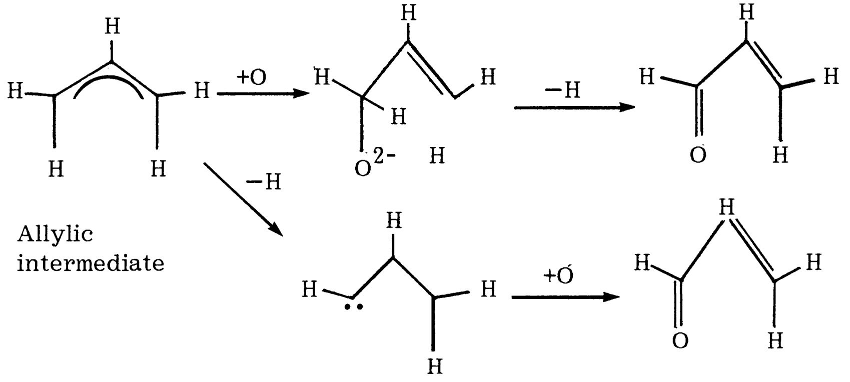

Studies of the reaction of ^2D- and ^{18}O- labelled allyl alcohols enabled the discrimination between these two reaction pathways.

It has been shown in the experiments [74] (Table 7.7) using 1,1-d_2-allyl alcohol in the presence and absence of pyridine, that on MoO_3 and $Bi_2Mo_3O_{12}$ catalysts the alcohol molecules react on Brönsted acid sites. What results is diallyl ether formation with scrambling of deuterium atoms via carbonium ion mechanism, and also on oxidizing sites, where scrambling also takes place via the formation and interconversion of two isomeric 1,1-d_2- and 3,3-d_2-allyl alcoxides (Fig. 7.20) but is accompanied by the production of 1-d- and 3,3-d_2-acrolein, respectively. Accordingly, on unpoisoned MoO_3 containing considerable number of Brönsted acid centers at its side faces (100), (001), and (110) (see Section III.D), a very rapid isomerization of 1,1-d_2-allyl alcohol molecules takes place resulting in uniform distribution of deuterium atoms between carbon atoms 1 and 3. Allyl ether is formed on acid centers, whereas on oxidizing centers both isomers are oxidized to appropriately labeled acrolein molecules.

TABLE 7.7 Product and Isotopic Distribution for Pulse Reaction of Allyl Alcohol-d_2 and Propene-d_2 at 320°C[a].

			Percentage yields[b]							Acrolein (%)[d]		AA (%)[d]	
Catalyst	Diluent[c]	AA	AA:solvent	$C_3^{=}$	Acrolein	AA	HD	PhH	AE	1-d_1	3,3-d_2	1,1-d_2	3,3-d_2
MoO_3	n-Octane	1,1-d_2	1.7	4.4	30.1	38.2	7.1	1.5	19.0	41.8	58.2	56.7	43.3
MoO_3	2-MPyr	1,1-d_2	1.7	0.6	27.4	64.5	6.9	0.0	0.8	56.0	44.0	72.2	27.8
MoO_3	Pyr	1,1-d_2	0.4	0.0	48.8	46.5	4.7	0.0	e	57.0	43.0	77.3	22.7
$Bi_2O_3 \cdot 3MoO_3$	n-Octane	1,1-d_2	1.7	25.1	37.0	30.2	3.8	3.1	0.8	52.0	48.0	73.0	27.0
$Bi_2O_3 \cdot 3MoO_3$	Pyr	1,1-d_2	1.7	19.8	35.1	38.8	4.5	1.3	0.4	69.8	30.2	82.3	17.7
$Bi_2O_3 \cdot 3MoO_3$	Pyr	1,1-d_2	0.4	20.4	44.2	29.5	5.4	0.5	0.0	66.8	33.2	f	f
$Bi_2O_3 \cdot 3MoO_3$	Pyr	1,1/3,3-d_2[g]	0.4	26.9	54.0	10.3	8.9	0.0	0.0	31.6	68.4	f	f
$Bi_2O_3 \cdot 3MoO_3$	Pyr	1,1/3,3-d_2[g,h]	0.4	6.0	20.0	70.4	3.6	0.0	0.0	f	f	55.7	44.3
$Bi_2O_3 \cdot 3MoO_3$	—	$C_3^{=}$—1,1-d_2[i]	—	91.5	8.5	0.0	0.0	0.0	0.0	29.4	70.6	—	—

[a] 0.25-sec contact time, 0.7 m^2 catalyst, AA + solvent = 32 µmole total, unless otherwise stated.

[b] $C_3^{=}$ = propene; AA - allyl alcohol; HD = 1,5-hexadiene; PhH = benzene; AE = diallyl ether.

[c] 2-MPyr = 2-methoxy pyridine, Pyr = pyridine.

[d] Ratios by NMR.

[e] Masked by pyridine peak.

[f] Not enough collected to analyze by NMR.

[g] 55:45 (1,1-d_2:3,3-d_2) mixture used.

[h] Contact time - 0.025 sec, 0.07 m^2 catalyst.

[i] Feed = 24.5 µmole C_3^{2-}—1,1-d_2; 3.0 cm^3 (2.48 g, 4.2 m^2) $Bi_2O_3 \cdot 3MoO_3$: 15-sec contact tinme.

Source: Ref. 74.

When acid centers at the surface of MoO_3 become poisoned by pyridine, allyl ether disappears from the products whereas the yield of acrolein remains unchanged indicating that oxidized centers have not been affected. Deuterium is no more uniformly scrambled between C_1 and C_3 atoms, and the ratio 77:23 of 1,1-d_2- and 3,3-d_2-allyl alcohol reflects the operation of oxidizing centers, which simultaneously isomerize the alcohol molecules and convert them to acrolein. It is noteworthy that the same ratio is observed in the case of $Bi_2Mo_3O_{12}$ catalyst both in the absence and in the presence of pyridine. This is understandable in view of the fact that no acid centers have been observed on the surface of this catalyst. Comparison of the behavior of labeled 1,1 d_2-propene with that of allyl alcohols indicates that only in the case of using the 1:1 mixture of 1,1-d_2- and 3,3-d_2-allyl alcohol molecules is the ratio of the 1-d_1-

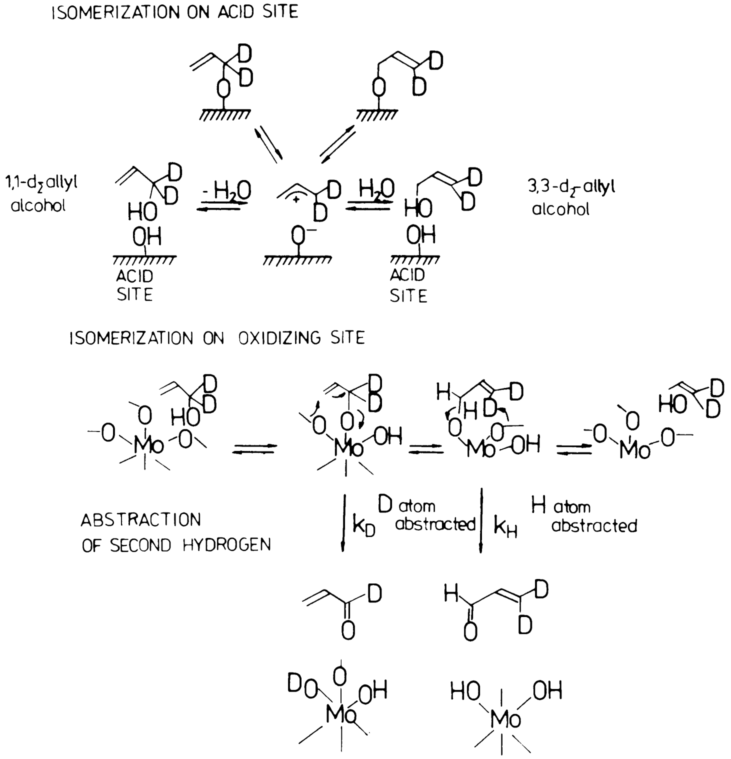

FIGURE 7.20 Reactions of deuterated allyl alcohol molecules at the surface of MoO_3 catalyst [74].

and 3,3-d_2 acrolein molecules produced similar to that obtained from 1,1-d_2-propene. This observation is consistent with the conclusion that π-allyl species are formed in the first step of propene oxidation, the direct formation of the σ-bonded allyl alcoxide being impossible. There is equal probability that nucleophilic addition of oxygen will take place on either side of the allyl species, producing the two isomeric precursors of acrolein in 50:50 proportion.

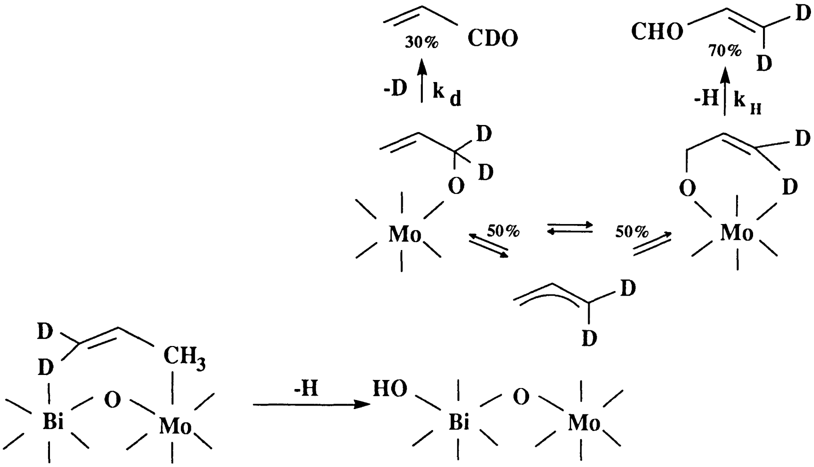

Because of the kinetic isotope effect, the abstraction of H being more facile than abstraction of D, the theoretical ratio of rate constants amounts to $k_H/k_D = 2.13$. The observed ratio of 1-d_1- and 3,3-d_2 acrolein is in agreement with these predictions.

Our discussion of the consecutive steps in the oxidation of propene may be now summarized in form of a mechanistic scheme, shown in Fig. 7.21, in which Bi_2O_3–MoO_3 catalyst was taken as the example. In the first step, dissociative chemisorption of propene takes place through α-hydrogen abstraction by bridging the O^{2-} ion of basic character and formation of a π-allyl complex, linked to the bismuth ion. The allyl radical thus generated undergoes a nucleophilic attack by another bridging oxygen ion, that forming either the Bi—O—Mo or Mo—O—Mo bridge depending on the surface structure of the catalyst, and becomes σ-bonded to this oxygen ion as an allyl alcoxide (2). The allylic hydrogen of the latter now becomes split

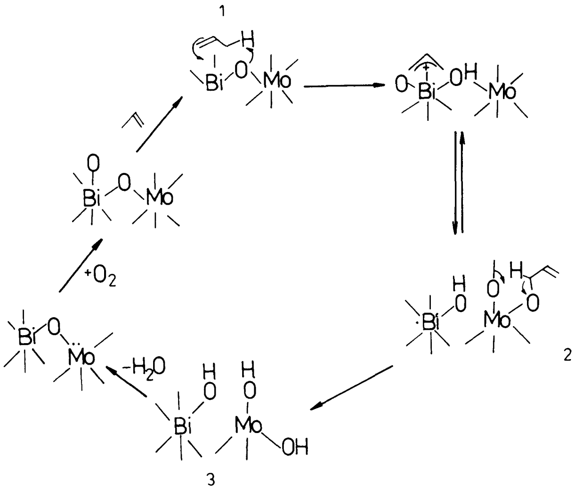

FIGURE 7.21 Mechanism of the oxidation of propene on bismuth molybdate catalysts.

by the adjacent bridging oxygen ion in the concerted reaction resulting in the desorption of acrolein and formation of an oxygen vacancy and an OH group (3). Dehydroxylation restores one of the Bi—O—Mo bridges, generating another oxygen vacancy. In an efficient catalyst the oxygen vacancies rapidly diffuse into the bulk and react with gas phase oxygen at some other surface site, the processes of generation of vacancies in the course of the catalytic reaction and their annihilation by reaction with gas phase oxygen are separated in time and space.

E. Ammoxidation of Propene

Ammoxidation of propene, i.e., its oxidation in the presence of ammonia,

$$CH_3CH{=}CH_2 + NH_3 + 3/2O_2 \xrightarrow{400-460°C} CH_2{=}CHCN + 3H_2O$$

shows a number of similarities to oxidation in the basic elements of its mechanism [75] (Fig. 7.22). Both reactions produce the same relative rates and isotopic distribution of allylic products of oxygen or nitrogen insertion, respectively, obtained from propenes D-labeled either in allyl or vinyl positions, indicating the k_H/k_D value of 1.82 [50], which is nearly the theoretical maximum at this reaction tem-

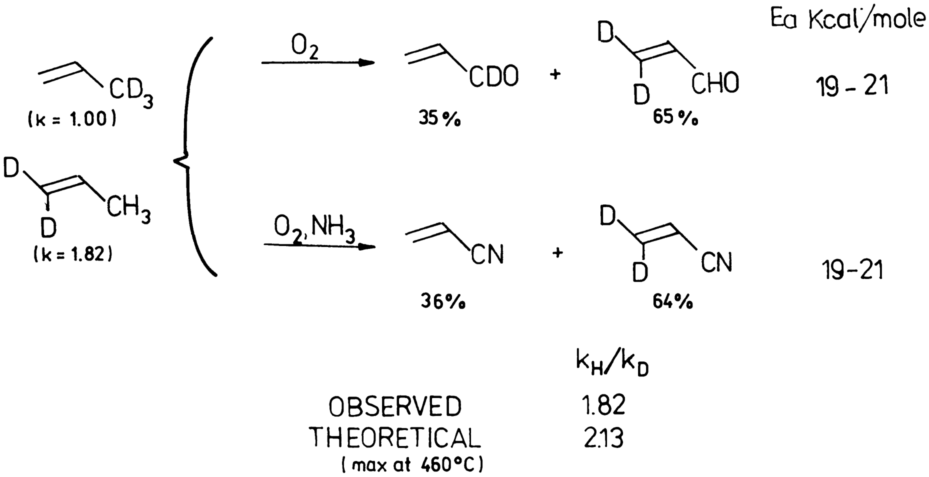

FIGURE 7.22 Comparison of oxidation and ammoxidation over $Bi_2Mo_3O_{12}$ catalyst at 460°C [75].

perature. Moreover, both reactions have the same overall activation energy. These observations indicate a common rate-determining step, which is the α-hydrogen abstraction, described in detail in Section III.B. This is followed by nucleophilic attack of NH^{2-} species on the π-allyl.

Ammoxidation must usually be carried out at temperatures higher than oxidation. At 320°C the oxidation of propene to acrolein proceeds with high conversion and selectivity of almost 100%. The addition of ammonia at this temperature causes a dramatic decrease in conversion, indicating that the surface becomes poisoned. The poisoning effect disappears at higher temperatures, so that at 430°C conversion remains high independent of the increasing ammonia propene ratio, and selectivity to acrylonitrile increases slightly with this ratio.

It should be borne in mind that the nucleophilic attack of NH^{2-} species on the π-allyl results in the formation of an intermediate allyl σ-bonded to the NH^{2-}. Its conversion to nitrile requires removal of three hydrogen atoms. At the surface populated by NH^{2-} ions the removal of two hydrogen atoms may be carried out by the adjacent NH^{2-} ion to form an NH_3 molecule, with the last hydrogen being taken away by an O^{2-} ion, diffusing from the subsurface layer to fill the vacancy left by desorbed ammonia. It may then be expected that ammoxidation would require two ammonia molecules per propene molecule. At constant propene pressure the ratio of acrylonitrile and acrolein in the products should thus be proportional to $\underline{k}_N \tau\ NH^2/\underline{k}_O \tau_O$, where $\underline{k}_N$ and $\underline{k}_O$ are the rate constants of the nucleophilic addition of NH^{2-} and O^{2-} to the allylic species, respectively, and τ_{NH} and τ_O are the surface coverage with NH^{2-} and O^{2-} ions. As indicated by the results of Table 7.8, $\tau_{NH} + \tau_O = 1$, the ratio of acrylonitrile to acrolein should thus be proportional to the pressure of ammonia or, at constant propene pressure, also to the ratio of ammonia and propene pressures. Indeed the acrylonitrile-acrolein product ratio obtained on the multicomponent molybdate catalyst is a linear function of the $(NH_3)^2/C_3H_6$ ratio [75].

Interesting results were obtained by comparing the results of ammoxidation of D-labeled allyl alcohol and allyl ammine [74]. Both 1,1-d_2- and 3,3-d_2-allyl alcohols gave the same nitrile product composition containing 70% of 3,3-d_2- and 30% of d_0-acrylonitrile molecules. The authors point out that the formation of a common intermediate of the π-allyl type must be postulated in which equal probability of C—N bond formation on either side of the allyl species occurs, which is similar to C—O bond formation in propene oxidation. In this case, however, the process requires the rapid migration of the carbon bond from oxygen to nitrogen at the catalyst surface, and then the rapid isomerization of the allyl species σ-bonded to NH^{2-} ions, through a π-allyl intermediate.

TABLE 7.8 Interaction of Propene and Ammonia Pulses over Bi^{3+}/MoO_3 Catalyst[a]

Time lag between NH_3 and C_3H_6 pulses (s)	Yield (%)		Conv. (%)	Selectivity (%)	
	C_2H_3CHO	C_2H_3CN		C_2H_3CHO	C_2H_3CN
3	—	6.92	7.9	—	87.6
15	2.64	4.44	8.0	33.0	55.5
25	4.36	2.81	8.0	54.5	35.1
40	5.95	1.70	8.1	73.5	21.0
60	5.95	1.71	8.0	74.4	21.2

[a] Catalyst: $Bi_{0.5}/MoO_3$. Conditions: 450°C, 1 ml NH_3, 0.3 ml C_3H_6.
Source: Ref. 60.

F. Catalysts

A great number of different mono-, bi-, and multicomponent oxide systems have been studied as catalysts in allylic oxidation of propene and many of them have been patented. The most important are those based on two component oxides, one of these components being bismuth, uranium, tin, or iron oxide, and the other component the oxide of molybdenum, tungsten, or antimony. These systems may form definite chemical compounds of the oxy salt type as bismuth molybdates and uranium antimonates, or they may constitute solid solutions as in the case of tin-antimony oxide. By far the most extensively studied are the catalysts based on Bi_2O_3 and MoO_3, which serve as the basis for many of today's highly active and selective commercial catalytic systems.

1. Bi_2O_3–MoO_3 System

Bismuth molybdate catalysts display extremely high activity and selectivity in both oxidation of propene to acrolein and ammoxidation of propene to acrylonitrile. As was described in Section III.B, the bismuth oxide component is responsible for the activation of a hydrocarbon molecule, whereas the role of the molybdate sublattice is to perform the nucleophilic addition of oxygen or nitrogen. The two oxides form several compounds of varying composition, but it has been established that superior catalytic properties appear only within the Bi/Mo composition range 2:3 and 2:1 [1]. Three different compounds exist in this composition range, which can be described by chemical formulas $Bi_2(MoO_4)_3$ (phase α), $Bi_2Mo_2O_9$ (phase β), and Bi_2MoO_6 (phase γ). Upon heating the latter undergoes several polymorphic transformations. The γ phase has the layer structure of the orthorhombic koechlinite [76], made up of $(Bi_2O_2)_{\underline{n}}^{2+}$ and $(MoO_2)_{\underline{n}}^{2-}$ units connected through O^{2-} ions. The idealized structure of the $\overline{M}oO_2$ sheet may be viewed as a two-dimensional ReO_3-type layer of corner-sharing octahedra. The presence of layers provides low-energy pathways for the diffusion of oxygen vacancies, which makes the reoxidation of the catalyst to proceed with the activation energy of only 8–9 kcal mol^{-1}.

The α-phase $Bi_2(MoO_4)_3$ crystallizes with a structure which can be derived from the scheelite structure ($CaWO_4$) [77]. In the ABO_4-type scheelite, the A cation is usually divalent and is eight-coordinated by oxygen, while the B cation is hexavalent and present in the structure in the form of discrete BO_4 tetrahedra. When molybdate or tungstate of trivalent metal cations crystallize with a scheelite structure, three of the divalent A cations are replaced by two trivalent cations producing a cation vacancy in the structure. These vacancies may be disordered or ordered into different substructures. Thus, the α phase of bismuth molybdate is more accurately described as $Bi_{2/3}\square_{1/3}MoO_4$, where □ represents a vacant cation site. The vacancy ordering in the α phase is such that some of the oxygen atoms are bonded to only one Mo cation at a distance of 1.68 Å, which corresponds to an Mo═O double bond. All $(MoO_4)^{2-}$ ions occur as pairs, Mo_2O_8. Each Bi^{3+} secures its eightfold surrounding, all oxygens being shared with Mo anions.

In the structure of the β-phase elements from the scheelite and koechlinite structures are combined [78]. The structure is built of square clusters of four MoO_4 tetrahedra, Mo_4O_{16}, bound together by Bi ions located halfway on the axis passing through the centers of the squares [87]. Some Bi cations are surrounded by eight oxygen ions from the MoO_4 tetrahedra; in the coordination sphere of others oxygen associated only with Bi is also present. Thus, the structure may be visualized as composed of rows of oxygen ions, connected only to Bi cations, running parallel to the $(Mo_4O_{16})-Bi-(Mo_4O_{16})$ units. These resemble the ribbons of Bi_2O from the Bi_2O_2 layers in koechlinite. As emphasized by Matsuura [79], not all Bi sites are filled, but one in every four sites is empty. The structure may be thus represented by $Bi(Bi_3\square O_2)(Mo_4O_{16})$, the first Bi being associated only with the (Mo_4O_{16}) units, and the Bi cations in parentheses being bonded to the oxygens associated only with Bi as well as to those shared with the (Mo_4O_{16}) units. Schuit [87] drew attention to the fact that the changes occurring in the structure on passing from Bi_2MoO_6 through $Bi_2Mo_2O_9$ into $Bi_2Mo_3O_{12}$ are indicated by three features:

1. Change in the Bi coordination, which in Bi-rich compound is essentially determined by the Bi_2O_2 layer structure, whereas in Mo-rich compound all oxygens of the cubic arrangement are shared by Bi and Mo.
2. Change in the degree of clustering of the Mo–O polyhedra, which passes from an infinite two-dimensional ReO_3 structure via Mo_4O_{16} to Mo_2O_8 clusters.
3. Gradual appearance of vacant cation sites.

These differences are summarized in Table 7.9.

One of the methods of characterizing the reactivity of oxygen in oxide lattices is the measurement of the rate and activation energy of the reduction of these oxides, with hydrogen often being used as the reducing agent. Figure 7.23 shows the kinetics of the reduction of α-, β-, and γ-bismuth molybdate as well as Bi_2O_3 carried out at 440°C in 29 Torr of hydrogen [88]. A linear dependence of the amount of hydrogen consumed on time was observed in all cases. The highest rate of reduction is observed in the case of Bi_2O_3, the reduction of the γ phase is slower, and the β and α phases are the slowest. The reduction of MoO_3 under these conditions is unmeasurably slow.

TABLE 7.9 Structural Peculiarities of Bismuth Molybdate

Formula	Number of oxygens bound only to Bi (per formula)	Number of Bi^{3+} vacancies	Degree of clustering of MoO_4
$Bi_2Mo_3O_{12}$		1	2
$Bi_2Mo_2O_9$	1	1/2	4
Bi_2MoO_6	2		Infinite

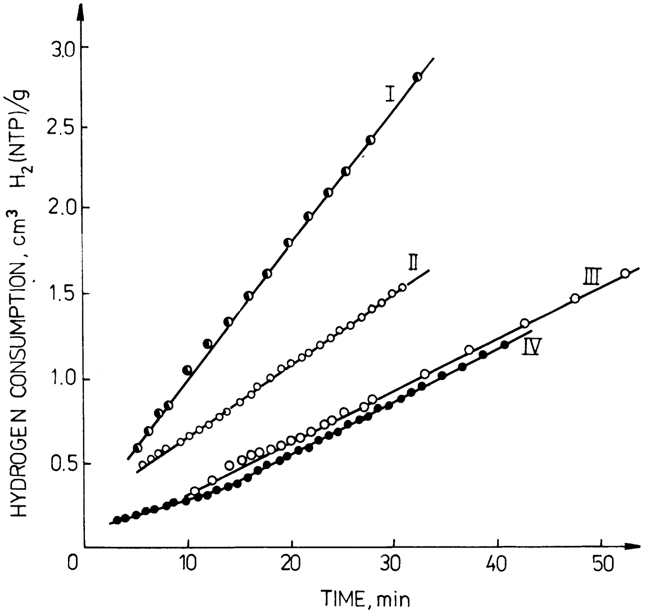

FIGURE 7.23 Kinetics of the reduction of Bi_2O_3 and bismuth molybdates in 29 Torr of hydrogen at 440°C. I-Bi_2O_3, II-Bi_2MoO_6, III-$Bi_2Mo_2O_9$, IV-$Bi_2(MoO_4)_3$ [88].

Reduction may be described by the general equation:

$$O^{2-}_{surf} + H_2 \longrightarrow H_2O + V_O$$

where V_O is the oxygen vacancy. As the reaction was proceeding under quasi-isobaric conditions, the linear dependence of the degree of reduction on time indicates that the surface concentration of O^{2-} ions remained constant, i.e., the rate of diffusion of oxygen through the lattice must have been much higher than the rate of consumption at the surface. Under these conditions the rate equation simplifies to

$$\underline{r}_{red} = \underline{k}\underline{p}_{H_2}$$

in agreement with the observed first order of the reaction with respect to hydrogen. The rates at 440°C and the activation energies of the reduction of Bi_2O_3, MoO_3, and the three bismuth molybdates are summerized in Table 7.10 [88]. It can be seen that the activation energies differ considerably whereas the rates assume values of the same order. This indicates that the compensation effect takes place. In fact, the linear relation between the logarithm of the pre-exponential factor and the activation energy is well obeyed (Fig. 7.24).

TABLE 7.10 Rates and Activation Energies of the Reduction in Hydrogen at a Pressure of 29 Torr

Catalyst	Rate at 440°C $\frac{cm^3 H_2(NTP)}{g \cdot min} 10^2$	E_{act} (kcal mol^{-1})
Bi_2O_3	6.35	21.5
$Bi_2MoO_6(\gamma)$	4.09	19.4
$Bi_2Mo_2O_9(\beta)$	2.90	29.0
$Bi_2(MoO_4)_3(\alpha)$	2.36^{+} 3.04^{++}	32.6^{+} 27.1^{++}
MoO_3	—	21

$^{+}$–Slow step; $^{++}$–rapid step.
Source: Ref. 88.

Since in the course of the reduction oxygen ions are removed from the surface of the oxide, their bonds with the surface must be disrupted. The activation energy may be thus represented by the relation:

$$\underline{E}_{act} = \underline{E}_{\underline{o}} + \underline{a}\cdot\underline{q}_{\underline{o}}$$

where $\underline{q}_{\underline{o}}$ is the energy of oxygen to surface bond, broken in the course of the reaction. The activation energy of the reduction with hydrogen may thus be taken as a measure of the oxygen bond strength in the catalyst. The data summarized in Table 7.10 indicate that the activation energies differ considerably for the three molybdates, suggesting differences in the strength of the oxygen bonding. Indeed, Bi_2MoO_6 with its layer structure has oxygen less tightly bonded than in the other two molybdates.

Measurements of the rate of the reverse process of oxidation of prereduced oxides may in turn supply information on the mobility of

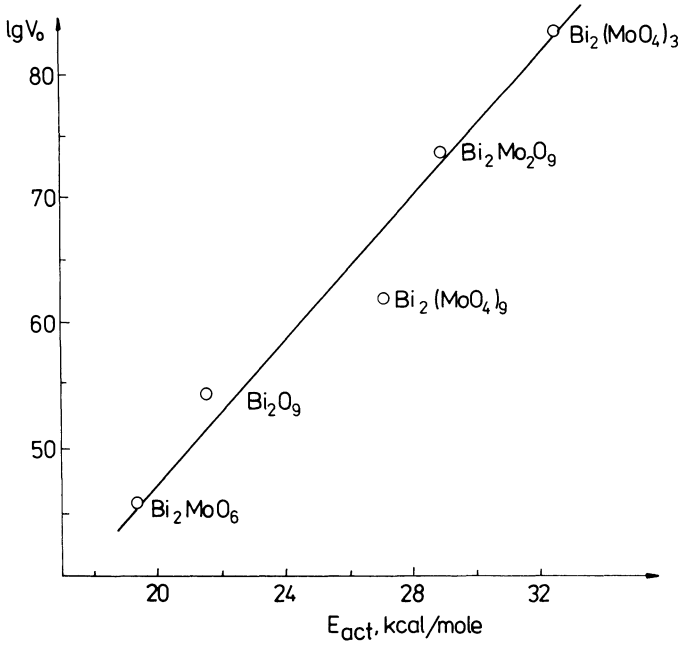

FIGURE 7.24 Logarithm of the rate of reduction of Bi_2O_3 and bismuth molybdates in hydrogen at 440°C as a function of the activation energy of reduction [88].

oxygen ions in the oxide lattice. For mildly reduced bismuth molybdates the rate of reoxidation decreases in the order $\gamma > \beta > \alpha$. At low levels of reduction, when oxygen vacancies are confined primarily to the surface, the energy barrier for reoxidation is 1–2 kcal mol^{-1}. The values of the activation energy for reoxidation of more deeply reduced bismuth molybdates, summarized in Table 7.11 [89], show that the energy barrier for oxygen transport is much smaller in the γ phase than it is in the α or β phase.

A large number of contradictory results were published concerning the catalytic properties of different bismuth molybdate phases. Margolis et al. [80] determined the specific rate constants for the formation of the major products in the oxidation of propene over α, β, and γ phase and found that the β phase was most active and selective, followed by α and γ phases. These results were essentially similar to those of Bereś et al. [81] who also found that the β phase displayed superior properties, whereas the Dutch group

TABLE 7.11 Activation Energies for Catalyst Reoxidation (temperature range = 320–460°C)

Catalyst	Initial reduction (Atoms O × 10^{19} m^2)	Activation energy (kcal mol^{-1})
$Bi_2Mo_3O_{12}$	0.2	1.3
	0.5	1.4 (430–460°C)
	1.4	24.5 (320–400°C)
		25.9
$Bi_2Mo_2O_9$	0.1	8.1
	0.3	9.6
	0.8	26.6
	1.5	25.8
Bi_2MoO_6	0.2	1.2
	0.5	0.7 (430–460°C)
		8.1 (320–380°C)
	1.3	7.9
$Bi_3FeMo_2O_{12}$	0.1	4.0
	0.4	6.6
	0.9	8.0
	1.4	8.2
Multicomponent catalyst	0.1	3.6
	0.5	5.2 (430–460°C)
		27.1 (350–400°C)
	1.3	1.4

Source: Ref. 88.

[82,83] obtained results indicating that the γ phase was equally good. In a more recent study Agaquseinova et al. (after ref. [137]) observed that in the oxidation of propene activity decreased in the order $\alpha > \beta > \gamma$ whereas the order of selectivity was $\beta > \alpha > \gamma$. These results are at variance with those of Monnier and Keulks (after ref. [137]), who found the order of decreasing activity $\beta > \alpha > \gamma$ at approximately the same selectivity.

It seems that these differences in assessment of the catalytic properties of the bismuth molybdate phases are due to the very high mobility of MoO_3 on the one hand and to the considerable reactivity in the solid state of these phases on the other hand. As the result, dynamic changes of the surface structure may occur in the course of pretreatment and during the catalytic reaction. Indeed, the results of the photoelectron spectroscopic studies of the surface composition of the three bismuth molybdate phases after different vacuum and thermal treatments as well as after having worked in the catalytic reactor indicate [90] that on annealing in vacuum the surface layer of grains becomes enriched in molybdenum, whereas in the oxidizing atmosphere of the reacting mixture the composition of the surface remains the same as that of the fresh sample. Therefore the surface composition of the three molybdates will depend strongly on the redox properties of the gas phase, i.e., they may strongly depend on the conditions under which the catalytic reaction is carried out. This may be an important factor determining the catalytic properties of molybdate catalysts as indicated by the observation that strictly stoichiometric molybdates are inactive in the oxidation of propene and the presence of excess MoO_3 is necessary to render them active [79].

As mentioned, ample experimental evidence was accumulated in recent years indicating that in the atmosphere of the reacting catalytic mixture the surface of bismuth molybdate catalysts shows the ratio of Bi/Mo to be about one independently of the composition of the bulk. This led Matsuura to postulate that bismuth molybdate multicomponent catalysts are covered by surface domains of $Bi_2Mo_2O_9$ which constitute the catalytically active phase exposing the A-sites and B-sites responsible for the transformation of olefins [111]. As the abstraction of hydrogen from the hydrocarbon molecule and its desorption in the form of water or the insertion of oxygen from the catalyst surface into the hydrocarbon molecule take place at different sites than those at which the catalyst surface is reoxidized by gas phase oxygen, the efficient transport of oxygen between these two sites through the lattice is a condition of the operation of an active catalyst. Measurements of the rate of isotopic oxygen exchange between bismuth molybdates and $C^{18}O_2$ indeed revealed that catalysts with high activity in oxidation also show high rate of oxygen exchange reaction, whereas exchange of oxygen hardly occurs with the catalysts showing low activity in oxidation. The operation of such catalysts has been called by Matsuura a hydroponic type model [111].

It should be borne in mind that the catalytic properties may be crucially dependent on the microstructural changes taking place at the catalyst surface in the course of its pretreatment or during the catalytic reaction. This may be of particular importance in the case of oxide catalysts, whose surface lattice oxygen ions are removed from certain surface sites in one step of the catalytic reaction and replaced by gas phase oxygen in another step of the reaction, not necessarily at the same surface sites. Such a redox-type mechanism requires a high mobility of lattice oxygen ions, which may facilitate the local restructuring of the surface.

Important information concerning the microstructural surface transformations may be obtained by combining high-resolution electron microscopy (HREM) with in situ dynamic studies as well as microanalytical methods (STEM and AEM) [91]. As an example, results may be quoted that were obtained by exposing the γ phase to C_3H_6 in situ in the electron microscope. At around 400°C the formation of an ordered superstructure with spacing of 8.4 × 10.8 Å was observed on the (001) plane of γ phase (Fig. 7.25). When the

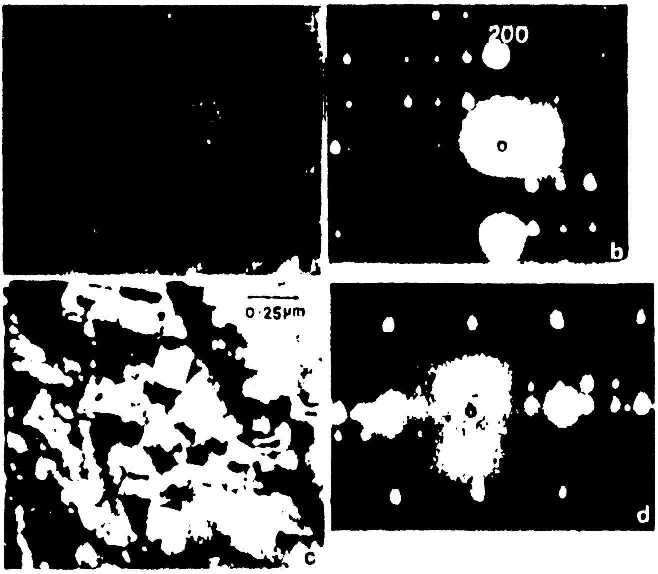

FIGURE 7.25 In situ reduction sequence in C_3H_6 of γ-Bi_2MoO_6: (a) sample at room temperature, (b) diffraction pattern, (c) sample at around 400°C with defects, (d) diffraction pattern showing supperlattice. 1 MeV [91].

(010) samples of the α phase were analyzed in the same way, they also exhibited the superstructure with spacing of 8.4 × 10.5 Å, similar to that observed in the case of γ phase. Microanalysis indicated that this superstructure corresponded to a Bi/Mo ratio of 1:1. The diffraction patterns and the images of these superlattices were consistent with the diffraction patterns and images obtained in (101) projection of the β phase. Thus the appearance of the superstructure may signify the formation of the β phase. The structure of this phase may be derived from the γ phase by removing Bi atoms and some rearrangement of cations, in the transformation of layers written as

$$(Bi_2)(Mo) \longrightarrow (BiMo_{2/3}\square_{1/3})(Mo_{2/3}B_{1/3})$$

where (Bi_2) represents the layer built of (Bi_2O_2) units and (Mo) the layer of (MoO_2) units. The presence of vacancies may enhance oxygen mobility and activity.

2. Bi_2O_3—Fe_2O_3—MoO_3 and Multicomponent Molybdate Systems

In the scheelite structure ABO_4 either the A sites or the B sites may be occupied by more than one type of cations. Thus it was shown [92,93] that in the Bi–Fe–Mo–O system two compounds appear crystallizing in the scheelite structure: $Bi_3FeMo_2O_{12}$ and $Bi_2Fe_2Mo_2O_{12}$. Both may be derived from the $Bi_2\square(MoO_4)_3$ formula. In the first compound, the trivalent ions substitute one-third of hexavalent molybdenum ions in the anionic sublattice. The resulting increase of the negative charge of anions (three negative charges per formula) are compensated by filling the cation vacancies with trivalent bismuth ions. The compound may thus be represented as $Bi_3(Mo_{2/3}Fe_{1/3}O_4)_3$. In the second compound the excess charge of anions becomes compensated by filling the cation vacancies with trivalent iron ions. The compound is thus properly described as $Bi_2Fe(Mo_{2/3}Fe_{1/3}O_4)_3$. The XPS determination of the surface composition showed that it roughly corresponded to their bulk composition. The two compounds are isostructural, giving identical X-ray diagrams and Raman as well as IR spectra [93], but $Bi_2Fe_2Mo_2O_{12}$ showed much higher catalytic activity in the oxidation of propene to acrolein [94]. This activity may be increased still further by introducing other additives. In recent years a large number of multicomponent molybdate catalysts have been investigated and patented. The patent literature implies that there are always several molybdate phases present comprising $CoMoO_4$, $NiMoO_4$, $Fe_2(MoO_4)_3$, and $Bi_2(MoO_4)_3$. The catalyst formulations also include alkali and alkaline-earth metal cations as well as such elements as phosphorus, arsenic, antimony, and vanadium. They are usually supported on silica and operate at much lower temperatures than bismuth molybdate catalysts. The X-ray analysis of the multicomponent catalytic system Bi—Fe—Co—Mo—O showed [134] that it was composed of four separate phases: $Fe_2(MoO_4)_3$ coherent with $Bi_2(MoO_4)_3$, β—$CoMoO_4$, and excess MoO_3. Studies of XRD and Mössbauer spectra in situ in the course of the oxidation of propene revealed [135] that $Bi_2(MoO_4)_3$ and β—$CoMoO_4$ remained unchanged with the time-on-stream, whereas $Fe_2(MoO_4)_3$ transformed into β—$FeMoO_4$, its conversion being higher the higher the content of propene in the gas phase (Fig. 7.26). After several hours of reaction the X-ray reflexes of $Fe_2(MoO_4)_3$ disappeared, but the presence of Mössbauer lines indicated that it remained transformed in a highly dispersed phase. Figure 7.27 shows the temperature dependence of the isomeric shift of $Fe_2(MoO_4)_3$ in the spectrum of multicomponent catalyst registered in air and in situ in the course of propene oxidation. When measured in air (curve 1) or under the conditions of catalytic reaction below 520 K (curve 2), the temperature dependence followed the theoretical relation. In this temperature range the total oxidation of propene was observed. Above

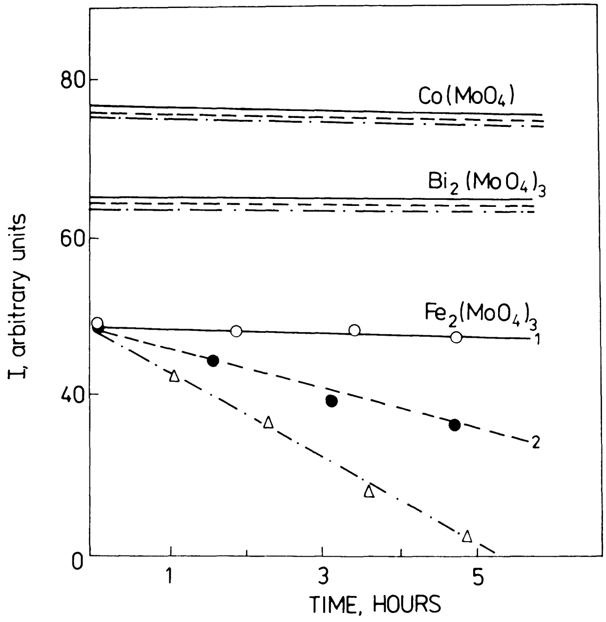

FIGURE 7.26 Changes of intensities of X-ray lines characteristic for different molybdates in the course of the oxidation of propene in the C_3H_6/O_2 mixture of composition (1) 1:3, (2) 1:2, and (3) 1:1 [135].

520 K when selective oxidation of propene set in as indicated by a rapid increase in its rate (curve 4), an anomalous divergence from the theory was observed. After the reaction a linear dependence was again observed but with a different slope (curve 3). These results indicate that under the conditions of catalytic reaction the iron(III) molybdate transforms into a defect structure according to the equation:

$$Fe_2Mo_3O_{12} \longrightarrow Fe_2Mo_3O_{12-\underline{x}}\square_{\underline{x}} + \frac{\underline{x}}{2}O_2$$

where $\square$ = anionic vacancy and $\underline{x}$ = nonstoichiometry factor. Thermal activation of vacancies $\square = \square^{\beta+} + \beta\, e^-$ results in the appearance of the excess negative charge which polarizes the Fe—O bond in the molybdate. The $Fe^{3+}(3d^5)$ state in the initial molybdate is transformed into the activated state $3d^{5+\beta}$ intermediate between Fe(III)

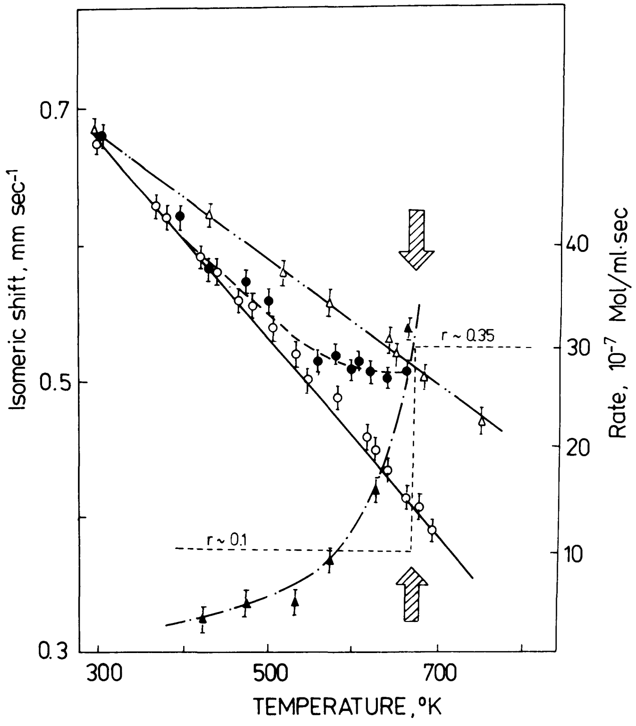

FIGURE 7.27 Dependence of the isomeric shift on the Fe(III) molybdate in the Mössbauer resonance spectrum (curves 1—3) and dependence of the rate of propene oxidation on temperature (curve 4) [135]. o—1, •—2, Δ—3, ▲—4.

and Fe(II). The complete reduction to β–$FeMoO_4$ takes place at the interface with the isostructural β-$CoMoO_4$ where the energy of nucleation of β–$FeMoO_4$ is considerably lower. The switch from total to selective oxidation range taking place around 680 K is marked in Fig. 7.27 by an arrow. It corresponds to the change of normalized areas of Mössbauer peaks:

$$\underline{r} = \frac{[Fe^{2+}]}{[Fe^{2+} + Fe^{3+}]}$$

from 0.1 to 0.35 (reduction of 35% of Fe^{3+} to Fe^{2+} ions). The role of different phases in the multicomponent catalyst may thus be explained as follows. Activation of hydrocarbon molecules and insertion of oxygen into the allyl species takes place at the surface of $Bi_2(MoO_4)_3$. Oxygen molecules are activated at the surface of β–$FeMoO_4$ and then oxygen is transported through the defected $Fe_2(MoO_4)_3$ phase to replenish the reduced sites at the surface of $Bi_2(MoO_4)_3$. The role of β–$CoMoO_4$ consists of stabilization of β–$FeMoO_4$ nuclei, and MoO_3 is necessary to make the interconverstion of iron(III) and iron(II) possible:

$$Fe_2(MoO_4)_3 \longrightarrow 2FeMoO_4 + MoO_3 + O_2$$

Indeed, experiments showed [136] that substitution of β–$CoMoO_4$ by isostructural manganese or zinc molybdate produces similar catalytic properties.

G. U_3O_8–Sb_2O_4 System

The phase diagram of this system indicates the existence of two compounds: $USbO_5$ and USb_3O_{10} [84,85]. They may be represented, similarly to bismuth molybdates, as layer structures, the $USbO_5$ being composed of alternating uranium oxide or antimony oxide layers, whereas in USb_3O_{10} every second uranium atom in the layer is substituted by an antimony atom, so that every U atom is isolated by Sb atoms and there are no adjacent U—O—U elements:

U Sb U	U U U
Sb Sb	Sb Sb
Sb U Sb	U U U
Sb Sb	Sb Sb
U Sb U	U U U
USb_3O_{10}	$USbO_5$

The USB_3O_{10} phase is orthorhombic, belonging to the D_{2h}-F_{ddd} space group with $\underline{Z}$ = 8 and 112 atoms in the unit cell, analogous to UNb_3O_{19} and UTa_3O_{10}.

Figure 7.28 compares the catalytic activity in ammoxidation of propene, the intensity of the X-ray peak at d = 3.18 Å characteristic for the USb_3O_{10}, and the intensity of the IR-band at 930 cm^{-1} also characteristic of this phase [84]. A distinct correlation may be seen between the catalytic activity in nitrile formation and the presence of the USb_3O_{10} phase, the latter being responsible for the production of acrylonitrile. The $USbO_5$ phase is also catalytically active but only in total combustion. It has been proposed that the active centers for the allylic oxidation are generated in the course of the dehydroxylation of the surface of the USb_3O_{10} crystallites [86].

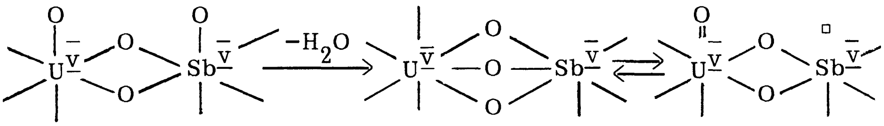

There is not enough experimental data to formulate the detailed mechanism of the reaction at the surface of this catalyst. In particular, no information is available as to whether the allyl species is generated at the uranium or antimony ion.

H. Oxidation of Propene and Acrolein to Acrylic Acid

Acrylic acid is widely used as a monomer for the production of polyacrylic acid and polyacrylates. Considerable research effort has been devoted to disentangle the mechanism of the transformation of propene into this acid. Two types of commercial processes have been developed: one-stage oxidation of propene directly into acrylic acid; and two-stage oxidation, involving the transformation of propene into acrolein in the first stage and then oxidation of acrolein to acrylic acid in the second stage.

Examination of the patent data shows that on some catalysts, such as bismuth molybdate or tin antimony, only acrolein is formed (besides the products of the degradation of the propene molecule) whereas with other catalysts, e.g., cobalt and nickel molybdates, acrolein and acrylic acid are obtained in different proportions depending on the experimental conditions. The ability to transform the aldehyde into an acid seems to be a more general property as indicated by the data of Table 7.12 which summarizes results [95] concerning the selectivity of these two groups of catalysts in the oxidation of $\underline{o}$-xylene. On catalysts which oxidize propene only to acrolein,

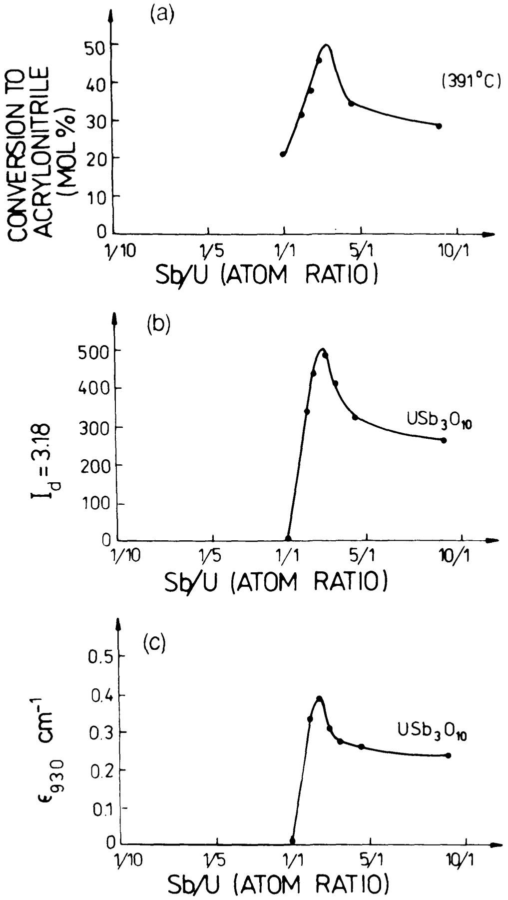

FIGURE 7.28 Correlation between catalytic properties and phase composition: (a) yield of acrolynitrile in ammoxidation of propene, (b) intensity of X-ray line, and (c) intensity of IR band characteristic of USb_3O_{10} [84].

o-xylene is oxidized only to tolualdehyde, whereas phthalic anhydride is formed only with those catalysts on which acrylic acid appears as the result of the oxidation of propene. Thus, it may be concluded that at the surface of the catalysts a special type of active centers must be present, which has the ability to transform the aldehyde groups into the carboxylic groups irrespective of the type of organic molecule.

Studies of the behavior of transition metal molybdates led to the observation that the selectivity of these systems in the formation of acrylic acid may be related to the presence of excess molybdenum trioxide; this is illustrated by the results [96] presented in Fig. 7.29,

TABLE 7.12 Oxidation of o-Xylene on Olefin Oxidation Catalysts

			Selectivity (%)		
Catalyst	Temp. (°C)	Conv. (%)	Tolualdehyde	Phthalic anhydride	CO_2
$Bi_2Mo_2O_9$	370	5.5	54.4	—	52.8
	430	35.0	33.7	—	54.3
	470	49.5	29.9	—	52.9
Bi_2MoO_6	370	18.5	45.4	—	45.9
	430	52.5	34.7	—	54.5
	470	71.7	25.6	Trace	58.0
Sn—Sb—O	390	7.5	45.3	—	49.3
	450	21.0	34.8	—	54.8
Sn/Sb = 1:4	490	42.0	24.0	—	70.2
$CoMoO_4$	390	30.0	12.0	10.6	60.0
	410	56.0	5.2	26.4	57.0
	450	94.0	Trace	36.4	48.0
	470	98.0	Trace	31.2	48.0
$NiMoO_4$	370	40.0	6.8	13.0	62.8
	390	76.0	2.5	19.5	71.0
	410	93.0	1.0	29.0	62.4
	450	99.0	Trace	25.2	56.0
MoO_3	450	15.0	50.0	3.3	32.7
	490	30.5	51.1	2.3	30.8
V_2O_5—TiO_2	350	29.0	14.5	34.8	32.4
	370	65.0	7.1	49.2	21.4
V/Ti = 1:2	390	99.0	—	64.5	27.6

Source: Ref. 95.

in which the yield of acrylic acid obtained by the direct oxidation of propene and the selectivity of its formation are plotted as the function of the chemical composition of the NiO–MoO_3 catalysts. It may be seen that acrylic acid appears in the composition range corresponding to excess MoO_3.

Important information concerning the nature of centers responsible for the transformation of the aldehyde group into the acid group was supplied by studies of the oxidation of acrolein on heteropoly acids and their salts.

Heteropoly compounds are composed of heteropoly anion, countercation, and crystal water. The heteropolyanions of acid (H_3PM $o_{12}O_{40}$) and its salts from a structure called a Keggin unit (Fig. 7.30). The Keggin units together with countercations and water are arranged in a three-dimensional secondary structure. This secondary structure depends on the type of cation and changes readily upon dehydration-hydration processes. Water and alcohol molecules are quickly exchanged even at room temperature. When D_2O was introduced at room temperature into $H_3PMo_{12}O_{40}$, the H_2O of the acid was exchanged completely with D_2O within 1–2 min.

In situ IR experiments showed [97] that the isotopic exchange of oxygen between $H_2{}^{18}O$ and the Keggin unit was also rapid, with exchange of both the terminal Mo=O as well as the bridging Mo—O—Mo oxygen atoms (36 out of 40 atoms). Only the internal oxygen atoms bridging the central phosphorus atom with the Mo—O octahedra remained on their sites. This indicates that oxygen atoms

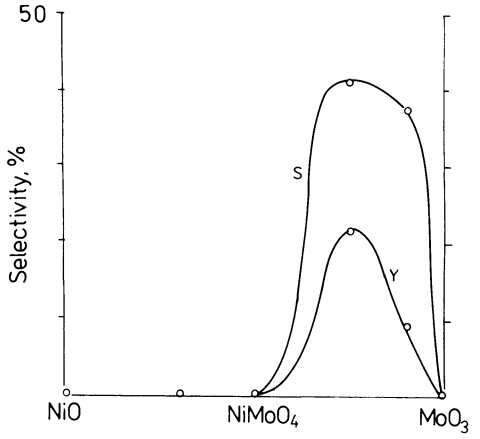

FIGURE 7.29 Yield and selectivity of acrylic acid obtained in the oxidation of propene over NiO–MoO_3 catalysts of different composition. Reaction temperature 425°C [96].

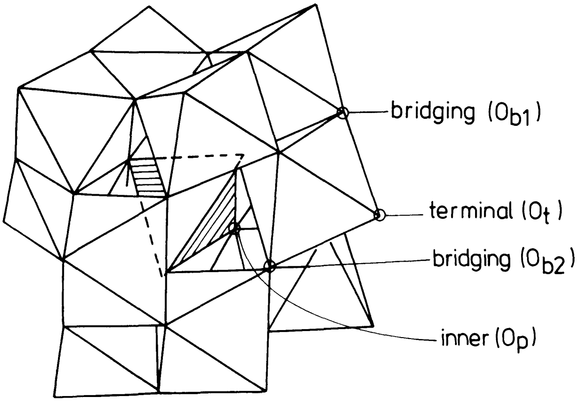

FIGURE 7.30 Structure of the Keggin unit.

in the Keggin unit are very mobile. Experiments with pyridine showed that protons can be quantitatively replaced by pyridinium ions indicating the Brönsted acidity of all three protons. The temperature at which pyridinium ions were removed ($\geq$300°C) shows that these compounds are strong solid acids.

The behavior of $H_3PMo_{12}O_{40}$ and its salts in the course of reduction and reoxidation depends on the type of countercation [98]. The acids and salts of such cations as Mg, which are soluble in water, decompose on reduction to give MoO_{3-x} and P_2O_5. The degree of decomposition depends on the conditions of reduction and results in the irreversibility of this process. Although formally such a reduced sample may be completely reoxidized, the structure of the collapsed Keggin units is no more restored, and the samples are mixtures of initial $H_3PMo_{12}O_{40}$, P_2O_5, and MoO_3.

Conversely, insoluble salts as $K_3PMo_{12}O_{40}$ can be reduced reversibly if the reduction does not exceed about two electrons per Keggin unit. The in situ IR measurements showed that on reduction the intensity of the Mo—O—Mo band decreases whereas that of Mo=O band remains practically constant, which was taken as an indication that it is the bridging oxygen atom of the Keggin unit which is involved in catalytic oxidation [97].

In the pulse reactor studies of the oxidation of methacrolein (MAC) it was found that when the O_2 supply was stopped the oxidation of methacrolein to methacrylic acid continued to proceed at the same selectivity, although the conversion decreased. This clearly demonstrated that the lattice oxygen is used for oxidation. In line with this conclusion the rate of methacrolein oxidation could be expressed by the equation:

$$-\frac{d[MAC]}{dt} = k p_{MAC} p_{O_2}^{0.6-1.0} p_{H_2O}^{0-0.2}$$

A mechanism was thus postulated in which a geminal diol species was proposed as the first intermediate complex resulting from the interaction of acrolein with the acid centers of the catalyst. This complex then undergoes dehydrogenation to form methacrylic acid and an oxygen vacancy in the Keggin unit, which is then refilled by oxygen from the gas phase:

$$\mathrm{R{-}CHO} \underset{-\mathrm{H_2O}\ \text{or}\ \mathrm{H^+}}{\overset{+\mathrm{H_2O}\ \text{or}\ \mathrm{H^+}}{\rightleftarrows}} \begin{matrix} \mathrm{RCH(OH)_2} \\ \text{or} \\ \mathrm{RCH(OH){-}O{-}Mo} \end{matrix} \xrightarrow{-\mathrm{H_2}} \mathrm{R{-}COOH}$$

Vital new observations contributing to our understanding of the detailed mechanism of the insertion of oxygen into the aldehyde group were obtained by studying the EPR and IR spectra in situ in the course of the oxidation of acrolein on 12-molybdophosphoric acid and its potassium salt [99]. In the temperature range 300–450 K the chemisorption of acrolein was observed accompanied by the appearance of an electron delocalized over 12 Mo^{+6} centers in the Keggin units. The IR spectrum registered in the course of adsorption could be interpreted by assuming that the chemisorbed acrolein is present in the form of acrylate type species. Above 450 K desorption of an acrylic acid molecule takes place, the proton being recaptured by the acrylate ion. Diffuse reflectance IR spectra of the catalyst reduced in situ in acrolein vapor at different temperatures show that the $Mo{=}O_t$ bond remains unperturbed in the course of the reduction, whereas the intensity of bands characteristic for the $Mo{-}O_b{-}Mo$ vibrations markedly decreases (Fig. 7.31). This indicates that it is the bridging oxygen of the Keggin unit, to which acrolein becomes bonded and which is then removed on its desorption. Subsequent reoxidation restores the original appearance of the IR spectrum. Desorption leaves an oxygen vacancy and two electrons, at least one of them becoming trapped at a neighboring Mo^{+6} to generate an ESR active Mo^{+5} ion, responsible for the asymetric EPR signal shown in Fig. 7.32.

Thus, it may be concluded that chemisorption of acrolein proceeds with the transfer of two electrons and a proton to the Keggin unit, the resulting chemisorbed species of an acrylate type being attached to the bridging oxygen of the catalyst:

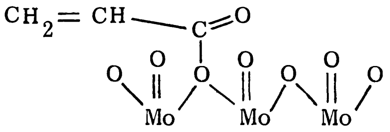

There are three different lattice oxygen environments present in the Keggin anion: terminal oxygen O_t, two types of bridging oxygens O_b, and an inner oxygen O_p (Fig. 7.30). From among the two exposed oxygens, O_t and O_b, the bridging oxygens O_b are more basic and their lone pairs constituting the HOMO of the Keggin unit are capable of performing a nucleophilic attack on the hydrocarbon molecule. The LUMO of the unit is the Mo4d orbital but this orbital is relatively inaccessible to the reactants because it is screened by the close-packed surface oxygen atoms. The HOMO and LUMO of

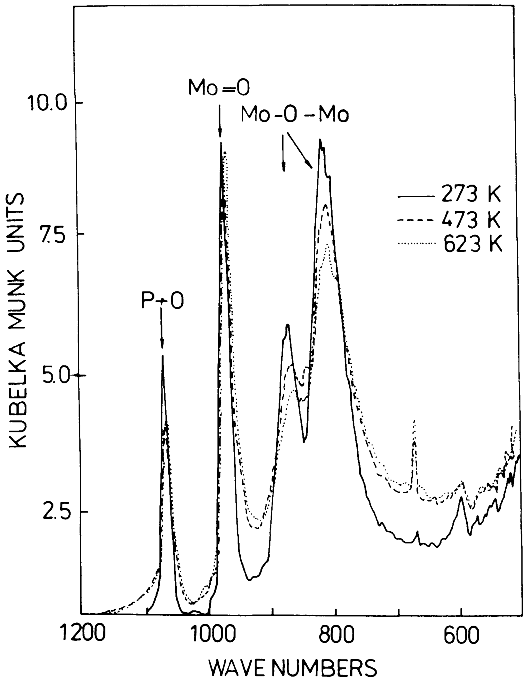

FIGURE 7.31 IR spectrum of $KPMo_{12}O_{40}$ after desorption of acrolein at different temperatures [99].

the acrolein molecule are illustrated in Fig. 7.33 [99]. The HOMO is the lone pair of acyl oxygen (13a'), although the 2a" orbital (essentially the C═C π-bond) lies very close to it in energy. The LUMO consists of the first unoccupied orbital 3a" of the π system of acrolein; its largest coefficient is associated with the carbonyl carbon. The reaction between acrolein and the Keggin unit to form a chemisorbed species is governed by HOMO-LUMO interaction consisting of a nucleophilic attack by the surface O_b lone pair orbitals on the empty 3a" orbital of acrolein.

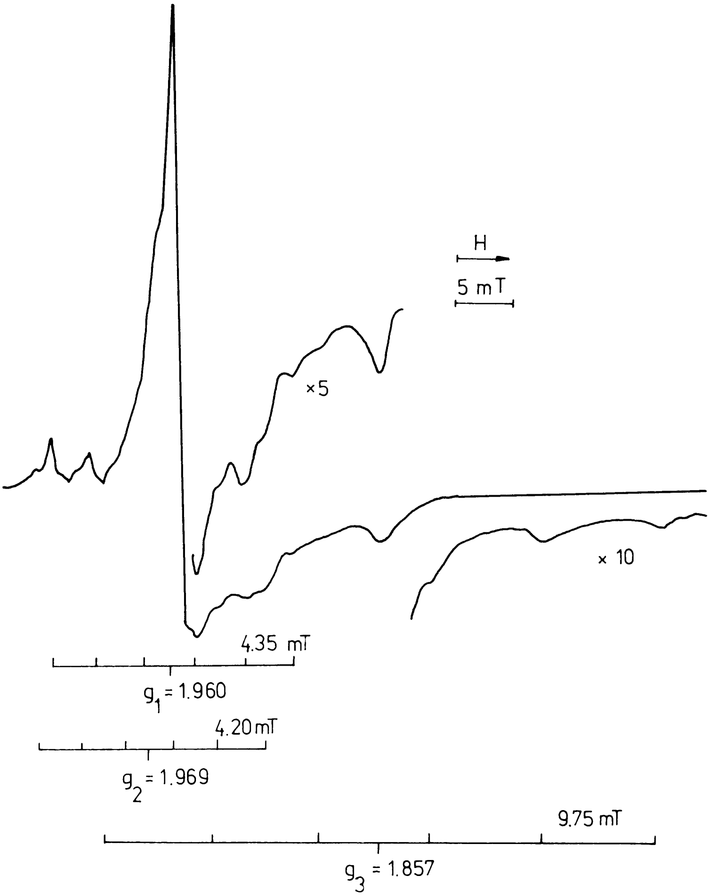

FIGURE 7.32 ESR spectrum of $KPMo_{12}O_{40}$ after desorption of acrolein [99].

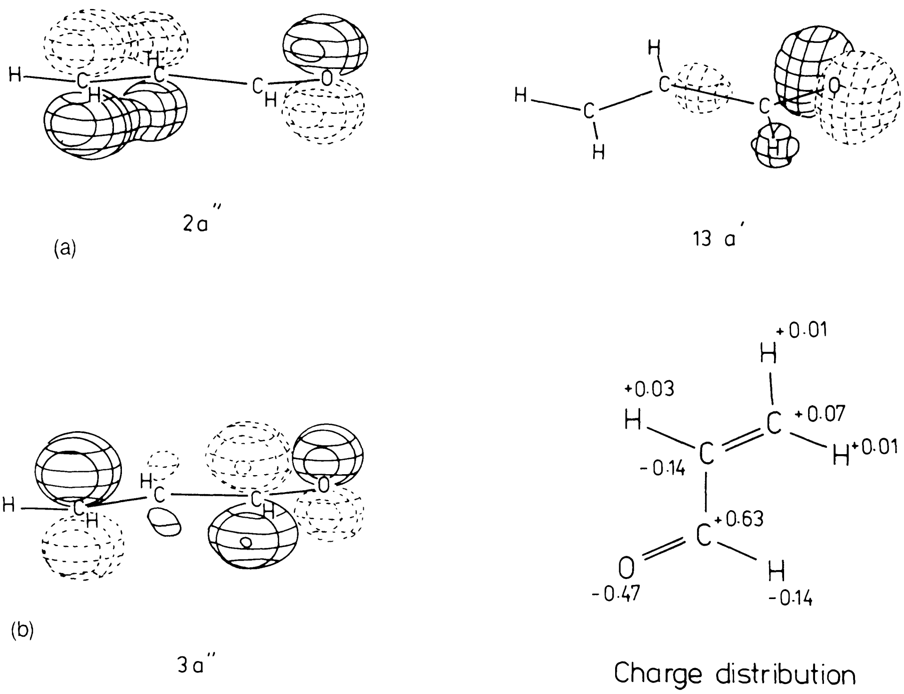

FIGURE 7.33 HOMO (a) and LUMO (b) of acrolein [99].

H. Oxidation of Propene to Acetone

As discussed in Section III.B, the activation of the propene molecule to form allyl species may be considered as an acid-base process, involving the participation of surface O^{2-} ions of base character. A different type of propene activation will take place on surfaces containing Brönsted acid centers, where carbonium ion mechanism may operate, resulting in the formation of propoxide type adsorption complex. In the presence of water the complex decomposes to produce isopropyl alcohol and regenerated surface Brönsted acid centers. When redox centers are also present at the catalyst surface, dehydrogenation of isopropyl alcohol may follow its formation on acid centers, resulting in the appearance of acetone. This reaction was discovered in 1968 [100,101] and since then is known as oxyhydration. Many mixed transition metal oxides containing MoO_3 have been shown to be active in the oxyhydration of propene. The best catalysts found so far are SnO_2—MoO_3 and Co_3O_4—MoO_3. In both cases the highest activity was observed for samples containing no more than about 30% of MoO_3, the reaction being carried out in the temperature range

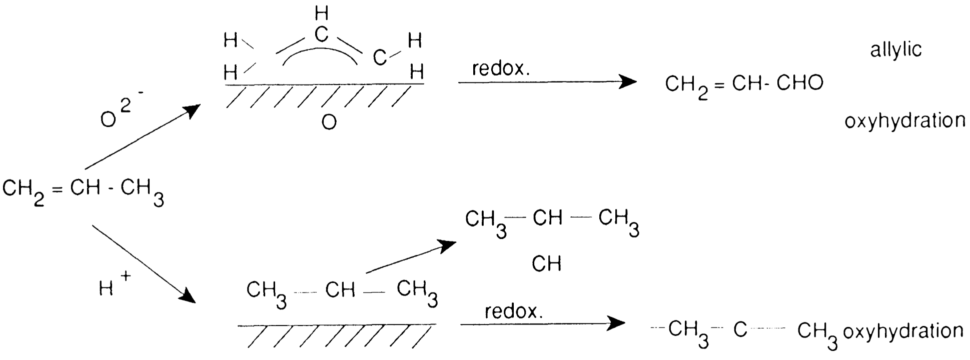

100—200°C. In the case of the SnO_2—MoO_3 catalyst with the Sn/Mo ratio of 9:1, propene was converted at 135°C to acetone with the selectivity of 90%. The participation of the OH groups has been confirmed by isotope labeling. It was shown [100], for example, that the H—D exchange between propene and D_2O, which is practically nonexistent in the presence of MoO_3 and slow on SnO_2, becomes extremely rapid in the presence of the SnO_2—MoO_3 catalyst (Table 7.13). On the other hand, experiments with $H_2{}^{18}O$ proved [102] that oxygen atom in the product acetone comes from water as expected by the carbonium ion mechanism and not from molecular oxygen. The kinetic studies of the oxidation of propene to acetone on SnO_2—MoO_3 at 130°C confirmed that the initial step in the formation of acetone involves the hydration of propene to give isopropanol with an initial selectivity of almost 100%. In the next step dehydrogenation of isopropanol follows yielding actone. The presence of acetone in the feed hindered the oxidation of propene.

TABLE 7.13 Reaction Rate Constant for H—D Exchange between Propene and D_2O

Catalyst	Surface area (m^2 g^{-1})	Rate constant ($mmol/h \cdot m^2 \cdot atm$)
MoO_3	9	5
SnO_2	21	55
SnO_2—MoO_3	4.6	2500

Source: Ref. 100.

IV. OXIDATION OF BUTENES

A. Introduction

Butenes, like propene, contain hydrogen atoms in the α position with respect to the double bond which are more reactive than other hydrogen atoms and are readily abstracted to form an allylic moiety. However, at variance with propene, this allylic moiety may react with oxygen along several different reaction pathways. The majority of oxide surfaces, particularly those used as supports, contain acid centers. In their presence isomerization of but-1-ene to but-2-ene takes place. Indeed, on many oxidation catalysts this is the reaction pathway prevailing at lower temperatures. At higher temperatures, the surface oxide ions which exhibit basic properties abstract hydrogen atoms from the α position in both but-1-ene and but-2-ene to form allylic species and OH^- groups, which are then removed from the surface in the course of its dehydroxylation. The allyl species, thereby generated at the surface, have several possibilities of further transformations. The simplest is the repetition of the hydrogen abstraction from the α position, but now in respect to the allylic bond, i.e., at the C4 atom. This results in the formation of butadiene, which may be desorbed or react further. The allyl species may also undergo a nucleophilic attack by lattice oxygen ions when the surface of the catalyst has the ability to perform such an attack. Depending on the properties of the catalyst, the nucleophilic addition of the O^{2-} ion may take place either at the C3 position to form methyl vinyl ketone, or at the C1 position, leading to the appearance of crotonaldehyde. When electrophilic oxygen species are simultaneously present at the catalyst surface, they may react with butadiene to form furan, reacting further to give maleic anhydride. When only electrophilic oxygen species are present at the surface, an electrophilic attack on the double bond of but-2-ene may take place, resulting in the oxygenolysis of this bond and formation of acetaldehyde or acetic acid. The possible reaction pathways are shown in Fig. 7.34. In the presence of electrophilic oxygen further consecutive reactions can take place, essentially all the intermediate compounds being liable to undergo combustion to CO, CO_2, and H_2O. The steps leading to total oxidation were omitted from Fig. 7.34 to avoid unnecessary complication of the reaction network. In the case of isobutene the properties of the allyl species resemble those observed in the case of propene. The nucleophilic O^{2-} addition may be performed only at two equivalent terminal carbon atoms of the three-atom chain, giving methacrolein as the final product. Thus, the mechanism of the reaction is similar to that described in the case of propylene oxidation.

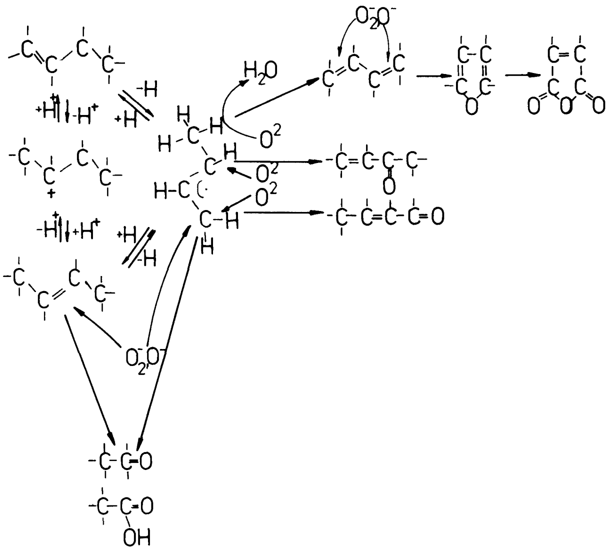

FIGURE 7.34 Reaction network of butenes at oxide surfaces.

B. Oxidative Dehydrogenation of n-Butenes to Butadiene

The major turning point in this important industrial process was the observation that butadiene and other diolefins may be obtained from C4 and higher alkenes by oxidative dehydrogenation over bismuth molybdate catalysts [104]. This stimulated an intensive research effort which resulted in the development of many active and selective catalytic systems. To illustrate the broad spectrum of oxides used, Table 7.14 summarizes some of the commercial catalysts operating in the oxidative dehydrogenation of butene to butadiene.

A relatively large number of studies were devoted to bismuth molybdate catalysts. Oxidation of butene-1 over this catalyst proceeds toward butadiene with a very high selectivity ranging as high as 90–95%, even at very high conversion [54]. The butene-2 molecules are less reactive than butene-1. An experiment in which mixtures of butene-1 and ^{14}C-labeled cis- and trans-butene-2 were passed over bismuth molybdate catalysts showed that but-1-ene is the primary source of butadiene [105]. Over a very wide range of temperature the reaction rate can be expressed by the equation:

$$\underline{r} = \underline{k}\, p_{C_4H_8}^{1}\, p_{O_2}^{0}$$

TABLE 7.14 Selected Commercial Catalysts for Oxidative Dehydrogenation of Butene to Butadiene

Company	Catalyst	Temp. (°C)	Butadiene yield (%)	Selectivity (%)
Dow Chemical	CoNi phosphate + 2% Cr_2O_3	500	—	92
Japanese Geon Ltd.	Mo—Bi—Te—Sb—P oxides	415	70.9	83.8
Petrotex Chem.	Fe_2O_3 + Al_2O_3	621	26	76
Inst. Franc. du Petrole	10% ZnO, 5% Fe_2O_3 ε-Al_2O_3	580	80	—
Phillips Petroleum	P—Sn—Bi oxides	1000°F	87	
Nippon Kagaku Ltd.	$Ni_{2.5}Co_{4.5}Fe_3BiP_{3.5}K_{0.03}Mo_{12}O_{54}$ on silica	305	88	
Gul Res.	$MgCrFeO_4$	325	69	91

The conversion-selectivity data indicate the following reaction scheme [106]:

$$\text{but-1-ene} \xrightarrow{k_1} \text{butadiene} \xrightarrow{k_2} \text{furan}$$

$$CO_2$$

Values for k_3/k_1 of 0.05 and for $(k_2 + k_4)/k_1$ of 0.05 were found, explaining the very high selectivity.

Comprehensive studies, carried out by Schuit and his school in the late 60s, considerably contributed to the understanding of many features of this reaction. They proposed [107] that the reaction starts by abstraction of the α-hydrogen and formation of a π-allyl complex:

$$C_4H_8 + O^{2-} \longrightarrow C_4H_7^- + OH^- \qquad \text{(a)}$$

The allyl species then loses the second hydrogen and desorbs as butadiene, whereas the two OH^- groups recombine to desorb as water, leaving a vacancy at the catalyst surface:

$$C_4H_7^- + O^{2-} + Mo^{6+} \longrightarrow Mo^{4+} + OH^- + C_4H_6 \qquad (b)$$

$$2OH^- \rightleftarrows O^{2-} + \square + H_2O \qquad (c)$$

where $\square$ denotes an anion vacancy. The vacancies then become filled by oxygen from the gas phase; the reduced Mo ions being simultaneously reoxidized. The kinetic data indicated that this latter step proceeds very rapidly.

Reaction (a) simultaneously provides a pathway for isomerization, although the latter may also proceed by the carbonium ion mechanism if Brönsted acid centers are present at the surface [108].

By recirculating but-1-ene/helium mixture over Bi_2O_3, MoO_3, and Bi_2MoO_6 at 530°C it was shown [109] that Bi_2O_3 was reduced to Bi and CO_2 was mainly formed, MoO_3 was reduced to MoO_2 and isomerization was the main product, whereas in the course of reduction of Bi_2MoO_6 butadiene was mainly produced and the rate of its formation was the same as the rate of butene oxidation in the presence of gaseous oxygen. These results indicated that lattice oxygen was responsible for the abstraction of hydrogen, as assumed in the proposed scheme.

Interesting results were obtained by studying the adsorption of butenes and butadiene on bismuth molybdates [110]. On fully oxidized catalysts neither oxygen nor water was adsorbed but their adsorption occurred on partially reduced catalysts and increased with the degree of reduction. Conversely, adsorption of hydrocarbons took place and two types of adsorption sites were found to operate: one involved in the single-site Langmuir adsorption isotherm and the other in dual-site Langmuir adsorption isotherm. They were called A sites and B sites. It was assumed that the A sites may be assigned to oxygen ion surrounded by two oxygen vacancies on Bi ion. The adsorption of butene or butadiene on B sites was found to be rapid and reversible, and as these adsorptions obeyed dual-site Langmuir isotherm, two adsorption centers must be involved in formation of the B site. It was thus postulated that this site comprised an anion vacancy on a Mo^{6+} ion surrounded by corner-shared O^{2-} ions.

According to the authors [110], the active site for butene dehydrogenation on the surface of Bi_2MoO_6 catalyst contains one A site and two B sites and, as represented schematically in Fig. 7.35, the transformation of butene starts by abstraction of the hydrogen atom from the α position, the H atom becoming located on one of the

O_B atoms, and the allyl group on the other. The second hydrogen atom, now in the α position to the allyl group, i.e., at C4, begins to interact with the O_B atom of the second B site and is abstracted to form the OH group and a butadiene molecule, weakly attached to the B site. At that point two alternative ways exist: either the butadiene molecule is desorbed and the two protons migrate to O_A and are desorbed as a water molecule, or the weakly adsorbed butadiene becomes strongly attached to O_A and becomes further

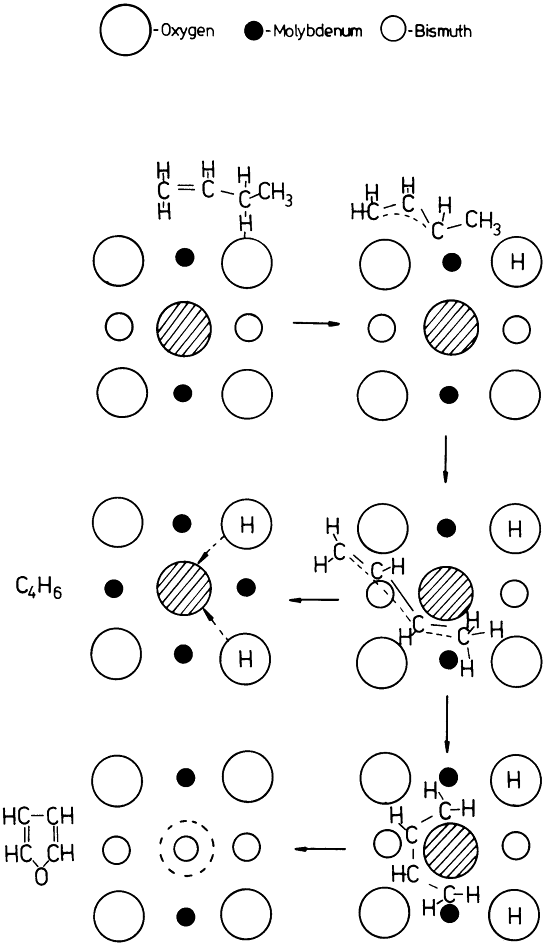

FIGURE 7.35 Mechanism of the transformation of butene into butadiene on B sites and A sites at the surface of Bi_2MoO_6 catalysts. Adapted from [110]. A site oxygen atoms are hatched.

oxidized to furan and then to CO, CO_2, leaving the catalyst reduced. The catalyst is then reoxidized at the A site either by diffusion of an O^{2-} ion from the bulk or by gas phase oxygen.

A considerable number of studies were also devoted to the oxidative dehydrogenation of butenes to butadiene on spinel-type catalysts. Some of the catalysts used are given in Table 7.15. It may be seen that different types of zinc iron spinels operate with very high selectivity at a considerable conversion [120]. In addition, studies on the use of inverse spinels $CoFe_2O_4$ and $CuFe_2O_4$ have been reported [121]. The mechanism must involve a redox cycle, and it may thus be expected that the catalytic properties would be related to the ability of the catalyst lattice to withstand reduction and the facility of reoxidation. In the case of zinc chromium ferrite the redox cycle involving the Fe^{2+}/Fe^{3+} pair was confirmed by ESR spectroscopy [122]. It was postulated that the active site for adsorption of but-1-ene consists of an oxygen vacancy and an adjacent adsorbed radical O^- which is responsible for the hydrogen abstraction. During the desorption of butadiene, iron is reduced to Fe^{2+} and desorption of water leaves the site empty for subsequent adsorption of oxygen in the form of an O^- ion, Fe^{2+} being simultaneously reoxidized to Fe^{3+}:

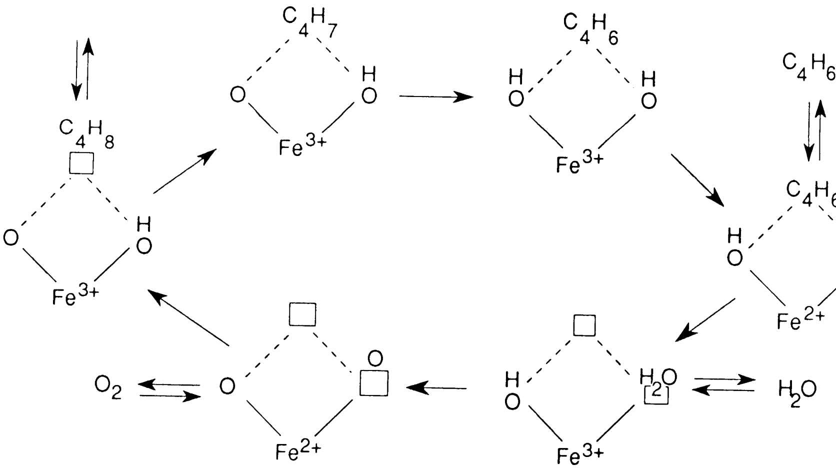

C. Oxidation of Butenes to Maleic Anhydride

As discussed in Section III.E, in the series of elementary oxidative steps propene ⟶ allyl ⟶ aldehyde ⟶ acid the step involving the addition of the second oxygen necessary to transform the aldehyde

TABLE 7.15 Catalytic Properties of Some Spinels in the Oxidation of 2-Butene to Butadiene at 325°C

Catalyst	Conversion (%)	Selectivity (%)
$ZnCrFeO_4$	58	91
$ZnCr_{0.25}Fe_{1.75}O_4$	56	90
$ZnCr_{0.1}Fe_{1.9}O_4$	46	92
$ZnFe_2O_4$	20	89
$ZnCr_2O_4$	15	16
$MgCrFeO_4$	64	90
$MgFe_2O_4$	53	86
$MgCr_2O_4$	28	32
α-Fe_2O_3	35	83

Source: Ref. 120.

group into an acid group requires presence at the catalyst surface of separate active sites, so that the catalysts may be divided into those which form aldehyde and those which are able to carry the reaction series to the formation of acid. This division seems to be a general feature and apply also to the reaction series butene $\longrightarrow$ butadiene $\longrightarrow$ anhydride. Ample experimental evidence [112] indicates that catalysts for the oxidation of butadiene to maleic anhydride require different surface properties as compared to those of the catalysts for oxidative dehydrogenation of butene to butadiene. Butadiene is formed on a very wide class of molybdates, bismuth molybdate being the best known example, whereas only $MnMoO_4$ and β-$FeMoO_4$ possess the specific centers for furan and maleic acid synthesis. Other known catalysts include heteropoly acids of molybdenum, tungsten, and vanadium, and vanadium-phosphorus mixed oxides, the latter being by far the most selective catalysts for this reaction [113–115].

The increasing demand for maleic anhydride has stimulated the search for new, cheap feedstocks. The low-cost C4 hydrocarbon stream obtained from naphtha cracker is a very attractive source as an alternative raw material to benzene for producing maleic anhydride on a large scale. Presently large-scale plants of maleic anhydride based on C4 fraction are already operated by many companies. Some patented catalysts are listed in Table 7.16.

An interesting conclusion concerning the participation of different types of oxygen species in the consecutive steps of butene oxidation were obtained from the comparison of $Fe_2(MoO_4)_3$ catalyst in the pulse and flow catalytic reactor on changing the composition of the reacting mixture. Figure 7.36 shows [116] the dependence of the yield of different products when oxygen content in the feed of the flow reactor was changed. At very low oxygen concentration butadiene was the main product, confirming that it is the lattice oxygen which is involved in the hydrogen abstraction step. X-ray analysis showed that under these conditions $Fe_2(MoO_4)_3$ was transformed into $\beta{-}FeMoO_4$. On increasing the oxygen content the yield of butadiene decreased and maleic anhydride appeared in the products, its yield attaining maximum and then decreasing. This was accompanied by the transformation of the catalyst to $Fe_2(MoO_4)_3$ and rapid increase of the yield of CO_2 + CO, which were the main products at an oxygen content higher than about 8%. This behavior may be compared [117] with that observed in the pulse experiments shown in Fig. 7.37. When pulses of pure butene were introduced on

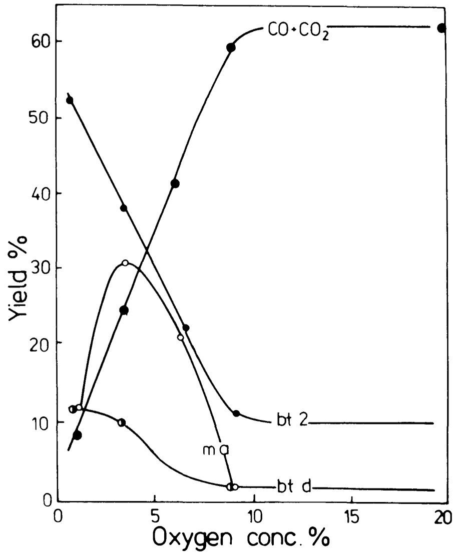

FIGURE 7.36 Oxidation of 1-butene on $Fe_2(MoO_4)_3$ as a function of the oxygen partial pressure. Temperature 390°C, 1% (vol) of 1-butent, GHSV 4140 h^{-1} [116].

TABLE 7.16 Some Patented Catalysts for the Oxidation of C_4 Unsaturated Hydrocarbons to Maleic Anhydride

Catalyst	Temp. (°C)	Yield (%)	Company
V—P—O	400	38	Mitsubishi Chem. Ind. Ltd.
V—P—O/silica gel	200–420	45.7	Mitsubishi Chem Ind. Ltd.
V—P—O/alumina ($\underline{P}/\underline{V} > 0.6$)	450	62.4	Kuraray Ltd.
V—P—Zr (1:3:9.8)		61.8	Ube Industries Ltd.
V—P—Li, V—P—Cu + alkali metal ($\underline{P}/\underline{V} = 1:1.6$)	480	87	Petro-Tex Chemical
V—P—Cu—Nb oxides (1:1.35:0.082:0.021) 20% on alumina	446	84	Petro-Tex Chemical
V—U—P—O (24% V_2O_5, $\underline{V}/\underline{U} = 9.9$)	511	55.2	Gulf Res. & Dev.
W—P—Ti—O (3.2:1:0.5)	410	64	Kiraray Ltd.
$MoO_3—P_2O_5$		30.5	Mitsubishi Chem. Ind.
Mo—Sn—O (1:1)	400	56	Ube Industries Ltd.
Mo—Bi—V—Fe—Co		70	Toyo Soda Mfg. Ltd.
P—W—Ga—O (1:3.2:0.1)	460	58	Kuraray Ltd.
$PMo_{12}Bi_{0.36}Fe_{0.52}Co_{0.8}O_{40.0}$	350	37.5	Mitsubishi Chemical Ind.
V—I—Zr—Bi—O (1:3:10:0.5)	360	57.5	Ube Industries Ltd.

$Fe_2(MoO_4)_3$ at 350°C total oxidation was observed in the first pulse, decreasing rapidly with the number of pulses, which was accompanied by a rapid increase of the butadiene yield. No traces of maleic anhydride were detected. Apparently the initial $Fe_2(MoO_4)_3$ surface, at which total oxidation occurred, was reduced by the pulses of butene to $\beta-FeMoO_4$, where butadiene was selectively formed. As in the presence of oxygen in the gas phase in flow experiments (cf. Fig. 7.36), maleic anhydride was formed on $\beta-FeMoO_4$ as an important product, it may be concluded that it is the adsorbed oxygen which is involved in the oxidation of butadiene to maleic anhydride. When the temperature of pulse experiments is raised to 405°C only total oxidation is observed because the diffusion of oxygen in the $Fe_2(MoO_4)_3$ lattice becomes so rapid that its surface can no longer be locally reduced to $\beta-FeMoO_4$.

The interplay of the two types of sites in the oxidation of butenes is well illustrated by the results presented in Fig. 7.38, in which the yields of butadiene and maleic anhydride are shown, as obtained by the oxidation of 1-butene on vanadium phosphorus mixed-oxide catalyst (1:1) in a flow reactor [118]. At low butene partial pressure maleic anhydride is the only product. On increasing the partial pressure of butene, butadiene appears in rising

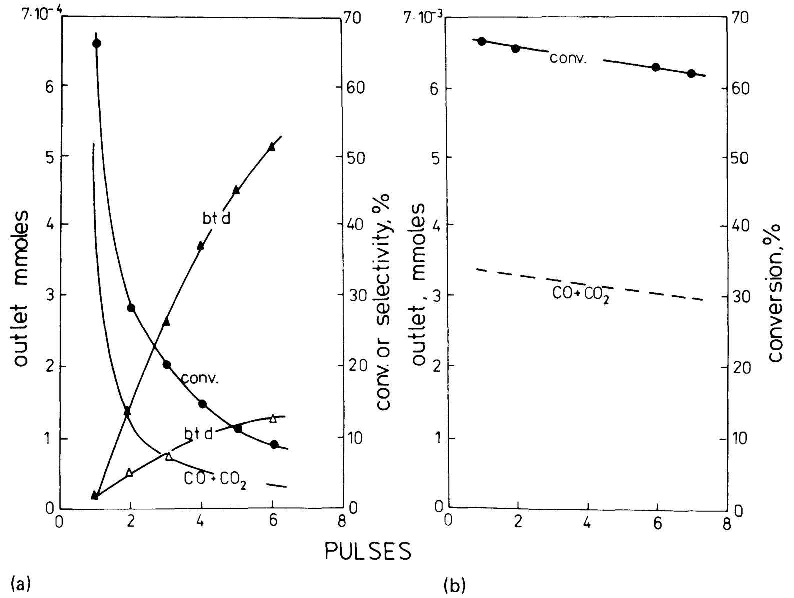

FIGURE 7.37 Oxidation of 1-butene in a pulse reactor on $Fe_2(MoO_4)_3$ at (a) 350 and (b) 405°C [112].

amounts whereas the formation of maleic anhydride becomes inhibited. The inhibition can be completely removed by increasing oxygen partial pressure, which restores the original activity in the formation of maleic anhydride and depresses the yield of butadiene. These results clearly demonstrate that different active centers operate in the formation of butadiene and its transformation into maleic anhydride. The selectivity of butadiene (considering the sum of butadiene formed and butadiene converted to furan + maleic anhydride) is independent of oxygen concentration, whereas the selectivity to furan + maleic anhydride strongly depends on oxygen concentration. Moreover, butadiene is formed in a pulse reactor even without oxygen in the gas phase, the presence of the latter being necessary, however, for the synthesis of furan and maleic anhydride [119]. The rate of butene oxidation may be adequately represented by a Langmuir-Hinschelwood type of model assuming different sites for olefin and oxygen adsorption [118]. The volcano-shaped curve of the dependence of the formation rate for maleic anhydride on butene partial pressure may be satisfactorily explained in terms of a surface

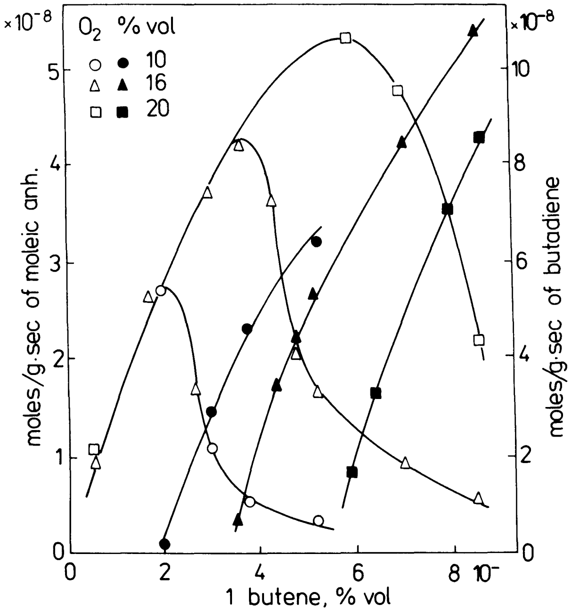

FIGURE 7.38 Amounts of maleic anhydride (open symbols) and butadiene (full symbols) formed in the oxidation of 1-butene in a flow reactor on a vanadium-phosphorus (1:1) mixed oxide catalysts as a function of the partial pressure of butene [112].

reaction between adsorbed oxygen and butadiene as an intermediate, adsorbed on two neighboring sites. The competition between 1-butene and 1,3-butadiene for the same kind of sites is the cause of the inhibition of the selectivity to maleic anhydride at high concentrations of butene.

D. Allylic Oxidation of Butenes

In Section IV.A the mechanism of activation of butene molecules was discussed and it was shown that the allylic intermediate may either lose the second hydrogen atom and transform into butadiene, or undergo a nucleophilic attack by oxide ion to give the carbonyl compounds (cf. Fig. 7.34). Depending on the position in the allylic intermediate, in which the nucleophilic addition of oxygen takes place, either crotonaldehyde or methyl vinyl ketone may be formed. Thus it was found that 1-butene is oxidized to methyl vinyl ketone and 2-butene to crotonaldehyde on metal selenites and tellurites [129]. On the other hand, Cu_2O was shown to be an active catalyst in the oxidation of both 1-butene and 2-butene to methyl vinyl ketone [130].

In the presence of SnO_2-MoO_3 (9:1) and $Co_2O_4-MoO_3$ (9:1) catalysts, which convert propene to acetone at low temperatures, butene was found to be converted to methyl ethyl ketone with a very high yield of 83.5%.

The limited number of experimental data does not yet permit discussion of the factors determining the selection of the reaction pathway by the reacting molecule at two steps where the reaction may be branched: allyl intermediate to butadiene or carbonyl compounds, and the addition of oxygen to C1 or C2 carbons. One of the parameters which may play an important role is the surface structure of the catalysts. This is illustrated by the behavior of the $CuO-Cu_2O-MoO_3$ system.

The subsolidus phase diagram of the $Cu_2O-CuO-MoO_3$ system is shown in Fig. 7.39 [131]. Five chemical compounds were found to be formed; two of them are the Cu(II) molybdates $CuMoO_4$ and $Cu_3Mo_2O_9$, two are the Cu(I) molybdates $Cu_2Mo_3O_{10}$ and $Cu_6Mo_4O_{15}$, and the nonstoichiometric phase $Cu_{4-\underline{x}}Mo_3O_{12}$ composed of Cu(II) and CU(0), its formula being $Cu_3^{II}Cu_{(1-x)}^{0}Mo_3^{VI}O_{12}$. On reduction of $Cu^{II}Mo^{VI}O_4$ the $Cu^{I}Mo^{VI}$ compounds are formed, but not the $Cu^{I}Mo^{IV}$, further reduction leading to the formation of metallic copper and MoO_2.

Figure 7.40 shows the conversion and selectivities to different products when 1-butene pulses were introduced on $Cu_2Mo_3O_{10}$ and $Cu_6Mo_4O_{15}$ catalysts, respectively [132,133]. In the case of $Cu_2Mo_3O_{10}$ the majority reaction is isomerization of 1-butene to 2-butenes, cis- and trans-butenes being the main products obtained. The considerable amount of butadiene which is also formed indicated that on interaction of 1-butene with the surface of $Cu_2Mo_3O_{10}$ allyl species appear as intermediates. On the other hand, experiments carried out with 3,3-dimethylbutene-1 showed that 2,3-dimehtylbutene-2 is formed indicating that isomerization at least partially proceeds also through the carbonium ion mechanism with participation of the surface Brönsted acid centers.

Different behavior is observed in the case of $Cu_6Mo_4O_{15}$. Here the majority product of the reaction is crotonaldehyde, formed with a selectivity of about 70%. The most striking feature is the complete absence of isomerization. Thus, although both $Cu_2{}^IMo_3{}^{VI}O_{10}$ and $Cu_6{}^IMo_4{}^{VI}O_{15}$ are composed of the same chemical elements in the same valence state, they show an entirely different catalytic behavior: The former is active in isomerization and dehydrogenation, whereas the latter mainly inserts oxygen into the organic molecule.

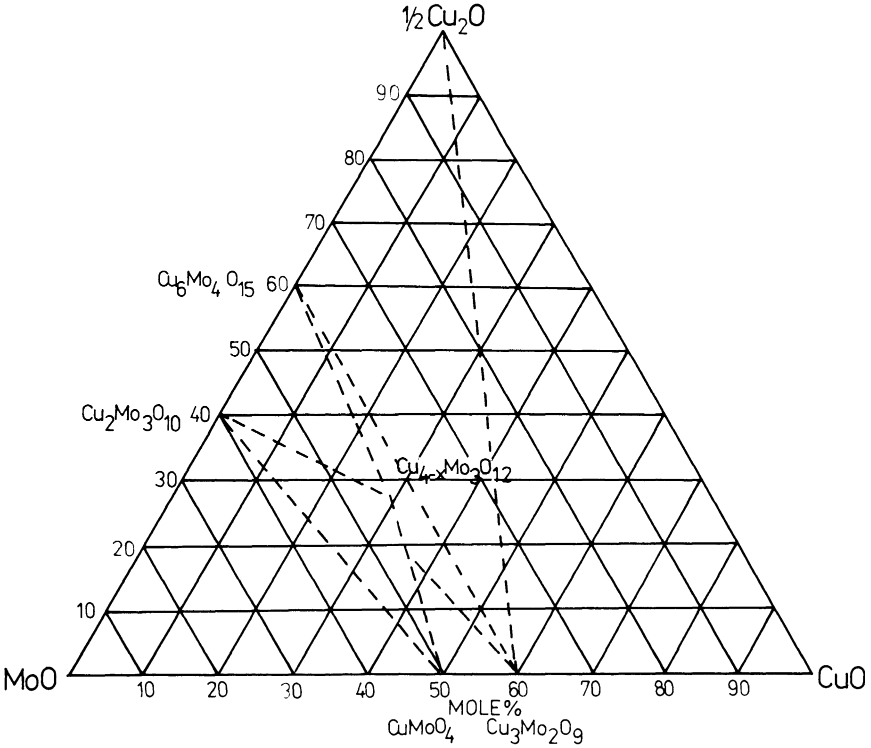

FIGURE 7.39 Subsolidus phase diagram of the $Cu_2O-CuO-MoO_3$ system [131].

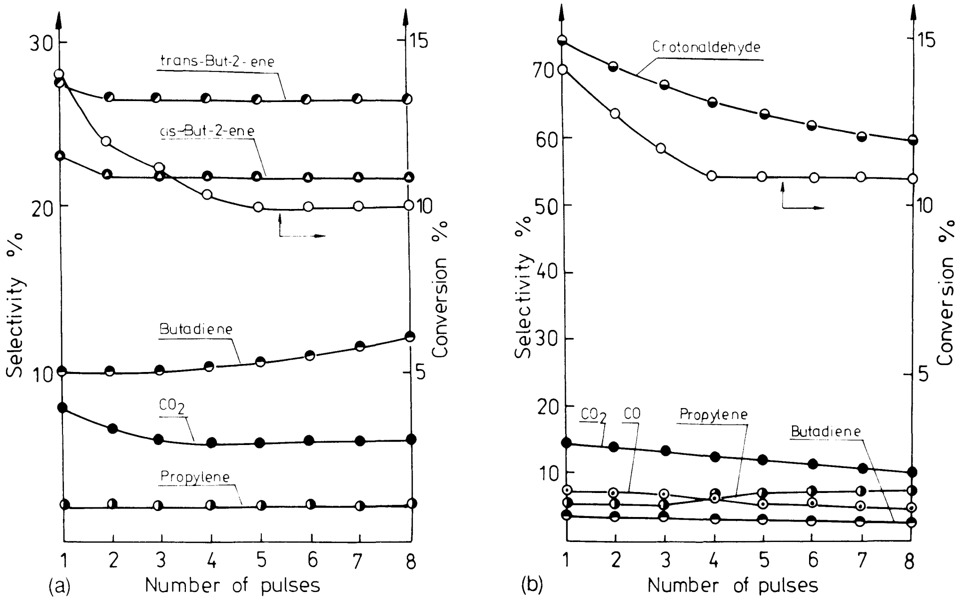

FIGURE 7.40 Conversion and selectivities to different products as a function of the number of pulses of butene-1 on (a) $Cu_2Mo_3O_{10}$ and (b) $Cu_6Mo_4O_{15}$ at 370°C [133].

An interesting behavior is shown by $CuMoO_4$ containing a small excess of MoO_3, of which the example is shown in Fig. 7.41. The fresh $CuMoO_4$ + 0.05 MoO_3 catalyst, when exposed to pulses of pure butene-1, at first showed high selectivity in isomerization, the only other important product being CO and CO_2. Progressively as the surface became more and more reduced by pulses of butene, more and more oxygenated products, i.e., crotonaldehyde and methyl vinyl ketone appeared and after 20 pulses of butene the selectivity of the formation of crotonaldehyde reached a level of about 30% and that of methyl vinyl ketone 10%. When pulses of the mixture of butene and oxygen were injected after pulses of pure butene, the seletivity to crotonaldehyde and methyl vinyl ketone remained high at a high conversion of 70%. Results of these experiments show that in the case of the $Cu_2O-CuO-MoO_3$ system, in which different redox and phase equilibria may be established at the surface, different

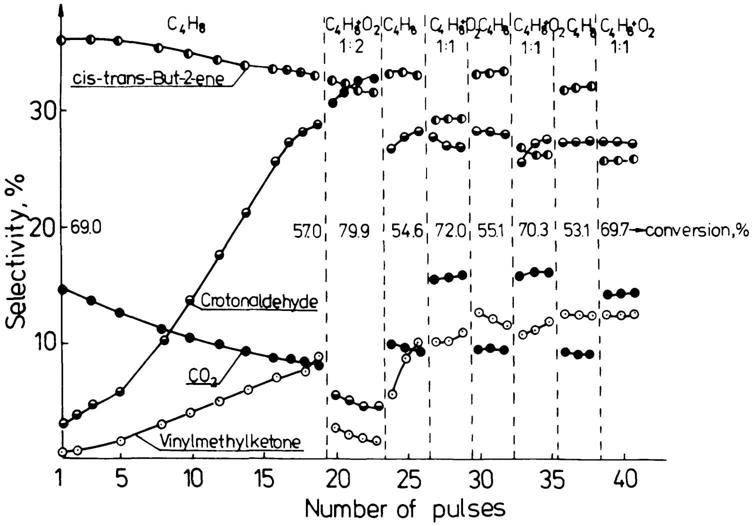

FIGURE 7.41 Conversion and selectivities to different products of the interaction of butene-1 and the mixture of butene-1/oxygen with $CuMoO_4$ + 0.05 MoO_3 as a function of the number of pulses [133].

active centers may be generated which can selectively direct the transformation of butene molecules either to dehydrogenation or to oxygenation. It has not yet been possible, however, to answer the question of which is the structure of these active centers and which parameters are responsible for their operation.

V. OXIDATION OF PARAFFINS

One of the few examples of industrial utilization of a paraffin through a catalytic oxidation reaction is the selective oxidation of n-butane. The use of n-butane for the production of maleic anhydride has enjoyed wide interest in recent years because it is considered more favorable than the traditional process from benzene. Two factors are being taken into consideration: a substantial price difference between benzene and n-butane feedstocks in favor of the latter, and the possibility of avoiding pollution of the atmosphere with benzene, which is subjected to strict control because of its high toxicity.

Most catalysts for this reaction contain mainly vanadium and phosphorus oxides in a P/V atomic ratio near 1.0. Many preparation procedures have been described in the literature [123,124], differing in the solvent utilized (water or an organic solvent), the source of vanadium (V_2O_5, NH_4VO_3, or $VOPO_4$), the reducing agent, and the P/V ratio.

The crucial factors in determining the phase composition, i.e., the final characteristic features of V—P—O catalysts, are the P/V ratio during precipitation, which defines the type of precursor formed, and the gaseous atmosphere during calcination. When, say, ammonium salts are used, ammonia diffuses in the course of calcination into the pores and reduces V^{5+} to V^{4+} (when $P/V \leq 1{:}1$) or to V^{4+} and V^{3+} (at $P{:}V > 1{:}1$). Generally, well-crystallized phases may be obtained only after prolonged thermal treatment at or above 450°C in an inert or oxidizing atmosphere. Several phases have been fully characterized: α—$VOPO_4$ and β—$VOPO_4$, $(VO)_2P_2O_7$, $VPO_5 \cdot 2H_2O$, $VO(PO_3)$, and $VO(H_2PO_4)_2$—but the existence of many others has been postulated by different authors [124].

The structural features of the solid phases in the P—V—O system are similar to those observed in V_2O_5 and its suboxides in spite of the presence of PO_4 tetrahedra and P_2O_7 units. The layer structure of these phases results from the alternation of short covalent $\sigma\pi$ bonds in the vanadyl group V=O and long bonds in the direction perpendicular to the natural cleavage planes. The low symmetry of the vanadium environment is thus expected to remain unchanged at the surface.

Pure $VOPO_4$ crystallizes in two forms, α and β, isostructural with the α and β—$VOSO_4$. Their main characteristic feature is a layer structure. $VO(O)_5$ octahedra share corners with PO_4 tetrahedra giving ribbons or sheets in the (001) plane for the α form and the (010) plane for the β form. $(VO)_2P_2O_7$, in which vanadium is four-valent, has the space group $C_{2v}{}^5$. In the plane parallel to (010) the framework is composed of pairs of $VO(O)_5$ octahedra sharing an edge (the two vanadyl groups being in trans position) and linked together by phosphate tetrahedra (Fig. 7.42). The layers are held together by asymmetric V═O-----V bonds similar to those in V_2O_5 and P—O—P (bent) bonds of P_2O_7 pyrophosphate groups in the b direction [125]. The XRD patterns of spent reduced catalysts revealed additional interesting features. Frequently, the texture is cross-hatch-oriented; superstructures, microdomains, and antiphase boundaries can be seen. Streaking along (001) or (011) is often observed, indicating that disorder occurs in these directions.

The$VO(PO_3)_2$ phase appearing when $P/V > 1.6$ is composed of infinite chains of metaphosphate anion and $VO(O)_5$ octahedra.

Studies of the oxidation of n-butane as a function of the composition of the P—V—O system have shown that the conversion is very

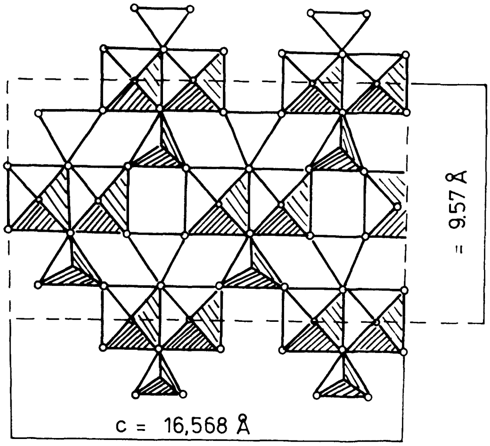

FIGURE 7.42 Crystal structure of $(VO)_2P_2O_7$; the (010) plane [125].

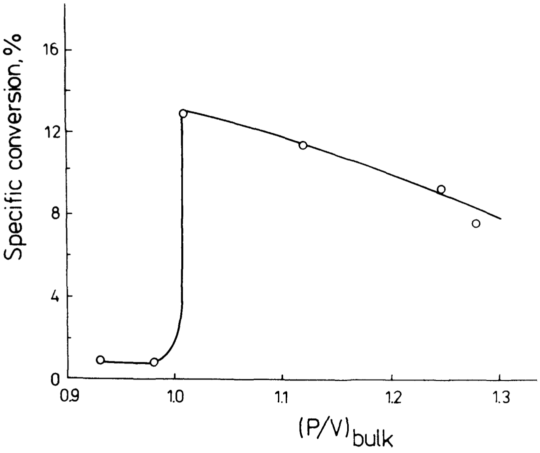

FIGURE 7.43 Total n-butane conversion at 623 K as a function of the P/V ratio on the P–V–O catalysts [126].

low for samples of P/V < 1 (Fig. 7.43) and sharply increases by an order of magnitude when P/V ≥ 1 [126], whereas the specific surface area remained practically constant. Also the selectivity of the oxidation of n-butane to maleic anhydride changes in the same manner Fig. 7.44) [127].

These and many other observations lead to a general consensus that it is the $(VO)_2P_2O_7$ phase which is responsible for the catalytic properties of the P—V—O system in the oxidation of n-butane. This phase may be obtained by a rapid reduction of α-$VOPO_4$, or directly from the appropriate precursor by heat treatment. It has been found that on using the $VOHPO_4 \cdot 0.5H_2O$ compound as precursor one can convert it by a topotactic reaction into $(VO)_2P_2O_7$ of particular morphology, having a strong laminar structure [125]. This is a result of the pseudomorphic relations between the starting and final

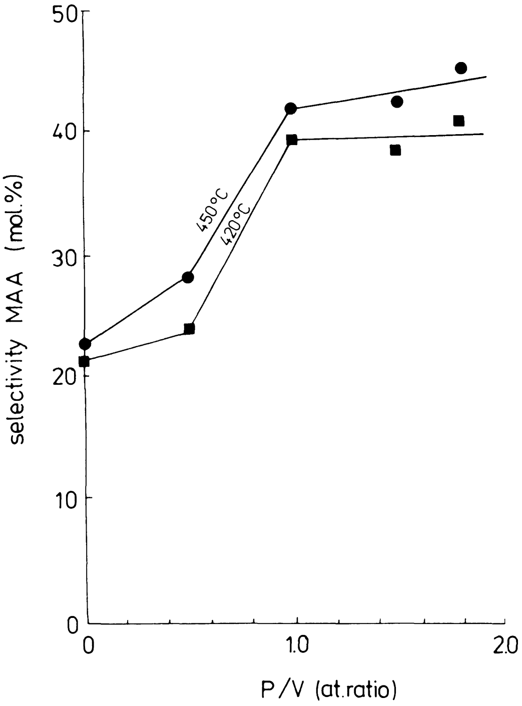

FIGURE 7.44 Selectivity of the formation of maleic anhydride from the oxidation of n-butane as a function of the P/V ratio in P—V—O catalysts [127].

products obtained by a topotactic transformation. This modification has been called $\gamma-(VO)_2P_2O_7$.

The hydrated vanadyl phosphate $VOHPO_4 \cdot 0.5H_2O$ may be also obtained by precipitation from the solution of V_2O_5 and H_3PO_4 in the mixture of higher alcohols. The alcohol molecules trapped between the layers of the phosphate structure may generate in the course of the thermal treatment various kinds of defects in the layers of the resulting vanadyl pyrophosphate, which may have a pronounced influence on the catalytic properties. As an example, Fig. 7.45 compares the specific rates of the formation of maleic anhydride from butene and butane as a function of the reaction temperature, using the $(VO)_2P_2O_7$ prepared from precipitates obtained in water and in the mixture of isobutyl and benzyl alcohols [128]. Two important conclusions can be drawn from the analysis of these results. The rate of the oxidation of n-butane to maleic anhydride is many times higher on preparations obtained by precipitating in the organic medium than on those precipitated in water. At the same time, no great differences between these two preparations are found in their

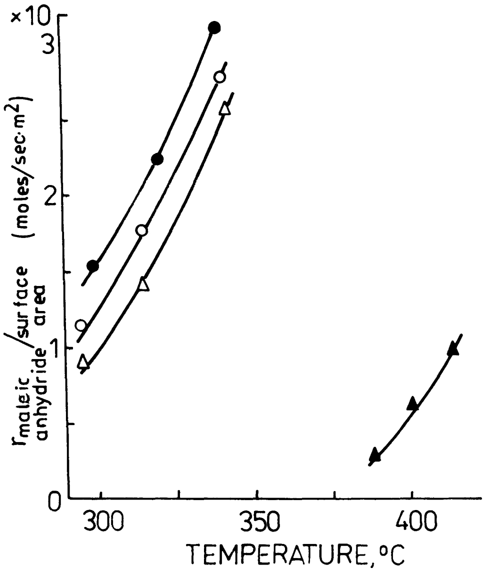

FIGURE 7.45 Comparison of the specific rate of maleic anhydride formation from n-butane (filled-in symbols) and from 1-butene (open symbols) as a function of the reaction temperature for active phases prepared in an aqueous medium (△,▲) and in an organic medium (○,●) [128].

activities in the selective oxidation of 1-butene. The first step in the selective oxidation of n-butane is its oxidative dehydrogenation to an intermediate, which under particular conditions in which its successive total oxidation can be avoided can be desorbed as butenes, or react further to form butadiene, furan and maleic anhydride. The dramatic influence of the texture of the catalyst on the rate of the oxidation of n-butane but not that of 1-butene suggests that the specific nature of the active phase mainly affects this first step of paraffin oxidation, i.e., the activation of the paraffin molecule. Structural analysis indicates that in both cases the same $\gamma-(VO)_2P_2O_7$ phase is present in the catalysts. It is also noteworthy that the surface ratio $(P/V)_s$ as determined by the XPS is directly proportional to the bulk ratio $(P/V)_b$ only in the region of $(P/V)_b < 1$. At higher values the surface ratio remains constant (Fig. 7.46) [126]. The $(P/V)_s$ values are twice higher than expected on the basis of bulk composition. It was suggested that phosphorus acts

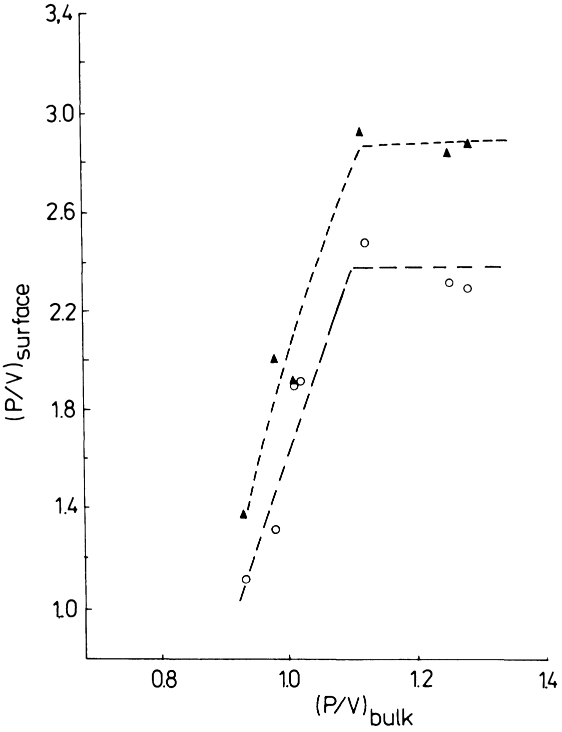

FIGURE 7.46 Surface versus bulk P/V ratio in P–V–O catalysts after drying (o) and reaction (▲) [126].

as a diluent on the surface, isolating V ion sites and thus increasing the selectivity. The EXAFS data are in line with the presence of a tetrahedral oxygen coordination around phosphorus and the excess of phosphorus has no structural effect on its coordination. This would suggest that a special modification of the surface is responsible for the increased rate of the activation of n-butane molecules. It was suggested that the surface defect structure caused by the presence of alcohol molecules in the course of the formation of the layer structure may consist of the local inversion of the trans into a cis arrangement in the pair of $VO(O)_5$ edge-linked octahedra in the presence of oxygen vacancies or in the modification of the V—O bond strength. The studies of the reducibility of the catalyst system led to the conclusion that the stabilization of V(IV) against its oxidation to V(V) is one of the important factors rendering the catalyst selective in the n-butane oxidation and the presence of excess phosphorus hinders this process. A high rate of V(IV) to V(V) oxidation causes over oxidation of the surface of the catalyst. This enhances the oxygen attack on the activated n-butane intermediate as well as increases the rate of consecutive oxidations of other intermediates and maleic anhydride to CO_2, drastically decreasing the yield of maleic anhydride.

REFERENCES

1. D. J. Hucknall, Selective Oxidation of Hydrocarbons, Academic Press, New York, 1974.
2. G. W. Keulks, L. D. Krenzke, and T. M. Notermann, Adv. Catal., 27, 183 (1978).
3. R. K. Grasselli and J. D. Burrington, Adv. Catal., 30, 133 (1981).
4. B. C. Gates, R. Katzer, and G. C. Schuit, Chemistry of Catalytic Processes.
5. D. B. Dadyburjor, S. S. Jewur, and E. Ruckenstein, Catal. Rev., 19, 293 (1979).
6. Chemical and Physical Aspects of Catalytic Oxidation (J. L. Portefaix and F. Figueras, eds.), Editions du CNRS, Paris, 1980.
7. L. Ya. Margolis, Okislenje uglievodorodov na geterogennykh katalizatorakh, Izd. Khimija, Moscow, 1977.
8. J. Haber, in Solid State Chemistry in Catalysis (R. K. Graselli and Brazdil, eds.), ACS Symposium Series 279, Washington, D.C., 1985.
9. B. E. Leach, in Applied Industrial Catalysis (B. E. Leach, ed.) Academic Press, Orlando, 1983, p. 1.
10. J. C. Zomerdijk and M. W. Hall, Catal. Rev., Sci. Eng., 23, 163 (1981).

11. V. Ponec, *Catal. Rev., Sci. Eng.*, **11**, 1 (1975).
12. H. R. Gerberich, N. W. Cant, and W. K. Hall, *J. Catal.*, **16**, 204 (1970).
13. W. M. H. Sachtler, C. Backx, and R. A. van Santen, *Catal. Rev., Sci. Eng.*, **23**, 127 (1981).
14. X. E. Verykios, F. P. Stein, and R. W. Coughlin, *Catal. Rev. Sci. Eng.*, **22**, 197 (1980).
15. V. E. Ostrovskii and M. I. Temkin, *Kinet. Katal.*, **7**, 529 (1966).
16. P. A. Kilty, N. C. Rol, and W. M. H. Sachtler, *Proc. 5th Int. Congress on Catalysis* (Palm Beach, 1972) Vol. 2, (J. Hightower, ed.), North Holland, Amsterdam, 1973, p. 929.
17. R. B. Clarkson and A. Cirillo, *J. Catal.*, **33**, 392 (1974).
18. S. Tanaka and T. Yamashima, *J. Catal.*, **40**, 140 (1975).
19. W. Shimizu, K. Shimokoshi, and I. Yasumori, *Bull. Chem. Soc. Japan*, **46**, 2929 (1973).
20. R. W. Joyner and M. W. Roberts, *Chem. Phys. Lett.*, **60**, 459 (1979).
21. C. Backx, C. P. M. de Groot, and P. Biloen, *Surf. Sci.*, **104**, 300 (1981).
22. A. E. Marcinkowsky and J. M. Berty, *J. Catal.*, **29**, 494 (1973).
23. W. H. Flank and H. C. Beachell, *J. Catal.*, **8**, 316 (1967).
24. D. O. Hayward and B. M. W. Trapnell, *Chemisorption*, 2nd ed., Butterworths, London, 1964, pp. 231–232.
25. R. G. Meisenheimer and J. N. Wilson, *J. Catal.*, **1**, 151 (1962).
26. E. L. Force and A. T. Bell, *J. Catal.*, **38**, 440 (1975).
27. J. L. Carter, D. J. C. Yates, P. J. Lucchesi, V. V. Elliott, and V. Kevorkian, *J. Phys. Chem.*, **70**, 1126 (1966).
28. C. Backx, C. P. M. de Groot, and P. Biloen, *Appl. Surf. Sci.*, **6**, 256 (1980).
29. S. V. Gerci, K. M. Kholyarenko, and M. Ya. Rubanik, *Ukr. Khim.*, **31**, 449 (1965).
30. J. M. Berty, in *Applied Industrial Catalysis*, Vol. 1 (B. E. Leach, ed.), Academic Press, New York, 1983, P. 207.
31. A. Orzechowski and K. E. Mac Cormack, *Can. J. Chem.*, **32**, 415, 443 (1954).
32. G. H. Twigg, *Trans. Faraday Soc.*, **42**, 284, 657 (1946).
33. P. Kripylo, L. Mögling, H. Ehrchen, I. Harkanyi, D. Klose, and L. Beck, *Chem. Tech. (Leipzig)*, **31**, 82 (1979).
34. W. Herzog, *Ber. Bunsenges Phys. Chem.*, **74**, 216 (1970).
35. S. Kagawa, K. Kono, H. Futata, and T. Seiyama, *Kogyo Kagaku Zasshi*, **74**, 819 (1971).
36. J. Mikami, Sh. Satoh, and H. Kobayashi, *J. Catal.*, **18**, 265 (1970).
37. R. A. van Santen, J. Moolhuysen, and W. M. H. Sachtler, *J. Catal.*, **65**, 478 (1980).
38. R. W. Clayton and S. V. Norval, in *Catalysis, Specialists Periodical Reports*, Vol. 3, The Chemical Society, London, 1980, p. 70.

39. J. V. Porcelli, Catal. Rev., Sci. Eng., 23, 151 (1981).
40. G. W. Hearne and M. L. Adams, U.S. Patent 2,451,485 (1948).
41. H. H. Voge and C. R. Adams, Adv. Catal., 17, 151 (1967).
42. L. Ya. Margolis, Adv. Catal., 14, 429 (1963).
43. R. J. Sampson and D. Shooter, Oxide Combust. Rev., 1, 225 (1965).
44. F. Veatch, J. L. Callahan, E. C. Milberger, and R. Forman, Proc. 2nd Int. Congr. Catalysis, Vol. 2 (Paris, 1960), Editions Techniq, Paris, 1961, p. 2647.
45. F. Veatch, J. L. Callahan, I. D. Idol, and E. C. Milberger, Chem. Eng. Prog., 56, 65 (1960).
46. I. D. Idol, U.S. Patent 2,904,580 (1959).
47. G. W. Hearne and K. W. Furman, U.S. Patent 2,991,320 (1961).
48. C. C. McCain, G. Gough, and G. Godin, Nature, 198, 989 (1963).
49. W. M. H. Sachtler and N. H. de Boer, Proc. 3rd Int. Congr. Catalysis, Vol. 1 (Amsterdam, 1964), North Holland, Amsterdam, 1965, p. 252.
50. C. R. Adams and T. J. Jennings, J. Catal., 2, 63 (1963); 3, 549 (1964).
51. B. Grzybowska, J. Haber, and J. Janas, J. Catal., 49, 150 (1977).
52. E. G. Gamid-Zade, A. R. Kuliyev, E. A. Mamedov, R. G. Rizayer, and V. A. Sokolovski, React. Kinet. Catal. Lett., 3, 191 (1975).
53. J. D. Burrington and R. K. Grasselli, J. Catal., 59, 79 (1979).
54. C. R. Adams, Proc. 3rd Int. Congress Catalysis, Vol. 2 (Amsterdam, 1964), North Holland, Amsterdam, 1965, p. 252.
55. T. Seijama, M. Egashira, T. Sakamoto, and I. Aso, J. Catal., 24, 76 (1972).
56. R. P. Buckley and M. Szwarc, Proc. Roy. Soc., A240, 396 (1957).
57. A. A. Davydov, IK spektroskopija v khimii povierhnosti okislov, Izd. Nauka, Novosibirsk, 1984.
58. A. A. Davydov, V. G. Mikhaltchenko, V. D. Sokolovskii, and G. K. Boreskov, J. Catal., 55, 299 (1978).
59. R. Grabowski, J. Haber, and J. Sloczyński, React. Kinet. Catal. Lett., 12, 119 (1979).
60. K. Brückman, J. Haber, and J. Wiltowski, J. Catal., 106, 188 (1987).
61. J. Haber and M. Witko, J. Mol. Catal., 9, 399 (1980).
62. J. Haber and M. Witko, Acc. Chem. Res., 14, 1 (1981).
63. A. B. Anderson, D. W. Ewing, Yunsoo Kim, R. K. Grasselli, J. D. Burrington, and J. F. Brazdil, J. Catal., 96, 222 (1985).
64. J. Haber, Proc. 8th Int. Congress on Catalysis, Vol. 1 (Berlin, 1984), Dechema Chemie Verlag, Frankfurt/Main, 1984, Plenary Lectures, p. 85.

65. J. Haber and E. Mielczarska, and W. Turek, (unpublished results).
66. J. Goodenough, Progress Solid State Chem., 5, 145 (1971).
67. F. S. Stone, J. Solid State Chem., 12, 271 (1975).
68. J. Haber, J. Janas, M. Schiavello, and R. J. D. Tiley, J. Catal., 82, 395 (1983).
69. L. Kihlborg, Ark. Kemi, 21, 357 (1963).
70. J. M. Dominguez-Esquivel, S. Fuentes-Moyado, G. Diaz-Guerrero, and A. Vazquez-Zavala, Surf. Sci., 175, L701 (1986).
71. A. Anderson, Y. Kim, D. Ewing, R. K. Grasselli, and M. Tenhover, Surf. Sci., 134, 237 (1983).
72. K. Brückman, R. Grabowski, J. Haber, A. Mazurkiewicz, J. Sloczyński, and T. Wiltowski, J. Catal., 104, 71 (1987).
73. L. I. Firment and A. Ferretti, Surf. Sci., 129, 155 (1983).
74. J. D. Burrington, C. T. Kartisek, and R. K. Grasselli, J. Catal., 63, 235 (1980).
75. J. D. Burrington, C. T. Kartisek, and R. K. Grasselli, J. Catal., 81, 489 (1983).
76. L. Ya. Erman, E. L. Galperin, Zh. Nieorg. Khim., 13, 927 (1968).
77. A. F. Van den Elzen and G. D. Rieck, Acta Crystallogr., Sect. B, 2433 (1973).
78. A. F. Van den Elzen and G. D. Rieck, Mater. Res. Bull., 10, 1163 (1975).
79. I. Matsuura, R. Schut, and K. Hirakawa, J. Catal., 63, 152 (1980).
80. A. P. Gorshkov, I. K. Kolchin, I. M. Gribov, and L. Margolis, Kinet. Katal., 9, 1068 (1968).
81. J. Bereś, A. Janik, and J. Wasilewski, J. Catal., 15, 101 (1969).
82. Ph. A. Batist, A. H. W. M. Der Kinderen, Y. Leeuwenburgh, F. A. M. G. Metz, and G. C. A. Schuit, J. Catal., 12, 45 (1968).
83. Ph. A. Batist, C. G. M. van der Moesdijk, I. Matsuura, and G. C. A. Schuit, J. Catal., 20, 40 (1971).
84. R. K. Grasselli and A. L. Callahan, J. Catal., 14, 93 (1969).
85. R. K. Grasselli, D. D. Suresh, and K. Knox, J. Catal., 18, 356 (1970).
86. R. K. Grasselli and D. D. Suresh, J. Catal., 25, 273 (1972).
87. G. C. A. Schuit, in Ref. 4.
88. J. Bereś, K. Brückman, J. Haber, and J. Janas, Bull. Acad. Polon. Sci., Ser. Sci. Chim., 20, 813 (1972).
89. R. K. Grasselli, J. D. Burrington, and J. P. Brazdil, Disc. Faraday Soc., 203 (1981).
90. B. Grzybowska, J. Haber, W. Marczewski, and L. Ungier, J. Catal., 42, 327 (1976).
91. P. L. Gai, Proc. 3rd Int. Conference Chemistry and Uses of Molybdenum (Ann Arbor, 1979) (H. F. Barry, P. C. H. Mitchell,

eds.), Climax Molybdenum, 1979, p. 143; Proc. 4th Intern. Conference Chemistry and Uses of Molybdenum (Golden, Colorado, 1982) (H. F. Barry and P. C. H. Mitchell, eds.), Climax Molybdenum, 1982, p. 296.

92. M. Lo Jacono, T. Noterman, and G. W. Keulks, J. Catal., 40, 19 (1975).
93. B. Grzybowska, E. Payen, L. Gengembre, and J. P. Bonnelle, Bull. Acad. Polon. Sci., Ser. Sci. Chim., 31, 245 (1983).
94. K. Brückman and B. Grzybowska, React. Kinet. Catal. Lett., 26, 117 (1984).
95. B. Grzybowska and M. Gasior, J. Catal., 52, 534 (1978).
96. C. Mazzocchia, F. Di Renzo, P. Centola, and Del Rosso, Proc. 4th Int. Conference Chemistry and Uses of Molybdenum (Golden, Colorado, 1982) (H. F. Barry and P. C. H. Mitchel, eds.), Climax Molybdenum, 1982, p. 406.
97. M. Misono, K. Sakata, Y. Yoneda, and W. Y. Lee, Proc. 7th Intern. Congr. Catalysis (Tokyo, 1980) (T. Seiyama and A. Ozaki, eds.), Elsevier, New York, 1980, p. 1047.
98. K. Brückman, J. Haber, and J. Niedziólka, Bull. Acad. Polon. Sci., Ser. Sci. Chim., 35, 373 (1987).
99. E. Serwicka, J. B. Black, and J. Goodenough, J. Catal., 106, 23 (1987).
100. J. Buiten, J. Catal., 10, 188 (1968); 13, 373 (1969).
101. Y. Moro-oka, S. Tan, and A. Ozaki, J. Catal., 12, 241 (1968).
102. Y. Moro-oka, Y. Takita, and A, Ozaki, J. Catal., 27, 177, 185 (1972).
103. Y. Takita, Y. Moro-oka, and A. Ozaki, J. Catal., 52, 95 (1978).
104. G. W. Hearne and K. W. Furman, U.S. Patent 2,991,320 (1961).
105. S. Z. Roginskii, M. I. Yanorski, and R. A. Zimin, Neftekhim, 7, 166 (1967).
106. C. R. Adams, H. H. Voge, C. Z. Morgan, and W. F. Armstrong, J. Catal., 3, 379 (1964).
107. Ph. A. Batist, B. C. Lippens, and G. C. A. Schuit, J. Catal., 5, 55 (1966).
108. T. G. Alkhazov, M. S. Belenkii, W. M. Khiteva, and R. I. Alekseeva, Proc. 4th Int. Congr. Catalysis (Moscow, 1968), (V. B. Kazanskii, ed.), Akademiai Kiado, Budapest, 1971.
109. Ph. Batist, C. J. Kaptejns, B. C. Lippens, and G. C. A. Schuit, J. Catal., 7, 33 (1967).
110. I. Matsuura and G. C. A. Schuit, J. Catal., 20, 19 (1971).
111. I. Matsuura, in Succesful Design of Catalysts, (T. Inui, ed.), Elsevier, New York, 1989, p. 111.
112. G. Centi and F. Trifiro, Appl Catal., 12, 1 (1984).
113. B. K. Hodnett, Ph. Permanne, and B. Delmon, Appl. Catal., 6, 231 (1983).
114. E. Bordes and P. Courtine, J. Catal., 57, 236 (1979).
115. R. L. Varma and D. M. Saraf, Ind. Eng. Chem. (Product R&D), 18, 7 (1979).

116. I. Pasquon, F. Trifiro, and G. Caputo, Chim. Ind. (Milan), 55, 168 (1973).
117. M. Carbucicchio, F. Trifiro, and P. L. Villa, Z. Phys. Chem. N. F., 106, 237 (1977).
118. F. Cavani, G. Centi, I. Manenti, A. Riva, and F. Trifiro, Ind. Eng. Chem. (Product R&D), 22, 565, 570 (1983).
119. L. Morselli, F. Trifiro, and L. Urban, J. Catal., 75, 112 (1982).
120. R. J. Renmard and W. L. Kehl, J. Catal., 21, 282 (1971).
121. W. R. Cares and D. W. Hightower, J. Catal., 23, 193 (1971).
122. F. E. Massoth and D. A. Scarpiello, J. Catal., 21, 294 (1971).
123. K. Wohlfahrt and G. Emig, Hydrocarbon Process, 6, 83 (1980).
124. B. K. Hodnett, Catal. Rev., Sci. Eng., 27, 373 (1985).
125. E. Bordes and P. Courtine, J. Solid State Chem., 55, 270 (1984).
126. F. Garbassi, I. C. I. Bart, R. Tassinari, G. Vlaic, and P. Lagarde, J. Catal., 98, 317 (1986).
127. E. Bordes and P. Courtine, J. Catal., 57, 236 (1979).
128. G. Busca, F. Cavani, G. Centi, and F. Trifiro, J. Catal., 99, 400 (1986).
129. A. Clark and R. S. Shutt, U.S. Patent 2,383,711 (1945).
130. G. W. Hearne and M. L. Adams, U.S. Patent 2,451,485 (1948).
131. T. Machej and J. Ziólkowski, J. Solid State Chem., 31, 135 (1980).
132. J. Haber and T. Wiltowski, Bull. Acad. Polon. Sci., Ser. Sci. Chim., 29, 563 (1983).
133. J. Haber, Proc. 4th Intern. Conf. Chemistry and Uses of Molybdenum, Golden Colorado, 1982, (H. F. Barry and P. C. H. Mitchell, eds.), Climax Molybdenum, 1982, p. 395.
134. Yu. V. Maksimov, M. Sh. Zurmukhtashvili, I. P. Suzdalev, L. Ya. Margolis, and O. V. Krylov, Kinet. Katal., 25, 948 (1984).
135. M. Sh. Zurmukhtashvili, Yu. V. Maksimov, M. Yu. Kutyrev, L. Ya. Margolis, D. P. Shashkin, and O. V. Krylov, Kinet. Katal., 25, 955 (1984).
136. W. L. Jorgensen and L. Salem, The Organic Chemists Book of Orbitals, Academic Press, New York, 1973.
137. C. F. Cullis, D. J. Hucknall, in Catalysis (C. Kemball and D. A. Dowden, eds.), Specialist Periodical Reports, The Chemical Society, London, 1982, Vol. 5. 273.

8

Selective Oxidation of Aromatic Hydrocarbons

I. INTRODUCTION

Processes of partial oxidation of aromatic hydrocarbons in the vapor phase represent an important class of catalytic reactions, many of which are of great importance in chemical technology [1]. The oxidation of aromatic hydrocarbons obtained by pyrolysis of coal is one of the first organic gas phase oxidation processes introduced into industrial practice. Now oxidation of naphthalene or o-xylene to phthalic anhydride, anthracene to anthraquinone, acenaphthene in naphthenic anhydride are operated on a large scale in the chemical industry.

Commercial production of phthalic anhydride was started in 1872 based on the liquid phase catalytic oxidation of naphthalene. The method was steadily improved until 1917, when it was replaced by the vapor phase oxidation of naphthalene over vanadium oxide catalysts, although catalytic oxidation of aromatic hydrocarbons in the vapor phase over a vanadium oxide catalyst was reported in the scientific literature as early as 1895 [2]. In the last three decades a dynamic growth of phthalic anhydride production has been observed, from 695,000 t/a in 1961, to 2 million t/a in 1972, to 2.7 million t/a in 1976, due to its wide use in the manufacture of phthalate plasticizers, polyester and alkyl resins, paints, lacquers, insecticides, and numerous other industrial products [3,4]. Until 1945 naphthalene was the only raw material used commercially to produce phthalic anhydride. Since then o-xylene has been introduced in increasing amounts so that at present about 75% of world production of phthalic anhydride is based on o-xylene.

Catalytic vapor phase oxidation of benzene was commercialized in the 1930s as an efficient and economic route to maleic anhydride, with the production level in the 1950s and 1960s increasing rapidly in view of the rising consumption of maleic anhydride used as a feedstock to make polyesters, paints, and varnishes. In the last decade catalytic oxidation of C4 aliphatic hydrocarbons has become an increasingly important route to maleic anhydride.

Two classes of aromatic oxidations can be distinguished:

The side chain oxidation of alkyl aromatics and, in particular, methyl aromatics, which yields aldehydes and acids or anhydrides without affecting the π-electron system of the aromatic ring. They belong to the nucleophilic type oxidation.

The more severe oxidation involving destruction of the aromatic nucleus to form acid anhydrides and proceeding along the electrophilic oxidation route.

It is remarkable that the V_2O_5-based catalysts introduced originally in the first industrial processes are still used today and remain superior to any other type of catalyst. The result is that depending on the type of additives and support they may function in both electrophilic and nucleophilic oxidation. In the first type of process, e.g., oxidation of benzene to maleic anhydride, they are modified by mixing with MoO_3 and adding some promoters, and are usually supported on alumina [5]. For the nucleophilic process, as in the oxidation of o-xylene to phthalic anhydride, V_2O_5 is usually supported on an anatase modification of TiO_2. The problems connected with the manufacture of phthalic anhydride are presented in [6]. Earlier literature concerning the oxidation of aromatic hydrocarbons has been reviewed in several articles [7-10].

II. OXIDATION OF BENZENE TO MALEIC ANHYDRIDE

A. Introductory Remarks

With most transition metal oxide catalysts benzene is completely oxidized to CO, CO_2, and H_2O [11]. The only notable exceptions are the oxides of V > Mo > W on which benzene can be oxidized selectively, with the selectivity decreasing in the above order [12]. Hence the catalysts for the selective oxidation of benzene to maleic anhydride are based exclusively on the V_2O_5-MoO_3 system. Usually they contain about 30 mol % MoO_3 and various promoting additives, e.g., the oxides of P, Na, Ni, etc. With such industrial catalysts benzene is oxidized with 67–72% of the theoretical yield of maleic anhydride.

The mechanism of selective catalytic oxidation of benzene is fairly complicated and the results published in the literature frequently involve various discrepancies. An additional complication is the fact that the V_2O_5-MoO_3 system is very labile and, depending on conditions, the working catalyst may contain a number of different phases produced in the course of interactions of the catalyst with the feed [13].

B. V_2O_5-MoO_3 System

A V_2O_5-MoO_3 phase diagram is shown in Fig. 8.1 [14-17]. A vast region of solubility of MoO_3 in solid V_2O_5 (α phase) and a congruently melting intermediate compound (β phase) are seen in the diagram. However, there is no appreciable solubility of V_2O_5 in MoO_3. The solubility limit of MoO_3 in V_2O_5 reaches a value somewhat less than 30 mol % at the eutectic temperature (about 610°C) but it decreases with decreasing temperature [17] and at 350°C is between 10 and 15 mol % MoO_3.

V_2O_5 and α phase are built of layers parallel to the (010) plane (Fig. 8.2). Within the layer each V atom is situated in a deformed square pyramid of oxygen atoms. The pyramids partly directed above and partly below the layers are joined either by the

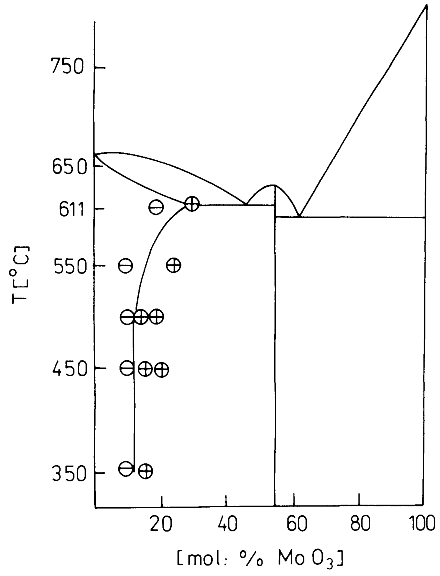

FIGURE 8.1 V_2O_5-MoO_3 phase diagram [15].

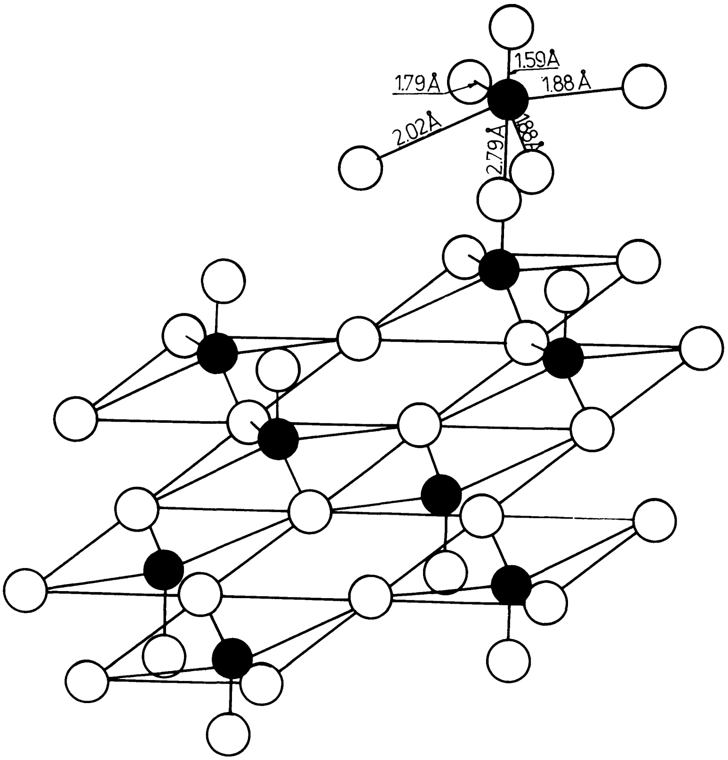

FIGURE 8.2 Structure of the layers parallel to the (010) plane in V_2O_5 crystal lattice.

common corners or by common edges. The length of oxygen-vanadium bonds is shown in Fig. 8.2. The shortest and hence the strongest bond is formed between vanadium atoms and oxygen atoms situated at the free apices of the pyramids. It is considered to be a double V=O bond and is characterized by a stretching frequency of about 1025 cm^{-1} in the IR spectrum. The neighboring layers are situated in such a way that the doubly bonded oxygen atoms from one layer occupy positions below the square bases of pyramids in the next layer as shown in Fig. 8.2. Hence the coordination number of vanadium in the lattice is completed to six. V_2O_5 and $(Mo_xV_{1-x})_2O_5$ solid solutions with $x \leq 0.2$ are orthorhombic but at $x \approx 0.28$ monoclinic [18]. The difference between the structures consists of the different displacement of metal ions from the centers of the irregular octahedra. In the orthorhombic structure all metal ions within an ReO_3-type slab are displaced in the same direction whereas in the monoclinic structure they are shifted pairwise in the opposite directions. In both structures metal ions in the edge-sharing octahedra are displaced in opposite directions to minimize the electrostatic repulsions.

Vanadia-molybdena solid solutions when dissolved in H_2SO_4 reduce certain amounts of $KMnO_4$. This is due to the fact that they contain vanadium (IV) atoms as can be proved by EPR measurements [19,20]. The formation of V(IV) is evidently the result of doping vanadia with hexavalent molybdenum, which can be represented by the equation:

$$2MoO_3 \rightarrow 2Mo_V^{\bullet} + 5O_O + 2e^- + \frac{1}{2}O_{2(g)} \qquad (8.1)$$

in which Kröger-Vink symbols are used. Electrons are localized on vanadium atoms in the vicinity of Mo(VI) atoms, thus forming V^{IV}-O-Mo^{VI} donor centers.

The structure of the intermediate compound (β phase) in the V_2O_5-MoO_3 system was studied by Eick and Kihlborg [21] and Magneli and Oughton [22], who ascribed to it the V_2MoO_8 formula. The authors described the structure of this compound as a shear structure of octahedra forming ReO_3-type slabs which are infinitely long in the b and c directions but only three octahedra thick. Such slabs are jointed by component octahedra having common edges across the plane $\underline{x} = 1/4$ and $\underline{x} = 3/4$ which can be described as the shear planes. This structure may be considered as the second member of a homologous series of structures with the general formula M_nO_{3n-1} (n = 2,3,...). Eick and Kihlborg, who prepared their samples by heating equimolar mixture of oxides at 630 and 580°C, found β phase with the same small amounts of α phase, which according to them justified the V_2MoO_8 formula. However, Munch and Pierron [23] detected pure β phase as the only one at the composition $3V_2O_5 \cdot 4MoO_3$ (samples heated at 600°C for 2 weeks). When the composition was changed there always appeared either an α or a MoO_3 phase. Considering that the intermediate β phase was always oxygen-deficient, the authors proposed the $V_9Mo_6O_{40}$ formula. Similar results were obtained in [15] where the samples were obtained by the fusion of appropriate mixtures of oxides and a distinct maximum on the liquidus curve was observed at a 3:4 molar ratio of V_2O_5 and MoO_3 (Fig. 8.1). Eon et al. [24] suggested that the β phase may change its composition within limits corresponding to the formulas V_2MoO_8 and $V_9Mo_6O_{40}$. The controversy between the two formulas seems to be solved by more recent work by Jarman et al. [25,26], who confirmed that prolonged heating of 3:4 molar mixtures of V_2O_5 at 600—700°C results in the formation of β phase as the only phase; in the case of a 1:1 molar ratio α phase appears along with β phase. On the other hand, when a sample with V:Mo atom ratio 0.93 was prepared by the evaporation of a solution of ammonium vanadate and molybdate and calcined at 500°C, only β phase was detected without α-phase or MoO_3 contamination. Hence the authors conclude that β phase always has M_3O_8 composition but the limits in which the ratio of V and Mo atoms can vary depends on the calcination temperature. The molybdenum-rich phase limit is close to $(V_{0.5}Mo_{0.5})_3O_8$ at 500°C but as the temperature rises the following reaction occurs:

$$\frac{0.5 + \underline{y}}{0.5}(V_{0.5}Mo_{0.5})_3O_8 \xrightarrow{O_2} (V_{0.5+\underline{y}}Mo_{0.5-\underline{y}})_3O_8 + 6\underline{y}MoO_3 \tag{8.2}$$

At 600°C $\underline{y} = 0.1$ and $V_9Mo_6O_{40}$ composition is obtained.

The portion of the phase diagram corresponding to the higher content of MoO_3 than in $V_9Mo_6O_{40}$ represents a typical two-component phase diagram without the formation of solid solution in the usual orthorhombic modification of MoO_3. However, it should be mentioned that Grussenmeyer [27] showed that the samples which initially contained the mixture of $V_9Mo_6O_{40}$ and orthorhombic MoO_3 reinvestigated after 15 years changed their phase composition: the β phase vanished and instead a solid solution of V_2O_5 in hexagonal MoO_3 appeared which evidently is more stable at room temperature.

The magnetic, optical, and electrical properties of the V_2O_5-MoO system were investigated in [19,28,29].

The phases appearing in the V_2O_5-MoO_3 system can easily be reduced, which may occur also in the atmosphere of air saturated with benzene vapors under the conditions of catalytic reaction. Moreover, Bielański and Inglot [30] showed that a certain degree of reduction is necessary to activate the catalyst. Their catalysts obtained by fusing the mixtures of both oxides in the atmosphere of air when fresh were practically inactive in benzene oxidation at 350°C and acquired activity only in the course of their reduction. Figure 8.3 shows Arrhenius plots corresponding to a series of experiments carried out with a sample of undoped V_2O_5 which has been stepwise reduced with a benzene vapor-air mixture. After each state of reduction a catalytic run was carried out over a range of temperature, a small amount of catalyst taken for chemical analysis and reduction—catalytic test—and chemical analysis cycles repeated several times. It is seen that after the first treatment, resulting in the reduction of 55.1% of V^V to V^{IV}, the catalyst became active (curve I in Fig. 8.3); the second treatment

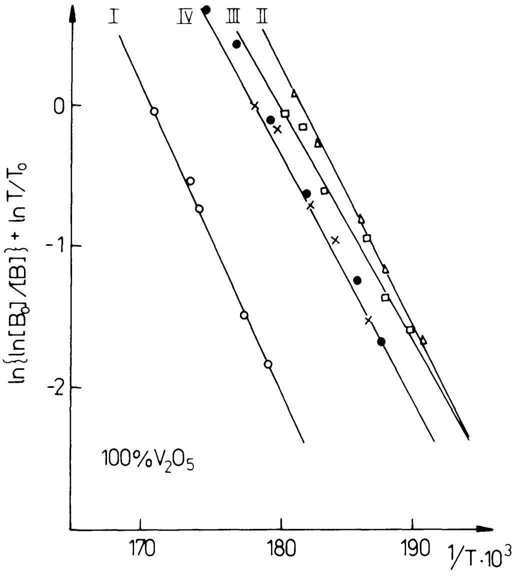

FIGURE 8.3 Arrhenius plots for the catalytic oxidation of benzene on V_2O_5 catalyst after successive stages of reduction with air-benzene vapors (curve I) or nitrogen-benzene vapors (curves II—IV) at 350°C. $\underline{B}_0$ and $\underline{B}$, concentrations of benzene in the gas entering and the gas flowing out of reactor, respectively; $\underline{T}$, temperature of experiment; $\underline{T}_0$, correction factor allowing for the change of volume of the gases due to heating them to various temperatures [30].

(curve II) gave still higher activity and in this case chemical analysis indicated 90% of V^{IV} and 10% of V^{III}. Further reduction resulted in a certain decrease of activity (curve III and IV). It can be clearly seen that the best activity was reached when the composition of the catalyst sample corresponded roughly to V_2O_4, which must have been the predominant phase. Similar enhancement of activity was also observed in all catalysts containing MoO_3 additives. However, the process of reduction of such samples is more complicated because it is accompanied by the segregation of elements occurring at least in the external layers of catalyst grains. This was shown by Bielański et al. [31] by carrying out under an electron scanning microscope quantitative analysis with the X-ray microprobe at fixed points of the catalyst surface. The ratio of the numbers of characteristic X-ray quanta of molybdenum and vanadium $\underline{N}_{Mo}/\underline{N}_V$ was taken as the relative measure of molybdenum concentration. The analyses were performed with the fresh sample after oxidizing it at 450°C and reducing it with benzene vapors at the same temperature. Owing to the scanning microscopic photographs it was always possible to carry out the analysis at the same points of the flat surface of the chosen microcrystallites. The results are given in Table 8.1. It is seen that both treatments resulted in distinct changes in Mo concentration in the near-to-surface layer penetrated by the electron beam. In all cases oxidation led to a decrease in the Mo/V atomic ratio, while reduction led to an increase. The effect was stronger in the case of sample A containing only α phase and sample β containing α and β phase than in the case of sample C containing only β phase. Najbar and Niziol [32] showed that both treatments can locally result in such enrichment in Mo that the β phase separates from the α phase. Further experiments enabling a deeper insight into the process of new phase formation upon the reduction of model samples were carried out by Najbar and Bielańska [33]. In this work small samples cut off from the body of a previously fused oxide mixture after exposing them to the action of a reducing agent were embedded in the epoxy resin. Subsequently, thin slices (600—700 Å thick) were cut parallel to the flat surface of the sample using an ultramicrotome. Crystallites from the layer about 2000 Å thick were transferred on a grid and investigated under electron microscope working with a scanning attachment and X-ray spectrometer. The apparatus enabled the investigators to carry out electron diffraction and also X-ray quantitative analysis on the same crystallite. It should be observed that this method renders it possible to detect, identify, and analyze the phases present in the near-to-surface layer in amounts too small to be detected by the usual X-ray analysis. In the case of "mild" reduction (benzene vapors at 350°C) of the sample containing 10 mol % MoO_3 and originally containing only the α phase, the crystallites of $V_9Mo_6O_{40}$ appeared in the most external layer besides which α phase was present. The latter was the only phase in the second and the following deeper layers. However, the X-ray microanalysis showed that the Mo/V ratio was the highest in the first and the second investigated layers, and then decreased in the direction of the bulk of the sample.

A much more pronounced segregation was reached when reduction of the sample in benzene vapors was carried out at 450°C [33] (Table 8.2). In this case only the oxides of molybdenum MoO_3 and $Mo_{17}O_{47}$ were detected in the most external layer. The intermediate compound and both molybdenum oxides were present in the second and third layers. The former was the only or the predominant phase in the fourth, fifth, and sixth layers. Vanadium oxides were detected first in the fifth (V_3O_7) and sixth (α phase) layers at a distance of the order of 10,000 Å from the catalyst grain surface.

TABLE 8.1 X-Ray Microprobe Point Analysis of V_2O_5-MoO_3 Samples

Sample	Site	N_{Mo}/N_V Fresh sample	 After oxidation	 After reduction
A	1	0.036	0.025	0.064
	2	0.049	0.028	0.062
	3	0.047	0.024	0.060
B	1	0.082	0.081	0.145
	2	0.084	0.078	0.117
	3	0.104	0.082	0.140
C	1	0.667	0.610	0.649
	2	0.733	0.625	0.667
	3	0.746	0.625	0.676

A: 10 mol % MoO_3.
B: 30 mol % MoO_3.
C: 56.8 mol % MoO_3.
Source: Refs. 31 and 34.

It is of interest to compare these results with those obtained with an industrial catalyst which was working in an industrial reactor for 16 months [34]. This catalyst initially contained α and β phases as well as sodium-vanadia-molybdena bronze. As the data in the Table 8.3 show, in this case strong segregation of elements took place and the formation of similar phases occurred as was observed in the case of the "strong" reduction of the model sample. The data in Table 8.3 concern catalyst sample taken from the upper part of the reactor tube (gas inlet) where temperature is the highest and so also is the concentration of benzene vapors. The catalyst from the lowest parts of the reactor tube remained practically unchanged and in the laboratory exhibited unchanged activity. The catalyst from the upper part of the tubing has lost an appreciable amount of molybdenum, which was considered to explain the observed drop it its activity. The data in Table 8.2 suggest that the departure of molybdena from the catalyst is due to the segregation of elements leading to the formation of volatile molybdenum oxide the vapors of which are taken off by the flowing reaction gases.

TABLE 8.2 Chemical and Phase Composition of Consecutive Layers of V_2O_5-MoO_3 Solid Solution Reduced in Benzene Vapors at 450°C

Number of layer	Total number of identified crystallites	Phase identified	Number of crystallites of phase
I	6	MoO_3	4
		$Mo_{17}O_{47}$	2
II	8	$Mo_{17}O_{47}$	1
		MoO_3	2
		$V_9Mo_6O_{40}$	5
III	3	$V_9Mo_6O_{40}$	3
IV	2	$V_9Mo_6O_{40}$	2
V	7	$V_9Mo_6O_{40}$	6
		V_3O_7	1
VI	11	$V_9Mo_6O_{40}$	4
		V_2O_5	3
		Mo_5O_{14}	4

Source: Data from Ref. 33.

All of the above results clearly indicate that the catalysts for selective benzene oxidation represents fairly complicated system, the chemical and phase composition of which may differ considerably from those of the fresh samples. The changes in the original catalytic mass occurring when the catalyst is working depend strongly on the conditions and this may be the source of discrepancies with the results obtained in different laboratories.

The mechanism of the segregation of cations in the solid α and β phases can be interpreted as the "demixing" process described by Schmaltzried [36], who showed that in the binary oxide solid solutions exposed to the oxygen potential gradient the segregation of elements occurs which is connected with different mobilities of both cations. In our case the surface of the catalyst is always exposed to a different oxygen chemical potential than the bulk of crystallites. The direction of the observed segregation indicates that the mobility of vanadium atoms is greater then that of molybdenum atoms [31]. The diffusion of cations is also induced by the removal of oxygen from the surface layer by reduction. Faster diffusion of

TABLE 8.3 Chemical and Phase Composition of an Industrial Catalyst for Benzene Oxidation Determined After 16 Months of Working in the Industrial Reaction

Number of layer	Total number of identified crystallites	Phase identified	Number of crystallites of phase
I	11	Mo_5O_{14}	1
		MoO_3	1
		$Mo_{17}O_{47}$	4
		$V_9Mo_6O_{40}$	3
		$V_6Mo_4O_{25}$	2
II	23	$Mo_{17}O_{47}$	8
		MoO_3	6
		Mo_4O_{11}	1
		V_6O_{13}	1
		$V_9Mo_6O_{40}$	7
III	11	$V_9Mo_6O_{40}$	5
		$V_6Mo_4O_{25}$	4
		V_6O_{13}	1
		$Na_2O.V_2O_4.5V_2O_5$	1

Source: Data from Ref. 34.

vanadium results in the enrichment of the surface layer in molybdenum. In the oxidation the outward diffusion of vanadium results in the enrichment of the surface layer in this latter element. The reversibility of these effects was studied in [32].

Najbar and Stadnicka [37] studied the structural relationships in the evolution of vanadia-molybdena catalysts. They pointed out that in V_2O_5 interstitial cavities with a diameter of about 2.2 Å exist which are linked by the windows of about 1.4 × 2.2 Å along the directions (001) and (010). The diameter of the interstitial positions is much larger than the diameter of the Mo^{6+} (1.24 Å) and V^{5+} (1.18 Å) ions. Such rows of interstitial cavities represent the most plausible easy diffusion paths. When comparing the crystal structure of V_2O_5 and α phase with that of the intermediate compound, the authors arrived at the conclusion that there exists a crystallographic fit between (001) planes of both phases and also between (001) plane of V_2O_5 and the (100) plane of the intermediate compound. This enables the formation of "hybrid" crystals during the reduction in which an epitaxial layer of intermediate compound develops on α-phase crystallites. If (001) planes of both phases fit one another the easy diffusion channels run in the same direction and the epitaxial layer does not prevent further reduction. On the other hand, a (100) epitaxial layer of intermediate compound on the (001) plane of the α phase would hinder the reduction because of the fact that easy diffusion channels would not run in the same direction. In the same way Najbar [38] investigated the formation of epitaxial layers of MoO_3 on the (001) face (best developed) of the intermediate compound.

The anisotropy of cation diffusion in α and β phase was confirmed by the same author [39] in a series of experiments carried out in the following way: A small amount of pulverized sample prepared by fusing the mixtures of both oxides was placed on the sticky strip subsequently fastened to a scanning microscope holder. The platelet-like crystals elongated in the [010] direction (width 5—6 μm, length several tens of μm) were stuck to the strip by their best developed (001) face. Using an optical microscope silver glue was placed by thin needle on the (010) or (001) face of the chosen crystals and on the strip thus connecting electrically crystals to the holder. The holder was then introduced into the microprobe X-ray analyzer. The electron beam entering in the [001] direction was used simultaneously as the second electrode and as the probe for chemical analysis. The electrical field imposed between the electron beam entering the crystal and the silver electrode was assumed to influence the chemical composition of analyzed areas. In neither case did the concentration of vanadium in the area of beam penetration significantly change with time if the electric field was imposed in the [100] direction in which no easy diffusion channels exist in α and β phase. However, the changes were distinct when the electrical field was applied in the [010] direction parallel to which easy diffusion channels run.

C. Interactions of Oxygen and Benzene with V_2O_5 and V_2O_5-MoO_3 Surface

Owing to the lability of the V_2O_5-MoO_3 system, the discrimination between the chemisorbed and the lattice oxygen from the most external layers of crystallites is difficult. The only study of oxygen chemisorbed species was possible in the case of silica-supported V_2O_5. Shvets and Kazansky [40] showed that adsorption of oxygen at −196°C results in the formation of O_2^- ion radicals. The EPR signal of this species decreased after heating the sample to −78°C when the O^- signal appeared. The latter could also be obtained after chemisorption of N_2O at room temperature. This species exhibited rather high thermal stability and could still be observed at 350°C. That is why the authors suggested that it may be the active species in the catalytic reaction of benzene. The oxygen anion radicals are stabilized close to vanadium ions as was indicated by the hyperfine structure of the EPR spectra. Signals of V^{4+} ions in the prereduced V_2O_5/SiO_2 were observed only at liquid air temperature but vanished at room temperature, indicating the tetrahedral coordination of vanadium. Yoshida et al. [41] when investigating the same type of V_2O_5/SiO_2 prereduced catalyst showed that the O^-/O_2^- ratio of peak intensities increased with the increasing reduction degree, i.e., with the availability of electron donor centers. In their experiments the total amount of paramagnetic oxygen species O^- and O_2^- was less than 10% of the total amount of adsorbed oxygen, thus indicating the predominant adsorption of oxygen in the form of the species nonvisible by EPR as O_2 or O^{2-}. Good accordance with the Langmuir isotherm for nondissociative adsorption was considered to support the possibility of molecular neutral adsorption.

Different results concerning the forms of chemisorbed oxygen were obtained with nonsupported V_2O_5 and V_2O_5-MoO_3. Dyrek [42] and Bielański, Dyrek and Serwicka [43] did not observe any EPR signals upon adsorption of oxygen on slightly reduced V_2O_5, which indicated that oxygen was incorporated into the external layers of crystallites in the form of O^{2-} ion. In these samples the concentration of V^{4+} detected by EPR in the initial samples was always lower than that calculated on the basis of chemical analysis. This justified the conclusion that besides V^{4+} ions detectable by EPR there were also present non-Kramers V^{3+} ions which do not give an EPR signal. The confirmation was found in the fact that the intensity of V^{4+} signal passed over maximum in the course of oxygen chemisorption at temperatures up to 200°C, thus showing a two-step oxidation:

$$V^{3+} \longrightarrow V^{4+} \longrightarrow V^{5+} \tag{8.3}$$

in which only surface or near-to-the-surface V atoms participated. Above 300°C a monotonous decrease of intensity was observed indicating nearly complete disappearance of V^{4+}, which must have been connected with the diffusion into the bulk of crystallites. In a series of similar experiments carried out with slightly reduced V_2O_5-MoO_3 solid solutions, Dyrek and Labanowska [44] observed two maxima on the curves showing the intensity of the EPR signal as a function of the amount of oxygen consumed. The position of the first of them did not change with the changing concentration of molybdenum. On the other hand, the second one shifted toward shorter adsorption times upon increasing content of molybdenum. Such a result indicated that two kinds of oxygen adsorption centers were present in the samples, attributed to the reduced vanadium ions stabilized by oxygen lattice vacancies and the other to the reduced vanadium ions stabilized by Mo^{6+} ions incorporated into the crystal lattice.

Although no O^- or O_2^- species was detected on the nonsupported vanadia and fast irreversible formation of O^{2-} was observed, Dziembaj [45] detected by TPD-type experiments the presence of loosely bonded oxygen on this oxide. The desorption peak of this presumably molecular oxygen was observed at 130°C and under vacuum conditions. The TPD curves indicated also the evolution of oxygen from V_2O_5 above 450°C. This was the departure of lattice oxygen. The subsequent study of the equilibria in the system V_2O_3-O_2 led to the conclusion that at $0 < \underline{x} < 0.02$ [46,47] and 575—615°C the nonstoichimetric V_2O_5 phase exists. However, further departure of oxygen results in the formation of a lower oxide (in the reversible reaction):

$$3V_2O_5 \rightleftarrows V_6O_{13} + O_2 \tag{8.4}$$

The lability of V_2O_5 phase renders the determination of oxygen adsorption isobars questionable [48].

The adsorption of benzene on V_2O_5 and V_2O_5-MoO_3 catalysts has been tackled in a few studies. Jones et al. [49] studied benzene adsorption on alumina-supported V_2O_5 and V_2O_5-MoO_3 samples at 288—381 K, conditions which are not very interesting from the catalytic point of view. The authors determined the differential adsorption heats, which decreased from the values of the order of 60 kcal mol^{-1} for small coverages to a value corresponding to the vaporization heat of benzene at coverages higher than a monolayer. More recently, Belokopytov et al. [50] studied the thermoprogrammed desorption of benzene from V_2O_5-MoO_3 catalyst. Two TPD peaks were observed: a strong one at 422 K and a much weaker one at 516 K. The desorption in the former case followed the first-order law, which indicated that it was a monomolecular process and dissociatively adsorbed oxygen departed from the surface. The activation energy determined for this process was only 50 kJ mol^{-1}. The reaction order determined for the second peak was two and hence in the desorption act characterized by the activation energy 143 kJ mol^{-1} two chemisorbed species were involved. The authors suggested that the formation of two forms of adsorbed benzene was due to the presence of two different types of surface centers, e.g., Mo and V atoms. Following the suggestion of Ioffe and Wolkenstein [51] they considered the possibility of formation of benzene surface complex with the dissociation of either a σ or a π bond in the C_6H_6 molecule. In either case the molecule would be oriented perpendicularly to the surface. However, it should also be observed that the flat orientation of the adsorbed benzene molecule on the surface should be taken into account. In such a case benzene would be bonded by its π-orbitals in the same way as it occurs in sandwich type complexes such as di-benzene chromium $/C_6H_6/_2Cr$, or in the "piano stool" type molecule of benzene-tricarbonyl chromium $/C_6H_6/Cr/CO/_3$. Easily accessible vanadium atoms are present at (010) face of V_2O_5. Assuming coordination of such atoms as fifefold one could expect the formation of the complex $/C_6H_6/VO_5$ in which all oxygen atoms are lattice oxygen atoms.

D. The Mechanism and Kinetics of the Oxidation of Benzene on V_2O_5-MoO_3 Catalysts

1. Reaction Patterns

The main products of the catalytic oxidation of benzene on vanadia-molybdena catalysts are maleic anhydride and carbon oxides. Already in the early investigation it has been understood that the latter can be produced either by the direct oxidation of benzene or by the oxidation of maleic anhydride. This led Hammar to accept the following reaction scheme [52]:

$$\begin{tikzcd} & C_4H_2O_3 \arrow[dr, "k_2"] & \\ C_6H_6 \arrow[ur, "k_1"] \arrow[rr, "k_3"] & & CO + CO_2 + H_2O \end{tikzcd} \tag{8.5}$$

which subsequently became the basis for most of kinetics studies. However, the fact that besides maleic anhydride some amount of benzoquinone was also detected along with, less frequently reported, hydroquinone (the presence of which is questioned by some authors) and traces of formaldehyde and diphenyl [53] led to the reaction schemes postulating different intermediate products of the transformation of benzene to maleic anhydride. Germain and Peuch [54] proposed the following scheme:

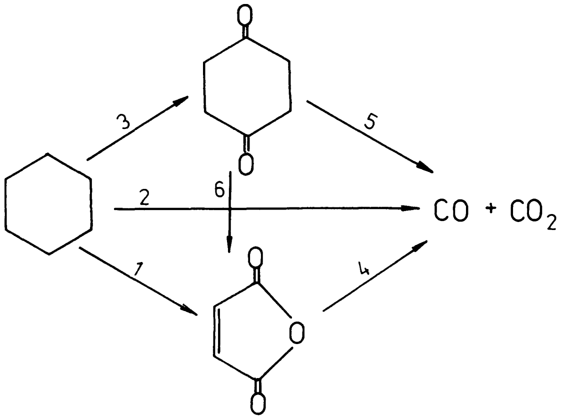

(8.6)

In the case of a catalyst in which the V:Mo atomic ratio was 6 and at low conversion of benzene the ratio of reaction rates was estimated to be $\underline{v}_1:\underline{v}_2:\underline{v}_3 = 1:0.53:0.08$. Scheme (8.6) was considered by the authors to be equivalent to the "rake" scheme:

$$\begin{tikzcd} \text{Gas phase} & B \arrow[d, shift left] & Q \arrow[d, shift left] & M \arrow[d, shift left] & & \\ \text{Adsorbed phase} & B \arrow[u, shift left] \arrow[r] & Q \arrow[u, shift left] \arrow[r] & M \arrow[u, shift left] \arrow[r] & C & CO + CO_2 \end{tikzcd} \qquad (8.7)$$

Reaction 1 of scheme (8.6) corresponds in (8.7) to a fraction of quinone (Q), the molecules of which were oxidized without desorption, while reactions 3 and 6 correspond to the quinone molecules which were readsorbed after desorption. This mechanism was supported by the experiments carried out by Beydoun et al. [55] who observed maxima on the reaction yield versus contact time curves for both quinone and maleic anhydride (M). Quinone was oxidized to maleic anhydride with the selectivity of 90% while benzene only in 60%. This observation confirms the existence of a direct path (reaction 2 in 8.6) of the total oxidation of benzene. It should be noticed that the latter reaction predominates in the case of fully oxidized catalyst, and the selectivity to maleic anhydride distinctly increases with the reduction of the catalyst [55,30].

A more developed reaction scheme was proposed by Ahmad et al. [56] who were using V_2O_5–MoO_3 and Cr_2O_3–V_2O_5 catalysts and fluidized bed reactor. Kinetic investigations and especially the study of the effect of contact time gave the authors the basis for the formulation of the following scheme of consecutive and parallel reactions:

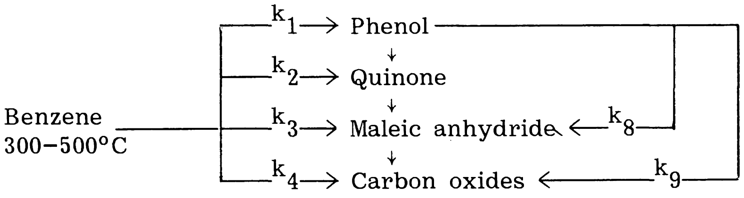

(8.8)

Taking into account a high excess of air throughout the study, the authors assumed zero order reaction with respect to oxygen and simultaneously first order of reactions of the particular organic reagents. Consequently, the rate constants k_1–k_9 could be evaluated. It should be emphasized that activation energies obtained for particular reactions are definitely low: 4–6 kcal mole^{-1} for V_2O_5–MoO_3 with the exception of 17.3 kcal mole^{-1} for reaction 8) and 2–6 kcal mol^{-1} for Cr_2O_3–V_2O_5 catalysts (with the exception of 12 kcal mol^{-1} for reaction 5). Such values clearly indicate that the reactions were diffusion-controlled, i.e., they occurred within the narrow pores of silica-supported catalyst. This circumstance might be the reason that Ahmad et al. obtained an exceptionally high yield of quinone and phenol in comparison with that of maleic acid. For example, at 400°C the following proportion of products was found: $P:Q:M:CO_2 = 0.010:0.016:0.414:0.560$.

Recently the problem of the participation of particular reaction paths in the overall oxidation of benzene was also tackled by Inglot who studied on the same vanadia-molybdena catalyst (30 mol % MoO_3) kinetics of the oxidation of benzene [57], maleic anhydride [58], phenol [59], and p-benzoquinone [60]. The main results can be summarized as follows: on the undoped catalyst the participation of route 1 in the scheme (8.5) in the total conversion of benzene at 322°C was 0.62 while 0.38 corresponded to the direct oxidation to CO and CO_2. The ratio $\underline{k}_1/\underline{k}_3$ amounted to 1.29 thus indicating a distinct overoxidation of maleic anhydride. However, the doping of V_2O_5-MoO_3 catalyst with 0.5–5 mol % of P_2O_5 resulted in a decrease of $\underline{k}_3$ by a factor of 2 and the overall selectivity increased to about 60%. In Inglot's experiments phenol was oxidized to maleic anhydride and quinone with selectivities of 10 and 12%, respectively, while the selectivity of benzene oxidation was 60%. This indicated that under the conditions of his experiments the reaction route of selective oxidation of benzene via phenol as intermediate can play only a minor role (1–3%). On the other hand, analysis of kinetic data led to the conclusion that quinone can be the main intermediate product in the transformation of benzene into maleic anhydride.

Krylova et al. [61] showed that besides the products already mentioned, a very small amount of side products of much more complicated molecular structure can be formed in the course of catalytic oxidation of benzene on the industrial catalysts. These products were identified chromatographically and mass spectroscopically in the residue after extraction from an aqueous solution of crude technical maleic anhydride. In particular they detected phthalic anhydride, p-benzoquinone, 2-piron, benzaldehyde, pirocatechine carbonate, benzoic acid, anthraquinone, and 1,4-naphthoquinone. The authors also proposed the hypothetical scheme of side reactions leading to all these products.

2. Kinetics of the Catalytic Oxidation of Benzene

As mentioned in Section II of Chapter 4, Mars and van Krevelen in their now classical paper on the catalytic oxidation of aromatic hydrocarbons [62], assumed that such reactions comprise two independent steps, i.e., reaction between hydrocarbon molecules and oxygen atoms at the surface of catalyst, and reoxidation of the partly reduced surface by oxygen from gas phase. Assuming that the former step is a first-order reaction with respect to the partial pressure of the substance to be oxidized p_R, one can express the oxidation rate v_R by the equation:

$$v_R = k_1 p_R \theta \tag{8.9}$$

based on the supposition that the reaction rate is proportional to the degree of occupation of the surface by oxygen atoms participating in the reaction (θ).

The rate of reoxidation of the surface was assumed to be proportional to a certain power m of oxygen partial pressure and to the catalyst's surface area not covered by active oxygen $(1 - \theta)$:

$$v_{O_2} = k_2 p_{O_2}^m (1 - \theta) \tag{8.10}$$

In the steady state of the reaction the rates of both processes, reduction and reoxidation, are equal, and if for one aromatic molecule β molecules of oxygen are required we can write:

$$\beta k_1 p_R \theta = k_2 p_{O_2}^m (1 - \theta)$$

and

$$\theta = \frac{k_2 p_{O_2}^m}{\beta k_1 p_R + k_2 p_{O_2}^m} \tag{8.11}$$

From (8.9) and (8.11) we find that the overall reaction rate is:

$$v_R = \frac{1}{1/k_1 p_R + \beta/k_2 p_{O_2}^{m}} \qquad (8.12)$$

The validity of the equation with $m = 1$ for the oxidation of benzene was verified by Mars and van Krevelen. An important argument for the correctness of their reaction scheme has been found in the fact that the value of the rate constant k_2 of the reoxidation process studied on a V_2O_5-MoO_3/Al_2O_3 catalyst was identical when determined in the catalytic oxidation of benzene, naphthalene, and anthracene. Mars and van Krevelen's model does not specify which kind of surface oxygen participates in the catalytic reaction: chemisorbed or lattice oxygen. However, the authors believed that it is doubly bonded terminal oxygen in V=O groups. They also observed that in the steady state of the reaction a certain degree of surface reduction must always be present. Otherwise the reoxidation process would be stopped.

The Mars and van Krevelen equation ($m = 1$) was also applied by Germain et al. [63]. Tufan and Angkerman [64], who examined 11 theoretical models and corresponding kinetic equations, proved the best applicability of Eq. (8.12) with m equal to 1 or 1/2. A similar result was obtained in [65] where seven different kinetic equations were tested. The applicability of Eq. (8.12) limited only to the initial period of the catalytic reaction was observed in [66]. The author recommended instead an equation based on the Houghen-Watson model in the general form:

$$r = k p_B \frac{1}{1 + \Sigma p_i k_i} \qquad (8.13)$$

based on the assumption that the reaction rate was controlled either by the adsorption of benzene or maleic anhydride (k rate constant, k_i adsorption coefficient of the reactant i).

Generally speaking, the steady-state kinetic equation adequately describes the rate of overall benzene consumption and the values of apparent activation energies determined by different authors are in most cases in reasonable accordance. However, this equation can only be taken as an empirical one giving the first approximation. The model on which it is based does not take into account the fact that in reality catalytic oxidation of benzene comprises a rather complicated pattern of parallel and consecutive reactions, the simplest representation of which is given by the scheme of Hammar [Eq. (8.5)]. Ioffe and Liubarskii [67] determined the rates of all three reactions mentioned therein when studying the oxidation of benzene on V_2O_5-MoO_3/Al_2O_3 catalyst in a circulating flow reactor where the rate of benzene conversion and maleic anhydride formation could be determined either in the presence of maleic anhydride in the gas phase at the stationary state of reaction or in the situation where maleic anhydride vapors were removed by freezing them out. The rate of transformation of benzene into maleic anhydride [reaction 1 in scheme (8.5)] and the rate of direct degradation of benzene (reaction 3) in the absence of maleic anhydride in the gas phase could be given as:

$$\underline{r}_1 = \underline{k}_1[B]^{0.78} \tag{8.14}$$

and

$$\underline{r}_3 = \underline{k}_3[B]^{0.71} \tag{8.15}$$

Both equations are valid independent of the partial pressure of oxygen. The order of reaction with respect to maleic anhydride (reaction 2) has been determined separately [68] as equal to one:

$$\underline{r}_2 = \underline{k}_2[M] \tag{8.16}$$

Much more complicated was the dependence of reaction rate on the concentration of oxygen in the gas phase. At $[O_2] < 4 \times 10^{-3}$ mol liter^{-1} reactions 1 and 3 were of the order two with respect to oxygen. However, at $[O_2] > 4 \times 10^{-3}$ mol liter^{-1} reaction was zero order with respect to oxygen. The change of reaction order with the changing oxygen partial pressure was also observed by Germain et al. [69].

Ioffe et al. also showed that the rate of benzene consumption in both reactions 1 and 2 is inversely proportional to the concentration of maleic anhydride in the gas phase raised to the 0.74 power independent of oxygen partial pressure. The rate of benzene conversion can therefore be represented by the equations:

$$\underline{r} = \underline{r}_1 + \underline{r}_3 = \frac{[O_2]^2}{[M]^{0.74}}\left\{\underline{k}_1[B]^{0.78} + \underline{k}_3[B]^{0.71}\right\}$$

$$\text{for } [O] < 4 \times 10^{-3} \text{ mol liter}^{-1} \tag{8.17}$$

$$\underline{r} = \underline{r}_1 + \underline{r}_3 = \frac{1}{[M]^{0.74}}\left\{\underline{k}_1[B]^{0.78} + \underline{k}_3[B]^{0.71}\right\}$$

$$\text{for } [O_2] > 4 \times 10^{-3} \text{ mol liter}^{-1} \tag{8.18}$$

Inhibition of the reaction by the presence of maleic anhydride strongly suggests that both reagents B and M are chemisorbed on the same sites on the catalyst surface.

The kinetic model of the catalytic oxidation of benzene based on reaction scheme (8.5) represents a good approximation at high conversions of benzene, i.e., when the formation of products such as quinone, phenol, etc., can be neglected. However, more elaborate studies must also take into account the formation of these secondary products. Most such studies comprise not only the kinetics of benzene oxidation but also oxidation of maleic anhydride, quinone, and phenol as was done by Ahmad et al. [56] and Inglot [57-60], as was already mentioned in Section II.D.1. It should here be mentioned that the former authors gave the most complete set of kinetic equations from which rate constants of processes indicated in scheme (8.8) could be calculated. However, their detailed presentation seems outside the scope of this text.

3. Molecular Mechanism of the Catalytic Benzene Oxidation

In the two last sections dealing with the reaction patterns and kinetics of catalytic benzene oxidation the problem of molecular mechanism of benzene transformations was not raised. The main question is the nature of the first attack: H abstraction or O addition [70]. Dolgov [71] proposed a highly hypothetical but chemically feasible sequence of reactions consistent with the H-abstraction mechanism:

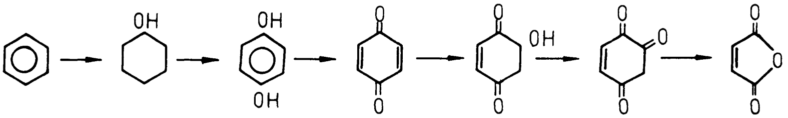

(8.19)

Since no clear evidence of 1,2 or 1,4 oxygen addition to olefins and diens exists, Germain [70] proposed that the first step is a nuclear H abstraction followed by the second identical process in the para position, and an O addition to these radicals, all π-bonded to a surface cation.

The addition of an O_2 molecule to the benzene ring was suggested by Dmuchovsky et al. [72]. It was proposed that in the rate-limiting step benzene can add molecular oxygen either in 1,2 or 1,4 fashion to yield an activated complex in the form:

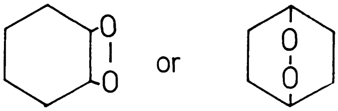

(8.20)

The idea of a peroxy intermediate is strongly supported by the recent papers of Waugh et al. [73-75] and Haber et al. [76,77]. The first group of investigators carried out a series of TPD experiments with a mass spectrometer on-line in which adsorption of benzene and maleic anhydride over alumina-supported V_2O_5-MoO_3 catalyst was studied. On the same catalyst the oxidation of benzene, quinone, and hydroquinone was also investigated. The main results obtained by the authors can be summarized as follows:

1. Adsorption of maleic anhydride on the catalyst was definitely poor and never exceeded 6×10^{12} molecules per cm^2. This suggested that maleic anhydride was adsorbed on the defects present on the surface, e.g., anionic vacancies. The DTA experiments showed two desorption peaks:

At 220–250°C $\quad \underline{E}_{des} = 138–148\ \text{kJ mol}^{-1} \quad \Delta\underline{H} = -79.9\ \text{kJ mol}^{-1}$

and

At 340–350°C $\quad \underline{E}_{des} = 171–181\ \text{kJ mol}^{-1} \quad \Delta\underline{H} = -1024\ \text{kJ mol}^{-1}$

The high values of the activation energies of desorption $\underline{E}_{des}$ and high values of adsorption enthalpy show that chemisorption of maleic anhydride is strong and that the desorption of maleic anhydride can be the rate-limiting step in the oxidation of benzene. Such a conclusion is in accordance with the already mentioned kinetic Eqs. (8.17) and (8.18) given by Ioffe according to which the rate of benzene oxidation is slowed down by the presence of maleic anhydride in the gas phase.

2. Similarly to the case of maleic anhydride, the concentration of benzene adsorbed on the same catalyst is small and never exceeds 4×10^{11} molecules per cm^2. Benzene chemisorbed was partially transformed into maleic anhydride desorbing at the same temperature as in the experiments in which the latter was directly adsorbed from the gas phase. Waugh concluded that maleic anhydride was produced on the same sites at which its precursor, benzene, was adsorbed. Both molecules are considered to be not mobile on the surface and the transformation $C_6H_{6(ads)} \rightarrow C_4H_2O_{3(ads)}$ is very easy. It occurs with activation energy as low as 31.4 kJ mol^{-1}. The immobility of both organic molecules suggests that it is oxygen species participating in the reaction which must be mobile. It seems unlikely that such mobility can be exhibited by lattice oxygen; rather it is chemisorbed oxygen, e.g., O_2^- species, which is migrating.

3. Catalytic experiments show that the selectivity of quinone oxidation to maleic anhydride was very small (3–5%), while that of

benzene and hydroquinone was high (∿60%) and equal for both latter reagents. Therefore Waugh accepted that hydroquinone is the intermediate in the selective oxidation of benzene and quinone the intermediate in the nonselective oxidation. The logical consequence of accepting hydroquinone as the intermediate was to accept the previously mentioned suggestion of Dmuchovsky that the first product of oxygen attack on the benzene molecule is a peroxidic adduct. The reaction scheme proposed by Waugh is represented by the scheme (8.21) in a somewhat simplified form. It should also be observed that, according to the experiments carried out by Inglot [60], quinone can be oxidized to maleic anhydride with much higher selectivity (up to 60%) than was observed by Waugh et al. That is why in scheme (8.21) a dotted line has been introduced by the authors of this book indicating this latter possibility. Waugh et al. also showed that all the steps proposed in their reaction scheme are symmetry-allowed.

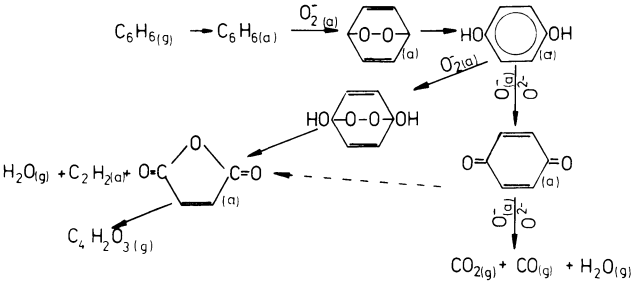

(8.21)

The ideas developed by Waugh et al. found strong support in the quantum-chemical calculations carried out by Broclawik et al. [76,77]. These authors assumed three main reaction paths as most probable for the reaction between benzene and dioxygen molecules (Fig. 8.4):

1. The reaction path is in the plane of the benzene ring; the O_2 molecule is approaching with its axis parallel to the side of the ring.
2. The reaction path is in the plane of the ring; the O_2 molecule is approaching with its axis perpendicular to the ring.
3. The reaction path is directed perpendicular to the center of the benzene ring; the O_2 molecule approaching with its axis parallel to the diagonal of the ring.

The proposed mutual positions of C_6H_6 and O_2 molecules are fairly reasonable considering the fact, mentioned in Section II.C of this chapter, that we can expect two positions of a C_6H_6 adsorbed molecule, parallel and perpendicular to the surface, and also

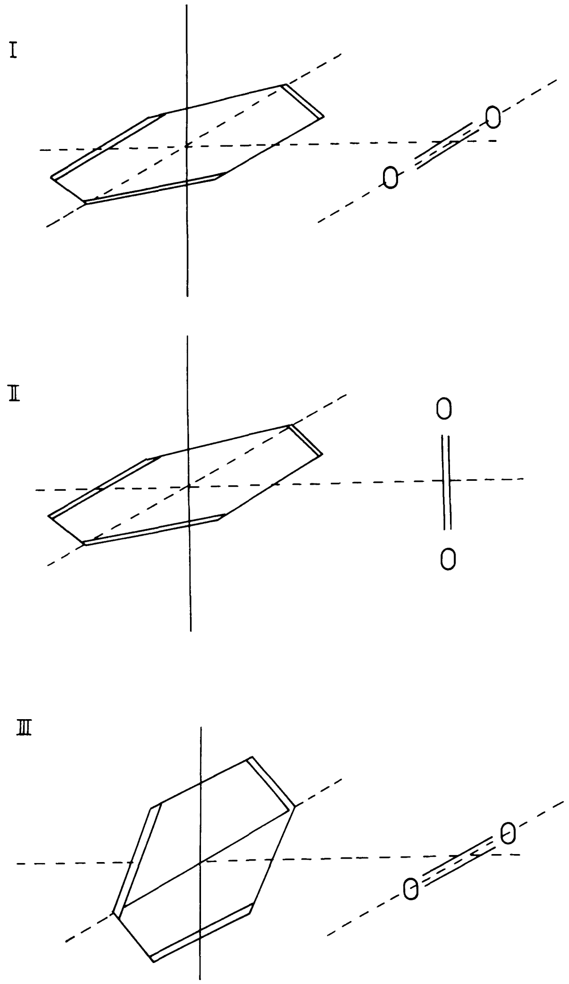

FIGURE 8.4 Chosen paths for the reaction of benzene with oxygen molecule [77].

the fact, mentioned in Section I.C.2 of Chapter 2, that dioxygen can also be oriented "side-on" and "end-on" to the surface.

Figure 8.5 shows the dependence of the potential energy of the quantum-chemical system in path 1 on the distance of both molecules. In the case when O_2 molecule is in the triplet ground state (curve a) a monotonous increase of the energy occurs upon the approach of the O_2 molecule to the C—C bond. The calculations also indicate that no change in the O—O bond length occurs and the

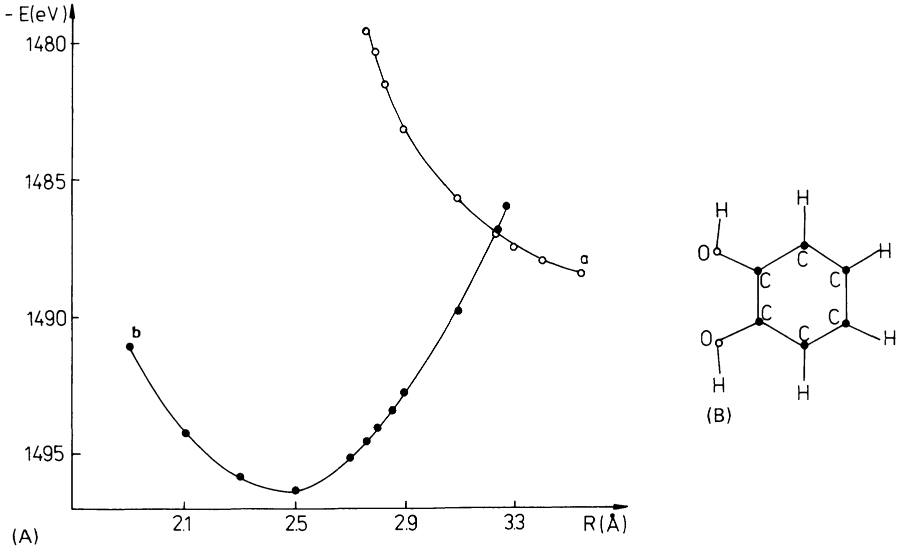

FIGURE 8.5 (A) Potential energy curves for reaction path 1. (a) starting $\underline{R}_{O\text{-}O}$ = 1.20 Å; (b) starting $\underline{R}_{O\text{-}O}$ = 1.49 Å.(B) optimal geometry for the O_2 + C_6H_6 system corresponding to the minimum on curve b [77].

charge transfer from benzene to oxygen is small. On the other hand, stretching the initial O—O bond distance to 1.49 Å (a value not very different from that in the case of O_2^- ion equal to 1.28 Å) results in the appearance of a potential curve of attractive character (curve b) exhibiting a minimum at the reaction coordinate 2.5 Å at which the distance between the C—C and O—O bonds is 1.239 Å. The optimal geometry of the complex forming from C_6H_6 and O_2 molecules, then, is close to the geometry of the o-dihydroxybenzene presented at the right side of Fig. 8.5. The presence of dihydroxybenzene in the products of catalytic oxidation was postulated in [61] as the intermediate product of traces of double-ring aromatic compounds. However, in no case has it been detected experimentally. The fact that the reaction route including formation of this species was not confirmed experimentally may be taken as an indication that chemisorption of oxygen "side-on" on V_2O_5 occurs only exceptionally.

The potential energy curve calculated for reaction path 2 and presented in Fig. 8.6 is composed of three distinct sections apparently belonging to three different states. The first section corresponding to high values of the reaction coordinate is repulsive; the

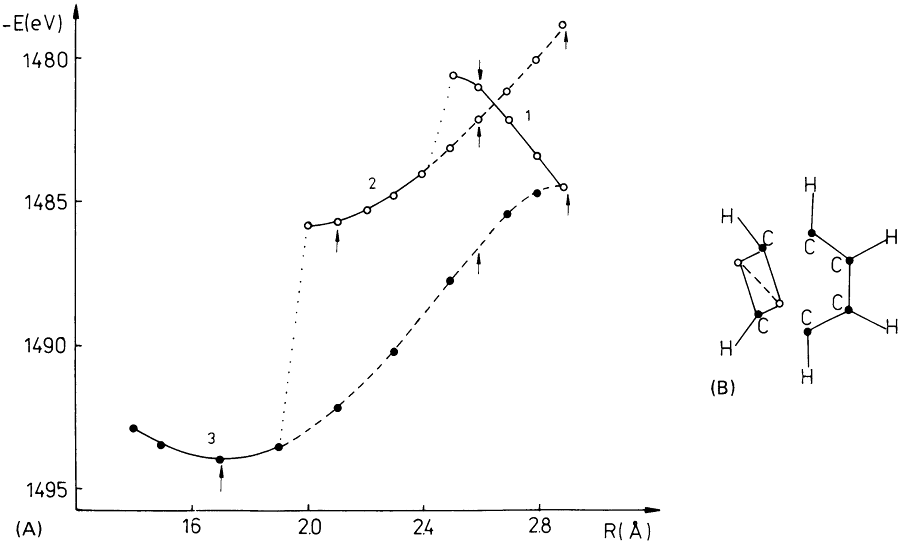

FIGURE 8.6 (A) Potential energy curves for reaction path 2. Full line corresponds to the energy curve obtained on decreasing reaction coordinate; dashed lines describe energy curves obtained when the optimal geometries at the reaction coordinate equal to 1.7 and 2.3 Å, respectively, were taken as the input and the reaction coordinate was increased. (B) Optimal geometry of the complex corresponding to the minimum on curve 3 [77].

second and third sections are attractive. The system represented by the intermediate curve 2 can be considered as composed of the deformed benzene ring with C1 and C2 carbon atoms pulled strongly apart and the oxygen molecule with a considerably elongated O—O bond. Curve 3 refers to the situation in which oxygen atoms already far apart interact strongly with C1 and C2 carbon atoms pulled together with their hydrogen atoms away from the remainder of the benzene ring. At the reaction coordinate 1.7 Å, corresponding to the minimum of potential energy, the benzene molecule becomes split into two fragments, represented on the right side of Fig. 8.6, which are expected to be highly reactive intermediates of complete oxidation of the aromatic molecule to water and carbon oxides.

Figure 8.7 shows that in the case of reaction path 3 potential energy curve a, corresponding to the oxygen molecule in its ground state, the interactions are repulsive. However, a shallow local minimum appears when the starting O—O bond length is 1.49 Å. At the minimum the O—O bond becomes strongly stretched and the charge on oxygen atoms is increased. This suggests the formation

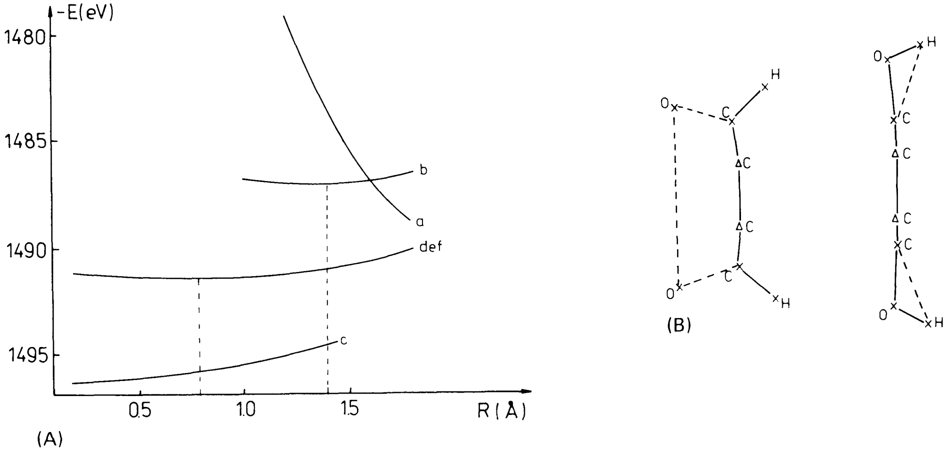

FIGURE 8.7 (A) Potential energy curves for reaction path III. a and d, initial value of $\underline{R}_{O-O}$ = 1.20 Å. b and e, initial value of $\underline{R}_{O-O}$ = 1.49 Å. c and f, initial value of $\underline{R}_{O-O}$ = 3.9 Å. Curves a, b, c refer to the system $O_2 + C_6H_6$, curves d, e, f to the system $O_2^{2-} + C_6H_6$. (B) Optimal geometries of the $O_2 + C_6H_6$ complex for the value of $\underline{R}_{O_2-C_6H_6}$ = 1.4 Å (minimum on curve b), and $\underline{R}_{O_2-C_6H_6}$ = 0.2 Å (close to the minimum on the reaction path c) [76].

of a metastable intermediate in which the oxygen molecule is bridge-like bonded to the diagonal 1,4 carbon atoms of the benzene molecule. The geometry of such a complex is shown at the right side of Fig. 8.7. It corresponds fairly well to the C_6H_6-O_2 adduct proposed by Dmuchovsky [72] and Waugh et al. [73,74], already presented in this section.

The elongation of the stretching O—O bond to 3.8 Å results in the potential energy curve c. Here the situation is completely different from two previous cases. The energy of the C_6H_6-O_2 system decreases monotonously at first and then reaches a minimum for a hydroquinone-like complex. Oxygen atoms displace hydrogen atoms at the diagonal 1,4-carbon atoms and assume a position intermediate between carbon and hydrogen with a C-O distance of 1.37 Å and an H-O distance of 0.95 Å e.g., the value virtually equal to that of typical H-O distance in organic molecules. The configuration of this complex is shown on the right side of Fig. 8.7. A significant charge transfer is observed from benzene to oxygen. It can be concluded that in this case reaction between benzene and oxygen results in the formation of σ bonds between the oxygen and carbon atoms whereas in the case of curve b a π-like complex is produced. It is seen that quantum chemical calculations fully confirm the possibility of the first two steps postulated by Waugh and also indicate a plausible mechanism of the direct degradation of benzene. The essential result of quantum mechanical calculations is the conclusion that selective oxidation of benzene occurs via the formation of a bridge-like adduct between adsorbed benzene and dioxygen species which then rearranges into hydroquinone. This sequence of elementary steps may be then repeated with the second oxygen molecule again forming a bridge-like intermediate with hydroquinone, the latter finally rearranging to give an adsorbed molecule of maleic anhydride as is shown in (8.21).

However, it is necessary to notice that there also exists in the literature a different approach accepting that it is the doubly bonded terminal oxygen atom in the V=O group which participates in the catalytic oxidation of benzene. This was suggested by Tarama [78], who postulated it on the basis of structural considerations. As shown in Fig. 8.2, such atoms are exposed and easily accessible on the (010) face generally best developed in V_2O_5 crystallites. Although the V=O bond is the shortest and hence the strongest of all vanadium-oxygen bonds in V_2O_5, this oxygen atom was considered, apparently for geometric reasons, to be the most reactive one. Tarama's hypothesis was accepted in many later papers. Weiss et al. [79] proposed a mechanism of the selective oxidation of benzene in which C_6H_6 molecules are adsorbed in the first stage of reaction on doubly bonded oxygen atoms. On the other hand, Bielański and Inglot [80] when investigating the IR spectra of V_2O_5 and V_2O_5-MoO_3 catalysts obtained by fusion of the oxides stated that the fresh catalysts exhibiting a distinct peak at 1025 cm^{-1} characteristic of the V=O bond showed only weak catalytic activity and were nonselective. In contrast, the same catalysts when reduced by benzene vapors and not exhibiting a 1025 cm^{-1} peak were active and selective, thus showing that the presence of the V=O group is not necessary for the selective oxidation of benzene.

More recently, Inomata et al. [81–85] when studying the reaction between NO and NH_3 occurring on the surface of V_2O_5 with the formation of N_2 and H_2O proposed the following mechanism for this process:

$$NO + NH_3 + {}^{5+}V{=}O \longrightarrow N_2 + H_2O + {}^{4+}V{-}OH \qquad (a)$$

$$2\,{}^{4+}V{-}OH \xrightarrow{O_2 \text{ or lattice oxygen}} 2\,{}^{5+}V{=}O + H_2O \qquad (b)$$

The first step is the reduction of the catalyst surface; the second one the reoxidation either by oxygen from gas phase or by the diffusion of bulk oxygen to the surface with the reproduction of V=O groups. Both processes (a) faster and (b) slower in the absence of oxygen in the gas phase can be separated. In this way, according to the authors, the number of surface oxygen atoms participating in the reaction assumed to be the doubly bonded oxygen can be determined [83]. Using their analytical method the authors stated an approximately linear correlation between the number of active oxygen atoms supposed to be bonded in V=O groups and the activity of titania-supported V_2O_5 catalyst in the oxidation of benzene [85].

The assuption that Inomata's reaction occurs on the surface V=O centers was seriously questioned by Gasior et al. [86], who showed that this reaction occurs with the participation of ammonia adsorbed on Brönsted acid sites in the form of NH_4^+ ions and loosely bonded NO molecules. According to the latter authors, Inomata's process can be described by the overall reactions:

$$ {}^{5+}V{-}OH + NH_3 \longrightarrow {}^{5+}V{-}O\cdots NH_4 \qquad (c) $$

and

$$ 2\,{}^{5+}V{-}O\cdots NH_4 + {}^{5+}V{-}O{-}V + 2NO \longrightarrow 2N_2 + 3H_2O + {}^{5+}V{-}OH + {}^{4+}V{-}\square{-}{}^{4+}V \qquad (d) $$

where □ represents an oxygen vacancy at the surface of V_2O_5. In the absence of gas phase oxygen the reduced surface sites are rapidly regenerated to their initial state by the diffusion of oxide ions from the bulk of crystallites, the reaction being in fact not catalytic but stoichiometric, whereas in the presence of gas phase oxygen the lattice becomes reoxidized according to the equation:

$$ {}^{4+}V\,\square\,{}^{4+}V + \frac{1}{2}O_2 \longrightarrow {}^{5+}V{-}O{-}{}^{5+}V \qquad (e) $$

The argument of Gasior et al. is based on the following experiments carried out with monocrystalline and powdered V_2O_5 samples differing by the habitus of crystallites, which was characterized by the morphological factor *f* introduced by Ziólkowski and Janas [87] [$f = I_{(101)}/I_{(010)}$ is the ratio of X-ray intensities of the (101) and (010) reflections].

1. The XPS study of the exposed (010) planes of V_2O_5 monocrystals besides V2p doublet found only a simple line at 529.6 eV corresponding to the O1s characteristic of lattice oxygen in

V_2O_5. There were no changes in the XPS spectrum after argon sputtering the surface. On the other hand, the spectrum taken from the exposed (100) plane exhibited, in addition to the 529.6-eV line, a line at 532.2 eV typical of OH groups in transition metal hydroxides and oxides. On sputtering the intensity of this latter line decreased while that of 529.6 eV assigned to lattice oxygen increased.

2. The IR study of NH_3 adsorption indicated only the presence of NH_3 bonded on Brönsted acid sites as NH_4^+ ions, the coordinatively bonded NH_3 on Lewis acid sites being absent. The intensity of the 1416 cm^{-1} peak corresponding to deformation vibrations of NH_4^+ ion was distinctly increasing with the increase of morphological factor, i.e., with the decreasing ratio of surface area of (010) plane (at which V=O groups are present) to the surface area of planes perpendicular to it: (101) and (100).
3. Increasing with the morphological factor was the amount of N_2 obtained in the reaction between NO and NH_3 over powdered V_2O_5 catalysts.

All the above facts clearly indicate that Inomata's reaction does not occur on the (010) plane and hence the yield of N_2 can not be taken as a measure of the concentration of surface V=O groups.

It should be noted that Inomata et al. [81] observed the decrease of the 1025 cm^{-1} IR peak intensity in the course of the reaction between NO and NH_3, and this was considered as confirmation that V=O groups really participate in this process. However, Gasior et al. stated that V_2O_5 is reduced to V_2O_4 by ammonia at temperatures well below 300°C. This was also observed in [89]. Taking into account the fact that IR spectra reflect primarily the behavior of the bulk of crystallites, the decrease in the intensity of the 1025 cm^{-1} bond should be linked with the disappearance of V_2O_5 phase due to reduction to V_2O_4, which does not contain doubly bonded oxygen in its structure.

E. Selectivity in the Catalytic Oxidation of Benzene to Maleic Anhydride

Selectivity in the catalytic oxidation of benzene to maleic anhydride depends on a number of factors: phase and chemical composition of the catalyst, degree of reduction, degree of benzene conversion, temperature and other experimental conditions. No clear-cut discrimination between the particular effects can be done at present. However, looking over the literature certain correlations can be found.

As was stated in Section II.B, fully oxygenated vanadia represents a definitely poor and nonselective catalyst for benzene oxidation and quite appreciable reduction is necessary to activate it. Such reduced V_2O_5 frequently constitutes a mixture of lower oxides which may not only exhibit high activity but also good selectivity. The lower oxides of vanadium are catalytically active without a pretreatment [90] and the highest activity is reached in the case of V_2O_4 [91]. All these oxides are nonselective catalysts. However, the selectivity of V_6O_{13} and V_2O_4 could be strongly enhanced by doping them with MoO_3. Facing the fact that particular lower vanadium oxides are not selective as catalysts, it is rather unexpected that the product of reduction of V_2O_5 in benzene vapors representing a mixture of different lower oxides may exhibit satisfactory selectivity as was observed in [90].

The enhancement of selectivity by molybdena introduced into vanadium catalysts depends on the concentration of the dopant and the selectivity reaches a flat maximum at about 30 mol % of MoO_3 [92-94]. One of the reasons for selectivity improvement by the addition of MoO_3 may be the increase of oxygen bond strength which manifests itself by the retardation of the reduction observed in [95]. It was also observed that maximum selectivity was accompanied by maximum catalytic activity [5,94]. Selectivity is generally poor at low benzene conversion.

The selectivity reached in two-component vanadia-molybdena catalysts is not fully satisfactory for industrial purposes and a number of promoters—the oxides of Ag, Ti, P, Co, Na, Li, K, B, Ni, Ta, and Sn—were mentioned in the patent literature [5]. However, the information concerning the physicochemical effects and the mechanism of modification of V_2O_5-MoO_3 catalysts with such additives is scarce.

Bielański et al. [96] and Inglot [97] studied the effect of P_2O_5 additive and showed that small amounts of promoter (1–5 mol %) improved the selectivity simultaneously decreasing the activity of the catalyst containing 30 mol % MoO_3. Further increase of P_2O_5 concentration was accompanied by the decrease of selectivity and the appearance of an increasing amount of amorphous (glassy) phase. No new crystalline phases due to the presence of P_2O_5 were detected.

The effect of Ag_2O additive strongly depends on its concentration. According to [98], 1.02 mol % Ag_2O improved the selectivity of vanadia-molybdena catalyst (30 mol % MoO_3) from 29.5 to 63.3%. On the other hand, when the content of Ag_2O was increased to 12.1 mol % and the predominant phase was Ag-V-Mo-O bronze, the catalyst completely lost its activity. Later on it was shown that vanadia-molybdena catalysts obtained by the fusion of the oxides can be rendered more selective by impregnating them with small amounts of $AgNO_3$ solution and subsequently calcining them at 700 K [99]. Selectivity enhancement was strongest (from 27.3 to 49.5% at practically unchanged activity) when catalyst containing 28.5 mol % MoO_3 was doped with 5.9×10^{-2} mol Ag per g of catalyst. This optimal concentration corresponded to 1 Ag atom per 1000 (V + Mo) atoms. The XPS spectrum of such catalyst did not contain peaks characteristic of silver. This indicated that Ag atoms were either incorporated into the subsurface layers or were present in the form of a small number of aggregates which might be missed during XPS experiments. The subsequent scanning microscope and electron probe examination did not uncover any silver aggregates.

The addition of 0.89 mol % of sodium oxide to the fused V_2O_5-MoO_3 catalyst resulted in a distinct decrease in catalytic activity. Increasing its content to 9.4 mol % gave catalyst composed almost exclusively of Na-V-Mo-O bronze and still less active and selective. Such result seems to be in contradiction to the fact that numerous industrial catalysts contain sodium as the promoter. This problem was studied by Najbar et al. [100], who investigated an industrial catalyst obtained by the evaporation on the sintered corundum support of an aqueous solution of ammonium vanadate, molybdic acid, oxalic acid, phosphoric acid, as well Na, Ni, and Ta promoters introduced in the form of chlorides. After calcination in air at 320°C, the X-ray analysis indicated both in fresh catalyst and in the catalyst which was used for 16 months in an industrial reactor the presence of sodium-vanadium bronzes as the only detectable phase. However, the IR spectrum of the fresh catalyst, besides having the bands characteristic for bronze, also contained a 1010 cm^{-1} band which was taken as an indication of the presence of V_2O_5-MoO_3 solid solution. This was confirmed by an electron diffraction study of the crystallites in thoroughly powdered catalyst. The crystallites of the intermediate compound were also present. They were all of too small size (∿100 Å) to be detected by X-ray analysis. In the catalyst studied, after the use in industry, besides bronze forming relatively large crystallites strongly dispersed products of the reduction and phase segregation of the V_2O_5-MoO_3 solid solution and the intermediate compound were detected by electron diffraction as listed in Table 8.3. It has been hence concluded that in this fairly complicated catalytic system the nonactive bronze phase stabilizes the dispersion of the catalytically active phases.

It was already mentioned that selectivity in the catalytic oxidation of benzene also depends in some measure on the conditions of the experiment. First of all when temperature is raised selectivity passes over a flat maximum at 350—400°C [5]. Its decrease at temperatures above maximum seems to be connected with the increased degradation of maleic anhydride, the primary product of the reaction. Chrzaszcz et al. [5] also studied the effect of catalyst bed length (0.3—3.0 m) on the conversion and selectivity in the production of maleic anhydride using a flow reactor which corresponded in its size and heating conditions to a unit tube in the industrial reactor. In the initial section of the tube 1 m long about 90% of benzene was converted to yield ∿60% of maleic anhydride. Over the remaining section of the tube the overall conversion of benzene and conversion to maleic anhydride increased to 98 and 74%, respectively, whereas the conversion to carbon oxides increased only from 20 to 24%. Thus it may be concluded that over this 2-m-long bed section the yield to maleic anhydride increased primarily at the expense of some intermediates now being oxidized up. On the other hand, the slight increase in the oxidation to carbon oxides indicated that the resulting maleic anhydride, most of which had already formed over the initial section of catalyst bed, is oxidized to a minor extent.

III. OXIDATION OF o-XYLENE TO PHTHALIC ANHYDRIDE

A. V_2O_5-TiO_2 System

Vanadium oxide does not form chemical compounds with TiO_2. Thus, when vanadium ions are supported at the surface of TiO_2 by impregnation or chemical deposition (grafting), a heterogeneous mixture is formed built of a layer of V_2O_5 enveloping the grains of TiO_2. The catalytic properties of such a composite system depend on type of support, mode of dispersion of the active component, and conditions of the pretreatment. These factors may influence both physical properties (size and orientation of crystallites, porosity of the resulting system) as well as the nature and extent of chemical interactions between the two phases. The latter in turn affect the catalytic behavior of the active phase, modifying the properties of existing active sites or generating new sites.

It has now been well established [101,102] that the catalytic properties of V_2O_5, both activity and selectivity, are considerably improved when it is supported on anatase, not rutile, although both of these polymorphic modifications of TiO_2 are catalytically inactive in the oxidation of hydrocarbons. As an example, Table 8.4 summarizes results of the measurements of some physicochemical properties and of selectivity of the oxidation of o-xylene to phthalic anhydride on vanadia supported in different amounts on anatase and rutile, as obtained by Grzybowska-Świerkosz and Gasior [101]. For comparison the data obtained with pure V_2O_5 prepared by coprecipitation or decomposition of ammonium metavanadate are also given. It can be seen that the catalysts containing vanadia deposited on rutile are much less selective in phthalic anhydride formation than vanadia deposited on anatase, irrespective of vanadia concen-

Comparison of Physicochemical and Catalytic Properties of V_2O_5-TiO_2 Catalysts of Diffe
dification

Vanadia content (mol %)	Sp. surface area (m^2 g^{-1})	Reduction degree % V_2O_4		Max. selectivity in oxygen o-xylene ox. %		Isopropanol decomposition	
		Initial	After reaction	PA	MA	Dehydrat. mol C_3H_4/pulse × 10^7	Dehydro C_3H_4O/ × 10^7
2.5	—	4.2	21.3	74	—	3	21
5.0	4.6	4.7	9.5	72	3.0	44	26
10.0	5.0	3.1	6.6	75	4.0	30	21
20.0	5.2	3.2	6.2	69	3.5	38	20
2.5	6.5	5.2	27.1	29	—	47	6
5.0	—	5.3	37.5	44	10	124	6
10.0	—	4.7	25.6	47	10	124	5
20.0	6.5	2.8	23.6	45	11	123	2
100	2.1	1.2	13.2	60	9	130	2
100	4.6	1.0	7.2	56	5	—	—

ethod; coprecipitation.
decomposition.
ef. 101.

tration. Both series show also completely different behavior in isopropanol decomposition, which may be used to differentiate between the acidic and redox sites at the catalyst surface [103], namely, for catalysts deposited on rutile the main reaction of isopropanol is its dehydration to propene, similar to the case of pure vanadia, indicating high acidity of the surface, whereas catalysts containing anatase show much smaller amounts of propene (i.e., much lower acidity) and also exhibit activity in dehydrogenation to acetone, characteristic for redox sites. In the same conditions pure anatase and rutile showed practically no activity in the reaction with isopropanol, which supports the argument that the observed changes are due to different properties of the vanadia phase deposited on the two modifications of TiO_2. It may thus be concluded that deposition of vanadia on anatase drastically reduces its acidity. The reducibility of vanadia in the course of the reaction is much higher in the case of samples supported on rutile than on anatase.

Figure 8.8 shows the conversion of o-xylene to phthalic anhydride as a function of the content of vanadia in V_2O_5-anatase samples. It can be seen that the conversion rises from a small value at low vanadia content to almost 100% at 2% of vanadia and then remains high on further increase of the vanadia content. In addition, selectivity also rises attaining for the 2% vanadia sample a value of about 60%. It is noteworthy that pure vanadia shows much lower conversion and lower selectivity. The amount of vanadia required to achieve a monolayer of the surface vanadia species on the surface of anatase grains may be estimated from the area occupied per $VO_{2.5}$ unit of bulk V_2O_5 which is 0.105 nm^2. For the anatase used in the discussed experiments this amount would correspond to about 1% mol of vanadia in V_2O_5-TiO_2. The level of almost 100% conversion of o-xylene on vanadia-anatase catalyst is attained for the sample containing 2% mol of vanadia. Thus a conclusion can be formulated that the improvement of the catalytic properties of vanadia in oxidation of o-xylene is due to the formation of a surface monolayer of vanadia on anatase grains. This conclusion was confirmed by Bond and Brückman [104], who prepared catalyst composed of a monolayer of vanadia deposited by grafting on anatase grains. Analysis of the laser Raman spectra showed that after approximately a monolayer of the surface vanadia species has been formed on the anatase surface, crystallites of V_2O_5 begin to grow [105]. The amount of vanadia which can be accommodated at the surface of the anatase support depends on its surface area.

The structure of the V_2O_5-TiO_2 system and the mechanism of the promotion of catalytic properties of vanadia by supporting it on anatase has recently been the subject of intensive studies [114-116]. At loadings lower than that corresponding to the monolayer coverage,

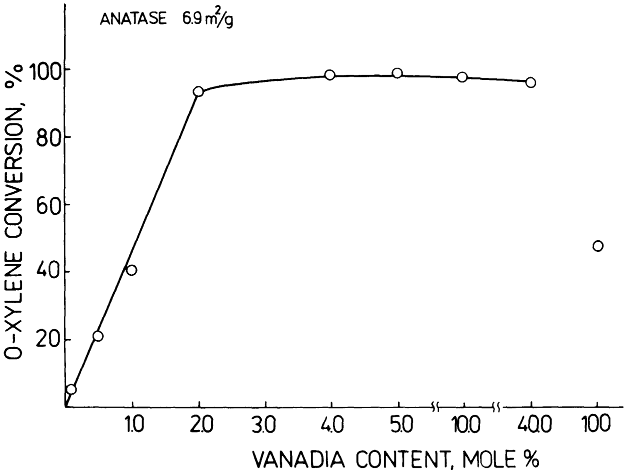

FIGURE 8.8 Conversion of o-xylene as a function of the content of V_2O_5 in V_2O_5/anatase catalysts [101].

the structure of the layer depends on the method of preparation. When grafting, i.e., chemical deposition in water-free conditions, is used, isolated monomeric vanadate tetrahedra become anchored at the OH groups of anatase. EXAFS and XANES measurements [113] showed that these isolated vanadate tetrahedra have two terminal oxygens with the bond length 1.65 Å and two bridging oxygens (bond length 1.90 Å). The bulk structure of anatase is built up of TiO_6 octahedra edge-linked to form zig-zag ribbons running in a and b directions at two different levels and bound together in such a way that each O^{2-} ion has three Ti^{4+} neighbors. Boehm [117] advanced a simple structural model of the anatase surface. A clean (001) plane contains unsaturated Ti^{4+} ions with one O^{2-} missing in their coordination sphere and two types of O^{2-} bridging ions: those coordinating three Ti^{4+} ions and those bridging only two Ti^{4+} ion with the third one missing. Therefore formally the unbalanced charges appear: +2/3 on Ti^{4+} and −2/3 on unsaturated O^{2-}. A decrease of these local excess charges could be achieved by dissociative chemisorption of water with a proton going to oxygen and OH group becoming attached to Ti^{4+} (Fig. 8.9). The resulting formal charge would be +1/3 and −1/3, respectively. The hydroxyl density on the fully hydroxylated most prevalent (001) plane should be 14 OH groups per nm^2. A lower value of 9.3 OH/nm^2 was found with NMR [118], and the amount of vanadium which could be bound to the surface was found to be eight vanadium atoms per nm^2. The simplest model which emerges from these re-

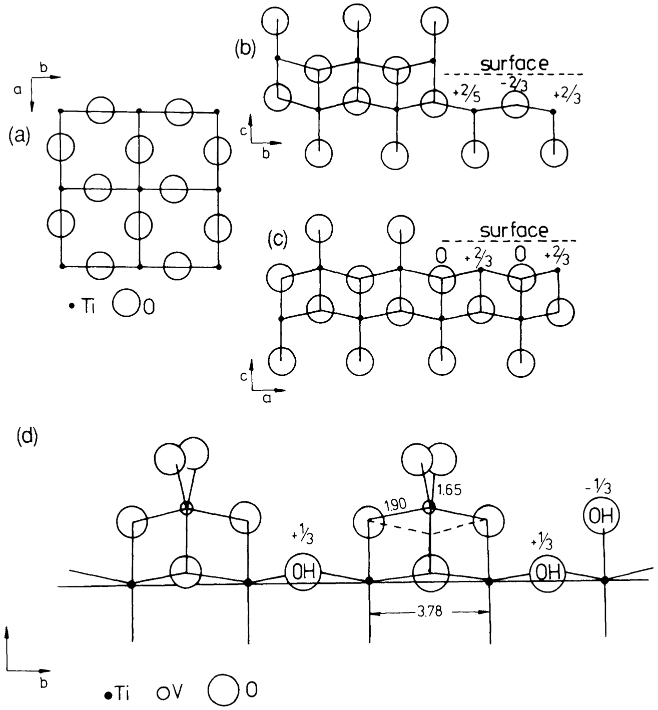

FIGURE 8.9 Anatase structure projected on (a) (001), (b) (100), (c) (010) plane; (d) shows VO_4 polyhedra located on the (001) plane.

sults [114] involves bonding of vanadate ions to the surface through esterification of three hydroxyl groups as shown in Fig. 8.9. Vanadium would in this case occupy roughly a position which another Ti^{4+} would occupy had the bulk structure continued. This should bring about almost perfect balance of local charges rendering the vanadium complex particularly stable. Indeed, the length of the V—O—V bond established by EXAFS to be 1.90 Å is very near to the value of 1.93 Å characteristic of the Ti—O—Ti bond in anatase. Thermogravimetric experiments showed that such a vanadate layer on reduction with H_2, CO, or hydrocarbons gives off stoichiometrically one oxygen atom for each vanadium polyhedron, this number being independent of the reducing agent and of the surface coverage of the carrier with vanadium ions for coverages less than monolayer. The reoxidation is fast and complete at low temperatures and the redox cycles are fully reversible.

When deposition is carried out by impregnation from the water solution, two-dimensional polymeric clusters of VO_6 octahedra are formed as revealed by the Raman spectra [105,110]. At vanadia loadings exceeding that corresponding to the monolayer capacity small crystallites of V_2O_5 form on the anatase support in addition to the monolayer of the surface vanadia species. The morphology of the supported vanadia phase also depends on the calcination temperature. At low calcination temperatures (100—200°C) the vanadia exists in the form corresponding to that prevailing in the impregnating solution. At intermediate calcination temperatures (350—575°C) vanadia is present as a complete monolayer of surface vanadia species linked to the anatase support, and V_2O_5 crystallites. In this temperature range the anatase support experiences sintering manifested by a loss of surface area. The portion of vanadia present as crystalline V_2O_5 increases at the expense of the surface vanadia species in the monolayer, which is reflected in the changes of the appropriate bands in the Raman spectra [115] and the increase of the V/Ti peak intensity ratio in the XPS spectra [119]. At calcination temperatures of 575°C and higher the TiO_2 (anatase) support under the influence of vanadia undergoes a structural transformation to rutile with simultaneous formation of a solid solution $V_{\underline{x}}Ti_{1-\underline{x}}O_2$ accompanied by further decrease of surface area and change of catalytic properties.

Calcination temperature also influences markedly the catalytic properties of the V_2O_5-TiO_2 (anatase) system in o-xylene oxidation. Calcination at intermediate temperatures (350—450°C) yields active and selective catalysts, whereas calcination at high temperatures results in inferior catalysts. Analyses of the spent catalysts showed that the monolayer of surface vanadia species remain intact and crystalline V_2O_5 is reduced by the reaction medium. However, as it is the monolayer of vanadia species at the surface of anatase grains which is the active phase in o-xylene oxidation, the reduction of crystalline V_2O_5 present in the catalyst does not affect the catalytic performance.

A surface layer of vanadia on anatase can also be obtained by taking advantage of the phenomenon of wetting of an oxide by another oxide [129]. Spreading of a solid over the surface of another solid may result from surface diffusion of constituents of the lattice under the influence of the concentration gradient. Taking into account the relatively high values of the lattice energy of oxides, one can expect surface diffusion to be slow in the temperature range usually used for the preparation of catalysts. However, rapid surface migration may occur due to operation of the forces of surface tension as manifestation of the phenomenon of wetting. For such migration to proceed the overall free energy change $\Delta \underline{F}$ of the process must be negative. $\Delta \underline{F}$ is given by

$$\Delta\underline{F} = \gamma_{I/\underline{g}}\Delta\underline{A}_I - \gamma_{II/\underline{g}}\Delta\underline{A}_{II} + \gamma_{I/II}\,\Delta\underline{A}_{I/II}$$

where $\gamma_{I/\underline{g}}$ and $\gamma_{II/\underline{g}}$ are surface tensions of the oxide I which is migrating and oxide II on which spreading occurs, in equilibrium with the gas phase $\underline{g}$. $\gamma_{I/II}$ is the interfacial tension at the interface of the two oxides, and $\Delta\underline{A}$ are the respective surface area changes. As in the course of spreading

$$\Delta\underline{A}_I = \Delta\underline{A}_{II} = \Delta\underline{A}_{I/II}$$

the free energy change $\Delta\underline{F}$ is negative if $(\gamma_{I/\underline{g}} + \gamma_{I/II}) < \gamma_{II/\underline{g}}$. Simple recalculation shows that this condition is fulfilled if $\underline{W}_{I/II} - \underline{W}_I > 0$, where $\underline{W}_{I/II}$ is the energy of adhesion of the two oxide phases, and $\underline{W}_I$ is the energy of cohesion of the oxide I. It may thus be concluded that spreading occurs only if the phase moving adheres to the immobile phase more strongly than it coheres to itself.

Experiments showed [130] that the behavior of the two modifications of TiO_2 anatase and rutile with respect to wetting by V_2O_5 is completely different. Namely, when a V_2O_5 crystallite is placed on an anatase pellet and heated, vanadium ions migrate over the surface of anatase grains. XPS studies showed that a surface layer of vanadia is formed, its properties being strongly modified by interaction with the anatase support. Contrary to that no migration is observed on rutile. It may thus be concluded that V_2O_5 is wetting anatase but not rutile. It should be noted that because of the high value of the surface free energy of many solids used as supports, the driving force of the surface migration may attain considerable value and spreading may take place at relatively low temperatures.

The phenomenon of wetting of oxides by other oxides is of paramount importance for the preparation of catalysts and their stability. Indeed, when a mechanical mixture of V_2O_5 and anatase was used as catalyst in the oxidation of o-xylene to phthalic anhydride [131], at the beginning it showed a poor performance, resembling that of pure vanadia. However, evolution of its catalytic properties took place with time-on-stream, manifested by a multiple increase of conversion and selectivity to phthalic anhydride, which finally attained values comparable with those characteristic for the best catalysts obtained by impregnation or grafting (Fig. 8.10). This is due to the spontaneous spreading of V_2O_5 over the grains of anatase, resulting in the formation of a surface layer. No such spreading occurs on rutile. Therefore, when vanadia was dispersed over the surface of rutile by grafting, the catalytic properties were in the beginning

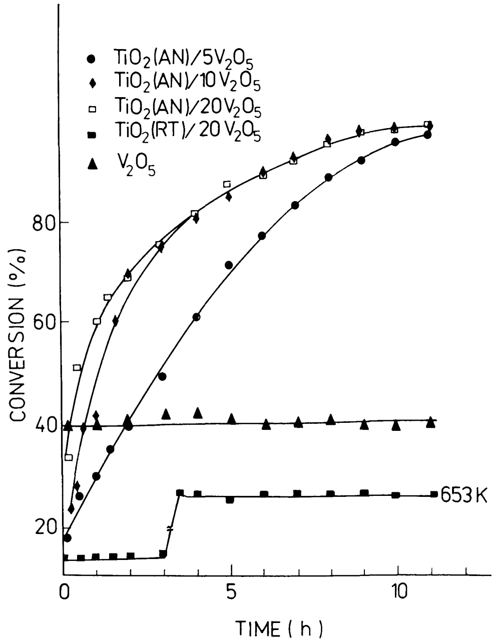

FIGURE 8.10 Conversion of o-xylene in the gas phase oxidation at 633 K over V_2O_5 and its mechanical mixtures with anatase and rutile, as a function of the time on-stream [131].

fairly good, but rapidly deteriorated with time-on-stream because vanadia layer is in this case unstable and shrinks to form a heterogeneous mixture of V_2O_5 crystallites and rutile.

B. Mechanism of o-Xylene Oxidation

The kinetics and mechanism of o-xylene oxidation were extensively studied because of the industrial importance of this reaction. The process is usually carried out in the temperature range 350—400°C with a maximum yield of 70—75 mol %. The main byproducts are carbon oxides besides smaller amounts of tolualdehyde and maleic anhydride. In the first step one methyl group is oxidized to form tolualdehyde as the main intermediate product, which is then oxidized further to phthalic anhydride. Maleic anhydride is the side product made by direct oxidation of o-xylene, and phthalide a side product formed from tolualdehyde. Carbon oxides may be formed either directly from o-xylene, from any of the intermediates, or by oxidation of the final product. The reaction scheme is illustrated in Fig. 8.11. An important contribution to clarification of the reac-

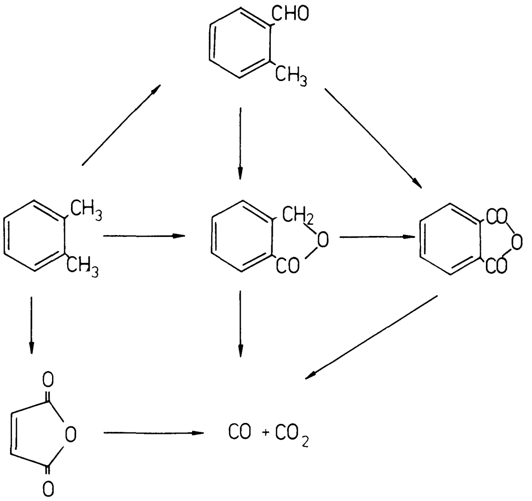

FIGURE 8.11 Reaction scheme of the oxidation of o-xylene.

tion network came from experiments in which labeled o-xylene (methyl-^{14}C) and phthalic anhydride (-^{14}CO) were oxidized over V_2O_5 [120]. It turned out that maleic anhydride is formed only from carbon atoms of the nucleus. This seems to indicate that maleic anhydride is formed as the result of an attack by electrophilic oxygen on the π-electron system of the benzene ring.

Oxidation of o-xylene in the presence of oxygen and in its absence provided evidence [121] for the redox mechanism proposed by Mars and van Krevelen and discussed in Section II.D.2 of this chapter. In the case of o-xylene it consists of two consecutive reduction-oxidation steps in which o-xylene is stepwise oxidized by lattice oxygen of the vanadium catalyst. On the other hand, studies of the kinetics of o-xylene oxidation on an industrial V_2O_5-TiO_2 catalyst, carried out in an integral nonisothermal tubular reactor [122], were interpreted in terms of the Langmuir-Hinshelwood model. It should, however, be emphasized that both models lead to identical rate expression for the overall rate of reaction and the mechanisms cannot be distinguished simply by kinetic measurements.

C. Mechanism of Naphthalene Oxidation

Naphthalene is oxidized over vanadium oxide-based catalysts in a series of parallel and consecutive reactions. This is similar to the oxidation of benzene in that it belongs to the electrophilic-type oxidations. Although naphthoquinone is the intermediate in the reac-

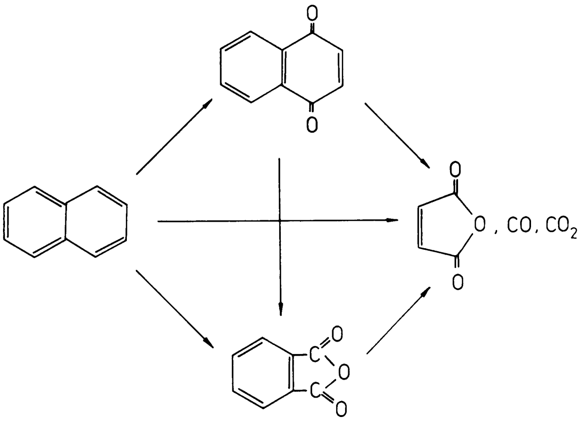

FIGURE 8.12 Reaction scheme of the oxidation of naphtalene.

tion sequence, this is not the only route to phthalic anhydride [6]. The simplified reaction network is shown in Fig. 8.12.

The reaction mechanism may be described by the redox model. The initial selectivities are almost independent of temperature which implies that the activation energies of all steps have similar values. Steps 1—3 proceed with rates of the same order and approximately the same amounts of naphthoquinone and phthalic anhydride are initially formed from naphthalene.

The large exothermic effect due to the oxidation of naphthalene to the anhydride and to complete combustion of a portion of naphthalene feedstock requires that the reaction space be cooled with an appropriate cooling medium through the tubes of the reactor. Steam generators serve as a secondary heat sink. Furthermore, the excess of air contained in the reaction gas stream is an additional heat-removing agent.

D. Active Sites at the Surface of V_2O_5-Based Catalysts

The crystal of V_2O_5 as already mentioned in Section II.A of this chapter may be considered to be built either from distorted tetragonal pyramids (five V—O bond lengths of 1.58—2.02 Å) or distorted octahedra (the sixth V—O bond length of 2.79 Å). Figure 8.13a shows ribbons of double tetragonal pyramids sharing edges and forming sheets by sharing corners with adjacent ribbons on both sides. All pyramids in one row of the ribbon point up and in the second row point down. The sheets form a three-dimensional network being stacked one over the other in such a manner that apices of pyramids of one sheet are positioned over basal planes of

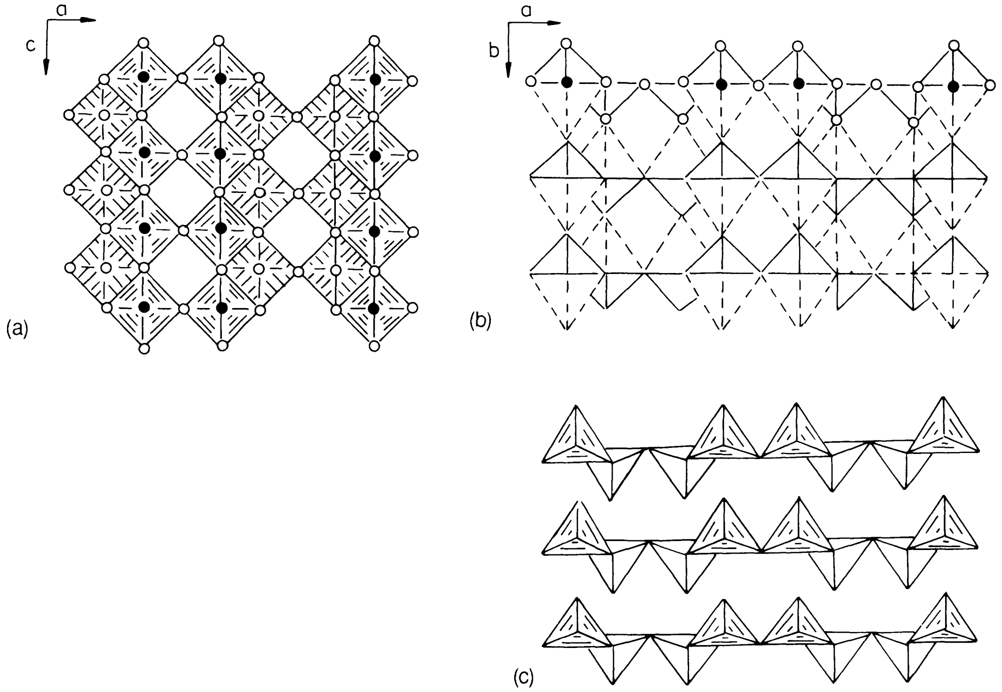

FIGURE 8.13 Idealized structure of V_2O_5: (a) projection of (010) and (b) (100) plane drawn as tetragonal pyramids; (c) (100) projection drawn as idealized trigonal pyramids. •-vanadium. o-oxygen.

pyramids of the sheet beneath, thus completing the distorted octahedron (Fig. 13b). These weak V—O bonds give rise to perfect cleavage between the sheets. Figure 8.13c is the same projection as Fig. 8.13b but drawn as idealized trigonal bipyramids.

Two types of crystal faces may be distinguished from the point of view of chemical bonding type [123]. The basal (010) plane is composed of terminal oxygen $\sigma\pi$-bonded to vanadium ions, two types of bridging oxygen ions and vanadium ions with all chemical bonds almost fully saturated, leaving a negligible excess positive charge of 0.04. The exposed vanadium ions in the adjacent rows of square pyramids in every two ribbons have empty d_{xz} and d_{yz} orbitals, which are LUMOs of the oxide and can play the role of Lewis acid sites. Oxygen ions bridging the ribbons have free electron pairs at the HOMOs and because of the displacement of V^{5+} ions toward the $\sigma\pi$-bonded terminal oxygens they acquire more negative charge and are rendered more basic. When a toluene or xylene molecule approaches this surface, the C—H bond of the methyl group reacts with the empty d orbitals of vanadium, the proton being shifted to the bridging oxide ion and the benzyl radical attached end-on to vanadium [123], as indicated by the in situ IR studies of toluene and o-xylene adsorbed at the surface of V_2O_5 [126,127]. The nucleophilic addition of the other bridging oxygen ion of the surface to the carbon atom of the $—CH_2$ group of the adsorbed benzyl radical may now be performed, resulting in the formation of a precursor of the aldehyde which is then desorbed after abstraction of the second hydrogen, generating a surface oxygen vacancy.

Different interactions prevail at crystal planes perpendicular to the (010) basal plane, such as (100) or (001). Cleavage leaves on the (100) plane coordinatively unsaturated vanadium ions with about +0.5 excess formal charge and oxygen ions with about −1.0 excess charge, as estimated from the bond strength model [124], and on the (001) plane V_{cus} and O_{cus} with excess formal charges of about +0.7 and −0.7, respectively. These planes should thus show a strong tendency to dissociatively adsorb water and to develop acid-base interactions with the reacting molecule. On heating at higher temperatures dehydration of the surface takes place, leaving coordinatively unsaturated V^{5+} cations and O^{2-} anions, on which considerable excess formal charge is accumulated. Such sites may induce a heterolytic bond scission in the adsorbed reactant molecules. Simultaneously, the reducing atmosphere of the hydrocarbon reaction medium usually causes some reduction of the catalyst surface so that V^{4+} ions are generated. Such ions may function as sites activating oxygen molecules to their electrophilic active forms, which may initiate the electrophilic oxidation route. Under the conditions of a heterogeneous catalytic process this route may end in total oxidation.

Experiments in which the catalytic activity of V_2O_5 crystallites of different crystal habit in the oxidation of o-xylene was studied permitted the location of active sites responsible for the different pathways of o-xylene transformation [125]. The results of these experiments are shown in Fig. 4.24, in which selectivities of the oxidation of o-xylene to phthalic anhydride and to products of total combustion are plotted as a function of the morphological factor f defined as the ratio of intensity of the (110) reflection to the intensity of the (010) reflection in the X-ray diffraction pattern of V_2O_5 crystallites. It may be seen that samples characterized by a low value of f, i.e., composed of platelike crystallites exposing predominantly the basal (010), showed very high selectivity to phthalic anhydride, whereas on crystallites of needlelike habit, characterized by higher values of f, i.e., exposing mainly (100), (001), and (110) planes, total oxidation became the predominant reaction pathway.

TABLE 8.5 Concentrations (mol cm^{-2}) of Adsorbed Benzene (B), Toluene (T), Pyridine (P), and 3-Methyl Pyridine (MP) on V_2O_5

Temp. (°C)	B	T	P	(T + P)	MP
250	0.00	0.17	0.28	0.45	0.45
350	0.00	0.17	0.03	0.20	0.19

Source: Ref. 132.

Comparative studies of the adsorption of benzene (B), toluene (T), pyridine (P), and 3-methyl pyridine (MP) on polycrystalline V_2O_5 samples at 250 and 350°C [132] revealed that benzene is practically not adsorbed as compared to other hydrocarbons (Table 8.5). This indicates that π electrons of the aromatic ring do not participate in the adsorption bond and the other aromatic molecules are adsorbed end-on through their functional groups. The amount of toluene adsorbed does not change on raising the temperature, which indicates that it must be strongly held at the surface at variance with pyridine which is only weakly adsorbed. The sum of the amounts of toluene and pyridine adsorbed was equal to the amount of adsorbed 3-methyl pyridine, which was taken as an indication that toluene and pyridine are adsorbed on different crystal planes. It may be assumed that pyridine will be adsorbed on the highly polar non-(010) planes either on Bronsted or Lewis acid sites; toluene and—by analogy—o-xylene must be thus adsorbed on the basal (010) plane through the donor-acceptor interactions.

The molecular mechanism of the oxidation of o-xylene discussed above was confirmed by quantum chemical calculations of the system composed of o-xylene and oxygen in different mutual geometric orientations, taking as reactants the ground state hydrocarbon molecule and oxygen activated to its reactive electrophilic forms, the hydrocarbon molecule activated by abstraction of hydrogen from one of the methyl groups and activated electrophilic oxygen, as well as the activated hydrocarbon molecule and the nucleophilic oxygen form O^{2-} [128]. Several reaction pathways are possible as shown in Fig. 8.14. Results of the calculations showed that no reaction can take place with oxygen in its ground state and when oxygen is activated by stretching the O—O bond only the epoxide-type product is formed. When o-xylene is activated by abstraction of hydrogen, the type of product formed depends on the form of oxygen involved in the reaction. With activated electrophilic molecular oxygen unstable peroxide complexes are formed, whereas attack by nucleophilic O^{2-} ions results in the formation of alcohol or aldehyde depending on the direction

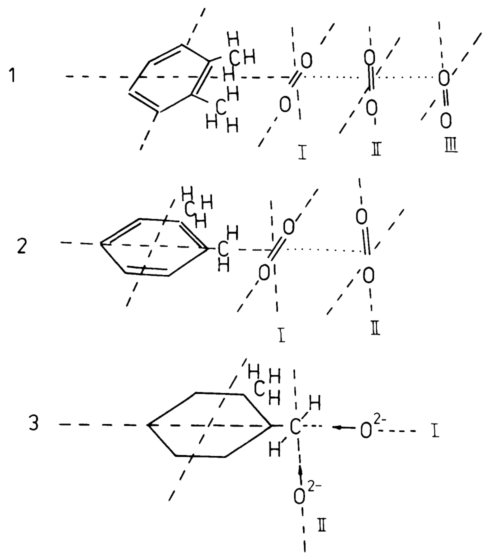

FIGURE 8.14 Geometric models for the attack of oxygen on o-xylene [128].

of the attack. Tolualdehyde appears as the stable product if the O^{2-} ion approaches the $-CH_2$ group of o-xylene from the direction perpendicular to the plane of the benzene ring (reaction pathway 3-II in Fig. 8.14). Such mutual orientation of the o-xylene molecule adsorbed end-on and surface lattice O^{2-} ion indeed prevails on the (010) plane of V_2O_5.

The increase of selectivity of o-xylene oxidation by supporting vanadia on TiO_2 (anatase) can now be easily explained. As discussed in Section III.A, the monolayer of vanadia on the surface of anatase epitaxially is oriented in such a way that the (010) crystal plane is exposed, on which the nucleophilic selective oxidation takes place, whereas the non-(010) planes, which in V_2O_5 are responsible for total combustion, are practically nonexistent.

REFERENCES

1. H. Heinemann, in Catalysis: Science and Technology, Vol. 1 (J. R. Anderson and M. Boudart, eds.), Springer-Verlag, Berlin, 1981, p. 1.
2. J. Walter, J. Prakt. Chem., 51, 107 (1985).
3. A. Suter, Phthalsäureanhydrid und seine Vervendung, Darmstad, 1972.

4. R. A. Duckworth, Chem. Process Eng., 50, 69 (1969).
5. J. Chrzaszcz, J. Oblój, W. Ormaniec, and W. Wal, in Vanadia Catalysts for Processes of Oxidation of Aromatic Hydrocarbons (B. Grzybowska and J. Haber, eds.), Polish Scientific Publishers, Kraków, 1984, p. 11.
6. M. S. Wainwright and N. R. Foster, Catal. Rev. Sci. Eng., 19, 211 (1979).
7. J. K. Dixon and J. E. Longfield, in Catalysis, Vol. 7 (P. H. Emmeett, ed.), Reinhold, New York, 1960, p. 183.
8. K. van der Wiele and P. J. van den Berg, Heterogeneous oxidation processes, in Chemical Kinetics, Vol. 20 (C. H. Bamford and C. F. H. Tipper, eds.), Elsevier, New York, 1978, p. 123.
9. R. Higgins and P. Hayder, in Catalysis-Specialist Periodical Report, Vol. 1, The Chemical Society, London, 1977, p. 168.
10. Yu. I. Piatnitskii, in Problems of Kinetics and Catalysis (in Russian), Izd. Nauka, Moscow, 1985, p. 132.
11. O. N. Kimkhai, V. U. Popovskii, G. K. Boreskov, T. V. Andrushkevich, and T. B. Dneprovskaya, Kinet. Katal., 12, 371 (1971).
12. J. E. Germain and L. Laugier, Bull. Soc. Chim. France, 2910 (1972).
13. A. Bielański, in Dynamique de la reaction catalytique et chimie quantique dans la catalyse (J. Haber and K. Dyrek, eds.), Polish Scientific Publishers, Warszawa-Kraków, 1982, p. 143.
14. N. Strupler and A. Morette, Compt. Rend., 260, 1971 (1965).
15. A. Bielański, K. Dyrek, J. Poźniczek, and E. Wenda, Bull. Pol. Ac.: Chem. 19, 507 (1971).
16. V. L. Volkov, G. Sh. Tynkacheva, A. A. Fotiev, and E. V. Tkachenko, J. Inorg. Chem. (Russian), 17, 2803 (1972).
17. A. Bielański and M. Najbar, Polish J. Chem., 52, 883 (1978).
18. L. Kihlborg, Acta Chem. Scand., 21, 2495 (1967).
19. A. Bielański, K. Dyrek, I. Kracik, and E. Wenda, Bull. Pol. Ac. Sci.: Chem., 19, 513 (1971).
20. F. Y. Robb, W. S. Glausinger, and P. J. Courtine, J. Solid State Chem. 30, 171 (1979).
21. H. A. Eick and L. Kihlborg, Acta Chem. Scand., 20, 1658 (1966).
22. A. Magneli and B. Oughton, Acta Chem. Scand., 5, 581 (1951).
23. R. H. Munch and E. D. Pierron, J. Catal., 3, 406 (1964).
24. J. G. Eon, E. Bordes, and P. Courtine, Compt. Rend., 288, 485 (1979).
25. R. H. Jarman, P. G. Dickens and A. J. Jacobson, Mater. Res. Bull., 17, 325 (1982).

26. R. H. Jarman and A. K. Cheetham, Mater. Res. Bull., 17, 1011 (1982).
27. J. Grussenmeyer, Thesis, Claude Bernard University, Lyon, 1978.
28. A. Bielański, K. Dyrek, and A. Kozlowska-Róg, Bull. Pol. Ac.: Chem., 20, 1055 (1972).
29. A. Bielański, M. Najbar, and M. Szymońska-Stachura, Bull. Pol. Ac.: Chem., 26, 2491 (1978).
30. A. Bielański and A. Inglot, Bull. Pol. Ac.: Chem., 22, 773 (1974).
31. A. Bielański, J. Camra, and M. Najbar, J. Catal., 57, 326 (1979).
32. M. Najbar and M. Niziol, J. Solid State Chem., 26, 3 (1978).
33. M. Najbar and E. Bielańska, in Reactivity of Solids: Proceedings of 9th Int. Symposium on the Reactivity of Solids (K. Dyrek, J. Haber, and J. Nowotny, eds.), Elsevier, Amsterdam, 1982, p. 657.
34. M. Najbar, Thesis, Jagiellonian University, Kraków, 1984.
35. A. Bielański, M. Najbar, J. Chrzaszcz, and W. Wal, in Catalyst Deactivation (B. Delmont and G. F. Froment, eds.), Elsevier, Amsterdam, 1980, p. 127.
36. H. Schmaltzried, Reactivity of Solids, 1, 117 (1986).
37. M. Najbar and K. Stadnicka, J. Chem. Soc., Faraday Trans. 1, 79, 27 (1983).
38. M. Najbar, J. Chem. Soc., Faraday Trans. 1, 82, 1673 (1986).
39. M. Najbar and J. Camra, Proc. 9th Int. Congr. on Catalysis, Calgary, 1988.
40. V. A. Shvets and V. B. Kazanskii, J. Catal., 25, 123 (1972).
41. S. Yoshida, T. Matsuzaki, T. Kashivazaki, K. Mori, and K. Tarama, Bull. Chem. Soc. Jap., 47, 1564 (1974).
42. K. Dyrek, Bull. Pol. Ac.: Chem., 22, 605 (1974).
43. A. Bielański, K. Dyrek, and E. Serwicka, J. Catal., 66, 316 (1980).
44. K. Dyrek and M. Labanowska, J. Catal., 66, 32 (1985).
45. R. Dziembaj, Bull. Pol. Ac.: Chem., 24, 965 (1976).
46. R. Dziembaj and J. Piwowarczyk, J. Solid State Chem., 21, 387 (1977).
47. R. Dziembaj, J. Solid State Chem., 26, 159 (1978).
48. A. Bielański and R. Dziembaj, Bull. Pol. Ac.: Chem., 21, 547 (1973).
49. L. F. Jones, D. Dollimore, R. Robinson, and R. Sh. Mikhail, J. Colloid Interf. Sci., 64, 237 (1978).
50. Y. V. Belokopytov, Yu. N. Grebennikov, and G. P. Korneichuk, React. Kinet. Catal. Lett., 16, 409 (1981).
51. I. I. Ioffe and F. F. Wolkenstein, Dokl. Acad. Sci. USSR, 118, 747 (1958).

52. C. G. B. Hammar, Svensk. Chem. Tridskr., 64, 165 (1952), citation according to Ref. 7.
53. K. Vaidyanathan, Chem. Age India, 19, 366 (1968).
54. J. E. Germain and J. C. Peuch, Bull. Soc. Chim. France, 1844 (1969).
55. A. Beydoun, F. Figueras, and L. de Mourgues, Bull. Soc. Chim. France, 806 (1971).
56. S. I. Ahmad, S. H. Ibrahim, and N. R. Kuloor, Ind. J. Technol., 8, 8, 85, 131, 136, 251 (1970).
57. A. Inglot, Bull. Pol. Ac.: Chem., 27, 155 (1979).
58. A. Inglot, Pol. J. Chem., 57, 223 (1983).
59. A. Inglot, Pol. J. Chem., 60, 841 (1986).
60. A. Inglot, Pol. J. Chem., 61, 165 (1987).
61. E. K. Krylova, B. P. Luzyanin, and A. M. Yakobson, Neftekhimia, 23, 255 (1983).
62. P. Mars and D. W. van Krevelen, Chem. Eng. Sci. Special Suppl., 3, 41 (1954).
63. J. E. Germain, F. Gaschka, and A. Mayeux, Genie chimique, 95, 1371 (1966).
64. G. Tufan and G. Angkerman, Ind. Eng. Chem. Process Des. Dev., 20, 604 (1981).
65. T. Q. Phung Quach, D. Rouleau, C. Chavarie, and C. Laguerie, Can. J. Chem. Eng., 56, 72 (1978).
66. K. Vaidyanathan, Ind. J. Technol., 8, 175 (1970).
67. I. I. Ioffe and A. G. Liubarskii, Kinet. Katal., 3, 261 (1962).
68. I. I. Ioffe and A. G. Liubarskii, Kinet. Katal., 4, 294 (1963).
69. J. E. Germain, F. Gaschka, and A. Mayeux, Bull. Soc. Chim. France, 1445 (1965).
70. J. E. Germain, Intra-Science Chem. Rep., 6, 101 (1972).
71. B. N. Dolgov, Die Katalyse in der organischen Chemie, Deutscher Verlag der Wissenschaften, Berlin, 1963, p. 215.
72. B. Dmuchovsky, M. C. Freerks, E. D. Pierron, R. H. Munch, and F. B. Zienty, J. Catal., 4, 291 (1965).
73. J. Lucas, D. Vandervell, and K. C. Waugh, J. Chem. Soc. Faraday Trans. 1, 77, 15 (1981).
74. J. Lucas, D. Vandervell, and K. C. Waugh, J. Chem. Soc. Faraday Trans. 1, 77, 31 (1981).
75. R. Petts and K. C.Waugh, J. Chem. Soc. Faraday Trans. 1, 78, 803 (1982).
76. E. Broclawik, J. Haber, and M. Witko, J. Molec. Catal., 26, 249 (1984).
77. M. Witko, E. Broclawik, and J. Haber, J. Molec. Catal., 35, 179 (1986).
78. K. Tarama, S. Teranishi, S. Yoshida, and N. Tamura, Proc. 3rd Int. Congr. Catalysis, Vol. 1, North-Holland, Amsterdam, 1965, p. 282.

79. F. Weiss, J. Marion, J. Metzger, and J. M. Cognon, Kinet. Katal., 14, 45 (1973).
80. A. Bielański and A. Inglot, React. Kinet. Catal. Lett., 6, 140 (1977).
81. M. Inomata, A. Miyamoto, and Y. Murakami, J. Catal., 62, 140 (1980).
82. A. Miyamoto, Y. Yamazaki, M. Inomata, and Y. Murakami, Chem. Lett., 1355 (1978).
83. A. Miyamoto, Y. Yamazaki, M. Inomata, and Y. Murakami, J. Phys. Chem., 85, 236 (1981).
84. M. Inomata, K. Mori, A. Miyamoto, T. Vi, and Y. Murakami, J. Phys. Chem. 87, 754 (1983).
85. K. Mori, M. Inomata, A. Miyamoto, and Murakami, J. Phys. Chem., 87, 4560 (1983).
86. M. Gasior, J. Haber, T. Machej, and T. Czeppe, J. Molec. Catal., 43, (1988).
87. J. Ziólkowski and J. Janas, J. Catal., 81 298 (1983).
88. N. I. Ilchenko, J. M. Avilova, and G. N. Golodets, Kinet. Katal., 16, 697 (1975).
89. R. Gajerski, S. Komornicki, A. Malecki, and A. Podgórecka, School of Mining and Metallurgy Cracow, Mat. Fiz. Chem., 4, 135 (1979).
90. A. Bielański, J. Piwowarczyk, and J. Pozniczek, J. Catal., 113, 334 (1988).
91. H. Schaeffer, Z. Elektrochem., Ber. Bunsen Ges. Physik. Chem., 71, 222 (1967).
92. I. I. Ioffe, Z. I. Eshkova, and A. G. Lyubarskii, Zh. Fiz. Khim., 35, 2348 (1961).
93. M. Blanchard, G. Longuet, G. K. Boreskov, and V. S. Muzykantov, Bull. Soc. Chim. France, 814 (1971).
94. A. Bielański and A. Inglot, Bull. Pol. Ac.: Chem., 22, 785 (1974).
95. M. Szymońska, Thesis, Jagiellonian University, Kraków, 1978.
96. A. Bielański, J. Poźniczek, and E. Wenda, Bull. Pol. Ac.: Chem., 24, 147, 374 (1976).
97. A. Inglot, Bull. Pol. Ac.: Chem., 27, 155 (1979); 29, 273 (1981).
98. A. Bielański, J. Poźniczek, and E. Wenda, Bull. Pol. Ac.: Chem., 24, 394 (1976).
99. A. Bielański and J. Poźniczek, React. Kinet. Catal. Lett., 33, 417 (1987).
100. M. Najbar, A. Bielański, J. Camra, E. Bielańska, W. Wal, J. Chrzaszcz, and W. Ormaniec, in Preparation of Catalysts IV (B. Delmon, P. A. Jacobs, and G. Poncelet, eds.), Elsevier, Amsterdam, 1987, p. 217.

101. M. Gasior and B. Grzybowska-Swierkosz, in Vanadia Catalysts for Process of Oxidation of Aromatic Hydrocarbons (B. Grzybowska-Świerkosz and J. Haber, eds.), Polish Scientific Publ., Kraków, 1984, p. 133.
102. M. Gasior, I. Gasior, and B. Grzybowska, Appl. Catal., 10, 87 (1984).
103. O. V. Krylov, Catalysis by Non-metals (in Russian), Izd. Khimya, Moscow, 1967.
104. G. C. Bond and K. Brückman, Disc. Faraday Soc., 72, 235 (1981).
105. I. E. Wachs, R. Y. Saleh, S. S. Chan, and C. C. Chersich, Appl. Catal., 15, 339 (1985).
106. D. VanHove and M. Blanchard, Bull. Sci. Chim. France, 3291 (1971).
107. R. Grabowski, B. Grzybowska, J. Haber, and J. Sloczyński, React. Kinet. Catal. Lett., 2, 81 (1975).
108. G. C. Bond and P. Konig, J. Catal., 77, 308 (1982).
109. A. J. Van Hengstum, J. G. Van Ommen, H. Bosch, and P. J. Gellings, Appl. Catal., 5, 207 (1983); 8, 369 (1983).
110. F. Roozeboom, M. C. Mittelmeijer-Hazeleger, J. A. Moulijn, J. Medema, V. H. J. de Beer, and P. J. Gellings, J. Phys. Chem., 84, 2783 (1980).
111. F. Roozeboom, A. Jos van Dillen, J. W. Gens, and P. J. Gellings, Ind. Eng. Chem., Prod. Res. Dev., 20, 304 (1981).
112. P. J. Gellings, Catalysis (Specialist Periodical Report), Vol. 7, The Royal Society of Chemistry, London, 1983.
113. R. Kozlowski, R. F. Pettifer, and J. M. Thomas, J. Phys. Chem., 87, 5172 (1983).
114. J. Haber, A. Kozlowska, and R. Kozlowski, J. Catal., 102, 52 (1986).
115. R. Y. Saleh, I. E. Eachs, S. S. Chan, and C. C. Chersich, J. Catal., 98, 102 (1986).
116. G. Hausinger, H. Schmelz, and H. Knözinger, Appl. Chem., 39, 267 (1988).
117. H. P. Boehm, Adv. Catal., 16, 249 (1966).
118. M. A. Enriquez, C. Doremieux-Morin, and J. Fraissard, J. Solid State Chem., 40, 233 (1981).
119. J. Haber and J. Stoch, React. Kinet. Catal. Lett., 9, 319 (1978).
120. M. Blanchard and D. Vanhove, Bull. Soc. Chim. France, 4134 (1971).
121. M. S. Wainwright and T. W. Hoffman, Can. J. Chem. Eng., 55, 552 (1977).
122. J. Skrzypek, M. Galantowicz, M. Grzesik, J. Tejszerski, C. Masal, J. Soliński, and M. Madej, in Vanadia Catalysts for Processes of Oxidation of Aromatic Hydrocarbons (B. Grzy-

bowska-Świerkosz and J. Haber, eds.), Polish Scientific Publishers, Kraków, 1984, p. 127.
123. J. Haber, Proc. Intern. Conference on Structure and Reactivity of Surfaces, Trieste, 1988, (C. Morterra and A. Zecchina, eds.), Elsevier, New York, 1989.
124. A. Anderson, J. Solid State Chem., 42, 263 (1982).
125. M. Gasior and T. Machej, J. Catal., 83, 472 (1983).
126. A. J. van Hengstum, J. Pranger, S. M. van Hengstum-Nijhuis, J. G. van Ommen, and P. J. Gellings, J. Catal., 101, 323 (1986).
127. G. Busca, F. Cavani, and F. Trifiro, J. Catal., 106, 471 (1987).
128. M. Witko, E. Broclawik, and J. Haber, J. Molec. Catal., 45, 183 (1988).
129. J. Haber, Pure and Appl. Chem., 56, 1663 (1984).
130. J. Haber, T. Machej, and T. Czeppe, Surf. Sci., 151, 301 (1985).
131. M. Gasior, J. Haber, and T. Machej, Appl. Catal., 33,1 (1987).
132. A. Andersson, in Adsorption and Catalysis on Oxide Surfaces (M. Che and G. C. Bond, eds.), Elsevier, New York, 1985, p. 38.

9

Oxidation of Methane

I. INTRODUCTION

Methane is the major component of natural gas, often constituting more than 90% of the hydrocarbon fraction of the gas. At present it is primarily used as a fuel. In the chemical industry it is used as a basis for the generation of synthesis gas, production of hydrogen, and manufacturing of the halogen derivatives of methane, acetylene, hydrogen cyanide, technical carbon, and many other products [1]. The recognized deposits of natural gas are, however, large enough for methane to be considered as the raw material substitute for oil in the next century. Functionalization of methane to make it a useful reactant for organic synthesis is therefore of great prospective importance. Since one of the processes used to functionalize hydrocarbon molecules is their partial oxidation, much research effort is now being devoted to the conversion of methane to useful chemicals by partial oxidation [2] and oxidative coupling [3].

Currently in the chemical industry methane is converted by the steam reforming process into synthesis gas [4]

$$CH_4 + H_2O \longrightarrow CO + 3H_2 \qquad (9.1)$$

using the NiO/Al_2O_3 catalyst promoted with K_2O. The synthesis gas is then used to manufacture methanol over $Cu/ZnO/Al_2O_3$ catalysts

$$CO + 2H_2 \longrightarrow CH_3OH \qquad (9.2)$$

which in turn may be subjected to oxidative dehydrogenation on silver or iron molybdate catalysts:

$$CH_3OH + \frac{1}{2}O_2 \longrightarrow HCHO + H_2O \qquad (9.3)$$

to obtain formaldehyde as the important starting reagent for many technological processes. The steam-methane reaction (9.1) is strongly endothermic and involves the expenditure of considerable energy equal to 206 $kJmol^{-1}$ at 970–1100 K. It is accompanied by a water-gas shift reaction and a Boudouard reaction, which may cause carbon deposition. These disadvantages have stimulated intensive research efforts aimed at the development of active and selective catalysts for direct oxidation or oxidative coupling of methane.

II. THERMODYNAMICS OF METHANE REACTIONS

Simple dehydrogenative coupling of methane is thermodynamically unfavorable [Eq. (9.4)], whereas all reactions involving oxygen such as, say, partial oxydation of methane to formaldehyde [Eq. (9.5)] or methanol [Eq. (9.6)] are thermodynamically favored. However, a much larger decrease of Gibbs free energy accompanies the total oxidation of methane to CO, CO_2, and H_2O [Eqs. (9.7) and (9.9)] and therefore one can expect that they will preferentially take place. The $\Delta\underline{G}$ change of the oxidative coupling of methane [Eq. (9.8)] is comparable to that of its total oxidation; the main problem in upgrading methane is therefore the question of how to achieve high conversion without significant loss of methane in complete combustion. Because methanol and formaldehyde are more easily oxidized than methane, their subsequent oxidation as well as the parallel reaction of direct oxidation of methane must be suppressed.

	$\Delta\underline{G}_{700K}$ (kcal mol^{-1})	
$2CH_4 \longrightarrow C_2H_6 + H_2$	+71.0	(9.4)
$CH_4 + O_2 \longrightarrow HCHO + H_2O$	−70.0	(9.5)
$CH_4 + \frac{1}{2}O_2 \longrightarrow CH_3OH$	−22.0	(9.6)
$CH_4 + \frac{3}{2}O_2 \longrightarrow CO + 2H_2O$	−136.0	(9.7)
$2CH_4 + \frac{1}{2}O_2 \longrightarrow C_2H_6 + H_2O$	−159.7	(9.8)

$$CH_4 + 2O_2 \longrightarrow CO_2 + 2H_2O \qquad -189.0 \qquad (9.9)$$

III. OXIDATION OF METHANE TO METHANOL AND FORMALDEHYDE

Kinetic studies have shown [5] that the reaction which mainly contributes to the disappearance of HCHO is

$$HCHO + \frac{1}{2}O_2 \longrightarrow CO + H_2O \qquad (9.10)$$

In the gas phase the free radical mechanism operates [6]. Thus, to obtain higher yields of methanol and formaldehyde from the oxidation of methane the reaction products must be quenched immediately after leaving the reaction zone.

At high pressures, high flow rates and low ratios of air-to-methane methanol prevail in the products. Low pressure and a lower flow rate favors the production of formaldehyde.

The catalysts most widely studied in the oxidation of methane to methanol and formaldehyde are those based on MoO_3. Table 9.1 summarizes some of the results obtained at high pressures of 50 atm [7]. In order to obtain high selectivity to methanol the conversion of methanol was kept low and the products were rapidly cooled by injecting liquid water. Another oxide catalyst which seemed promising was CuO-MoO_3 [8]. The results were improved when small amounts of ethane were added to the feed. MoO_3 when supported on aluminosilicate proved to be a selective catalyst for the production of formaldehyde [2]. Its yield increased with the CH_4/O_2 ratio and was strongly dependent on the loading of the support with molybdena, as shown in Fig. 9.1. It is interesting that the addition of water strongly inhibited the production of CO but decreased the conversion of methane.

Important conclusions concerning the mechanism of methane activation could have been drawn from experiments in which N_2O instead of O_2 was used for the oxidation of methane over MoO_3-SiO_2 catalysts [10,11]. Selectivities to 60% of methanol were obtained at conversions of 10%. On reacting at liquid nitrogen temperature CH_4 with O^- species obtained by decomposition of N_2O on Mo^V sites methyl radicals were observed by ESR spectroscopy, whereas at room temperature methoxy groups were identified by IR spectroscopy. It was concluded that O^- species formed at the surface of the catalyst were responsible for the activation of the CH_4 molecule. The mechanism thus comprised the reduction of the catalyst surface due to the reaction of total oxidation:

TABLE 9.1 Activities of some MoO_3-Based Oxide Catalysts in Methane Partial Oxidation

	Conversion,%	yield,%	
		CH_3OH	HCHO
MoO_3	2.3	19	2
$ZnO.MoO_3$	2.3	51	8
$Fe_2O_3MoO_3$	2.1	65	8
UO_2MoO_3	3.5	75	5
VO_2MoO_3	2.6	49	4

Temperature 430-500°C, CH_4O_2 = 97.3

Source: Data from Ref. 7.

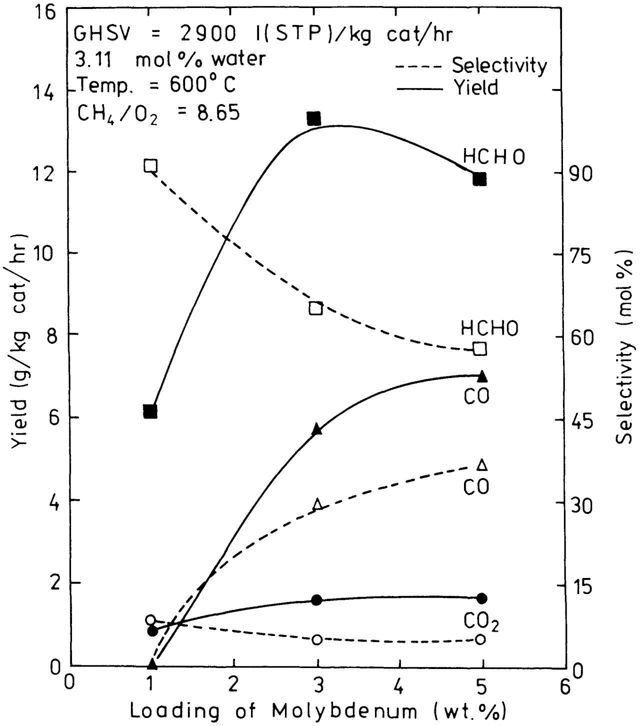

FIGURE 9.1 Effect of loading of molybdenum on the yields and selectivities of products of the partial oxidation of methane [9].

$$8Mo^{VI} + 4O^{2-} + CH_4 \longrightarrow 8Mo^{V} + 2H_2O + CO_2 \qquad (9.11)$$

generation of O^- species by decomposition of N_2O:

$$Mo^{V} + N_2O \longrightarrow Mo^{VI} - O^- + N_2 \qquad (9.12)$$

and the chain reaction:

$$Mo^{VI} - O^- + CH_4 \longrightarrow Mo^{VI} - OH^- + CH_3\cdot \qquad (9.13)$$

$$CH_3\cdot + Mo^{VI}O^{2-} \longrightarrow Mo^{V}O\text{-}CH_3^- \qquad (9.14)$$

$$Mo^{V}O\text{-}CH_3^- + H_2O \longrightarrow Mo^{V}OH^- + CH_3OH \qquad (9.15)$$

$$Mo^{VI}OH^- + Mo^{V}OH^- \longrightarrow Mo^{V} + Mo^{VI}O^{2-} + H_2O \qquad (9.16)$$

Parallel to the generation of surface O^- species by reaction (9.12) the decomposition of N_2O may also proceed as the two-electron transfer resulting in the reoxidation of the surface:

$$2Mo^{V} + N_2O \longrightarrow 2Mo^{VI} + N_2 + O^{2-} \qquad (9.17)$$

The type of product formed from methane thus depends on the relative rates of reactions (9.12) and (9.17). They can be related to the influence of experimental conditions on the formation of O^- ions from N_2O adsorbed on reduced grafted MoO_3-SiO_2 and the role of these ions in surface charge transfer reactions [12].

Recently, studies have been reported on the kinetics of the partial oxidation of methane with N_2O over MoO_3-SiO_2 and V_2O_5-SiO_2 catalysts in a broader temperature range [13,14]. At low temperatures methanol and formaldehyde seemed to be formed from the same intermediate by parallel processes, while at higher temperatures formaldehyde was formed in a consecutive step from methanol.

Formation of formaldehyde requires two operations to be performed by oxygen atoms of the oxide surface: an electrophilic attack on the C—H bond to abstract hydrogen from methane and a nucleophilic attack on the adsorbed methoxy group to abstract a proton. The rates of these operations will depend on the charge on oxygen atoms of the oxide surface and on the charge accumulated on the methyl groups, which in turn will also be determined by the charge on surface oxide ions. One can expect that the quantity of the negative charge on oxide ions of the metal oxide lattice would change depending on the electronegativity of the cations of the oxides, i.e., the more electronegative the cations, the more electrophilic the surface oxygens. They would increasingly withdraw the charge from the methyl group rendering hydrogen atoms more and more positive and therefore easier and easier to abstract. Simultaneously, however, the surface oxide ions become less and less basic and therefore less active in abstracting protons from the adjacent methoxy groups. The volcano-shaped correlation between the rate of methane conversion and electronegativity should thus appear. Such a correlation was indeed found for various oxides supported on SiO_2 as shown in Fig. 9.2 [15,16].

IV. OXIDATIVE COUPLING OF METHANE

Methyl radicals generated in reaction (9.13), instead of reacting with surface oxygen to form methoxy species, may combine to give ethane, which readily undergoes dehydrogenation to ethylene. Activity in oxidative coupling will thus be determined by the rate at which methane is activated to methyl radicals, and the selectivity of C2 formation will depend on the relative rates of recombination of methyl radicals and their reaction with oxygen molecules to form superoxo radicals. As the latter is very rapid at the high temperatures required to generate methyl radicals, higher selectivities to C2 hydrocarbons can be obtained only at a high methane/oxygen ratio when methane conversion is very low. A great variety of oxides

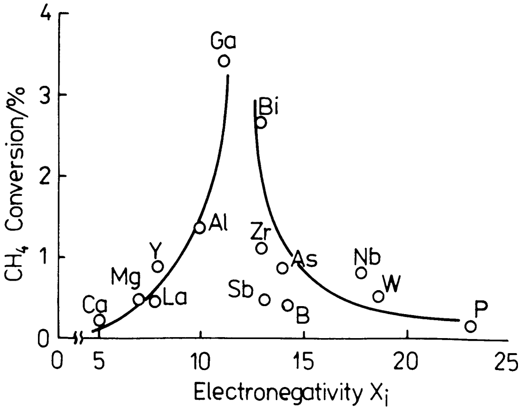

FIGURE 9.2 Conversion of CH_4 as function of the electronegativity of metal cations in simple oxides [16].

have been shown to be effective catalysts in oxidative coupling of methane [35]. Some of them are listed in Table 9.2. In some cases these oxides are used in stoichiometric reactions with methane and then are regenerated in a separate consecutive oxidation step. Interesting results were recently obtained with layered structures composed of infinite sheets of bismuth oxide interleaved with other layers [9].

Using the matrix isolation technique direct evidence was recently provided that gas phase methyl radicals may be the main intermediates in the oxidative coupling of methane [17,18]. When the reaction mixture of methane and oxygen or N_2O was passed over MgO in a special apparatus permitting the trapping of products in a solid argon matrix on a sapphire rod cooled to 13.5 K [19] and their analysis in the ESR spectrometer, ESR spectra shown in Fig. 9.3 were obtained. Signal a is the pure methyl radical $CH_3\cdot$ spectrum, which also appeared when very-low-partial-pressure N_2O or oxygen was the oxidant. At a large excess of oxygen the spectrum of methyl peroxy radical $CH_3O_2\cdot$ was observed as shown by signal b. Signal c is a mixture of the spectra of methyl and methylperoxy radicals and was registered in all reactions when O_2 was present at measurable pressures. The type of pretreatment of MgO had a significant

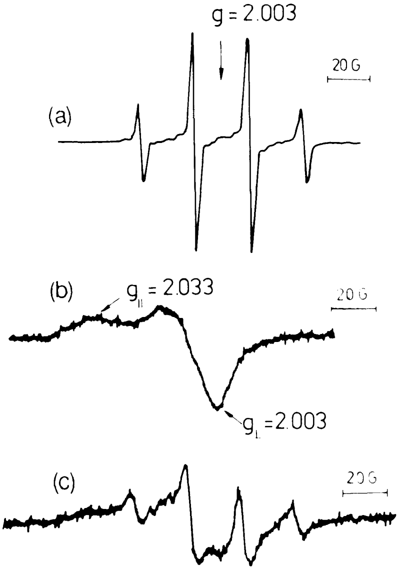

FIGURE 9.3 Radical ESR spectra: (a) pure methyl radical ($CH_3^\cdot$); (b) pure methyl peroxy radical ($CH_3O_2^\cdot$); (c) mixture of methyl and methyl peroxy radicals.

TABLE 9.2 Activity of Various Oxides in the Oxidative Coupling of Methane

Catalyst	Temperature °C	Conversion of CH_4 %	Selectivity to $C_2H_4 + C_2H_6$ %	Ref.
BeO	750	9	22	29
MgO	750	12	47	29
CaO	750	11	55	29
SrO	750	8	72	29
BaO	750	14	70	29
La_2O_3	725	9	47	24
Li_2O/CaO	750	14	72	29
Na_2SO_4/CaO	750	16	78	29
Na_2O/CaO	750	16	76	29
$Li_2O/Ce_2O_3/MgO$	700	23.5	98.4	34
$Li_2O/Pr_2O_3/MgO$	700	44.7	43.9	34
$Li_2O/Nd_2O_3/MgO$	700	24.7	95.6	34
$PbMoO_4$	750	1	19	29
$PbCrO_4$	750	10	4	29
$PbSO_4$	750	8	63	29

effect on its initial activity in the production of methyl radicals, which were observed only when MgO was exposed to O_2 at elevated temperatures, whereas after vacuum treatment no radicals were found. When CH_4 and O_2 were used as reactants at moderate or low flow rates, a steady state was reached and the activity showed no change in time. The stable products were ethane, ethylene, and methanol. Their distribution indicated that the primary reaction was the coupling of methyl radicals to form ethane, its amount being of the same order of magnitude as the amount of $CH_3\cdot$ radicals that would have been collected under similar conditions.

A dramatic increase in activity was observed when MgO was doped with lithium (Fig. 9.4) [21,22]. The X-ray diffraction pattern of the Li-doped samples indicated that two phases were present, MgO and Li_2CO_3, but ESR spectra registered after quenching the samples to liquid nitrogen temperature revealed the formation of $[Li^+O^-]$ centers. The striking correlation between the amount of $CH_3\cdot$ radicals formed and the amount of these centers indicates that

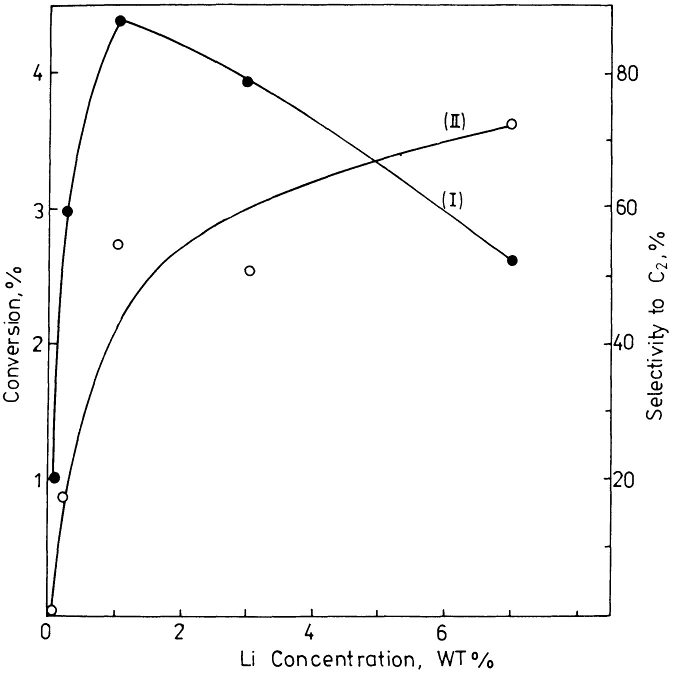

FIGURE 9.4 Conversion (curve I) and selectivity to C_2 hydrocarbons (curve II) in the oxidative dimerization of CH_4 over Li-doped MgO catalysts as function of the Li concentration. Reaction temp. 650°C. (Based on data from [20].)

they play the role of active sites in the generation of $CH_3\cdot$ radicals. Detailed study of these centers showed [21] that the concentration of $[Li^+O^-]$ centers increases with the temperature of annealing, the presence of oxygen being essential for their formation. In the case of powdered MgO they are thermally unstable at temperatures above 200 K. Studies of the Li-doped MgO and CaO monocrystals led to the conclusion [23] that gas phase oxygen is necessary to provide the positive holes at the crystal surface:

$$O_2 + 2O^{2-} \longrightarrow 4O^- \tag{9.18}$$

which become associated with Li^+ ions to form the $[Li^+O^-]$ centers. The observation that Na^+ ions were less effective in generating such active centers than Li^+ suggests that the latter replace Mg^{2+} cations in the MgO lattice. In order to maintain charge neutrality the substitutional Li^+ ions trap holes provided by molecular oxygen interacting with the MgO surface. These holes, i.e., the surface O^- ions, are the active sites abstracting hydrogen from CH_4:

$$Li^+O^- + CH_4 \longrightarrow Li^+OH^- + CH_3\cdot \tag{9.19}$$

These sites are then regenerated by dehydration:

$$2Li^+OH^- \longrightarrow Li_2^+O^{2-} + H_2O \tag{9.20}$$

and subsequent interaction with molecular oxygen:

$$Li_2^+O^{2-} + \tfrac{1}{2}O_2 \longrightarrow 2Li^+O^- \tag{9.21}$$

thus closing the catalytic cycle.

Recent results show [22] that centers of the type $[M^+O^-]$, where M^+ is a substitutional group IA ion, may also be generated in CaO and are active for the formation of $CH_3\cdot$ radicals, being therefore catalysts for oxidative coupling reactions. In pure MgO it is the cation vacancies which act as electron acceptor centers, the localization of an electron generating the V^- center and an adjacent hole in the form of an O^- ion. This latter may then be effective in the abstraction of hydrogen from CH_4.

Kinetic studies demonstrated [20] that selectivity to C2 products increases with rising temperature and CH_4 pressure, but passes through a maximum and then rapidly drops with rising O_2 pressure. They also indicated that the dominant route to product CO and CO_2

is not the consecutive oxidation of C2 products, but parallel reaction of CH_4. The following reaction scheme can thus be visualized:

$$2CH_3\cdot \longrightarrow C_2H_6 \tag{9.22}$$

$$C_2H_6 + O^- \longrightarrow C_2H_5\cdot + OH^- \tag{9.23}$$

$$C_2H_5\cdot + O^{2-} \longrightarrow O\text{-}C_2H_5^- + e^- \tag{9.24}$$

$$O\text{-}C_2H_5^- \longrightarrow C_2H_4 + OH^- \tag{9.25}$$

and formation of CO and CO_2 by parallel routes:

$$CH_3\cdot + O^{2-} \longrightarrow O\text{-}CH_3^- \longrightarrow CO, CO_2 \tag{9.26}$$

$$CH_3\cdot + O_2 \longrightarrow CH_3O_2\cdot \longrightarrow CO, CO_2 \tag{9.27}$$

Evidence has now accumulated indicating that surface O^- ions are not the only sites capable of abstracting hydrogen from methane. Namely, it was found that La_2O_3 has the ability to generate gas phase $CH_3\cdot$ radicals [24] and therefore this oxide and several others of the lanthanide sesquioxides show considerable activity in converting methane to ethane and ethylene [24,25]. Selectivities to C2 compounds as high as 70% were observed at low conversion, when a high excess of CH_4 over O_2 was present in the reactant mixture. On increasing the O_2 content the conversion rose but the selectivity to C2 compounds dropped because more CO_2 was formed. The ESR spectrum obtained after quenching the catalyst to −196°C contained no features which could be assigned to O^- ions but revealed the presence of O_2^- ions [26]. This may be taken as a hint that it is the superoxide ion O_2^- formed on chemisorption of oxygen at the La_2O_3 surface which is responsible for the abstraction of hydrogen from methane:

$$CH_4 + O_2^- \longrightarrow O_2H^- + CH_3\cdot \tag{9.28}$$

although the possibility cannot be ruled out that transient O^- species are formed by dissociation of O_2^- and in the presence of CH_4 they generate the $CH_3\cdot$ radicals. Carbon oxides may be formed either by surface reactions:

$$CH_3\cdot + O^{2-} \longrightarrow CO, CO_2 \tag{9.29}$$

or by gas phase reactions:

$$CH_3\cdot + O_2 \longrightarrow CH_3O_2\cdot \longrightarrow CO,CO_2 \qquad (9.30)$$

The equilibrium concentration of $CH_3O_2\cdot$, which leads to CO and CO_2, decreases upon rising temperature. Thus, with rising temperature, under oxygen-limiting conditions, the amount of CO and CO_2 decreases. The fact that simultaneously the selectivity to C_2H_4 increases as compared to C_2H_6 may be explained by consecutive reactions of C_2H_6 as the primary product of coupling:

$$C_2H_6 + CH_3\cdot \longrightarrow CH_4 + C_2H_5\cdot \qquad (9.31)$$

$$C_2H_5\cdot + O_2 \longrightarrow C_2H_4 + HO_2\cdot \qquad (9.32)$$

It should be emphasized that both M^+-doped alkaline earths oxides as well as lanthanide oxides behave in these reactions as oxidation catalysts although they do not contain transition metal ions of variable oxidation states.

Among many oxides tested as catalysts for oxidative coupling of methane lead oxide and lead oxysalts were found to be particularly effective [27,28,29]. As illustration Fig. 9.5 shows, the selectivities to C_2 hydrocarbons observed when CH_4-O_2 mixtures with large excess of O_2 were passed over the PbO/γ-Al_2O_3 catalysts with different PbO content. It may be seen that selectivities as high as 60% of ethylene+ethane were obtained at practically 100% conversion of

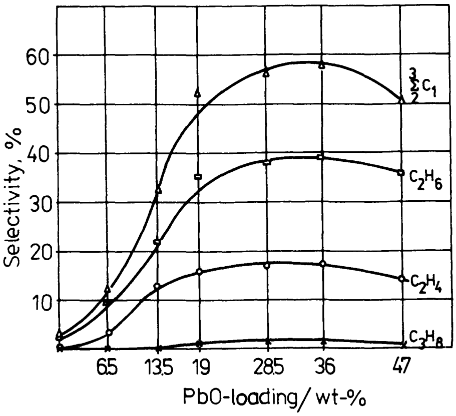

FIGURE 9.5 Effect of PbO loading on selectivity in oxidative coupling of methane at 740°C [28].

oxygen. The activity and the selectivities were strongly affected by the addition of alkali, which hindered the formation of CO.

Kinetic analysis leads to the conclusion that methane reacts by dissociative adsorption to methyl species, which are then converted either to ethane by recombination or to carbon oxides by attack of oxygen. Since the generation of methyl species is the rate determining step, the rates of formation of ethane and carbon oxides are direct functions of methane pressure. As C_2H_4 is formed by catalytic dehydrogenation of C_2H_6, it is necessary to take the sum of both to obtain the measure of the disappearance of methane. A following scheme of the reaction emerges from the kinetic measurements:

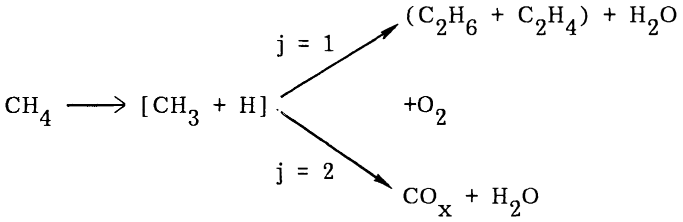

(9.33)

The evaluation of the integral kinetic data was carried out by using the power law rate equation for reaction pathways 1 and 2:

$$r_j = k_j \, p_{CH}{}^{m_{1,j}} \, p_{O_2}{}^{m_{2,j}} \qquad (9.34)$$

Reaction orders $\underline{m}_{1,j}$ and $\underline{m}_{2,j}$ were found to depend on temperature, which was taken as an indication that the kinetically significant elementary steps change with temperature.

Comparison of the behavior of PbO with that of $PbMoO_4$, which has much more mobile lattice oxygen, showed that the latter gives much poorer selectivity to C_2^+ but forms a significant amount of formaldehyde, which at high temperatures is an intermediate product on the route to carbon oxides. This confirms the conclusion that the reaction of methyl radicals with surface lattice oxygen to form methoxy species [Eq. (9.26)] competing with their recombination to ethane is responsible for the decrease of selectivity. It is conceivable that due to the low ionization potential of Pb^{2+} ions O_2^- species may be formed as the result of adsorption of oxygen and abstract hydrogen from methane, generating $CH_3\cdot$ radicals. Depending on the character of oxide ions in the lattice either recombination of methyl radicals or their reaction with surface oxide ions is favored determining the selectivity of the reaction. It is noteworthy that lead oxy salts of anions with a high degree of covalency, such as phosphate and sulfate, show high selectivity to C_2^+ products similar to PbO, whereas this selectivity is very low in the case of $PbMoO_4$, $PbWO_4$, and $PbCrO_4$. Very high selectivity to C_2^+ products was also observed in alkaline earth oxide catalysts, the selectivity being higher the more basic the material. BaO or SrO albeit highly selective were rapidly deactivated because of their facile transformation into molten hydrated hydroxides under the influence of water formed as a reaction product, and CaO showed lower selectivity. It could have been promoted by the addition of alkali metal compounds. Indeed, selectivities as high as 80% were observed on catalysts composed of CaO impregnated with sodium carbonate or sodium sulfate.

In order to elucidate the role of different oxygen species the transient response was followed after the cut of oxygen feed when the steady-state mixed gas of methane, oxygen, and nitrogen was passed over the PbO-MgO catalyst [30,31]. The results are shown in Fig. 9.6. Conversion of methane to CO_2 and ethylene decreased dramatically whereas the formation of ethane decreased only slowly, so that selectivity of C2 hydrocarbons was considerably improved.

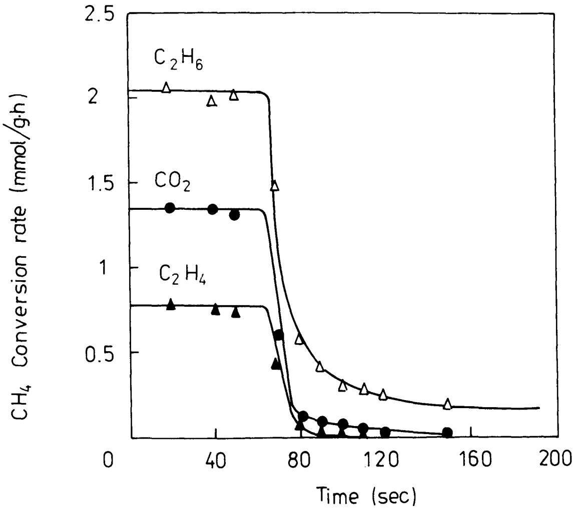

FIGURE 9.6 Effect of stopping O_2 feed on the conversion of methane at the steady-state on PbO-MgO catalyst at 750°C [31].

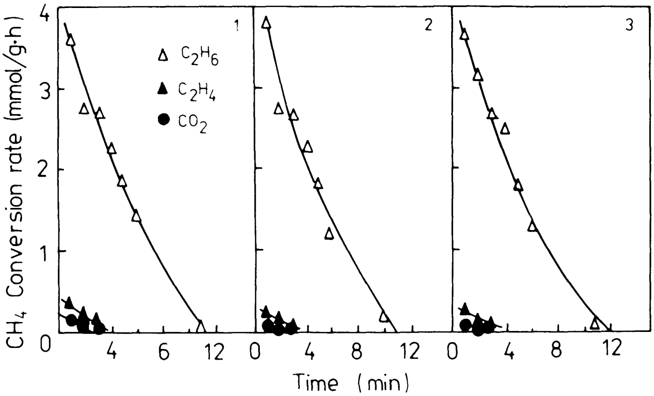

FIGURE 9.7 Transient-response of CH_4 conversion on PbO/MgO catalyst at 750° in three consecutive reduction-oxidation cycles [31].

It could be concluded that bulk oxygen of the catalyst was the species active in the formation of C2 hydrocarbons. This conclusion was confirmed by carrying periodic oxidation-reduction cycles. Figure 9.7 shows the transient response when nitrogen, air, and methane were passed consecutively over the catalyst. The oxidation-reduction cycles were repeated three times and the results were practically the same. Over all periods of the reaction ethane was the predominant product. XRD analysis of the catalyst in different moments of the periodic reaction showed that after the oxidation period the catalyst contained PbO, whereas after CH_4 conversion metallic Pb appeared in considerable amounts. This indicates that PbO is reduced to Pb by reacting with methane and is reoxidized by O_2, the oxidative coupling of methane being carried out by the redox cycle between Pb(0) and Pb(II). The fact that the presence of oxygen in the gas phase promoted the complete oxidation of CH_4 and that this product was observed only in the early stage of the periodic reaction suggested that adsorbed oxygen is the active species of the total oxidation. In the case of PbO/Al_2O_3 catalysts with high surface area mainly total oxidation of CH_4 was observed. This is consistent with the observation that the selectivity to carbon oxides in the mixed-gas reaction is higher the higher the oxygen partial pressure and the lower the temperature because adsorption of oxygen is then favored. The following reaction mechanism can thus be suggested:

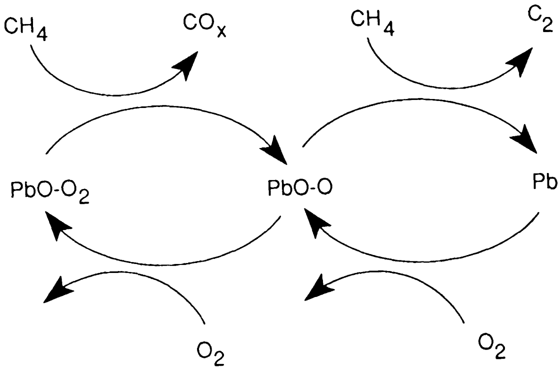

Ethane was assumed to be the primary product, which is then dehydrogenated to ethylene. The reaction network is thus expressed by a set of equations:

$$2CH_4 + PbO \xrightarrow{k_3} 2CH_3\cdot(ads) + Pb + H_2O \tag{9.36}$$

$$2CH_3(ads) \xrightarrow{k_4} C_2H_6 \tag{9.37}$$

$$Pb + \frac{1}{2}O_2 \xrightarrow{k_5} PbO \tag{9.38}$$

$$PbO + \frac{x}{2}O_2 \xrightarrow{k_6} PbO\text{-}O_2(ads) \tag{9.39}$$

$$PbO\text{-}O_2(ads) + CH_4 \xrightarrow{k_7} PbO + CO_x + H_2O \tag{9.40}$$

Assuming that generation of methyl radicals is the rate determining step the rate of ethane formation may be expressed by the equation:

$$r_C = \frac{k_3k_5f_3(p_{CH_4})f_5(p_{O_2})}{k_3f_3(p_{CH_4}) + k_5f_5(p_{O_2})} \tag{9.41}$$

$$r_{CO} = \frac{k_6k_7f_6(p_{O_2})f_7(p_{CH_4})}{k_6f_6(p_{O_2}) + k_7f_7(p_{CH_4})} \tag{9.42}$$

If the rate of oxidation (k_5f_5) is much larger than that of reduction (k_3f_3), apparent orders of r_C in respect to oxygen and methane vary between 0 and 1, and those of r_{CO} — 1 and 1, respectively, in agreement with the experimental data.

An alternative route of oxidative methane coupling was also proposed [32] consisting of the decomposition of methane into carbene followed by its reaction with the second molecule of methane to give ethane. The existence of such a route was substantiated by experiments in which ethylene was added to the mixture of methane and oxygen passing over Li-MgO catalysts and the presence of cyclopropane was detected in the products. Carbene species are known to react easily with olefins to form a cyclopropanic ring. The proposed mechanism involves as the first step of methane activation the abstraction of a proton on a strongly basic surface oxygen ion of the lattice in agreement with the observed activity of basic catalysts:

$$CH_4 + O^{2-} = CH_3^- + OH^- \qquad (9.43)$$

followed by the hydride transfer with formation of carbene species, in good keeping with the promoting role of lithium:

$$Li^+ + CH_3^- = Li^+H^- + CH_2 \qquad (9.44)$$

The carbene is then inserted into the C—H bond of methane:

$$CH_2 + CH_4 = CH_3{-}CH_3 \qquad (9.45)$$

Carbene species may appear in two electronic states, either as a triplet (diradical-like structure) or as a singlet. In the triplet state carbene could abstract hydrogen from methane to form free radicals:

$$CH_2 + CH_4 = 2CH_3\cdot \qquad (9.46)$$

This could be the source of the free radicals in the gas phase observed by ESR spectroscopy. Obviously, the question remains open as to the importance of these two reaction pathways.

The formation of C2 hydrocarbons was found [33] to be considerably promoted by combining the coupling of methane with the reverse shift reaction of CO_2 to CO over modified PbO-based catalysts:

$$2CH_4 \longrightarrow C_2H_6 + H_2 \qquad (9.47)$$

$$CO_2 + H_2 \longrightarrow CO + H_2O \qquad (9.48)$$

$$2CH_4 + CO_2 \longrightarrow C_2H_6 + CO + H_2O \quad \underline{G} = -27\ \mathrm{kJmol^{-1}} \qquad (9.49)$$

In such a combined process the decrease of Gibbs free energy in the second reaction compensates its increase in the first reaction, making the overall process thermodynamically possible. CO_2 is used here as an oxygen source which permits the elimination of the unwanted parallel total oxidation competing with coupling in the presence of gas phase oxygen.

REFERENCES

1. W. Keim (ed.), Catalysis in C_1 Chemistry, Reidel, Dordrecht, 1983.
2. R. Pitchai and K. Klier, Catal. Rev., Sci. Eng., 28, 13 (1986).
3. J. S. Lee and S. T. Oyama, Catal. Rev., Sci. Eng. 30, 249 (1988).
4. J. P. van Hook, Catal. Rev., Sci. Eng., 20. (1980).
5. D. W. E. Axford and R. G. W. Narrish, Proc. Roy. Soc., A192, 518 (1948).
6. J. E. Walker, Formaldehyde, 3rd ed., Reinhold, New York; 1964.
7. D. A. Dowden and G. T. Walker, UK Patent 1,244,001 (August 25, 1971).
8. H. J. F. Stroud, UK Patent 1,398,385 (June 18, 1975).
9. J. M. Thomas, W. Veda, J. Williams, K. D. M. Harris, Faraday Discuss. Chem. Soc., 87, 33 (1989).
10. R. S. Lin, M. Iwamoto, and J. H. Lunsford, J. Chem. Soc. Chem. Commun., 78 (1982).
11. H. F. Lin, R. S. Lin, K. Y. Liew, R. E. Johnson, and J. H. Lunsford, J. Am. Chem. Soc., 106, 4117 (1984).
12. M. Che, K. Dyrek, and L. Louis, J. Phys. Chem., 89, 4526, 4531 (1985).
13. M. M. Khan and G. A. Samorjai, J. Catal., 91, 263 (1985).
14. K. J. Zhen, M. M. Khanm, C. H. Mak, K. B. Lewis, and G. A. Samorjai, J. Catal., 94, 501 (1985).
15. K. Tanaka and A. Ozaki, J. Catal., 8, 1 (1967).
16. K. Otsuka and M. Hatano, J. Catal., 108, 252 (1987).
17. D. J. Driscoll, W. Martir, Ji-Xiang Wang, and J. H. Lunsford, in Adsorption and Catalysis On Oxide Surfaces (M. Chen and G. C. Bond, eds.), Elsevier, New York, 1985, p. 403.
18. D. J. Driscoll, W. Martir, Ji-Xiang Wang, and J. H. Lunsford, J. Am. Chem. Soc., 107, 58 (1985).
19. D. J. Driscoll and J. H. Lunsford, J. Phys. Chem., 87, 301 (1983).

20. T. Ito, Ji-Xiang Wang, C. H. Lin, and J. H. Lunsford, J. Am. Chem. Soc., 107, 5062 (1985).
21. Ji-Xiang Wang and J. H. Lunsford, J. Phys. Chem., 90, 5883 (1986).
22. C. H. Lin, T. Ito, Ji-Xiang Wang, and J. H. Lunsford, J. Am. Chem. Soc., 109, 4808 (1987).
23. D. N. Olson, V. M. Orera, Y. Chen, and M. M. Abraham, Phys. Rev., B21, 1258 (1980).
24. C. H. Lin, K. O. Campbell, Ji-Xiang Wang, and J. H. Lunsford, J. Phys. Chem., 90, 534 (1986).
25. K. Otsuka, K. Jinno, and A. Morikawa, Chem. Lett., 499 (1985).
26. Ji-Xiang Wang and J. H. Lunsford, J. Phys. Chem., 90, 3830 (1986).
27. M. Baerns, Catalysis Today, 1, 357 (1987).
28. W. Bytyn, W. Hinsen, and M. Baerns, Proc. 8th Int. Cong. Catalysis, Vol. 3, Berlin, 1984, Verlag Chemie, Dechema, 1984, p. 581.
29. J. A. S. P. Carreiro, G. Follmer, L. Lehmann, and M. Baerns, Proc. 9th Int. Cong. Catalysis, Vol. 2, Calgary, 1988, (M. J. Phillips and M. Ternan, eds.), The Chemical Institute of Canada, p. 891.
30. K. Asami, S. Hashimoto, T. Shimada, K. Fujimoti, H. Tominaga, Ind. Eng. Chem. Res., 26, 1485 (1987).
31. K. Asami, T. Shikada, K. Fujmoto, H. T. Tominaga, Ind. Eng. Chem. Res., 26, 2348 (1987).
32. C. Mirodatos, G. A. Martin, Proc. 9th Intern. Congress Catalysis, Vol. 2, Calgary, 1988, (M. J. Phillips and M. Ternan, eds.), p. 899.
33. K. Aika, T. Nishiyama, ibid, p. 907.
34 Bi Yinghi, Zhen Kaiji, Jiang Yutao, Teng Chiwen, Yuang Xiangguong, Appl. Catal., 39, 185 (1988).

10

Homogeneous Catalytic Oxidation

I. INTRODUCTION

One of the oldest applications of homogeneous catalysis in the chemical industry is the oxo reaction, catalyzed originally by cobalt carbonyl, which even today remains one of the most important industrial homogeneous catalytic processes [1]. It involves hydroformylation, the reaction of an olefin with carbon monoxide and hydrogen to produce aldehydes, e.g., butyraldehyde from propene or propionaldehyde from ethylene, and fatty alcohols from higher olefins:

$$CH_3CH{=}CH_2 + CO + H_2 \longrightarrow C_3H_7CHO \qquad (10.1)$$

$$RCH{=}CH_2 + CO + H_2 \longrightarrow RCH_2CH_2CH_2OH \qquad (10.2)$$

A major improvement in the catalytic oxo process was made by introducing the production of butyraldehyde from xylene employing homogeneous rhodium catalysts containing a phosphine ligand.

An important breakthrough in the use of metalloorganic catalysis was the introduction of the Wacker process for production of acetaldehyde from ethylene—the first industrial homogeneous oxidation. The oxidation is carried out using either air or oxygen, the oxidizing catalyst being an aqueous solution of cupric chloride and palladium chloride:

$$CH_2{=}CH_2 + H_2O + PdCl_2 \longrightarrow CH_3CHO + Pd + 2HCl \qquad (10.3a)$$

$$Pd + 2CuCl_2 \longrightarrow PdCl_2 + 2CuCl \qquad (10.3b)$$

$$2CuCl + \tfrac{1}{2}O_2 + 2HCl \longrightarrow 2CuCl_2 + H_2O \qquad (10.3c)$$

$$CH_2{=}CH_2 + \tfrac{1}{2}O_2 \xrightarrow{Pd(II),Cu(II)} CH_3CHO \qquad (10.3)$$

The Wacker process is now the main route for the production of acetaldehyde and has largely displaced the old methods based on ethanol or acetylene. The same type of homogeneous catalyst is used to produce vinyl acetate from ethylene and acetic acid:

$$CH_2{=}CH_2 + CH_3COOH + \tfrac{1}{2}O_2 \xrightarrow{Pd(II)} CH_2{=}CHOCOCH_3 \qquad (10.4)$$

The largest commercialized homogeneous catalytic oxidation is the production of terephthalic acid, which is obtained by oxidizing p-xylene with air using soluble cobalt or manganese salts as catalysts. This and some other applications of homogeneous oxidation catalysis in the chemical industry are summarized in Table 10.1 [2]. It should be emphasized that homogeneous catalytic processes are particularly advantageous in the field of fine chemicals, where such factors as the loss of catalyst, choice of raw materials, recuperation of energy, etc., are much less important than in the case of the production of large volume petrochemicals. The most important requirements in transformations of complex organic molecules are high selectivity and high specificity; these two features are well fulfilled by homogeneous organometallic catalysts. In recent years more and more attention has been paid to stereo-specific transformations, for which homogeneous catalysis is particularly well suited. For a more complete review of oxidations catalyzed by transition metal complexes the reader is referred to specialized articles and books [3-6].

II. CATALYTIC OXIDATION AND OXYGEN TRANSFER REACTIONS

Hydrocarbon molecules in liquid phase may become activated by abstraction of hydrogen resulting in the formation of free radicals which then participate in chain reaction. For the last 20 years the studies of liquid phase slow chain reactions were the subject of continuous interest because of their technological importance [7]. Generation

TABLE 10.1 Major Applications of Homogeneous Oxidation Catalysis in Industry

$$CH_2{=}CH_2 + O_2 \longrightarrow CH_3CHO$$

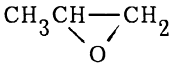

$$CH_3CH{=}CH_2 + ROOH \longrightarrow CH_3\underset{\diagdown O \diagup}{CH{-}CH_2} + ROH$$

$$c\text{-}C_6H_{12} \xrightarrow{O_2} c\text{-}C_6H_{11}OH + c\text{-}C_6H_{10}{=}O \xrightarrow{O_2 \text{ or } HNO_3} \text{adipic acid}$$

$$c\text{-}C_{12}H_{24} \xrightarrow{O_2} c\text{-}C_{12}H_{23}OH + c\text{-}C_{12}H_{22}{=}O \xrightarrow{HNO_3} \text{dodecanedioic acid}$$

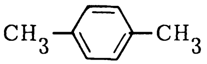

$+ O_2 \longrightarrow$ terephthalic acid and esters

$$n\text{-}C_4H_{10} + O_2 \longrightarrow CH_3COOH$$

$$CH_3CHO + O_2 \longrightarrow CH_3COOH$$

Source: Ref. 1.

of radicals may be accelerated by the presence of transition metal cations due to the reaction:

$$RCH_3 + M^{\underline{n}+} \longrightarrow [RCH_3]^+ + M^{(\underline{n}-1)+} \tag{10.5}$$

$$[RCH_3]^+ \longrightarrow RCH_2\cdot + H^+ \tag{10.6}$$

The free radical interacts with dioxygen dissolved from the gas phase to form peroxy radicals:

$$RCH_2\cdot + O_2 \longrightarrow RCH_2O_2\cdot \tag{10.7}$$

which enter into a chain reaction producing peracids, acids, aldehydes and carbon oxides:

$$RCH_2O_2\cdot + RCH_3 \longrightarrow RCH_2O_2H + RCH_2\cdot \tag{10.8}$$

These processes are called the autooxidation of hydrocarbons and are responsible for the degradation of many organic materials such as plastics, rubber, fibers, lubricating oils and fats, etc. The facility of electron transfer from the hydrocarbon molecule to the metal to produce the cation radical is related to the ionization potential of the organic substrate and the oxidizing power of the metal cation. As the low values of ionization potential are characteristic for alkylbenzenes, the liquid phase oxidation of p-xylene to terephthalic acid in acetic acid with dioxygen mediated by a cobalt catalyst was the first commercialized homogeneous catalytic oxidation:

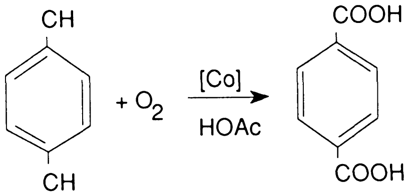

(10.9)

Some organometallic complexes also have the ability to activate dioxygen and make it react with the organic substrate. Dioxygen in the ground state is a triplet and therefore its reactions with the organic compounds, which are singlets, are restricted by spin conservation rule. This may be overcome by forming an adduct of dioxygen with a metal complex [8]. If the adduct is formed reversibly, it may serve for transporting oxygen. Synthetic oxygen carriers are interesting because of their relation to natural oxygen carriers such as hemaglobin and myoglobin.

As described in Chapter 1, the interaction of dioxygen with metal complexes can lead to successive transfers of electrons from the metal orbitals, giving superoxo and peroxo complexes:

$$\mathrm{M} \xrightarrow{+\mathrm{O}_2} \mathrm{MO}_2 \xrightarrow{+\mathrm{M}} \mathrm{MO}_2\mathrm{M} \longrightarrow 2\mathrm{MO} \xrightarrow{+\mathrm{M}} \mathrm{MOM}$$

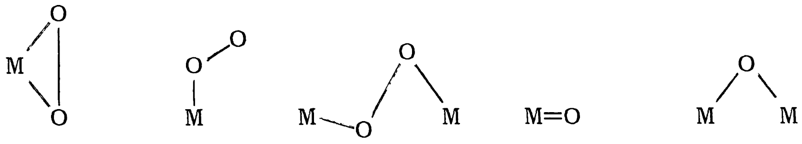

Peroxo Superoxo μ-peroxo Oxo μ-oxo

Table 10.2 [9] summarizes the metals which form different types of oxygen complexes and the main characteristics of these complexes. They may perform the addition of the oxygen atom to the organic

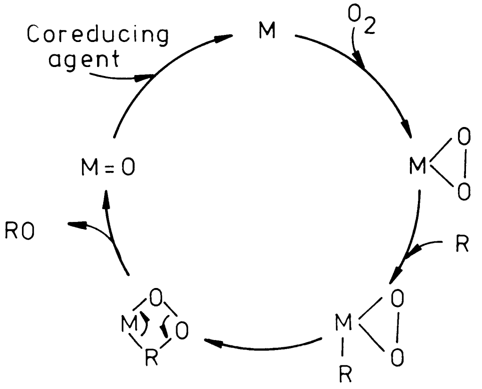

FIGURE 10.1 Mechanism of homogeneous catalytic oxidation in the presence of coordination compound as catalyst.

molecule which is being oxidized. Figure 10.1 illustrates the general mechanism of the oxidation processes involving metal peroxo complexes. In the first step dioxygen and substrate become coordinated at the same metal on two adjacent sites. The substrate is then inserted into a metal-oxygen bond forming a peroxo metallocycle. The latter decomposes evolving the oxygenated substrate and oxo metal complex, which must be reduced to the initial metal state to close the catalytic cycle. Thus, for regenerating the reduced metal from the oxo metal complex a co-reducing agent is required. This co-reducing agent can be a hydrogen donor, water being produced in the course of the reaction, or the substrate itself which would be oxidized.

The sequence of reactions shown in Fig. 10.1 and representing the process of homogeneous oxidation of an organic substrate S by gas phase oxygen to form a product P in the presence of an organometallic catalyst may be described by a following set of equations:

$$\text{Cat} + O_2 \longrightarrow \text{Cat}.O_2 \qquad (10.10)$$

$$\text{Cat}.O_2 + S \rightleftarrows \text{Cat}.O_2.S \qquad (10.11)$$

$$\text{Cat}.O_2.S \longrightarrow \text{Cat}.O + P \qquad (10.12)$$

$$\text{Cat}.O + \text{Red} \longrightarrow \text{Cat} + H_2O \qquad (10.13)$$

TABLE 10.2 Transition Metal Dioxygen Complexes

Complex	Metal	Ligand	X	Structure	ν(O–O)	d(O–O) (Å)
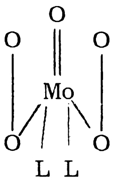	Cr	Py, DMF	–	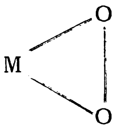		1.4
	Mo	HMPT			870	1.5
	W	PPh_3O				
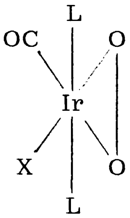	Ir	PPh_3	Cl	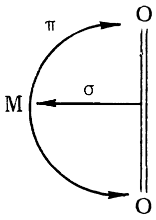	858	1.3
		PPh_3	Br		862	1.36
		PPh_3	I		862	1.5
		PPh_2Et	Cl			1.46
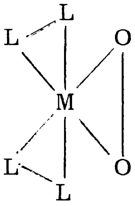	Rh	$Ph_2CH_2CH_2PPh_2$		$O_2 \longrightarrow M$	–	1.41
	Ir			σ-bonding	845	1.48
	Co	$Ph_2PCH{=}CHPPh_2$		$M \longrightarrow O_2$	909	1.42
				π-bonding		

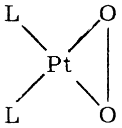	Pt	PPh_3	Peroxo (σ + π)	830	1.46
$Co(CN)_5O_2^{3-}$	Co	CN	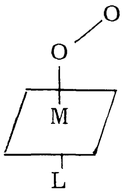 superoxo (σ + π)		1.24
$CoLPyO_2$	Co				
CoL(Bz Imid)O_2	Co	t B salten		–	1.27
FeL(N Me Imid)O_2	Fe	α_4tPiVPP		1385	1.23
(CoL DMF)$_2$	Co	Salen	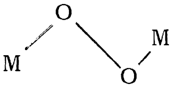 μ peroxo (σ + π)		1.35
$(L_5Co)O_2$	Co	NH_3			1.65

Source: Ref. 9.
Abbreviations:
Bz acen: $(C_6H_5C(O^-)=CHC(CH_3)=NCH_2-)_2$
Salen: NN'bisethylene (salicylidene iminato)
a_4tPivPP: mesotetra (ααααo-pivalamidophenylporphyrin)
tB salten: NN'(1,1,2,2 tetramethyl)bisethylene(3 tert butyl salicylideniminato)

The mass balance equations have the form:

$$[\text{Cat}]_0 = [\text{Cat}] + [\text{Cat.O}_2] + [\text{Cat.O}_2\text{.S}] + [\text{Cat.O}] \tag{10.14}$$

and

$$[\text{S}]_0 = [\text{S}] + [\text{Cat.O}_2\text{.S}] + [\text{P}] \tag{10.15}$$

The rate of change of the concentration of intermediate complex $[\text{Cat.O}_2\text{.S}]$ may be expressed by:

$$\underline{v}_{\text{Cat.O}_2\text{.S}} = \underline{k}_1[\text{Cat.O}_2][\text{S}] - \underline{k}_{-1}[\text{Cat.O}_2\text{.S}] - \underline{k}_2[\text{Cat.O}_2\text{.S}] \tag{10.16}$$

The rate of appearance of the product P is:

$$\underline{v} = \underline{k}_2[\text{Cat.O}_2\text{.S}] \tag{10.17}$$

Under steady-state conditions $\underline{v}_{\text{Cat.O}_2\text{.S}} = 0$ and, assuming that decomposition of the intermediate complex (10.12) is rate determining and that (10.10) and (10.13) are very rapid, it follows from Eqs. (10.16) and (10.14) that

$$[\text{Cat.O}_2\text{.S}] = \frac{\underline{k}_1[\text{Cat}]_0[\text{S}]}{\underline{k}_1[\text{S}] + (\underline{k}_{-1} + \underline{k}_2)} \tag{10.18}$$

Substituting (10.18) into (10.17) we finally obtain the rate of formation of the product:

$$\underline{v} = \frac{\underline{k}_2[\text{Cat}]_0[\text{S}]}{(\underline{k}_{-1} + \underline{k}_2)/\underline{k}_1 + [\text{S}]} = \frac{\underline{k}_2[\text{Cat}]_0[\text{S}]}{\underline{K}_M + [\text{S}]} \tag{10.19}$$

where $\underline{K}_M = (\underline{k}_{-1} + \underline{k}_2)/\underline{k}_1$ is the Michaelis constant, and Eq. (10.19), which expresses the rate of reaction, is called the Michaelis-Menten equation and is used to describe the rate of enzymatic and homogeneous catalytic reactions. It was demonstrated by Schwab [15] that this equation is equivalent to the Hinshelwood-Langmuir equation used in heterogeneous catalysis.

TABLE 10.3 Single Oxygen Atom Donors

Donor	Molecular weight	Byproduct
H_2O_2	34	H_2O
t-BuO_2H	90	t-BuOH
Me_3NO	75	Me_3N
NaClO	74	NaCl
$NaClO_2$	90 (45)	NaCl
$NaClO_3$	106 (35)	NaCl
NaBrO	119	NaBr
$NaBrO_2$	135 (68)	NaBr
$NaBrO_3$	151 (50)	NaBr
$KHSO_5$	152	$KHSO_4$
$K_2S_2O_8$	275 (135)	K_2SO_4
NaH_2BO_4	100	$Na_2B_4O_7$
$NaIO_3$	198	NaI
$NaIO_4$	214	NaI
PhIO	220	PhI

Note: Figures in parentheses are molecular weights per active oxygen.

Instead of using the coreducing agent in situ in the reaction mixture, dioxygen may be reduced in a separate operation to form molecules such as H_2O_2, t-BuO_2H, NaOCl, etc., which can then be coordinated to the catalyst to perform the function of single oxygen donors. They are economically attractive and usually more acceptable environmentally. Oxidation reactions involving single oxygen donors may be classified as catalytic oxygen transfer processes:

$$S + X{-}O{-}Y \xrightarrow{\text{catalyst}} SO + XY \qquad (10.20)$$

where S = substrate, SO = oxidized substrate, X-O-Y = R-O-OH, Na-O-Cl, $R_3N{=}O$, etc.

The various commonly used oxygen donors are listed in Table 10.3 [6]. From the industrial point of view, the most important properties of single oxygen donors are the type of byproduct which should be easily disposable or recyclable and the molecular weight per active oxygen. The latter should be as small as possible because the weight of byproducts contributes to the costs of the production. Thus, commercially most attractive single oxygen donors are hydrogen peroxide, sodium hypochlorite and tert-butyl hydroperoxide.

III. MECHANISM OF OXYGEN TRANSFER

There are two pathways by which the oxygen transfer reactions may proceed [6]. They may be illustrated by a following scheme representing the oxygen transfer from an alkyl hydroperoxide as single oxygen donor:

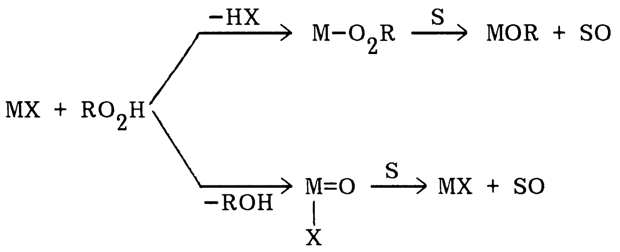

(10.21)

These two pathways are referred to as the oxo-metal and the peroxo-metal pathway, respectively. In the case of oxo-metal pathway the active oxidant is the same irrespectively of which oxygen donor is used whereas when the reaction proceeds through the pathway involving the metal-oxidant complex a different active oxidant is involved with each oxygen donor.

Oxygen transfer reactions may be used in many different types of organic processes to obtain a variety of products. Some of these processes are summarized in Table 10.4. Since the epoxidation of olefins is by far the most important industrial application of homogeneous oxidation, and paraffin functionalization the most prospective, these two types of reactions will be discussed in detail.

TABLE 10.4 Homogeneous Catalytic Oxidations

Reaction	Catalyst	Oxygen donor	Product
Allylic oxidation	SeO_2	$t\text{-}BuO_2H$	Alcohol, aldehyde
Vicinal hydroxylation	OsO_4	H_2O_2 $t\text{-}BuO_2H$, R_3NO, $KClO_3$	Glycol
Epoxidation	Mo^{VI}, W^{VI} $(P)Cr^{III}$	RO_2H, H_2O_2 PhlO	Epoxide
Oxidative cleavage	$RuCl_3$, RuO_4	$NaClO_3$	Aldehyde, ketone Acid
$R_3N \rightarrow R_3NO$	Mo^{VI}, V^{V}	$t\text{-}BuO_2H$	Amine oxide
Oxidation of alcohols	$Mo^{VI}{=}O$	H_2O_2	Aldehyde, ketone

IV. HOMOLYTIC AND HETEROLYTIC CATALYSIS

One of the most important classes of single-oxygen donors widely used in organic synthesis is hydrogen peroxide and the hydroperoxides [10]. Their reactions catalyzed by metal ions can be divided into two groups, proceeding by different mechanisms. The first group involves homolytic, one-electron processes in which free radicals appear as intermediates. The second group involves heterolytic, two-electron processes, the metal catalyst operating by increasing the electrophilic properties of the peroxide.

The metal-catalyzed homolytic decomposition of alkyl hydroperoxides formed as the result of reactions (10.5) to (10.8) is the most common further transformation taking place in the autooxidation of hydrocarbons. Two principal reactions of alkyl hydroperoxides with metal complexes may be considered, depending on the redox potential of the metal. When the latter has strong reducing properties, reduction takes place:

$$RO_2H + M^{(\underline{n}-1)+} \longrightarrow RO\cdot + M^{\underline{n}+} + HO^- \qquad (10.22)$$

whereas with metals with oxidizing power oxidation occurs:

$$RO_2H + M^{\underline{n}+} \longrightarrow RO_2\cdot + M^{(\underline{n}-1)+} + H^+ \qquad (10.23)$$

They are followed by further steps of the radical process of hydroperoxide decomposition:

$$2RO_2\cdot \longrightarrow 2RO\cdot + O_2 \qquad (10.24)$$

$$RO\cdot + RO_2H \longrightarrow RO_2\cdot + ROH \qquad (10.25)$$

As alkyl hydroperoxides are stronger oxidants than reducing agents, reaction (10.22) usually prevails. In the case of complexes of such metals as cobalt and manganese, which have two oxidation states of comparable stability, both reactions (10.22) and (10.23) proceed, which is equivalent to the catalytic decomposition of alkyl hydroperoxide into alkoxy and alkylperoxy radicals:

$$2RO_2H \xrightarrow{Co(II)/Co(III)} RO_2\cdot + RO\cdot + H_2O \qquad (10.26)$$

These reactions are generally characterized by low selectivity and therefore are limited in their applicability. However, considerable efforts are devoted to finding means by which hydroperoxides could be stabilized for periods long enough to undergo selective reaction to more stable oxidation products.

There is, however, a second possible reaction pathway, in which the hydroperoxide becomes coordinated to the metal complex in such a way that its terminal peroxy oxygen is rendered more electrophilic and, hence, more susceptible to reactions with π-electron systems of olefins. Oxygen transfer in a two-electron reaction of heterolytic cleavage of the O–O bond follows:

$$S + RO_2H \longrightarrow SO + ROH \qquad (10.27)$$

Such reactions being usually much more selective. Complexes of transition metal ions of group VA and VIA in high oxidation state are particularly efficient in these reactions.

V. EPOXIDATION OF OLEFINS

Interaction of peroxidic species with metal complexes of groups IVA–VIA transition metals results in the formation of peroxo complexes. Acidic oxides such as WO_3, MoO_3, CrO_3, V_2O_5, and TiO_2 catalyze the reactions of hydrogen peroxide through the formation of peracids [11]. They resemble the organic peracids in that they react readily with nucleophiles with scission of the O–O bond. Therefore, similar mechanisms operate in the epoxidation of olefins by both organic and inorganic peracids:

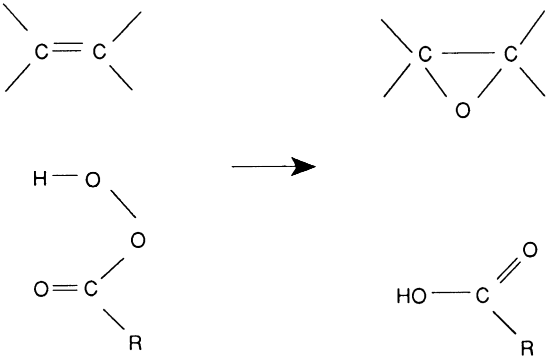

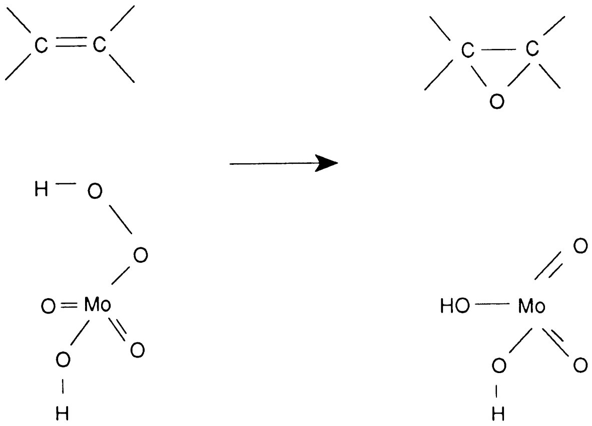

However, when hydrogen peroxide is used, it reacts easily with the epoxide, the perhydrolysis being also catalyzed by molybdenum complexes and glycol appears as the final product:

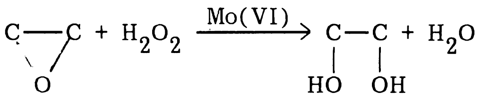

$$\underset{O}{C{-}C} + H_2O_2 \xrightarrow{Mo(VI)} \underset{HO}{C}{-}\underset{OH}{C} + H_2O \qquad (10.28)$$

Therefore, alkyl hydroperoxide ROOH is used to form the peroxo complexes of molybdenum and to obtain high selectivity to epoxide.

On the basis of kinetic evidence, structure-reactivity relationships, induction periods and inhibition by alcohol as the byproduct [12,13] a schematic mechanism for the molybdenum catalyzed epoxidation of olefins has been proposed:

$$\mathrm{Mo^{VI} + ROOH \longrightarrow Mo^{VI}(ROOH)} \qquad (10.29a)$$

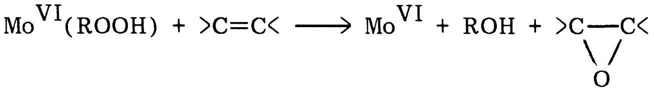

$$\mathrm{Mo^{VI}(ROOH) + {>}C{=}C{<} \longrightarrow Mo^{VI} + ROH + {>}\underset{\diagdown O \diagup}{C{-}C}{<}} \qquad (10.29b)$$

$$\mathrm{Mo^{VI} + ROH \longrightarrow Mo^{VI}(ROH)} \qquad (10.29c)$$

Equation (a) represents the initial formation of catalytically active species by interaction of the hydroperoxide with Mo(VI) complex; Eq. (b) describes the rate-determining step of the transfer of the oxygen atom to the olefin molecule. The coordination site at the Mo(VI) complex may be blocked by coordination of the product alcohol [Eq. (c)] which thus inhibits the reaction. The intermediate complex $\mathrm{Mo^{VI}(ROOH)}$ formed in reaction (a) may, however, also undergo a homolytic reaction resulting in the appearance of radicals:

$$\mathrm{Mo^{VI}(ROOH) \longrightarrow Mo^{V} + RO_2\cdot + H^+} \qquad (10.29d)$$

$$\mathrm{Mo^{V} + ROOH \longrightarrow Mo^{VI} + RO\cdot + OH^-} \qquad (10.29e)$$

and a decrease in selectivity of epoxidation which is determined by the relative rates of reactions (b) and (d). Reaction (b) consists of the nucleophilic attack of the olefin on one of the oxygen atoms of the peroxidic group. The principal function of the catalyst, a Lewis acid, is to withdraw electrons from the peroxidic oxygens, rendering them more susceptible to this nucleophilic attack. Reaction (d) becomes more facile as the oxidation power of the metal complex increases. The high activity of Mo(VI) complexes as epoxidation catalysts is due to the fact that MoO_3 shows high Lewis acidity but is at the same time a very weak oxidant. The Lewis acidity of transition metal oxides decreases in the order CrO_3, MoO_3, WO_3, TiO_2, V_2O_5, UO_3. Cr(VI) should also be a good catalyst for reaction (b). However, because Cr(VI) is also a strong oxidant which accelerates reaction (d), it is consequently a poor epoxidation catalyst.

The mechanism of the nucleophilic attack of the olefin molecule on the peroxidic oxygen in reaction (b) may be described by the following scheme:

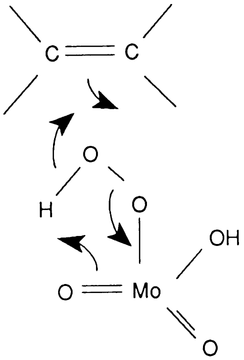

Recently a different mechanism of the epoxidation of olefins by Mo(VI) complexes was suggested [9] on the basis of the very high activity and selectivity of complexes of composition $Mo^{VI}O(O_2)_2L_2$ synthesized by the interaction of organic bases (amides, phosphines, aromatic amines, etc.) with a solution of MoO_3 in hydrogen peroxide. In this mechanism (Fig. 10.2) it is assumed that in the first stage of the reaction the ligand L is displaced by the olefin which then forms a five membered ring with the side bonded dioxygen. Rearrangement of bonds results in the formation of the epoxide leaving the complex with one vacant coordination site which may again accommodate an olefin molecule that reacts then with the second dioxygen. Finally, MoO_3 which results from these reactions interacts with hydrogen peroxide and the organic base to regenerate the initial peroxo complex.

In like manner, other nucleophilic reagents can undergo oxygen transfer reactions with metal hydroperoxide systems. Examples are the oxidations by tert amyl hydroperoxide in the presence of molybdenum catalysts of the following molecules:

nitrogen heterocycles

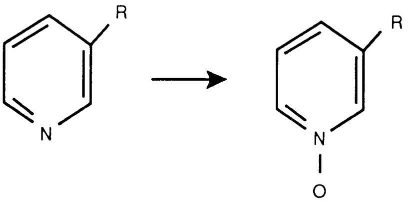

(10.30)

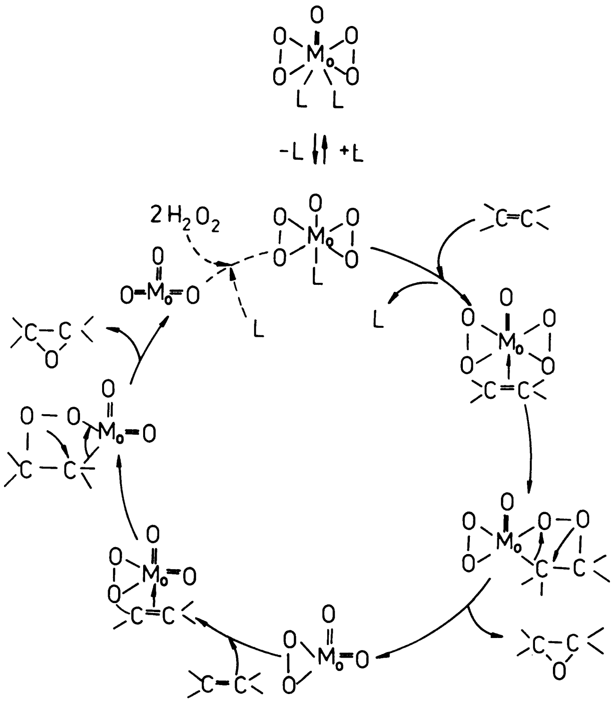

FIGURE 10.2 Mechanisms of the epoxidation of olefins by peroxometal complexes [9].

nitrosamines

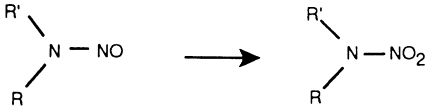

(10.31)

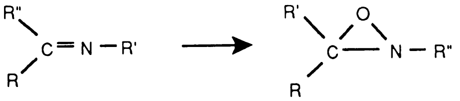

(10.32)

Aniline is oxidized to nitrobenzene

$$ArNH_2 \longrightarrow ArNO_2 \qquad (10.33)$$

and sulphides are oxidized to sulphoxides and sulphones

$$BuS_2 \longrightarrow Bu_2SO \longrightarrow Bu_2SO_2 \qquad (10.34)$$

By properly modifying the coordination sphere of the metal complex steric constraints can be imposed on the reaction permitting regioselective and stereoselective control. Thus, geraniol is regioselectively epoxidized to a monoepoxide with tert $BuO_2H/VO(acac)_2$ system

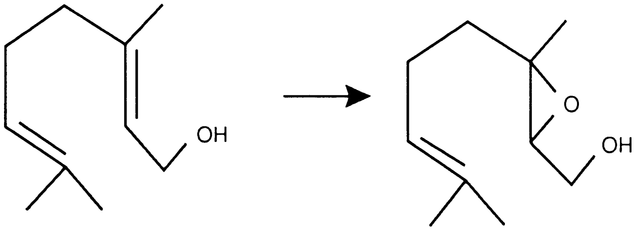

(10.35)

An example of a stereoselective reaction is epoxidation of the homoallylic alcohol to syn-epoxy alcohol, carried out by tert-$BuO_2H/Mo(CO)_6$ system:

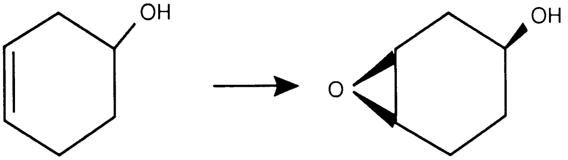

(10.36)

VI. ACTIVATION OF HYDROCARBONS BY COORDINATION

Platinum group metals in low oxidation states show the properties of soft centers activating the coordinated hydrocarbon molecule toward nucleophilic attack resulting in an oxidative nucleophilic substitution of hydrogen with a simultaneous two-electron reduction of the metal catalyst. Pd(II) is particularly efficient in this group of oxidative processes [14].

In water solutions Pd(II) salts act as catalysts of the oxidation of olefins to aldehydes or ketones. Ethylene is oxidized to acetaldehyde in what is known as the Wacker process, Pd(II) being reduced to Pd(0), which is reoxidized by molecular oxygen in the presence of Cu(II) salts. Under similar conditions propene is oxidized to acetone, and 1-butene to methyl ethyl ketone. In all these reactions the yields are very high, attaining 95% in the case of the oxidation of ethylene.

The reaction starts with the formation of a π-complex of the olefin with the metal center:

$$PdCl_4^{2-} + C_2H_4 \rightleftharpoons [PdCl_3C_2H_4]^- + Cl^- \qquad (10.37)$$

The transfer of electrons to metal orbitals reduces the electron density on the olefin molecule rendering it prone to a nucleophilic attack. As the reaction takes place in aqueous solution, chlorine ligands are exchanged for water:

$$[PdCl_3C_2H_4]^- + H_2O \rightleftharpoons [PdCl_2(H_2O)C_2H_4] + Cl^- \qquad (10.38)$$

The next step consists of the π-σ rearrangement of the coordinated olefin. Such rearrangement may involve any of the π-ligands such as olefins, allylic species, aromatics, is a general phenomenon and usually can proceed in both directions resulting in the establishment of an equilibrium between both species:

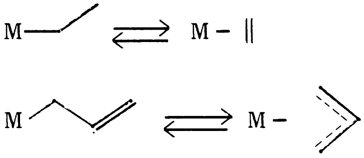

This equilibrium may be shifted by coordination or abstraction of other ligands at the given atom center, or by attack of a nucleophile:

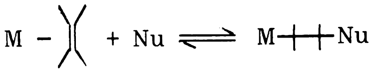

The π-σrearrangement of Pd-ethylene π complex in aqueous solution is facilitated by the attack of water molecules acting as nucleophiles proceeding with the trans-symmetry:

$$[PdCl_2(H_2O)C_2H_4] + H_2O \rightleftharpoons [HOCH_2CH_2PdCl_2(H_2O)]^- + H^+ \qquad (10.39)$$

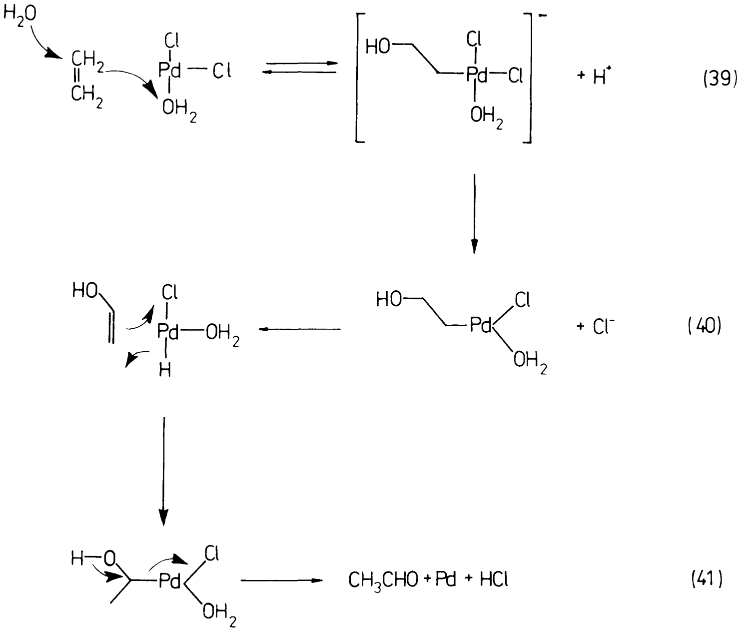

FIGURE 10.3 Mechanism of ethylene oxidation in the presence of Pd(II) complexes.

The mechanism proposed for such rearrangement [16,17] is shown in Fig. 10.3. The reversible hydroxypalladation step (39) representing the π-σ equilibrium is followed by the rate determining loss of chloride ion from the σ complex. The resulting coordinately unsaturated 14 electron intermediate, easily undergoes a rapid β-hydride elimination in step (40):

$$[HOCH_2CH_2PdCl_2(H_2O)]^- \longrightarrow HOCH_2CH_2PdCl(H_2O) + Cl^- \qquad (10.40)$$

$$HOHO_2CH_2PdCl(H_2O) \longrightarrow CH_3CHO + Pd + HCl + H_2O \qquad (10.41)$$

The external attack on the coordinated alkene resulting in trans symmetry may also be performed by nucleophiles such as acetate, alcohols and amines. Nucleophiles such as aryl, alkyl and hydride of only low concentration outside the coordinate sphere of palladium prefer an intramolecular pathway, resulting in cis-addition.

In non-aqueous solvents such as acetic acid it is the acetate ions, which perform the external nucleophilic attack on the coordinated olefin molecule, resulting in the acetoxypalladation:

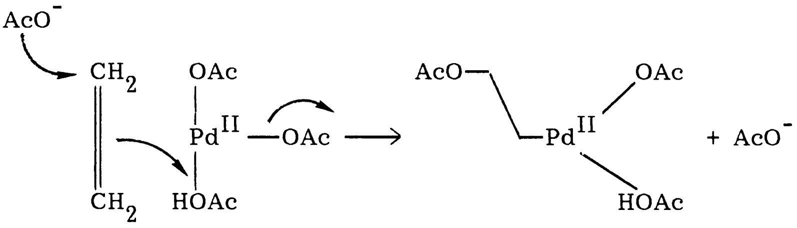

(10.42)

The subsequent β-hydride elimination gives vinyl acetate:

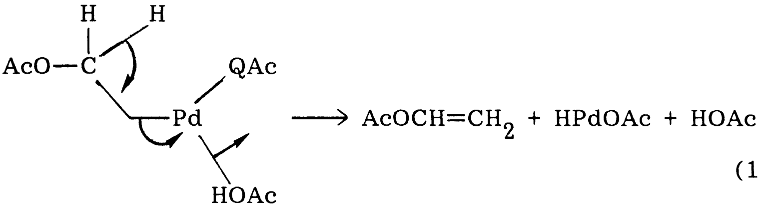

(10.43)

This is an example of a general class of Pd(II) mediated nucleophilic substitutions at an sp^2 carbon center as given by the general equation:

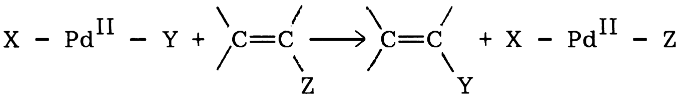

$$X - Pd^{II} - Y + {>}C{=}C{<}_{Z} \longrightarrow {>}C{=}C{<}_{Y} + X - Pd^{II} - Z \tag{10.44}$$

When Z is the hydrogen atom the result is oxidative substitution, which may be carried out with different nucleophiles:

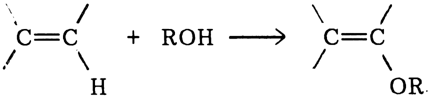

$$ {>}C{=}C{<}_{H} + ROH \longrightarrow {>}C{=}C{<}_{OR} \tag{10.45}$$

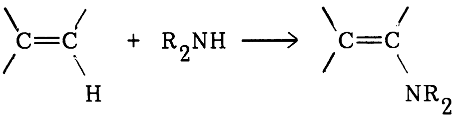

$$ {>}C{=}C{<}_{H} + R_2NH \longrightarrow {>}C{=}C{<}_{NR_2} \tag{10.46}$$

This reaction may be used to carry out arylation of olefins which otherwise is difficult to achieve:

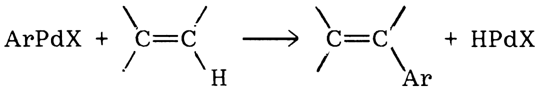

(10.47)

At variance with the external attack of strong nucleophiles this reaction is believed to proceed by an intramolecular nucleophilic addition of the aryl ligand to the coordinated olefin, followed by β-hydride elimination:

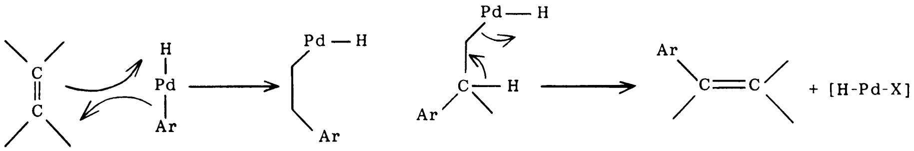

An important reaction catalyzed by Pd(II) complexes is the oxidative carbonylation. It may be used to obtain e.g. acrylic acid:

$$CH_2 = CH_2 + CO + \tfrac{1}{2}O_2 \longrightarrow CH_2CHCOOH \qquad (10.48)$$

Alcohols in the presence of group VIII metals are oxidized to carbonyl compounds. In the first step a metal alkoxide intermediate is formed, which then undergoes the β-hydride elimination to give the carbonyl group:

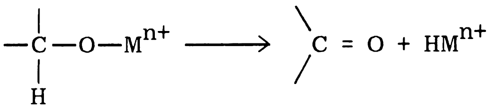

$$-\underset{\displaystyle H}{\overset{|}{\underset{|}{C}}}-O-M^{n+} \longrightarrow {>}C = O + HM^{n+} \qquad (10.49)$$

When copper salts are added the catalytic cycle is closed and the reaction becomes catalytic:

$$RCH_2OH + \tfrac{1}{2}O_2 \xrightarrow{Pd(II),Cu(II)} RCHO + H_2O \qquad (10.50)$$

In the presence of both dioxygen and carbon monoxides alcohols undergo oxidative carbonylation on Pd(II) complexes to form oxalate esters. When Cu(II) is added as cocatalyst the reaction becomes catalytic:

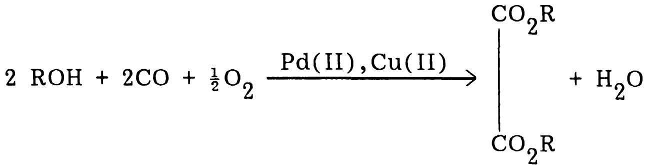

$$2\ ROH + 2CO + \tfrac{1}{2}O_2 \xrightarrow{Pd(II),Cu(II)} \begin{array}{c} CO_2R \\ | \\ CO_2R \end{array} + H_2O \qquad (10.51)$$

Recently considerable attention is devoted to the search of conditions in which the insertion of a low-valent Group VIII metal complex into a C–H bond would take place:

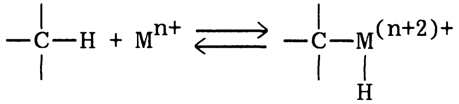

$$-\overset{|}{\underset{|}{C}}-H + M^{n+} \rightleftharpoons -\overset{|}{\underset{|}{C}}-\underset{\underset{H}{|}}{M}^{(n+2)+} \qquad (10.52)$$

by analogy with oxidative addition of molecular hydrogen to such complexes:

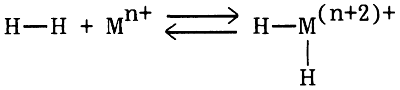

$$H-H + M^{n+} \rightleftharpoons H-\underset{\underset{H}{|}}{M}^{(n+2)+} \qquad (10.53)$$

It should be remembered that activation of C–H and C–C bonds with supported platinum group catalysts is the basis of many important heterogeneous catalytic processes used in petrochemical industry.

REFERENCES

1. H. Heinemann, in *Catalysis: Science and Technology*, Vol. 1 (J. R. Anderson and M. Boudart, eds.), Springer-Verlag, New York, 1981, p. 1.
2. G. W. Parshall, *J. Molec. Catal.*, 4, 243 (1978).
3. R. A. Sheldon and J. K. Kochi, *Adv. Catal.*, 25, 272 (1976).
4. J. E. Lyons, in *Fundamental Research in Homogeneous Catalysis*, (M. Tsutsui and R. Ugo, eds.), Plenum Press, New York, 1977, p. 1.
5. R. A. Sheldon and J. K. Kochi, *Metal-Catalyzed Oxidations of Organic Compounds*, Academic Press, New York, 1981.
6. R. A. Sheldon, *Bull. Soc. Chim. Belg.*, 94, 651 (1985).
7. N. M. Emanuel, *Oxidation Commun.*, 1, 125 (1980).
8. R. D. Jones, D. A. Summerville, and F. Basolo, *Chem. Rev.*, 79, 139 (1979).

9. H. Mimoun, in chemical and Physical Aspects of Catalytic Oxidation, (J. Portefaix and F. Figueras, eds.), CNRS, Paris, 1980, p. 15.
10. R. A. Sheldon, in The Chemistry of Functional Groups: Peroxides (S. Patai, ed.), John Wiley, New York, 1983, p. 161.
11. J. A. Connor and E. A. V. Ebsworth, Adv. Inorg. Chem. Radiochem., 6, 280 (1964).
12. R. Sheldon and J. Van Doorn, J. Catal., 31, 427 (1973).
13. R. Sheldon, J. Van Doorn, C. Schram, and A. DeJong, J. Catal., 31, 438 (1973).
14. P. M. Henry, Palladium Catalyzed Oxidation of Hydrocarbons, D. Reidel Publ. Co., (Boston, 1980).
15. G. M. Schwab, H. Noller, and J. H. Block, in Handbuch der Katalyse (G. M. Schwab, ed.), Springer Verlag (Wien, 1957), p. 160.
16. J. E. Backwell, B. Akermark, and S. O. Ljunggren, J. Am. Chem. Soc., 101, 2411 (1979).
17. J. K. Stille and R. Divakaruni, J. Organometal. Chem., 169, 239 (1979).

Index